Modelling Neuron-Glial Network Interactions at the Whole-Brain Scale for Human Neuroimaging Applications

Obaï Bin Ka'b Ali

A Thesis

In the Department

of

Physics

Presented in Partial Fulfillment of the Requirements

For the Degree of

Doctor of Philosophy (Physics) at

Concordia University

Montreal, Quebec, Canada

February 2024

CONCORDIA UNIVERSITY

SCHOOL OF GRADUATE STUDIES

This is to certify that the thesis prepared

By: Obaï Bin Ka'b Ali

Entitled: Modelling Neuron-Glial Network Interactions at the Whole-Brain Scale for Human Neuroimaging Applications

and submitted in partial fulfillment of the requirements for the degree of

Doctor of Philosophy (Physics)

complies with the regulations of the University and meets the accepted standards with respect to originality and quality.

Signed by the final examining committee:

_____ Chair
Dr. Emily Coffey

_____ External Examiner
Dr. Hugues Berry

_____ Arm's Length Examiner
Dr. Yasser Iturria-Medina

_____ Examiner
Dr. Hassan Rivaz

_____ Examiner
Dr. Alexandre Vidal

_____ Thesis Co-Supervisor
Dr. Christophe Grova

_____ Thesis Co-Supervisor
Dr. Habib Benali

Approved by _____
Dr. Pablo Bianucci, Graduate Program Director

March 27, 2024 _____
Dr. Pascale Sicotte, Dean, Faculty of Arts and Science

Abstract

Modelling Neuron-Glial Network Interactions at the Whole-Brain Scale for Human Neuroimaging Applications

Obaï Bin Ka'b Ali, Ph.D.
Concordia University, 2024

Glial cells, together with their neighboring neurons, constitute an integral functional unit within brain circuitry, rather than isolated elements. Astrocytes, for instance, are strategically situated around neurons and profoundly modulate neuronal circuits. They achieve this by forming gap-junction networks that actively monitor and regulate synaptic and extrasynaptic transmission of glutamate and GABA. Consequently, recent neuroscientific research firmly proposes that our understanding of brain function should incorporate a neuron-glial perspective. This approach necessitates an in-depth comprehension of neuron-glial interactions and emphasizes the critical role of computational modelling, which is essential due to the inherent nonlinearity and multiscale nature of these interactions. Despite this recognition, there is a notable deficiency in computational frameworks that elaborate on the neuron-glial perspective, particularly at the whole-brain level. This thesis addresses this significant gap.

The objective of this thesis is to underscore the significance of neuron-glial network interactions to whole-brain computational processes, particularly at the scale relevant to neuroimaging data. It conceptualizes the brain as a dynamic network-of-networks, wherein glial assemblies and neuronal populations communicate via various channels (mediated by glutamatergic and GABAergic transmission systems) and across diverse spatiotemporal scales, with structural constraints imposed by gap-junctional and axonal densities. The thesis introduces a biophysically plausible dynamical model of neuron-glial network interactions at the whole-brain scale, employing neural mass network and compartmental modelling techniques. It reveals how glial networks contribute to whole-brain activity and the emergence of functional connectivity patterns, using simulations grounded in multilayer network and dynamic system theories. The thesis further presents two neuroimaging applications. The first elucidates the influence of glial networks in the non-invasive electrophysiological reconstruction of resting-state functional networks. This offers a biologically informed computational framework to refine and assess empirical methodologies in whole-brain electrophysiological connectomics. The second generates credible mechanistic hypotheses for large-scale network dysfunctions, resistance, and adaptations in brains afflicted by Alzheimer disease. This aims to inform potential empirical investigations.

This timely thesis represents a critical step towards resolving longstanding neuron-glial questions through computational approaches, setting a foundation for an era where real-world experimentation and computational modeling mutually inform and advance our understanding of the brain.

Acknowledgements

This doctoral thesis was financially supported by:

- a Canada Research Chair (holder – supervisor: *Habib Benali*) from the Natural Sciences and Engineering Research Council of Canada,
- a Research Team Grant (holder – supervisor: *Christophe Grova*) from the Fonds de Recherche du Québec – Nature et Technologies,
- a Discovery Grant (holder – supervisor: *Christophe Grova*) from the Natural Sciences and Engineering Research Council of Canada,
- and a Graduate Fellowship from the Physics Department in the Faculty of Arts and Science of Concordia University.

Contribution of Authors

This thesis was written by me and guided by the expertise of Dr. Habib Benali (director of the Biomedical Imaging for Healthy Aging laboratory) and Dr. Christophe Grova (director of the Multimodal Functional Imaging laboratory). It comprises four original studies, each with contributions outlined as follows.

Neuron-astrocyte mass network model — foundations for whole-brain modelling
by Obaï Bin Ka'b Ali, Alexandre Vidal, Christophe Grova, Habib Benali

- Conceptualization: *all authors*. Biophysical modelling: *OBKA*, *AD*, and *HB*. Methods, analyses, and manuscript drafting: *OBKA*. Manuscript revision: *all authors*. Funding and supervision: *CG* and *HB*. Principal investigators: *OBKA* and *HB*. Final manuscript approval: *all authors*.
- In this study's acknowledgement section, the authors thank Dr. Maxime Descoteaux (Sherbrooke University) and Dr. Etienne St Onge (Université du Québec en Outaouais) for providing *OBKA* with training in diffusion magnetic resonance imaging tractography analyses.

Dialogue mechanisms between astrocytic and neuronal networks — a whole brain modelling approach
by Obaï Bin Ka'b Ali, Alexandre Vidal, Christophe Grova, Habib Benali

- Conceptualization: *all authors*. Biophysical modelling: *OBKA*, *AD*, and *HB*. Methods, analyses, and manuscript drafting: *OBKA*. Manuscript revision: *all authors*. Funding and supervision: *CG* and *HB*. Principal investigators: *OBKA* and *HB*. Final manuscript approval: *all authors*.
- In this study's acknowledgement section, the authors thank Dr. Maxime Descoteaux (Sherbrooke University) and Dr. Etienne St Onge (Université du Québec en Outaouais) for providing *OBKA* with training in diffusion magnetic resonance imaging tractography analyses.

A neuron-glial perspective of MEG connectomics — establishing a biologically plausible computational framework to guide and evaluate empirical methodologies
by Obaï Bin Ka'b Ali, Habib Benali, Christophe Grova

- Conceptualization: *all authors*. Methods, analyses, and manuscript drafting: *OBKA*. Manuscript revision: *all authors*. Funding and supervision: *HB* and *CG*. Final manuscript approval: *all authors*.
- In this study's acknowledgement section, the authors thank Jawata Afnan (McGill University) for allowing *OBKA* to use her wMEM code, and Dr. Ümit Aydin (University of Reading) for providing *OBKA* with training in encephalography real data analyses.

Exploring mechanisms of network dysfunction, resistance, and adaptation in Alzheimer disease — a research proposal for empirical insight
by Obaï Bin Ka'b Ali, Christophe Grova, Habib Benali

- Conceptualization: *all authors*. Methods, analyses, and manuscript drafting: *OBKA*. Manuscript revision: *all authors*. Funding and supervision: *CG* and *HB*. Final manuscript approval: *all authors*.

Table of Contents

List of Figures

List of Tables

Introduction

This doctoral thesis ventures into the uncharted territory of incorporating glial cells into biophysical models of whole-brain activity, aiming to bridge this gap at the spatiotemporal resolution pertinent to human neuroimaging data. The significance of this endeavor is underscored by the current state of neuroscientific research, where the potential contributions of glial cells to brain dynamics are yet to be fully integrated into computational models at the mesoscales and macroscales.

(De Pittà & Berry, 2019), in their seminal review which serves as the introductory chapter to the "*Computational Glioscience*" book, underscore the conspicuous absence of modeling efforts dedicated to elucidating neuron-glial interactions beyond the microscales. Their exhaustive review of the field revealed a specific lack of whole-brain models that consider glial cells, with only a limited number of models addressing neural assembly scales. Notably, the model developed by (Garnier et al., 2016), which constitutes a foundational element of this thesis, stands out as one of the few attempts in this direction.

This gap in glial modeling is further evidenced by the comprehensive review conducted by (Griffiths et al., 2022), which surveys key advancements in whole-brain modeling spanning from the 1940s to 2021. This review traces the evolution of neural models from their origins to contemporary implementations, offering insights into current models and speculating on future trajectories for the field. Remarkably, their discourse omits any reference to "glia", "astrocyte", or "oligodendrocyte", highlighting the fact that these critical cellular components have not yet been systematically incorporated into mainstream whole-brain modeling frameworks.

(Kastanenka et al., 2020) further illuminate the neuron-centric bias pervasive in systems neuroscience. An analysis of recent editions (years: 2015–2017) of three leading international conferences in Systems and Computational Neuroscience (Conference and Workshop on Neural Information Processing Systems: NIPS, Organization for Computational Neurosciences: OCNS, and Computational and Systems Neuroscience: COSYNE) revealed that among approximately 3000 presentations, less than 1% addressed non-neuronal cells. This stark statistic underscores the overwhelming focus on neuronal perspectives. This oversight is also particularly perplexing from the perspective of glial research given the burgeoning evidence of glial cells' vital contributions across the spectrum of brain physiology and pathology, at times rivaling or even superseding neuronal functions.

The disparity in attention to glial cells versus neurons in the broader neuroscientific discourse is highlighted by provocative and insightful titles from leading figures in the field, such as "*Astrocytes, from brain glue to communication elements: the revolution continues*" by (Volterra & Meldolesi, 2005), "*The Other Brain: The Scientific and Medical Breakthroughs That Will Heal Our Brains and Revolutionize Our Health*" by (Fields, 2011), "*Glia as architects of central nervous system formation and function*" by (Allen & Lyons, 2018), "*Astrocytes usurp neurons as a disease focus*" by (Liddelow & Sofroniew, 2019), and "*Glial Man: A Revolution in Neuroscience*" by (Agid & Magistretti, 2020). These works, among others, underscore a paradigm shift in neuroscience, advocating for a more inclusive understanding that recognizes glial cells as central to brain function and not merely as ancillary components.

Despite the significant advancements in neuroscience, critical gaps in our understanding persist, particularly regarding the roles of glial cells in brain functioning. The traditional neuron-centric view of the brain is increasingly challenged by emerging evidence, prompting a reassessment of brain function through a *neuron-glial perspective* (De Pittà & Berry, 2019). This reevaluation is not merely academic but carries profound implications for our understanding of brain physiology, the etiology of neurological disorders, and the development of therapeutic interventions (De Pittà & Berry, 2019).

The adoption of computational modeling approaches, complemented by empirical data, stands as a promising avenue for exploring neuron-glial interactions (De Pittà & Berry, 2019). Biophysical models, by design, distill complex real-world systems into their most salient features, allowing for systematic exploration and hypothesis testing through simulations. These models serve as invaluable tools for generating predictions, guiding experimental inquiries, and synthesizing disparate mechanisms into one coherent framework of brain function (Griffiths et al., 2022).

In this computational context, the exploration of glial roles in brain functioning emerges as a critical contemporary endeavor (De Pittà & Berry, 2019). The integration of glial cells into computational models of brain activity not only enriches our conceptualization of neural dynamics but also aligns with the evolving recognition of glial cells as integral to the brain's *connectome* and pivotal actors for cerebral computation (Fields et al., 2015; Kastanenka et al., 2020). This shift towards a more inclusive neuron-glial mindset represents a frontier in neuroscience, promising to unveil new dimensions of brain function and offering fresh perspectives on longstanding questions in the field (De Pittà & Berry, 2019).

The overarching aim of this doctoral thesis is to illuminate the pivotal role of neuron-glial network interactions within the computational landscape of the whole brain, especially as it pertains to the resolutions accessible through neuroimaging technologies, through a biophysical whole-brain neuron-glial model. The thesis posits the brain as a dynamic *network-of-networks*, where glial assemblies and neuronal populations engage in intricate communication through mechanisms mediated by glutamatergic and GABAergic transmission systems, navigating across various spatiotemporal scales within the structural confines dictated by gap-junctional and axonal densities.

The inaugural chapter (Background, starting on page 4) lays a robust foundation by providing an in-depth background necessary for comprehending the biophysical model at the core of this thesis. This chapter doubles as a literature review, setting the stage for a nuanced discussion that encapsulates the thesis's contributions to the field while acknowledging the broad scope of the topics covered.

The second chapter (Neuron-astrocyte mass network model — foundations for whole-brain modelling, starting on page 92) marks the first of several original contributions within this thesis, detailing the mathematical framework underpinning the whole-brain neuron-glial model. It elucidates the model's foundational hypotheses and introduces a strategy for its parameterization based on biologically plausible criteria, setting a precedent for subsequent chapters.

Building on the foundations laid in the previous chapter, the third chapter (Dialogue mechanisms between astrocytic and neuronal networks — a whole brain modelling approach, starting on page 117) presents the second original contribution, elucidating the significant impact of astrocytic

networks on modulating whole-brain activity and connectivity patterns. The insights garnered here are crucial and form a cornerstone for the remainder of the thesis.

The fourth chapter (A neuron-glial perspective of MEG connectomics — establishing a biologically plausible computational framework to guide and evaluate empirical methodologies, starting on page 169), representing the third original contribution, applies the developed model to a specific neuroimaging application centered around electrophysiological connectomics. Given the inherent challenges associated with empirical electrophysiological connectomics methods, this chapter aims to provide a biologically informed computational framework to refine and evaluate these methodologies. This endeavor not only champions the neuron-glial perspective in a field traditionally focused on neurons, but also strives to enhance the methodological rigor in whole-brain electrophysiological connectomics, with the ultimate aim of aligning model predictions with empirical electrophysiological data.

The fifth chapter (Exploring mechanisms of network dysfunction, resistance, and adaptation in Alzheimer disease — a research proposal for empirical insight, starting on page 220) outlines a future research trajectory that builds directly on this thesis, offering preliminary insights into generating mechanistic hypotheses, that can be tested empirically, for understanding large-scale network dysfunctions, resistance, and adaptations in brains afflicted by Alzheimer disease.

The penultimate chapter (Discussion, starting on page 239) serves as a general discussion, reflecting on the thesis's contributions to enriching scholarly discourse and advancing the field.

The concluding chapter (Conclusion, starting on page 249) encapsulates the aspirations of this thesis, articulating the hope that the presented multidisciplinary work will foster a deeper appreciation for the complexity of brain function and encourage further exploration of the integral roles played by both neuronal and glial components in shaping the brain's computational landscape.

Chapter 1 Background

1.1 Neuro-glial–vascular interactions: from cellular to assemblies to large-scale networks

The neuro-glial–vascular perspective (Giaume et al., 2010) posits that brain functioning is the result of dynamic interactions between neurons (e.g., glutamatergic pyramidal cells, GABAergic interneurons), glia (e.g., astrocytes, oligodendrocytes, microglia), and the vasculature (e.g., blood capillaries, pericytes). It further asserts that our understanding of brain complexity and functioning is bound to stagnate at an impasse as long as non-neuronal cells remain absent from neuroscientific theories, because non-neuronal cells (glia in particular) are as pertinent to the brain's *connectome* (i.e., the complete mapping of anatomical and functional connectivity in the brain) as any neuronal cells (De Pittà & Berry, 2019; Fields et al., 2015).

In this section, we delve into significant research on the intricate connections between neurons, glial cells, and the vascular system. The aim of this section is to illuminate the fundamental biological principles underpinning these interactions, providing sufficient insight to grasp the biophysical model that constitutes the essence of this thesis.

1.1.1 Neuro-glial–vascular cellular unit

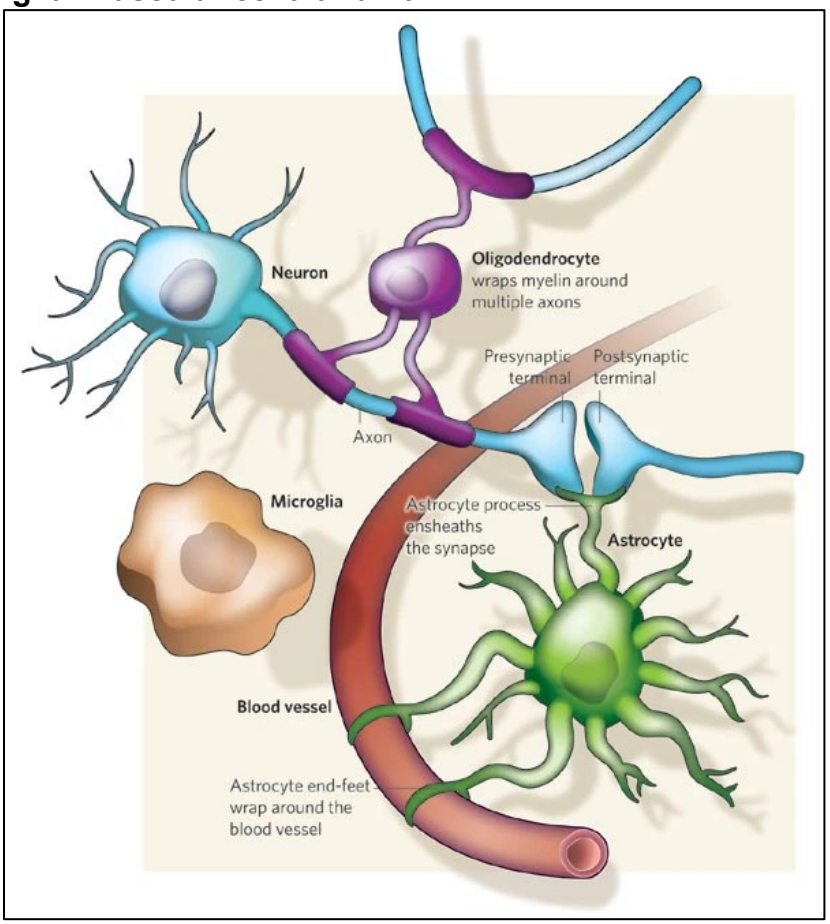

Figure 1.1. Neuro-glial–vascular unit. Figure from: (Allen & Barres, 2009). Permission obtained. — See text for explanation.

Figure 1.1 presents a basic sketch of the anatomical arrangement between neuronal, glial, and vascular compartments.

On the one hand, neurons intercommunicate through chemical synapses (though not exclusively, e.g., gap-junctions are also used and are orders of magnitude faster than chemical synapses at relaying signals (Coombes & Wedgwood, 2023; Nagy et al., 2018). At chemical synapses, neuronal signalling between two neurons (i.e., presynaptic and postsynaptic) includes electrical action potential propagation down axons to a presynaptic terminal, which then triggers presynaptic terminal depolarization and neurotransmitter releases, which in turn induces neurotransmitter bindings to the receptors of the postsynaptic membrane, which subsequently encourages depolarization of the postsynaptic neuron, to finally propagate the signal further to (potentially) other neurons (Allen & Barres, 2009).

On the other hand, glial cells envelop and wrap around every structural part of neurons across the central nervous system, owing to their intricate branched morphology, all the while remaining electrically non-excitable. For example, astrocytes make contact with and ensheath synapses and blood vessels to fuel, maintain, and modulate neurotransmission, oligodendrocytes wrap myelin around axons to speed up neuronal transmission, and microglia engulf dead cells and debris while keeping the brain under surveillance for damage or infection (Allen & Barres, 2009).

1.1.2 Zooming into astrocytes at the tripartite synapse

Figure 1.2 goes a step beyond the previous section by illustrating astrocytic functions at glutamatergic synapses. Astrocytes are the most prominently studied glial type in current literature, and a central focus in this thesis. Below, I encapsulate some of its key properties and functions, particularly those integral to the materials presented in the subsequent chapters of this thesis which will focus on neuron-astrocyte interactions.

Before starting, it is worth mentioning that the underlying findings are based on decades of research, yet some aspects remain debated and subject to revision. Recent authoritative references that provide foundational knowledge in this field include an introduction to the "*Computational Glioscience*" book (De Pittà & Berry, 2019) and an encyclopedia entry (De Pittà, 2020).

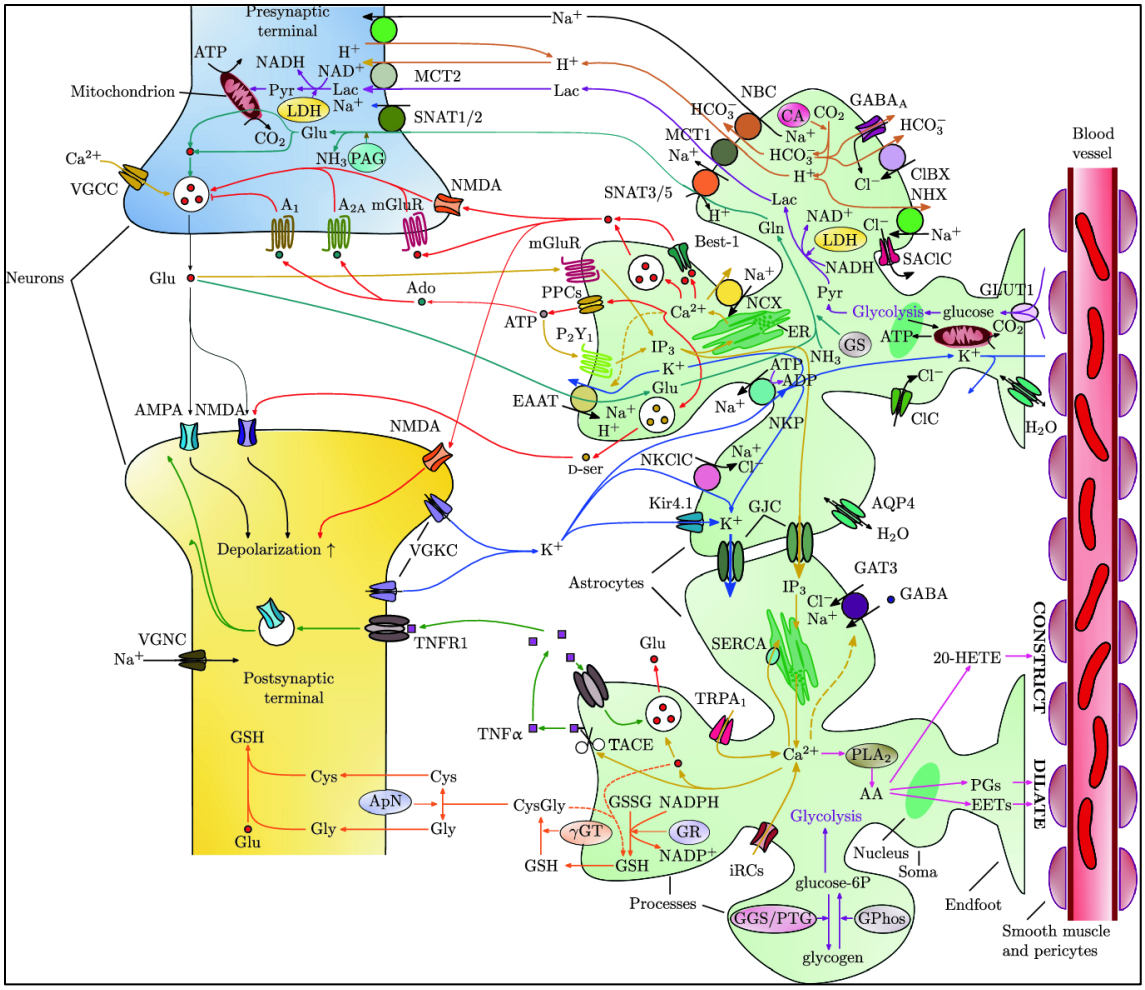

Figure 1.2. Interactions between glutamatergic neurons, astrocytes, and vasculature. Figure from: (De Pittà & Berry, 2019). Permission obtained. — See text for explanation. Pathways: yellow (calcium signaling); red (gliotransmission); green (cytokine signaling); turquoise (glutamate–glutamine cycle); blue (potassium buffering); purple (lactate shuttle); brown (pH buffering); orange (glutathione metabolism); magenta (vascular coupling). Relevant acronyms alphabetically ordered: 20-HETE (20-hydroxy-eicosatetraenoic acid); AA (arachidonic acid); ADP (adenosine diphosphate); ATP (adenosine triphosphate); Ca^{2+} (calcium); EAAT (excitatory amino acid transporter); EETs (epoxyeicosatrieonic acids); ER (endoplasmic reticulum); GABA (gamma-aminobutyric acid); GAT3 (gamma-aminobutyric acid transporter 3); GJC (gap junction channels); Gln (glutamine); Glu (glutamate); GLUT1 (glucose transporter); GS (glutamine synthetase); IP_3 (inositol 1,4,5-trisphosphate); Lac (lactate); LDH (lactate dehydrogenase); MCT1 and MCT2 (monocarboxylate transporters); mGluR (metabotropic glutamate receptor); Na^+ (sodium); NMDA (N-methyl-D-aspartate; a ionotropic glutamate receptor); PAG (phosphate-activated glutaminase); PLA_2 (phospholipase A2); PGs (prostaglandins); SNAT1/2 (sodium-coupled neutral amino acid transporters).

Astrocytic network anatomy. Astrocytes provide a tiled arrangement of brain space (i.e., they each are characteristically territorial by occupying non-overlapping domains) where each tile is a mini-circuit (i.e., composed of an astrocyte contacting many synapses, e.g., in the human brain, one astrocyte can ensheath 270–2000 thousand synapses), and they form a gap-junction-coupled syncytium (i.e., a multinucleate mass of cytoplasm resulting from the fusion of cells; e.g., GJC in Figure 1.2) supporting cell-cell (i.e., network) communication mediated by calcium signalling (yellow pathway in Figure 1.2) (De Pittà, 2020; Giaume et al., 2010; Kastanenka et al., 2020; Vasile et al., 2017). Gap junctions (see Figure 1.3) are specialized structures, constructed from connexin proteins, facilitating direct cell-to-cell communication through channels that regulate the

exchange of ions and small molecules, with mechanisms to open and close as needed (Lallouette et al., 2019; Stephan et al., 2021; Vasile et al., 2017). The suggested functional purpose of this astrocytic anatomical configuration posits that astrocytes act as physical barriers between the synaptic connections of neighbouring neurons while finely regulating extracellular neurotransmitter diffusion (De Pittà, 2020).

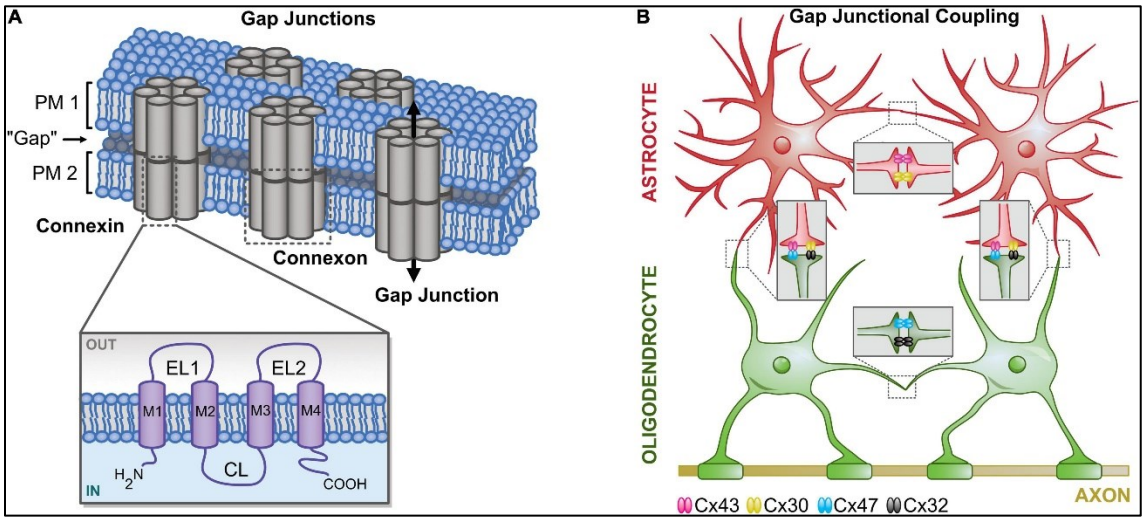

Figure 1.3. Principle of gap junctional coupling. Caption and figure from: (Stephan et al., 2021). Publisher's permission: http://creativecommons.org/licenses/by/4.0/. — (A) Structural organization of gap junctions. Gap junctions are integral membrane proteins that connect the cytosol of neighboring cells. Two pairs of connexons (hexamers of connexins; Cx) form a pore enabling diffusion for ions and small molecules. EL, extracellular loop; CL, cytoplasmic loop; M, transmembrane helix. (B) (Pan-/)glial coupling. Astrocytes mainly express Cx43 and Cx30, whereas oligodendrocytes mainly express Cx47 and Cx32. Homotypic gap junctions couple astrocytes (Cx43:Cx43, Cx30:Cx30) and oligodendrocytes (Cx47:Cx47, C30:Cx30). Heterotypic gap junctions are formed by different connexons connecting astrocytes and oligodendrocytes (Cx43:Cx47, Cx30:Cx32).

Astrocytic neurotransmitter regulation. Critically, astrocytes are equipped with excitatory amino acid transporters (EAAT in Figure 1.2) to play a pivotal role in maintaining cerebral homeostasis, which serve as two mechanisms. On the one hand, they serve as the principal mechanism for the uptake and regulation of glutamate in the mature brain (e.g., turquoise pathway in Figure 1.2). Given that glutamate acts as an exclusively excitatory neurotransmitter, its excessive presence can induce neuronal overstimulation and potentially lead to excitotoxicity (De Pittà, 2020; Pankevich et al., 2011; Scimemi, 2019). On the other hand, they serve as an intrasynaptic pathway of neural excitability modulation (De Pittà, 2020). It is noteworthy that neurons can participate in glutamate reuptake though at a negligible rate compared to astrocytes. They can do so thanks to e.g., vesicular glutamate transporters (not drawn in Figure 1.2), in, e.g., a recycling process maintaining an adequate supply of glutamate for neurotransmission whereby the taken-up glutamate can be reused as a neurotransmitter (Hori & Takahashi, 2012; Vigneault et al., 2015).

Astrocytic network calcium-mediated signaling. Intercommunications among astrocytes can be initiated by glutamatergic neurotransmission and perpetuated in a feedback loop via glutamatergic gliotransmission (yellow and red pathways in Figure 1.2). For example, when glutamate is released into the extracellular space in response to neuronal firing, a spillover portion reaches the glutamate receptors of an astrocyte (mGluR in Figure 1.2). This event sets off a series of action, including intracellular productions of inositol 1,4,5-trisphosphate (IP_3) within the targeted astrocyte. This, in turn, promotes calcium (Ca^{2+}) release from the astrocyte's endoplasmic reticulum (ER) as well as

diffusion through gap junctions to adjacent astrocytes whereby the diffusing molecule induces intracellular calcium releases within the adjacent astrocytes via their endoplasmic reticulum. Consequently, this cascade of events may lead to astrocytic glutamate releases (i.e., gliotransmitter releases) into the extracellular space, facilitated, e.g., by exocytosis. Importantly, the astrocytic glutamate releases may diffuse and bind to both pre-terminal and post-terminal neuronal glutamate receptors (NMDA), ultimately inducing, independently of neuronal firing, both *de novo* glutamate release from the pre-synaptic neuron and depolarization of the post-synaptic neuron.

Astrocytic neurometabolism regulation. In addition to neurotransmission, astrocytes also play a crucial role in neurometabolism. Neurometabolism (not to be confused with neurotransmission) refers to the processes involved in the production, breakdown, and utilization of molecules that provide energy and support the functioning of neural cells. The glutamate-glutamine cycle and the astrocyte-to-neuron lactate shuttle are two examples of metabolic pathways relying on glutamate (and GABA) uptake by astrocytic transporters.

The glutamate-glutamine cycle (turquoise pathway in Figure 1.2) starts by converting the taken-up glutamate into glutamine (Gln) through the glutamine synthetase (GS) enzyme within astrocytes. The synthetized glutamine is then shuttled back to neurons via sodium-coupled neutral amino acid transporters (SNATs in Figure 1.2), before undergoing reconversion to glutamate through phosphate-activated glutaminase (PAG) activity. The resulting glutamate can finally undergo either oxidative metabolism within mitochondria or be used to replenish synaptic vesicles. It is noteworthy that at GABAergic inhibitory synapses, GABA can be synthetized from glutamate through the glutamate decarboxylase enzyme within neurons, and possibly involve astrocytic uptake via GABA transporters (GAT3). See also Figure 1.4 and (Angulo et al., 2008; Yoon & Lee, 2014) for more information on GABA's role, as a gliotransmitter. Moreover, the expression of astrocytic excitatory amino acid transporters and GABA transporters can be influenced by intracellular calcium.

In a glutamate-mediated lactate shuttle (purple pathway in Figure 1.2), astrocytic glutamate uptake leads to an increase in the ratio of adenosine diphosphate to adenosine triphosphate (ADP and ATP in Figure 1.2) within the astrocyte. The elevated ratio then triggers the utilization of glucose through anaerobic glycolysis in astrocytes. This glycolytic process may be accompanied by glycogenolysis (breakdown of glycogen) or the uptake of glucose from the blood circulation via glucose transporters (GLUT1). Afterwards, lactate dehydrogenase (LDH) catalyzes the conversion of pyruvate (Pyr), a product of glycolysis, into lactate and *vice versa*. Finally, lactate (Lac), as produced in astrocytes, is transported to neurons through monocarboxylate transporters (MCTs), and once in neurons, lactate can be converted back to pyruvate and used as an energy substrate.

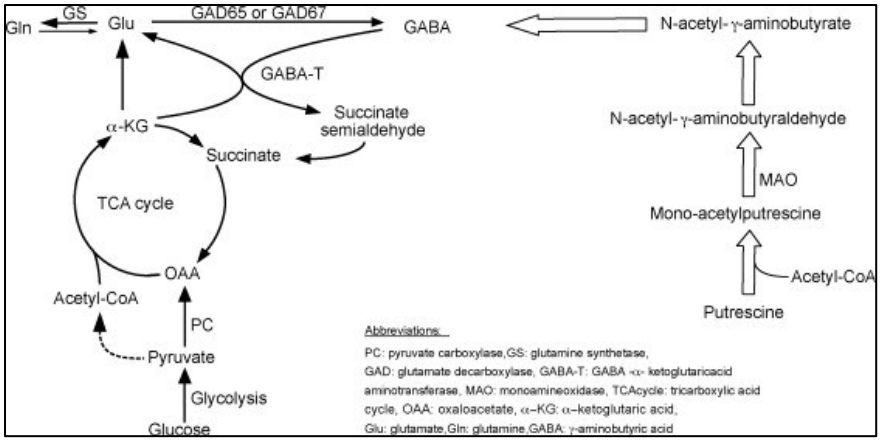

Figure 1.4. Two potential pathways for GABA production in glial cells. Caption and figure from: (Angulo et al., 2008). Permission obtained. — Glucose oxidation and glutamate–glutamine cycle pathway: As in neurons, GABA can be produced in glial cells from glutamate accumulated by uptake or generated in the TCA cycle. Glutamate decarboxylase activity was reported in glial cells; this enzyme can convert glutamate into GABA. Note that in glial cells glutamate is also converted into glutamine by the action of the glia-specific enzyme glutamine synthetase (GS), and that pyruvate generated by glycolysis would enter the TCA cycle through oxaloacetate rather than through acetyl-CoA as it is the case in neurons. Putrescine oxidation pathway: GABA can also be produced from putrescine through the monoamine oxidase pathway which requires acetyl coenzyme A (acetyl-CoA). Putrescine is acetylated in mono-acetylputrescine before oxidation by monoamine oxidase in N-acetyl-γ-aminobutyraldehyde. A second oxidation step leads to N-acetyl-γ-aminobutyrate, which is then de-acetylated into GABA. This pathway can continue with GABA entering the TCA cycle for further oxidation via the successive actions of the GABA-α-ketoglutaric acid aminotransferase and of the succinate semialdehyde dehydrogenase, but GABA produced from putrescine can also accumulate in glial cells and be released (see text from (Angulo et al., 2008) for details).

Astrocytic blood flow regulation. With respect to the vascular system, astrocytes are master regulators of cerebral blood flow through calcium-dependent vasoconstriction and vasodilation processes (magenta pathway in Figure 1.2). Both processes start with calcium-induced production of arachidonic acid (AA in Figure 1.2) from phospholipase A_2 (PLA_2). Subsequently, arachidonic acid can be converted into prostaglandis (PGs) and epoxyeicosatrieonic acids (EETs) by cyclooxygenases; or it can move through the endfeet to the smooth muscle surrounding capillaries where it is transformed into 20-hydroxy-eicosatetraenoic acid (20-HETE) by ω-hydroxylase. The former pathway leads to vasodilation at astrocytic endfeet processes, while the latter leads to vasoconstriction.

Astrocytic other processes. Figure 1.2 illustrates additional significant interaction pathways between astrocytes and glutamatergic neurons. These pathways include *cytokine signaling* (green pathway), *potassium buffering* (blue pathway), *pH buffering* (brown pathway), and *glutathione metabolism* (orange pathway). However, a detailed exposition of these pathways is not provided here, as they are not central to the subsequent sections of this thesis. Instead, functional diagrams are presented in Figure 1.5, which serve as a complementary synthesis to Figure 1.2. The diagrams are also useful for the modeling sections that will follow, offering a cohesive visual representation that aids in understanding the complex interactions discussed.

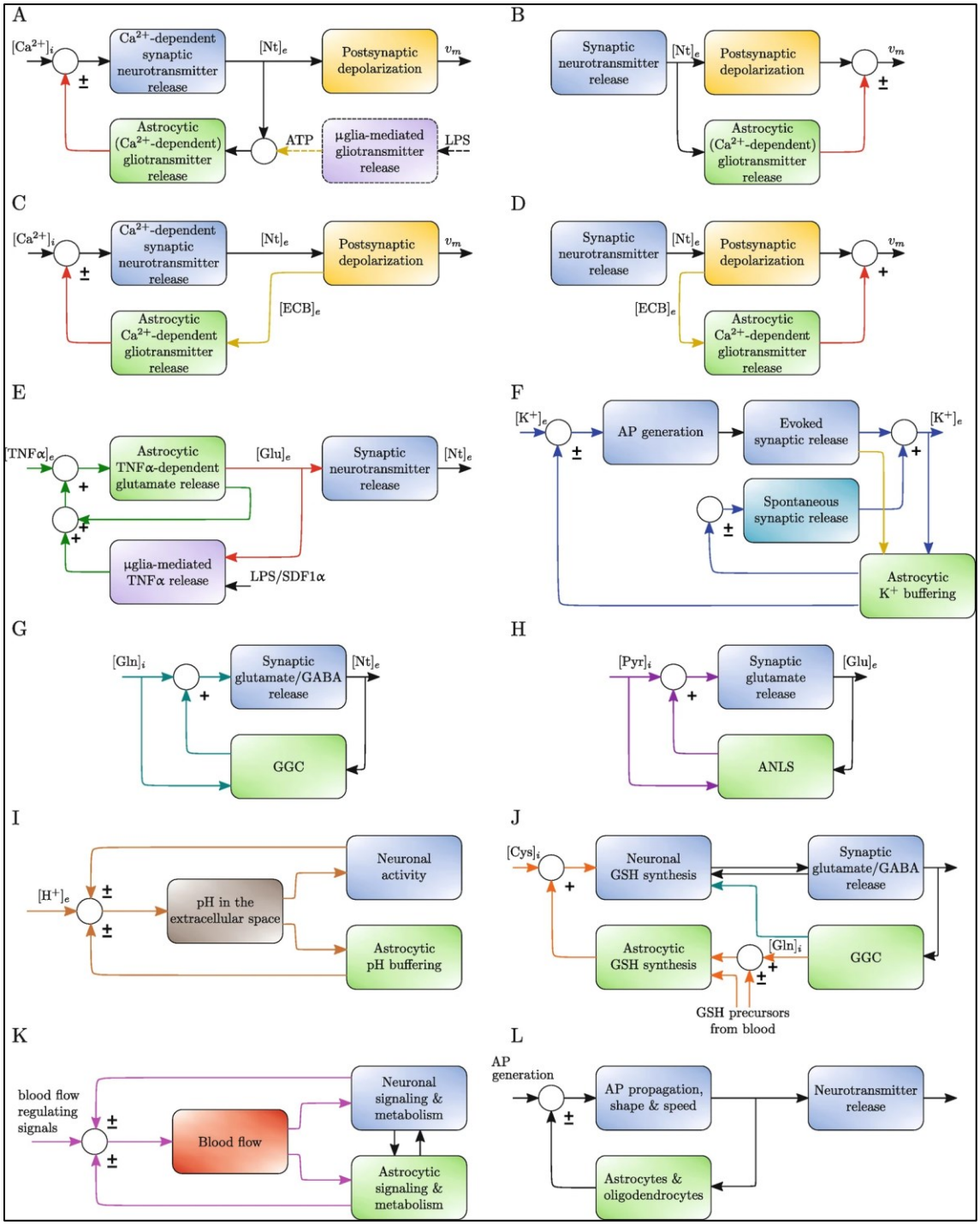

Figure 1.5. Feedback and feedforward pathways in neuron-glial interactions. Caption and figure from: (De Pittà, 2020). Permission obtained. — (A) Presynaptic pathway of gliotransmission stimulated by presynaptically released neurotransmitters; (B) postsynaptic pathway of gliotransmission stimulated by presynaptically released neurotransmitters; (C) presynaptic pathway of gliotransmission triggered by postsynaptic endocannabinoid release; (D) postsynaptic pathway of gliotransmission mediated by postsynaptic endocannabinoid release; (E) modulation of glutamatergic gliotransmission by cytokine tumor necrosis factor alpha (TNFα). (F) Potassium (K^+) buffering and regulation of neuronal activity; (G) glutamate-glutamine cycle (GCC); (H) astrocyte-to-neuron lactate shuttle (ANLS); (I) extracellular pH homeostasis; (J) glutathione synthesis; (K) neurovascular coupling; and (L) glia-mediated regulation of action potential conduction. $[Ca^{2+}]_i$ intracellular (cytosolic) calcium concentration; $[Cys]_i$ ($[Gln]_i$)

intracellular cysteine (glutamine) concentration, $[ECB]_e$ ($[TNF\alpha]_e$) extracellular endocannabinoid (TNFα) concentration, $[K^+]_e$ ($[H^+]_e$) extracellular K^+ (H^+) concentration, $[NT]_e$ ($[Glu]_e$) extracellular neurotransmitter (glutamate) concentration, v_m membrane potential, AP action potential, LPS lipopolysaccharide, SDF1α stromal cell-derived factor 1 alpha. i indicates that activities can be described either for neuronal or glial ensembles.

Astrocytic hypothesized neuromodulator regulation. Neuromodulators (e.g., norepinephrine, serotonin, acetylcholine, dopamine) play a crucial role in governing brain states by regulating key processes including brain plasticity, response to important stimuli, and the sleep-wake cycle (Bargmann, 2012; Katz, 1999; Marder, 2012; Mattson & Arumugam, 2018; Pacholko et al., 2020; Shine, 2019; Shine et al., 2019). Given their wide-reaching influence, it is notable how neuromodulators impact extensive and diverse brain regions, a phenomenon that extends beyond the scope of simple extracellular diffusion. Astrocytes, due to their strategic positioning and unique capabilities, are hypothesized to significantly enhance the impact of neuromodulators across broad neuronal networks. Indeed, as we have reported earlier, astrocytes form networks, and each astrocyte interacts with numerous synapses while releasing various gliotransmitters like glutamate and adenosine triphosphate (ATP) which influence various brain mechanisms. Additionally, astrocytes play a role in regulating the balance between excitation and inhibition in neuronal circuits by modulating extracellular potassium levels (Figure 1.2). Importantly, they express receptors for all major neuromodulators, positioning them as key players in neuromodulatory processes. It is therefore without surprise that astrocytes are hypothesized to not only influence individual synapses, but also play a pivotal role in broader synaptic communication and brain state transitions by extending the reach of neuromodulators (Pacholko et al., 2020). The potential of astrocytes to amplify neuromodulator effects on neuronal networks is thought to occur through several mechanisms (e.g., see Figure 1.6) such as: alterations in astrocytic calcium dynamics, the release of gliotransmitters, and the regulation of potassium homeostasis.

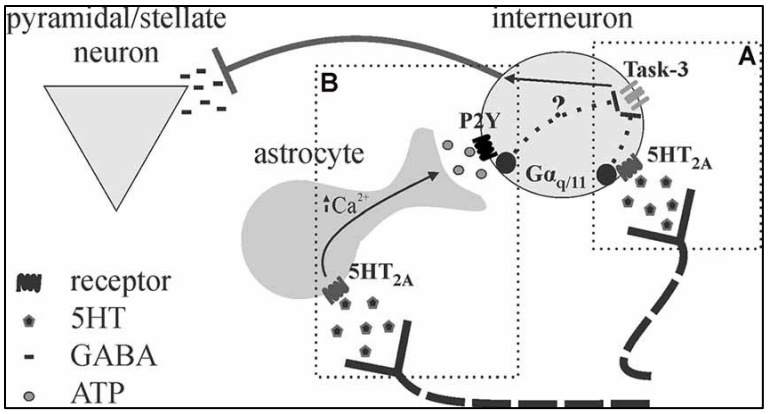

Figure 1.6. Proposed schematic for astrocytes as intermediary or amplifier of serotonin-mediated (5HT) inhibition. Caption and figure from: (Pacholko et al., 2020). Publisher's permission: http://creativecommons.org/licenses/by/4.0/. — (A) Deng and Lei (Deng & Lei, 2008) show 5HT effects on inhibition in the auditory cortex are mediated by $5HT_{2A}$ receptors, $G\alpha_{q/11}$, and task-3 potassium channel inhibition. (B) Evidence was recently provided that astrocytes may be an intermediary in the effects of 5HT on cortical inhibition in the somatosensory cortex (Quon et al., 2018; Wotton et al., 2018), as the application of purinergic antagonists and disruption of astrocytic metabolism blocked the effects of 5HT. It appears possible that 5HT promotes astrocytic ATP release downstream of $5HT_{2A}$ stimulation, leading to interneuron depolarization (P2Y also linked to $G\alpha_{q/11}$). It is not clear whether astrocytes mediate 5HT effects entirely or merely serve to amplify the effects given their strategic position.

1.1.3 Zooming into astrocytes along the vascular tree

The previous section was thorough in discussing astrocytic roles and neuron-astrocyte interactions, but it slightly underrepresented the vascular components' contributions in comparison. This section provides a more balanced depiction of the neuro-glia–vascular unit by underscoring the importance of the blood-brain barrier and the blood circulation system in supporting brain function.

The regulation of cerebral blood flow involves complex interactions between neurons, astrocytes, endothelial cells (which are cells forming the inner cellular lining of all blood vessels), and mural cells (i.e., smooth muscle cells (SMCs) and pericytes), with various signaling molecules mediating these interactions (e.g., see Figure 1.7). These findings come from a variety of studies conducted in different parts of the central nervous system and through both *in vivo* and *in vitro* research methods (Kugler et al., 2021; Sweeney et al., 2018).

Neuron–mural-cells interaction. E.g., see Figure 1.7. Adenosine triphosphate (ATP) and noradrenaline (NA) released by neurons cause SMCs and pericytes to either constrict or relax, affecting blood flow. This is mediated through specific receptors on the cells. Neurons produce nitric oxide (NO), leading to the relaxation of these cells and an increase in blood flow. The effect of NO on pericytes may vary across different brain regions. During neuronal activity, extracellular potassium (K^+) can either relax or constrict SMCs and pericytes by acting on potassium and calcium channels.

Astrocyte–mural-cells interaction. E.g., see Figure 1.7. ATP affects astrocytes and may lead to changes in calcium levels within these cells. This is still debated in scientific research. Increased calcium in astrocytes triggers the production of various compounds (like arachidonic acid (AA) and its metabolites) that regulate blood flow by acting on SMCs and pericytes.

Endothelial–mural-cells interaction. E.g., see Figure 1.7. Acetylcholine (ACh) from neurons or blood interacts with receptors on endothelial cells, increasing NO production. This relaxes mural cells, thereby increasing blood flow. Shear stress and other factors also enhance the production of NO and other compounds in endothelial cells, leading to the relaxation of SMCs and increased blood flow. ACh or raised extracellular potassium levels can cause endothelial cells to hyperpolarize, which can spread through gap junctions to increase blood flow.

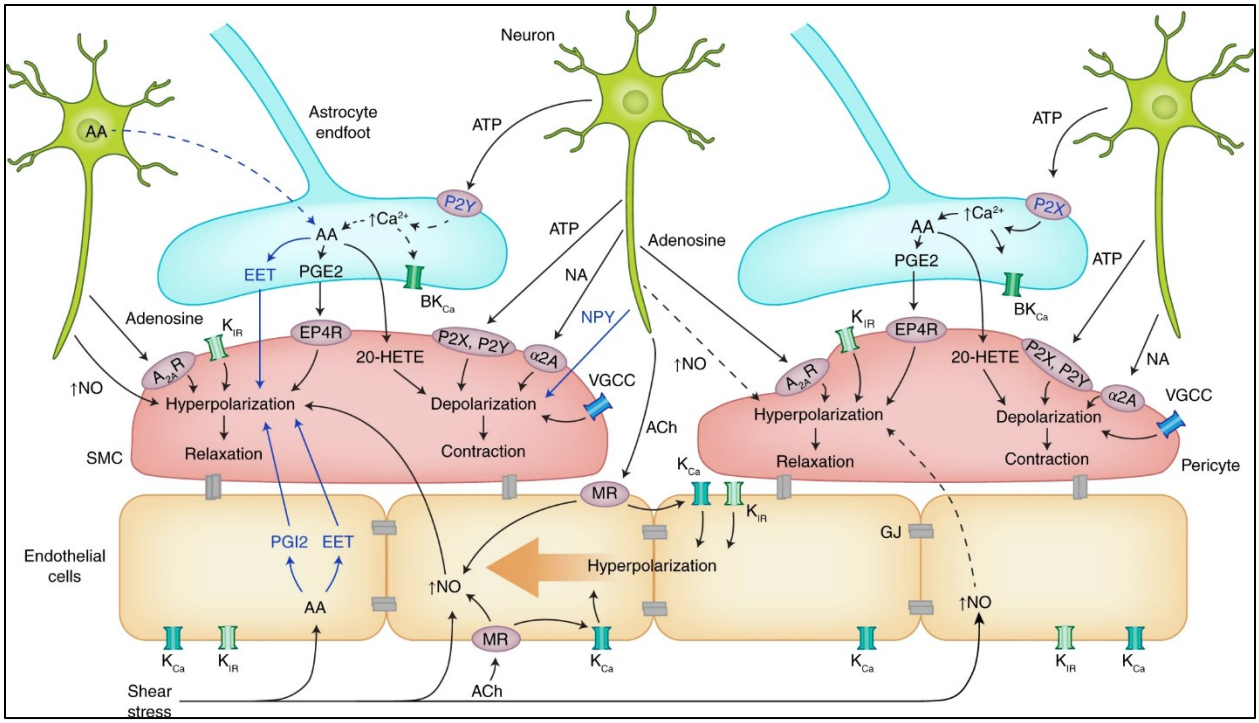

Figure 1.7. Key cellular and molecular pathways regulating cerebral blood flow. Caption and figure from: (Sweeney et al., 2018). Permission obtained. — See also text for summary. Neuron–mural cells crosstalk: ATP and noradrenaline (NA) released by neurons (green) act on SMCs and pericytes through adenosine A_{2A} receptors ($A_{2A}R$) or α2-adrenergic receptors (α2A), respectively, causing cell depolarization and constriction, which reduces blood flow. Adenosine acts via purinergic P2X and P2Y receptors to hyperpolarize SMCs and pericytes (pink), which increases blood flow. Neuropeptide Y (NPY) causes SMCs contraction. In both SMCs and pericytes, NO produced by neurons leads to hyperpolarization resulting in blood flow increase. Pericyte response to NO may vary by brain region, indicated by dashed arrows. Extracellular K^+ released during neuronal activation can act on K^+ (inward rectifier, K_{IR}) and Ca^{2+} (voltage-gated, VGCC) channels in SMCs and pericytes to hyperpolarize and relax the cells, or depolarize and contract cells. Astrocyte–mural cells crosstalk: ATP acts on P2X or P2Y receptors on astrocytes, which (according to some studies) can increase intracellular [Ca^{2+}]. However, the role of arteriolar astrocyte [Ca^{2+}] changes remains debatable (indicated by dashed arrows). [Ca^{2+}] increase triggers production of AA and its metabolites (PGE2, through PGE2 receptor EP4, EP4R; 20-HETE; epoxyeicosatetraenoic acids, EETs) that act on SMCs and pericytes to regulate blood flow. Alternatively, neurons may release AA to be further metabolized by astrocytes, indicated by dashed line. Endothelial–mural cells crosstalk: ACh released from neurons or blood-derived ACh act on endothelial muscarinic ACh receptors (MRs) to increase endothelial NO production, causing hyperpolarization and relaxation of mural cells (yellow), which increases blood flow. Shear stress can also increase NO endothelial production, as well as production of AA, EETs, and prostacyclin (PGI2), which hyperpolarize and relax SMCs, increasing arteriolar blood flow. ACh or an increase in extracellular [K^+] can activate K_{IR} or calcium-activated K^+ (K_{Ca}) channels on endothelial cells, leading to endothelial hyperpolarization that can propagate via gap junctions (GJs) between endothelial cells in a retrograde direction to increase blood flow. Altogether these findings are informed from various central nervous system regions and from both in vivo and in vitro studies.

The integrity of the blood-brain barrier (BBB), e.g., see Figure 1.8, is also the result of complex interactions among neurons, astrocytes, endothelial cells, and mural cells, each contributing through specific signaling pathways to maintain the barrier's stability and function (Kugler et al., 2021; Sweeney et al., 2018).

BBB integrity and cell signaling. E.g., see Figure 1.8. The BBB is maintained by special proteins in endothelial cells. These proteins include tight junction (TJ) and adherens junction (AJ) proteins,

which essentially act as barriers. Additionally, the BBB controls the movement of substances from the blood into the brain, a process known as transcytosis, which is normally kept at low levels.

Pericyte–endothelial-cells interaction. E.g., see Figure 1.8. Notch ligands from endothelial cells interact with Notch3 receptors on pericytes, promoting pericyte survival. Platelet-derived growth factor-BB (PDGF-BB) binds to receptors on pericytes, aiding their survival, proliferation, and migration. Vascular endothelial growth factor-A (VEGFA) binds to receptors on endothelial cells, supporting their survival. Pericyte-derived Notch ligands bind to endothelial Notch1 receptors, contributing to BBB stability. Transforming growth factor-β (TGFβ) signaling occurs between pericytes and endothelial cells in both directions. Pericyte-secreted angiopoietin-1 (Angpt1) binds to receptors on endothelial cells to encourage their proliferation.

Astrocyte–pericyte and astrocyte–endothelial-cells interactions. E.g., see Figure 1.8. Astrocytes secrete certain proteins (APOE2 and APOE3) that suppress inflammatory pathways in pericytes to maintain BBB stability. Astrocyte-produced laminin also maintains BBB integrity. Astrocyte-secreted Sonic hedgehog (Shh) interacts with receptors on endothelial cells to further enhance BBB stability.

Smooth-muscle–endothelial cells interaction. E.g., see Figure 1.8. SMCs interact with endothelial cells through various signaling molecules to promote BBB stability and SMC survival.

Neuron–endothelial-cells interaction. E.g., see Figure 1.8. Neurons secrete signaling molecules such as Wnt proteins that interact with receptors on endothelial cells, promoting endothelial cell differentiation during brain vasculogenesis.

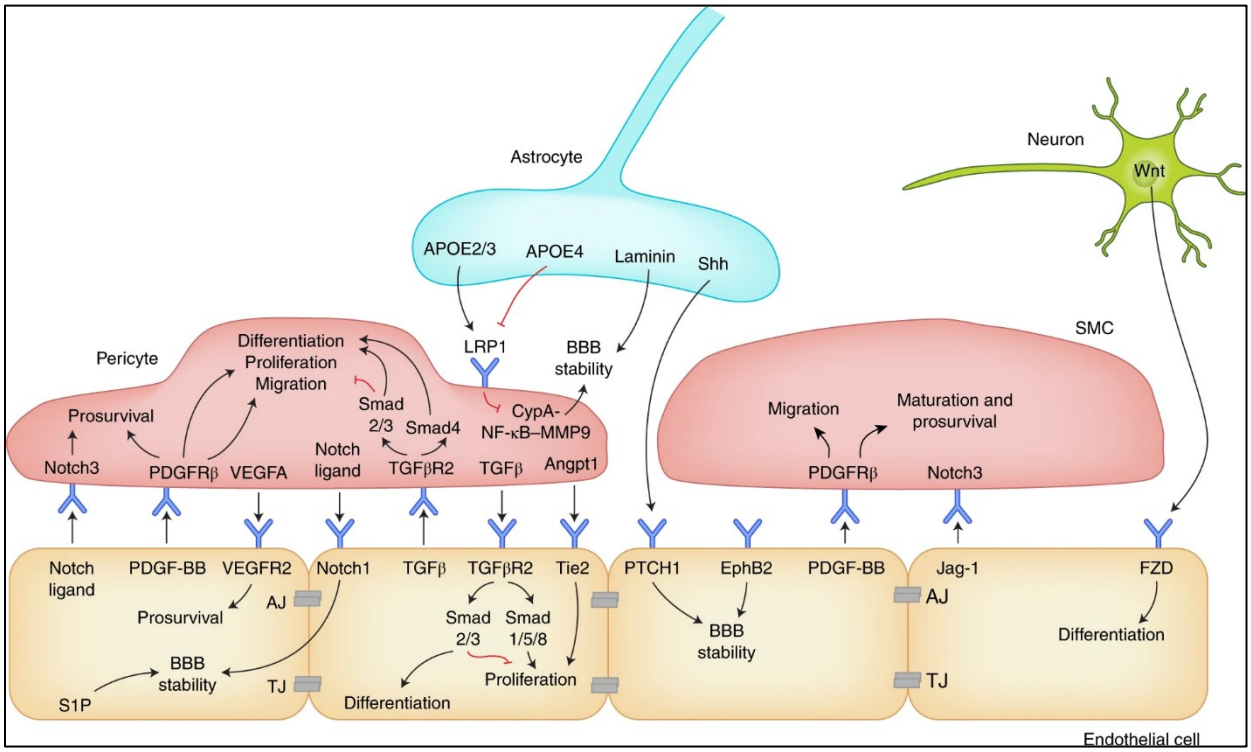

Figure 1.8. Key cellular and molecular pathways regulating blood-brain barrier (BBB) integrity. Caption and figure from: (Sweeney et al., 2018). Permission obtained. — See also text for summary. BBB integrity is maintained by tight junction (TJ) and adherens junction (AJ) proteins between endothelial cells and low-level bulk-flow transcytosis. Pericyte–endothelial cells crosstalk: Notch ligands–Notch3 receptor signaling promotes pericyte survival. Platelet-

derived growth factor-BB (PDGF-BB) binds to PDGFRβ on pericytes, causing pericyte survival, proliferation, and migration. Vascular endothelial growth factor-A (VEGFA) binds to endothelial VEGF receptor-2 (VEGFR2) mediating endothelial survival. Pericyte-derived notch ligands bind to endothelial Notch1 receptor, which mediates BBB stability, as does endothelial sphingosine-1 phosphate (S1P). Transforming growth factor-β (TGFβ) and TGFβ receptor-2 (TGFβR2) signaling occurs bidirectionally between pericytes and endothelial cells. Pericyte-secreted angiopoietin-1 (Angpt1) binds Tie2 receptors on endothelial cells to promote proliferation. Astrocyte–endothelial cells crosstalk: astrocyte-secreted APOE2 and APOE3, in contrast to APOE4, suppress the pro-inflammatory signaling cyclophilin A–NF-κB–matrix metalloproteinase-9 (MMP9) pathway in pericytes to maintain BBB stability. Similarly, astrocyte-produced laminin maintains BBB stability. Astrocyte-secreted sonic hedgehog (Shh) interacts with patched-1 (PTCH1) at the endothelium to further promote BBB stability. SMC–endothelial cells crosstalk: ephrin B2 (EphB2) on the endothelium promotes BBB stability. PDGF-BB binds PDGFRβ on SMCs to promote survival and migration. Endothelial-secreted jagged-1 (Jag-1) binds Notch3 to promote SMC maturation and survival. Neuron–endothelial cells crosstalk: neuron-secreted Wnt is a ligand of frizzled (FZD) at the endothelium that promotes endothelial cell differentiation.

1.1.4 Zooming out to neuro-glial–vascular networks, the connectome

Reflecting on the previous figures, it becomes clear that glial cells, especially astrocytes, exhibit structural and functional characteristics that profoundly influence neuronal activity and connectivity, as well as neurovascular coupling, across a spectrum of spatiotemporal scales (De Pittà & Berry, 2019; Fields et al., 2015; Giaume et al., 2010; Kastanenka et al., 2020). Such insights call for a re-evaluation of existing neuron-based modelling paradigms to incorporate glial-mediated effects.

The connectome. A prime example of this shift in perspective is the concept of the *connectome*, exemplified by Fields and colleagues (Fields et al., 2015), and central to this thesis. Historically, the term connectome predominantly referred to the mapping of neuronal and synaptic connections. For instance, in their review, Park and Friston (Park & Friston, 2013) acknowledged the fundamental role of non-neuronal cells in the brain's connectome, primarily through a graphical representation of the brain microscopic scale (see Figure 1.9). However, this recognition did not extend to detailed examination and discussion, as the review predominantly focused on neuronal aspects. Yet, as our preceding discussions reveal, a comprehensive depiction of the connectome must also integrate glial cells and vascular components alongside neuronal elements. This expanded view is gaining traction in recent research (Blanchard et al., 2016; Figley & Stroman, 2011; Jolivet et al., 2015; Kugler et al., 2021; Lu et al., 2019; Magistretti & Allaman, 2015; Schaeffer & Iadecola, 2021), which highlight the necessity of *integrative approaches*. It is noteworthy that while many studies contribute to this evolving understanding of the connectome, they do not always explicitly focus on or label their research as investigating the neuro-glia–vascular unit, despite clearly examining aspects closely related to it (Ahmed et al., 2016; Del Guerra et al., 2018; J. Y. Hansen et al., 2022; Mattson & Arumugam, 2018; Shafiei et al., 2023; Tesler et al., 2023; Voigt et al., 2023; Zhang et al., 2014). This can occur due to various reasons, such as differences in research focus and researchers' specialized knowledge, terminology used, or the rapidly evolving nature of the neuroscientific field. Nonetheless, the consensus seems to be that by considering neurons, glia, and vascular components in unison within the connectome, we can more effectively decode the complexities of brain function in health and disease (e.g., see Figure 1.10). This unified perspective not only propels forward the field of neuroscience but also lays the foundation for innovative neuroscientific investigations and the development of new therapeutic approaches (Barreto et al., 2012; Blanco-Suárez et al., 2017; W. S. Chung et al., 2015; Haim et al., 2015; Kugler et al., 2021; B. Liu et al., 2017; Mattson & Arumugam, 2018; Rowley et al., 2012; Sweeney et al., 2018; Q. Wang et al., 2017).

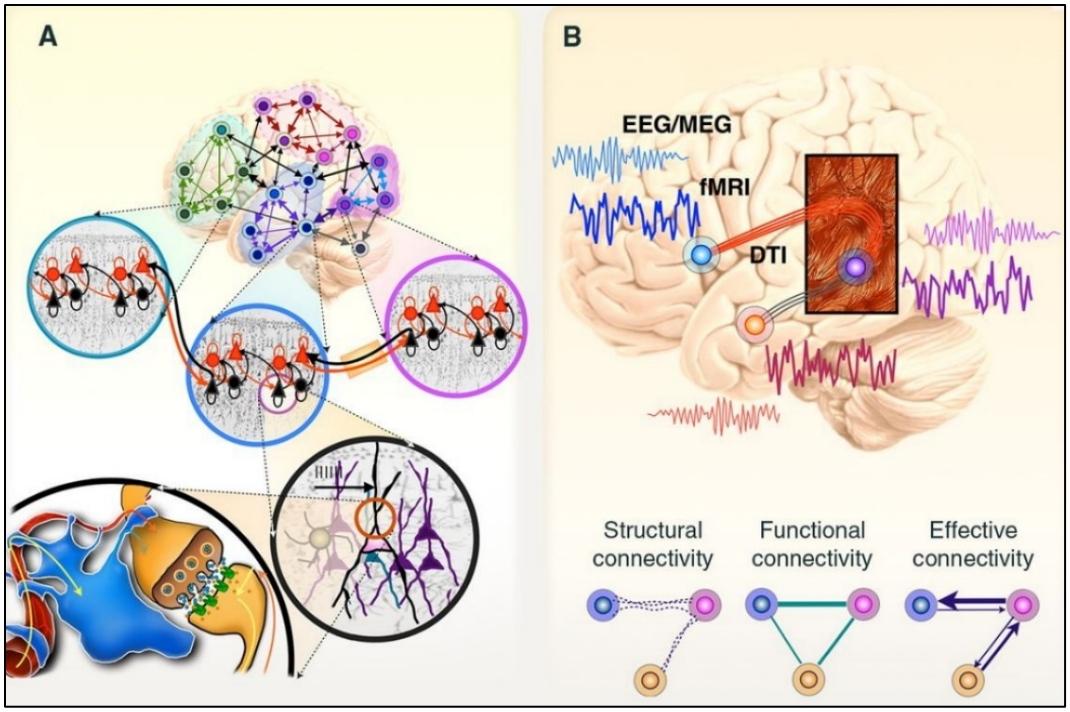

Figure 1.9. Node, edge, and organization in the brain network. Caption and figure from: (Park & Friston, 2013). Reprinted with permission from AAAS. — (A) Schematic of the multiscale hierarchical organization of brain networks: from neurons and macrocolumns to macroscopic brain areas. A network is composed of nodes and their links, called edges. A node, defined as an interacting unit of a network, is itself a network composed of smaller nodes interacting at a lower hierarchical level. (B) Depictions of "edges" in a brain network, as defined by three types of connectivity: structural, functional, and effective. Structural connectivity refers to anatomical connections and (macroscopically) is usually estimated by fiber tractography from diffusion tensor MRI (DTI). These connections are illustrated with broken lines in the bottom images. Functional and effective connectivity are generally inferred from the activity of remote nodes as measured by using BOLD-fMRI or EEG/MEG signals. Functional connectivity, defined by the correlation or coherence between nodes, does not provide directionality or causality and is therefore depicted without arrows. Because effective connectivity is estimated by using a model of neuronal interactions, it can evaluate directionality. This is illustrated by the one-sided arrows. Adjacency (or connectivity) matrices subserve graph theoretical analyses of brain systems and encode structural and functional connectivity between pairs of nodes.

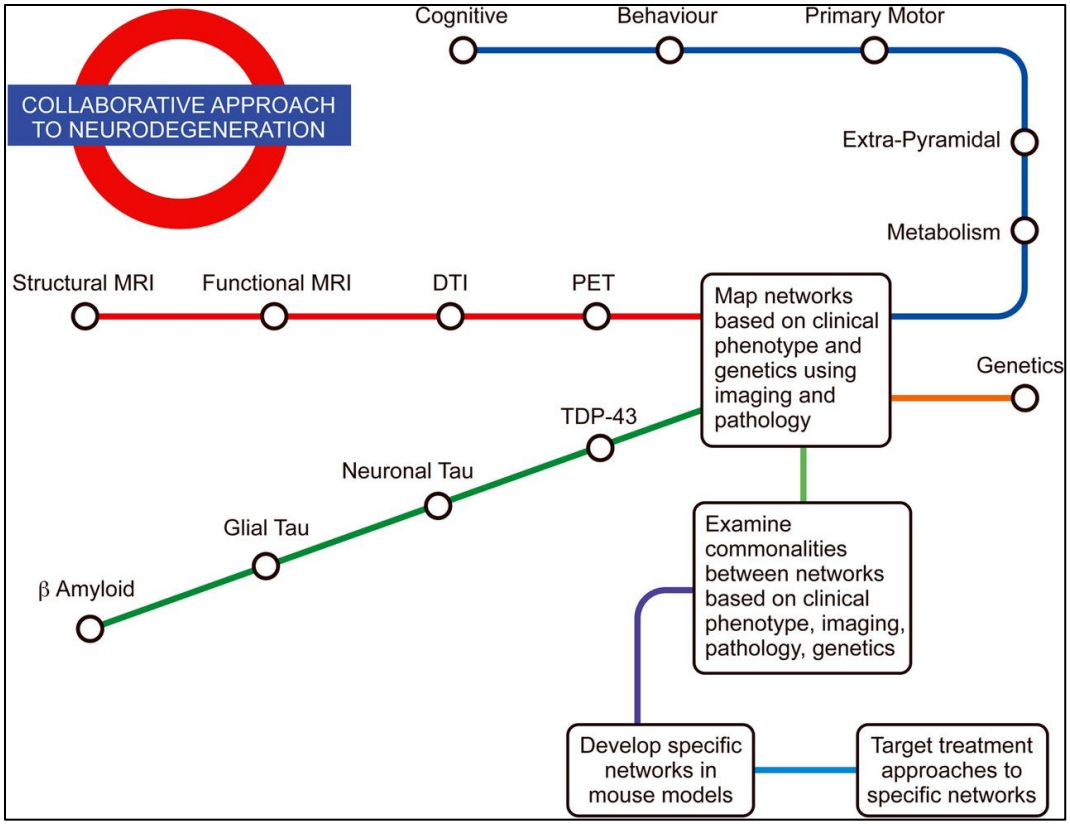

Figure 1.10. Collaborative approach to neurodegeneration. Caption and figure from: (Ahmed et al., 2016). Publisher's permission: http://creativecommons.org/licenses/by-nc/4.0/. — Neurodegenerative network map: proposed way forward for a collaborative approach based on phenotypic variation, imaging, pathology and genetics for investigating the neural networks and their contribution to the pathophysiological bases of neurodegenerative conditions. A better understanding of the neural networks involved is likely to translate into better targeted treatments based on these networks. DTI, diffusion tensor imaging; PET, positron emission tomography.

Spatiotemporal scales of neuro-glial–vascular network interactions. The spatiotemporal scale of neuro-glial–vascular interactions in neural networks is remarkably diverse and multifaceted, where neurons and glia serve as functional agents, and where astrocytes serve as bridges between neuronal and vascular processes (Fields et al., 2015). Spatially, they span from subcellular levels, where astrocytes and microglia interact with individual synapses, to extensive brain networks where oligodendrocytes influence large-scale communication through myelination. Temporally, these interactions range from rapid synaptic changes to slower modifications in myelination influenced by learning throughout development and aging.

Astrocytes in neural networks. Astrocytes support neuronal function by supplying nutrients, maintaining ion balance, and removing waste (Fields et al., 2015). They convert glucose to lactate for neurons and are involved in brain repair after injury by forming glial scars. Additionally, they help form and maintain synapses and modulate neurotransmitter levels in synapses, preventing excitotoxicity and releasing various gliotransmitters with profound influences on neuronal dynamics. Astrocytes also maintain the blood-brain barrier and regulate cerebral blood flow through neurovascular coupling, responding to neuronal activity and adjusting blood vessel diameter.

Microglia in neural networks. Microglia, as the central nervous system's resident immune cells, are crucial for synaptic pruning, immune defense, and responding to neural injuries (Fields et al., 2015). They modulate synaptic activity and support neurogenesis. Disruptions in microglia's functioning can lead to neurological diseases like Alzheimer disease, and they play varying roles in traumatic brain injury and synaptic plasticity.

Oligodendrocytes in neural networks. Oligodendrocytes are key for myelination in the central nervous system, wrapping axons with myelin sheaths for efficient signal transmission (Fields et al., 2015). Myelination begins prenatally and is influenced throughout aging by environmental factors. Oligodendrocytes are crucial for saltatory conduction and are dynamically regulated by neuronal activity, indicating their role in neural plasticity.

Vascular contributions to neural networks. Vascular components are essential for supporting neural networks, with neurovascular interactions forming a crucial metabolic network (Fields et al., 2015). Astrocytes regulate cerebral blood flow, and neural activity influences vascular patterning. Vascular cells also contribute to neuronal development and differentiation.

Astrocytic networks as integral pathways of information transfer. To go a step further, it has been shown that astrocytic gap-junction networks offer a parallel and alternative path for information transfer (not necessarily through computations) within the brain alongside neuronal pathways (De Pittà, 2020; De Pittà & Berry, 2019; Fields et al., 2015; Kastanenka et al., 2020; Kiyoshi & Zhou, 2019; Stephan et al., 2021). These astrocytic networks are posited to cover the whole-brain and naturally encompass all the temporal scales mentioned above and even more (De Pittà, 2020; Fields et al., 2015). Moreover, the fact that astrocytic networks mediate neurovascular couplings adds yet another dimension whereby the properties of the vascular network itself (e.g., including the cross-sectional area, length, and elasticity of vessels, the heterogeneity of the vascularization of brain regions, e.g., see Figure 1.11) constrain neural dynamics (L.-P. Bernier et al., 2021; M. Bernier et al., 2018; Hösli et al., 2022; Reichold et al., 2009; Schaeffer & Iadecola, 2021; Tesler et al., 2023; Uludağ & Blinder, 2018) in a non-trivial way. This means that the complete knowledge of all structural paths amongst and between glia and neurons do not represent all the possible ways information transfer may be constrained. Finally, dynamic diffusion-based information transfer (e.g., as discussed earlier with neuromodulators) are also prominent in the brain (Marder, 2012; Pacholko et al., 2020).

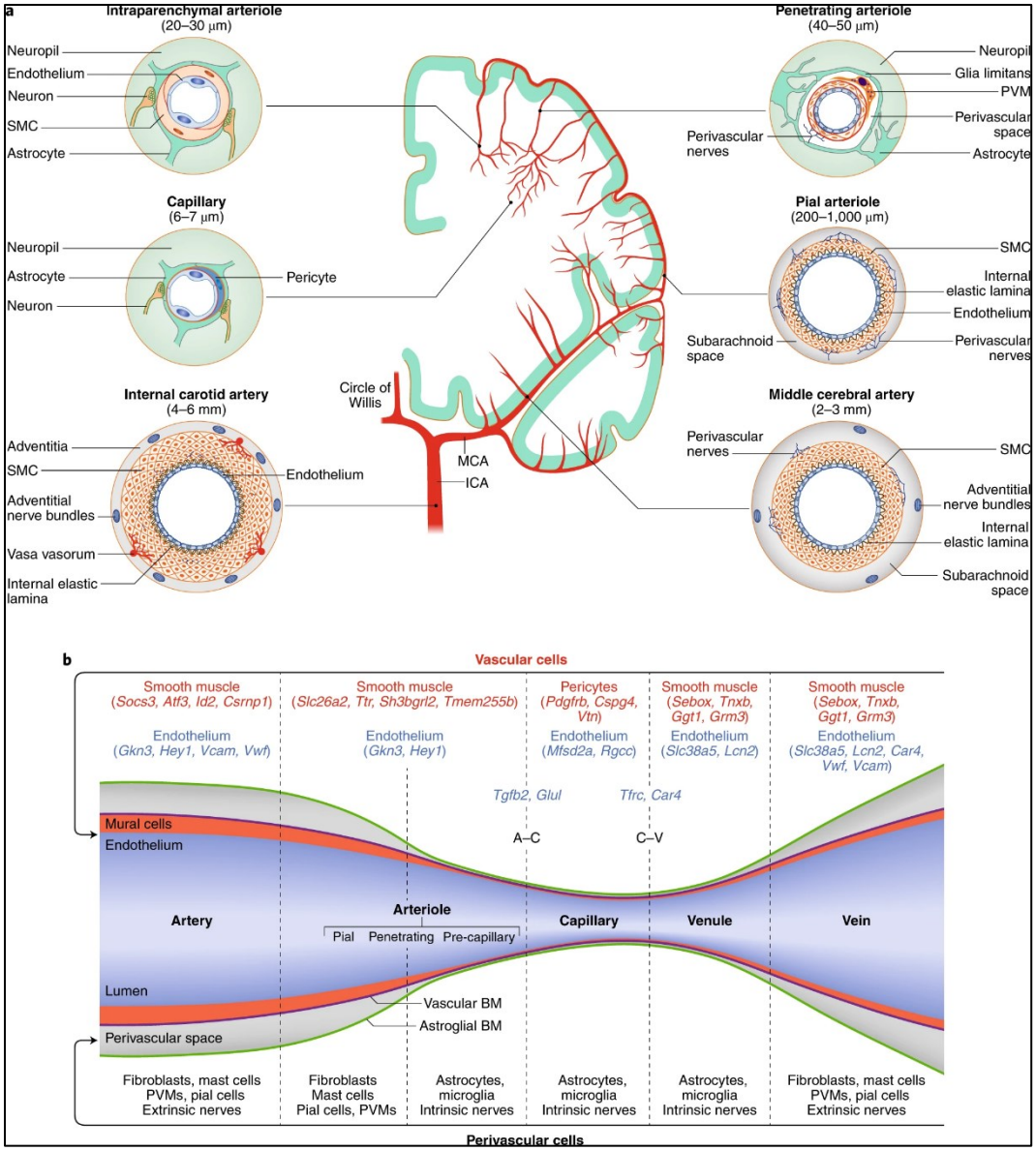

Figure 1.11. Segmental heterogeneity of cerebral arteries and diversity of vascular and perivascular cells. Caption and figure from: (Schaeffer & Iadecola, 2021). Permission obtained. — (a) The internal carotid artery has a thick layer of SMCs surrounded by nerves arising from cranial autonomic ganglia (extrinsic innervation) embedded in perivascular connective tissue (adventitia). The internal elastic lamina separates SMCs from the endothelial cell monolayer. In the middle cerebral artery (MCA) and pial arteriolar branches, the SMC layer becomes progressively thinner, and a perivascular nerve plexus surrounds the vascular wall. Penetrating arterioles dive into the substance of the brain surrounded by a perivascular space where perivascular macrophages (PVMs) and other cells reside. As the vessel becomes smaller (intraparenchymal arterioles), the vascular basement membrane fuses with the glial basement membrane and perivascular nerves are replaced by nerve terminals from interneurons or subcortical pathways (intrinsic innervation). In capillaries, SMCs are replaced by pericytes. Vascular diameters indicated under the vascular segments refer to the human cerebral circulation. Venous SMCs are morphologically, functionally and molecularly distinct from arterial SMCs. (b) Each segment of the cerebrovascular tree is characterized by diverse vascular and perivascular cells. The vascular and astroglial membranes delimit the perivascular space, which disappears when these membranes fuse together. Pial arterioles give rise to penetrating arterioles, the first-order branch of which is defined as precapillary arterioles (Hartmann et al., 2021). For mural and endothelial cells, genes enriched in each vascular segment are also indicated. For SMCs, the database from ref. (Vanlandewijck et al., 2018) was used, in which segmental assignment was validated by in situ hybridization. For endothelial cells, ref. (Kalucka et al., 2020) was

used, in which the segmental assignment was predicted in silico. A–C represents marker endothelial genes at the arteriolar–capillary transition and C–V at the capillary–venular transition. BM, basement membrane; ICA, internal carotid artery.

Spatiotemporal scales of neuro-glial–vascular interactions in aging and disease. In anticipation for the discussion chapter of this thesis, it is worth briefly mentioning the spatiotemporal scales of the aging brain in a context where lifestyle factors including diet, physical and mental exercise, and sleep contribute to shaping the connectome. This adds yet another dimension to the complex interplay between neurons, glial cells, and vascular elements within neural networks (e.g., see Figure 1.12). Indeed, in the context of brain aging and susceptibility to neurodegenerative diseases, the coupling between neurons, glial cells, and vascular components take other forms than the ones described earlier (Mattson & Arumugam, 2018). Neurons undergo functional decline and degeneration, significantly impacting synaptic transmission and cognitive capabilities. Glial cells assume pivotal roles in maintaining brain homeostasis, but their altered functions in aging can contribute to inflammatory processes and exacerbate neuronal damage. Neuroinflammation, primarily mediated by microglial activation, is a key pathological feature in aging brains and neurodegenerative diseases. Furthermore, vascular dysfunctions, such as impaired blood flow and blood-brain barrier breakdown, further contribute to the pathophysiology of neurodegenerative conditions. Collectively, these interdependent roles which are profoundly modulated by lifestyle factors, and which reflect spatial interactions extending from the subcellular level to encompass large-scale networks throughout the brain as well as temporal interactions ranging from milliseconds to years, underscore the complexity of brain aging and the pathogenesis of neurodegenerative diseases.

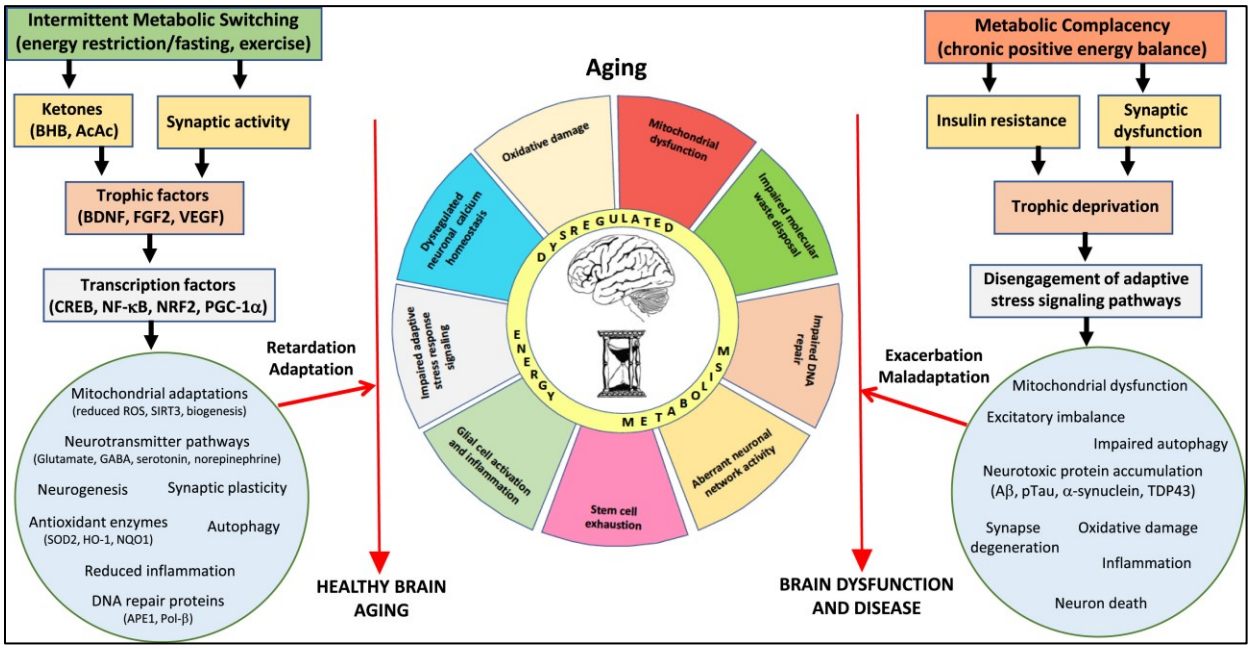

Figure 1.12. Working model for how intermittent metabolic challenges bolster brain health during aging, whereas a chronic positive energy balance hastens brain aging and associated brain diseases. Caption and figure from: (Mattson & Arumugam, 2018). Permission obtained. — Left: eating and lifestyle patterns that result in intermittent depletion of liver glycogen stores and mobilization of fatty acids to generate ketones (fasting and exercise) also typically increase neuronal network activity in many brain regions. Signaling pathways are activated in brain cells that upregulate the expression of trophic factors and activate transcription factors that induce the expression of genes encoding proteins that enhance neural plasticity and resilience during aging. These adaptations to intermittent metabolic switching

include mitochondrial biogenesis and stress resistance; adaptive modifications of neurotransmitter signaling pathways; upregulation of autophagy, antioxidant defenses, and DNA repair; stimulation of neurogenesis; and suppression of inflammation. In these ways intermittent metabolic switching counteracts core brain aging mechanisms, thereby slowing age-related declines in neurological function and reducing the risk of AD, PD, and stroke. Right: sedentary overindulgent lifestyles accelerate brain aging and increase the risk of AD, PD, and stroke. A chronic positive energy balance results in metabolic morbidity (insulin resistance and dyslipidemia) and reduced activation of signaling pathways that promote synaptic plasticity and cellular stress resistance. As a consequence, neurons suffer: impaired mitochondrial function, autophagy, and DNA repair; excessive oxidative stress; dysregulated neuronal network activity and Ca^{2+} homeostasis; the accumulation of potentially toxic protein aggregates; and inflammation. In these ways, metabolic complacency accelerates age-related decrements in brain function and increases the risk of AD, PD, and stroke.

Glial contributions to brain structures. Highly relevant to this thesis is how brain architecture involves an intricate interplay between white-matter axons, cortical folding, and glia (notably, radial glia and astrocytes). Radial glial cells not only provide structural support for neuron migration but also regulate neuronal proliferation and contribute to mechanical forces required for cortical folding (Van Essen, 2020). *Astrocytes*, serve as stem cells in neurogenic regions of the adult brain, like the hippocampal dentate gyrus, and contribute to the generation of new neurons (Morrens et al., 2012). These glial cells create an environment that supports neurogenesis and are themselves generated alongside new neurons. This ongoing neurogenesis in adulthood is linked to cognitive functions and could be related to the structural changes observed in gyrification.

Recent research emphasizes that understanding these dynamics is key to unraveling the complexities of not only brain development but also cognitive ability throughout lifespan, particularly in species with highly folded cortices like humans (Pang et al., 2023; Van Essen, 2020). Disruptions in these processes have profound implications in neurodevelopmental and neuropsychiatric disorders, highlighting the significance of glia in brain architecture. Additionally, though this is of lesser importance, these processes have direct consequences on the ability to non-invasively image electrophysiological activity, as I will detail later.

Concerning the relation between white-matter axons and cortical folding, white-matter axons facilitate communication between brain regions and crucially contribute to the brain's structural and functional connectivity, but the relationship between axonal arrangement and cortical folding is nuanced. For instance, white matter wiring significantly influences gray matter and folding patterns to the extent that diffusion tensor imaging data can be used to predict T1-weighted data (Zaman et al., 2020). Similarly, the interplay between cerebral cortex growth and axonal fiber tension has been identified as a key factor in the formation of regular cortical folding patterns, with neural wiring possibly being the major regulator of these patterns (Chavoshnejad et al., 2021). Conversely, tension-induced fiber growth plays a role in white matter organization during brain folding, with mechanical feedback contributing to brain connectivity (Garcia et al., 2021).

Regarding the relation between glia and cortical development, advances in imaging, genetics, and molecular biology have deepened our understanding of glial cells in cortical folding. For instance, tension-based morphogenesis is a significant concept that describes how mechanical tension along axons, dendrites, and glial processes contributes to central nervous system morphogenesis, including cortical folding (Van Essen, 2020). Similarly, the *glial framework* concept in white matter tracts (which refers to the spatial alignment of astrocytes and myelinating oligodendrocytes along their neighboring axons) provides insights into white matter fiber architecture in human and primate brains, highlighting the significance of radial glia in guiding axonal orientations (Schurr & Mezer, 2021).

Beyond morphogenesis and development, it is worth also motivating further research on how the interplay between glial cells, white-matter axons, and cortical folding affect the large-scale brain

networks subserving behavior and cognition throughout lifespan (Pang et al., 2023). In the discussion chapter of this thesis, I will be specifically talking about the topology of astrocytic networks throughout the brain and its relationships with cortical folding, and how such topology support brain architectures. How this is relevant could be highlighted by few specialized research. For instance, during adolescence, age-related changes in cortical folding in the frontoparietal cortex have been shown to contribute to cognitive development in this period (Y. S. Chung et al., 2017). In mid-life adults, increased cortical gyrification, particularly in the frontal regions, is positively related to working memory and mental flexibility, suggesting that greater cortical folding is associated with better cognitive function (Gautam et al., 2015). More generally, the degree of gyrification, particularly in the neocortical regions, has been linked to general cognitive ability in humans. Regions like the prefrontal cortex, inferior parietal lobule, and temporoparietal junction, which show increased gyrification, are correlated with higher general cognitive ability (Gregory et al., 2016). Studies in schizophrenia, a condition marked by cognitive deficits, show a relationship between altered gyrification patterns and disruptions in neural connectivity (White & Hilgetag, 2011). How glial anatomy and function as well as neuron-glial interactions contribute to these structure-function relationships?

Altogether, these studies, amongst others (Llinares-Benadero & Borrell, 2019; Mota et al., 2019; Shinmyo et al., 2022), underscore the complex interplay between the structural features of the brain, such as gyrification, and the functional roles of glial cells in supporting neuronal health and neurogenesis, which are crucial for cognitive abilities throughout life. Further research in this area could provide deeper insights into how these relationships evolve in adulthood and contribute to cognitive resilience or decline.

1.2 Dynamical systems theory

Dynamical systems and differential equations. Dynamical systems theory fundamentally revolves around the concept of *differential equations*. These equations, typically denoted as $\mathrm{d}X/\mathrm{d}t = F_\mu(X)$, are the formal framework describing the temporal evolution of a system's *state variable* X (which quantifies the system's characteristics) in conformity with a *governing law* F_μ. Here, μ usually represents a constant vector-parameter, encapsulating certain system-specific parameters or external conditions. Generally, the analytical resolution of differential equations is a non-trivial if not impossible endeavor, instead, a triangulation of algebraic, geometric, and numerical methodologies is employed (Strogatz, 2018).

Phase space and trajectories. In a geometrical perspective, a system's solution can always be represented in a *phase space*. The phase space is the geometric space spanned by the state variables. For example, a one-dimensional system is represented on a phase line, while a two-dimensional system uses a phase plane. Each point in this space uniquely represents a system's *state*, and a *velocity vector* at any point in this space indicates the direction and magnitude of the system's *motion* (i.e., the change in the system's state) at that point. The collection of all such vectors constitutes a *vector field*. This vector field serves as a guide for the system's *flow* (i.e., the system's dynamics) which specifies how a system's state may evolve over time for all possible initial conditions. Given an initial condition, the system's unique solution traces out a curve in the phase space, known as *phase trajectory* or *orbit*, that follows the system's flow. The graphical representation of phase trajectories is termed *phase portrait*. These trajectories and portrait help in qualitatively predicting the system's dynamics and its sensitivity to initial conditions. It is noteworthy that this prediction approach does not require the analytical solving of the differential equation, since the right-hand side of the differential equation, $F_\mu(X)$, provides the velocity vectors. As trajectories evolve, they tend to converge to specific sets known as *attractors*. These attractors can take various forms, such as *fixed-points*, *limit cycles*, or *strange attractors*, each with distinct characteristics. A fixed-point attractor corresponds to a steady state or equilibrium point, where the system settles into a stable configuration. Limit cycles represent simple closed orbits leading to periodic oscillations in the system. Strange attractors are more complex, characterized by a fractal structure, and they signify *chaotic* behavior, where the system exhibits deterministic yet aperiodic oscillations. An attractor is considered *structurally stable* if small changes in the system's parameters lead to only small changes in its form. When a system contains multiple attractors, it exhibits *multistability*, meaning that the system's long-term behavior depends on its initial conditions. Each attractor is associated with a *basin of attraction*, comprising all initial conditions that eventually lead to that attractor. These basins are separated by *boundaries*, which can sometimes be fractal in nature. The complexity of basin boundaries is essential for understanding the predictability and stability of dynamical systems (e.g., see (Dudkowski et al., 2016)). Figure 1.13 illustrates the main concepts discussed thus far.

Bifurcation analysis. Bifurcation analysis (Strogatz, 2018) is crucial for cataloging the dynamic behaviors of a system, particularly in observing changes such as the emergence or disappearance of oscillatory behavior. This process involves systematically characterizing the different types of solution X that arise for different values of the parameter μ. A bifurcation occurs when a qualitative change in the system's output is observed due to a smooth change in μ, indicating a transition in the system's dynamical state.

Bifurcation types. Bifurcations are either *local* or *global*, based on whether they can be detected by stability analysis near fixed points. They are also characterized by their *codimension*, i.e., the number of parameters that must be varied for the bifurcation to occur. This classification (Strogatz, 2018) helps in comprehensively understanding the dynamics and potential transitions in the system (though it has limitations, as I will explain later).

In more details, local bifurcations occur near fixed points and are detectable through stability analysis, often involving the evaluation of the system's Jacobian matrix. These bifurcations are characterized by changes in asymptotic stability, indicated by the crossing of the real parts of one or several eigenvalues of the Jacobian matrix through zero. This leads to changes in the local stability of the system's fixed points or limit cycles. Local bifurcations in models of neural populations encompass a variety of types such as Andronov–Hopf, saddle-node, saddle-focus, saddle-saddle, pitchfork, transcritical, and period-doubling bifurcations (e.g., see Figure 1.14). Of theses examples, all are typically codimension-1 bifurcations except for the saddle-focus and saddle-saddle. Altogether, these types of bifurcations are essential for understanding complex behaviors in neural population models, as they represent different ways in which the dynamics of these systems can change in response to variations in parameters.

- *Andronov–Hopf bifurcations.* These arise when a pair of complex conjugate eigenvalues traverse the imaginary axis. This marks a pivotal change from a stable state (indicated by a negative real part) to cyclic behavior (positive real part), often resulting in system oscillations. The harmonicity of these oscillations is influenced by the system's amplitude and degree of nonlinearity.
- *Saddle-node and saddle-focus bifurcations.* Known alternatively as *tangential or fold bifurcations*, they occur when a stable fixed point (node or focus) and an unstable fixed point (saddle) collide and annihilate each other due to parameter variations.
- *Saddle-saddle bifurcations:* These take place when the colliding fixed points are both saddle points. At the critical juncture of these bifurcations, the points become non-hyperbolic, characterized by a zero second derivative, indicating a loss of asymptotic stability.
- *Pitchfork bifurcations.* These occur in systems where there's a symmetry. A pitchfork bifurcation can be either supercritical or subcritical. In a supercritical pitchfork bifurcation, a stable fixed point bifurcates into two stable fixed points and one unstable fixed point as a parameter changes. In a subcritical pitchfork bifurcation, the opposite occurs: two unstable fixed points and one stable fixed point merge into a single stable fixed point as the parameter is varied.
- *Transcritical bifurcations.* These involve the exchange of stability between two intersecting fixed points as a parameter is varied. In this type of bifurcation, a stable and an unstable fixed point collide and swap their stability, meaning that the previously stable point becomes unstable and *vice versa*.
- *Period-doubling bifurcations.* Also known as *flip bifurcations*, these occur when a system with a periodic orbit (cycle) undergoes a bifurcation resulting in a new periodic orbit with double the period of the original. This type of bifurcation is often associated with the onset of chaos, as repeated period-doubling can lead to increasingly complex, chaotic behavior in the system.

Global bifurcations, also referred to as *catastrophic bifurcations*, necessitate a comprehensive analysis of the system's vector field, extending beyond the local vicinity of fixed points. These bifurcations, often involving interactions between larger invariant sets of the system, are marked

by significant alterations in the system's structure, characterized by the sudden emergence or disappearance of fixed points and limit cycles as parameters are smoothly varied. Such transformations indicate a fundamental change in the system's structural stability.

- A key family within global bifurcations is the *saddle family*, where the interaction and subsequent annihilation of colliding fixed points typify global bifurcation phenomena. An archetypal example of this is the *infinite period bifurcation*. In this scenario, a stable fixed point (either a node or focus) is linked to a saddle point through a specific path known as a *heteroclinic orbit*. As a system parameter is adjusted towards a critical value, these two fixed points converge progressively until they collide and cease to exist. Consequently, the heteroclinic orbit transforms into a periodic orbit, initiating continuous oscillations within the system. Conversely, approaching this bifurcation from the opposite parameter direction leads to a deceleration of oscillations, culminating in an infinite period at the critical point where the periodic orbit reverts to a heteroclinic orbit.
- Furthermore, global bifurcations encompass *homoclinic and heteroclinic bifurcations*. These involve interactions where periodic orbits either collide with saddle points (homoclinic) or with orbits from different saddle points (heteroclinic). Such collisions are instrumental in understanding the intricate dynamics of systems, including the transition to chaotic behavior.

To finish, when it is useful to consider higher-dimensional parameter spaces in the analysis of the behavior and stability of neural population models, the following higher codimension bifurcations typically occur.

- *Bautin (or generalized Hopf) bifurcation.* This bifurcation, occurring at codimension 2, is observed when an Andronov–Hopf bifurcation undergoes a transition from supercritical to subcritical due to the alteration of a second system parameter. In this scenario, the system experiences a change in the nature of the bifurcation, affecting the stability and type of periodic orbits that emerge.
- *Bogdanov–Takens bifurcation.* This bifurcation, also of codimension 2, is a critical point where Andronov–Hopf bifurcations, saddle-node bifurcations, and homoclinic curves intersect. This convergence signifies complex dynamical behaviors, including the potential for the emergence of homoclinic orbits and complex oscillatory patterns.
- *Cusp bifurcation.* Characterized as a codimension 2 bifurcation, the cusp bifurcation occurs when two branches of the saddle-node bifurcation curve meet tangentially. This interaction leads to the phenomenon of hysteresis, where the system's response to changing parameters exhibits a form of lag or delayed reaction.

Bifurcation diagrams. Bifurcation diagrams (Strogatz, 2018) are a crucial tool for investigating bifurcations in dynamical systems. In their simplest form, which pertains to codimension-1 bifurcations, these diagrams illustrate how stable and unstable fixed points (equilibrium points where the time derivatives of state variables are zero) and limit cycles (closed, repeating trajectories in state space) vary as a function of one or more system parameters. This representation allows for the visualization of how small changes in parameters can qualitatively change the behavior of a system and help in pinpointing exact values of parameters where qualitative changes in the system's behavior occur (i.e., the bifurcation points). Each type of bifurcation reviewed earlier has distinct characteristics that can be visually represented.

Limitations. Bifurcation analysis, as a qualitative approach is particularly useful in systems where exact solutions to the differential equations are complex or infeasible to obtain. However, it is also

essential to recognize that such predictions have limitations. For instance, in systems exhibiting chaotic behavior, small variations in initial conditions can lead to vastly different outcomes, a phenomenon known as sensitivity to initial conditions or the *butterfly effect* (Vannitsem, 2017). This sensitivity implies that long-term predictions in chaotic systems can be inherently uncertain, even though the systems are deterministic. Furthermore, in complex systems, the dynamics can be influenced by various factors, including nonlinear interactions, which may not be fully captured by simple trajectory analysis. Therefore, while trajectory analysis in phase space is a powerful tool, it must be used with an understanding of its limitations and in conjunction with other analytical and computational methods (Breakspear, 2017; Kotyrba, 2015; Strogatz, 2018).

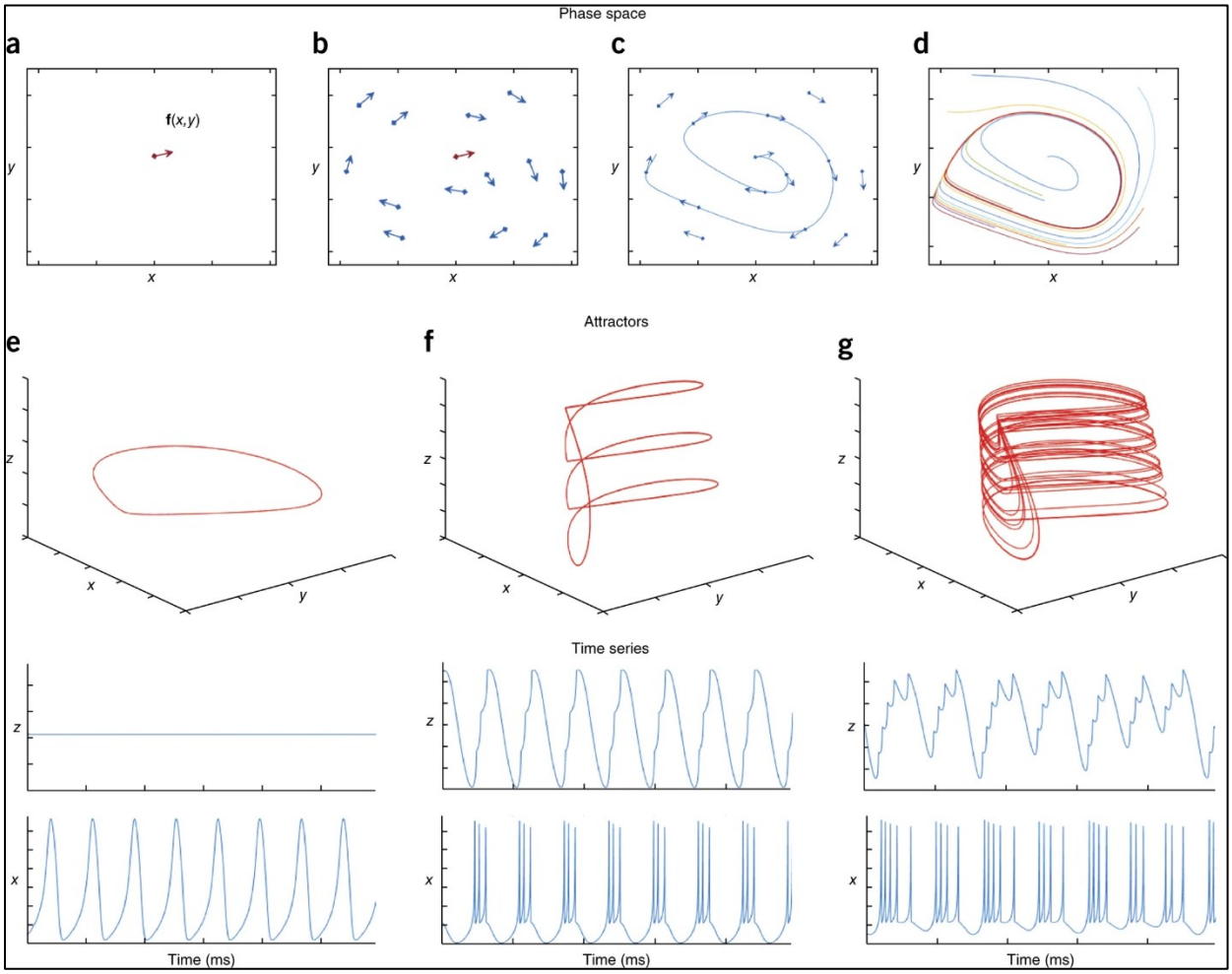

Figure 1.13. Dynamical system. Caption and figure from: (Breakspear, 2017). Permission obtained. — A dynamical system is defined by a differential equation $\mathrm{d}X/\mathrm{d}t = f(X)$. Here X is composed of the two state variables x (the cell membrane potential) and y (the conductance of a fast-depolarizing ion channel). (a) The phase space is the geometric space spanned by the state variables: in this case, simply the Cartesian plane composed of axes for x and y. The dynamical system then defines a vector of length and direction given by $f(x; y)$ at each point—that is, for each combination of membrane potential and ion channel conductance. (b) The flow (also called a vector field) is the set of all such vectors and shows how the dynamical system will flow through phase space: here, a distinctive clockwise flow is evident. (c) An orbit is a solution to the flow—a smooth line that is tangent to the flow. (d) Orbits converge onto the attractors, the long-term solutions of the system. Here there is just a single limit cycle attractor (red) reached from many different starting points (other colors). (e–g) By adding a slow recovery variable z (middle), the system can show a simple limit cycle (e, top), corresponding to regular spiking (e, bottom); or a more complex limit cycle (f,

top), yielding regular bursting (f, bottom); or a chaotic (strange) attractor (g, top) with irregular spiking (g, bottom) when the time scales of the spiking and recovery variable mix.

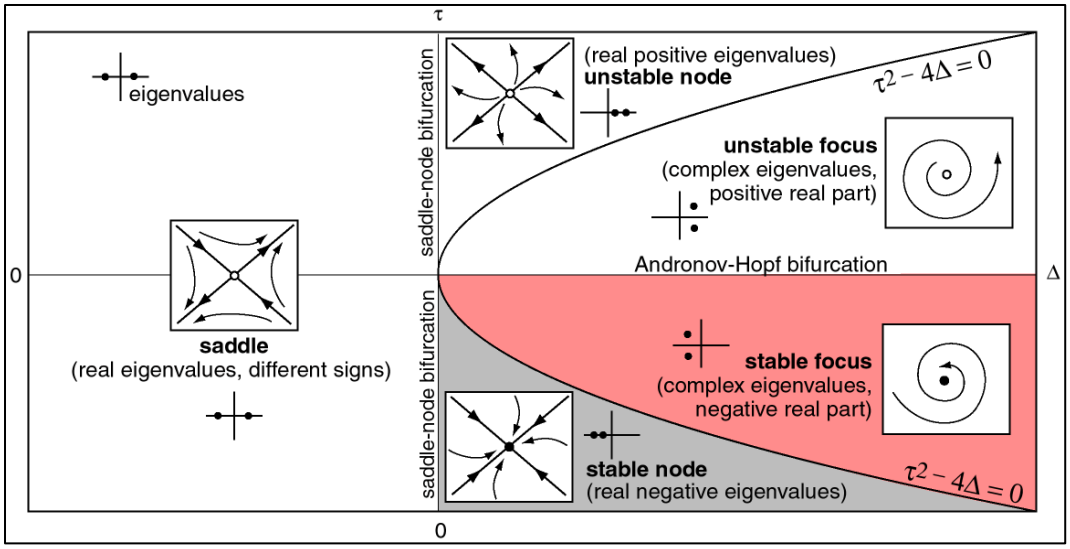

Figure 1.14. Equilibria of a two-dimensional dynamical system. Caption and figure from: (Izhikevich, 2007). Publisher's permission: http://creativecommons.org/licenses/by-nc-sa/3.0/deed.en_US. — Classification of equilibria of a two-dimensional dynamical system according to the trace (τ) and the determinant (Δ) of the Jacobian matrix. The shaded region corresponds to stable equilibria.

1.3 Neural network modelling: from the past 50 years to the present

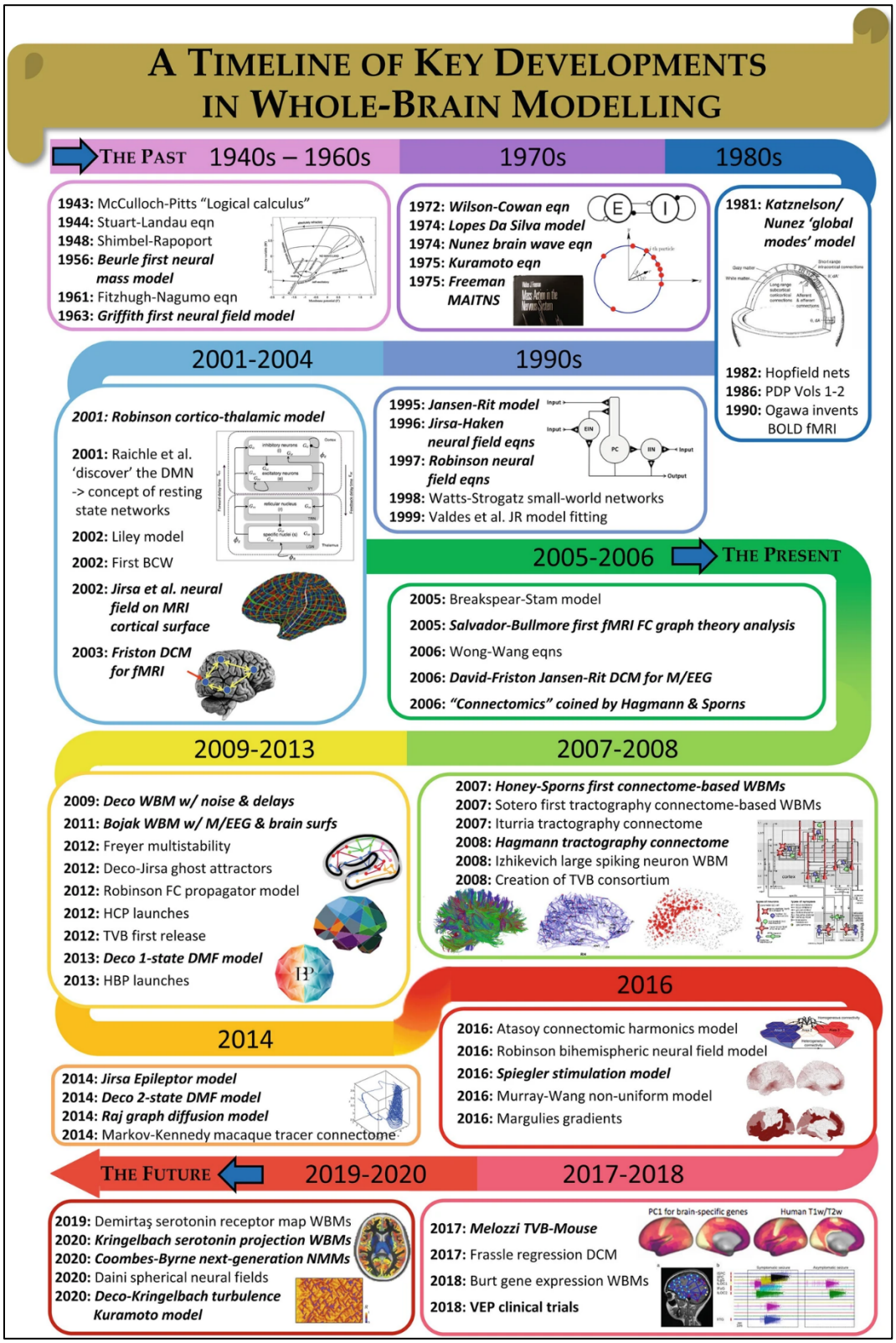

Figure 1.15. Timeline of major developments in and pertaining to whole-brain modelling. Caption and figure from: (Griffiths et al., 2022). Permission obtained. — Shown are a selection of key publications and events that have had a

major influence on the development of whole-brain modelling and adjacent fields. Particularly important entries are indicated in bold italics. The earliest neural population model formulations were outlined by (Shimbel & Rapoport, 1948), (Beurle, 1956), and (Uttley, 1955), building on the seminal work of (McCulloch & Pitts, 1943). Arguably most central in the entire timeline is the period 1970–1975, during which the key contributions of (Wilson & Cowan, 1972), (F. H. Lopes da Silva et al., 1974), (Freeman, 1972), (Freeman, 1975), and (Nunez, 1974) were published.

The field of biophysical neural population modeling, which explores the collective behavior of neural assemblies (predominantly neurons), has a rich history that extends back to the 1940s (e.g., see Figure 1.15). This long-standing tradition of research has led to significant advancements in our understanding of neural dynamics at the population and whole-brain levels (Breakspear, 2017; Cook et al., 2022; Coombes & Wedgwood, 2023; Griffiths et al., 2022; Hutt, 2015; Liley, 2015).

In this section, history starts in the 1970s for the sake of conciseness, and the focus is on the seminal works of Wilson and Cowan, and Lopes da Silva and colleagues, whose pioneering models and perspectives have significantly shaped contemporary neural modeling practices (Griffiths et al., 2022). Notably, the Wilson–Cowan and Lopes da Silva models and their various modern variants or extensions are central to the current landscape of neural modeling (Breakspear, 2017; Cook et al., 2022; Coombes & Wedgwood, 2023; Griffiths et al., 2022; Hutt, 2015; Liley, 2015). These models uniquely encapsulate the collective dynamics of neuronal populations, arising from the intricate interactions of different neuronal subtypes. Additionally, while they share similarities with single-neuron behaviors, they offer a distinct perspective as their properties and behaviors are not entirely deducible from studies of individual neurons. The essence of these low-dimensional models lies in their ability to simplify neural complexity based on some neurobiological principles. They achieve this by representing the interplay between excitatory and inhibitory neuron pools at a mesoscopic scale (see Figure 1.16 bottom) through average metrics or *mean fields*, representing for instance mean firing rates or mean soma membrane potentials (e.g., as illustrated in Figure 1.16 top). Such mesoscale models are attractive because they align with the widely accepted view that behavior is a manifestation of macroscopic neuronal activity, and their spatial domain closely matches the millimeter to centimeter resolution of non-invasive neuroimaging techniques like functional magnetic resonance imaging, electroencephalography, and magnetoencephalography, thereby making them particularly relevant for human brain function studies (Breakspear, 2017; Cook et al., 2022; Coombes & Wedgwood, 2023; Griffiths et al., 2022; Hutt, 2015; Liley, 2015).

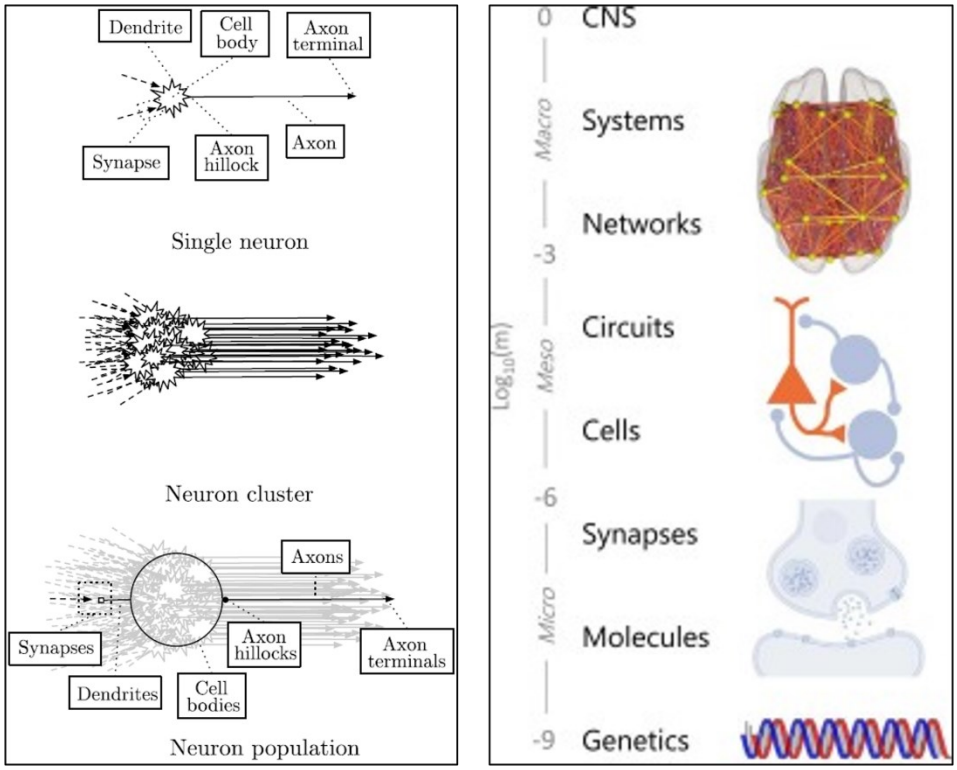

Figure 1.16. Diagram of neural mass approximation and hierarchical spatial organization of the brain. Left figure. Caption and figure adapted from: (Cook et al., 2022). Publisher's permission: https://creativecommons.org/licenses/by/4.0. — Diagram of neural mass approximation. A single neuron description starts on the top, where models such as Hodgkin–Huxley are appropriate to describe quantities such as membrane potential and spike frequency. Increasing in scale, abstracted neuronal models such as leaky integrate-and-fire are used to model signal transmission amongst interconnected neurons. At larger scales on the bottom, individually addressing neurons becomes mathematically intractable, so a continuum approximation is typically made. Models at this scale include neural field models and neural mass models, which describe the evolution of aggregate quantities across different populations of neurons. Neurons are grouped together by the type and time-scale of post-synaptic signals they send. Aggregate quantities used in ensemble descriptions of neural dynamics include mean membrane potential and mean spike rate of sub-populations, which are closely related by a sigmoidal wave-to-pulse transfer function. | Right figure. Caption and figure from: (Lawn et al., 2023). Publisher's permission: http://creativecommons.org/licenses/by/4.0/. — The hierarchical micro-, macro-, and meso-scale organisation of the brain. The brain is a complex system whose constitutive parts span vastly different spatial resolutions. Here, these are described as a hierarchy with interactions across micro-, meso-, and macro-scale levels. The definitions of these levels are somewhat arbitrary, but this loose demarcation has proven conceptually useful (Fornito et al., 2019; Suárez et al., 2020; Swanson & Lichtman, 2016; van den Heuvel et al., 2019; Wong-Lin et al., 2021).

In delving deeper into this thesis, it is also pertinent to clarify certain terminologies that have emerged in the field of modeling mesoscopic and macroscopic neural dynamics, and which have been used interchangeably at times, leading to some confusion. While terms like *neural mass models*, *neural population models*, *neural field models*, and *mean field models* are related, they each have distinct features. Adopting the classification proposed by Bojak (Bojak, 2014), neural mass models and neural population models are synonymous. These models, originating from Freeman's pioneering work on neural mass action (Freeman, 1975), describe the dynamics of neuronal populations at a singular spatial point, emphasizing collective temporal behavior while overlooking spatial variation. They are particularly useful in EEG and MEG signal simulations, offering insights into the temporal patterns of brain activity (Byrne et al., 2020, 2022). Neural field models represent a broader category, encompassing the attributes of neural mass models while also

incorporating the spatial characteristics of neural activity. This category is instrumental in unraveling spatially dependent neural phenomena, such as the propagation of neural waves, thereby providing a more comprehensive understanding of neural dynamics across both space and time (Byrne et al., 2020, 2022). Mean field models in neuroscience is a class of models that simplify neural network dynamics by averaging neuronal behaviors. This approach is conceptually different from the mean-field approximation in statistical mechanics, which simplifies a network of interacting neurons to a single average unit (Martínez-Cancino & Sotero Diaz, 2011), even though recent publications use this latter concept in yet another way (Bandyopadhyay et al., 2022), indicating a dynamic and evolving usage of the term.

1.3.1 Neural mass models

Neural mass modelling is a sophisticated and refined framework that facilitates a nuanced understanding of localized mesoscale neural dynamics (Breakspear, 2017; Cook et al., 2022; Coombes & Wedgwood, 2023; Griffiths et al., 2022; Liley, 2015). It also adeptly navigates the intricacies inherent in spatially extended neural populations such as the neocortex (Breakspear, 2017; Cook et al., 2022; Coombes & Wedgwood, 2023; Griffiths et al., 2022; Liley, 2015). The framework involves abstracting from the intricate neurophysiology of individual neural cells (primarily neurons in historical contexts) to elucidate collective neural behavior through meticulous mathematical formulations spanning various layers of abstraction, from fully phenomenological to rigorously exact, all aligned with the principles of physics (Breakspear, 2017; Cook et al., 2022; Coombes & Wedgwood, 2023; Griffiths et al., 2022; Liley, 2015).

This modelling approach relies on two fundamental tenets (Liley, 2015): on the one hand, there is a deliberate decision to consider the enumeration of individual cells within a specified population as unnecessary; on the other hand, it posits that structural connectivity among these cells is both random and nonspecific, eliminating the need for detailed inner circuitry specifications. Consequently, the complexities associated with spatial and temporal intricacies in neural activity within a delimited population are set aside in favor of characterizing the dynamic state through effective averages (mean fields) or *macrostates* (Liley, 2015). Critically, this characterization assumes negligible interneural propagation delays, as described in the next sections, and lacks specific spatial structures in connectivity (Liley, 2015). Accordingly, extensions must be made when modeling spatially extended neural populations, such as the neocortex, where there is a discernible spatial organization in neural connectivity (Liley, 2015). For instance, see also Sections 1.3.7 and 1.3.8, models must either instantiate networks of neural populations or posit a continuous spatial distribution with interactions governed by spatially dependent connectivity functions (Liley, 2015).

Within the *neuronal* mass modelling context, the notion of a “mean neuron” materializes as a mathematical abstraction resulting from spatially averaging functionally homogeneous and densely coupled neurons across a defined physical domain where the hypotheses of “dispensable inner circuitry details” as well as “uncorrelated membrane potential fluctuations due to spiking” both hold (Liley, 2015). The dynamics of neural populations are then conceptualized as a cascade of physiological transformations, encompassing synaptic input, transduction of postsynaptic potentials, neuronal cable delays, and action potential generation; all encapsulated within the representation of a mean neuron (Liley, 2015). The pioneering works of Wilson and Cowan (Wilson & Cowan, 1972) illustrate well these concepts.

Wilson and Cowan derived a pair of coupled nonlinear ordinary differential equations describing the short-time averaged dynamics of the spatial mean firing rates of interacting excitatory and inhibitory neuronal populations. Of crucial significance was their introduction of the sigmoidal firing rate function and an explicit cortical meso-circuit quantitatively defined by population (synaptic) connectivity coefficients. These two conceptual innovations are what virtually all subsequent mean field formulations have retained. The sigmoidal firing rate function formally represents the relationship between mean (soma) neuronal population membrane potential and the generation of axonal spike trains, and the cortical meso-circuit captures all possible feedforward and feedback connections between spatially circumscribed populations of excitatory and inhibitory neurons.

1.3.2 The Wilson–Cowan model

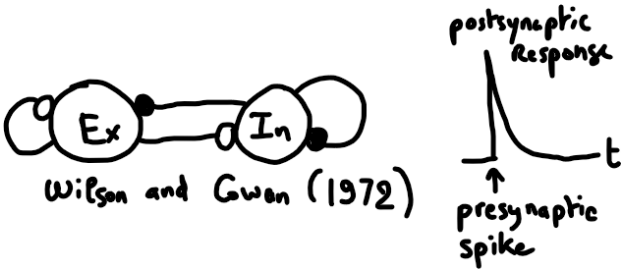

Figure 1.17. The Wilson–Cowan mass model. Schematic representation of the Wilson–Cowan neuronal population model circuit topology and the form of its postsynaptic response (Wilson & Cowan, 1972). This model considers functionally differentiated excitatory (Ex) and inhibitory (In) neuronal populations. Open circles represent excitatory connections and filled circles inhibitory ones. Figure inspiration from: (Liley, 2015).

Wilson and Cowan modelled cortical and thalamic neural tissue as comprised of two interacting, but functionally distinct, excitatory (Ex) and inhibitory (In) neuronal subpopulations. They derived the following pair of equations describing, in an inherently straightforward way, the proportion of excitatory or inhibitory cells firing per unit time ($F_\bullet$) at time $t + \tau_\bullet$:

$$\begin{aligned} F_{\mathrm{Ex}}(t+\tau_{\mathrm{Ex}}) &= \left(1 - \int_{t-r_{\mathrm{Ex}}}^{t} F_{\mathrm{Ex}}(T)\,\mathrm{d}T\right) S_{\mathrm{Ex}}\big(V_{\mathrm{Ex}}(t)\big) \\ F_{\mathrm{In}}(t+\tau_{\mathrm{In}}) &= \left(1 - \int_{t-r_{\mathrm{In}}}^{t} F_{\mathrm{In}}(T)\,\mathrm{d}T\right) S_{\mathrm{In}}\big(V_{\mathrm{In}}(t)\big) \end{aligned} \tag{1.1}$$

where the first factor in both equations represent the proportion of excitatory or inhibitory cells which are sensitive (i.e., not refractory) at time t, and the second factors maps, through postulated subpopulation response functions ($S_\bullet$), the average levels of excitation within the subpopulations ($V_\bullet$) at time t to expected proportion of cells receiving at least threshold excitation per unit time. The constants $r_\bullet$ are the absolute refractory periods and the constants $\tau_\bullet$ are synaptic operating delays (i.e., time lapses between excitation reaching threshold and the consequent appearance of action potentials). It is noteworthy that in these equations, it is posited that the probability of a neuron being sensitive to input is independent of the probability that it is currently excited above its threshold. This assumption allows for the representation of neuronal firing rates, $F_\bullet$, as the product of these two probabilities. While acknowledging that this assumption may not always hold, given the likely correlation between a neuron's recent firing activity and its subsequent propensity to fire, Wilson and Cowan argued that it serves as a reasonable approximation in the context of a densely interconnected population of neurons. Indeed, within large neuronal populations featuring

random and nonspecific connectivity, excitability levels of subpopulations are subject to spatial and temporal fluctuations, and the thresholds for activation among individual neurons are also variable. This inherent variability across the population justifies the simplifying assumption of negligible correlation and thereby statistical independence between sensitivity and excitation above threshold.

The subpopulation response functions ($S_\bullet$) are typically given a sigmoidal or logistic form, consistent with empirical observations, and such functions formally represent the relationship between mean (soma) neuronal population membrane potential and the generation of axonal spike trains. For example,

$$S_\bullet(v) = \frac{S_\bullet^\infty}{1 + \mathrm{e}^{-\gamma_\bullet(v-\theta_\bullet)}} \tag{1.2}$$

which for large v saturates to $S_\bullet^\infty$ (for Wilson–Cowan model, $S_\bullet^\infty = 1$), and where $\theta_\bullet$ are thresholds at which the value $S_\bullet^\infty/2$ (i.e., here, 0.5) is attained, and $\gamma_\bullet$ are positive steepness parameters. Noting that, this functional form is not derived from a biophysical model, rather it is seen as a physiologically consistent choice. Wilson and Cowan called $S_\bullet$ response functions because these functions give the expected proportion of cells in a subpopulation which would respond to a given level of excitation if none of them were initially in the absolute refractory state.

The average levels of excitation within the subpopulations ($V_\bullet$) at time t, typically incorporate the interactions between subpopulations whereby excitatory (inhibitory) neurons make their neighbors more (less) likely to become active. Concretely, assuming that individual cells sum their inputs in an all-to-all topology of interactions (as in Figure 1.17), they take the following convolution integral forms:

$$\begin{aligned} V_{\mathrm{Ex}}(t) &= \int_{-\infty}^{t} h_{\mathrm{Ex}}(t-T)\Big(C^{\mathrm{Ex}\to\mathrm{Ex}}F_{\mathrm{Ex}}(T) - C^{\mathrm{In}\to\mathrm{Ex}}F_{\mathrm{In}}(T) + q_{\mathrm{Ex}}(T)\Big)\,\mathrm{d}T \\ V_{\mathrm{In}}(t) &= \int_{-\infty}^{t} h_{\mathrm{In}}(t-T)\Big(C^{\mathrm{Ex}\to\mathrm{In}}F_{\mathrm{Ex}}(T) - C^{\mathrm{In}\to\mathrm{In}}F_{\mathrm{In}}(T) + q_{\mathrm{In}}(T)\Big)\,\mathrm{d}T \end{aligned} \tag{1.3}$$

where the positive constants $C^{▲\to■}$ describe the synaptic connection density strengths from subpopulation of type ▲ to type ■, the time-varying quantities $q_\bullet$ encode external inputs (e.g., from distant brain regions) to each subpopulation, and the convolution kernels $h_\bullet$ are the subpopulation postsynaptic impulse responses.

From a physiological perspective, the time course of the postsynaptic potential felt at the neuronal soma represents a combination of the kinetics of neurotransmitter action such as glutamate and GABA, and neuronal cable delays. For instance, if these effects are ignored, the Dirac delta impulse response corresponding to the arrival of a single presynaptic action potential become the simplest of all models (1.4).

$$h_\bullet(t) = \Gamma_\bullet \delta(t) \tag{1.4}$$

where $\Gamma_\bullet$ is the peak amplitude (positive for excitatory postsynaptic potentials, negative for inhibitory postsynaptic potentials) and δ is the Dirac delta function. In practice, it is desirable to describe the postsynaptic impulse responses (also called synaptic filters) more flexibly, and so

common choices include the exponential function (1.5), the difference of two exponential functions (1.6), and Rall's α-function (1.7).

$$h(t) = \frac{1}{\mu} \mathrm{e}^{-t/\mu} \Theta(t) \tag{1.5}$$

$$h(t) = \frac{1}{\mu - \tilde{\mu}} \left(\mathrm{e}^{-t/\mu} - \mathrm{e}^{-t/\tilde{\mu}} \right) \Theta(t) \tag{1.6}$$

$$h(t) = \frac{1}{\mu^2} t \mathrm{e}^{-t/\mu} \Theta(t) \tag{1.7}$$

where e is Euler's number, Θ is the Heaviside step function, and the parameters μ and $\tilde{\mu}$ are time constants. In Equation (1.6), μ is a decay time constant while $\tilde{\mu}$ is a rise time constant, and $\mu > \tilde{\mu}$.

For instance, assuming unitary Dirac delta impulse responses, and by reinterpreting $\tau_\bullet \ll r_\bullet$ as the combined characteristic time scale for uniform synaptic, cable, and axonal delays, we obtain from (1.1) and (1.3), after first-order Taylor expansion about $\tau_\bullet$:

$$\begin{aligned} \tau_{\mathrm{Ex}} \dot{F}_{\mathrm{Ex}} &= -F_{\mathrm{Ex}} + (1 - r_{\mathrm{Ex}} F_{\mathrm{Ex}}) S_{\mathrm{Ex}} (C^{\mathrm{Ex}\to\mathrm{Ex}} F_{\mathrm{Ex}} - C^{\mathrm{In}\to\mathrm{Ex}} F_{\mathrm{In}} + q_{\mathrm{Ex}}) \\ \tau_{\mathrm{In}} \dot{F}_{\mathrm{In}} &= -F_{\mathrm{In}} + (1 - r_{\mathrm{In}} F_{\mathrm{In}}) S_{\mathrm{In}} (C^{\mathrm{Ex}\to\mathrm{In}} F_{\mathrm{Ex}} - C^{\mathrm{In}\to\mathrm{In}} F_{\mathrm{In}} + q_{\mathrm{In}}) \end{aligned} \tag{1.8}$$

This pair of coupled ordinary differential equations is the well-known spatially lumped Wilson–Cowan equations (Wilson & Cowan, 1972).

It is noteworthy that in their original paper, Wilson and Cowan assumed a rapidly decaying exponential form for the postsynaptic impulse response, e.g., as given by Equation (1.5) instead of a Dirac delta impulse responses, and they dealt away with the integrals in Equation (1.1) and Equation (1.3) using the first mean value theorem for definite integrals (which is one procedure of time coarse graining), to end up with a mathematically equivalent system defined by Equation (1.8), of course up to multiplicative constants. Moreover, they assessed the appropriateness of the resulting system of ordinary differential equations by comparing solutions to Equation (1.1) with those obtained from Equation (1.8). The major difference that is observed between the two cases is that the solution to Equation (1.1) generally involves a damped oscillation with period equal to twice the refractory period, whereas the solution to Equation (1.8) approaches the same asymptotic value monotonically. Wilson and Cowan argued that the temporally coarse-grained equations are valid in physiologically reasonable conditions because the damped oscillations, being almost entirely dependent on the length of the absolute refractory period (1–2 ms), are not of great functional importance. In current practices of mesoscale modelling, the refractory periods are often if not always ignored (i.e., set to zero).

The system of equations defined by Equation (1.8) and subsequent extensions and modifications, are widely used in the modeling of coupled neuronal population activity. Additionally, there are direct extensions of these equations (Breakspear, 2017; Cook et al., 2022; Coombes & Wedgwood, 2023; Griffiths et al., 2022; Hutt, 2015; Liley, 2015; Wilson & Cowan, 1973) to continuously distributed populations of interacting excitatory and inhibitory neurons in planar sheets (i.e., accounting for spatial domain, through partial differential equations; see also Section 1.3.7).

In preparation for the model extensions to come below, it is worth discussing more about the postsynaptic impulse responses h. In general, h can be written as Green's function of a linear differential operator Q, so that:

$$Qh(t) = \delta(t) \tag{1.9}$$

In practice, the operator Q is found by taking the Laplace transform of h with respect to t and identifying, Laplace's variable s with $\mathrm{d}/\mathrm{d}t$, s^2 with $\mathrm{d}^2/\mathrm{d}t^2$, etc. For concrete examples, the operators associated with Equation (1.5), Equation (1.6), and Equation (1.7) are, respectively:

$$Q = \mu\left(\frac{1}{\mu} + \frac{\mathrm{d}}{\mathrm{d}t}\right) \tag{1.10}$$

$$Q = \mu\tilde{\mu}\left(\frac{1}{\mu} + \frac{\mathrm{d}}{\mathrm{d}t}\right)\left(\frac{1}{\tilde{\mu}} + \frac{\mathrm{d}}{\mathrm{d}t}\right) \tag{1.11}$$

$$Q = \mu^2\left(\frac{1}{\mu} + \frac{\mathrm{d}}{\mathrm{d}t}\right)^2 \tag{1.12}$$

With these formulations, integrals (i.e., in fact convolutions, herefrom denoted $*$) as in Equation (1.3) are readily replaced by differential equations, so that, for instance, if h is the α-function as defined in Equation (1.7), then:

$$V(t) = (F * h)(t) \Leftrightarrow \left(\frac{\mathrm{d}^2}{\mathrm{d}t^2} + \frac{2}{\mu}\frac{\mathrm{d}}{\mathrm{d}t} + \frac{1}{\mu^2}\right)V(t) = \frac{1}{\mu^2}F(t) \tag{1.13}$$

Using these formulations, the forthcoming sections will delve into voltage-based models, presenting an alternative to the Wilson–Cowan model, which is rate-based or activity-based. Unlike the Wilson–Cowan model, which is formulated in terms of firing rates, voltage-based models are described in terms of membrane potentials.

Before going to other models, it is interesting to portray some of the dynamical behaviors of the Wilson–Cowan model, following the preceding chapter on bifurcation theory.

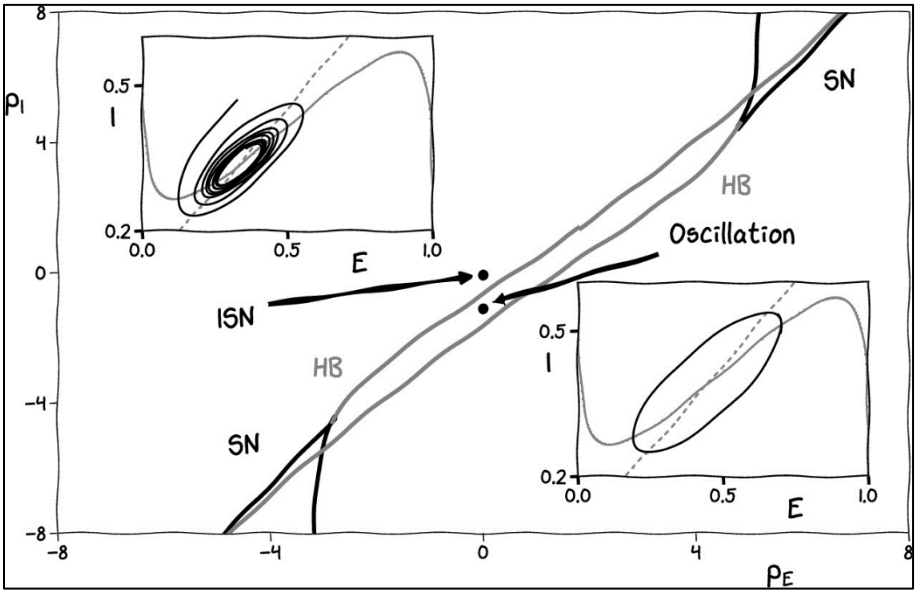

Figure 1.18. Bifurcation diagram of the Wilson–Cowan mass model. Caption and figure from: (Coombes & Wedgwood, 2023), in the chapter "*Population models*". Permission obtained. — Hopf (HB) and saddle-node (SN) bifurcation curves in the Wilson–Cowan model. Here, $S_\bullet(V) = (1 + \mathrm{e}^{-V})^{-1}$, $r_{\mathrm{Ex}} = r_{\mathrm{In}} = 0$, $\tau_{\mathrm{Ex}} = 3$, $\tau_{\mathrm{In}} = 8$, $C^{\mathrm{Ex}\to\mathrm{Ex}} = C^{\mathrm{In}\to\mathrm{In}} = C^{\mathrm{Ex}\to\mathrm{In}} = 10$, and $C^{\mathrm{In}\to\mathrm{Ex}} = 12$. The insets show the phase plane (F_{Ex}-nullcline (called E-

nullcline in the figure) in grey and F_{In}-nullcline (called I-nullcline in the figure) in dashed grey) for a parameter set supporting an inhibition-stabilised network with $(q_{\mathrm{Ex}}; q_{\mathrm{In}}) = (0; -0.647)$ and a sustained oscillation with $(q_{\mathrm{Ex}}; q_{\mathrm{In}}) = (0; -1)$; In the figure $q_{\mathrm{Ex}} = p_E$ and $q_{\mathrm{In}} = p_I$. Black lines denote numerically determined trajectories. The Wilson–Cowan model also supports Bogdanov–Takens bifurcations which occur when the saddle-node and Hopf curves intersect, as well as a saddle-node-on-an-invariant-circle bifurcations when the saddle-node curve lies between the two Hopf curves, and a saddle-separatrix loop and a double limit cycle.

The two insets of Figure 1.18 show phase planes $(F_{\mathrm{Ex}}; F_{\mathrm{In}})$ for a parameter set $(q_{\mathrm{Ex}}; q_{\mathrm{In}})$ supporting damped oscillations (a so-called *inhibition-stabilised network*) and a parameter set supporting sustained oscillations, both assuming r_{Ex} and r_{In} are null. The primary focus of the figure is a two-parameter bifurcation diagram, plotted in the $(q_{\mathrm{Ex}}; q_{\mathrm{In}})$ parameter space. This diagram traces both Hopf and saddle-node bifurcations, the latter indicating where the number of fixed points shifts from one to three. Transitioning between a regime of damped and sustained oscillations can be achieved by crossing the supercritical Hopf bifurcation line. Thanks to the straightforward structure of the Wilson–Cowan equations, the two-parameter bifurcation diagram depicted in Figure 1.18 can be derived analytically. Indeed, to determine equilibrium points $(\bar{F}_{\mathrm{Ex}}; \bar{F}_{\mathrm{In}})$, one can solve the system (1.14) after expressing the reciprocal function of $S_\bullet$, denoted as ${S^{-1}}_\bullet$.

$$\begin{aligned} q_{\mathrm{Ex}} &= {S^{-1}}_{\mathrm{Ex}}(\bar{F}_{\mathrm{Ex}}) - C^{\mathrm{Ex}\to\mathrm{Ex}}\bar{F}_{\mathrm{Ex}} + C^{\mathrm{In}\to\mathrm{Ex}}\bar{F}_{\mathrm{In}} \\ q_{\mathrm{In}} &= {S^{-1}}_{\mathrm{In}}(\bar{F}_{\mathrm{In}}) - C^{\mathrm{Ex}\to\mathrm{In}}\bar{F}_{\mathrm{Ex}} + C^{\mathrm{In}\to\mathrm{In}}\bar{F}_{\mathrm{In}} \end{aligned} \tag{1.14}$$

Choosing $S_\bullet(V) = (1 + \mathrm{e}^{-V})^{-1}$, provides ${S^{-1}}_\bullet(F) = \ln(F/(1-F))$, and the Jacobian matrix, evaluated at $(\bar{F}_{\mathrm{Ex}}; \bar{F}_{\mathrm{In}})$ is:

$$J = \begin{bmatrix} \left(-1 + C^{\mathrm{Ex}\to\mathrm{Ex}}\bar{F}_{\mathrm{Ex}}(1-\bar{F}_{\mathrm{Ex}})\right)/\tau_{\mathrm{Ex}} & -C^{\mathrm{In}\to\mathrm{Ex}}\bar{F}_{\mathrm{Ex}}(1-\bar{F}_{\mathrm{Ex}})/\tau_{\mathrm{Ex}} \\ C^{\mathrm{Ex}\to\mathrm{In}}\bar{F}_{\mathrm{In}}(1-\bar{F}_{\mathrm{In}})/\tau_{\mathrm{In}} & \left(-1 - C^{\mathrm{In}\to\mathrm{In}}\bar{F}_{\mathrm{In}}(1-\bar{F}_{\mathrm{In}})\right)/\tau_{\mathrm{In}} \end{bmatrix} \tag{1.15}$$

In the Wilson–Cowan model, it is possible to configure a scenario where two stable fixed points are separated by a saddle, as illustrated in Figure 1.19. In this setup, the stable manifold of the saddle point serves as a threshold. Consequently, when stochastic forces are introduced, the system exhibits bistable switching behavior. This dynamic is characterized by networks of neurons alternating between periods of elevated membrane potentials (referred to as the *up* state), lasting about 4 seconds, and phases of inactivity (the *down* state). Ermentrout and Terman (Ermentrout & Terman, 2010) have proposed this model configuration as a simplified representation of up-down state transitions, which are commonly observed in both extracellular and intracellular neuronal recordings. Coombes and Wedgwood, in the chapter "*Population models*" of (Coombes & Wedgwood, 2023), also provide further discussion on this subject, highlighting its practical applications in modeling neuronal behaviors.

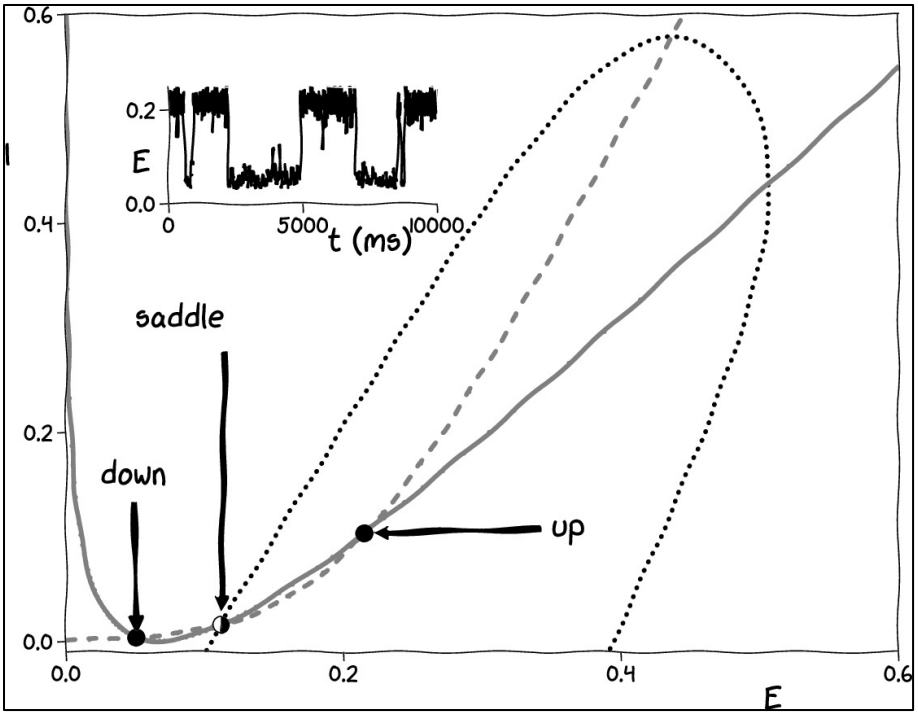

Figure 1.19. Bistability in the Wilson–Cowan mass model. Caption and figure from: (Coombes & Wedgwood, 2023), in the chapter "*Population models*". Permission obtained. — Bistability in the Wilson–Cowan model (F_{Ex}-nullcline (called E-nullcline in the figure) in grey and F_{In}-nullcline (called I-nullcline in the figure) in dashed grey). The dotted black line shows the stable manifold of the saddle point. With the addition of coloured noise, the system can switch back and forth between the *up* and *down* states as shown in the inset. Here, $S_{\bullet}(V) = (1 + \mathrm{e}^{-V})^{-1}$, $r_{\mathrm{Ex}} = r_{\mathrm{In}} = 0$, $\tau_{\mathrm{Ex}} = 5$, $\tau_{\mathrm{In}} = 3$, $C^{\mathrm{Ex}\to\mathrm{Ex}} = 16$, $C^{\mathrm{In}\to\mathrm{Ex}} = 10$, $C^{\mathrm{In}\to\mathrm{In}} = 6$, $C^{\mathrm{Ex}\to\mathrm{In}} = 24$, $q_{\mathrm{Ex}} = -3.7$, and $q_{\mathrm{In}} = -6.7$.

To conclude, the Wilson–Cowan model effectively mimics the overall activity (though not specifically the EEG) of a neural network comprising both excitatory and inhibitory neuron populations. Furthermore, as will be shown next, when enhanced by incorporating more realistic synaptic and network interactions, these models demonstrate considerable success in aligning with neuroimaging data (Breakspear, 2017; Cook et al., 2022; Coombes & Wedgwood, 2023; Griffiths et al., 2022; Liley, 2015). One of the earliest and notable examples in this context is the Zetterberg model (Zetterberg et al., 1978) for EEG rhythm analysis, described hereinafter in Section 1.3.4. This model, drawing on earlier concepts developed by Lopes da Silva and colleagues (F. H. Lopes da Silva et al., 1974), also described below in Section 1.3.3, is structured around three interacting neural mass models that together represent a simplified cortical column. It includes distinct populations for pyramidal cells, inhibitory interneurons, and secondary excitatory neurons. Since its inception, the Zetterberg model has gained broader recognition, particularly through the works of Jansen and Rit (Jansen & Rit, 1995), described in Section 1.3.5, and has been instrumental in advancing our understanding of many brain dynamics, such as epileptic and mesoscopic gamma-band electrophysiological activities (Liley et al., 2012).

1.3.3 The Lopes da Silva models

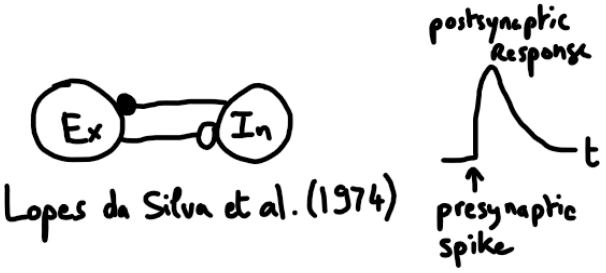

Figure 1.20. The Lopes da Silva 1974-model. Schematic representation of the Lopes da Silva neuronal population model circuit topology and the form of its postsynaptic response (F. H. Lopes da Silva et al., 1974). This model considers functionally differentiated excitatory (Ex) and inhibitory (In) neuronal populations. Open circles represent excitatory connections and filled circles inhibitory ones. Figure inspiration from: (Liley, 2015).

Lopes da Silva and colleagues (F. H. Lopes da Silva et al., 1974) proposed a *lumped* neuronal population model to explain the rhythmic origins of the mammalian alpha rhythm. In this neuronal mass model, a feedforward population of excitatory neurons receives external excitatory input and inhibitory feedback from inhibitory interneurons (e.g., see Figure 1.20). The equations describing the model are succinctly written as:

$$\begin{gathered} V_{\mathrm{Ex}}(t) = (q_{\mathrm{Ex}} * h_{\mathrm{Ex}} - C^{\mathrm{In}\to\mathrm{Ex}} F_{\mathrm{In}} * h_{\mathrm{In}})(t) \\ V_{\mathrm{In}}(t) = (C^{\mathrm{Ex}\to\mathrm{In}} F_{\mathrm{Ex}} * h_{\mathrm{Ex}})(t) \\ F_{\mathrm{Ex}}(t) = S_{\mathrm{Ex}}\big(V_{\mathrm{Ex}}(t)\big);\ F_{\mathrm{In}}(t) = S_{\mathrm{In}}\big(V_{\mathrm{In}}(t)\big) \end{gathered} \tag{1.16}$$

where the symbols are defined as in the previous section, and now $h_{\bullet}$ describe the shape of postsynaptic impulse responses using the difference of two exponential functions (1.6) with time constants that differ between subpopulations. It is worth recognising here the subpopulation response functions ($S_{\bullet}$), as introduced earlier, which specify the nonlinear (sigmoidal) relationship between average membrane potential and mean neuronal population firing rate, and, compared to the Wilson–Cowan model, the disregard of the influence of the refractory period (i.e., thereby assuming that the proportion of excitatory neurons and of inhibitory neurons firing per unit of time at instant t is equal to the impulse density of the populations of excitatory and inhibitory neurons). These response functions will be called wave-to-pulse functions from now onwards.

It is noteworthy that the works of Lopes da Silva and colleagues (F. H. Lopes da Silva et al., 1974) came around the same time as the works of Wilson and Cowan (Wilson & Cowan, 1972, 1973), with a focus on EEG signal generation and it was inspired by the works of Freeman (Freeman, 1975) who introduced the system approach to study neural masses, and it represents an alternative approach to formulating a neuronal population model by developing equations of motion in terms of the mean (soma) membrane potential of the respective neural masses instead of firing rates. The inclusion of such lumped postsynaptic dynamics was found sufficient to produce oscillatory activity in the alpha (8–13 Hz) electroencephalographic band (F. H. Lopes da Silva et al., 1974). A particular advantage to this formulation is that the mean soma membrane potential can be more naturally linked to mesoscopic and macroscopic physiological measurements such as the local field potential, the EEG, and the electrocorticogram.

It is also worth mentioning that in their 1974 publication, Lopes da Silva and colleagues (F. H. Lopes da Silva et al., 1974) intentionally reduced the complexity of their population model (in terms of connection topology) by not assuming any explicit interactions within the subpopulations

themselves nor any external input upon the inhibitory interneurons (i.e., compared to the Wilson–Cowan model, it was assumed that $C^{\mathrm{Ex}\to\mathrm{Ex}} = C^{\mathrm{In}\to\mathrm{In}} = 0$ and $q_{\mathrm{In}} = 0$). An extension with four subpopulation of neurons was soon after published (F. H. Lopes da Silva et al., 1976) assuming the meso-circuit shown in Figure 1.21. In this extended model, a main subpopulation of excitatory neurons simultaneously feedforwards to a main inhibitory subpopulation and a secondary excitatory subpopulation. The same main excitatory subpopulation receives an external excitatory input as well as feedback from both the main inhibitory subpopulation and the secondary excitatory subpopulation. This external input also drives an *intermediate* excitatory subpopulation which inhibits the main inhibitory subpopulation. Additionally, but not represented in Figure 1.21, the main inhibitory subpopulation receives its own external inputs, one excitatory and the other inhibitory. Finally, to remain consistent between the two publications (F. H. Lopes da Silva et al., 1974, 1976), the self feedback loops of the main subpopulations were kept inactive in this extended model. This extended model (the analysis of which was still in its preliminary phase in 1976) was found sufficient to produce oscillatory activity in the theta (4–8 Hz) electrophysiological band as well as some epileptiform discharges.

Figure 1.21. The Lopes da Silva 1976-model. Schematic representation of the updated Lopes da Silva neuronal population model circuit topology (F. H. Lopes da Silva et al., 1976) which emphasizes excitatory and inhibitory feedback. Explanation in text.

The next section further extends the models of Lopes da Silva and colleagues (F. H. Lopes da Silva et al., 1974, 1976). But before going further, it is useful to introduce an alternative representation, a block diagram, as in Figure 1.22.

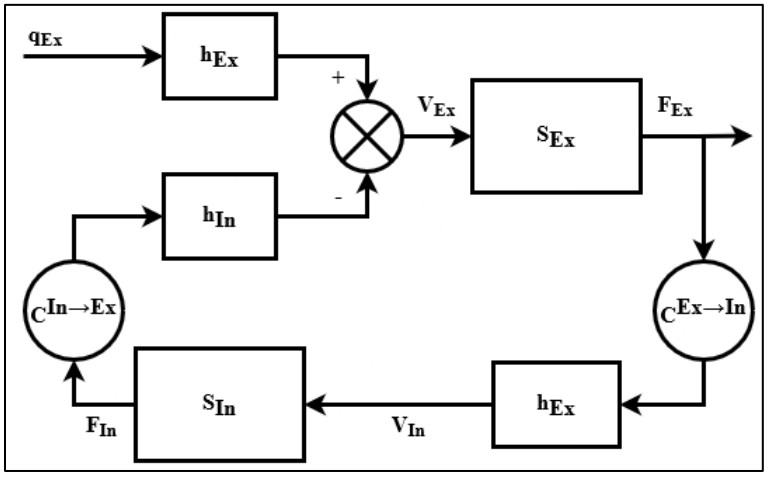

Figure 1.22. Block diagram for the Lopes da Silva 1974-model. Reproduced from (F. H. Lopes da Silva et al., 1974) by using the symbols introduced in equation (1.16).

The block diagram of Figure 1.22 illustrates two primary types of blocks: linear dynamic blocks (i.e., filters) and non-linear blocks. The linear blocks represent the synaptic dynamics through their

impulse response (i.e., h_{Ex} or h_{In}), modeling postsynaptic potentials. They capture how synaptic inputs from other neurons are integrated over time, reflecting the temporal processing of excitatory and inhibitory inputs at the synapses. The non-linear blocks represent the generation process of neuronal firing rates as a static non-linear function (i.e., S_{Ex} or S_{In}) of membrane potentials (i.e., V_{Ex} or V_{In}). The outputs F_{Ex} and F_{In} from these blocks denote the corresponding intensities of action potentials for excitatory and inhibitory neuron subpopulations, respectively. Additionally, the diagram includes a summation unit representing cell soma. In this unit, the excitatory and inhibitory postsynaptic potentials are aggregated, with excitatory inputs contributing positively and inhibitory inputs negatively to the overall membrane potential. This summation mimics the integrative nature of neuronal processing. The interconnectivity between the two neuron subpopulations, excitatory and inhibitory, are depicted through the coefficients $C^{\mathrm{Ex}\to\mathrm{In}}$ and $C^{\mathrm{In}\to\mathrm{Ex}}$. From the perspective of the excitatory subpopulation, this arrangement forms a negative feedback loop.

1.3.4 Zetterberg model

The two-population model proposed by Lopes da Silva et al. (F. H. Lopes da Silva et al., 1974) was further developed by Zetterberg et al. (Zetterberg et al., 1978) by extending it to a three-population model (see diagram in Figure 1.23) consisting of a main population of excitatory neurons (Ex), a main population of inhibitory interneurons (In), and a secondary population of excitatory neurons (ex). The model allows the main excitatory neurons to interact with inhibitory interneurons giving negative feedback and with a third set of excitatory neurons giving positive feedback. It also allows for a linear positive feedback loop for the main excitatory subset to represent collateral connections. The equations describing it are succinctly written as:

$$\begin{gathered} V_{\mathrm{Ex}}(t) = \Big((C^{\mathrm{Ex}\to\mathrm{Ex}}F_{\mathrm{Ex}} + q_{\mathrm{Ex}}) * h_{\mathrm{Ex}} + (C^{\mathrm{ex}\to\mathrm{Ex}}F_{\mathrm{ex}} + q_{\mathrm{ex}}) * h_{\mathrm{dEx}} \\ - C^{\mathrm{In}\to\mathrm{Ex}}F_{\mathrm{In}} * h_{\mathrm{In}}\Big)(t) \\ V_{\mathrm{In}}(t) = (C^{\mathrm{Ex}\to\mathrm{In}}F_{\mathrm{Ex}} * h_{\mathrm{Ex}})(t) \\ V_{\mathrm{ex}}(t) = (C^{\mathrm{Ex}\to\mathrm{ex}}F_{\mathrm{Ex}} * h_{\mathrm{Ex}})(t) \\ F_{\mathrm{Ex}}(t) = S_{\mathrm{Ex}}\big(V_{\mathrm{Ex}}(t)\big);\ F_{\mathrm{In}}(t) = S_{\mathrm{In}}\big(V_{\mathrm{In}}(t)\big);\ F_{\mathrm{ex}}(t) = S_{\mathrm{Ex}}\big(V_{\mathrm{ex}}(t)\big) \end{gathered} \tag{1.17}$$

where two types of excitatory impulse responses, h_{Ex} and h_{dEx}, are distinguished through a delay τ_{d} whereby $h_{\mathrm{dEx}}(t) = h_{\mathrm{Ex}}(t - \tau_{\mathrm{d}})$; two types of excitatory inputs, q_{Ex} and q_{ex}, represent specific and non-specific inputs, respectively; and all other symbols remain consistent with the previous sections. In this model, the difference of two exponential functions (1.6) was retained to describe the shape of postsynaptic potentials $h_{\bullet}$, and the subpopulation wave-to-pulse functions $S_{\bullet}$ were revisited to account for the refractory periods introduced by Wilson and Cowan (see Section 1.3.2) while assuming a sigmoidal shape defined piecewise as in Equation (1.18).

$$S_{\bullet}(V_{\bullet}) = S_{\bullet}^{\infty}\left(\mathrm{e}^{\gamma_{\bullet}(V_{\bullet}-\theta_{\bullet})}\mathbf{1}_{V_{\bullet}\le\theta_{\bullet}}(V_{\bullet}) + \left(2 - \mathrm{e}^{-\gamma_{\bullet}(V_{\bullet}-\theta_{\bullet})}\right)\mathbf{1}_{V_{\bullet}>\theta_{\bullet}}(V_{\bullet})\right) \tag{1.18}$$

where $\mathbf{1}_A$ is the characteristic function of a set A. For practical purposes, Zetterberg and colleagues assumed that $S_{\mathrm{Ex}} = S_{\mathrm{In}}$.

This three-population model has been found sufficient to produce signals that resemble EEG background activity and certain types of paroxysmal activity, in particular spikes. Moreover, the model supported the hypothesis that epileptic spikes are generated in a population of neurons that operate close to dynamic instability.

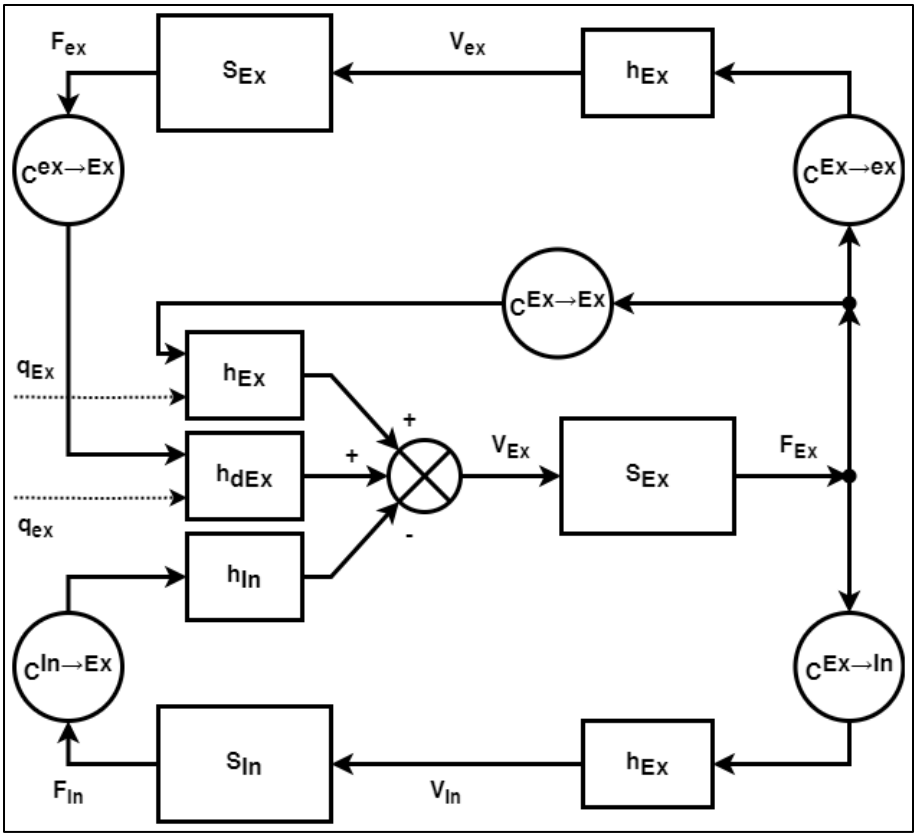

Figure 1.23. The Zetterberg model. Block diagram for the Zetterberg model. Reproduced from (Zetterberg et al., 1978) by using the symbols introduced in equation (1.16).

1.3.5 The Jansen–Rit model

Jansen and Rit, in their seminal work (Jansen & Rit, 1995), built upon the foundational models of Lopes da Silva and colleagues as well Zetterberg and colleagues (F. H. Lopes da Silva et al., 1974, 1976; Zetterberg et al., 1978). Their research focused on systematically varying the parameters of the postsynaptic impulse response. This approach was aimed at accounting for the observed variations in spontaneous EEG signals and in the visual evoked potential. Concurrently, they rigorously constrained the parameterization of connectivity constants, reflecting the evolving and maturing literature at the time. Initially conceptualized to model thalamic tissue, their model has since been adapted and is now prevalently employed for simulating cortical neuronal population dynamics. This model, with block diagram representation in Figure 1.25, assumes that a subpopulation of feedforward pyramidal cells (Pyr) receives feedback from inhibitory interneurons (InIn) and excitatory interneurons (ExIn) as well as arbitrary excitatory inputs. It is clearly a simplification of the Zetterberg model, such that its equations read:

$$\begin{gathered} V_{\mathrm{Pyr}}(t) = \left((C^{\mathrm{ExIn}\to\mathrm{Pyr}} F_{\mathrm{ExIn}} + q_{\mathrm{Ex}}) * h_{\mathrm{Ex}} - C^{\mathrm{InIn}\to\mathrm{Pyr}} F_{\mathrm{InIn}} * h_{\mathrm{In}} \right)(t) \\ V_{\mathrm{InIn}}(t) = \left(C^{\mathrm{Pyr}\to\mathrm{InIn}} F_{\mathrm{Pyr}} * h_{\mathrm{Ex}} \right)(t) \\ V_{\mathrm{ExIn}}(t) = \left(C^{\mathrm{Pyr}\to\mathrm{ExIn}} F_{\mathrm{Pyr}} * h_{\mathrm{Ex}} \right)(t) \\ F_{\mathrm{Pyr}}(t) = S\left(V_{\mathrm{Pyr}}(t)\right);\ F_{\mathrm{InIn}}(t) = S\left(V_{\mathrm{InIn}}(t)\right);\ F_{\mathrm{ExIn}}(t) = S\left(V_{\mathrm{ExIn}}(t)\right) \end{gathered} \tag{1.19}$$

where symbols remain consistent with the previous sections. Here, α-functions as defined in Equation (1.7) were chosen to describe the shapes of postsynaptic impulse responses. Besides, a single wave-to-pulse function S was specified for all subpopulations using a sigmoid function as defined in Equation (1.2). These modelling choices, together with the empirically motivated parameterization of the other constants will prove highly influential, laying a foundation for numerous scientific studies for decades.

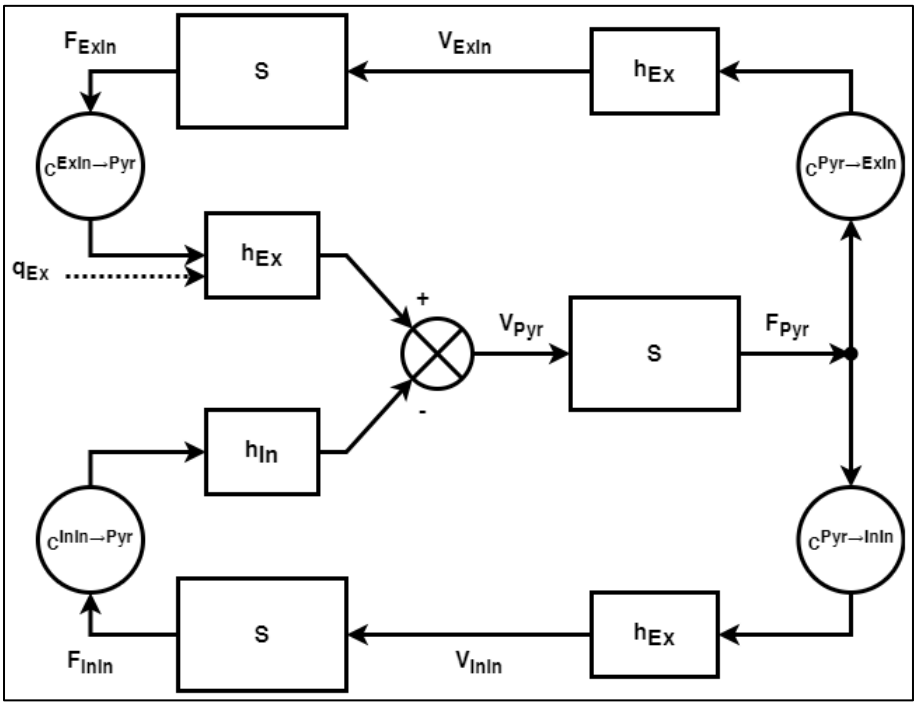

Figure 1.24. The Jansen–Rit model. Block diagram for the Jansen–Rit model. Redrawn from (Jansen & Rit, 1995) by using the symbols introduced in equation (1.20).

In practice, the model is equivalently reformulated using a different set of variables as in Figure 1.25. In this case, using the equivalence stated earlier in Equation (1.13), the resulting second order ordinary differential equations are succinctly given by:

$$\begin{gathered}
\frac{\mu_{\mathrm{Ex}}}{\Gamma_{\mathrm{Ex}}}\left(\frac{1}{\mu_{\mathrm{Ex}}}+\frac{\mathrm{d}}{\mathrm{d}t}\right)^2 E_{\mathrm{Pyr}} = F_{\mathrm{Pyr}} \\
\frac{\mu_{\mathrm{Ex}}}{\Gamma_{\mathrm{Ex}}}\left(\frac{1}{\mu_{\mathrm{Ex}}}+\frac{\mathrm{d}}{\mathrm{d}t}\right)^2 V_{\mathrm{Ex}} = C^{\mathrm{ExIn}\to\mathrm{Pyr}} F_{\mathrm{ExIn}} + q_{\mathrm{Ex}} \\
\frac{\mu_{\mathrm{In}}}{\Gamma_{\mathrm{In}}}\left(\frac{1}{\mu_{\mathrm{In}}}+\frac{\mathrm{d}}{\mathrm{d}t}\right)^2 V_{\mathrm{In}} = C^{\mathrm{InIn}\to\mathrm{Pyr}} F_{\mathrm{InIn}} \\
F_{\mathrm{Pyr}} = S(V_{\mathrm{Ex}} - V_{\mathrm{In}});\ F_{\mathrm{ExIn}} = S\left(C^{\mathrm{Pyr}\to\mathrm{ExIn}} E_{\mathrm{Pyr}}\right);\ F_{\mathrm{InIn}} = S\left(C^{\mathrm{Pyr}\to\mathrm{InIn}} E_{\mathrm{Pyr}}\right)
\end{gathered} \tag{1.20}$$

or, equivalently, after expansions:

$$\ddot{E}_{\mathrm{Pyr}} = \frac{\Gamma_{\mathrm{Ex}}}{\mu_{\mathrm{Ex}}} S(V_{\mathrm{Ex}} - V_{\mathrm{In}}) - \frac{2}{\mu_{\mathrm{Ex}}} \dot{E}_{\mathrm{Pyr}} - \frac{1}{{\mu_{\mathrm{Ex}}}^2} E_{\mathrm{Pyr}}$$
$$\ddot{V}_{\mathrm{Ex}} = \frac{\Gamma_{\mathrm{Ex}}}{\mu_{\mathrm{Ex}}} \left(C^{\mathrm{ExIn}\to\mathrm{Pyr}} S\left(C^{\mathrm{Pyr}\to\mathrm{ExIn}} E_{\mathrm{Pyr}} \right) + q_{\mathrm{Ex}} \right) - \frac{2}{\mu_{\mathrm{Ex}}} \dot{V}_{\mathrm{Ex}} - \frac{1}{{\mu_{\mathrm{Ex}}}^2} V_{\mathrm{Ex}} \qquad (1.21)$$
$$\ddot{V}_{\mathrm{In}} = \frac{\Gamma_{\mathrm{In}}}{\mu_{\mathrm{In}}} C^{\mathrm{InIn}\to\mathrm{Pyr}} S\left(C^{\mathrm{Pyr}\to\mathrm{InIn}} E_{\mathrm{Pyr}} \right) - \frac{2}{\mu_{\mathrm{In}}} \dot{V}_{\mathrm{In}} - \frac{1}{{\mu_{\mathrm{In}}}^2} V_{\mathrm{In}}$$

where the positive constants μ_{Ex}, Γ_{Ex}, μ_{In}, and Γ_{In} determine the shape of the postsynaptic response functions as $h_{\mathrm{Ex}}(t) = \Gamma_{\mathrm{Ex}}/\mu_{\mathrm{Ex}}\, t\mathrm{e}^{-t/\mu_{\mathrm{Ex}}}\Theta(t)$ and $h_{\mathrm{In}}(t) = \Gamma_{\mathrm{In}}/\mu_{\mathrm{In}}\, t\mathrm{e}^{-t/\mu_{\mathrm{In}}}\Theta(t)$, the positive constants $C^{\blacktriangle\to\blacksquare}$ describe the connection strengths from neurons of type ▲ to neurons of type ■, the time varying quantity q_{Ex} is an external input, the sigmoidal firing rate function S instantaneously transforming average membrane potential into average firing rates, and the overdots denote temporal derivatives. The formulation in Equation (1.22) is the one frequently encountered in literature.

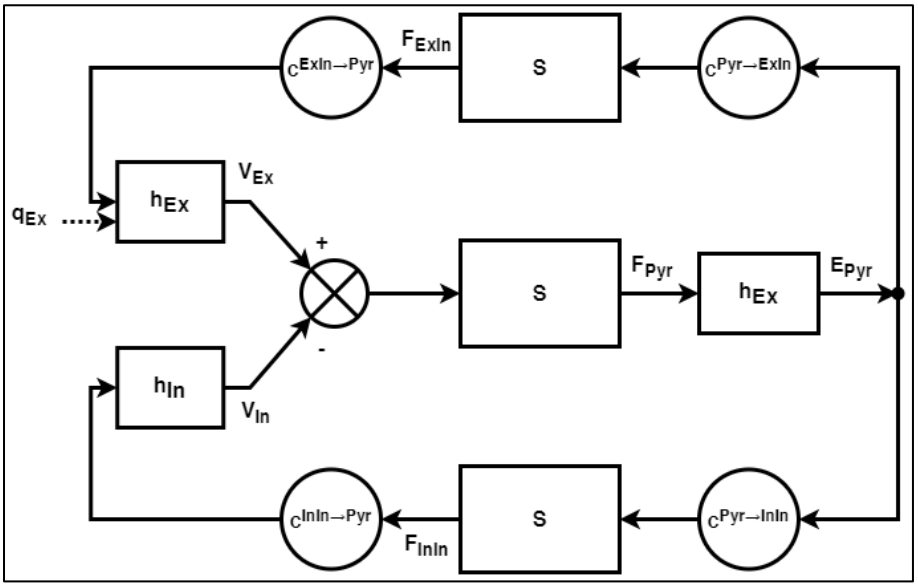

Figure 1.25. Alternative block diagram for the Jansen–Rit model. Block diagram for the Jansen–Rit model. Redrawn from (Jansen & Rit, 1995) by using the symbols introduced in equation (1.22).

It is noteworthy that the aspect of self-feedback, as discussed and modelled by Zetterberg and colleagues (Zetterberg et al., 1978), specifically the parameter $C^{\mathrm{Pyr}\to\mathrm{Pyr}}$ (see diagram in Figure 1.23), initially didn't gain much attention but resurfaced decades later in the works of Sotero and colleagues (Sotero et al., 2007) and others. This aspect, along with other simplifications made by Jansen and Rit, was revisited and incorporated into newer models. The revised set of equations, with the addition of the self-feedback term emphasized in bold font, now reads:

$$\begin{gathered}
\frac{\mu_{\mathrm{Ex}}}{\Gamma_{\mathrm{Ex}}}\left(\frac{1}{\mu_{\mathrm{Ex}}}+\frac{\mathrm{d}}{\mathrm{d}t}\right)^{2} E_{\mathrm{Pyr}} = F_{\mathrm{Pyr}} \\
\frac{\mu_{\mathrm{Ex}}}{\Gamma_{\mathrm{Ex}}}\left(\frac{1}{\mu_{\mathrm{Ex}}}+\frac{\mathrm{d}}{\mathrm{d}t}\right)^{2} V_{\mathrm{Ex}} = C^{\mathrm{ExIn}\rightarrow\mathrm{Pyr}} F_{\mathrm{ExIn}} + \boldsymbol{C^{\mathbf{Pyr}\rightarrow\mathbf{Pyr}}} \boldsymbol{F_{\mathbf{Pyr}}} + q_{\mathrm{Ex}} \\
\frac{\mu_{\mathrm{In}}}{\Gamma_{\mathrm{In}}}\left(\frac{1}{\mu_{\mathrm{In}}}+\frac{\mathrm{d}}{\mathrm{d}t}\right)^{2} V_{\mathrm{In}} = C^{\mathrm{InIn}\rightarrow\mathrm{Pyr}} F_{\mathrm{InIn}} \\
F_{\mathrm{Pyr}} = S(V_{\mathrm{Ex}} - V_{\mathrm{In}});\ F_{\mathrm{ExIn}} = S\left(C^{\mathrm{Pyr}\rightarrow\mathrm{ExIn}} E_{\mathrm{Pyr}}\right);\ F_{\mathrm{InIn}} = S\left(C^{\mathrm{Pyr}\rightarrow\mathrm{InIn}} E_{\mathrm{Pyr}}\right)
\end{gathered} \tag{1.22}$$

Sotero and colleagues (Sotero et al., 2007), employed this updated neural mass model within a realistically coupled network (see Section 1.3.8) to explore the generation of EEG rhythms. Their research demonstrated that the model could effectively replicate many characteristics of the temporal dynamics and the spectrum of human EEG rhythms. Garnier and colleagues (Garnier et al., 2015) provided a thorough modern bifurcation analysis of the same neuronal mass model, highlighting the significance of incorporating such excitatory self-feedback mechanism, while identifying new parameter sets with practical implications for neuroscience research. Concurrently, Youssofzadeh and colleagues took additional steps by exploring the impact of self-feedback across all neuronal subpopulations, not just pyramidal neurons (Youssofzadeh et al., 2015). Their research, particularly focused on event-related potentials, illustrated that self-feedback mechanisms are crucial for generating more robust and consistent neuronal rhythms. Their research also served to unify earlier key developments from many groups, e.g., such as those of Moran and colleagues (Moran et al., 2007). Moran and colleagues have sought to account for self-connectivity that are not excitatory and introduced a self-loop among inhibitory interneurons to generate oscillatory activity in the gamma (40–70 Hz) electrophysiological band.

More generally, since the seminal work of Jansen and Rit, the topic of self-feedback connectivity has received increased attention in an attempt to enrich many dynamics that the Jansen–Rit model is unable to plausibly generate (Youssofzadeh et al., 2015). Indeed, from a modelling perspective, adding self-feedback connectivity generalizes to adding subpopulations (see Section 1.3.6). Additionally, self-feedback connectivity is intrinsic to neural field models (see Section 1.3.7) and it can also coincides with the intrinsic parameters of a network model of neural masses (see Section 1.3.8).

In closing this section, it is noteworthy that Garnier and colleagues (Garnier et al., 2016) integrated the neuronal mass model expressed in Equation (1.22) as a neuronal compartment within a neuron-astrocyte mass model, the intricacies of which will be discussed in a forthcoming manuscript-chapter of this thesis.

1.3.6 Notable neural mass models

In this section, I aim to highlight several models that have enhanced the realism of early neuronal mass models by introducing additional populations with varied kinetics, refining postsynaptic potential shapes through complex exponential combinations, or incorporating dendritic compartmentalization, among other advancements.

The Jansen–Rit model is known for its capability to generate alpha band rhythms with narrow-band spectra. However, it struggles to replicate higher frequency phenomena within plausible parameter ranges due to its temporal kernels acting as low-pass filters. Addressing this limitation, particularly in the context of epilepsy, Wendling and colleagues (Wendling et al., 2005) introduced

a fourth neuronal subpopulation of slow inhibitory interneurons. This addition enabled the model to replicate the high-gamma activity observed in EEGs of epileptic patients (see also comprehensive mathematical analysis in (Touboul et al., 2011)). From another angle, David and Friston (David & Friston, 2003) proposed a model that represents a cortical area with multiple parallel subpopulations, each exhibiting distinct kinetics (both excitatory and inhibitory). They achieved this by decomposing the postsynaptic potential impulse responses into probabilistic sums of multiple terms, each representing a different subpopulation kinetics. This model successfully reproduced oscillatory rhythms across broad-band and multi-band spectra. Another notable model by Liley and colleagues (Liley et al., 2002, 2010) emphasizes conductance-based synapses and the significance of synaptic reversal potentials. It describes cortical activity through the mean soma membrane potentials of excitatory and inhibitory subpopulations, interconnected with an all-to-all connectivity topology including self-feedback. The mesoscopic synaptic model accounts for shunting currents and realistic post-synaptic conductance changes, allowing the model to support a rich repertoire of dynamical states and particularly model the human EEG alpha rhythm.

Despite these advancements, neural mass models remain phenomenological, grounded in neurobiological principles but unable to fully capture the vast array of responses observed in real neuronal tissue (Byrne et al., 2020; Coombes, 2023; Coombes & Byrne, 2016). Indeed, most models rely on an assumed, rather than derived, wave-to-pulse function, typically sigmoidal, with parameters that align with empirical data but are not directly informed by it. Addressing these limitations, a new generation of neural mass models has been proposed. These *next-generation* models offer a precise mesoscopic description of underlying microscopic spiking neurodynamics, making them suitable for future large-scale human brain simulations (Byrne et al., 2020; Coombes, 2023; Coombes & Byrne, 2016). A key feature of these next-generation models is their detailed account of neural population synchrony evolution.

For a more detailed understanding of neural mass modeling, the following references are highly recommended: "*Neuroimaging, Neural Population Models for*" (Bojak & Breakspear, 2015), "*Dynamic models of large-scale brain activity*" (Breakspear, 2017), "*Neural Field Models: A mathematical overview and unifying framework*" (Cook et al., 2022), "*Next generation neural population models*" (Coombes, 2023), "*Population models*" and "*Firing rate tissue models*" chapters from (Coombes & Wedgwood, 2023), "*Wilson–Cowan Equations for Neocortical Dynamics*" (Cowan et al., 2016), "*The dynamic brain: From spiking neurons to neural masses and cortical fields*" (Deco et al., 2008), "*The Wilson–Cowan model, 36 years later*" (Destexhe & Sejnowski, 2009), "*A constructive mean-field analysis of multi-population neural networks with random synaptic weights and stochastic inputs*" (Faugeras et al., 2009), "*Whole-Brain Modelling: Past, Present, and Future*" (Griffiths et al., 2022), "*Neural Field Model, Continuum*" (Hutt, 2015), "*Neural Population Model*" (Liley, 2015), "*Co-operative Populations of Neurons: Mean Field Models of Mesoscopic Brain Activity*" (Liley et al., 2012), "*Sleep, Neural Population Models of*" (Phillips, 2015), "*Neural masses and fields: modeling the dynamics of brain activity*" (Pinotsis et al., 2014), and "*Gap Junctions, Neural Population Models and*" (Steyn-Ross et al., 2015). It is important to note that neural mass and field models have an intertwined development history, with many key researchers contributing to both areas. As a result, literature reviews in this field often cover both neural mass and field models, reflecting their shared evolutionary trajectory and the cross-pollination of ideas between these modeling approaches.

In concluding this section, it is pertinent to revisit our previous deliberations on the *connectome* delineated in Section 1.1.4. There, we clarified the profound impact of various non-neuronal

components on neuronal excitability, necessitating their incorporation into models and theoretical frameworks of brain functionality. Astrocytes, in particular, have been spotlighted for their synaptic mutual engagements with cortical neurons, thereby probing and modulating neuronal firing patterns. The advancements on this topic (with a focus on computational modelling) have been extensively reviewed, notably by (De Pittà & Berry, 2019). Nevertheless, the integration of these insights with neural mass or field models, as we discussed here, has been limited, with each area progressing somewhat independently. Moreover, models that acknowledge glial contributions predominantly address neural activity at scales not readily applicable to macroscale functional analyses in humans, e.g., refer to "*A Neuron–Glial Perspective for Computational Neuroscience*" (De Pittà & Berry, 2019), "*Computational Models of Astrocytes and Astrocyte–Neuron Interactions: Characterization, Reproducibility, and Future Perspectives*" (Manninen et al., 2019), "*Modeling Neuron–Glia Interactions with the Brian 2 Simulator*" (Stimberg et al., 2019), or "*Computational Models of Pathophysiological Glial Activation in CNS Disorders*" (Volman & Bazhenov, 2019); albeit with a few noteworthy exceptions, such as the works of Blanchard or Garnier and colleagues (Blanchard et al., 2016; Garnier et al., 2016) within the context of mesoscale brain dynamics. Specifically, Blanchard and colleagues (Blanchard et al., 2016) enhanced our mesoscale comprehension of non-neuronal factors in brain activity by melding descriptions of neuronal dynamics from a neural mass model perspective with regional cerebral blood flow dynamics through a neuro-glial–vascular coupling framework. This model accentuates astrocytes' pivotal role in neurotransmitter recycling, such as glutamate and GABA, and their regulatory effects on neighboring vessels. Empirical data from rodents underpinned their biologically constrained simulations, which notably illustrated that non-linearities in the relationships between neuronal activity and cerebral blood flow were primarily due to astrocytic activity. This finding underscores the indispensable role of astrocytes in the interpretation of regional brain activity data. Building on this, Garnier and colleagues (Garnier et al., 2016) further explored the complex interactions between neurons and astrocytes at the mesoscopic scale. They focused on the theoretical effects of compromised astrocytic reuptake of glutamate and GABA on neural dynamics, introducing a model that integrates a bilaterally coupled neuron-astrocyte system. This model aims to elucidate the nuanced interplay between populations of astrocytes and neurons mediated by neurochemistry and its impact on neural functionality. Unlike the Blanchard model, this neuron-astrocyte mass model considers how dynamical changes in extracellular neurotransmitter concentrations influence neuronal excitability. The subsequent chapter of this thesis will provide an in-depth examination of this model, shedding light on the integral role of astrocytes in modulating neural activity within a broader network framework.

1.3.7 Neural field models

Neural field models represent an evolution of neural mass models by incorporating spatial dynamics through the utilization of partial differential equations, which articulate the spatial distribution of neural activity. For the purposes of this discussion, and to maintain clarity, I will not delve into neural field models with the same depth as was applied to neural mass models. Rather, I will illustrate how neural field modeling can be viewed as a broad generalization that encompasses a wide array of models, including those neural mass models previously discussed. An in-depth exploration of this subject is presented by Cook and colleagues (Cook et al., 2022). In their publication (Cook et al., 2022), they contend that while explicit derivations are seldom provided, many neural field models found within existing literature can be restructured to align with a set of standard equations, such as Equation (1.23). This reconfiguration unveils a shared foundational structure across models, which primarily diverge in their selection of spatiotemporal

kernels, the definitions of neuronal populations and connectivity patterns, and the foundational assumptions each model is built upon. This unified mathematical framework, which also coincides with the one proposed by (Sanz-Leon et al., 2015; Spiegler & Jirsa, 2013), facilitates a more straightforward comparison among different neural field models, allowing for clear identification and discussion of the core assumptions each model is predicated on. Hence, a generalized formulation for contemporary neural field models (describing the evolution of membrane potential) is articulated as:

$$\begin{aligned} u_{▲}(x,t) &= \sum\nolimits_{■} v_{▲,■} V_{▲,■}(x,t) \\ V_{▲,■}(x,t) &= \int_{-\infty}^{t} \psi_{▲,■}(t-T)\left(\phi_{▲,■}(x,T) + q_{▲,■}(x,T)\right) \mathrm{d}T \\ \phi_{▲,■}(x,t) &= \int_{\Omega} \omega_{▲,■}(x-X) f_{■}\left(u_{■}(X,t)\right) \mathrm{d}X \end{aligned} \tag{1.23}$$

where x designates position, t is time, ▲ and ■ are two neuronal subpopulations, and all other quantities are as in Table 1.1.

Table 1.1. Table of quantities used in general neural field models. Adapted from: (Cook et al., 2022). Publisher's permission: https://creativecommons.org/licenses/by/4.0.

Quantity	**Physical interpretation**
$u_{▲}(x,t)$	Mean membrane potential of subpopulation ▲ at the position x and time t
$\omega_{▲,■}(x)$	Spatial kernel of connections from subpopulation ■ to subpopulation ▲ at the position x
$\phi_{▲,■}(x,t)$	Pulse density of action potentials from subpopulation ■ to subpopulation ▲ at the position x and time t
$f_{▲}$	Wave-to-pulse transfer function for subpopulation ▲
$V_{▲,■}(x,t)$	Mean post-synaptic potential at subpopulation ▲ from subpopulation ■ at the position x and time t
$v_{▲,■}$	Magnitude and polarity of post-synaptic potentials at subpopulation ▲ from subpopulation ■
$\psi_{▲,■}(t)$	Membrane temporal kernel of transmissions from subpopulation ■ to subpopulation ▲
$q_{▲,■}(x,t)$	External input from subpopulation ■ to subpopulation ▲ at the position x and time t
Ω	Spatial neural medium (often subset of $\mathbb{R}$ or $\mathbb{R}^2$)

Compared to the preceding section, the only novelty here is the spatial convolution in the expression of the pulse density of action potentials $\phi_{▲,■}$. This can be concretely highlighted by deriving the Jansen–Rit model.

To obtain the Jansen–Rit model, with three subpopulations Pyr, InIn, and ExIn, we assume:

- reciprocal non-null interactions only between Pyr and InIn or between Pyr and ExIn, denoting by $C^{\mathrm{Pyr}\to\mathrm{InIn}}$, $C^{\mathrm{InIn}\to\mathrm{Pyr}}$, $C^{\mathrm{Pyr}\to\mathrm{ExIn}}$, and $C^{\mathrm{ExIn}\to\mathrm{Pyr}}$ the corresponding connectivity constants, as in Section 1.3.5;

- subpopulation activities with no spatial dependance, i.e., $\omega_{\blacktriangle,\blacksquare}(x) = C^{\blacksquare\to\blacktriangle}\delta(x)$, where $C^{\blacksquare\to\blacktriangle}$ are the connectivity constants defined just above;
- the same sigmoidal firing rate function S, as defined in Equation (1.2), for all subpopulations $f_{\mathrm{Pyr}} = f_{\mathrm{InIn}} = f_{\mathrm{ExIn}} = S$;
- α-functions temporal kernels, as defined in Equation (1.7), that are only specific to the type of synapse (i.e., excitatory or inhibitory) of the afferent subpopulations, i.e., such that $\psi_{\mathrm{InIn,Pyr}}(t) = \psi_{\mathrm{ExIn,Pyr}}(t) = \psi_{\mathrm{Pyr,ExIn}}(t) = h_{\mathrm{Ex}}(t)$ and $\psi_{\mathrm{Pyr,InIn}}(t) = h_{\mathrm{In}}(t)$;
- scaling factors of post-synaptic potentials with unit magnitudes and polarities determined by the type of synapse of the afferent subpopulations, i.e., such that $\nu_{\mathrm{InIn,Pyr}} = \nu_{\mathrm{ExIn,Pyr}} = \nu_{\mathrm{Pyr,ExIn}} = 1$ and $\nu_{\mathrm{Pyr,InIn}} = -1$;
- a single external input from ExIn to Pyr, $q_{\mathrm{Pyr,ExIn}}$ (more rigorously, the input acting on Pyr should be conceptualized as coming from an *external* excitatory population, but here this is equivalent to coming from ExIn).

With the above assumptions (and directly substituting $u_{\blacktriangle}$ and $\phi_{\blacktriangle,\blacksquare}$ by their expressions in $V_{\blacktriangle,\blacksquare}$), we get:

$$\begin{aligned}
V_{\mathrm{Pyr,InIn}}(t) &= \left(C^{\mathrm{InIn}\to\mathrm{Pyr}} S\left(V_{\mathrm{InIn,Pyr}}\right) * h_{\mathrm{In}}\right)(t) \\
V_{\mathrm{Pyr,ExIn}}(t) &= \left(\left(C^{\mathrm{ExIn}\to\mathrm{Pyr}} S\left(V_{\mathrm{ExIn,Pyr}}\right) + q_{\mathrm{Pyr,ExIn}}\right) * h_{\mathrm{Ex}}\right)(t) \\
V_{\mathrm{InIn,Pyr}}(t) &= \left(C^{\mathrm{Pyr}\to\mathrm{InIn}} S\left(V_{\mathrm{Pyr,ExIn}} - V_{\mathrm{Pyr,InIn}}\right) * h_{\mathrm{Ex}}\right)(t) \\
V_{\mathrm{ExIn,Pyr}}(t) &= \left(C^{\mathrm{Pyr}\to\mathrm{ExIn}} S\left(V_{\mathrm{Pyr,ExIn}} - V_{\mathrm{Pyr,InIn}}\right) * h_{\mathrm{Ex}}\right)(t)
\end{aligned} \tag{1.24}$$

which, as intended, simplifies to the same Jansen–Rit equations obtained earlier in Equation (1.19) after defining $V_{\mathrm{Pyr}} = V_{\mathrm{Pyr,ExIn}} - V_{\mathrm{Pyr,InIn}}$, $V_{\mathrm{InIn}} = V_{\mathrm{InIn,Pyr}}$, $V_{\mathrm{ExIn}} = V_{\mathrm{ExIn,Pyr}}$, and $q_{\mathrm{Pyr,ExIn}} = q_{\mathrm{Ex}}$.

It is noteworthy that in the formulation presented in Equation (1.23), the wave-to-pulse transfer function was implemented under the spatial integral in order to describe the evolution of membrane potentials, characterizing it as a voltage-based model (Cook et al., 2022; Hutt, 2015; Liley et al., 2012). However, an alternative formulation involves describing the evolution of firing rates, where spatial interactions are incorporated into the arguments of the transfer function, typifying it as a rate-based or activity-based model (Cowan et al., 2016; Hutt, 2015; Liley et al., 2012; Wilson & Cowan, 1973). This distinction becomes apparent when deriving a spatially continuous version of the Wilson–Cowan model which we exposed in Section 1.3.2. The neural field adaptation of this model, employing temporally coarse-grained spatiotemporal variables F_{Ex} and F_{In}, can be concisely expressed through these equations:

$$\begin{aligned}
\left(1 + \tau_{\mathrm{Ex}}\frac{\partial}{\partial t}\right) F_{\mathrm{Ex}}(x,t) &= \left(1 - r_{\mathrm{Ex}} F_{\mathrm{Ex}}(x,t)\right) S_{\mathrm{Ex}}\left(V_{\mathrm{Ex}}(x,t) + q_{\mathrm{Ex}}(x,t)\right) \\
\left(1 + \tau_{\mathrm{In}}\frac{\partial}{\partial t}\right) F_{\mathrm{In}}(x,t) &= \left(1 - r_{\mathrm{In}} F_{\mathrm{In}}(x,t)\right) S_{\mathrm{In}}\left(V_{\mathrm{In}}(x,t) + q_{\mathrm{In}}(x,t)\right) \\
V_{\mathrm{Ex}}(x,t) &= \int_{\Omega} \omega^{\mathrm{Ex}\to\mathrm{Ex}}(x-X) F_{\mathrm{Ex}}(X,t)\,\mathrm{d}X - \int_{\Omega} \omega^{\mathrm{In}\to\mathrm{Ex}}(x-X) F_{\mathrm{In}}(X,t)\,\mathrm{d}X \\
V_{\mathrm{In}}(x,t) &= \int_{\Omega} \omega^{\mathrm{Ex}\to\mathrm{In}}(x-X) F_{\mathrm{Ex}}(X,t)\,\mathrm{d}X - \int_{\Omega} \omega^{\mathrm{In}\to\mathrm{In}}(x-X) F_{\mathrm{In}}(X,t)\,\mathrm{d}X
\end{aligned} \tag{1.25}$$

where, $F_{\bullet}(x,t)$ are the proportion of neurons firing at the position x and instant t, $\tau_{\bullet}$ are membrane time constants, $r_{\bullet}$ are refractory periods (in practice, they are set to zero), $S_{\bullet}$ are wave-to-pulse transfer functions, $q_{\bullet}(x,t)$ are afferent excitation or inhibition at the position x and instant t, $\omega^{▲\to■}$ are spatial connectivity kernels such that the spatial convolutions $(\omega^{▲\to■} * F_{▲})(x,t)$ over the domain Ω represent the effective drive experienced by subpopulation ■ from subpopulation ▲ at the position x and instant t. Usually, transfer functions are sigmoidal, e.g., $S_{\bullet}(v) = (1+\tanh(v/2))/2$, while connectivity functions are exponential or Gaussians to represent a distance-dependent decay in cortical connectivity, e.g., $\omega^{▲\to■}(d) = w^{▲\to■}\mathrm{e}^{-|d|/\sigma^{▲\to■}}$ where $w^{▲\to■}$ represents the mean synaptic weight and $\sigma^{▲\to■}$ represents the width of the distribution. When the spatial kernel is taken as a function of distance alone between spatial locations, like in this example, we call it homogeneous, otherwise heterogeneous. It is also not uncommon to introduce an axonal delay term, e.g., rewriting the first term of $V_{\mathrm{Ex}}(x,t)$ as $\int_{\Omega} \omega^{\mathrm{Ex}\to\mathrm{Ex}}(x-X)F_{\mathrm{Ex}}(X, t-|x-X|/c_{\mathrm{Ex}\to\mathrm{Ex}})\,\mathrm{d}X$ (and similarly for other terms) where $c_{\mathrm{Ex}\to\mathrm{Ex}}$ is a velocity of propagation of action potentials between excitatory neurons. Further discussions on this model and variants can be found in (Cook et al., 2022; Coombes & Wedgwood, 2023; Cowan et al., 2016; Kilpatrick, 2015; Wilson & Cowan, 1973).

1.3.8 Large-scale network models

Large-scale network models, synonymous with whole-brain network models in our discourse, integrate neural mass or field models within a coupling framework adhering to structural constraints such as synaptic connections or gap junctions, incorporating time delays for neural signal propagation across different brain regions, and accounting for the inherent variability in brain activity through stochastic noise (Breakspear, 2017; Cabral et al., 2014; Deco et al., 2008; Deco & Jirsa, 2012; Griffiths et al., 2022; Sanz-Leon et al., 2015).

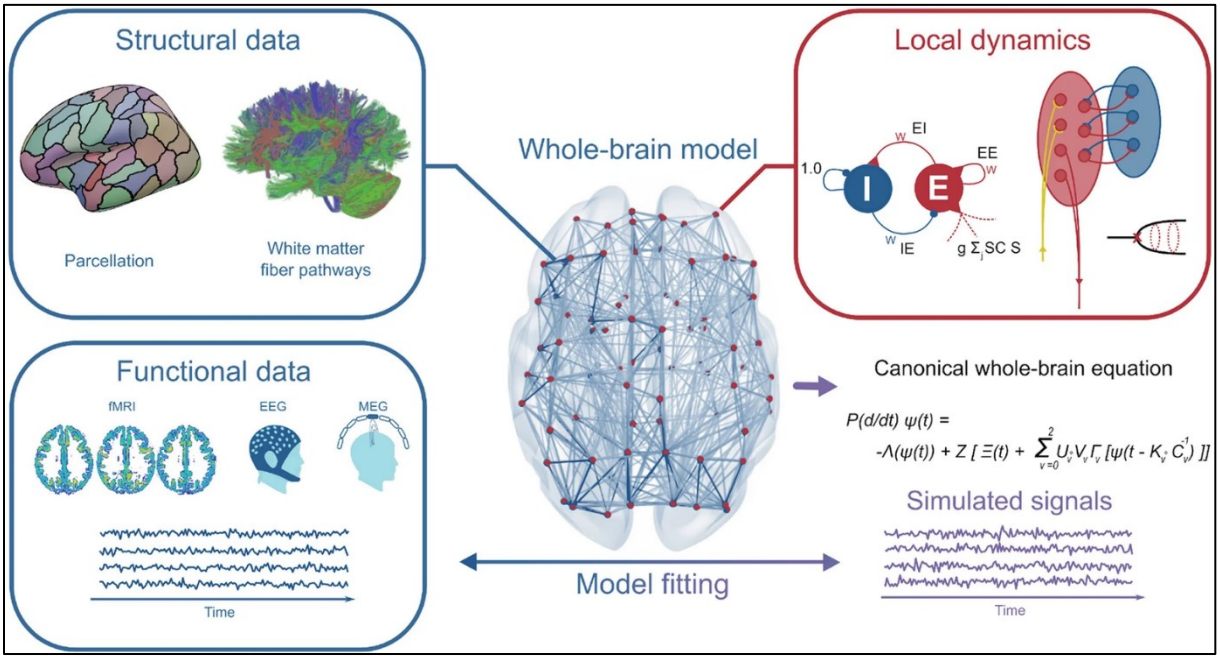

Figure 1.26. Schematic of the whole-brain modelling approach. Caption and figure from: (Griffiths et al., 2022). Permission obtained. — 'Local' neural dynamics are described by the activity of (1) millions of point-process spiking neuron (differential) equations, aggregated by connectivity into regions; OR (2) hundreds/thousands of point-process neural mass/mean field/neural field (differential and/or integral) neural population equations—variously termed; OR

(3) hundreds/thousands of point-process linear algebraic neural population equations (normally grouped into a single matrix-valued equation). Typically, all nodes in the network are described with the same local neural dynamics model and same parameters. Neural populations are coupled together based on a structural connectome, which is defined principally by noninvasive neuroimaging data, including T1-weighted MRI, diffusion-weighted MR tractography, and others. Simulated neural activity is compared against empirical measurements such as fMRI/EEG/MEG time series or covariance structure using brute-force or parameter optimization approaches. When coupled together in the regime achieving good fits with empirical data, the collective behaviour of the system produces quasi-periodic activity whose static/dynamic functional connectivity patterns are similar to those observed for empirical data. Theoretical analysis of these models provides insight into principles and physiological details of large-scale brain organization, and can be used for in silico perturbation studies.

The mathematical foundation for modeling whole-brain networks is encapsulated in a canonical differential equation, as illustrated in Figure 1.26 and first introduced by (Sanz-Leon et al., 2015; Spiegler & Jirsa, 2013). This equation, represented at time t, is given by:

$$\boldsymbol{P}(\mathrm{d}/\mathrm{d}t)\boldsymbol{\Psi}(t) = -\boldsymbol{\Lambda}\big(\boldsymbol{\Psi}(t)\big) + \boldsymbol{Z}\left(\mathbf{E}(t) + \sum_{\nu=0}^{2} \boldsymbol{U}_\nu \circ \boldsymbol{V}_\nu \boldsymbol{\Gamma}_\nu\big(\boldsymbol{\Psi}(t - \boldsymbol{K}_\nu \circ \boldsymbol{C}_\nu^{-1})\big)\right) \quad (1.26)$$

To demystify this formula, let us consider a network composed of l nodes, where each node symbolizes a neural mass model. Although mass models may differ across nodes, each node j is characterized by a vector $\boldsymbol{\Psi}_j$, which encapsulates the neural activity state of that node, including all state variables of the node's neural mass model. The differential operator $\boldsymbol{P}_j$ maps the current state $\boldsymbol{\Psi}_j(t)$ into the next.

Within this formulation, a neural mass model at any given node consists of m neural masses, with m potentially differing from one node to another. For simplicity and enhanced readability, we avoid overly detailed indexing by not explicitly denoting each node's index with, for instance, m_j. Each neural mass within a node is defined by n distinct state variables, where n also varies across neural masses. The interconnection of these state variables is governed by a specific state operator matrix, while a larger matrix $\boldsymbol{\Lambda}_j$ integrates the state operators for all m neural masses at node j.

Additionally, the function $\boldsymbol{Z}$, which can embody both linear and non-linear (e.g., a sigmoidal) transformations, alongside the vector $\mathbf{E}_j$ which introduces external inputs to node j, modulate the system's dynamics.

With these notations established, we define the l -dimensional vectors: $\boldsymbol{P}$ as $(\boldsymbol{P}_1, \boldsymbol{P}_2, \dots, \boldsymbol{P}_l)$, $\boldsymbol{\Psi}$ as $(\boldsymbol{\Psi}_1, \boldsymbol{\Psi}_2, \dots, \boldsymbol{\Psi}_l)$, and $\mathbf{E}$ as $(\mathbf{E}_1, \mathbf{E}_2, \dots, \mathbf{E}_l)$. The matrix $\boldsymbol{\Lambda}$ consolidates the state operator matrices $\boldsymbol{\Lambda}_j$ from each node j.

The model in Equation (1.26) further differentiates scales of interactions within the brain network using the dummy index ν. At each scale ν, various matrices and functions facilitate modeling different types of neural interactions:

- The matrix $\boldsymbol{V}_\nu$ outlines the topology of neural connections, while the matrix $\boldsymbol{U}_\nu$ assigns weights to these connections.
- The transformation function $\boldsymbol{\Gamma}_\nu$, similar to $\boldsymbol{Z}$, dictates how neural activity is processed and represented.
- $\boldsymbol{K}_\nu$ denotes a matrix of distances between neural elements, and $\boldsymbol{C}_\nu$ represents their conduction speeds. The form of $\boldsymbol{C}_\nu$ can vary from scalar to vector to matrix depending on the required granularity.

The operation $\circ$ denotes an element-wise multiplication, also known as the Hadamard or Schur product.

The functions $\boldsymbol{Z}$ and $\boldsymbol{\Gamma}_\nu$ are adjusted to reflect different types of neural models that are used to simulate brain activity (like in Section 1.3.7). For instance, voltage-based models like the Jansen–Rit model typically emerge when $\boldsymbol{Z}$ is linear and $\boldsymbol{\Gamma}_\nu$ is non-linear, whereas activity-based models such as the Wilson–Cowan model are more common when $\boldsymbol{Z}$ is non-linear and $\boldsymbol{\Gamma}_\nu$ is linear.

Each scale ν addresses a specific layer of interaction, from internal neural mass connections to long-range nodal interactions:

- At the scale $\nu = 0$, the model captures internal interactions between neural masses at individual nodes, utilizing intrinsic connections defined by $\boldsymbol{V}_0$ and weighted by $\boldsymbol{U}_0$. Here, $\boldsymbol{K}_0$ and $\boldsymbol{C}_0$ are not typically applicable.
- For $\nu = 1$, the focus shifts to short-range or local interactions between nodes, typically within the vicinity defined by axonal space constants. At this level, $\boldsymbol{V}_1$ delineates the local (or lateral) connection topology, and $\boldsymbol{U}_1$ applies biologically plausible weights to these connections. $\boldsymbol{K}_1$ and $\boldsymbol{C}_1$ are generally not relevant for these local interactions.
- At the $\nu = 2$ scale, the model extends to long-range interactions between nodes, beyond the limits set by axonal space constants. These long-range connections, often mediated by white matter fibers, are characterized by $\boldsymbol{V}_2$ for the topology and $\boldsymbol{U}_2$ for the connectivity weights, with $\boldsymbol{K}_2$ and $\boldsymbol{C}_2$ introducing explicit delays to account for the longer distances involved.

In prevalent whole-brain network models found in the literature, the focus is primarily on the interactions at scales $\nu = 0$ and $\nu = 2$. Taking the Wilson–Cowan neural mass model as a typical example, which is often used to represent each node within a whole-brain network of l nodes, we recall its formulation (as outlined in Section 1.3.2, on page 32). The model, assuming no refractory periods, is described by the following set of differential equations for each node:

$$\begin{aligned} \frac{\mathrm{d}}{\mathrm{d}t}\varphi_{1,1} &= -\varphi_{1,1} + S\big(a_{1,1}\varphi_{1,1} - a_{1,2}\varphi_{2,1} + \varepsilon_1\big) \\ \frac{\mathrm{d}}{\mathrm{d}t}\varphi_{2,1} &= -\varphi_{2,1} + S\big(a_{2,1}\varphi_{1,1} - a_{2,2}\varphi_{2,1} + \varepsilon_2\big) \end{aligned} \tag{1.27}$$

Here, $\varphi_{1,1}$ and $\varphi_{2,1}$ represent the activities of excitatory and inhibitory neurons, respectively; ε_1 and ε_2 are external inputs; $a_{1,1}$, $a_{1,2}$, $a_{2,1}$, and $a_{2,2}$ are connectivity constants; and S denotes a sigmoidal function.

At scale $\nu = 0$, the model incorporates two neural masses: one representing excitatory neurons and the other inhibitory neurons, each described by a single state variable (i.e., $n_1 = 1$ and $n_2 = 1$). The notation $\varphi_{m,i}$ in the equations signifies the i-th state variable of the m-th neural mass. Therefore, for each node j, $\boldsymbol{\Psi}_j$ is represented as $\boldsymbol{\Psi}_j = \begin{bmatrix}\varphi_{1,1}\\ \varphi_{2,1}\end{bmatrix}$, and the differential operator $\boldsymbol{P}_j$ is expressed as $\boldsymbol{P}_j(\mathrm{d}/\mathrm{d}t) = \begin{bmatrix}\mathrm{d}/\mathrm{d}t\\ \mathrm{d}/\mathrm{d}t\end{bmatrix}$. The state operator matrix $\boldsymbol{\Lambda}_j$ is simply $\boldsymbol{\Lambda}_j = \begin{bmatrix}1\\ 1\end{bmatrix}$. This model is an activity-based model where interactions are mediated through the sigmoidal function S. The vector of external inputs is $\mathbf{E}_j = \begin{bmatrix}\varepsilon_1\\ \varepsilon_2\end{bmatrix}$, with intrinsic connectivity matrices at node j given by

$\boldsymbol{V}_{0,j} = \begin{bmatrix} 1 & 1 \\ 1 & 1 \end{bmatrix}$ and $\boldsymbol{U}_{0,j} = \begin{bmatrix} a_{1,1} & -a_{1,2} \\ a_{2,1} & -a_{2,2} \end{bmatrix}$. These matrices are elements of larger block diagonal matrices $\boldsymbol{V}_0$ and $\boldsymbol{U}_0$, each of order $2l$.

At scale $\nu = 2$, the model expands to encompass large-scale networks by specifically coupling the excitatory populations across nodes. In this configuration, even-indexed rows and columns of $\boldsymbol{V}_2$ and $\boldsymbol{U}_2$ are set to zero, allowing for non-zero values in the remaining elements to facilitate the coupling of excitatory neural masses across the network's nodes. Additionally, temporal delays are incorporated through $\boldsymbol{K}_2$ and $\boldsymbol{C}_2$.

Thus, the general formulation of this model is given by:

$$\dot{\boldsymbol{\Psi}}(t) = -\boldsymbol{\Psi}(t) + S\big(\mathbf{E}(t) + \boldsymbol{U}_0 \circ \boldsymbol{V}_0 \boldsymbol{\Psi}(t) + \boldsymbol{U}_2 \circ \boldsymbol{V}_2 \boldsymbol{\Psi}(t - \boldsymbol{K}_2 \circ \boldsymbol{C}_2^{-1})\big) \tag{1.28}$$

However, in the literature, a more specific expression is often employed for practical applications:

$$\begin{aligned} \dot{\varphi}_e^j(t) &= -\varphi_e^j(t) \\ &+ S\left(a_{1,1}\varphi_e^j(t) - a_{1,2}\varphi_i^j(t) + \varepsilon_e^j(t) + \sum_{k=1}^{l} \Omega_{j,k}\, \varphi_e^k\big(t - \mathrm{T}_{j,k}\big) \right) \\ \dot{\varphi}_i^j(t) &= -\varphi_i^j(t) + S\left(a_{2,1}\varphi_e^j(t) - a_{2,2}\varphi_i^j(t) + \varepsilon_i^j(t) \right) \end{aligned} \tag{1.29}$$

In this equation, the superscript j denotes a network node, while the subscripts e and i distinguish between the excitatory and inhibitory neuronal populations, respectively. The matrix Ω represents structural connectivity derived from white-matter fiber tracking, and T accounts for the time delays associated with signal propagation though the tracks. Typically, the connectivity constants $a_{1,1}$, $a_{1,2}$, $a_{2,1}$, and $a_{2,2}$ are assumed to be uniform across the network.

In summary, the equation presented in Equation (1.26) is a comprehensive framework meant to encompass the wide array of connectome-based neural mass models, which are formulated through either ordinary or stochastic integrodifferential equations, as discussed by (Griffiths et al., 2022; Sanz-Leon et al., 2015; Spiegler & Jirsa, 2013). Despite its inclusive design, it is important to note that due to the equation's versatility and broad scope, actual implementations in the literature often adopt adapted or simplified versions of this formula. A discussion of neural field models (extending the Section 1.3.7) is also provided in (Sanz-Leon et al., 2015; Spiegler & Jirsa, 2013). Moving forward, rather than expanding further on this topic, the ensuing sections of this thesis will focus on the construction and exploration of a specific whole-brain neuron-glial network model.

Section 1.4, beginning on page 53, will explore how these whole-brain network models leverage structural and functional real data to decode the intricate dynamics of brain networks. This endeavor, which builds upon the foundational concepts introduced and exemplified in Figure 1.26, aims to enhance our understanding of the brain's intricate workings through advanced computational modeling techniques.

1.4 Multimodal neuroimaging data acquisition and analysis — providing non-invasive empirical whole-brain data complementing biophysical neural models

Non-invasive neuroimaging techniques—including diffusion magnetic resonance imaging (MRI), blood-oxygen-level-dependent (BOLD) functional MRI (fMRI), and electroencephalography (EEG) or magnetoencephalography (MEG)—are preferentially used to constrain human whole-brain biophysical models structurally and functionally (Figure 1.26). And as we have seen earlier, such whole-brain models can produce outputs comparable to neuroimaging data (often after accounting for a forward model), as shown also in Figure 1.27. This chapter specifically addresses diffusion MRI, EEG, and MEG, due to their direct relevance to this thesis (but see also Figure 1.28 for complements).

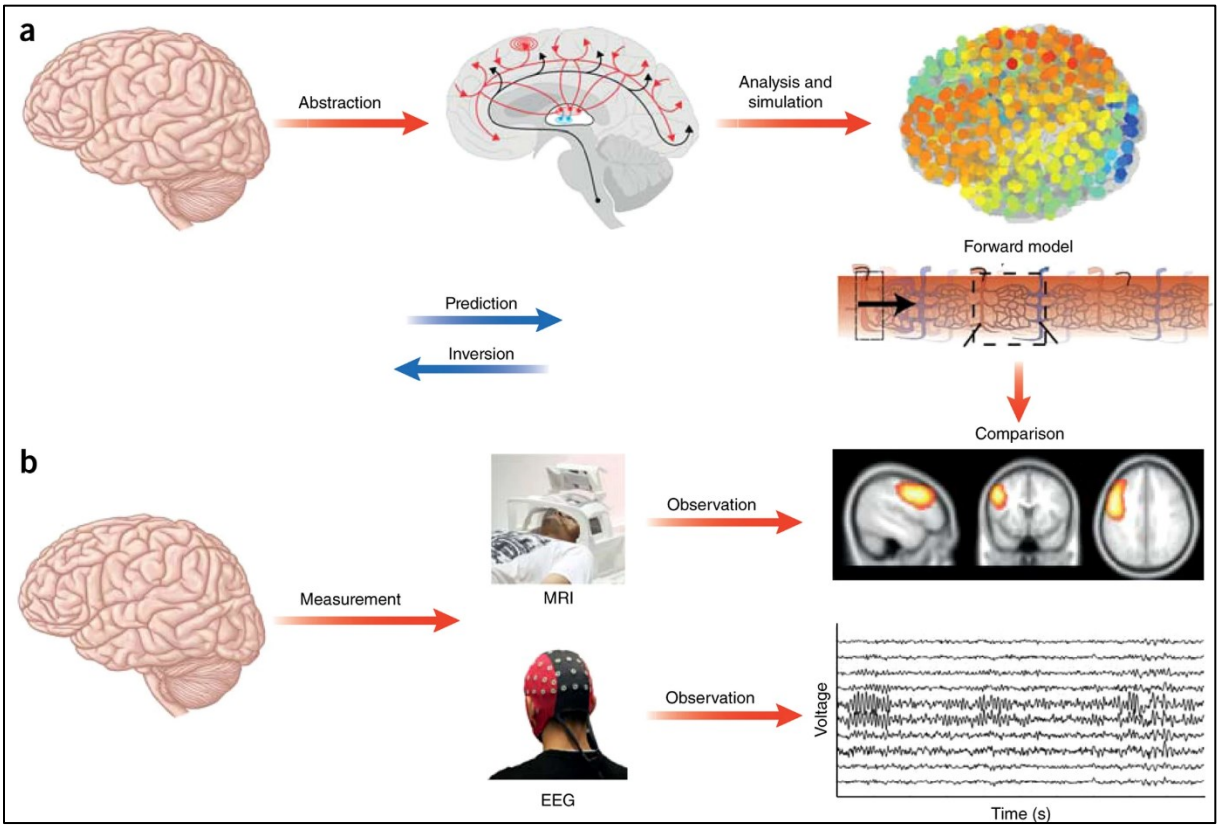

Figure 1.27. Technical and conceptual framework for empirical testing of neural mass models and neural field models. Caption and figure from: (Breakspear, 2017). Permission obtained. — (a) Models of large-scale dynamics are derived from detailed neurophysiology through abstraction. A combination of mathematical analysis and numerical simulations can then be employed to understand the emergent dynamics supported by these models. This step can be constrained by ensuring that neurophysiological parameters are constrained to lie within realistic values. A forward model (biomagnetic or hemodynamic; the latter is illustrated) is then required to predict empirical data from these models (Aquino et al., 2012). Bottom right panel adapted from (Aquino et al., 2012) under a Creative Commons CC BY 4.0 license. (b) Empirical experiments using brain imaging technology yield empirical data across a range of spatial and temporal apertures. High-quality fMRI and EEG can be acquired simultaneously to test model predictions. Going from neural models to empirical data corresponds to model prediction. Using variational schemes and appropriate penalties for model complexity, the mismatch between prediction and observation can be used for model inversion and comparison.

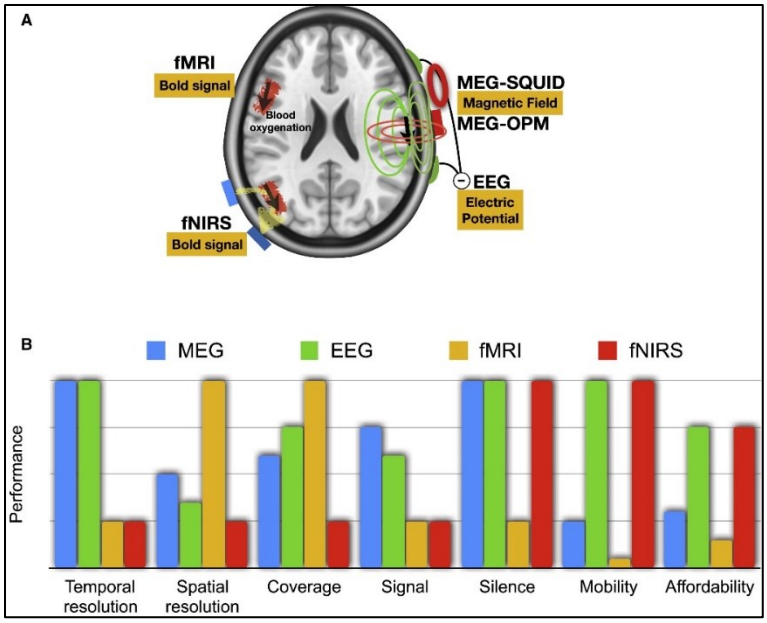

Figure 1.28. Neuroimaging recording techniques. Caption and figure from: (Gross, 2019). Permission obtained. — (A) Measuring brain activity: this schematic figure illustrates the recording of brain activity with fMRI, fNIRS, MEG, and EEG. Current flow (black arrow) is associated with magnetic fields (red lines) that can be recorded with MEG. SQUID sensors (red coil) operate in liquid helium and need a thermal insulation that leads to a physical separation from the scalp. OPM sensors (red rectangle) operate at near room temperature and in close proximity to the scalp. EEG electrodes (green) are attached to the scalp and record potential differences to a reference electrode. fMRI and fNIRS are sensitive to changes in blood oxygenation that are caused by neural activity. (B) MEG and other recording techniques. MEG is compared to EEG, fMRI, and fNIRS. The bar graph shows for each aspect a comparative ranking of all four methods. High bars indicate high performance. Temporal resolution: MEG and EEG have the same higher resolution compared to fMRI and fNIRS. Spatial resolution: fMRI has the highest spatial resolution followed by MEG where spatial resolution is less affected by models of head conductivity compared to EEG. Coverage: modern MEG and EEG system have sensors covering most of the scalp (and for EEG sometimes the face) but typically have reduced coverage of prefrontal areas and cerebellum, while fMRI does not have this limitation. fNIRS has limited coverage. Signal: MEG/EEG signals are more directly related to neuronal activity compared to fNIRS and fMRI. MEG signals are less distorted by changes in tissue conductivities compared to EEG. Silence: MEG, EEG, and fNIRS are silent recording techniques in contrast to fMRI where gradient coils produce noise during data acquisition. Mobility: mobile systems exist for EEG and fNIRS but not for fMRI. New MEG-OPM sensors can be integrated in more mobile MEG systems. Affordability: fMRI systems are most expensive, followed by MEG and more affordable EEG and fNIRS systems. This graph is not the result of a quantitative, precise assessment.

1.4.1 Diffusion MRI

Diffusion MRI data are probably the most important ones for the human whole-brain biophysical modelling (Bezgin et al., 2017; Breakspear, 2017; Deco et al., 2009; Melozzi et al., 2017; Messé et al., 2014; Sanz-Leon et al., 2015; Shen et al., 2019). All whole-brain models rely on data obtained thanks to diffusion MRI to define (using tractography methods) a biophysically plausible structural layer for interconnecting neuronal populations (through white matter tracts). This importance is evident, as I exposed in the previous chapter, because the resulting structural network can singularly explain a significant portion of the variance in empirical multimodal functional networks (J. Y. Hansen et al., 2022; Z.-Q. Liu et al., 2023). This explanatory power is largely due to multimodal connectivity overlap in unimodal cortices and the dominant activity spectral power in these same regions (J. Y. Hansen et al., 2022; Z.-Q. Liu et al., 2023). Furthermore, the neuronal structural layer is a fundamentally important parameter in whole-brain models as it not only constrains their primary spatial and temporal interactions but can typically, if not always, be informed by empirical data (Bezgin et al., 2017; Breakspear, 2017). It also aligns model outputs conveniently with a connectomics scale of empirical data (Bezgin et al., 2017; Breakspear, 2017).

The aim of this condensed subsection is to present the fundamental principles of diffusion MRI, focusing on brain white matter tractography, which represents its most advanced application to date. This understanding is crucial for comprehending the methodological choices I will make in subsequent manuscript-based chapters regarding neuronal structural layer tractography-based reconstructions. I first formally characterize the phenomenon of molecular diffusion and I specify the conceptual root of diffusion MRI. I then explain how diffusion measurements are made with MRI, and I briefly introduce three diffusion MRI techniques: the scalar diffusion-weighted imaging, the diffusion tensor imaging, and the diffusion spectrum imaging. Acquiring and then properly interpreting diffusion images require much care and so for each diffusion technique, I also summarize its underlying assumptions and hypotheses, and its main advantages and drawbacks. I conclude with brain white matter tractography, where I emphasize how detailed human brain anatomical connectomes can be portrayed in vivo and non-invasively through data obtained from brain diffusion imaging.

Molecular diffusion. In a homogeneous medium, molecular diffusion is best described on a statistical basis with the notion of displacement distribution in a three-dimensional (3D) space. This distribution (e.g., see Figure 1.29) is commonly depicted as an isotropic centered Gaussian with a single defining parameter: its variance σ^2 [m^2] expressed as $\sigma^2 = 2D\Delta$ (Le Bihan & Johansen-Berg, 2012). Here D [m^2/s] represents the diffusion coefficient, a property characterizing the medium's viscosity, while Δ [s] is the diffusion time. The diffusion coefficient varies depending on factors such as the mass of the molecules, temperature, and the viscosity of the medium (Le Bihan & Johansen-Berg, 2012). For instance, the self-diffusion coefficient of water at 37 °C is approximately equal to 3×10^{-3} mm^2/s (Le Bihan & Johansen-Berg, 2012).
On the contrary, in a heterogeneous medium, especially in highly heterogeneous environments such as biological tissues, molecular diffusion departs from a Gaussian distribution (e.g., see Figure 1.29) and becomes inherently anisotropic (Le Bihan & Johansen-Berg, 2012). Furthermore, the diffusion coefficient in such environments tends to be lower (though exceptions exist) compared to that in freely diffusible solvents. For instance, within tissues comprising membranes or macromolecules, water molecules follow intricate paths, involving bouncing, crossing, contouring, and interactions with the tissues' constituents (Le Bihan & Johansen-Berg, 2012). As

a result, the diffusion driven displacement is diminished in comparison to that in a freely diffusible solvent, and the anisotropy emerges from the spatial organization of the tissue's constituents.

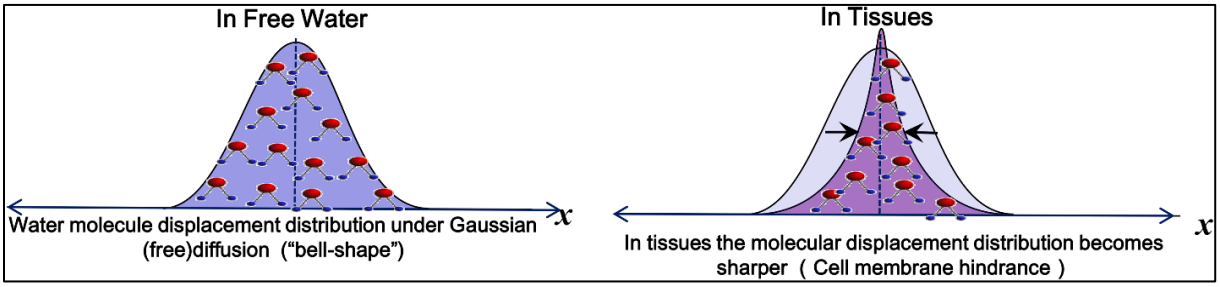

Figure 1.29. Molecular displacement distribution. Figure adapted from: (Le Bihan & Iima, 2015). Publisher's permission: http://creativecommons.org/licenses/by/4.0/. — Water molecule displacement distribution in a homogeneous and heterogeneous medium (see text for explanation).

Conceptual root of diffusion MRI. As a consequence of the previously mentioned phenomenon, in biological tissues such as the brain, the intrinsic viscosity of the tissue becomes apparent over a *short* diffusion time for water molecules (Le Bihan & Iima, 2015). However, over a *longer* diffusion time, the influence of obstacles becomes more pronounced, as the likelihood of interactions between water molecules increases (Le Bihan & Iima, 2015). In the context of MRI, the timescale typically ranging from tens to hundreds of milliseconds (for echo time) is what we consider as *long* (Le Bihan & Iima, 2015). This fundamental concept underlies diffusion MRI: even though the resulting images offer millimetric resolution (e.g., see Figure 1.30), they enable the exploration of tissue structure at the microscopic level (Le Bihan & Iima, 2015).
To date, diffusion MRI remains the most reliable non-invasive technique, providing direct, *in vivo* insight into the voxel-averaged microscopic tissues (Le Bihan & Iima, 2015).
At this point of our discussion, it is pertinent to note that, in the context of diffusion imaging, the primary focus often lies not in acquiring a detailed diffusion profile (Figure 1.31), but rather in identifying the direction of maximum diffusion because this directional parameter is believed to align with the orientation of axonal or other fibrillar structures within the brain tissue (Hagmann et al., 2006). Understanding the predominant direction of diffusion is key for mapping the brain's white matter tracts and reconstruct its structural connectivity.

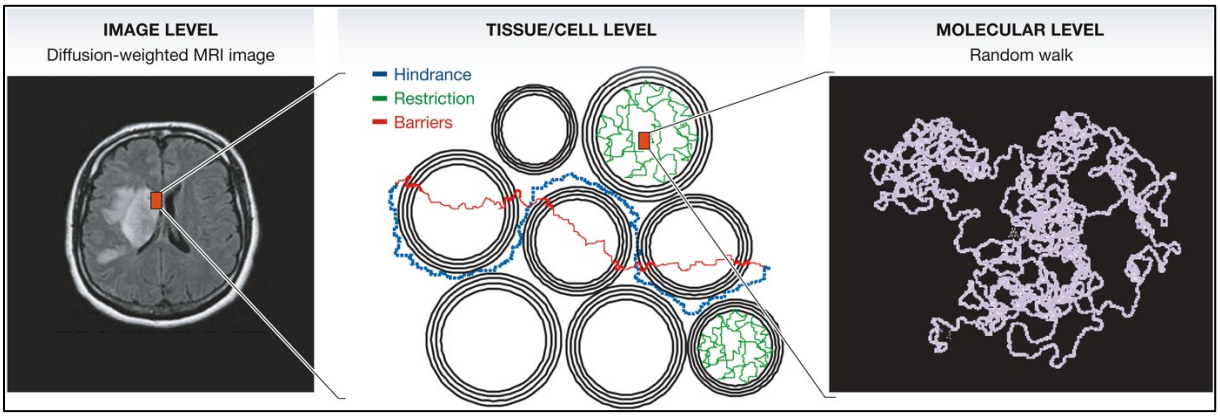

Figure 1.30. Conceptual root of diffusion MRI. Figure adapted from: (Le Bihan, 2014). Publisher's permission: http://creativecommons.org/licenses/by/4.0/. — With diffusion MRI, tissue structure is truly explored at the microscopic level.

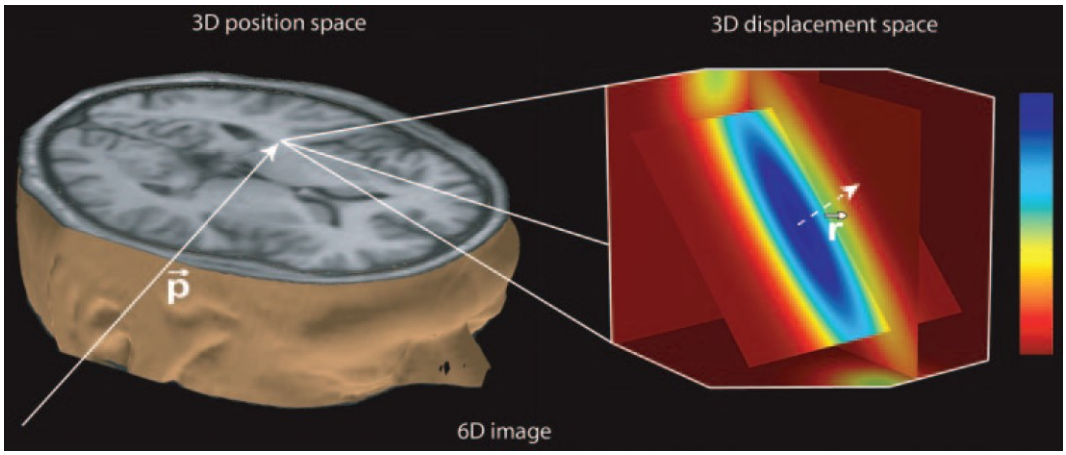

Figure 1.31. Diffusion represented by a six-dimensional image. Caption and figure from: (Hagmann et al., 2006). Permission obtained. — Left part of diagram shows that standard imaging methods provide one value (gray level) for every 3D position **p**. That value or gray level may code for the linear x-ray attenuation coefficient at CT or for the relative signal intensity at MR imaging. Right part of diagram shows that in diffusion imaging every 3D position **p** (voxel) is associated not with a gray level but with a 3D image that encodes the molecular displacement distribution in that voxel. The value measured at the coordinates $\mathbf{p}, \mathbf{r}$— $f(\mathbf{p}, \mathbf{r})$—indicates the proportion of molecules in the voxel that have moved the given distance **r**.

The link between diffusion and the signal intensity measured by MRI. In any MRI sequence, during the echo time, a tissue is exposed many times over to different gradient magnetic fields, such as those used for slice selection or frequency encoding (e.g., see Figure 1.32). Ergo, water molecules moving along the direction of a gradient experience a greater phase shift than the relatively *stationary* ones (bearing in mind that water molecules are never completely stationary but rather relative to the spatiotemporal resolution of MRI), and this leads to a greater signal loss (e.g., see Figure 1.33). Therefore, in any MRI image, the signal intensity at each voxel is *already* modulated by the presence of diffusion (Le Bihan & Iima, 2015).

Nevertheless, any MRI pulse sequence can be deliberately made sensitive to diffusion by adding a pair of gradient pulses with equal strength on both sides of a 180° radiofrequency pulse (e.g., see Figure 1.32). By applying a gradient and then exactly reversing it, only the water molecules flowing along the direction of the gradient magnetic field accumulate phase, while the others end up with no net phase shift (Le Bihan et al., 2006). In essence, the two gradients serve to label space for a specific time interval along a single direction and encode any displacement of water molecules along that direction (Le Bihan et al., 2006). The field strength of the gradient pulses, $G\,[\mathrm{T/m}]$, and the diffusion time interval (between the gradients), $\Delta\,[\mathrm{s}]$, are both adjustable parameters (Le Bihan et al., 1986). They are sometimes expressed in terms of the b-value where $b\,[\mathrm{s/m^2}]$ is proportional to $G^2\Delta$ (Le Bihan et al., 1986). The b-value indicates the degree of exposure to a diffusion gradient.

In summary, three fundamental factors determine the extent of MRI signal intensity change due to diffusion: the observation time and the gradient strength (summarized by the b-value), and the diffusion coefficient. For instance, faster diffusion, stronger gradient pulses, or longer observation times result in more pronounced signal intensity attenuation. It is noteworthy that increasing the strength of a gradient pulse can be achieved either by raising its magnitude or its duration. However, practical limitations often restrict the magnitude, so in practice, the duration is extended (Le Bihan et al., 2006).

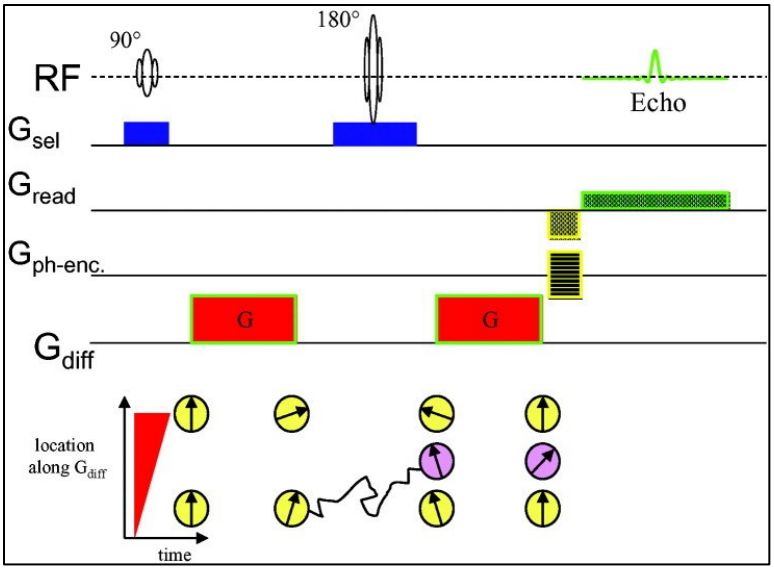

Figure 1.32. Diffusion MRI sequence. Caption and figure from: (Le Bihan et al., 2006). Permission obtained. — Spin-echo sequence sensitized to diffusion using a gradient pulse pair (G_{diff}). Spin phase-shift varies according to location along G_{diff}. Static spins are rephased by the 180° radiofrequency (RF) pulse and the second gradient pulse, while diffusing spins remain out of phase (G_{sel} = slice selection, G_{read} = readout, $G_{ph\text{-}enc}$ = phase encoding).

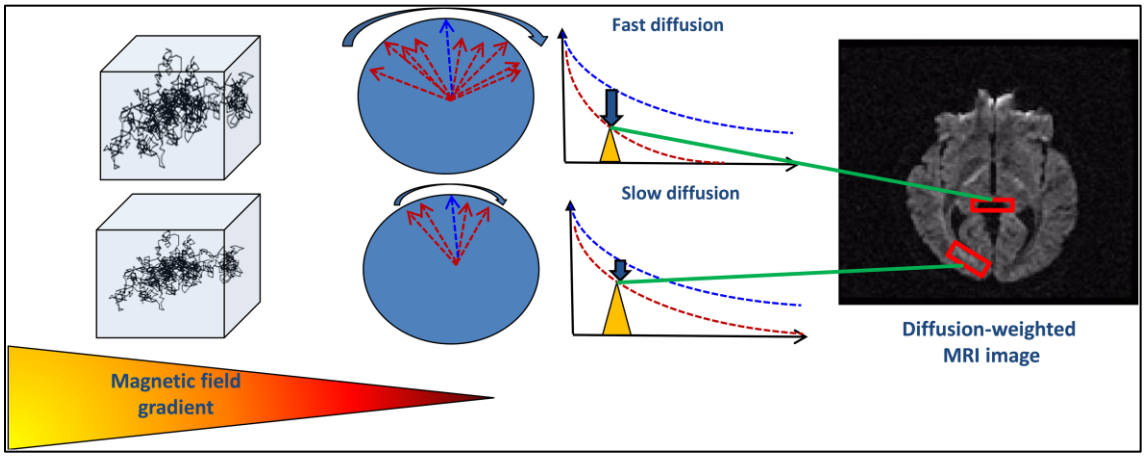

Figure 1.33. Diffusion-weighted image. Caption and figure adapted from: (Le Bihan & Iima, 2015). Publisher's permission: http://creativecommons.org/licenses/by/4.0/. — In the presence of a magnetic field gradient, the MRI resonant frequency will vary along the direction of the gradient. As a result, the phase of the radio waves emitted by the magnetized hydrogen nuclei of water molecules contained in a voxel (box representing the image elementary volume) will vary (red arrows) compared to otherwise static nuclei (blue arrow), depending on their displacement behavior. For the diffusion-driven random displacements, the average phase shift is zero but exhibits a distribution that is wider for water nuclei experiencing large displacements (fast diffusion, as in CSF, top) than for those experiencing small displacements (slow diffusion, as in white matter brain tissue, bottom). Considering the very large number of water molecules present in each image voxel, each with its own random displacement history, this phase distribution results in an attenuation of the MRI signal amplitude due to phase interference, and the MRI signal (red curve) decays faster than in the absence of diffusion (blue curve). This attenuation is larger in voxels where water movement is fast, and hence where diffusion is high, and *vice versa*. The MRI images obtained at a given time (yellow triangle) are then "diffusion weighted": regions of slow diffusion appear in "white" and those with fast diffusion in "black". Quantitative maps of the apparent diffusion coefficient can be calculated based on this differential signal attenuation.

Scalar diffusion-weighted imaging. The simplest among diffusion techniques is the result of applying a diffusion sequence, much like the one discussed earlier, but limited to a single direction (Hagmann et al., 2006). This produces an image known as a diffusion-weighted image (e.g., see Figure 1.32), with the degree of diffusion weighting controlled by the b-value. In these images, a conventional MRI grayscale is typically used, where brighter colors indicate slow diffusion (low signal intensity attenuation), and darker colors represent fast diffusion (high attenuation).

While this unidirectional measurement offers the shortest acquisition time among all techniques, it comes with limitations (Hagmann et al., 2006). Indeed, diffusion is inherently a 3D process, and as previously mentioned, the movement of water molecules in tissues can vary in different directions. Additionally, for a proper interpretation of such images, the two MRI relaxation times, T1 and especially T2, are of practical importance (Le Bihan & Johansen-Berg, 2012). Eliminating T1 effects is straightforward with a long repetition time. However, diffusion-weighted images are inherently T2-weighted, and mitigating T2 effects is more challenging due to the inclusion of gradient pulses. This complexity arises from several factors (Le Bihan & Johansen-Berg, 2012). Firstly, a long echo time is needed to accommodate both sufficient diffusion times and diffusion encoding. Secondly, tissues with very low diffusion require large b-values, and thirdly, achieving these large b-values involves increasing gradient pulse durations. Consequently, in this scenario, diffusion measurements become less well-defined because water diffusion displacement becomes large. In practice, diffusion-weighted images are always assessed alongside a b_0 image, which is acquired without diffusion weighting ($b = 0$) and servers as the reference image. The reference image aids in identifying T2 artifacts, such as the T2 shine-through effect.

Thus, due to relaxation effects, diffusion weighted images contain tissue properties other than the diffusion itself. To overcome the presence of tissue properties in diffusion-weighted images, quantitative diffusion images are often preferred (Le Bihan & Johansen-Berg, 2012). These quantitative images can be derived by assuming a model of a 3D isotropic Gaussian distribution. In this model, each voxel's signal intensity is calculated using the equation: $\mathrm{ADC} = -\ln(\mathrm{DWI}/b_0)/b$, where DWI is the intensity from a diffusion weighted image obtained for a specific b-value and direction, and b_0 is the reference image (e.g., see Figure 1.34). In this context, the diffusion coefficient (i.e., the D defined previously when discussing ***Molecular diffusion***) is estimated as ADC and termed the apparent diffusion coefficient (e.g., see Figure 1.34). This parametrization serves as a statistical bridge between millimetric (acquisition) and microscopic (diffusion phenomenon) scales. This technique requires only two acquisitions. However, ADC images are influenced by the diffusion encoding direction and the assumption of isotropy, limiting their ability to address questions related to anisotropy, such as those arising in brain connectomics. Unlike the previous images, brighter colors in ADC images indicate fast diffusion, while darker colors signify slow diffusion (e.g., see Figure 1.34).

In clinical practice, ADC images are often employed to assess acute brain ischemia, which was historically their first clinical application, as well as certain types of cancer (Le Bihan & Johansen-Berg, 2012).

In 2006, technical requirements for ADC imaging, considering the acquisition of 30 axial sections each with a 3 mm thickness, were outlined by Hagmann and colleagues (Hagmann et al., 2006). These requirements (encompassing hardware capabilities and acquisition time) included optional 3.0 T and high gradient strength capabilities; support for more than 3 gradient directions with a b-value $\leq 1000\ \mathrm{s/mm^2}$ (as the average of three orthogonal directions helps mitigate the dependence on the direction of diffusion encoding and provides a more accurate approximation of the diffusion

coefficient); an acquisition time of 2–4 minutes; utilisation of simple summations for postprocessing; and display on monitor of gray-scale sections.

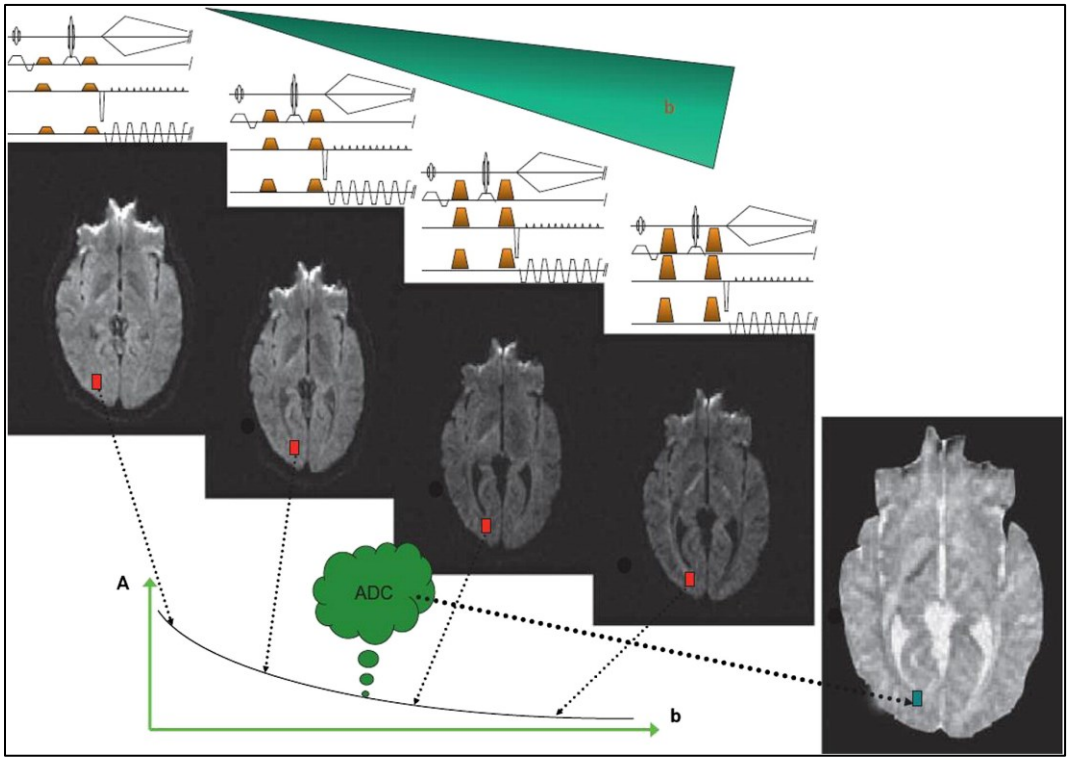

Figure 1.34. Diffusion-weighted and diffusion-calculated images. Caption and figure from: (Le Bihan & Johansen-Berg, 2012). Permission obtained. — Diffusion-weighted and diffusion-calculated (ADC) images. The set of diffusion-weighted images is obtained using different b-values, by changing the intensity of the diffusion gradient pulses (gold trapezoids) in the MRI sequence. In diffusion-weighted images, the overall signal intensity in each voxel decreases with the b-value. Tissues with high diffusion (such as ventricles) get darker more rapidly when the b-value is increased and become black. Tissues with low diffusion remain with a higher signal. As diffusion-weighted images also contain T1 and T2 contrast, one may want to calculate pure diffusion (or ADC) images. To do so, the variation of the signal intensity, $A_{x,y,z}$, of each voxel (red boxes) with the b-value is fitted using the equation $\mathrm{ADC}_{x,y,z} = \ln\left(A_{x,y,z}(b_0)/A_{x,y,z}(b)\right)/(b - b_0)$ to estimate the ADC for each voxel (green box). In the resulting image, the contrast is inverted: bright corresponds to fast diffusion and dark to low diffusion.

Diffusion tensor imaging. DTI for short, this technique overcomes the aforementioned limitations by employing a model based on anisotropic Gaussians, providing six degrees of freedom for each voxel (Hagmann et al., 2006). To fit this model, a minimum of six diffusion-weighted images, in addition to the reference image (b_0), are required. The outcome is a square matrix with three dimensions, referred to as the diffusion tensor. This tensor fully characterizes diffusion in all three spatial directions within a 3D space. Often, an ellipsoid is used to represent the diffusion tensor (e.g., see Figure 1.35). From the tensor, several scalar values can be derived to construct other diffusion images (Hagmann et al., 2006):

- the mean diffusion, formally defined as the matrix trace of the diffusion tensor, which provides a measure akin to an ADC image obtained from three orthogonal directions;
- the principal direction of diffusion, formally defined as the eigenvector corresponding to the largest eigenvalue (in absolute value);

- the fractional anisotropy, formally defined as $\mathrm{FA} = \sqrt{3/2}\sqrt{\sum_i (\lambda_i - \bar{\lambda})^2 / (\sum_i \lambda_i^2)}$, where the $(\lambda_i)_i$ are the eigenvalues of the diffusion tensor and $\bar{\lambda}$ is the mean eigenvalue.

This technique offers the advantage of a short acquisition time. However, similar to the previous model, it relies on certain underlying assumptions that may not always hold, particularly in brain connectomics studies. In cases where a region contains crossing fiber populations resulting in two maxima within the measured tensor, the principal direction may be biased and inaccurate. Nevertheless, the diffusion tensor model is well-suited for voxels where fiber populations align predominantly along a single direction.

In 2006, technical requirements for DTI, considering the acquisition of 30 axial sections each with a 3 mm thickness, were outlined by Hagmann and colleagues (Hagmann et al., 2006). These requirements (encompassing hardware capabilities and acquisition time) included optional 3.0 T and high gradient strength capabilities; support for more than 6 gradient directions with a b-value ≤ 1000 s/mm^2; an acquisition time of 3–6 minutes; utilisation of simple matrix operations for postprocessing; and display on monitor of gray-scale sections for derived scalars (e.g., trace, fractional anisotropy), and color-coded sections for diffusion direction, ellipsoid reconstruction of orientation distribution function, and tractography.

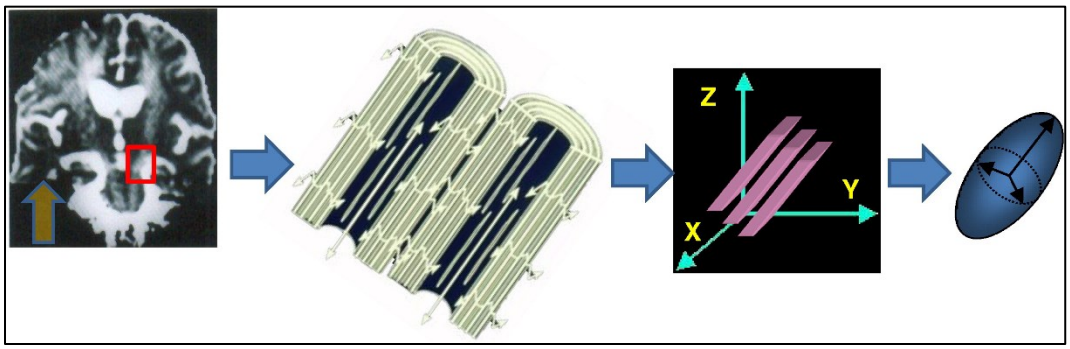

Figure 1.35. Diffusion anisotropy and diffusion tensor imaging. Caption and figure adapted from: (Le Bihan & Johansen-Berg, 2012). Permission obtained. — In the presence of anisotropic diffusion the ADC, as in white matter, depends on the measurement direction. From left to right: Measurement direction was vertical (yellow arrow). Vertical tracts (such as pyramidal tract) have high ADC, while horizontal tracts (as in corpus callosum) are dark. This results from the fact that diffusion is reduced perpendicularly to the white matter fibers due the presence of plasma membranes and myelin. With DTI it becomes possible to characterize diffusion in all 3 dimensions and to determine the direction of fastest diffusion. For each image voxel an ellipsoid can be produced the nature of which is related to key DTI parameters: overall ellipsoid volume and mean diffusivity, the shape (oblong) to the degree of fractional anisotropy and the orientation to the fiber main direction.

Diffusion spectrum imaging. This technique is primarily employed in the field of brain connectomics (Hagmann et al., 2006). It relies on acquiring a series of diffusion-weighted images with varying directions and strengths of the diffusion gradient, to sample a diffusion probability density function at each brain voxel. This data acquisition process is termed *q-space filling*. In q-space, each voxel in the brain corresponds to a point in a 3D space, where the MRI signal intensity is associated with a specific direction and strength of the diffusion gradient (Hagmann et al., 2006). Unlike other techniques, diffusion spectrum imaging does not require the assumption of a Gaussian distribution (in fact, no specific hypothesis about diffusion is made), which enables the accurate resolution of fiber crossings, a challenge in diffusion imaging (Hagmann et al., 2006). However, the ability to resolve the diffusion probability density correctly is contingent upon the q-space resolution. Additionally, compared to other methods, this technique demands a significantly longer

acquisition time due to the larger number of images required. To address this time limitation (especially in clinical settings), alternative methods have been proposed. One such approach is q-ball imaging (e.g., see Figure 1.36) or high angular resolution diffusion weighted imaging, which combines the advantages of both diffusion tensor and diffusion spectrum imaging techniques (Hagmann et al., 2006).

In 2006, technical requirements for diffusion spectrum imaging, considering the acquisition of 30 axial sections each with a 3 mm thickness, were outlined by Hagmann and colleagues (Hagmann et al., 2006). These requirements (encompassing hardware capabilities and acquisition time) included very desirable 3.0 T and high gradient strength capabilities; support for more than 200 gradient directions with a b-value > 8000 s/mm^2; an acquisition time of 15–60 minutes; utilisation of complex operations (filtered Fourier transform and radial projection with multiple parameters) for postprocessing; and display on monitor of mean diffusion, fractional anisotropy, probability density function, orientation distribution function, tractography.

In this thesis, I specifically used multi-shell (i.e., multiple b-values) high angular resolution diffusion-weighted imaging data obtained from the Human Connectome Project. This imaging technique involves acquiring diffusion data using a significantly higher b-value (i.e., > 1000 s/mm^2) and number of diffusion directions (e.g., > 40 directions) compared to DTI. For example, the Human Connectome Project data employed in this thesis were collected at a high spatial resolution of 1.25 mm isotropic using a 2D spin echo echo-planar imaging sequence and included 18 b_0-images and 90 diffusion-weighted images per b-shell, covering three different b-values (1000, 2000, and 3000 s/mm^2) totalling about 1 hour of acquisition time. I provide more details on this in the manuscript-based chapters.

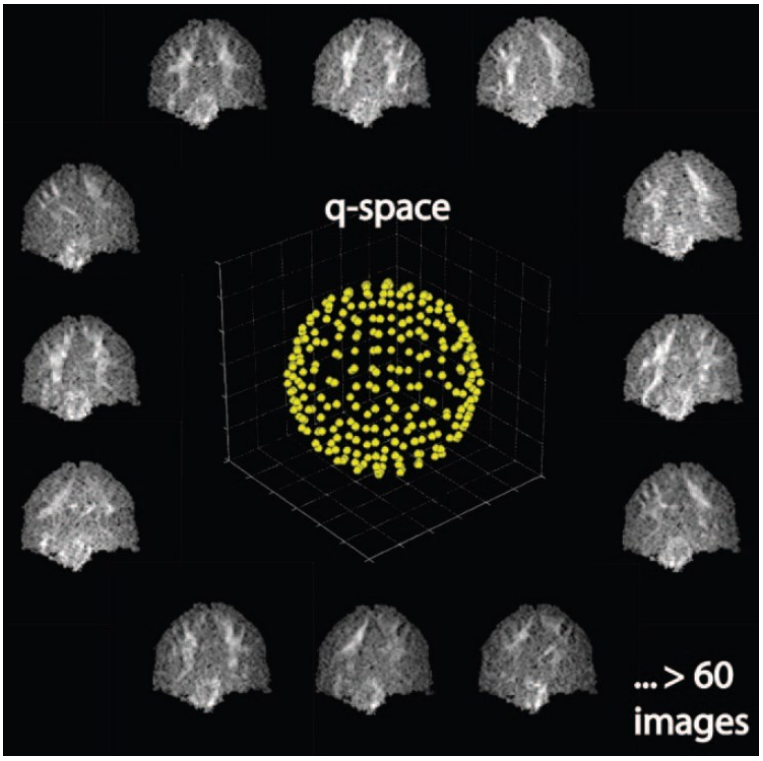

Figure 1.36. Q-space and q-ball imaging. Caption and figure from: (Hagmann et al., 2006). Permission obtained. — Diagram shows that in q-ball imaging, points on a shell with a constant b-value are acquired in q-space. At least 60 images are necessary to reconstruct an orientation distribution function that is realistic.

Brain tractography. In preceding sections, I delineated the collection methods for diffusion MRI images and the techniques for deducing the diffusion direction at any given point within the image. The fundamental principle underpinning brain tractography is as follows: within white matter, water molecules exhibit preferential diffusion; specifically, they diffuse more rapidly along the fiber direction and more slowly perpendicular to it (Hagmann et al., 2006; Le Bihan & Johansen-Berg, 2012). Consequently, starting from a seed voxel, tractography is able to reconstruct a fiber by sequentially linking adjacent voxels according to the principal diffusion direction (e.g., see Figure 1.37). It is critical to emphasize the term *fiber* here; fibers, as reconstructed by tractography, are representations of axonal bundles rather than individual axons. The latter have a diameter on the order of micrometers, which far exceeds the resolving power of contemporary human MRI technology (Hagmann et al., 2006; Le Bihan & Johansen-Berg, 2012). Furthermore, from a physical standpoint, the reconstructed fibers merely approximate the actual axonal architecture, as they are fundamentally representations of diffusion velocity (Hagmann et al., 2006; Le Bihan & Johansen-Berg, 2012).

Tractography methodologies are broadly classified based on three aspects (Hagmann et al., 2006): the diffusion model employed which pertains to the mathematical model used to interpret the diffusion data (e.g., diffusion tensor or diffusion spectrum), the tracking algorithm used which describes the method by which fiber pathways are inferred from the diffusion data (deterministic, which utilizes the most probable direction of diffusion to trace fiber pathways voxel-by-voxel, or probabilistic, which samples a distribution of fiber orientations), and the approach to constructing the trajectory of fiber tracts (local, which iteratively builds the fiber using a seed-based technique, or global, which utilises the entire diffusion dataset simultaneously to reconstruct all fibers in a holistic manner). For instance, Figure 1.38 compares two fiber tractographies based on the diffusion model employed.

The potential applications of brain tractography are vast (Le Bihan & Iima, 2015). For instance, structural brain connectivity alters with the progression of development, aging, or neurodegenerative diseases, and significantly influences functional connectivity. However, the challenges are equally substantial (Maier-Hein et al., 2017; Schilling, Daducci, et al., 2019; Schilling et al., 2020; Schilling, Nath, et al., 2019; C. Yeh et al., 2021). For example, a definitive ground truth is absent for validating tractography on human subjects, beyond a rudimentary understanding of brain wiring, including the major white-matter pathways. Often, ground truths are established *ex vivo*, via dissections on human donors or animal models. Chemical tracing offers another avenue for establishing a standard, despite its acquisition and labeling challenges (Delettre et al., 2019; Grisot et al., 2021). It can clarify ambiguities inherent in diffusion imaging. Nonetheless, numerous tractography methods fall short, primarily due to insufficient resolution (Le Bihan & Iima, 2015). Consequently, different tissue microstructures can yield identical diffusion profiles, rendering the problem unresolved, an inherent complexity of the methodology (Le Bihan & Iima, 2015; Ocampo-Pineda et al., 2021).

To go a step further, and in anticipation of the General Discussion of this thesis, it is pertinent to mention that, in the context of tractography, the premise that diffusion MRI signals are more sensitive to the coherent organization of axonal bundles than other white-matter structures such as glial cells, is being increasingly challenged. For instance, Garcia-Hernandez and colleagues presented a diffusion-weighted MRI method capable of imaging changes in glia morphology, particularly microglia and astrocytes, *in vivo* (Garcia-Hernandez et al., 2022). This method is sensitive to changes in glia morphology and proliferation, providing a quantitative account of neuroinflammation without necessitating neuronal loss or demyelinating injury. This approach

demonstrates the significant influence of glial cells on diffusion MRI signals, highlighting the need to account for such factors in the interpretation of imaging data. In subsequent chapters, I will delve into specific limitations of tractography, particularly concerning neuron-glial interactions and other nuanced aspects. These discussions will provide a more comprehensive understanding of the intricate landscape of brain tractography.

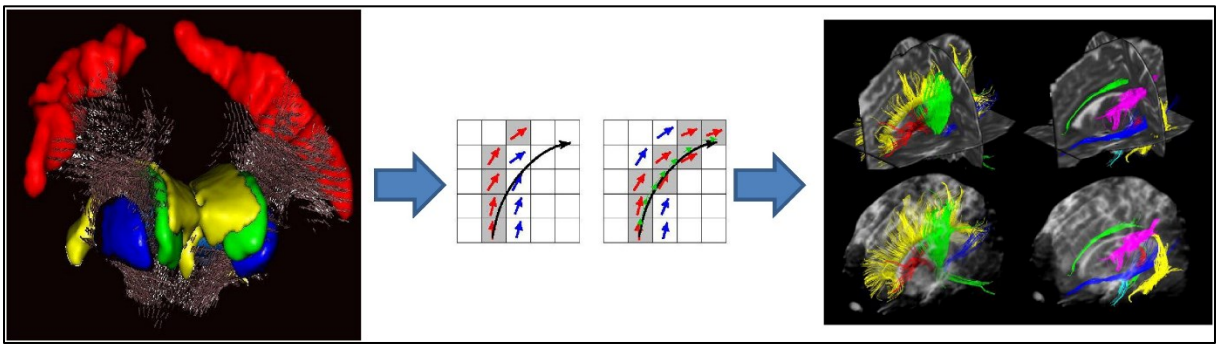

Figure 1.37. Fiber tracking. Caption and figure adapted from: (Le Bihan & Johansen-Berg, 2012). Permission obtained. — Complementary to Figure 1.35. Left to right: After the ellipsoids have been obtained for all voxels of the image (here for the cortico-spinal tract out of the motor cortex in red) an algorithm is used to determine whether adjacent voxels are likely to be connected (here with the FACT algorithm from (Mori et al., 1999)). Connected voxels within putative tracts are then displayed using pseudo-colors. It should be noticed that such color tracks are purely the results of a software and do not represent genuine anatomical structures.

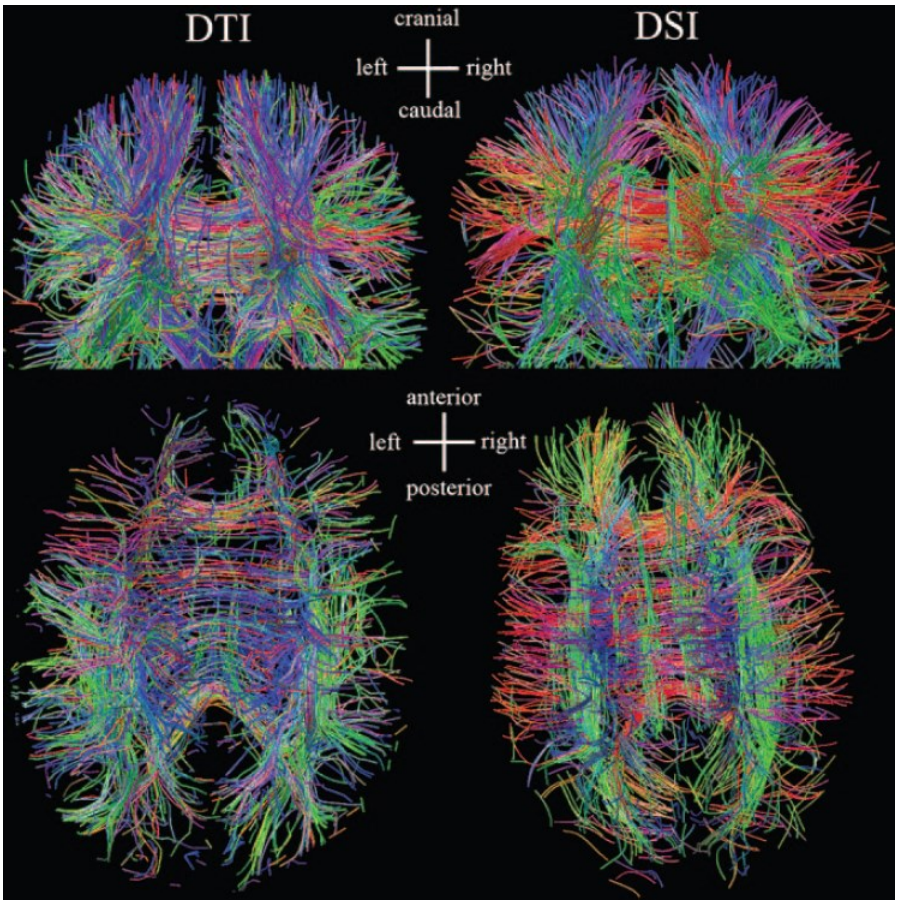

Figure 1.38. Diffusion tensor and spectrum imaging. Caption and figure from: (Hagmann et al., 2006). Permission obtained. — Comparison of fiber tractography based on diffusion tensor imaging (DTI) versus fiber tractography

based on diffusion spectrum imaging (DSI) in two healthy volunteers. [See acquisition details in (Hagmann et al., 2006)]. Because diffusion spectrum imaging provides higher angular resolution, fiber crossings are better resolved and fibers from different tracts are more clearly separated. The most visible differences between the two axial views (bottom row) are the greater predominance of red, which represents decussating callosal fibers that connect both the parietal and the temporal lobes, and the more uniform distribution of callosal fibers that project into the frontal lobe, on the diffusion spectrum image. These differences reflect typical errors of diffusion tensor imaging tractography in areas where fibers cross.

Structural connectome reconstruction. The preceding section elucidated the utility of tractography as a visualization tool that extracts pathways of maximal diffusion coherence from orientation distribution function maps, mirroring the anatomical pathways of axonal trajectories. Tractography finds application in diverse analyses, ranging from the examination of individual tracts to comprehensive assessments of whole-brain structural connectivity, the latter being of particular interest in this thesis. It was previously highlighted that all dynamic models of large-scale network activity depend on diffusion MRI-derived data to construct a structurally plausible connectivity layer that interlinks neuronal populations via white matter pathways.

In the realm of connectomics, the typical methodology for reconstructing an individual's structural connectome based on diffusion MRI data is depicted in Figure 1.39. Conceptually, the formulation of a structural connectome from an individual's diffusion-weighted images appears straightforward but necessitates numerous practical considerations (C. Yeh et al., 2021). These considerations include: (a) the selection of imaging sequences and parameters; (b) the preprocessing of diffusion-weighted images and correction of artifacts; (c) the choice of fiber orientation estimation methods; (d) the selection of streamline tractography techniques; (e) criteria for streamline selection; (f) the quantitative reconstruction of tractograms; (g) the adoption of a brain parcellation scheme; (h) the assignment of streamlines to network nodes; (i) post-processing of the connectome; and, when relevant, (j) the application of graph theoretical analyses.

In the context of this thesis, it is assumed that access to cutting-edge diffusion data and processing pipelines is available, allowing for an emphasis on critical elements starting from step (c). Specifically, in this section I aim to elucidate the two principal sources of bias in tractography during tractogram generation: the biases related to streamline termination and streamline quantification (C. Yeh et al., 2021). This discussion is pertinent as the thesis utilizes tractography-based connectome reconstruction pipelines applied to the high-resolution datasets from the Human Connectome Project, aiming to establish constraints for comprehensive biophysical models of the brain. The methodologies adopted here are designed to mitigate the biases associated with streamline termination and quantification inherent in tractography techniques.

- In the domain of diffusion MRI tractography, the initiation and propagation of streamlines through the cerebral white matter rely on the localized diffusion characteristics of water molecules, as deduced from MRI data (C. Yeh et al., 2021). These streamlines serve as virtual proxies, approximating the trajectories of axonal fibers within the brain. Nevertheless, determining the precise initiation and cessation points of these streamlines poses significant challenges, giving rise to what is termed streamline termination bias, as depicted in Figure 1.40. A promising approach to counter this bias is to integrate supplementary anatomical data, typically derived from high-resolution structural MRI, to inform the propagation and termination of streamlines. For instance, streamlines may be restricted to end at the interface between grey and white matter or within designated cortical areas (St-Onge et al., 2018, 2021).

  In this thesis, a novel strategy aimed at mitigating streamline termination bias employs particle filtering tractography, facilitating the generation of a surface-based tractogram for

each subject (St-Onge et al., 2018, 2021). This approach imposes geometrical constraints on the streamlines' reconstruction, grounded in a model of surface flow trajectory along the grey-white matter boundary. Consequently, this technique enables the reconstruction of tractograms with enhanced cortical representation, ensuring that all streamlines intersect the cortical surface of the brain. The efficacy of this method is illustrated in Figure 1.40.

- Streamline quantification bias in diffusion MRI tractography highlights the challenges in accurately depicting the true density or number of white matter fibers between brain regions (C. Yeh et al., 2021). This bias arises from the discrepancy between the real biological fiber pathways in the brain and their virtual representation by streamlines in tractography (C. Yeh et al., 2021). The core of this issue lies in the methodologies tractography algorithms employ to estimate streamline numbers, which serve as proxies for connectivity strength within structural networks (C. Yeh et al., 2021). One critical aspect of this bias is the inaccurate representation of fiber density. Direct measurement of axonal fiber density within a voxel or across brain regions is not feasible with diffusion MRI. Consequently, tractography algorithms resort to using streamline counts as estimates for fiber density, which may not align with the actual fiber density. Another dimension of this bias is the effect of pathway length on streamline density. The quantification of streamlines for extended connections might be inaccurately high or low, depending on the initiation and propagation methods used by the tractography algorithms. This discrepancy can distort the perceived strength of longer connections in the network, making them appear disproportionately influential or insignificant.

  The implications of quantification bias extend to the graph-theoretical analysis of structural connectomes or the simulations of large-scale network dynamics and related studies, which depend on the connectivity inferred from tractography. Misinterpretation of network connectivity can lead to incorrect assumptions about the significance or functionality of specific neural pathways (C. Yeh et al., 2021).

  To counteract streamline quantification bias, researchers have developed various advanced techniques designed to align connectivity measures more closely with the true biological architecture (C. Yeh et al., 2021). Among these techniques are seeding strategies that fine-tune the initiation points and methods for streamline generation, sophisticated weighting approaches that assign streamline weights based on additional information or constraints to more accurately reflect biological realities, and post-processing corrections that apply adjustments to the tractogram to rectify known biases in streamline counts. These efforts are directed towards ensuring that tractography-derived models of neural connectivity offer a more faithful representation of the brain's structural network.

  In the scope of this thesis, an advanced tractogram filtering technique (Daducci et al., 2015; Ocampo-Pineda et al., 2021; Schiavi et al., 2020) was utilized to refine tractograms by incorporating microstructural and anatomical constraints and attributing a quantitative weight to individual streamlines. The technique enhances tractogram fidelity by reconciling the observed diffusion MRI signals with a linear forward model that simulates tissue microstructure, incorporating anatomical priors that posit axonal organization within distinct bundles (e.g., see Figure 1.41). This process involves adjusting a global penalty coefficient, or regularization constant, to favor solutions that minimally yet accurately represent the observed diffusion signals with a select number of fiber bundles. This regularization approach is noteworthy for its ability to yield biologically plausible tractograms that vary in sparsity, aligning closely with known anatomical structures.

The resulting tractograms are then used to construct structural connectomes (e.g. see Figure 1.42). As I detail in the manuscript-chapters, for these constructions, a quantitative weight is assigned to each connection between brain regions, or parcels, based on the weights attributed to the streamlines. This methodology ensures that the resulting connectomes are not merely qualitative but quantitative, with each connection weight offering a microstructurally and anatomically informed measure of connectivity strength. This approach represents a significant advancement in deriving connectomes that are both biologically grounded and quantitatively accurate, facilitating a deeper understanding of the brain's complex network architecture.

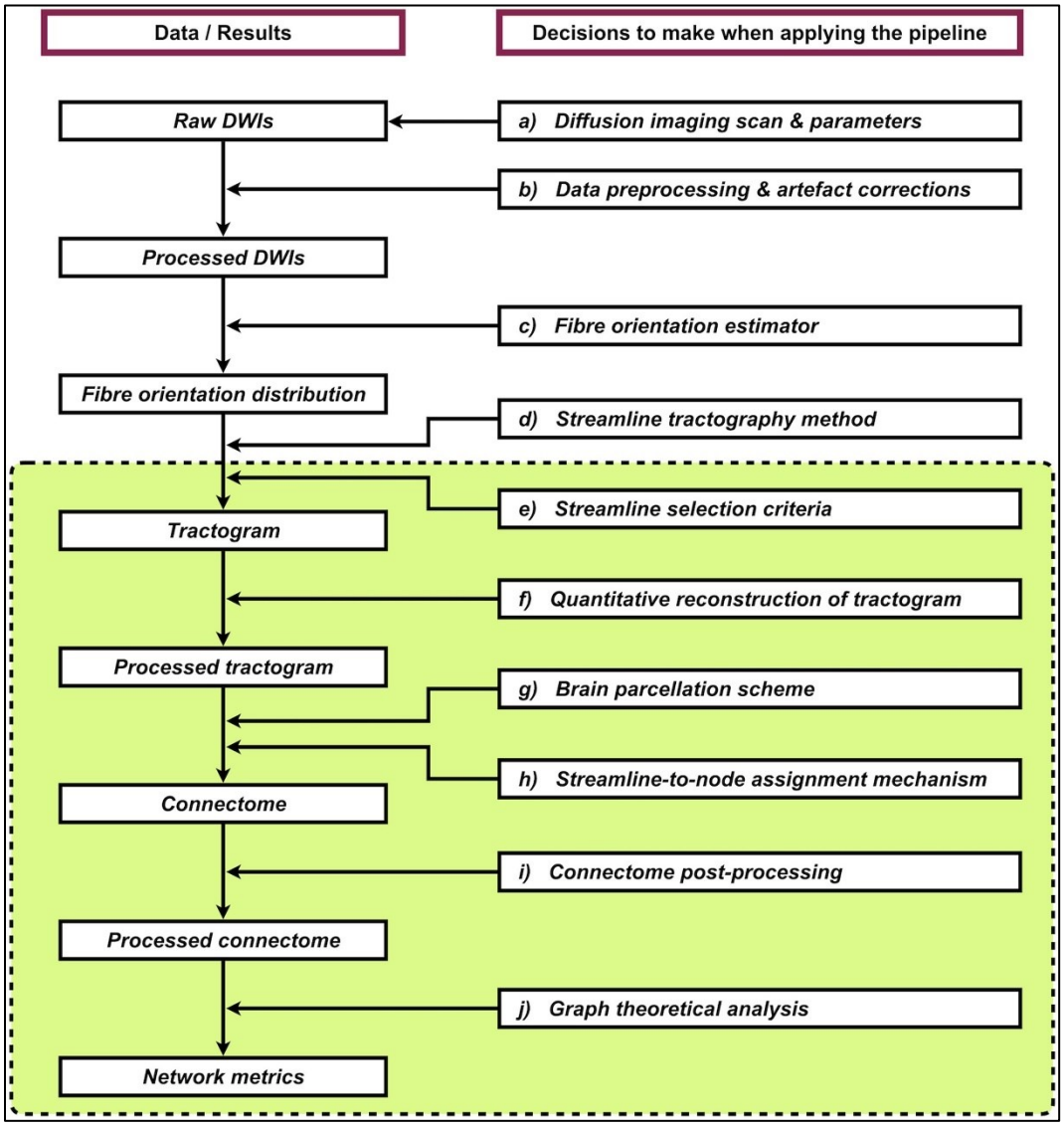

Figure 1.39. An example processing workflow for generating an individual's structural connectome using diffusion MRI data. Caption and figure from: (C. Yeh et al., 2021). Publisher's permission: http://creativecommons.org/licenses/by/4.0/. — Left column: Each box denotes the raw, interim, or final products of this pipeline. Right column: Each box describes the class of data processing involved in this pipeline. Within each procedure, there are many relevant options and parameters that have to be considered, where each choice can potentially affect the final output network metrics and the inference drawn from this technique. This shows the

complexity of data processing in tractography-based structural connectomics research. The green box indicates the processing steps that are specifically discussed in the article (C. Yeh et al., 2021).

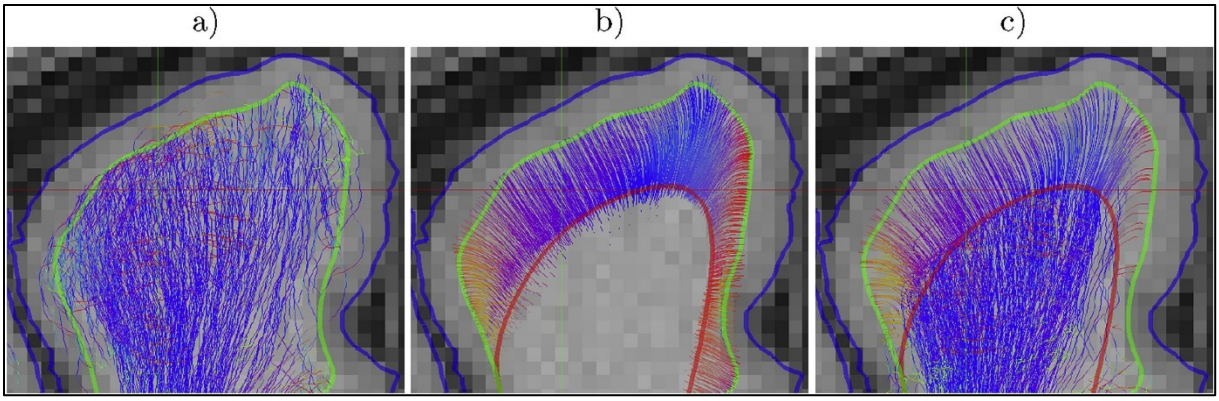

Figure 1.40. Surface-enhanced tractography. Caption and figure from: (St-Onge et al., 2018). Permission obtained. — Visualization of the Human Connectome Project subject tractography, seeded from the same initial vertices colored by their local orientation (left-right - red, anterior-posterior - green, inferior-superior - blue): a) probabilistic local tractography, b) surface flow used as streamline initial and terminal trajectory for c) surface-enhanced tractography + probabilistic local tractography. The red surface in b) and c) indicate the less-convoluted mesh generated from the surface flow shown in Figure 2 of (St-Onge et al., 2018).

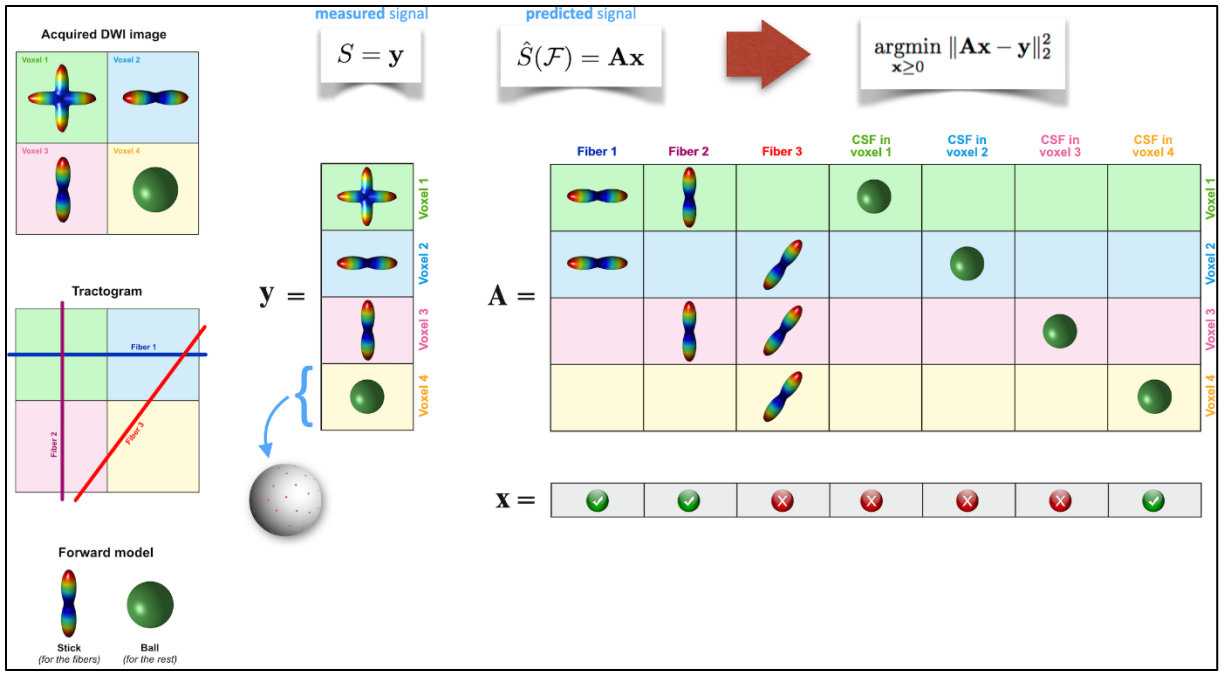

Figure 1.41. Convex optimization modeling for microstructure informed tractography (COMMIT). Caption and figure from: https://github.com/daducci/COMMIT. Publisher's permission: https://github.com/daducci/COMMIT/blob/ef88008ae2eae60b6a48ccd8ef7aad1dbfc0acf9/LICENSE. — Starting from an input set of candidate fiber-tracts estimated using standard fiber-tracking techniques, COMMIT, models the diffusion MRI signal in each voxel of the image as a linear combination of the restricted and hindered contributions generated in every location of the brain by these candidate tracts. Then, COMMIT seeks for the effective contribution of each of them such that they globally fit the measured signal at best. These weights can be efficiently estimated by solving a convenient linear system.

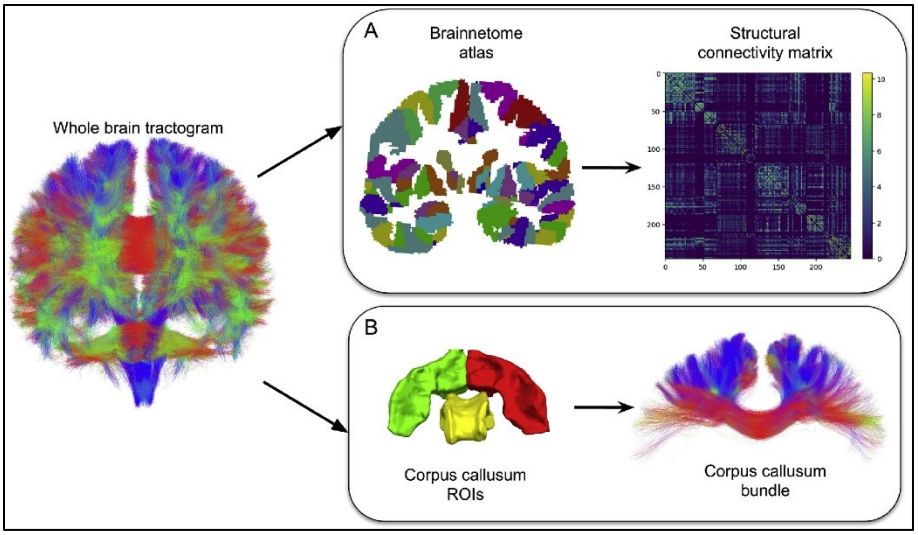

Figure 1.42. Structural connectome and fiber bundle. Figure from: (Theaud et al., 2020). Publisher's permission: http://creativecommons.org/licenses/by-nc-nd/4.0/. — For a given subject, a structural connectivity matrix can be generated from the whole-brain tractogram, with constraints applied based on a predefined parcellation atlas (A). Additionally, it is possible to isolate specific fiber bundles, such as the corpus callosum, by applying targeted filtering to the tractogram using designated regions of interest (B).

Summary and outlook. In the preceding sections, I delineated the foundational concepts of diffusion MRI, surveyed various diffusion imaging methodologies, and elucidated how diffusion data can be leveraged to delineate the architecture of cerebral white-matter pathways. It is imperative to recognize that diffusion imaging stands as a non-invasive, innocuous, and quantitative modality that facilitates the *in vivo* examination of water molecule diffusion in biological tissues. With technological advancements and the introduction of high-field MRI scanners, research in this domain is poised for significant expansion, promising enhanced insights into the intricate anatomical and functional processes of the human brain at microstructural levels. Nevertheless, accurate interpretation of diffusion data, to infer the microstructure of biological tissues reliably, necessitates a comprehensive understanding of both the capabilities of the utilized imaging equipment and the biophysical principles of the subject matter. In this thesis, I harness cutting-edge tractography-based connectome reconstruction methodologies applied to the high-resolution datasets from the Human Connectome Project, to impose constraints on whole-brain biophysical models. Specifically, I utilize pipelines designed to mitigate the biases associated with streamline termination and quantification inherent in tractography techniques. These methodologies will be expounded upon in the subsequent manuscript-centered chapters.

1.4.2 Electroencephalography and magnetoencephalography

Non-invasive electrophysiological techniques, such as electroencephalography (EEG) and magnetoencephalography (MEG), are central to the discussions in this thesis. This section aims to provide foundational knowledge on these technologies, similar to the purpose of the diffusion MRI section (1.4.1), offering critical insights necessary for understanding the subsequent chapters.

EEG and MEG are among the most crucial methodologies in whole-brain computational models due to their ability to capture a non-invasive glimpse of neural dynamics with unmatched temporal resolution (Griffiths et al., 2022). Their integration with connectomics substantially enhances our understanding of the brain's functional architecture. Furthermore, these modalities form the cornerstone of neural modeling, despite being influenced predominantly by neuron-centric perspectives.

I have specifically labeled this section as "Electroencephalography and magnetoencephalography" although EEG will not be utilized in the subsequent chapters. I did so because it is straightforward to provide a combined description of both modalities while delving into the specifics of MEG. Additionally, I intentionally adopt a neuron-centric perspective initially, but I will conclude with a more comprehensive view that includes neurons, glia, and vascular components (Buzsáki et al., 2012; Robertson, 2018).

Generators of EEG and MEG signals. In our preceding discussions, we established that to model the cerebral activity subserving behaviour and cognition, the mesoscales and macroscales of the brain become the building blocks. At these scales, cerebral activity arises from synchronized neuronal populations, typically located across various cortical areas and coupled through axonal projections (Buzsáki et al., 2012; F. Lopes da Silva, 2013; Wadman & Lopes da Silva, 2017). It is hypothesized that it is these spatially organized neuronal groups, when activated in unison, which generate detectable electrical and magnetic fields. These detectable fields can be recorded using electrodes in direct contact with or at a close distance from the scalp, enabling the non-invasive recording of specific cerebral activities through methods like EEG and MEG (Buzsáki et al., 2012; F. Lopes da Silva, 2013; Wadman & Lopes da Silva, 2017).

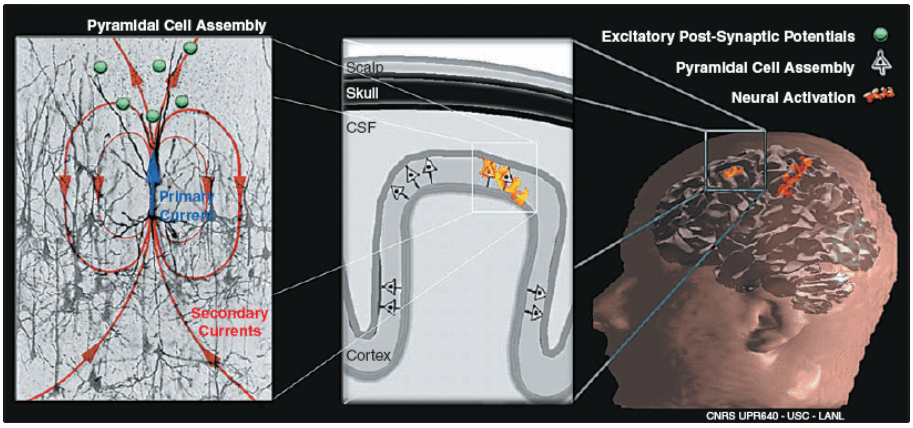

Figure 1.43. Networks of cortical neural cell assemblies are the main generators of EEG and MEG signals. Caption and figure from: (Baillet et al., 2001). Reprinted with permission from © 2001 IEEE. — *Left*: Excitatory postsynaptic potentials (EPSPs) are generated at the apical dendritic tree of a cortical pyramidal cell and trigger the generation of a current that flows through the volume conductor from the non-excited membrane of the soma and basal dendrites to the apical dendritic tree sustaining the EPSPs. Some of the current takes the shortest route between the source and the sink by travelling within the dendritic trunk (primary current in blue), while conservation of electric charges imposes that the current loop be closed with extracellular currents flowing even through the most distant part of the volume

conductor (secondary currents in red). *Center*: Large cortical pyramidal nerve cells are organized in macro-assemblies with their dendrites normally oriented to the local cortical surface. this spatial arrangement and the simultaneous activation of a large population of these cells contribute to the spatio-temporal superposition of the elemental activity of every cell, resulting in a current flow that generates detectable EEG and MEG signals. *Right*: Functional networks made of these cortical cell assemblies and distributed at possibly multiple brain locations are thus the putative main generators of MEG and EEG signals.

Figure 1.43 presents an idealized neuronal structure, focusing on pyramidal neurons, the predominant neuron type in the neocortex. These neurons are instrumental in producing the signals measured by EEG and MEG. Their dendritic trees are aligned parallel to each other while standing perpendicular to the cortical surface. This arrangement leads to additive longitudinal current flow and cancellative transverse components, thereby creating a laminar current flow along these neurons' main axes. Consequently, the combined postsynaptic activity of these concurrently active pyramidal neurons generates detectable electrical and magnetic fields, even at a considerable distance from the neuronal sources (Buzsáki et al., 2012; F. Lopes da Silva, 2013; Wadman & Lopes da Silva, 2017).

In essence, recording electrical and magnetic fields becomes feasible from the coordinated activity of a sufficiently large, spatially organized population of neurons; and this is the principle behind non-invasive techniques like EEG and MEG. EEG involves capturing the brain's electrical potentials via scalp electrodes, while MEG records the magnetic fields elicited by neuronal activity using induction coils placed around the head (see Figure 1.46). Both methods are rooted in the same fundamental process: the generation of ionic currents by excited neurons (Buzsáki et al., 2012; F. Lopes da Silva, 2013; Wadman & Lopes da Silva, 2017). Moreover, these non-invasive methods share key characteristics with invasive recordings like intracranial EEG and electrocorticograms as shown in Figure 1.44. Finally, both modalities boast the capability to monitor neuronal activity with temporal precision on the sub-millisecond scale.

The brain's natural folds significantly influence the sensitivity and orientation of its neuronal current sources, as depicted in Figure 1.43's center image. Signals originating in the gyri (the brain's convoluted ridges) typically have a quasi-radial orientation relative to the head's surface. In contrast, signals from the sulci (the brain's shallow grooves) exhibit a quasi-tangential orientation (Buzsáki et al., 2012; F. Lopes da Silva, 2013; Wadman & Lopes da Silva, 2017). MEG primarily detects these quasi-tangential dipoles, signifying activity in the sulci, while EEG is capable of detecting both radial and tangential dipoles, thus capturing activities in both gyri and sulci. Given that magnetic fields are less distorted and diffused than electrical fields by the brain's volume conductors (tissues with varying conductivities), MEG offers enhanced spatial precision in comparison to EEG (Baillet, 2017; Buzsáki et al., 2012; F. Lopes da Silva, 2013; Wadman & Lopes da Silva, 2017). Nonetheless, the topographies of EEG and MEG signals are nearly orthogonal to each other, suggesting their complementary nature, as shown in Figure 1.45. Simultaneous recordings from both modalities increase the likelihood of capturing comprehensive aspects of brain signal topographies, thus enhancing the accuracy and effectiveness of source reconstruction that we discuss next (Aydin et al., 2015; Chowdhury et al., 2015; Gross, 2019; Puce & Hämäläinen, 2017).

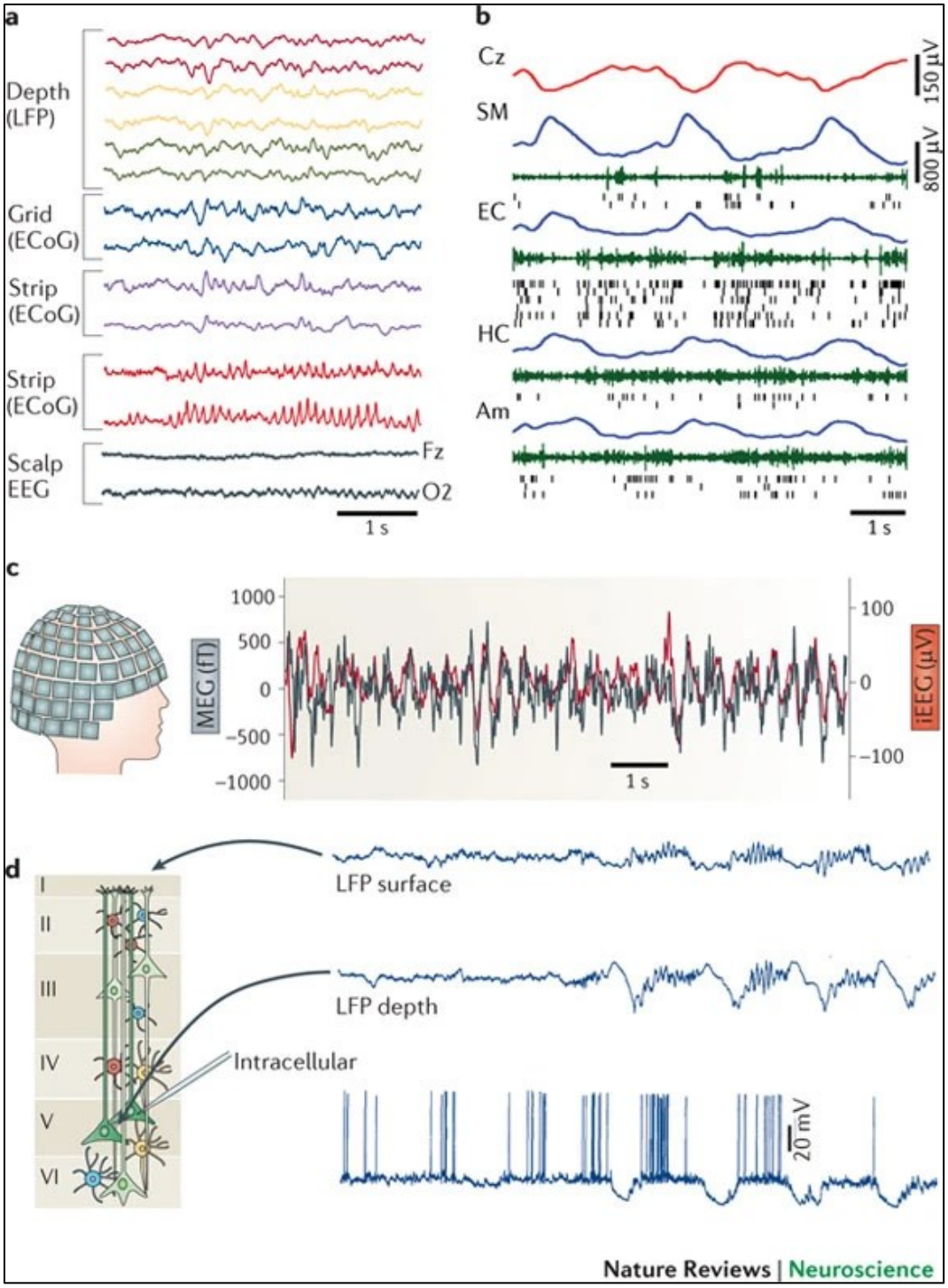

Figure 1.44. Extracellular traces using different recording methods are fundamentally similar. Caption and figure from: (Buzsáki et al., 2012). Permission obtained. — a | Simultaneous recordings from three depth electrodes (two selected sites each) in the left amygdala and hippocampus (measuring the local field potential (LFP)); a 3 × 8 subdural grid electrode array placed over the lateral left temporal cortex (measuring the electrocorticogram (ECoG); two four-contact strips placed under the inferior temporal surface (measuring the ECoG); an eight-contact strip placed over the left orbitofrontal surface (measuring the ECoG); and scalp electroencephalography (EEG) over both hemispheres (selected sites are the Fz and O2) in a patient with drug-resistant epilepsy. The amplitude signals are larger and the higher-frequency patterns have greater resolution at the intracerebral (LFP) and ECoG sites compared to scalp EEG.

b | A 6 s epoch of slow waves recorded by scalp EEG (Cz, red), and LFP (blue) recorded by depth electrodes placed in the deep layers of the supplementary motor area (SM) and entorhinal cortex (EC), hippocampus (HC) and amygdala (Am). Also shown are multiple-unit activity (green) and spikes of isolated neurons (black ticks). c | Simultaneously recorded magnetoencephalogram (MEG; black) and anterior hippocampus depth EEG (red) from a patient with drug-resistant epilepsy. Note the similar theta oscillations recorded by the depth electrode and the trace calculated by the MEG, without any phase delay. d | Simultaneously recorded LFP traces from the superficial ('surface') and deep ('depth') layers of the motor cortex in an anaesthetized cat and an intracellular trace from a layer 5 pyramidal neuron. Note the alternation of hyperpolarization and depolarization (slow oscillation) of the layer 5 neuron and the corresponding changes in the LFP. The positive waves in the deep layer (close to the recorded neuron) are also known as delta waves. iEEG, intracranial EEG. Part a courtesy of G. Worrell, Mayo Clinic, Minneapolis, Minnesota, USA, and S. Makeig, University of California at San Diego, USA. Part b is reproduced, with permission, from (Nir et al., 2011) © (2011) Cell Press. Part c courtesy of S. S. Dalal, University of Konstanz, Germany, and J.-P. Lachaux and L. Garnero, Université de Paris, France. Part d is reproduced, with permission, from (Contreras & Steriade, 1995) © (1995) Society for Neuroscience.

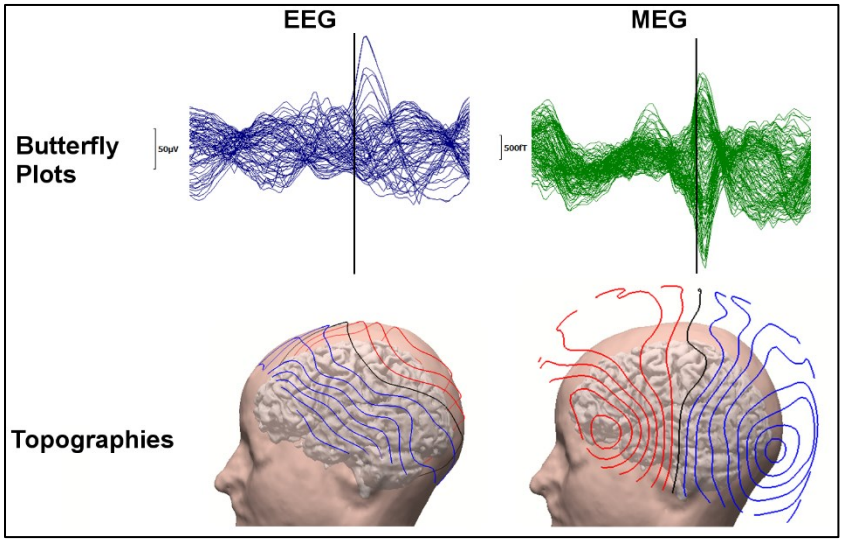

Figure 1.45. EEG and MEG topographies. Caption and figure from: (Aydin et al., 2014). Publisher's permission: http://creativecommons.org/licenses/by/4.0/. — The waveform and topography of an example epileptic spike. FT9 spike: 71 channel EEG (left column) and 129 channel MEG (right column) butterfly plots (upper row, time-point −13 ms marked with a black line) and corresponding topographies from left view at time-point −13 ms plotted on individual brain and skin (bottom row).

In EEG and MEG, we are interested in pinpointing (localizing, reconstructing) the current sources (generators) within the brain that gave rise to the sensor recordings. This mathematical problem is called the electromagnetic inverse problem (see Figure 1.46). Solving this problem requires initially to resolve the forward problem (based on Maxwell's equations, often using quasi-static approximations), which estimates the EEG and MEG data generated by known current sources in the brain (see Figure 1.46).

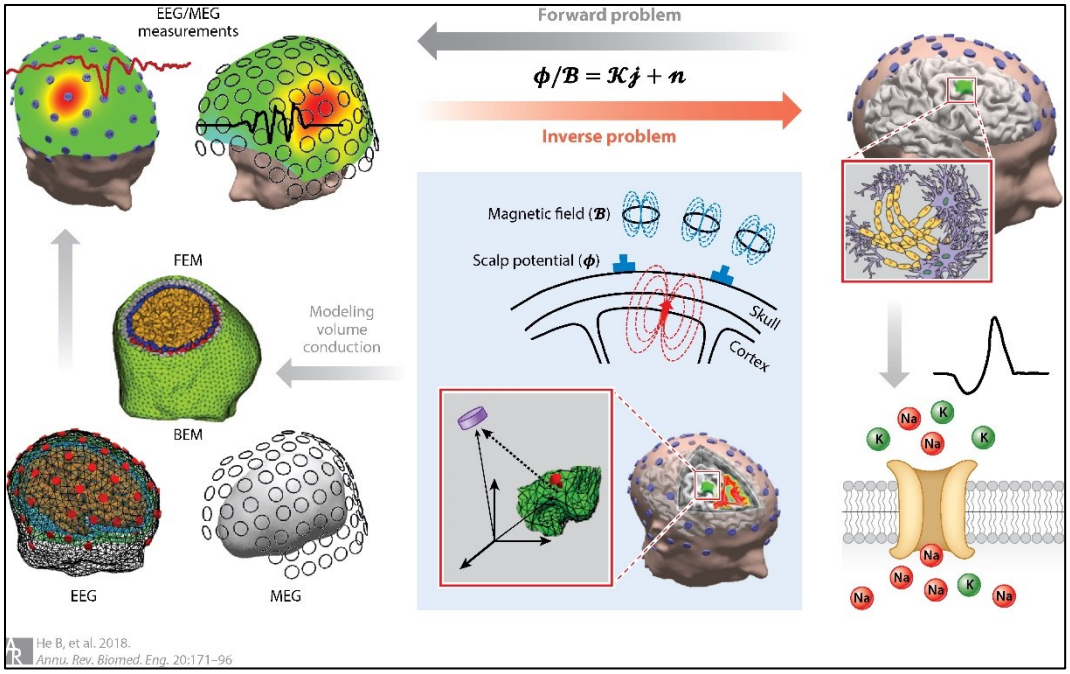

Figure 1.46. Physiological basis of EEG and MEG, and the biophysical modeling of the forward and inverse problems. Caption and figure from: (B. He et al., 2018). Permission obtained. — The electrical activity of the brain arises from the ions (charges) that enter and exit the selective membrane of neurons. EEG/MEG signals manifested on the scalp represent the underlying activation of synchronous neuronal ensembles, which encode brain function or dysfunction. Current dipoles can be used to model neuronal currents. Maxwell's equations can be solved to obtain the electric potential (EEG) and the magnetic field (MEG)—the so-called forward problem. Various numerical techniques, such as the boundary element method (BEM) and the finite element method (FEM), can be used to model the head volume conductor linking neuronal current dipoles to EEG/MEG. The current density distribution of brain activity can be estimated from scalp EEG/MEG by means of signal processing algorithms—the so-called inverse problem. The lead-field matrix is denoted by $\mathcal{K}$, the current density distribution as $\boldsymbol{j}$, and $\boldsymbol{n}$ is the additive noise in the recording EEG/MEG system.

Forward model. The forward model in EEG and MEG is a construct that indicates how neural activity within the brain translates to measurable signals at the sensors (B. He et al., 2018). Solving the forward problem in EEG and MEG requires precise knowledge of the measurement geometry, which involves the spatial relationship between the head and the sensors (Gross, 2019). This is accurately modeled using a three-dimensional representation of the head, incorporating detailed anatomical structures and the precise locations of sensors as set up during the recording session (Gross, 2019; He et al., 2018). The head model typically reflects various tissue types (e.g., scalp, skull, and brain tissues) derived from imaging data such as MRI, and their electrical conductivities derived, e.g., from electrical impedance tomography (Mansouri et al., 2021; Wadman & Lopes da Silva, 2017). With this head model and the known sensor positions, Maxwell's equations, which govern the behavior of electric and magnetic fields, can be applied (Gross, 2019; He et al., 2018). These equations allow for the computation of the electric and magnetic fields at each sensor location, resulting from a hypothetical current dipole placed at a specific location within the head model and oriented in a defined direction. In this context, the source model refers to all the probable spatial locations of the current dipoles within the brain (Gross, 2019; He et al., 2018). Ultimately, the forward model provides a lead field or gain matrix, which operates as a projector mapping neuronal activity from the source space (within the brain) to the sensor space (where measurements are taken).

For personalized analysis, subject-specific T1-weighted MRI is preferred for head modeling; otherwise, a standard anatomical template may suffice. Common head modeling methods in EEG and MEG include (B. He et al., 2018):

- *Single sphere method.* Simplifies head geometry as a homogenous sphere with uniform electromagnetic properties.
- *Overlapping spheres method.* Improves upon the single sphere model by fitting localized spheres to sensors, providing a better approximation of head geometry relative to sensors.
- *Boundary element method.* Uses segmented concentric surfaces from MRI for a more accurate head geometry and tissue boundary representation, assuming isotropic conductivity.
- *Finite element method.* Advances modeling further by accommodating anisotropic conductivity, allowing detailed modeling of tissue properties and geometries.

Each modeling approach balances computational complexity and realism, chosen based on study-specific needs and limitations (B. He et al., 2018). For instance, research shows that MEG's forward problem solution is less affected by the conductivity values of surrounding brain tissues (brain, skull, skin) than EEG's (Baillet, 2017; B. He et al., 2018). For example, the overlapping spheres method can be sufficient for MEG where a three-compartment boundary element method is necessary for EEG. This difference stems from MEG's focus on magnetic fields generated by neuronal currents, which are minimally influenced by tissue conductivities compared to EEG's electric fields. Magnetic fields traverse biological tissues with little distortion, whereas electric fields are significantly altered by tissue conductivities, especially by the skull's high resistance. Therefore, MEG offers a clearer representation of neuronal activity, enhancing spatial accuracy and simplifying forward modeling. Nonetheless, MEG's accuracy still depends on factors like neuronal current orientation and sensor placement, crucial for precise source localization and MEG data interpretation.

Inverse model. The EEG and MEG inverse problem is concerned with estimating neuronal sources within the brain from sensor-space data (B. He et al., 2018). It can be solved by minimizing the difference between the measured signals and those generated by source estimates through the head volume conductor model. Some illustrations are shown in Figure 1.47. Discussing in detail the many different techniques would add significant lengths to this thesis, so instead, I will describe only those that directly relate to the subsequent manuscript-chapters.

Mathematically, all inverse problems are founded on the same fundamental principle, encapsulated in the equation:

$$M = GJ + E \tag{1.30}$$

where $M \in \mathbb{R}^{N_C \times N_T}$ denotes the EEG or MEG data from N_C channels over N_T time samples, $J \in \mathbb{R}^{(3N_D) \times N_T}$ is the unknown current density distribution encompassing N_D dipolar sources with unconstrained orientations, the orientation-free lead-field matrix is denoted by $G \in \mathbb{R}^{N_C \times (3N_D)}$, and $E \in \mathbb{R}^{N_C \times N_T}$ is the additive noise in the recording system. The lead field matrix G is determined by the forward problem, as discussed previously, taking into account the chosen head model and the placement of electrodes, while inverse methods aim to provide an estimate of J, denoted as $\hat{J}$.

Before describing some inverse methods, it is important to understand that the task of solving the inverse problem is inherently challenging due to its ill-posed nature, where multiple intracerebral source configurations can produce identical sensor signal distributions, whether as electrical potentials or magnetic fields. Said otherwise, there is an *inherent non-uniqueness* of the problem (B. He et al., 2018). The complexity is further heightened by the discrepancy between the limited number of measurements (typically a few hundred channels, N_{C}) and the vast number of potential sources (several thousand dipolar sources, N_{D}), i.e., there are *practical limitations* (B. He et al., 2018). There are other limitations which I will address later below.

To address the two issues listed above, certain a priori assumptions about cortical current distributions are made (B. He et al., 2018). Commonly, it is assumed that brain activity generators can be modeled as distributed current dipoles across the cortical surface at a sufficient resolution allowing to represent sulci and gyri (this is called a distributed source model, typically encompassing from 4,000 to 164,000 sources per hemisphere; https://www.fieldtriptoolbox.org/tutorial/sourcemodel/). Furthermore, these dipoles are often constrained orientation-wise, aligning perpendicularly to the cortical surface, reflecting the orientation of pools of pyramidal neurons (though this can be relaxed). This incorporation of such anatomical constraints helps regularize the inverse problem. Consequently, solving this problem involves an underdetermined linear system where the aim is to deduce the current density of several thousand dipoles (N_{D}) using data from merely a few hundred sensors (N_{C}).

When anatomical priors are incorporated by constraining current dipole orientations to be perpendicular to the cortical surface at each vertex location, an oriented lead-field matrix $G_{\mathrm{fixed}} = G\Theta \in \mathbb{R}^{N_{\mathrm{C}} \times N_D}$ is used in Equation (1.30), instead of G. Here, the matrix Θ contains unit vectors representing the direction of current for each dipole. Therefore, the remaining of the discussion below maintains G, without loss of generality.

In addition to anatomical constraints imposed by the source model, various regularization strategies based on different assumptions are specified, each leading to a different source localization method (B. He et al., 2018). Depending on the physiological plausibility of the regularization introduced, the distributed source estimates bear different characteristics and affinity to neuronal activity on a mesoscopic scale.

Minimum norm solution family. The minimum norm (MN) approach is a foundational solution to the inverse problem, particularly for distributed source models (M. S. Hämäläinen & Ilmoniemi, 1994; B. He et al., 2018). It formulates the inverse problem as a least-squares optimization task and utilizes the l^2-norm for regularization, thereby addressing the underdetermined nature of the problem by selecting the least energetic source configuration that matches the observed data (B. He et al., 2018).

Although the MN approach is based on solid mathematical principles, offering a practical solution by favoring the simplest source distribution that explains the data, its physiological interpretability remains challenging (B. He et al., 2018). The premise that the most energy-*efficient* configuration reflects the true neuronal sources may not fully capture the complexities of brain activity, as neuronal sources may not adhere to *minimal* energy use. Furthermore, the MN approach inherently exhibits a predisposition towards superficial sources (Lin et al., 2006), a consequence of the lead-field matrix's construction, which inherently incorporates the electromagnetic field's decay from a dipole with the cube of the distance (M. Hämäläinen et al., 1993; Sarvas, 1987). This

characteristic may inadvertently overlook deeper neuronal activities that could be of significant physiological relevance.

Notwithstanding these considerations, the MN approach remains a popular choice for EEG and MEG source imaging, attributed to its simplicity, computational efficiency, and solid mathematical underpinnings (B. He et al., 2018). It proves particularly useful for general localization of brain activity where the precise delineation between deep and superficial sources is not critical. However, interpreting MN-derived results necessitates a cautious approach, taking into account the inherent biases and assumptions of the method. It is advisable that MN findings be corroborated with additional neuroimaging or physiological data to validate the proposed source distributions (B. He et al., 2018).

The mathematical formulation of the MN solution is expressed as:

$$\hat{J}_{\mathrm{MN}} = RG^{\top}(GRG^{\top} + \lambda^2 C)^{+}M \tag{1.31}$$

In this equation, $^{\top}$ denotes matrix transpose, $^{+}$ signifies the Moore–Penrose inverse, R and C represent the source covariance and data noise-covariance matrices, respectively, and λ^2 is the Tikhonov regularization parameter. The simplest MN solution treats R as a scalar matrix.

The regularization parameter λ^2 plays a critical role in balancing spatial smoothness and sensitivity to noise (P. C. Hansen, 1992). An increased λ augments the regularization term's impact on the solution, steering it towards spatial smoothness. This bias towards minimizing the current norm results in smoother estimated current distributions across the brain, attenuating high-frequency variations that could be attributed to noise. While this smoothness can mitigate noise effects, it risks underrepresenting the true amplitude of neuronal currents, potentially masking underlying neural activities. Conversely, a reduced λ prioritizes data fidelity, enhancing the solution's adherence to observed data fluctuations. This heightened data conformity may yield a more precise depiction of localized neuronal sources, reflecting variations in measured signals more faithfully. However, this advantage is tempered by a heightened susceptibility to measurement noise and the risk of ill-conditioning, which may inadvertently amplify noise alongside genuine neuronal signals. Selecting an optimal λ is thus a delicate balance between achieving a solution that is smooth enough to be robust against noise, yet detailed enough to accurately reflect the underlying neuronal activity. Various methods, such as the L-curve criterion or generalized cross-validation, are often employed to determine an appropriate value for λ that optimizes this trade-off (P. C. Hansen, 1992).

To ensure the noise covariance matrix retains essential statistical properties such as positive definiteness and good conditioning, it is often regularized. A common approach is to modify the matrix's spectrum, typically by truncating its smallest eigenvalues or setting them to a minimum threshold. This regularization helps stabilize the solutions to the inverse problem by reducing the impact of noise and numerical instabilities (for reference refer to https://mne.tools/stable/documentation/implementation.html).

Data whitening is frequently applied in practice, utilizing a whitening matrix $W = C^{-1/2}$. This leads to an adjusted formulation of the MN solution:

$$\hat{J}_{\mathrm{MN}} = R\tilde{G}^{\top}\left(\tilde{G}R\tilde{G}^{\top} + \lambda^2 I\right)^{+}\tilde{M} \tag{1.32}$$

Here, $\tilde{M} = WM$ is the whitened data, and $\tilde{G} = WG$ is the spatially whitened lead-field matrix. The whitening process aims to transform the data such that its covariance is the identity matrix, thereby normalizing the influence of noise across different sensors.

A depth-weighting prior is introduced through the source covariance matrix R to equitably account for sources at varying depths. This adjustment is particularly crucial for ensuring that deeper sources, which may be underrepresented in sensor data due to the attenuation of signals as they propagate through the head, receive adequate representation in the source reconstruction process. Depth weighting is typically implemented by scaling the diagonal elements of R corresponding to each source location i by a factor proportional to $\left(g_{x,i}{}^{\top} g_{x,i} + g_{y,i}{}^{\top} g_{y,i} + g_{z,i}{}^{\top} g_{z,i}\right)^{-\gamma}$, where $g_{x,i}$, $g_{y,i}$, and $g_{z,i}$ are the three columns of G at the source location i, and γ is a depth weighting exponent. Often the factor has an imposed upper limit to prevent excessive weighting. For more details, refer to (Lin et al., 2006) and https://mne.tools/stable/documentation/implementation.html.

Whitening the data also facilitates a data-driven approach for determining the regularization hyperparameter λ. As discussed by (Lin et al., 2006), λ^2 can be set based on the trace of the whitened gain matrix and the signal-to-noise ratio (SNR) of the whitened data: $\lambda^2 = \mathrm{tr}\left(\tilde{G}R\tilde{G}^{\top}\right)/(N_C \times \mathrm{SNR}^2)$. Here, N_C represents the number of channels, and SNR is the signal-to-noise ratio of the whitened data. A higher SNR implies that the data is less noisy, allowing for a smaller λ that prioritizes data fidelity. Conversely, a lower SNR indicates noisier data, necessitating a larger λ to enhance the smoothness and stability of the solution. The factor given by the trace of the gain matrix reflects the overall sensitivity of the sensor array to neuronal sources across the brain, ensuring that λ scales with the properties of the measurement system.

Employing these strategies, this thesis adopts a depth-weighted MN estimate approach, which will be further explored in Chapter 4 starting on page 169. Some other solutions of the MN family are presented in Figure 1.47.

Maximum entropy solution family. The principle of maximum entropy, popularized by E. T. Jaynes (E. Jaynes, 1968), is a cornerstone of information theory used to assign the most unbiased probability distribution to quantities underpinned by incomplete information, typically in the form of expected values. Unlike Bayesian or Laplacian inference, which updates probabilities based on new evidence, the maximum entropy approach focuses on maximizing the entropy of a distribution to reflect the state of maximal ignorance consistent with the given constraints (Cheeseman, 2004; Djafari, 1994; E. T. Jaynes, 1988; Mohammad-Djafari, 2015). Despite this distinction, the maximum entropy principle often employs the language of priors and posteriors, leading to a common misconception about its relation to Bayesian–Laplacian inference. In practice, the maximum entropy principle can be utilized to define *subjective* prior distributions within Bayesian–Laplacian frameworks, further illustrating the complementarities between these methodologies. The nuanced interplay and distinctions between maximum entropy and Bayesian–Laplacian inferences are explored in (Caticha, 2008; Caticha & Giffin, 2006; Cheeseman, 2004; Gamboa & Gassiat, 1997; Giffin & Caticha, 2007; J. He & Kolovos, 2018; E. T. Jaynes, 1988; Mohammad-Djafari, 2006, 2015; Toda, 2011; Waldrip & Niven, 2017).

Consider a random variable X, with an unknown probability density function ρ^X, and suppose our knowledge is limited to a set of expected values:

$$m_k = \mathrm{E}\{\phi_k(X)\} = \int \rho^X(x)\phi_k(x)\,\mathrm{d}x\,, \quad k \in [\![1, K]\!] \tag{1.33}$$

where $\{\phi_k\}_k$ represents a known set of functions. Given that an infinite array of distributions could satisfy these constraints, the principle of maximum entropy advocates for selecting the distribution that maximizes entropy, thus embodying the least number of additional assumptions.

To formalize as in (M. Djafari, 1994; Mohammad-Djafari, 2015), we define the set of feasible solutions as:

$$\mathcal{P}_X = \left\{\rho^X\colon \quad \int \rho^X \phi_k = m_k, \quad k \in [\![0, K]\!]\right\} \tag{1.34}$$

Here, ϕ_0 is defined as a constant function equal to 1 to ensure the normalization of ρ^X, making $m_0 = 1$. The maximum (*Shannon*) entropy principle then poses an optimization problem:

$$\rho^X_{\mathrm{ME}} = \underset{\rho^X \in \mathcal{P}_X}{\operatorname{argmax}} \left\{\mathrm{H}[\rho^X] \coloneqq -\int \rho^X \ln(\rho^X)\right\} \tag{1.35}$$

Addressing this problem, we introduce Lagrange multipliers λ_0 for normalization and $\lambda = (\lambda_1, \dots, \lambda_K) \in \mathbb{R}^{K\times 1}$ for other constraints, leading to the Lagrangian $\mathcal{L}$:

$$\mathcal{L}(\rho^X, \lambda_0, \lambda) = \mathrm{H}[\rho^X] - (\lambda_0 - 1)\left(\int \rho^X - 1\right) - \sum_{k=1}^{K} \lambda_k \left(\int \rho^X \phi_k - m_k\right) \tag{1.36}$$

Provided it exists, the optimization problem's unique solution corresponds to a saddle point of $\mathcal{L}$, verifying:

$$\begin{aligned} \frac{\partial}{\partial \rho^X}\mathcal{L}(\rho^X, \lambda_0, \lambda) &= -\ln(\rho^X) - \lambda_0 - \sum_{k=1}^{K} \lambda_k \phi_k = 0 \\ \frac{\partial}{\partial \lambda_0}\mathcal{L}(\rho^X, \lambda_0, \lambda) &= \int \rho^X - 1 = 0 \\ \frac{\partial}{\partial \lambda}\mathcal{L}(\rho^X, \lambda_0, \lambda) &= \sum_{k=1}^{K} \left(\int \rho^X \phi_k - m_k\right) = 0 \end{aligned} \tag{1.37}$$

This yields a maximum entropy solution ρ^X_{ME} in an exponential form:

$$\rho^X_{\mathrm{ME}}(x) = \frac{1}{Z(\lambda^{\mathrm{sol}})} \exp\left(-\sum_{k=1}^{K} \lambda_k^{\mathrm{sol}} \phi_k(x)\right) \tag{1.38}$$

where the partition function Z ensures normalization and is related to the Lagrange multipliers as:

$$Z(\lambda) = \exp(\lambda_0) = \int \exp\left(-\sum_{k=1}^{K} \lambda_k \phi_k(x)\right) \mathrm{d}x \tag{1.39}$$

With Z thus defined, the optimal Lagrange multipliers λ^{sol} are determined to satisfy the constraints, derived from the logarithm of the partition function:

$$-\frac{\partial}{\partial\lambda_k}\ln\big(Z(\lambda_1,\dots,\lambda_K)\big)=\int \rho^X\phi_k=m_k,\quad k\in[\![1,K]\!] \tag{1.40}$$

Consequently, we need to solve a system of K nonlinear equations with as many unknowns $\{\lambda_k\}_{1\le k\le K}$ as data $\{m_k\}_{1\le k\le K}$, which is summarized as the unconstrained dual optimization problem:

$$\lambda^{\mathrm{sol}}=\underset{\lambda}{\operatorname{argmin}}\big\{\ln\big(Z(\lambda)\big)+\lambda^{\top}m\big\},\quad m=(m_1,\dots,m_K)\in\mathbb{R}^{K\times 1} \tag{1.41}$$

where $^{\top}$ denotes matrix transpose. Solving this problem usually requires a numerical method such as Newton–Raphson's, as discussed in (M. Djafari, 1994).

The maximum entropy is finally computed as:

$$\mathrm{H}_{\max}=\int \rho^X_{\mathrm{ME}}\left(\ln\left(Z\left(\lambda^{\mathrm{sol}}\right)\right)+\sum_{k=1}^{K}\lambda_k^{\mathrm{sol}}\phi_k\right)=\ln\left(Z\left(\lambda^{\mathrm{sol}}\right)\right)+{\lambda^{\mathrm{sol}}}^{\top}m \tag{1.42}$$

Transitioning to maximum relative entropy (MrE), we replace $\mathrm{H}[\rho^X]$ with the relative entropy (i.e., the negative of the Kullback–Leibler divergence, in the present context) $\mathrm{D}[\rho^X:\rho_0^X]\coloneqq-\int\rho^X\ln\left(\frac{\rho^X}{\rho_0^X}\right)$ in the primal optimization from Equation (1.35), incorporating a known reference distribution ρ_0^X. This extension yields:

$$\begin{aligned}\rho^X_{\mathrm{MrE}}(x)&=\frac{1}{Z(\lambda^{\mathrm{sol}})}\rho_0^X(x)\exp\left(-\sum_{k=1}^{K}\lambda_k^{\mathrm{sol}}\phi_k(x)\right)\\ Z\left(\lambda^{\mathrm{sol}}\right)&=\int\rho_0^X(x)\exp\left(-\sum_{k=1}^{K}\lambda_k^{\mathrm{sol}}\phi_k(x)\right)\mathrm{d}x\end{aligned} \tag{1.43}$$

highlighting how prior information (ρ_0^X) can be seamlessly integrated into the entropy maximization framework.

When employing a uniform reference law ρ_0^X, the principles of maximum entropy and maximum relative entropy align. This convergence underscores the adaptability of Jaynes' original maximum entropy formulation to incorporate prior distributions, akin to the reference distribution in maximum relative entropy. While the term "relative" in "maximum relative entropy" highlights the inclusion of a reference or prior distribution, common usage, especially outside statistical circles, often simplifies this to "maximum entropy". Conceptually, through the maximum relative entropy principle, we update our knowledge of an unknown probability distribution based on new information, typically in the form of expected values, against an assumed reference distribution (Banavar & Maritan, 2007; Caticha & Giffin, 2006; Giffin & Caticha, 2007; Mohammad-Djafari, 2006, 2015; Muñoz-Cobo et al., 2017; Thurner et al., 2017; Toda, 2011).

It is noteworthy that the maximum relative entropy solution bears a deep connection with the solution of the maximum likelihood approach (see (Mohammad-Djafari, 2015) for a detailed

discussion). Moreover, by revisiting and potentially reframing the axioms underpinning the principle of maximum relative entropy, one can achieve a harmonization with Bayesian–Laplacian inference principles. This alignment allows for meaningful comparisons between distributions derived from maximum relative entropy and Bayesian–Laplacian methods, further enriching the dialogue between these inferential frameworks (for an in-depth exploration, see (Caticha, 2008; Caticha & Giffin, 2006; Cheeseman, 2004; Gamboa & Gassiat, 1997; Giffin & Caticha, 2007; Toda, 2011)). Finally, pertaining to the maximum entropy principle and its extensions, the following references offer a broad spectrum of perspectives on the concept of entropy *per se*, beyond Shannon's: (Jizba & Korbel, 2019; Koutsoyiannis & Sargentis, 2021; Thurner et al., 2017, 2018).

The preceding derivations focused on scalar variables. However, the extension of the scalar variable to the finite-dimensional vectorial case is straightforward. For a notable example, consider a non-degenerate multivariate normal distribution for an n-diemsional vector $X \sim \mathcal{N}(\mu, R)$ with mean vector μ and covariance matrix R, the (differential) entropy is then captured by the Equation (1.44). Furthermore, relative to a reference distribution $\mathcal{N}(\mu_0, R_0)$ where R_0 is non-singular, the relative entropy is articulated as Equation (1.45).

$$\frac{1}{2}\ln(|2\pi e R|) = \frac{1}{2}(n\ln(2\pi) + n + \ln(|R|)) \tag{1.44}$$

$$-\frac{1}{2}\left(\mathrm{tr}\left({R_0}^{-1}R\right) + (\mu_0 - \mu)^{\top}{R_0}^{-1}(\mu_0 - \mu) - n + \ln\left(\frac{|R_0|}{|R|}\right)\right) \tag{1.45}$$

Here $|\cdot|$ denotes the matrix determinant, e represents Euler's number, and $\mathrm{tr}(\cdot)$ is the matrix trace operator. Another extension of the scalar variable to the finite-dimensional vectorial case will be detailed in Chapter 4 starting on page 169, but see also (M. Djafari, 1994; Mohammad-Djafari, 2015).

In the preceding derivations, we assumed Lebesgue's standard measure as the reference, a useful simplification in maximum entropy problems. However, for a more generalized approach applicable to any measurable space, we may consider a reference measure P_0. The solution P, defined on the same space, is presumed absolutely continuous with respect to P_0 ($\mathrm{P} \ll \mathrm{P}_0$), and our objective is to maximize:

$$-\int \frac{\mathrm{dP}}{\mathrm{dP}_0}\ln\left(\frac{\mathrm{dP}}{\mathrm{dP}_0}\right)\mathrm{dP}_0 = -\int \ln\left(\frac{\mathrm{dP}}{\mathrm{dP}_0}\right)\mathrm{dP} \tag{1.46}$$

Here, $\frac{\mathrm{dP}}{\mathrm{dP}_0}$ denotes the Radon–Nikodym derivative of the measure P with respect to P_0 and can serve as a density function. This generalized construct enables us to express the optimization problem in a familiar form, even when the reference measure P_0 differs from the Lebesgue measure. For a random variable X with the measure P as its distribution, its density $\rho^X = \frac{\mathrm{dP}}{\mathrm{dP}_0}$ facilitates the maximization of $-\int \rho^X \ln(\rho^X)\,\mathrm{dP}_0$, seamlessly integrating into the earlier maximum entropy and maximum relative entropy derivations. Moreover, this approach allows for the incorporation of prior information, represented by a prior density ρ_0^X, into the reference measure P_0. Adopting a reference measure P_0 beyond the Lebesgue measure permits a broader application of maximum entropy principles to accommodate a variety of spaces and measures (Djafari, 1994; Gamboa, 1989; Gamboa & Gassiat, 1997).

In this thesis, we employ the maximum (relative) entropy on the mean (MEM) approach (Djafari, 1994; Gamboa, 1989; Gamboa & Gassiat, 1997), a nuanced application of the broader maximum (relative) entropy framework that emphasizes constraints related to the distribution's mean (first-order moment):

$$m_k = \mathrm{E}\{\phi_k(X)\} = \int x\rho^X(x)\,\mathrm{d}x\,, \quad k \in [\![1, K]\!] \tag{1.47}$$

This method has proven effective in addressing a wide array of inverse problems, as highlighted by many works across different fields (Amblard et al., 1999, 2004; Cai et al., 2022; Clarke, 1989; Clarke & Janday, 1989; M. Djafari, 1994; Mohammad-Djafari, 2015; Muñoz-Cobo et al., 2017; Rioux et al., 2020; Vaisbourd et al., 2022).

Formally, in solving the bioelectromagnetic inverse problem as earlier posited in Equation (1.30), we aim to determine the distribution ρ_{MEM} of current sources J given EEG and MEG data M, a lead field matrix G, and a reference distribution ρ_0:

$$\begin{aligned} \rho_{\mathrm{MEM}} &= \underset{\rho\in\mathcal{P}}{\operatorname{argmax}} \left\{ D[\rho:\rho_0] = -\int \rho(j) \ln\left(\frac{\rho(j)}{\rho_0(j)}\right) \mathrm{d}j \right\} \\ \mathcal{P} &= \left\{ \rho: \quad G\int j\rho(j)\,\mathrm{d}j = M \right\} \end{aligned} \tag{1.48}$$

which retains the exponential form:

$$\begin{aligned} \rho_{\mathrm{MEM}}(j) &= \frac{1}{Z(\lambda^{\mathrm{sol}})}\rho_0(j)\exp\left(-\lambda^{\mathrm{sol}^{\top}} G j\right) \\ Z\left(\lambda^{\mathrm{sol}}\right) &= \int \rho_0(j)\exp\left(-\lambda^{\mathrm{sol}^{\top}} G j\right)\,\mathrm{d}j \end{aligned} \tag{1.49}$$

The optimal distribution's mean, J_{MEM}, is subsequently determined:

$$J_{\mathrm{MEM}} = \int j\rho_{\mathrm{MEM}}(j)\,\mathrm{d}j \tag{1.50}$$

In contrast to previous derivations that assumed noise-free observations, we must now enhance the Lagrangian, originally formulated in Equation (1.36), by introducing an additional term (usually quadratic) to account for observation noise (Djafari, 1994). This adjustment leads to an additional term in the dual optimization problem in Equation (1.41), and allows to acknowledge the presence of independent, identically distributed, additive, normally centered noise with a known non-singular covariance matrix, just like the minimum norm approach. By incorporating the noise characteristics directly into the optimization process, the model's ability to handle the inherent uncertainties in EEG and MEG data is enhanced, leading to more robust and reliable solutions. Chapter 4 starting on page 169, will present a concrete example illustrating how this adjusted MEM approach is applied to solve a bioelectromagnetic inverse problem, as proposed by (Amblard et al., 2004), highlighting the practical integration of noise considerations into the entropy maximization framework and showcasing the method's applicability to real-world scenarios.

Additionally, when focusing on EEG and MEG inverse problems, a pivotal aspect of these MEM applications is the careful selection of the reference law, as suggested by (Amblard et al., 2004), which has seen active developments (Afnan et al., 2023; Amblard et al., 2004; Aydin et al., 2020;

Chowdhury et al., 2013, 2016; Deslauriers-Gauthier et al., 2020; Lina et al., 2014; Zerouali et al., 2013). This thesis will adopt the specific MEM extension proposed by (Afnan et al., 2023; Lina et al., 2014), which will be detailed in Chapter 4 starting on page 169.

A recurring theme in MEM extensions for EEG and MEG distributed source reconstructions is the assumption that EEG and MEG source model dipoles can be grouped according to a cortical parcellation (e.g., data-driven or based on template atlases), leading to a simplified model where each parcel is either active or inactive, represented by Gaussian distributions. This assumption, endorsed by works such as (Afnan et al., 2023; Amblard et al., 2004; Aydin et al., 2020; Chowdhury et al., 2013, 2016; Lina et al., 2014; Zerouali et al., 2013), facilitates a structured approach to the inverse problem, allowing for a more tractable analysis within the MEM framework.

In this framework, we delineate N_P cortical parcels, each parcel k characterized by a time-dependent latent state S_k (that can be either active or inactive) from a state vector $S = (S_1, \dots, S_{N_P})$, with joint density ρ^S (which reflects the collective states across all parcels). Assuming the current sources J_k within the k-th parcel depend solely on its state S_k the joint prior density is summarized as:

$$\rho_0(J, S) = \rho^S(S) \prod_{k=1}^{N_P} \rho_0(J_k|S_k) \tag{1.51}$$

This formulation allows for a modular approach to modeling brain activity, where the complexity of interdependencies is managed through the independent consideration of each parcel's state. Incorporating this joint prior into the MEM framework has yielded successes in reconstructing both normal and pathological brain activities under various conditions, from resting states to specific task engagements. These applications, as demonstrated in studies by (Afnan et al., 2023; Amblard et al., 2004; Aydin et al., 2020; Chowdhury et al., 2013, 2016; Lina et al., 2014; Zerouali et al., 2013), highlight the MEM approach's versatility and effectiveness in EEG and MEG source imaging.

However, the independence hypothesis may oversimplify the inherently networked nature of brain activity. Extensions to MEM, such as those proposed by (Deslauriers-Gauthier et al., 2020), introduce anatomical priors based on diffusion MRI to better reflect the brain's connectivity:

$$\begin{aligned} \rho_0(J, S, C) &= \varphi(C)\rho^S(S|C) \prod_{k=1}^{N_P} \rho_0(J_k|S_k) \\ &= \varphi(C) \prod_{k=1}^{N_P} \rho^S\left(S_k|C_{\gamma(k)}\right)\rho_0(J_k|S_k) \end{aligned} \tag{1.52}$$

Here, $C = (C_1, \dots, C_{N_C})$ represents the diffusion MRI connectome, capturing N_C white-matter connections between cortical parcels with density $\varphi(C)$, and $\rho^S\left(S_k|C_{\gamma(k)}\right)$ models the likelihood of the k-th parcel's state given the connectivity reaching it. This approach aims to incorporate the complex interdependencies observed in brain networks, promising a more nuanced understanding

of brain dynamics, as evidenced in preliminary applications like the localization of network dynamics in sensory-motor tasks (Deslauriers-Gauthier et al., 2019, 2020).

Chapter 4, starting on page 169, will further explore the MEM approach, providing a deeper dive into their theoretical foundations, practical applications, and implications for our understanding of brain function.

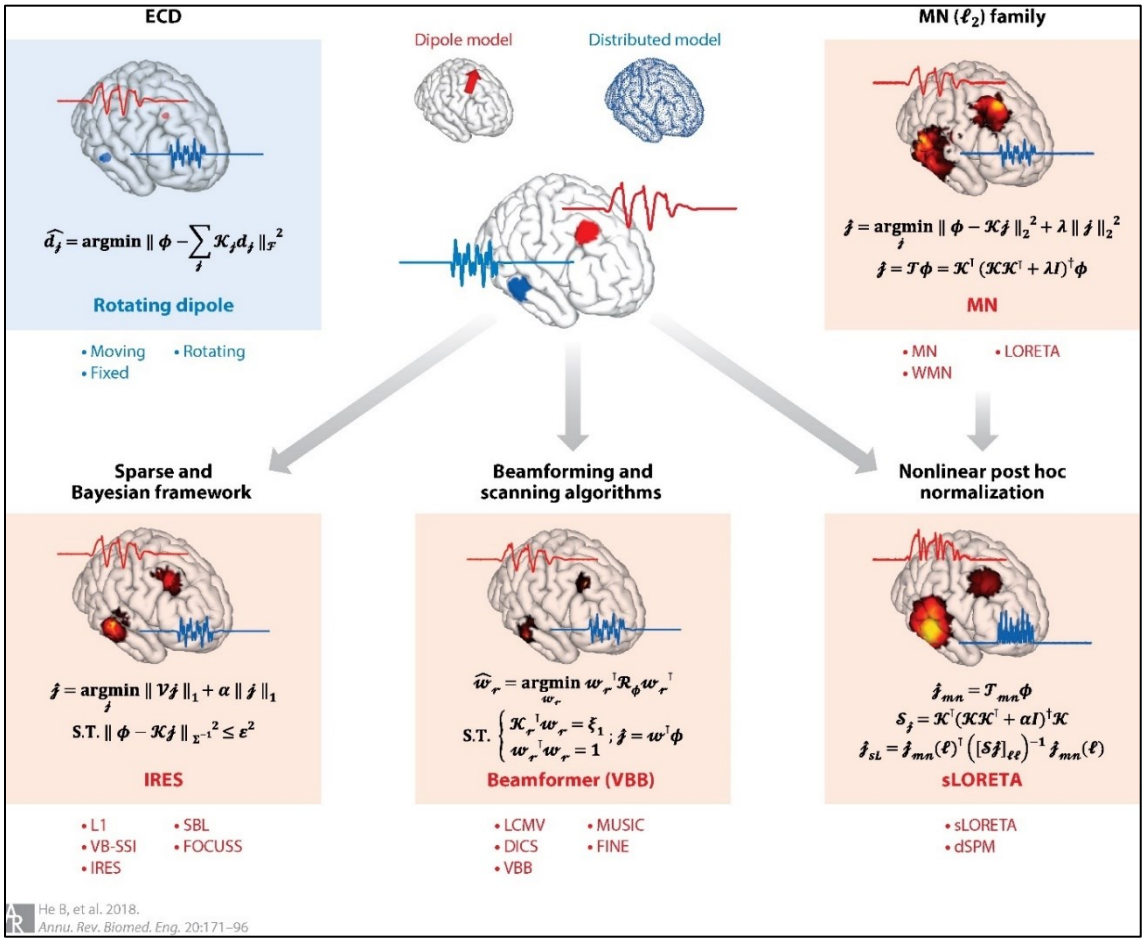

Figure 1.47. Electrophysiological source imaging at a glance. Caption and figure from: (B. He et al., 2018). Permission obtained. — Different classes and families of source imaging algorithms are depicted. In the center, an underlying brain activity with two separate sources and the corresponding time course of the activity are simulated; the forward problem is solved, and the scalp potential distribution is calculated (simulated EEG). The solution of the dipole localization method for the given example is depicted on the top left. The rest of the figure shows the major families of inverse algorithms, and bulleted lists show some of the well-known algorithms in each family as examples (the lists are by no means exhaustive). For each case, the algorithm used to solve and produce the result is shown in bold red font under the result. The mathematical formulation for the algorithm is provided for each solution. The lead-field matrix (a transformation from the current dipole distribution to the scalp potential) is denoted by $\mathcal{K}$, the scalp potential as $\boldsymbol{\Phi}$, the current density distribution as $\boldsymbol{j}$, and the dipole moment as $\boldsymbol{d_j}$ (the lead-field entries corresponding to $\boldsymbol{d_j}$ are denoted by $\mathcal{K}_j$). The inverse imaging operator (for the MN family) is denoted by $\mathcal{T}$, and $\boldsymbol{\lambda}$ and $\boldsymbol{\alpha}$ are regularization parameters. In the beamforming family, the data covariance is denoted by $\mathcal{R}_{\boldsymbol{\Phi}}$ and the spatial filter weights by $\boldsymbol{w_r}$. For the IRES algorithm, $\mathcal{V}$ is the discrete gradient operator, $\boldsymbol{\Sigma}$ is the estimated noise covariance, and $\boldsymbol{\mathcal{E}}$ is the estimated noise power. Abbreviations: DICS, dynamic imaging of coherent sources; dSPM, dynamic statistical parametric mapping; ECD, equivalent current dipoles; EEG, electroencephalography; ESI, electrophysiological source imaging; FINE, first-principle vector; FOCUSS, focal undetermined system solution; IRES, iteratively reweighting edge sparsity; LCMV, linearly constrained minimum variance; LORETA, low-resolution electromagnetic tomography; MN,

minimum norm; MUSIC, multiple classification algorithm; SBL, sparse Bayesian learning; sLORETA, standardized LORETA; VB-SSI, variation-based sparse source imaging; VBB, vector-based beamformer; WMN, weighted MN.

Connectivity. The preceding section highlighted how source estimation with EEG and MEG facilitates the dynamic mapping of neural activity with millisecond accuracy. Advancing beyond this, we can further explore the parallels with diffusion MRI. Just as structural networks are deduced from diffusion MRI data, EEG and MEG source-space data enable the reconstruction of functional neural networks. This advanced approach is exemplified in Figure 1.48, illustrating how these techniques extend our understanding of the brain's functional architecture. This process involves employing statistical measures such as bi-variate phase-amplitude coupling in different frequency bands and bi-variate directed coherence applied to the source time series (Bastos & Schoffelen, 2016; B. He et al., 2018; Sadaghiani et al., 2022).

The high temporal resolution of EEG and MEG is pivotal for dissecting network patterns and understanding the rapid evolution of neural interactions. This attribute is crucial in gaining insights into the timing and sequence of neural events, which are fundamental to cognitive processes and behaviors. The detailed temporal resolution is exceptionally valuable in research pertaining to cognitive functions, neural communication, and brain disorders (B. He et al., 2018).

The integration of non-invasive electrophysiology with connectomics provides a comprehensive view of the brain's functional mechanisms, thereby enriching our understanding of cognitive functions and related pathologies. In a subsequent chapter (A neuron-glial perspective of MEG connectomics — establishing a biologically plausible computational framework to guide and evaluate empirical methodologies, starting on page 169), an in-depth exploration of electrophysiological connectomics will be offered.

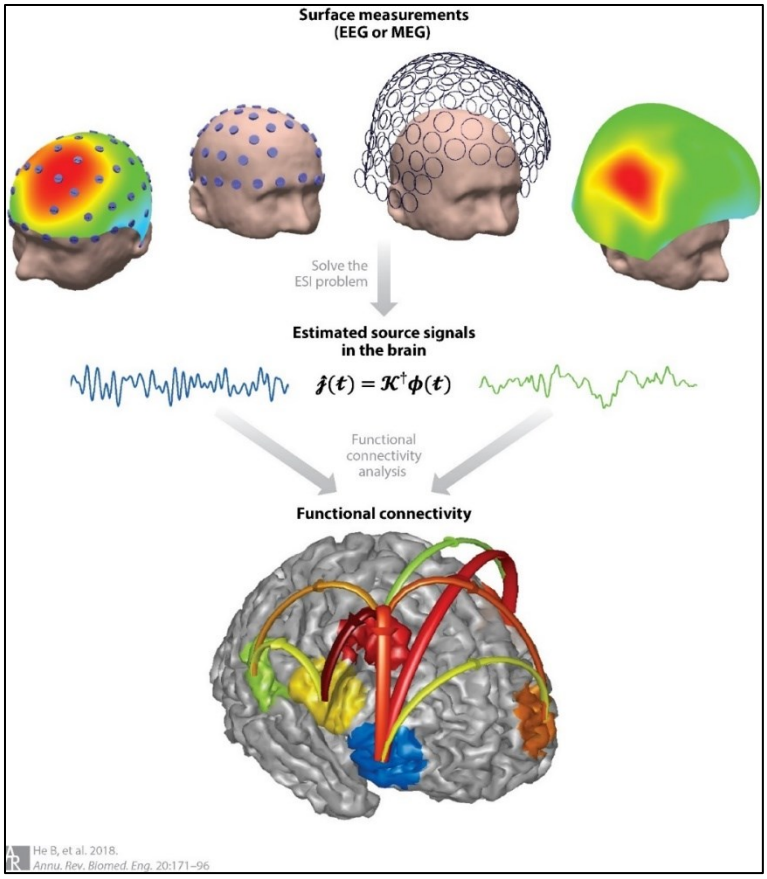

Figure 1.48. The concept of the electrophysiological connectome (eConnectome). Caption and figure from: (B. He et al., 2018). Permission obtained. — Electrophysiological source imaging (ESI) can image not only brain activity but also the functional connectivity of the brain. The eConnectome approach estimates brain network dynamics from noninvasive surface techniques, such as electroencephalography (EEG) and magnetoencephalography (MEG). The location of the activity (nodes), the time course of the activity at such nodes, and the dynamic connectivity among these nodes (links) can be estimated from EEG/MEG to reveal the underlying brain networks. ESI is a key element in realizing this goal. The eConnectome is effective and accurate in imaging brain network dynamics in the source domain. Arrows (colored arrows on the cortical surface) represent the direction of information flow and directional functional connectivity or causality. The inversion operator is denoted by $\mathcal{K}^{\dagger}$, and the estimated current density distribution is denoted by $\hat{\boldsymbol{j}}$.

1.5 Multilayer brain networks

Within the scope of this thesis, there has been a comprehensive utilization of the multilayer network theory to elucidate the characteristics of brain networks.

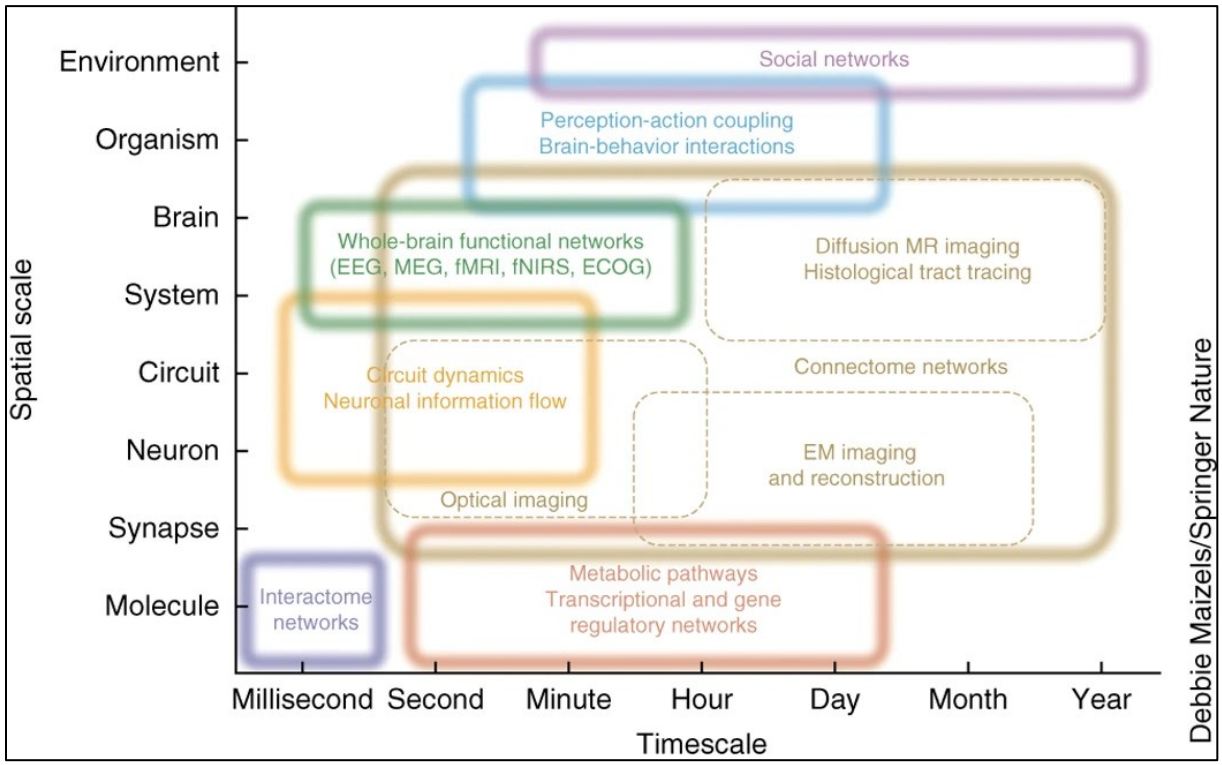

Figure 1.49. Networks on multiple spatial and temporal scales. Caption and figure adapted from: (Bassett & Sporns, 2017). Permission obtained — Network neuroscience encompasses the study of very different networks encountered across many spatial and temporal scales. Additionally, network neuroscience does not stop at the brain, but instead asks how these patterns of interconnectivity in the central nervous system drive and interact with patterns of behavior. Finally, network neuroscience asks how all of these levels of inquiry help us to understand the interactions between social beings that give rise to ecologies, economies and cultures.

The multilayer network theory transcends the limitations of the standard network theory by affording the capability to concurrently model and analyze graphs that exhibit a diverse array of natures and attributes (Boccaletti et al., 2014; De Domenico, 2017; Kivela et al., 2014). In fact, multilayer network modelling conceptualizes the very notion of *network-of-networks* or *a collection of interconnected networks* (Bassett & Sporns, 2017; Betzel & Bassett, 2017; Boccaletti et al., 2014; De Domenico, 2017; Kivela et al., 2014) which has been suggested to be the best integrative representation of the brain's intrinsic spatiotemporal facets (e.g., see Figure 1.49) as well as the brain's interactions with the rest of the body and the surrounding environment (e.g., see Figure 1.49 and Figure 1.50).

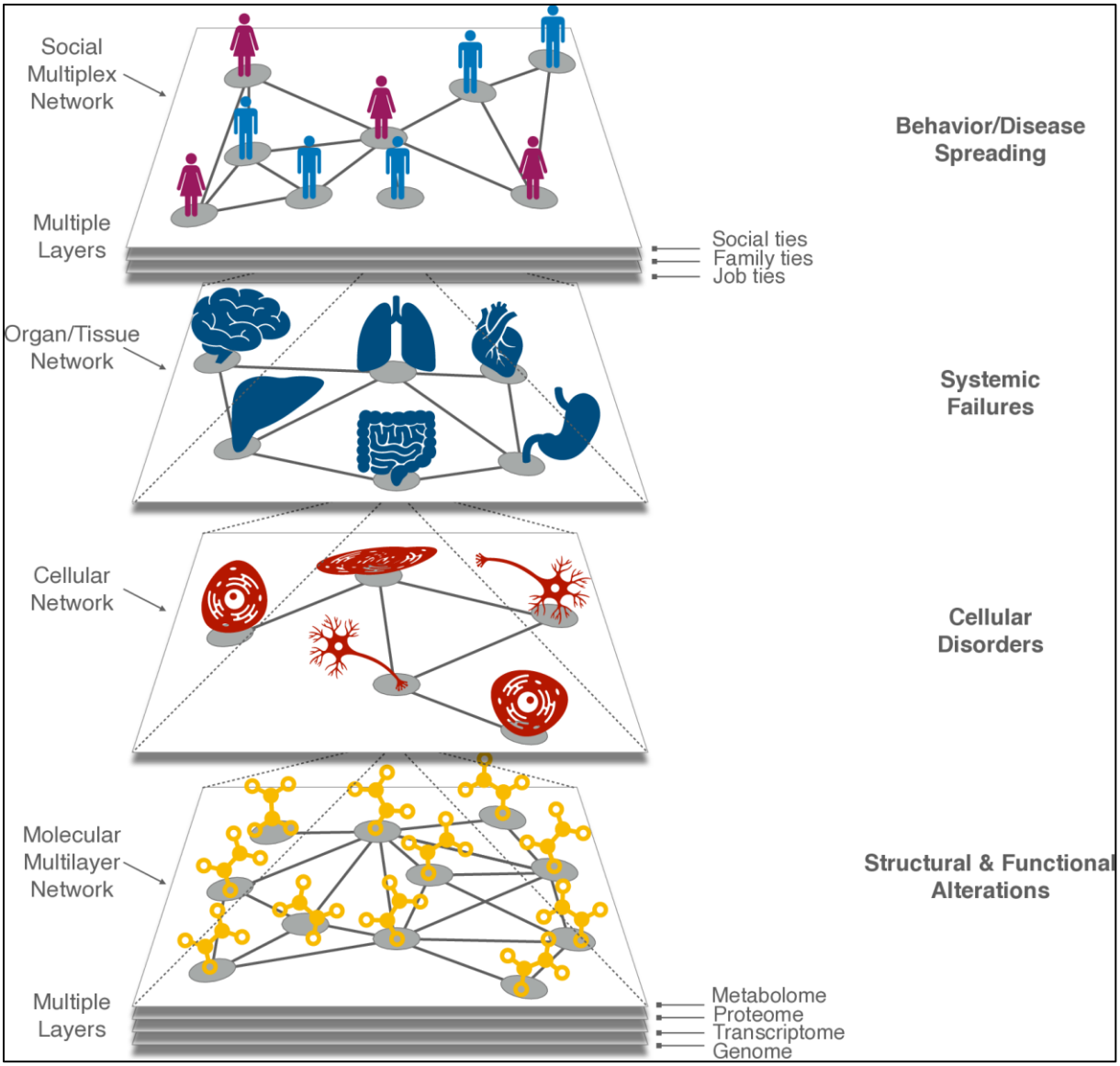

Figure 1.50. Multiscale and multiplex model of a social system, from the molecular to the population layers. Figure from: (De Domenico, 2020). Publisher's permission: https://github.com/manlius/muxViz/blob/69c1752539bb757df8222917999a8c299a6821a4/gui-old/theory/illustrations/LICENSE.md (CC BY-SA 4.0). — See text for explanation.

Mathematically, multilayer networks are represented by adjacency tensors (i.e., a higher-order mathematical construct of the classical adjacency matrix for standard networks). Formally, given a multilayer network with N nodes and L layers, each component of its adjacency tensor $M_{j,\beta}^{i,\alpha} \in \mathbb{R}$ encodes the connectivity between unit i in layer α and unit j in layer β where $i, j \in [\![1, N]\!]$ and $\alpha, \beta \in [\![1, L]\!]$ (Boccaletti et al., 2014; De Domenico, 2017; Kivela et al., 2014). As illustrated in Figure 1.9, in the investigation of brain networks, M can encode anatomical information (such as fiber densities) or functional information (such as correlations), or both.

For a concrete example, Figure 1.51.a draws on its left side a 4-node–3-layer weighted-directed multilayer network and on its right side the corresponding intra-layer connectivity matrices. In practice, the associated 4-rank tensor is flattened (without loss of information) into a rank-2 tensor

(i.e., the supra-adjacency matrix), as drawn in Figure 1.51.b, that possesses a block structure where diagonal and extra-diagonal blocks encode, respectively, intra-layer and inter-layer connectivity. For another example, Figure 1.50, shown earlier, draws a more complex multilayer network that encompasses multiple interdependent scales from genes and biomolecules whose structural and functional relationships shape and are shaped by cellular interactions, to the information shared between body organs and tissues whose processes, while bidirectionally coupled to cellular networks, drive and depends on social behavior and interactions.

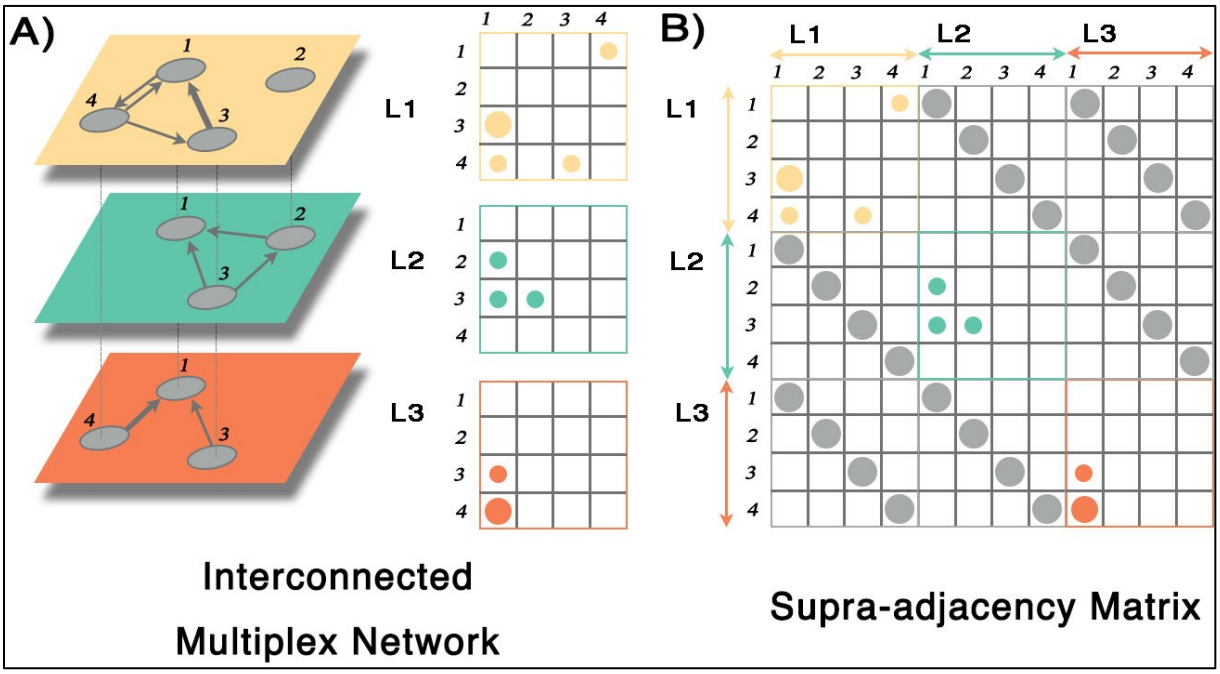

Figure 1.51. Multilayer network representation. Figure from: (De Domenico, 2020). Publisher's permission: https://github.com/manlius/muxViz/blob/69c1752539bb757df8222917999a8c299a6821a4/gui-old/theory/illustrations/LICENSE.md (CC BY-SA 4.0). — See text for explanation.

In the investigation of brain networks, the prevailing topologies that are commonly used for study include the *multiplex* and *interconnected multiplex* models (De Domenico, 2017). The multiplex model involves the consideration of multiple layers, each representing a distinct facet or modality of neural connectivity, while the interconnected multiplex model further extends this analysis by exploring the intricate interplay and interconnectedness between these individual layers (De Domenico, 2017). Besides, and importantly, both models operate under the assumption that a given node (e.g., classically a given brain region) exists across all layers, manifesting distinct connectivity patterns contingent upon the specific information encoded within each layer (De Domenico, 2017). Thus, using the notation introduced earlier (De Domenico, 2017), the multiplex topology satisfies for any $i,j \in [\![1,N]\!]$ and $\alpha,\beta \in [\![1,L]\!]$ such that $\alpha \neq \beta$, $M_{j,\beta}^{i,\alpha} = 0$ (i.e., no interconnections between layers); whereas the interconnected multiplex topology satisfies simultaneously $M_{j,\beta}^{i,\alpha} = 0$ for any $i \neq j$ and $\alpha \neq \beta$, and $M_{i,\beta}^{i,\alpha} \neq 0$ for $\alpha \neq \beta$ (i.e., interconnections between layers only consist of those among node replicas). For example, Figure 1.51 showed an interconnected multiplex topology (often simply called *multiplex* due to the fact that when interconnectivity is lacking, the examination of the multilayer adjacency tensor coincides with the standard graph theoretical analysis applied to each layer in isolation, thereby making the non-interconnected multiplex model unvaluable in practical settings, i.e., it is only a useful

mathematical model to show that multilayer network theory completely generalizes standard network theory; (De Domenico, 2017)).

It is worth mentioning that, although multiplex topologies are prevalent, there are notable neuroscientific applications that have successfully employed more complex topologies (e.g., see (Brookes et al., 2016) and Figure 1.52 for an investigation of pan-spectral electrophysiological connectomics, or see (Virkar et al., 2016) and Figure 1.53 for an investigation of glial network metabolic support of neuronal network learning activity). Additionally, it is noteworthy that many standard graph theoretical measures (e.g., see (Rubinov & Sporns, 2010)) have been extended to the multilayer realm (e.g., centrality indices, assortativity coefficients, network motifs; e.g., see (Boccaletti et al., 2014; De Domenico, 2017; Kivela et al., 2014)).

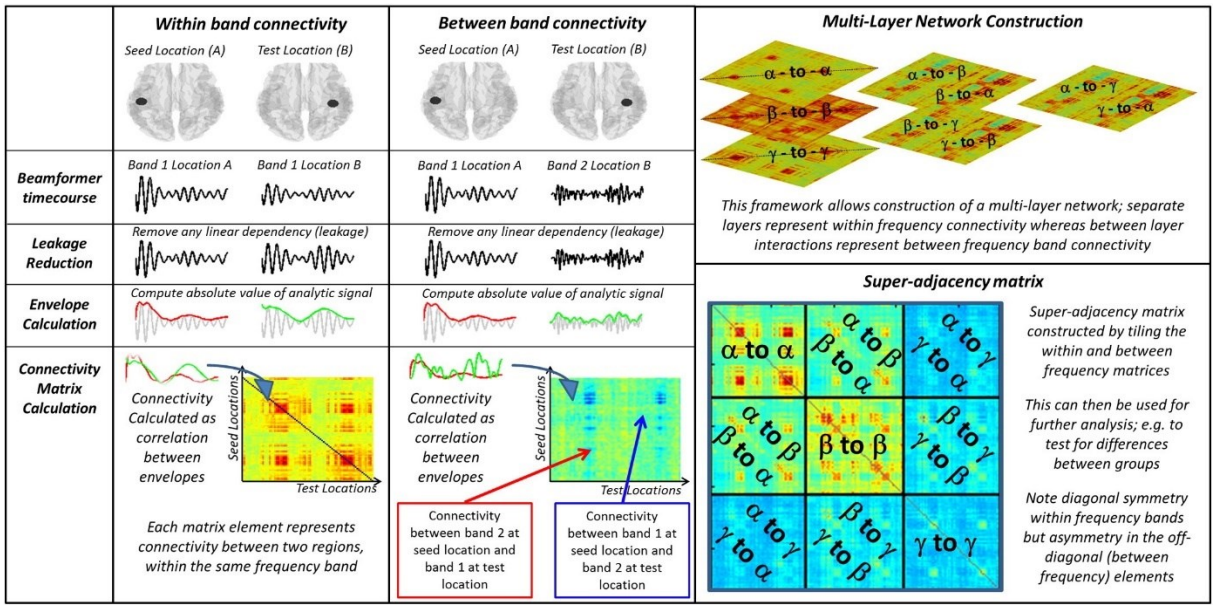

Figure 1.52. Multilayer functional network analysis of MEG data. Caption and figure from: (Brookes et al., 2016). Publisher's permission: http://creativecommons.org/licenses/by/4.0/. — Schematic diagram of the connectivity data analysis pipeline including construction of a multi-layer network. Note that, in the actual analysis, the gamma band was split into two, separating low gamma (30 Hz–50 Hz) and high gamma (50–100 Hz). However in order to simplify the Figure, this is not shown.

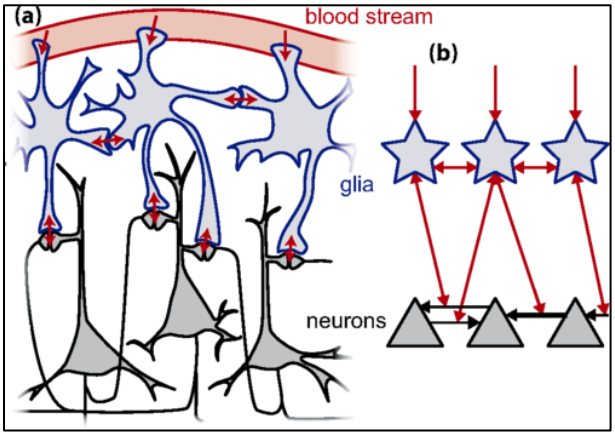

Figure 1.53. Multilayer glial-neuronal network. Caption and figure from: (Virkar et al., 2016). Reprinted with permission from © 2016 American Physical Society. — Glial-neuronal interactions: (a) Cartoon based on existing experiments, illustrating how glia serve to distribute metabolic resources from the bloodstream to neural synapses.

Red arrows indicate paths of metabolite transport. (b) A simplified directed graph representation of our two-layer network model. Black arrows indicate neural synaptic interactions. Arrow thickness indicates synaptic strength which evolves according to STDP. Red arrows which terminate on black arrows represent the resource supply to the corresponding synapse.

Throughout the manuscript-chapters of this thesis, the interconnected multiplex model is always adopted to study structural and functional connectivity. Although this may appear as a simplistic model (because it assumes that each node is consistently present across layers and only adapt its connectivity profile in response to the information encapsulated within each layer), I provide evidence that they nonetheless enable a nuanced and expansive exploration of the complex architecture and functionality inherent in brain networks, in particular I prove that such simplistic models greatly contribute to a deeper understanding of the multi-faceted nature of neuron-glial network interactions. As a matter of fact, I fully exploit the simplicity of the interconnected multiplex model in conjunction with bifurcation theory to derive new easy-to-grasp formalisms of brain large-scale network dynamics before further endorsing the use of more complex multilayer network topologies to overcome the limitations of the multiplex.

Chapter 2 Neuron-astrocyte mass network model — foundations for whole-brain modelling

2.1 Thesis storyline

Central to this thesis is a dynamic model that elucidates the complex interactions within neuron-astrocyte networks. The model is tailored to the spatiotemporal dimensions pertinent to human neuroimaging data for functional studies. It represents a *whole-brain* and strikes a balance between biological fidelity and computational feasibility by incorporating principles from neural mass network modelling and compartmental modelling.

The primary aim of this *introductory* chapter is to articulate the fundamental biophysical principles governing the bidirectional interactions between astrocytes and neurons in the whole-brain network model. It will methodically outline a mathematical procedure for parameterizing the network model, employing techniques from simulation, bifurcation theory, and compartmental modelling.

This chapter is pivotal as it establishes a rigorously parameterized network model, laying the groundwork for subsequent investigations into the astrocytic network's influence on whole-brain activity and the emergence of functional connectivity patterns. For the purposes of clarity and focus, this chapter will specifically address the parameterization criteria that most directly support the objectives of the following chapters. It will also highlight opportunities for generalizing these criteria to accommodate a broader range of applications.

In the following sections, temporal derivatives are indicated by overdots. Additionally, Table 2.2 and Table 2.3 provide a comprehensive overview of the symbols used to represent each variable and parameter introduced.

2.2 Network model

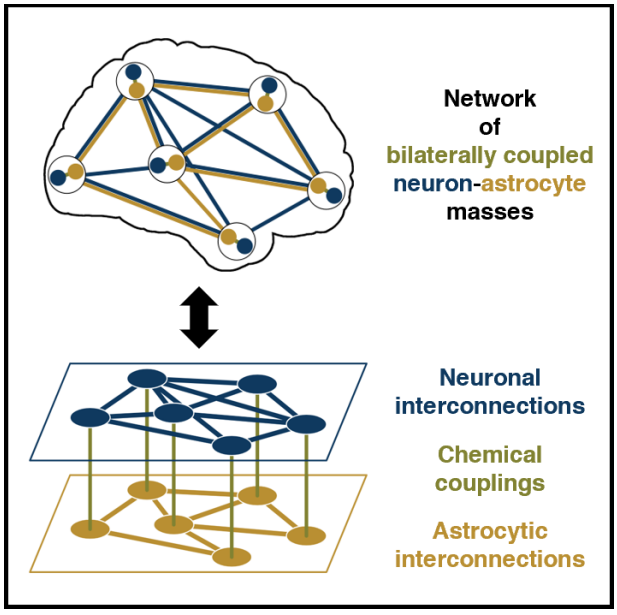

Figure 2.1. Network of bilaterally coupled neuron-astrocyte mass models. A biophysical model of whole-brain activity is introduced where large-scale astrocytic and neuronal networks couple their dynamics through glutamatergic and

GABAergic transmission systems, and where neural dynamics are constrained by a two-layered structural network interconnecting either astrocytic or neuronal populations.

In the proposed network model depicted in Figure 2.1, each node represents a mesoscopic brain region through a neuron-astrocyte mass model. This mass model characterises the coarse-grained temporal dynamics among four distinct, yet coupled, homogeneous subpopulations of neural cells: glutamatergic pyramidal neurons (Pyr), excitatory interneurons (ExIn), GABAergic inhibitory interneurons (InIn), and astrocytes (Ast). It extends the foundational work of (Garnier et al., 2016), by offering a nuanced portrayal of the interplay between neuronal and astrocytic subpopulations through glutamatergic and GABAergic neurotransmission pathways. Notably, this enhanced mass model incorporates the effects of glutamatergic gliotransmission as well as stochastic fluctuations arising from both distant regions and the immediate nodal environments.

At the nodal level, the mass model, indexed by n, articulates two primary types of interactions among the subpopulations: neuron-neuron and neuron-astrocyte.

On the one hand, neuron-neuron interactions are abstracted to the dendro-somatic transformation of subpopulation firing rates (F_{Pyr}, F_{ExIn}, and F_{InIn}) into average membrane potentials (E_{Pyr}, $E_{\mathrm{ExIn}\cup\mathrm{Pyr}}$, and E_{InIn}), and *vice versa*; assuming that feedforward pyramidal neurons receive self-feedback, as well as feedback from inhibitory and excitatory interneurons, and arbitrary excitatory inputs. These interactions are formalized in Equations (2.1) and (2.2).

Membrane potential dynamics:

$$\begin{aligned}
\ddot{E}_{\mathrm{Pyr}_{[n]}} &= AaF_{\mathrm{Pyr}_{[n]}} - 2a\dot{E}_{\mathrm{Pyr}_{[n]}} - a^2E_{\mathrm{Pyr}_{[n]}} \\
\ddot{E}_{\mathrm{ExIn}\cup\mathrm{Pyr}_{[n]}} &= Aa\left(C^{\mathrm{ExIn}\to\mathrm{Pyr}}F_{\mathrm{ExIn}_{[n]}} + C^{\mathrm{Pyr}\to\mathrm{Pyr}}F_{\mathrm{Pyr}_{[n]}} + q_{[n]} + \underbrace{Q_{\mathrm{Pyr}_{[n]}}}_{\substack{\text{neuroal}\\ \text{network}\\ \text{feedback}}}\right) \\
&\quad - 2a\dot{E}_{\mathrm{ExIn}\cup\mathrm{Pyr}_{[n]}} - a^2E_{\mathrm{ExIn}\cup\mathrm{Pyr}_{[n]}} \\
\ddot{E}_{\mathrm{InIn}_{[n]}} &= BbC^{\mathrm{InIn}\to\mathrm{Pyr}}F_{\mathrm{InIn}_{[n]}} - 2b\dot{E}_{\mathrm{InIn}_{[n]}} - b^2E_{\mathrm{InIn}_{[n]}}
\end{aligned} \tag{2.1}$$

Neuronal firing rates:

$$\begin{aligned}
F_{\mathrm{Pyr}_{[n]}} &= \mathrm{S}\left(E_{\mathrm{ExIn}\cup\mathrm{Pyr}_{[n]}} - E_{\mathrm{InIn}_{[n]}}, \nu_{\max}, v_{\mathrm{Pyr}_{[n]}}, r\right) \\
F_{\mathrm{ExIn}_{[n]}} &= \mathrm{S}\left(C^{\mathrm{Pyr}\to\mathrm{ExIn}}E_{\mathrm{Pyr}_{[n]}}, \nu_{\max}, v_{\mathrm{ExIn}_{[n]}}, r\right) \\
F_{\mathrm{InIn}_{[n]}} &= \mathrm{S}\left(C^{\mathrm{Pyr}\to\mathrm{InIn}}E_{\mathrm{Pyr}_{[n]}}, \nu_{\max}, v_{\mathrm{InIn}_{[n]}}, r\right)
\end{aligned} \tag{2.2}$$

Here S is a *sigmoidal function* defined as:

$$\mathrm{S}\colon (x, \nu, \theta, r) \longmapsto \nu/\big(1 + \exp\big(r(\theta - x)\big)\big)$$

On the other hand, neuron-astrocyte interactions are modeled as concurrent synaptic releases and uptakes of neurotransmitters into and from the extracellular space (e). The model specifically considers the two major neurotransmitters: glutamate (Glu) and GABA, for excitatory and inhibitory signaling, respectively, as detailed in Equations (2.3) and (2.4). Glutamate release (J_{Glu}) is modulated by the firing activity of pyramidal neurons (F_{Pyr}), while GABA release (J_{GABA}) is

controlled by the activity of inhibitory interneurons (F_{InIn}). The uptake of extracellular glutamate ($\mathrm{Glu_e}$) is primarily astrocytic, though neurons contribute to a lesser extent. In contrast, the uptake of extracellular GABA ($\mathrm{GABA_e}$) is primarily neuronal, with astrocytes playing a subsidiary role. Post-uptake, neurotransmitters are degraded within astrocytes, as captured by the state variables $\mathrm{Glu_{Ast}}$ and $\mathrm{GABA_{Ast}}$.

Glutamate dynamics:

$$\begin{aligned}
\ddot{J}_{\mathrm{Glu}[n]} &= W w_{\mathrm{r}} \left(\underbrace{F_{\mathrm{Pyr}_{[n]}}}_{\substack{\text{neuronal firing}\\ \text{induced Glu release}}} + \underbrace{Q^{\mathrm{Ast}}_{\mathrm{Glu}_{[n]}}}_{\substack{\text{astrocytic network}\\ \text{induced Glu release}}} \right) - (w_{\mathrm{r}} + w_{\mathrm{d}}) \dot{J}_{\mathrm{Glu}[n]} \\
&\quad - w_{\mathrm{r}} w_{\mathrm{d}} J_{\mathrm{Glu}[n]} \\
\dot{\mathrm{Glu}}_{\mathrm{e}[n]} &= J_{\mathrm{Glu}[n]} - \underbrace{\mathrm{S}\left(\mathrm{Glu}_{\mathrm{e}[n]}, V^{\mathrm{e}\to\mathrm{Ast}}_{\mathrm{Glu}}, v^{\mathrm{e}\to\mathrm{Ast,Pyr}}_{\mathrm{Glu}}, r^{\mathrm{e}\to\mathrm{Ast,Pyr}}_{\mathrm{Glu}}\right)}_{\text{astrocytic Glu uptake}} \\
&\quad - \underbrace{\mathrm{S}\left(\mathrm{Glu}_{\mathrm{e}[n]}, V^{\mathrm{e}\to\mathrm{Pyr}}_{\mathrm{Glu}}, v^{\mathrm{e}\to\mathrm{Ast,Pyr}}_{\mathrm{Glu}}, r^{\mathrm{e}\to\mathrm{Ast,Pyr}}_{\mathrm{Glu}}\right)}_{\text{neuronal Glu uptake}} \\
\dot{\mathrm{Glu}}_{\mathrm{Ast}[n]} &= \mathrm{S}\left(\mathrm{Glu}_{\mathrm{e}[n]}, V^{\mathrm{e}\to\mathrm{Ast}}_{\mathrm{Glu}}, v^{\mathrm{e}\to\mathrm{Ast,Pyr}}_{\mathrm{Glu}}, r^{\mathrm{e}\to\mathrm{Ast,Pyr}}_{\mathrm{Glu}}\right) - \underbrace{\mathrm{Glu}_{\mathrm{Ast}[n]}/\tau^{\mathrm{Ast}}_{\mathrm{Glu}}}_{\text{Glu degradation}}
\end{aligned} \tag{2.3}$$

GABA dynamics:

$$\begin{aligned}
\ddot{J}_{\mathrm{GABA}[n]} &= Z z_{\mathrm{r}} \left(\underbrace{F_{\mathrm{InIn}_{[n]}}}_{\substack{\text{neuronal firing}\\ \text{induced GABA release}}} + \underbrace{Q^{\mathrm{Ast}}_{\mathrm{GABA}[n]}}_{\substack{\text{astrocytic network}\\ \text{induced GABA release}}} \right) \\
&\quad - (z_{\mathrm{r}} + z_{\mathrm{d}}) \dot{J}_{\mathrm{GABA}[n]} - z_{\mathrm{r}} z_{\mathrm{d}} J_{\mathrm{GABA}[n]} \\
\dot{\mathrm{GABA}}_{\mathrm{e}[n]} &= J_{\mathrm{GABA}[n]} - \underbrace{\mathrm{H}\left(\mathrm{GABA}_{\mathrm{e}[n]}, V^{\mathrm{e}\to\mathrm{Ast}}_{\mathrm{GABA}}, K^{\mathrm{e}\to\mathrm{Ast}}_{\mathrm{GABA}}\right)}_{\text{astrocytic GABA uptake}} \\
&\quad - \underbrace{\mathrm{H}\left(\mathrm{GABA}_{\mathrm{e}[n]}, V^{\mathrm{e}\to\mathrm{InIn}}_{\mathrm{GABA}}, K^{\mathrm{e}\to\mathrm{InIn}}_{\mathrm{GABA}}\right)}_{\text{neuronal GABA uptake}} \\
\dot{\mathrm{GABA}}_{\mathrm{Ast}[n]} &= \mathrm{H}\left(\mathrm{GABA}_{\mathrm{e}[n]}, V^{\mathrm{e}\to\mathrm{Ast}}_{\mathrm{GABA}}, K^{\mathrm{e}\to\mathrm{Ast}}_{\mathrm{GABA}}\right) - \underbrace{\mathrm{GABA}_{\mathrm{Ast}[n]}/\tau^{\mathrm{Ast}}_{\mathrm{GABA}}}_{\text{GABA degradation}}
\end{aligned} \tag{2.4}$$

Here H is a *Michaelis–Menten function* defined as:

$$\mathrm{H}\colon (x, V, K) \mapsto Vx/(K + x)$$

Critically, the mass model establishes a relationship between extracellular neurotransmitter concentrations and neuronal firing rates through the excitability levels of targeted neuronal subpopulations, as formulated in Equation (2.5). This relationship manifests in two ways: an elevation in $\mathrm{Glu_e}$ generally leads to a bounded (potentially transient) decrease in the excitability thresholds of both pyramidal cells and inhibitory interneurons, and conversely, an elevation in $\mathrm{GABA_e}$ typically results in a bounded (potentially transient) increase in the excitability threshold

of pyramidal neurons. For simplicity, the model assumes that excitatory interneurons remain unaffected by changes in extracellular neurotransmitter levels.

Neuronal excitability levels:

$$\begin{aligned} v_{\mathrm{Pyr}_{[n]}} &= v_0^{\mathrm{Pyr}} + v_{\mathrm{GABA}_{[n]}} - v_{\mathrm{Glu}_{[n]}} \\ v_{\mathrm{ExIn}_{[n]}} &= v_0^{\mathrm{ExIn}} \\ v_{\mathrm{InIn}_{[n]}} &= v_0^{\mathrm{InIn}} - \mu_{\mathrm{Glu}}^{\mathrm{InIn/Pyr}} v_{\mathrm{Glu}_{[n]}} \\ v_{\mathrm{Glu}_{[n]}} &= \mathrm{S}\left(\mathrm{Glu}_{\mathrm{e}_{[n]}}, m_{\mathrm{Glu}}^{\mathrm{Pyr}}, v_{\mathrm{Glu}}^{\mathrm{Pyr,InIn}}, r_{\mathrm{Glu}}^{\mathrm{Pyr,InIn}}\right) \\ v_{\mathrm{GABA}_{[n]}} &= \mathrm{S}\left(\mathrm{GABA}_{\mathrm{e}_{[n]}}, m_{\mathrm{GABA}}^{\mathrm{Pyr}}, v_{\mathrm{GABA}}^{\mathrm{Pyr}}, r_{\mathrm{GABA}}^{\mathrm{Pyr}}\right) \end{aligned} \tag{2.5}$$

Given the concurrent nature of all the nodal processes described so far, complex interactions emerge between neuronal excitatory and inhibitory firings, and neuron-astrocyte uptakes and releases of neurotransmitters, fostering a wide repertoire of dynamics across various (fast-slow) timescales.

At the network level, each node is influenced by distal regions through a two-layered structural network, as illustrated in Figure 2.1. One of the layer interconnects neuronal populations across different regions, representing white matter tracts (denoted by the parameter matrix Ω_{Pyr}), and the other interconnects astrocytic populations, reflecting gap junctional densities (denoted by the parameter matrix Ω_{Ast}). For the purposes of this discussion, it is assumed that the matrices Ω_{Pyr} and Ω_{Ast} are well-defined and accessible. Detailed methodologies for their estimation from empirical MRI data will be elaborated in the subsequent chapter.

Consistent with established practices (Breakspear, 2017; Griffiths et al., 2022), neuronal interconnections across the network's nodes are presumed to be excitatory, involving solely the pyramidal cell subpopulations. The corresponding network interaction terms for these connections are detailed in Equation (2.6) and appear in the state variable $\ddot{E}_{\mathrm{ExIn}\cup\mathrm{Pyr}}$ in Equation (2.1). These terms are formulated as a linear combination of incoming firing rates (Q_{Pyr}), with the weights encapsulated in Ω_{Pyr}, and a global coupling parameter, ω_{Pyr}, modulates the relative impact of Ω_{Pyr} on nodal dynamics.

Neuronal network feedback:

$$Q_{\mathrm{Pyr}_{[n]}} = \omega_{\mathrm{Pyr}} \sum_{\tilde{n}} \Omega_{\mathrm{Pyr}_{[n,\tilde{n}]}} F_{\mathrm{Pyr}_{[\tilde{n}]}} \tag{2.6}$$

Due to the current lack of experimental astrocytic data for whole-brain modeling, it is necessary to develop a preliminary astrocytic network coupling model. This coupling model extrapolates from the structural concept of astrocytes being connected in a gap-junction-coupled syncytium, as well as the functional roles of glutamate neurotransmission in facilitating intercommunication between astrocytes and the impact of excitatory gliotransmission on neuronal pre-terminal receptors (Fields et al., 2015; Goldberg et al., 2010; Vasile et al., 2017). Structurally, the coupling model posits that astrocytic interconnections across network nodes adhere to a syncytial organization, where an astrocytic subpopulation within one region connects exclusively with other astrocytic subpopulations within adjacent regions along the cortical mantle. Functionally, it is assumed that astrocytic network's modulation of nodal neuronal glutamate and GABA release rates (J_{Glu} and J_{GABA}) can be represented by linear interaction terms ($Q_{\mathrm{Glu}}^{\mathrm{Ast}}$ and $Q_{\mathrm{GABA}}^{\mathrm{Ast}}$) with weights

distributed according to Ω_{Ast}. These terms are detailed in Equation (2.7) and influence the state variables J_{Glu} in Equation (2.3) and J_{GABA} in Equation (2.4). Additionally, two global coupling parameters, ω_{Glu} and ω_{GABA}, determine the relative impact of Ω_{Ast} on nodal dynamics. In essence, this postulated coupling model outlines a large-scale neuron-astrocyte network framework where regional glutamate dynamics prompt adjacent astrocytic populations to synchronize their activities. This synchronization is based on a topology determined by gap junctional densities, which is distinct from the neuronal population topology based on axonal densities (e.g., see Figure 2.1). This coordinated astrocytic network activity ultimately influences whole-brain patterns of neuronal excitatory and inhibitory firing rates through gliotransmission.

Astrocytic network feedback:

$$\begin{aligned} Q^{\mathrm{Ast}}_{\mathrm{Glu}[n]} &= \omega_{\mathrm{Glu}} \sum_{\tilde{n}} \Omega_{\mathrm{Ast}_{[n,\tilde{n}]}} \mathrm{S}\left(\mathrm{Glu}_{\mathrm{e}_{[\tilde{n}]}}, m^{\mathrm{Ast}}_{\mathrm{Glu}}, v^{\mathrm{Ast}}_{\mathrm{Glu}}, r^{\mathrm{Ast}}_{\mathrm{Glu}}\right) \\ Q^{\mathrm{Ast}}_{\mathrm{GABA}[n]} &= \omega_{\mathrm{GABA}} \sum_{\tilde{n}} \Omega_{\mathrm{Ast}_{[n,\tilde{n}]}} \mathrm{S}\left(\mathrm{Glu}_{\mathrm{e}_{[\tilde{n}]}}, m^{\mathrm{Ast}}_{\mathrm{Glu}}, v^{\mathrm{Ast}}_{\mathrm{Glu}}, r^{\mathrm{Ast}}_{\mathrm{Glu}}\right) \end{aligned} \tag{2.7}$$

Given the central role of astrocytic network feedback in our study, a deeper examination of its intricacies is warranted. Various studies have shed light on the activities within astrocytic networks (De Pittà, 2020; De Pittà et al., 2011; De Pittà & Berry, 2019; Fields et al., 2015; Goldberg et al., 2010; Manninen et al., 2019; Vasile et al., 2017). For instance, (De Pittà et al., 2011) describe a process where a portion of glutamate synaptically released by a neuron into the extracellular space can bind to the glutamate receptors of an astrocyte. This binding may initiate a cascade of events, including the production of inositol 1,4,5-trisphosphate within the astrocyte. This compound can trigger calcium release from the endoplasmic reticulum within the same astrocyte and propagate through gap junctions to stimulate calcium release in adjacent astrocytes. Subsequently, the calcium releases may lead these astrocytes to secrete glutamate into the extracellular space, which can diffuse extrasynaptically and bind to pre-terminal neuronal receptors, potentially inducing neurotransmitter release independently of neuronal firing.

Thus, in our network model, we propose that astrocytic network feedback ($Q^{\mathrm{Ast}}_{\mathrm{Glu}}$ and $Q^{\mathrm{Ast}}_{\mathrm{GABA}}$) partially modulates the nodal releases of neuronal glutamate and GABA (J_{Glu} and J_{GABA}) through excitatory gliotransmission initiated by nodal glutamate bindings. For simplicity, we assume that astrocytic glutamate binding and uptake share similar sigmoidal kinetics, allowing their sigmoidal parameters to be equated. This modelling choice implies that elevated glutamate levels can intensify astrocytic coupling and network feedback. To express how nodal neurotransmitter releases are modulated, we incorporate linear terms combining local (firing-induced) and distal (astrocytic network-induced) dynamics, with the latter structurally constrained by Ω_{Ast}. These terms, outlined in Equation (2.7), impact the state variables J_{Glu} and J_{GABA} as seen in Equations (2.3) and (2.4). To differentiate the astrocytic network's impact on glutamate release by pyramidal cells versus GABA release by inhibitory interneurons, we introduce two coupling parameters, ω_{Glu} and ω_{GABA}, which dictate the relative influence of Ω_{Ast} on nodal dynamics. This overall approach simulates the diffusion-like influence of distal extracellular glutamate concentrations on local neurotransmitter releases. We further simplify, by assuming that astrocytic glutamate release into the extrasynaptic cleft, triggered by local glutamate binding, is generally negligible compared to the effects induced by neighboring astrocytes, thereby maintaining a zero diagonal in Ω_{Ast} and omitting direct feedback mechanisms. Lastly, as the literature provides less evidence for astrocytic

network feedback mediated by GABA (Angulo et al., 2008; Manninen et al., 2019; Yoon & Lee, 2014), we exclude the considerations of GABA-induced gliotransmission in our current model.

To conclude this section, it is important to note that we have adopted the common practice of setting parameters (such A, a, etc.) uniformly across all network nodes (Breakspear, 2017; Griffiths et al., 2022). However, it is possible in a more detailed model for any given parameter to vary by region (i.e., to be indexed by n) and over time (e.g., like q).

2.3 Constraining dynamical regimes

As outlined in Section 2.1, the goal of this chapter is to set the stage for the next, which will investigate, through simulations, the contributions of astrocytic networks to whole-brain activity and the emergence of functional connectivity patterns. This investigation will entail a comprehensive examination of how variations in the global astrocytic network coupling parameters, ω_{Glu} and ω_{GABA}, introduced earlier, affect the dynamical network system. These parameters are crucial for determining the extent to which astrocytic network activity influences glutamatergic and GABAergic neurotransmissions.

Thus, our immediate objective is to establish a biologically plausible exploration plane for $(\omega_{\mathrm{Glu}}; \omega_{\mathrm{GABA}})$. To this end, we must define a set of criteria ensuring that key model outputs, such as local field potential ($\mathrm{LFP} = E_{\mathrm{ExIn\cup Pyr}} - E_{\mathrm{InIn}}$), $\mathrm{Glu_e}$, and $\mathrm{GABA_e}$, qualitatively reflect characteristics normally observed in empirical resting-state human data.

Constraining local field potentials appears to be straightforward, given that the neuronal compartment of our network model is based on the Jansen–Rit model (Jansen & Rit, 1995), which is well-regarded for its ability to simulate biologically plausible neuronal activity. Numerous studies have provided parameter sets for Jansen–Rit-based models, allowing them to replicate essential features of electrophysiological recordings, particularly α-band oscillatory patterns observed during rest (David & Friston, 2003; Ferrat et al., 2018; Forrester et al., 2020; Garnier et al., 2015; Sotero et al., 2007; Tewarie et al., 2021; Touboul et al., 2011).

In contrast, our understanding of the astrocytic and extracellular compartments of the network model is grounded in relatively more recent research (Blanchard et al., 2016; Garnier et al., 2016). The challenge here lies in the lack of methodologies or empirical data for fine-tuning these model aspects (De Pittà & Berry, 2019; Kastanenka et al., 2020). Nonetheless, bifurcation analysis at the nodal level offers a viable approach for setting nodal parameters within realistic bounds, even when factoring in network feedback terms (Garnier et al., 2016).

Subsequent sections will demonstrate that by adopting a strategic set of criteria, we can navigate the network model's capacity to produce various temporal behaviors, ensuring that (i) LFP dynamics mirror α-band characteristics found in electrophysiological recordings, including amplitude and phase network synchronizations, and (ii) neurotransmitter dynamics achieve a balance, resulting in quasi-stationary slow fluctuations of $\mathrm{Glu_e}$ and $\mathrm{GABA_e}$.

We now detail our parameterization strategy and delve into the pivotal roles of ω_{Glu} and ω_{GABA}. It is important to remember that this approach involves pinpointing dynamic regimes of interest, defined by particular parameter and state variable ranges. The goal is to traverse this dynamic terrain by adjusting ω_{Glu} and ω_{GABA}, thereby methodically exploring predefined sections of a bifurcation diagram to discern the combined effects of $(\omega_{\mathrm{Glu}}; \omega_{\mathrm{GABA}})$.

2.3.1 Reduction of parameters

Our parameterization approach significantly leverages the results of the bifurcation analyses of a neuron-astrocyte mass model conducted by (Garnier et al., 2016). We begin by selecting a widely accepted, physiologically plausible set of scalar parameters from existing literature (refer to Table 2.3 and references such as (David & Friston, 2003; Ferrat et al., 2018; Forrester et al., 2020; Garnier et al., 2015; Sotero et al., 2007; Tewarie et al., 2021; Touboul et al., 2011)), which allows us to focus on the network coupling parameters ω_{Pyr}, ω_{Glu}, and ω_{GABA}, along with the following nodal parameters: $q_{[\cdot]}$, v_0^{Pyr}, v_0^{InIn}, $m_{\mathrm{Glu}}^{\mathrm{Pyr}}$, $m_{\mathrm{GABA}}^{\mathrm{Pyr}}$, $v_{\mathrm{Glu}}^{\mathrm{Pyr}}$, $v_{\mathrm{GABA}}^{\mathrm{Pyr}}$, $r_{\mathrm{Glu}}^{\mathrm{Pyr}}$, $r_{\mathrm{GABA}}^{\mathrm{Pyr}}$, W, and Z. All these parameters, except for ω_{Glu}, ω_{GABA}, and $q_{[\cdot]}$, are to be fixed at scalar values.

Consistent with the model equations in Section 2.2 and common practices in the field (as noted by (Forrester et al., 2020; Sotero et al., 2007; Tewarie et al., 2021)), we apply a uniform setting across all nodal parameters, with the exception of $q_{[\cdot]}$, hence dropping all indices for simplicity unless specificity is required for clarity. Additionally, despite Table 2.3 indicating a null value for $C^{\mathrm{Pyr}\to\mathrm{Pyr}}$, our analysis will explore positive $C^{\mathrm{Pyr}\to\mathrm{Pyr}}$ values due to their intimate connection with ω_{Pyr} and their utility in illustrating the spectrum between a network of uniformly coupled nodes and a scenario where one node operates independently from its network counterparts. Furthermore, while Table 2.3 suggests that q is a stochastic variable, our discussion primarily focuses on deterministic bifurcation analysis. For more insights into stochastic scenarios, refer to works like (Ableidinger et al., 2017; Mendler et al., 2018).

2.3.2 Simplification of parameter dependencies

Our subsequent step involves characterising the bifurcation behavior of the nodal model's neuronal compartment, in isolation from the network. This is achieved by lumping its modulatory elements (i.e., $\mathrm{Glu_e}$ and $\mathrm{GABA_e}$) into a minimal set of scalars, defined as follows:

$$\begin{aligned} v_{\mathrm{Glu}} &= \mathrm{S}\left(\mathrm{Glu_e}, m_{\mathrm{Glu}}^{\mathrm{Pyr}}, v_{\mathrm{Glu}}^{\mathrm{Pyr,InIn}}, r_{\mathrm{Glu}}^{\mathrm{Pyr,InIn}}\right) - \Delta_{\mathrm{Glu}}^{v} \\ v_{\mathrm{GABA}} &= \mathrm{S}\left(\mathrm{GABA_e}, m_{\mathrm{GABA}}^{\mathrm{Pyr}}, v_{\mathrm{GABA}}^{\mathrm{Pyr}}, r_{\mathrm{GABA}}^{\mathrm{Pyr}}\right) - \Delta_{\mathrm{GABA}}^{v} \end{aligned} \tag{2.8}$$

Here, compared to Equation (2.5), the sigmoidal function S is extended by positive parameters $\Delta_{\mathrm{Glu}}^{v}$ and $\Delta_{\mathrm{GABA}}^{v}$, enabling v_{Glu} and v_{GABA} to take negative values for bifurcation analyses.

Specifically, with E_{Pyr} falling within the interval $]0; Av_{\max}/a[$ and setting $v_0 = v_0^{\mathrm{Pyr}} - \Delta_{\mathrm{Glu}}^{v} + \Delta_{\mathrm{GABA}}^{v} = v_0^{\mathrm{ExIn}} = v_0^{\mathrm{InIn}} - \mu_{\mathrm{Glu}}^{\mathrm{InIn/Pyr}}\Delta_{\mathrm{Glu}}^{v} = 6\ \mathrm{mV}$, singular points can be computed numerically using Equation (2.9), adhering to the methodologies elaborated in (Garnier et al., 2016).

$$\begin{aligned} & q - \frac{a}{A}v_{\mathrm{GABA}} - \frac{a}{A}\left(v_0 - v_{\mathrm{Glu}} - \frac{1}{r}\ln\left(\frac{Av_{\max}}{aE_{\mathrm{Pyr}}} - 1\right)\right. \\ & - \frac{A}{a}C^{\mathrm{ExIn}\to\mathrm{Pyr}}\mathrm{S}\left(C^{\mathrm{Pyr}\to\mathrm{ExIn}}E_{\mathrm{Pyr}}, v_{\max}, v_0, r\right) - C^{\mathrm{Pyr}\to\mathrm{Pyr}}E_{\mathrm{Pyr}} \\ & \left. + \frac{B}{b}C^{\mathrm{InIn}\to\mathrm{Pyr}}\mathrm{S}\left(C^{\mathrm{Pyr}\to\mathrm{InIn}}E_{\mathrm{Pyr}}, v_{\max}, v_0 - \mu_{\mathrm{Glu}}^{\mathrm{InIn/Pyr}}v_{\mathrm{Glu}}, r\right)\right) \\ & = 0 \end{aligned} \tag{2.9}$$

It is astute to note from Equation (2.9) that v_{GABA} is essentially equivalent to q up to a constant factor of a/A. This observation allows for the complete understanding of the neuronal

compartment's dynamics within the nodal model by drawing a codimension-2 bifurcation diagram with v_{Glu} and $p = q - v_{\mathrm{GABA}}\, a/A$ as the two parameters. Importantly, it should be noted that negative values for p are possible, which is of significant interest, even when q and v_{GABA} maintain positive values.

It is noteworthy that these simplifications, while focusing the analysis on the effects of glutamatergic and GABAergic neurotransmissions on neuronal dynamics, are nonetheless insightful. As previously mentioned, the neuronal compartment, *per se*, has been the subject of extensive research, primarily within the neuronal frameworks of Jansen–Rit-based models. Our approach, therefore, leverages the extensive knowledge base surrounding the neuronal compartment, facilitating a deeper understanding of the network model. Moreover, these simplifications do not compromise the general applicability of our findings, given the earlier assumption that neurotransmitter dynamics exhibit mean quasi-stationary slow fluctuations.

Further discussions in Sections 2.3.5 and 2.3.6 reveal that characterizing the neuronal compartment's behavior via v_{Glu} and p is instrumental in deciphering the network model's dynamics. This is attributed to straightforward relationships between the network coupling parameters (ω_{Pyr}, ω_{Glu}, and ω_{GABA}) and the bifurcation parameters (v_{Glu} and p). Specifically, increases in ω_{Pyr} (and ω_{GABA} respectively) are generally linked to increases (or decreases, respectively) in p, while increases in ω_{Glu} tend to raise v_{Glu}. It is crucial to recognize, however, that these relationships are somewhat transient, especially in the context of slowly fluctuating $\mathrm{Glu_e}$ and $\mathrm{GABA_e}$, as ω_{Glu} can indirectly influence GABAergic neurotransmission via inhibitory firing rates, just as ω_{GABA} can indirectly impact glutamatergic transmission via excitatory firing rates. This intricate balance between excitatory and inhibitory activities across different timescales is further explored in Section 2.4.

2.3.3 Identification of dynamical regimes of interest

Figure 2.2 presents the bifurcation diagram obtained when $C^{\mathrm{Pyr}\to\mathrm{Pyr}} = 0$, elucidating the parameterization for an individual node operating independently from the rest of the network. The analyses primarily utilized *MatCont* (Dhooge et al., 2008) version 7.3 available at https://gitlab.utwente.nl/m7686441/matcont and *PyDSTool* (Clewley, 2012) version 0.91.0 accessible at https://github.com/robclewley/pydstool. The diagram allows us to ascertain that approximately setting v_{Glu} within the range of [−0.5; 0.5] mV and p within [170; 370] Hz ensures that, with suitable initial conditions, the simulated LFP dynamics will converge to a self-sustaining oscillatory regime. This regime is characterized by a peak frequency within the [8; 13] Hz range and moderate peak-to-peak amplitudes, aligning with our objectives.

Importantly, the specified ranges for v_{Glu} and p confine the neuronal compartment of the nodal model, particularly when behaving independently from its network counterparts, to primarily exhibit stable limit cycles. These cycles are notably distant from saddle nodes and the regions prone to bi-stability and cusp catastrophes, where epileptic-like (instead of "normal" oscillatory) activities might emerge (refer to Section 2.4 or (Garnier et al., 2015) for more details). Furthermore, these ranges ensure that both glutamatergic pyramidal and GABAergic inhibitory neuron populations operate closer to the linear segments of their sigmoidal firing rate functions, which holds biophysical significance. Subsequent sections, starting from Section 2.3.4, provide further explanation for the narrow range chosen for v_{Glu}.

Interestingly, within the context of Figure 2.2, the Jansen–Rit model's parameterization for simulating α-band rhythms aligns precisely with $v_{\mathrm{Glu}} = 0\ \mathrm{mV}$, despite (Jansen & Rit, 1995) specifying for p a uniform distribution between 120 and 320 Hz. Moreover, the diagram illustrates how increases in v_{Glu} (reflecting rises in $\mathrm{Glu_e}$) and decreases in p (indicative of increased $\mathrm{GABA_e}$) correlate with larger limit cycle peak-to-peak amplitudes and reduced frequencies. Additionally, we understand that introducing temporal dependence between v_{Glu} and p (effectively between $\mathrm{Glu_e}$ and $\mathrm{GABA_e}$) yields a diverse range of dynamics, as further discussed in Section 2.4.

A comprehensive codimension-2 bifurcation analysis was beyond this study's scope. Therefore, Figure 2.2 omits extensive details such as limit cycle stabilities and bifurcation points of limit cycles, although these can be inferred to some extent (for more, see (Garnier et al., 2015, 2016)).

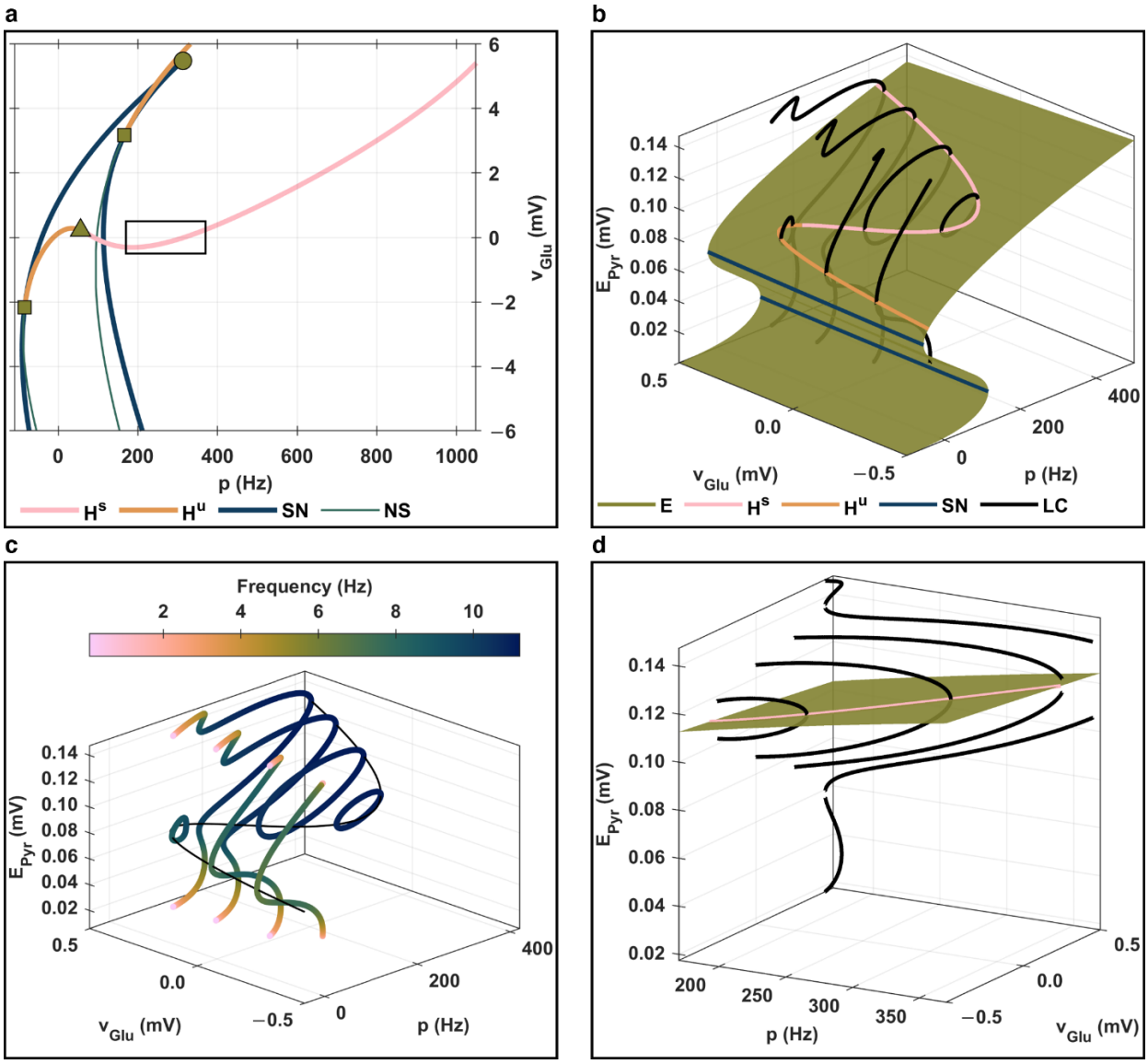

Figure 2.2. Two-parameter bifurcation diagram. Drawn with $C^{\mathrm{Pyr}\to\mathrm{Pyr}} = 0$. In panel (a), $\mathrm{H^s}$ refers to supercritical Hopf points, $\mathrm{H^u}$ refers to subcritical Hopf points, SN refers to saddle-node points, and NS refers to neutral saddle points (i.e., points associated with two real eigenvalues summing to zero). Saddle-node branches meet at a cusp bifurcation point represented as a circular green dot; Hopf branches meet at a Bautin (generalized Hopf) bifurcation point represented as a triangular green dot; and saddle-node, Hopf, and neutral saddle branches connect at Bogdanov–Takens

bifurcation points represented as rectangular green dots. The rectangular black border highlights the dynamic regimes under consideration, where $p \in [170; 370]$ Hz and $v_{\mathrm{Glu}} \in [-0.5; 0.5]$ mV. In panel (b), a three-dimensional view of the diagram in panel (a) is shown, maintaining the v_{Glu} range. The green surface represents singular points (E), the black solid lines represent maximal and minimal E_{Pyr} values along limit cycles (LC), and the other curves are the same as in panel (a). Limit cycle curves are represented only for $v_{\mathrm{Glu}} \in \{-0.25; 0; 0.25; 0.45\}$ mV for clarity, and neutral saddle curves are not drawn because they do not have a dynamic meaning for general equilibria. In panel (c), the same limit cycles from panel (b) are displayed alongside their respective frequencies, and the black solid thin lines represent Hopf bifurcations. Panel (d) magnifies the area within the black rectangular outline from panel (a), focusing on p values between 170 and 370 Hz, to provide a closer examination of the selected dynamic regimes. This panel counts also as a magnification of panel (b).

2.3.4 Backward parameterization

The definitions of $m_{\mathrm{Glu}}^{\mathrm{Pyr}}$, $m_{\mathrm{GABA}}^{\mathrm{Pyr}}$, $v_{\mathrm{Glu}}^{\mathrm{Pyr}}$, $v_{\mathrm{GABA}}^{\mathrm{Pyr}}$, $r_{\mathrm{Glu}}^{\mathrm{Pyr}}$, $r_{\mathrm{GABA}}^{\mathrm{Pyr}}$, $\Delta_{\mathrm{Glu}}^{v}$, and $\Delta_{\mathrm{GABA}}^{v}$ is established at the outset by selecting physiologically realistic ranges for the excitability thresholds (i.e., $v_{\mathrm{Pyr}} = v_0^{\mathrm{Pyr}} - v_{\mathrm{Glu}} + v_{\mathrm{GABA}}$ and $v_{\mathrm{InIn}} = v_0^{\mathrm{InIn}} - \mu_{\mathrm{Glu}}^{\mathrm{InIn/Pyr}} v_{\mathrm{Glu}}$; see Equation (2.5)) and by setting soft upper limits on extracellular neurotransmitter concentrations. We opted for the interval [3.5; 8.5] mV for both v_{Pyr} and v_{InIn} (for reference see (Ferrat et al., 2018)), and established approximate concentration ranges of [5; 15] µmol for $\mathrm{Glu_e}$ and [5; 35] µmol for $\mathrm{GABA_e}$.

The specified range for v_{Pyr} and v_{InIn} facilitated straightforward constraints for $m_{\mathrm{Glu}}^{\mathrm{Pyr}}$, $m_{\mathrm{GABA}}^{\mathrm{Pyr}}$, $\Delta_{\mathrm{Glu}}^{v}$, and $\Delta_{\mathrm{GABA}}^{v}$, as elucidated by the following inequalities:

$$\begin{gathered} (v_0 - 8.5)/\mu_{\mathrm{Glu}}^{\mathrm{InIn/Pyr}} \leq v_{\mathrm{Glu}} \leq (v_0 - 3.5)/\mu_{\mathrm{Glu}}^{\mathrm{InIn/Pyr}} \\ 3.5 + v_{\mathrm{Glu}}^{\mathrm{sup}} - v_0 \leq v_{\mathrm{GABA}} \leq 8.5 + v_{\mathrm{Glu}}^{\mathrm{inf}} - v_0 \\ 0 \leq v_{\mathrm{Glu}}^{\mathrm{sup}} - v_{\mathrm{Glu}}^{\mathrm{inf}} \leq 5 \end{gathered} \tag{2.10}$$

Here, $v_{\mathrm{Glu}}^{\mathrm{inf}}$ and $v_{\mathrm{Glu}}^{\mathrm{sup}}$ denote the infimum and supremum values of v_{Glu}, respectively. These constraints complement earlier stipulations, such as $v_{\mathrm{Glu}} \in [-0.5; 0.5]$ mV and $(q - 370)\, A/a \leq v_{\mathrm{GABA}} \leq (q - 170)\, A/a$, ensuring that p remains within the [170; 370] Hz range.

The validity of the chosen intervals for $\mathrm{Glu_e}$ and $\mathrm{GABA_e}$ is rationalized by analyzing the uptake functions depicted in Figure 2.3. For $\mathrm{Glu_e}$, the range [5; 15] µmol primarily aligns with the linear portion of the glutamate uptake sigmoidal functions, where the nodal model most effectively equilibrates release and uptake rates. This linear regime also facilitates more accurate numerical quantification of $\mathrm{Glu_e}$ variations, as the sigmoidal functions governing astrocytic network coupling (modeled after glutamate uptake functions) would otherwise approach their saturation points. Consequently, parameters such as $m_{\mathrm{Glu}}^{\mathrm{Pyr}}$, $v_{\mathrm{Glu}}^{\mathrm{Pyr}}$, $r_{\mathrm{Glu}}^{\mathrm{Pyr}}$, and $\Delta_{\mathrm{Glu}}^{v}$ were fine-tuned under the premise that glutamate's modulatory impact on neuronal excitability is most pronounced within the [5; 15] µmol range for $\mathrm{Glu_e}$, with saturated effects beyond this interval.

Similarly, the selected [5; 35] µmol range for $\mathrm{GABA_e}$ represents the optimal zone for balancing release and uptake rates. Given that the $\mathrm{GABA_e}$ uptake functions are formulated as rational polynomials, higher upper bounds could technically be set. However, doing so would likely extend simulation durations unless initial conditions are precisely defined to expedite the equilibrium between neurotransmitter release and uptake. As such, parameters including $m_{\mathrm{GABA}}^{\mathrm{Pyr}}$, $v_{\mathrm{GABA}}^{\mathrm{Pyr}}$, $r_{\mathrm{GABA}}^{\mathrm{Pyr}}$, and $\Delta_{\mathrm{GABA}}^{v}$ were calibrated to ensure that fluctuations of $\mathrm{GABA_e}$ within the [5; 35] µmol range significantly influence neuronal excitability levels.

As discussed in Section 2.3.3, a broader range than [−0.5; 0.5] mV could have been chosen for v_{Glu}, as further explored in Section 2.4. From the previous inequalities, it is clear that expanding the interval for v_{Glu} results in a corresponding narrowing of the range for v_{GABA}. Moving forward to Section 2.3.5, it is important to note that many Jansen–Rit-based studies typically attribute network (or exogenous) fluctuations along the p-axis to the variable Q_{Pyr} as outlined in Equation (2.6), or alternatively, to the parameter q. However, in this work, we opted to keep ω_{Pyr} and q constant, focusing instead on the influences of glutamatergic and GABAergic neurotransmissions. This decision is based on the observation made in Section 2.3.2 that variations in v_{GABA} can account for network fluctuations along the p-axis, as commonly seen in Jansen–Rit-based analyses.

In a stochastic network context, to be further discussed in Sections 2.3.5 and 2.3.6, the sigmoidal functions for $\mathrm{Glu_e}$ and $\mathrm{GABA_e}$ (specifically, the bounds for v_{Glu} and v_{GABA}) are fine-tuned in conjunction with an understanding of the network's potential dynamic behaviors. This includes considering the probabilistic distribution of Q_{Pyr} and q. Such adjustments help minimize simulations that do not yield insightful results. For instance, certain regions in the $(v_{\mathrm{Glu}}; p)$ or $(v_{\mathrm{Glu}}; v_{\mathrm{GABA}})$ parameter planes might exhibit relatively uniform dynamic characteristics, such as neighboring families of periodic orbits with very similar amplitudes and frequencies.

Consequently, we deemed it more appropriate in our current framework to define the broadest feasible interval for v_{GABA}, although further generalizations are discussed in Section 2.4. The sigmoidal functions for $\mathrm{Glu_e}$ and $\mathrm{GABA_e}$ were thus specifically calibrated to accommodate v_{Glu} within [−0.4; 0.4] mV and v_{GABA} within [−2.1; 2.1] mV, as also depicted in Figure 2.3 and detailed in Table 2.3.

To reiterate, our simulation strategy aims to traverse a predetermined section of a two-parameter bifurcation diagram, representing a dynamic landscape of interest, such as the area highlighted in Figure 2.2.a, using $(\omega_{\mathrm{Glu}}; \omega_{\mathrm{GABA}})$ as indirect controls. Moving forward, we initially consider, but subsequently refine, an exploration space defined by $\mathrm{Glu_e}$ within [5; 15] µmol, $\mathrm{GABA_e}$ within [5; 35] µmol, and p within [170; 370] Hz. This translates to v_{Glu} ranging from −0.34 to 0.34 mV and v_{GABA} from −2.00 to 2.00 mV, which further correspond to v_{GABA} a/A within [−62; 62] Hz and q within [232; 308] Hz.

It is crucial to note that these ranges serve as a guideline rather than rigid constraints, with the primary aim of minimizing computational burden. This approach helps streamline the simulation process by focusing on parameter sets likely to yield pertinent dynamics.

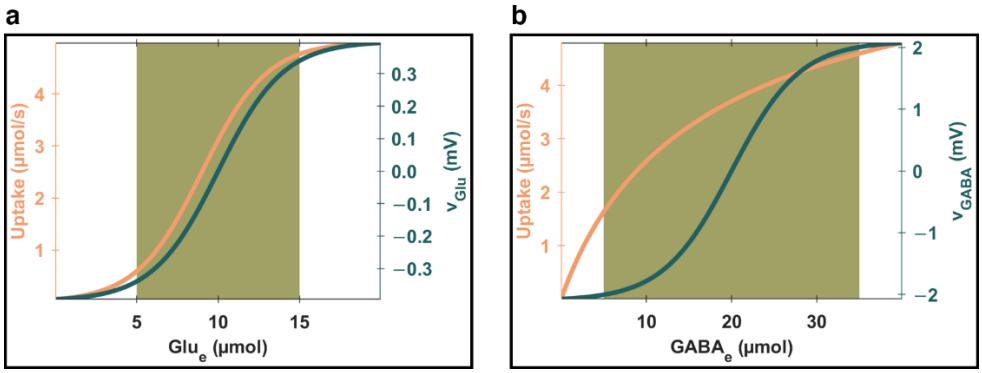

Figure 2.3. Parameterization of excitability feedback mechanisms. This figure specifies the parameters for the two sigmoidal functions that determine the impact of extracellular neurotransmitter concentration dynamics on neuronal excitability. The orange solid lines, corresponding to the left vertical axes, depict the uptake rate functions. For glutamate, this is represented by $\mathrm{Glu_e} \mapsto \mathrm{S}\left(\mathrm{Glu_e}, V_{\mathrm{Glu}}^{\mathrm{e\to Ast}} + V_{\mathrm{Glu}}^{\mathrm{e\to Pyr}}, v_{\mathrm{Glu}}^{\mathrm{e\to Ast,Pyr}}, r_{\mathrm{Glu}}^{\mathrm{e\to Ast,Pyr}}\right)$ as per Equation (2.3), and for GABA by $\mathrm{GABA_e} \mapsto \mathrm{H}\left(\mathrm{GABA_e}, V_{\mathrm{GABA}}^{\mathrm{e\to Ast}}, K_{\mathrm{GABA}}^{\mathrm{e\to Ast}}\right) + \mathrm{H}\left(\mathrm{GABA_e}, V_{\mathrm{GABA}}^{\mathrm{e\to InIn}}, K_{\mathrm{GABA}}^{\mathrm{e\to InIn}}\right)$ as per Equation (2.4). The dark green solid lines, linked to the right vertical axes, illustrate the modulatory functions. For glutamate, this is $v_{\mathrm{Glu}}\colon \mathrm{Glu_e} \mapsto \mathrm{S}\left(\mathrm{Glu_e}, m_{\mathrm{Glu}}^{\mathrm{Pyr}}, v_{\mathrm{Glu}}^{\mathrm{Pyr,InIn}}, r_{\mathrm{Glu}}^{\mathrm{Pyr,InIn}}\right) - \Delta_{\mathrm{Glu}}^{v}$, and for GABA, $v_{\mathrm{GABA}}\colon \mathrm{GABA_e} \mapsto \mathrm{S}\left(\mathrm{GABA_e}, m_{\mathrm{GABA}}^{\mathrm{Pyr}}, v_{\mathrm{GABA}}^{\mathrm{Pyr}}, r_{\mathrm{GABA}}^{\mathrm{Pyr}}\right) - \Delta_{\mathrm{GABA}}^{v}$. The parameters are set as follows: $m_{\mathrm{Glu}}^{\mathrm{Pyr}} = 0.8\ \mathrm{mV}$, $v_{\mathrm{Glu}}^{\mathrm{Pyr}} = 10\ \mu\mathrm{mol}$, $r_{\mathrm{Glu}}^{\mathrm{Pyr}} = 0.5\ \mu\mathrm{mol}^{-1}$, and $\Delta_{\mathrm{Glu}}^{v} = 0.4\ \mathrm{mV}$ for glutamate; and $m_{\mathrm{GABA}}^{\mathrm{Pyr}} = 4.2\ \mathrm{mV}$, $v_{\mathrm{GABA}}^{\mathrm{Pyr}} = 20\ \mu\mathrm{mol}$, $r_{\mathrm{GABA}}^{\mathrm{Pyr}} = 0.25\ \mu\mathrm{mol}^{-1}$, and $\Delta_{\mathrm{Glu}}^{v} = 2.1\ \mathrm{mV}$ for GABA. These parameters are also summarized in Table 2.3. The light green rectangular areas highlight the intended exploration spaces: $\mathrm{Glu_e}$ within [5; 15] μmol and $\mathrm{GABA_e}$ within [5; 35] μmol.

2.3.5 Forward parameterization

The bifurcation diagram in Figure 2.2 was drawn under the assumption of fully independent identical nodes. Nonetheless, this diagram can be conveniently expanded by incorporating the effects of the parameter $C^{\mathrm{Pyr\to Pyr}}$, enabling an exploration of certain form of network interactions between nodes, albeit within limited contexts. Specifically, in a setup where identical nodes are interconnected, referred to as a *homogeneous* network, $C^{\mathrm{Pyr\to Pyr}}$ can act as a substitute for ω_{Pyr} when the matrix Ω_{Pyr} is right stochastic, because then $Q_{\mathrm{Pyr}} = \omega_{\mathrm{Pyr}} F_{\mathrm{Pyr}}$. Therefore, under such a homogeneous network context, a bifurcation analysis incorporating $C^{\mathrm{Pyr\to Pyr}}$ provides a straightforward and systematic approach to determine ω_{Pyr} values by examining the dynamics of an individual node. This strategy avoids the complexities involved in performing detailed stability and bifurcation analyses on a complex (*heterogeneous*) and high-dimensional nonlinear network model, which remains a significant challenge in the field (for reference, see (Forrester et al., 2020)).

In practical applications, it is advisable to treat ω_{Pyr} as a free parameter, though such considerations were outside the purview of this study. However, we aim to delve into the intricate interplay among ω_{Pyr}, ω_{Glu}, and ω_{GABA} in subsequent research endeavors.

To establish values for ω_{Pyr}, our approach entailed a two-step process. Initially, bifurcation analyses of a single node (also conceptualized as a homogeneous network) were conducted using the parameter $C^{\mathrm{Pyr\to Pyr}}$. This was succeeded by stochastic simulations of a heterogeneous network, aimed at enhancing our comprehension and fine-tuning of the parameter settings.

Our bifurcation analysis aimed to identify suitable values for q and $C^{\mathrm{Pyr\to Pyr}}$ to ensure that $q + C^{\mathrm{Pyr\to Pyr}} F_{\mathrm{Pyr}} - v_{\mathrm{GABA}}\, a/A$ falls within the range [170; 370] Hz. This approach was chosen for its

convenience, especially since the bounds for $v_{\mathrm{GABA}}\, a/A$ were already established in Section 2.3.4, corresponding to $\mathrm{GABA_e}$ within [5; 35] µmol. This led to a straightforward specification for q: $370 + \inf(v_{\mathrm{GABA}}\, a/A) \geq q \geq 170 + \sup(v_{\mathrm{GABA}}\, a/A)$ where inf and sup denote the infimum and supremum, respectively. For example, we selected $q = 240$ Hz, which consequently provided a range of values for $C^{\mathrm{Pyr}\to\mathrm{Pyr}}$ due to $0 < F_{\mathrm{Pyr}} < \nu_{\max}$, though this range was too broad to be practical.

Further insights were gained by examining how the bifurcation landscape, particularly the branch of supercritical Hopf bifurcations, shifts as $C^{\mathrm{Pyr}\to\mathrm{Pyr}}$ varies, as shown in Figure 2.4 and Figure 2.5 (and also discussed in (Garnier et al., 2015) with different parameters). A notable observation was that increasing $C^{\mathrm{Pyr}\to\mathrm{Pyr}}$ maintained the presence of a supercritical Hopf bifurcation branch within the parameter plane defined by v_{Glu} within [−0.34; 0.34] mV and p within [170; 370] Hz (or equivalently, v_{GABA} within [−2.00; 2.00] mV). This bifurcation branch effectively divides the parameter space into two regions: an expanding oscillatory region characterized by stable limit cycles and a contracting non-oscillatory region marked by stable equilibria.

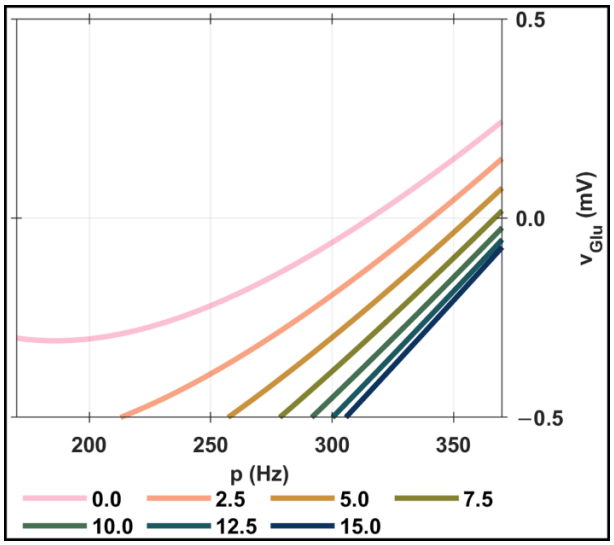

Figure 2.4. Branches of supercritical Hopf bifurcations. Hopf bifurcations within the $(v_{\mathrm{Glu}}; p)$ plane for $C^{\mathrm{Pyr}\to\mathrm{Pyr}} \in \{0; 2.5; 5; 7.5; 10; 12.5; 15\}$.

Although these dynamic characteristics were initially considered for convenience, they proved to be more broadly applicable across a wider range of v_{Glu} and p (or v_{GABA}) values, offering a robust framework for our analysis (as illustrated by comparing Figure 2.5.a to Figure 2.2.a, and then to Figure 2.4). Consequently, we could constrain the range of $C^{\mathrm{Pyr}\to\mathrm{Pyr}}$ values to ensure the network model operates near the critical boundary between steady-state and oscillatory behaviors (Deco et al., 2017), or within a continuum of oscillatory regimes, as pursued in this study.

More concretely, it is insightful to observe that for *smaller* $C^{\mathrm{Pyr}\to\mathrm{Pyr}}$ values, the equilibrium plane for an isolated node, as depicted in Figure 2.2.d, closely approximates that of any node within a homogeneous network, as shown in Figure 2.5.d. This relationship is directly tied to the p-axis, as described in Equation (2.9), with our approximations focusing on equilibria rather than limit cycle mean amplitudes. This insight allows us to refine the upper bound for $C^{\mathrm{Pyr}\to\mathrm{Pyr}}$, directly from the bifurcation diagram of an isolated node. We determined $F_{\mathrm{Pyr}} < 4.1$ Hz for v_{Glu} within [−0.34; 0.34] mV and p within [170; 370] Hz, leading to $C^{\mathrm{Pyr}\to\mathrm{Pyr}} \leq$

$(370 - q + \inf(v_{\mathrm{GABA}}\, a/A))/4.1 \approx 16.7$. Consequently, ω_{Pyr} was found to be viable within]0; 16.7].

To identify one suitable ω_{Pyr} value, we conducted simulations with the aim of finding a value that would facilitate the quantification of non-trivial functional connectivity patterns, particularly in stochastic and heterogeneous network conditions. This approach to defining ω_{Pyr} was critical for several reasons. Given our model's design, it was unlikely for functional network architectures to arise solely from variations in astrocytic network couplings. This was partly because we aimed for a balance between neurotransmitter uptake and release rates, minimizing the impact of neurotransmission on changes in nodal neuronal excitability levels. Furthermore, we selected a dynamic landscape where changes in the average levels of neuronal membrane potentials were generally minimal (not shown here), and we applied a uniform parameterization setting across nodes. Consequently, within our network model comprising uniformly parameterized coupled neuron-astrocyte masses, the neuronal structural layer Ω_{Pyr} emerged as the principal factor capable of engendering diverse attractors (primarily influencing the p-axis), which could then lead to complex functional connectivity patterns beyond mere linear correlations and phase locking.

Our objective was to ensure that motions on the bifurcation landscape would be predominantly driven by changes in astrocytic network couplings, while allowing the network model to express a range of functional states primarily influenced by neuron-neuron interconnections (i.e., Ω_{Pyr}). Therefore, it was desirable to select an ω_{Pyr} value that would, *a priori*, enhance the detectability and variety of network functional connections across the entire v_{Glu} spectrum. By specifying for q independently drawn samples from a normal distribution with a mean and standard deviation of 240 ± 10 Hz for each region independently, we found through *preliminary* simulations that $\omega_{\mathrm{Pyr}} = 7.5$ was appropriate. This ω_{Pyr} value is associated with the homogeneous network condition illustrated in Figure 2.5 with $C^{\mathrm{Pyr}\to\mathrm{Pyr}} = 7.5$. The value was strong enough to ensure that amplitude and phase network synchronizations are both present and quantifiable. Additionally, it was small enough to prevent the nodes from behaving too uniformly or too independently, relative to their stochastic baseline neuronal firing rates.

The preliminary simulations were conducted by interconnecting through the matrix Ω_{Pyr}, the *simplified* neuronal compartments, as detailed in Section 2.3.2, with parameterization based on v_{Glu} and v_{GABA}. In these simulations, each region was set to have the same $(v_{\mathrm{Glu}}; v_{\mathrm{GABA}})$ values, with v_{GABA} fixed at 0 mV and v_{Glu} chosen from the set $\{-0.3; 0; 0.3\}$ mV. Selecting v_{Glu} from this set offered a cost-effective insight into potential dynamics within the targeted landscape's core and periphery. The only variation between regions in each simulation was their stochastic component q, which was drawn from the same normal distribution independently for each region. It is important to note that the simulations of the forthcoming chapter will employ the *full* neuron-astrocyte network model, where $\mathrm{Glu_e}$ and $\mathrm{GABA_e}$ are dynamic state variables rather than fixed parameters.

Upon setting $\omega_{\mathrm{Pyr}} = 7.5$ through the preceding two-step process, we defined an *initial* state for the *main* simulations. This state is illustrated in Figure 2.5 as a circular black dot near a supercritical Hopf bifurcation locus, where the influence of astrocytic network activity on the *baseline* levels of $\mathrm{Glu_e}$ and $\mathrm{GABA_e}$, compared to neuronal activity, is minimal. Specifically, the initial conditions were set as ${\omega_{\mathrm{Glu}}}^{\mathrm{initial}} = {\omega_{\mathrm{GABA}}}^{\mathrm{initial}} = 0.01\ \mu\mathrm{mol}^{-1}$, ${v_{\mathrm{Glu}}}^{\mathrm{initial}} = -0.34$ mV

(equivalently, $\mathrm{Glu_e}^{\mathrm{initial}} \approx 4.98\ \mu\mathrm{mol}$), and $v_{\mathrm{GABA}}{}^{\mathrm{initial}} = -1.95\ \mathrm{mV}$ (equivalently, $\mathrm{GABA_e}^{\mathrm{initial}} \approx 6.82\ \mu\mathrm{mol}$). The insignificance of astrocytic network activity contributions relative to neuronal activity at this initial state is underscored by the following inequalities:

$$\begin{aligned} \omega_{\mathrm{Glu}}{}^{\mathrm{initial}} \mathrm{S}\left(\mathrm{Glu_e}^{\mathrm{initial}}, m_{\mathrm{Glu}}^{\mathrm{Ast}}, v_{\mathrm{Glu}}^{\mathrm{Ast}}, r_{\mathrm{Glu}}^{\mathrm{Ast}}\right) &\coloneqq Q_{\mathrm{Glu}}^{\mathrm{Ast}\,\mathrm{initial}} \ll F_{\mathrm{Pyr}}{}^{\mathrm{initial}} \\ \omega_{\mathrm{GABA}}{}^{\mathrm{initial}} \mathrm{S}\left(\mathrm{Glu_e}^{\mathrm{initial}}, m_{\mathrm{Glu}}^{\mathrm{Ast}}, v_{\mathrm{Glu}}^{\mathrm{Ast}}, r_{\mathrm{Glu}}^{\mathrm{Ast}}\right) &\coloneqq Q_{\mathrm{GABA}}^{\mathrm{Ast}\ \mathrm{initial}} \ll F_{\mathrm{InIn}}{}^{\mathrm{initial}} \end{aligned} \tag{2.11}$$

The establishment of an initial state also led to fixed values for W and Z, determined through steady-state calculations under the assumption that neurotransmitter uptake and release rates are in equilibrium (see also (Blanchard et al., 2016)):

$$\begin{aligned} W &= w_{\mathrm{d}} \frac{\mathrm{S}\left(\mathrm{Glu_e}^{\mathrm{initial}}, V_{\mathrm{Glu}}^{\mathrm{e}\to\mathrm{Ast}} + V_{\mathrm{Glu}}^{\mathrm{e}\to\mathrm{Pyr}}, v_{\mathrm{Glu}}^{\mathrm{e}\to\mathrm{Ast,Pyr}}, r_{\mathrm{Glu}}^{\mathrm{e}\to\mathrm{Ast,Pyr}}\right)}{F_{\mathrm{Pyr}}{}^{\mathrm{initial}} + Q_{\mathrm{Glu}}^{\mathrm{Ast}\,\mathrm{initial}}} \\ &\approx 4.9\ \mu\mathrm{mol/s} \\ Z &= z_{\mathrm{d}} \frac{\mathrm{H}\left(\mathrm{GABA_e}^{\mathrm{initial}}, V_{\mathrm{GABA}}^{\mathrm{e}\to\mathrm{Ast}}, K_{\mathrm{GABA}}^{\mathrm{e}\to\mathrm{Ast}}\right) + \mathrm{H}\left(\mathrm{GABA_e}^{\mathrm{initial}}, V_{\mathrm{GABA}}^{\mathrm{e}\to\mathrm{InIn}}, K_{\mathrm{GABA}}^{\mathrm{e}\to\mathrm{InIn}}\right)}{F_{\mathrm{InIn}}{}^{\mathrm{initial}} + Q_{\mathrm{GABA}}^{\mathrm{Ast}\ \mathrm{initial}}} \\ &\approx 50.6\ \mu\mathrm{mol/s} \end{aligned} \tag{2.12}$$

These calculated W and Z values are instrumental in sustaining the selected baseline concentrations at the initial state, factoring in the contributions from non-negligible astrocytic network activity.

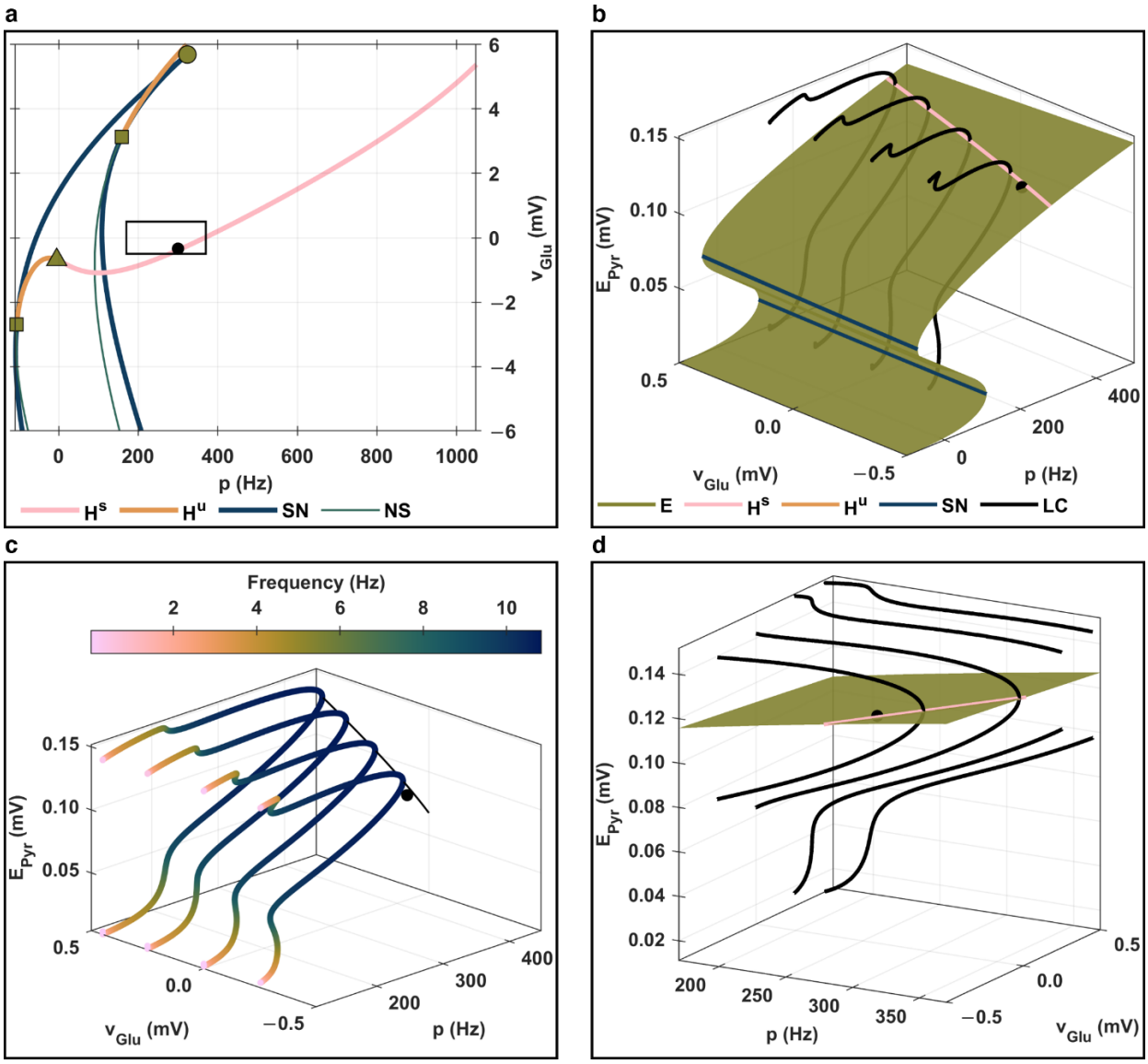

Figure 2.5. Two-parameter bifurcation diagram. Drawn with $C^{\mathrm{Pyr}\to\mathrm{Pyr}} = 7.5$. This is similar to the one shown in Figure 2.2. The circular black dot in panels (a)–(d) represent the initial state selected for this study (as detailed in the accompanying text).

2.3.6 Exploration parameter space

We successfully narrowed down the parameterization of our model to the two global astrocytic network coupling parameters: ω_{Glu} and ω_{GABA}. To establish a biologically relevant exploration grid for $(\omega_{\mathrm{Glu}}; \omega_{\mathrm{GABA}})$, we sampled the domain given by $(v_{\mathrm{Glu}}; v_{\mathrm{GABA}}) \in [-0.30; 0.15] \times [-2.00; 2.00]$ mV × mV using a 35×35 uniform grid. Through steady-state calculations, this gridding yielded $(\omega_{\mathrm{Glu}}; \omega_{\mathrm{GABA}}) \in [2.90; 6.47] \times [0.14; 1.94]$ $\mu\mathrm{mol}^{-1} \times \mu\mathrm{mol}^{-1}$. Thus, from the initial state, an increase in ω_{Glu} generally leads to a rise in $\mathrm{Glu_e}$ from its initial level to a maximum of 15 µmol, predominantly influencing the v_{Glu}-axis. Similarly, an increase in ω_{GABA} tends to elevate $\mathrm{GABA_e}$ from its initial level to a maximum of 35 µmol, primarily affecting the p-axis or v_{GABA}-axis.

The resulting grid comprises 1225 unique$(\omega_{\mathrm{Glu}}; \omega_{\mathrm{GABA}})$ pairs, which will be utilized in the next chapter. Figure 2.6.a illustrates the simulation parameter plane defined by these 1225 unique pairs. Figure 2.6.b displays the uniform grid on the parameter plane defined by $(v_{\mathrm{Glu}}; v_{\mathrm{GABA}})$ with 35x35 values, which was instrumental in deriving the $(\omega_{\mathrm{Glu}}; \omega_{\mathrm{GABA}})$ pairs.

Looking ahead to the discussions in the next chapter, it is important to note that the funnel-shaped parameter space depicted in Figure 2.6.a, defined by $(\omega_{\mathrm{Glu}}; \omega_{\mathrm{GABA}})$, highlights the highly nonlinear impact of ω_{Glu} on neuron-astrocyte interactions compared to ω_{GABA}. This is expected, considering that glutamate levels not only influence the excitability thresholds of both pyramidal cells and inhibitory interneurons but also drive astrocytic network feedback mechanisms. Additionally, despite the sparser sampling of lower ω_{GABA} values compared to higher ones, there was no significant advantage in conducting additional simulations with lower ω_{GABA} values for the purposes of this study.

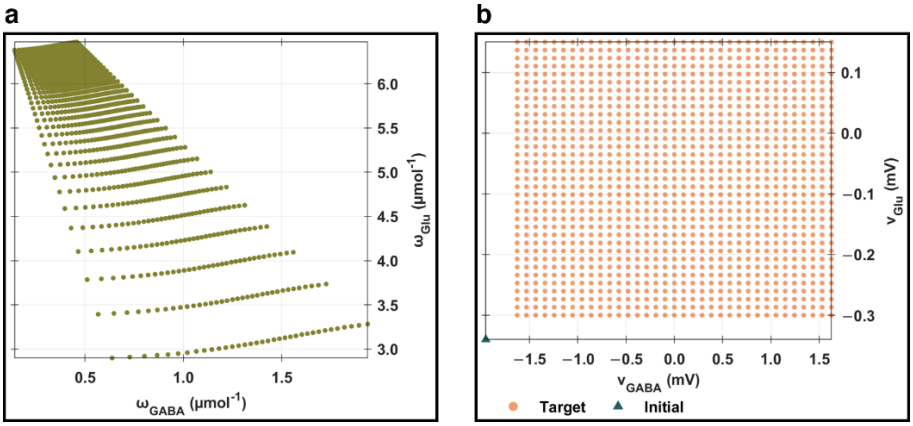

Figure 2.6. Simulation parameter planes. (a) Simulation parameter plane defined by $(\omega_{\mathrm{Glu}}; \omega_{\mathrm{GABA}})$. (b) The underlying parameter plane from which (a) was derived. The green triangular dot (on the bottom right corner) represents the initial state chosen for this study. To clarify, this initial state corresponds to ${\omega_{\mathrm{Glu}}}^{\mathrm{initial}} = {\omega_{\mathrm{GABA}}}^{\mathrm{initial}} = 10^{-2}\ \mu\mathrm{mol}^{-1}$, although it is not drawn in panel (a).

2.3.7 Summary and generalization

In summary, we established a biologically relevant exploration grid for $(\omega_{\mathrm{Glu}}; \omega_{\mathrm{GABA}})$ to ensure that $\mathrm{Glu_e}$ covers the range [5; 15] µmol and $\mathrm{GABA_e}$ spans [5; 35] µmol. The interplay between ω_{Glu} and ω_{GABA} facilitates the network model's exploration of diverse neuronal dynamical states. These states are characterized by stable periodic orbits with varying peak-to-peak amplitudes and α-band frequencies, along with distinctive excitatory and inhibitory activity patterns, contributing to a range of functional network architectures.

It is important to note that the decisions regarding the LFP frequency band, the concentration limits for $\mathrm{Glu_e}$ and $\mathrm{GABA_e}$, and the initial state are all adaptable. For instance, the LFP frequency band could be modified by scaling parameters A, a, B, and b (which define the neuronal postsynaptic potential impulse response functions), while maintaining the ratios A/a and B/b. Such adjustments leave singular points unaffected, as shown in Equation (2.9) and Figure 2.7, but they alter limit cycle frequencies through scaling. However, the biological realism of the resulting parameters may be questionable (for reference, see (Chehelcheraghi et al., 2016; David & Friston, 2003)). Regarding the concentration ranges for $\mathrm{Glu_e}$ and $\mathrm{GABA_e}$, these can also be varied, as partially demonstrated in Figure 2.3, by tweaking the parameters of the sigmoidal or Michaelis–

Menten functions. Naturally, this would necessitate corresponding adjustments to the parameters of the uptake, release, and feedback functions to ensure consistency.

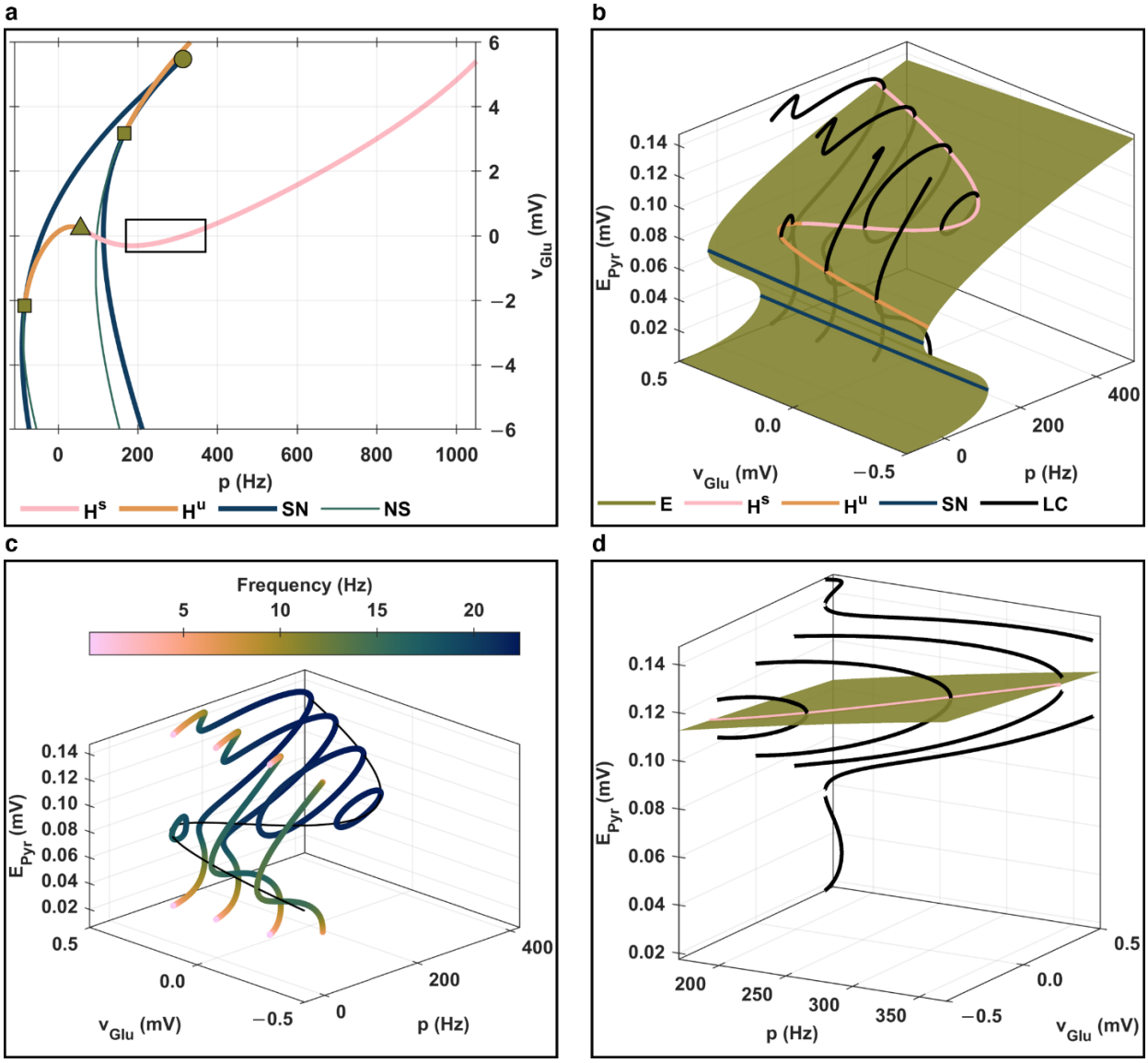

Figure 2.7. Two-parameter bifurcation diagram for simulating β-band activity. This is analogous to the one shown in Figure 2.2 but with the following adjustment: $A = 6.5\,\mathrm{mV}$, $a = 200\,\mathrm{Hz}$, $B = 44\,\mathrm{mV}$, and $b = 100\,\mathrm{Hz}$. This adjustment involved doubling the values of A, a, B, and b compared to those used in Figure 2.2. The purpose of this modification was to model β-band, rather than α-band, electrophysiological rhythms. For instance, in panel (c) the orbitally stable limit cycles that emerge from supercritical Hopf bifurcations exhibit frequencies around 21 Hz, indicative of β-band activity.

2.4 Simulated time series

2.4.1 Exotic scenarios

In this section, we demonstrate through simulations the significant versatility that a gliotransmission mechanism can introduce to the classical dynamical landscape of the Jansen–Rit model. We focus on phase trajectories within a network model consisting of a single node that incorporates astrocytic network self-feedbacks, i.e., such that $\Omega_{\mathrm{Ast}} = (1)$. The simulations adhere to the parameter settings listed in Table 2.3, except where modifications are specified in Table 2.1.

It is important to recognize that various parameters within the neuronal compartment could be adjusted to reproduce the rhythms depicted in the subsequent simulations, even without incorporating an astrocytic compartment (refer to (Forrester et al., 2020; Garnier et al., 2015) for examples). Nonetheless, we contend that relying solely on neuronal compartment adjustments to achieve these dynamics could potentially compromise biological realism. Our approach, which integrates astrocytic influences through glutamatergic and GABAergic transmission systems, aims to maintain a closer alignment with neurobiological evidence and thus enhance the model's biological plausibility.

Table 2.1. Parameters used in this study to perform single node simulations. Parameters used to simulate phase trajectories within a network model consisting of a single node featuring astrocytic network self-feedbacks, i.e., such that $\Omega_{\mathrm{Ast}} = (1)$. This table exclusively lists parameters that deviate from those presented in Table 2.3, to highlight the adjustments made for this particular simulation setup.

Name	**Value**
v_0^{Pyr}	2.2 mV
W	7.8 µmol/s
Z	59.0 µmol/s
$m_{\mathrm{GABA}}^{\mathrm{Pyr}}$	13.3 mV
ω_{Pyr}	0
ω_{Glu}	See texts or figure captions
ω_{GABA}	See texts or figure captions

In Table 2.1, for simplicity and illustrative purposes, we set an extreme value for $m_{\mathrm{GABA}}^{\mathrm{Pyr}}$ (and v_0^{Pyr}). As discussed in Section 2.3.2, the quantities $\mathrm{S}\left(\mathrm{GABA_e}, m_{\mathrm{GABA}}^{\mathrm{Pyr}}, v_{\mathrm{GABA}}^{\mathrm{Pyr}}, r_{\mathrm{GABA}}^{\mathrm{Pyr}}\right)$ and q serve analogous roles when constructing bifurcation diagrams relative to p, being essentially proportional. Thus, alternative pairs of $m_{\mathrm{GABA}}^{\mathrm{Pyr}}$ values and the mean of q could be chosen to yield similar outcomes.

As detailed in Section 2.3, the astrocytic compartment's relative simplicity allows for the application of insights previously gained from the neuronal compartment. In this context, we consider scenarios in which the extracellular dynamics act as slowly changing subsystems that spontaneously drive the neuronal subsystem through various states (such as spiking, resting, and oscillatory; or rhythmic bursting, tonic spiking, total quiescence, and bursting oscillations). These dynamics do so while being largely unaffected by the fast-changing values within the neuronal subsystem. The term *spontaneous* is particularly significant, as it highlights that these dynamic transitions occur without any temporal changes in the parameters.

Figure 2.8 presents a scenario with $\omega_{\mathrm{Glu}} = 3.82\ \mu\mathrm{mol}^{-1}$ and $\omega_{\mathrm{GABA}} = 0.38\ \mu\mathrm{mol}^{-1}$. The bifurcation diagram in this figure aligns with that in Figure 2.2.b, and the classical Jansen–Rit model is represented at $v_{\mathrm{Glu}} = 0$ mV, corresponding to $\mathrm{Glu_e} = 10.0$ µmol (refer to Figure 2.3 for comparison). In this setting, the neuronal populations primarily exhibit a *normal* oscillatory behavior, occasionally transitioning to a spiking regime for brief intervals. These transitions to spiking regimes represent dynamic fluctuations near a critical boundary between two distinct families of stable limit cycles.

Figure 2.9 illustrates a different scenario with $\omega_{\mathrm{Glu}} = 3.81\ \mu\mathrm{mol}^{-1}$ and $\omega_{\mathrm{GABA}} = 0.49\ \mu\mathrm{mol}^{-1}$. Unlike in Figure 2.8, the neuronal compartment does not predominantly stay in a *normal* oscillatory state but more frequently switches among *normal* oscillatory, spiking, and quiescent states. Notably, before shifting from *normal* oscillatory to spiking regimes, the neuronal populations momentarily enter quiescent phases, indicating that the neuronal compartment transitions to a lower manifold of stable singular points before encountering saddle-node on invariant cycle bifurcations. After entering spiking regimes, neuronal populations often revert to *normal* oscillatory states via fold bifurcations of limit cycles.

These dynamics underscore the intricate interplay between neuronal excitatory and inhibitory firings and the astrocytic modulation of glutamate and GABA neurotransmission. Moreover, by selecting various parameter combinations (such as those defining release transfer functions and uptake rate functions), it is possible to influence the duration within specific dynamical regimes and the frequency and speed of transitions between them.

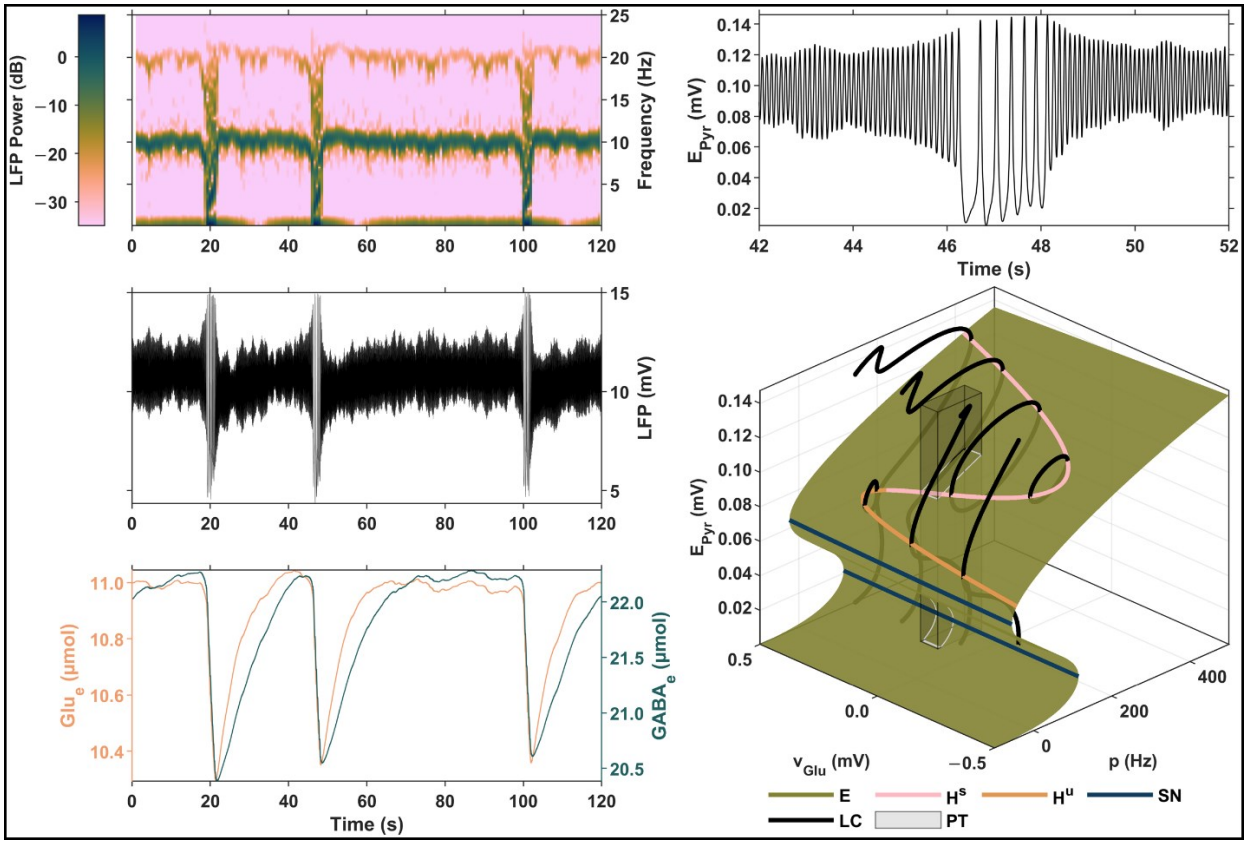

Figure 2.8. Simulation of sporadic spontaneous spiking. This figure presents a scenario characterized by $\omega_{\mathrm{Glu}} = 3.82\ \mu\mathrm{mol}^{-1}$ and $\omega_{\mathrm{GABA}} = 0.38\ \mu\mathrm{mol}^{-1}$. It includes time series plots for LFP, $\mathrm{Glu_e}$, and $\mathrm{GABA_e}$ over the interval [0; 120] s. Additionally, the spectrogram for LFP is displayed for the same time interval, and the time series for E_{Pyr} is illustrated for a specified period of interest. The bifurcation diagram corresponds to that shown in Figure 2.2.b. The three-dimensional grey rectangular region outlines the minimum and maximum values of the simulated phase trajectory (PT).

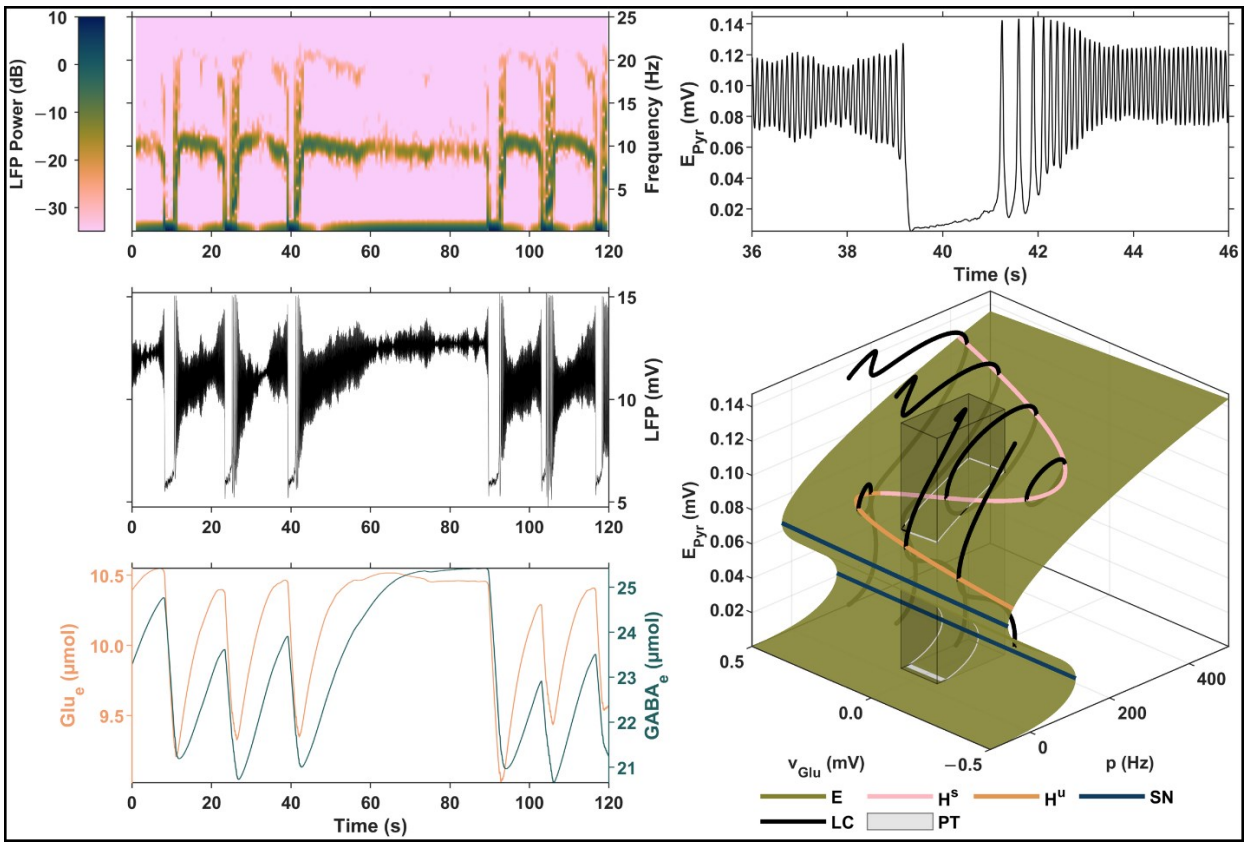

Figure 2.9. Simulation of spontaneous switches among normal oscillatory, spiking, and quiescent states. Similar to Figure 2.8, but in this scenario, $\omega_{\mathrm{Glu}} = 3.81\ \mu\mathrm{mol}^{-1}$ and $\omega_{\mathrm{GABA}} = 0.49\ \mu\mathrm{mol}^{-1}$ are used.

Figure 2.8 and Figure 2.9 collectively demonstrate how neurotransmission, augmented by gliotransmission, introduces remarkable adaptability to the conventional dynamical landscape of the Jansen–Rit model. As discussed in Section 2.3, constraining v_{Glu} and p (or v_{GABA}) within certain ranges and carefully choosing initial conditions are crucial for simulating normal oscillatory neuronal patterns. This modeling approach also opens new avenues for investigating physiological and pathological cortical activities, particularly epileptic patterns, from a neuron-glial perspective, aligning with contemporary neuroscientific research efforts (for instance, see (Touboul et al., 2011; Volman & Bazhenov, 2019; Wendling & Chauvel, 2008)).

2.4.2 Physiological scenario

Figure 2.10 and Figure 2.11 display two simulations from a network model comprising 216 nodes, with the parameters set precisely as outlined in Table 2.3. The specifics of these simulations will be elaborated upon in the upcoming chapter. In line with the simulation framework discussed throughout Section 2.3, Figure 2.10 and Figure 2.11 demonstrate that the LFPs feature amplitude modulations at frequencies significantly lower than their primary peak frequencies, which are around 10.5 Hz. Furthermore, $\mathrm{Glu_e}$ and $\mathrm{GABA_e}$ exhibit mean quasi-stationary slow fluctuations. These fluctuations are positively correlated, and mirror some aspects of the LFP envelopes (both upper and lower envelopes), indicating a complex interplay between neuronal and astrocytic activities within the network.

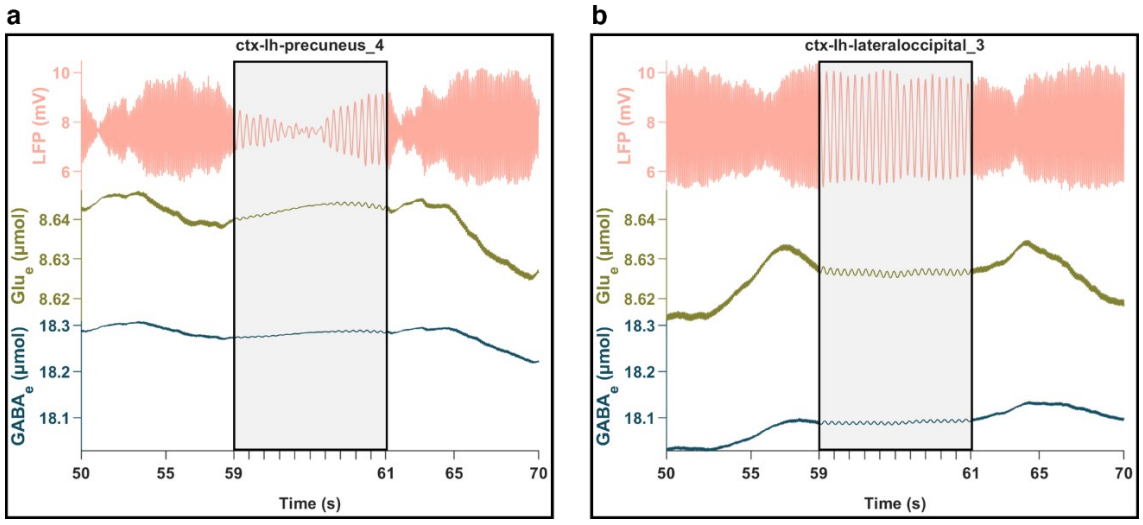

Figure 2.10. Physiological whole-brain network simulation bridging electrophysiology and neurotransmission. This figure illustrates a simulation with $\omega_{\mathrm{Glu}} = 5.64\ \mu\mathrm{mol}^{-1}$ and $\omega_{\mathrm{GABA}} = 0.52\ \mu\mathrm{mol}^{-1}$, corresponding to whole-brain levels of v_{Glu} and v_{GABA} given by $v_{\mathrm{Glu}} = -0.13$ mV and $v_{\mathrm{GABA}} = -0.49$ mV. Panel (a) displays the neural activity within a specific region of the left precuneus cortex, while panel (b) focuses on a region within the left lateral occipital cortex (further details on the brain parcellation will be provided in the subsequent chapter). The time series are depicted for the interval between 50 and 70 seconds, with the black rectangular frame highlighting a zoomed-in view of the activity from 59 to 61 seconds.

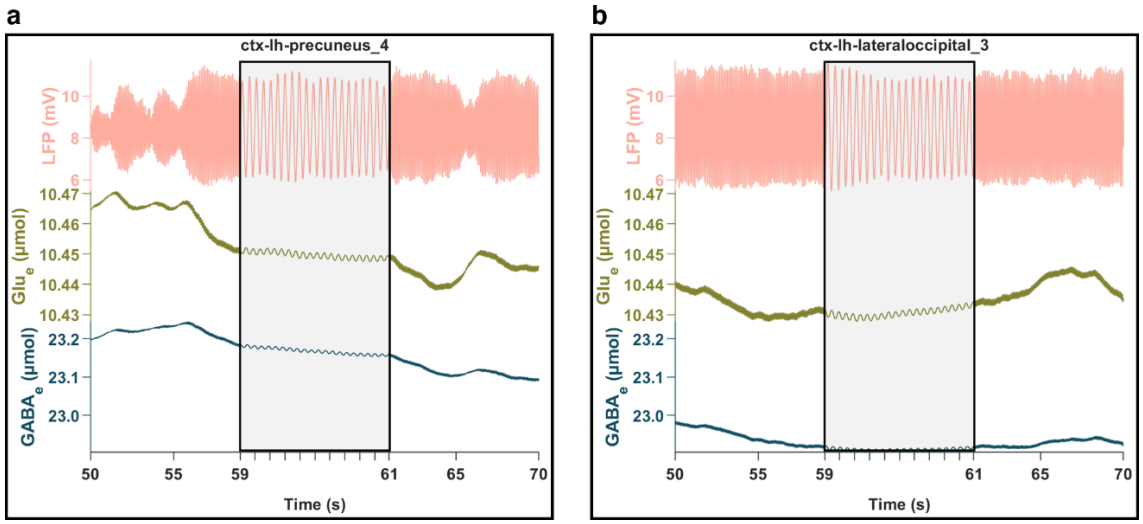

Figure 2.11. Physiological whole-brain network simulation bridging electrophysiology and neurotransmission. Similar to Figure 2.10, this figure represents a simulation with $\omega_{\mathrm{Glu}} = 6.30\ \mu\mathrm{mol}^{-1}$ and $\omega_{\mathrm{GABA}} = 0.46\ \mu\mathrm{mol}^{-1}$, which corresponds to whole-brain levels of v_{Glu} and v_{GABA} given by $v_{\mathrm{Glu}} = 0.04$ mV and $v_{\mathrm{GABA}} = 0.77$ mV.

2.5 SI — Tables

Table 2.2. Variables and abbreviations.

Name	Description
Pyr	Population of pyramidal cells
ExIn	Population of excitatory interneurons
InIn	Population of inhibitory interneurons
Ast	Population of astrocytes
Glu	Glutamate
GABA	Gamma-aminobutyric acid
E_{Pyr}	Average excitatory postsynaptic potentials from Pyr to ExIn and InIn
$E_{\mathrm{ExIn}\cup\mathrm{Pyr}}$	Average excitatory postsynaptic potentials from Pyr and ExIn to Pyr
E_{InIn}	Average inhibitory postsynaptic potentials from InIn to Pyr
J_{Glu}	Extracellular Glu release rate of Pyr
$\mathrm{Glu}_{\mathrm{e}}$	Extracellular Glu concentration
$\mathrm{Glu}_{\mathrm{Ast}}$	Intracellular Glu concentration of Ast
J_{GABA}	Extracellular GABA release rate of InIn
$\mathrm{GABA}_{\mathrm{e}}$	Extracellular GABA concentration
$\mathrm{GABA}_{\mathrm{Ast}}$	Intracellular GABA concentration of Ast
F_{Pyr}	Firing rate from Pyr
F_{ExIn}	Firing rate from ExIn
F_{InIn}	Firing rate from InIn
v_{Pyr}	Excitability threshold of Pyr
v_{ExIn}	Excitability threshold of ExIn
v_{InIn}	Excitability threshold of InIn
v_{Glu}	Excitability threshold offset induced by $\mathrm{Glu}_{\mathrm{e}}$ on Pyr and InIn
v_{GABA}	Excitability threshold offset induced by $\mathrm{GABA}_{\mathrm{e}}$ on Pyr
Q_{Pyr}	Neuronal network feedback on Pyr
$Q_{\mathrm{Glu}}^{\mathrm{Ast}}$	Astrocytic network feedback inducing Glu release from Pyr
$Q_{\mathrm{GABA}}^{\mathrm{Ast}}$	Astrocytic network feedback inducing GABA release from InIn

Table 2.3. Parameters used in this study to perform the primary simulations. $\mathcal{N}$: normal distribution; std: standard deviation; PSP: postsynaptic potentials; RTF: release transfer function.

Name	Description	Value
A	Tuning parameter of excitatory PSP maximal amplitude	3.25 mV
B	Tuning parameter of inhibitory PSP maximal amplitude	22 mV
a	Reciprocal of time constant of excitatory PSP	$100\ \mathrm{s}^{-1}$
b	Reciprocal of time constant of inhibitory PSP	$50\ \mathrm{s}^{-1}$
$\nu_{\max}$	Maximal neuronal firing rate	5 Hz
ν_0^{Pyr}	Baseline excitability threshold of Pyr	4.3 mV
ν_0^{ExIn}	Baseline excitability threshold of ExIn	6 mV
ν_0^{InIn}	Baseline excitability threshold of InIn	6.2 mV
r	Neuronal excitability rate	$0.56\ \mathrm{mV}^{-1}$
q	Baseline neuronal firing rate	$\mathcal{N}\begin{pmatrix}\mathrm{mean} = 240\ \mathrm{Hz}\\ \mathrm{std} = 10\ \mathrm{Hz}\end{pmatrix}$
$C^{\mathrm{Pyr}\to\mathrm{ExIn}}$	Nodal synaptic connection strength from Pyr to ExIn	135
$C^{\mathrm{ExIn}\to\mathrm{Pyr}}$	Nodal synaptic connection strength from ExIn to Pyr	108
$C^{\mathrm{Pyr}\to\mathrm{InIn}}$	Nodal synaptic connection strength from Pyr to InIn	33.75
$C^{\mathrm{InIn}\to\mathrm{Pyr}}$	Nodal synaptic connection strength from InIn to Pyr	33.75
$C^{\mathrm{Pyr}\to\mathrm{Pyr}}$	Nodal synaptic connection strength from Pyr to Pyr	0
W	Tuning parameter of Glu RTF gain	4.9 μmol/s
w_{r}	Reciprocal of rise time constant of Glu RTF	$90\ \mathrm{s}^{-1}$
w_{d}	Reciprocal of decay time constant of Glu RTF	$33\ \mathrm{s}^{-1}$
$V_{\mathrm{Glu}}^{\mathrm{e}\to\mathrm{Ast}}$	Maximal astrocytic Glu uptake rate	4.5 μmol/s
$V_{\mathrm{Glu}}^{\mathrm{e}\to\mathrm{Pyr}}$	Maximal neuronal Glu uptake rate	0.5 μmol/s
$\nu_{\mathrm{Glu}}^{\mathrm{e}\to\mathrm{Ast,Pyr}}$	Threshold parameter of Glu uptake rate sigmoid	9 μmol
$r_{\mathrm{Glu}}^{\mathrm{e}\to\mathrm{Ast,Pyr}}$	Rate parameter of Glu uptake rate sigmoid	$0.5\ \mu\mathrm{mol}^{-1}$
$\tau_{\mathrm{Glu}}^{\mathrm{Ast}}$	Time constant of astrocytic Glu degradation	1/9 s
Z	Tuning parameter of GABA RTF gain	50.6 μmol/s
z_{r}	Reciprocal of rise time constant of GABA RTF	$90\ \mathrm{s}^{-1}$
z_{d}	Reciprocal of decay time constant of GABA RTF	$33\ \mathrm{s}^{-1}$
$V_{\mathrm{GABA}}^{\mathrm{e}\to\mathrm{Ast}}$	Maximal astrocytic GABA uptake rate	2 μmol/s
$V_{\mathrm{GABA}}^{\mathrm{e}\to\mathrm{InIn}}$	Maximal neuronal GABA uptake rate	5 μmol/s
$K_{\mathrm{GABA}}^{\mathrm{e}\to\mathrm{Ast}}$	Michaelis–Menten concentration parameter for astrocytic GABA uptake rate	8 μmol
$K_{\mathrm{GABA}}^{\mathrm{e}\to\mathrm{InIn}}$	Michaelis–Menten concentration parameter for neuronal GABA uptake rate	24 μmol
$\tau_{\mathrm{GABA}}^{\mathrm{Ast}}$	Time constant of astrocytic GABA degradation	1/9 s

Name	Description	Value
$m_{\mathrm{Glu}}^{\mathrm{Pyr}}$	Maximal excitability threshold induced by $\mathrm{Glu_e}$ on Pyr	0.8 mV
$v_{\mathrm{Glu}}^{\mathrm{Pyr,InIn}}$	Threshold parameter of nodal $\mathrm{Glu_e}$ feedback sigmoid	10 µmol
$r_{\mathrm{Glu}}^{\mathrm{Pyr,InIn}}$	Rate parameter of nodal $\mathrm{Glu_e}$ feedback sigmoid	$0.5\ \mu\mathrm{mol}^{-1}$
$\mu_{\mathrm{Glu}}^{\mathrm{InIn/Pyr}}$	Maximal excitability threshold induced by $\mathrm{Glu_e}$ on InIn divided by $m_{\mathrm{Glu}}^{\mathrm{Pyr}}$	0.5
$m_{\mathrm{GABA}}^{\mathrm{Pyr}}$	Maximal excitability threshold induced by $\mathrm{GABA_e}$ on Pyr	4.2 mV
$v_{\mathrm{GABA}}^{\mathrm{Pyr}}$	Threshold parameter of nodal $\mathrm{GABA_e}$ feedback sigmoid	20 µmol
$r_{\mathrm{GABA}}^{\mathrm{Pyr}}$	Rate parameter of nodal $\mathrm{GABA_e}$ feedback sigmoid	$0.25\ \mu\mathrm{mol}^{-1}$
ω_{Pyr}	Gain of neuronal network feedback	7.5
ω_{Glu}	Diffusion coefficient for Glu-induced astrocytic network feedback on Glu release rates	$[2.90; 6.47]\ \mu\mathrm{mol}^{-1}$
ω_{GABA}	Diffusion coefficient for Glu-induced astrocytic network feedback on GABA release rates	$[0.14; 1.94]\ \mu\mathrm{mol}^{-1}$
$m_{\mathrm{Glu}}^{\mathrm{Ast}}$	Maximal amplitude of Glu-induced astrocytic network feedback sigmoid	$4.5\ \mu\mathrm{mol/s}$
$v_{\mathrm{Glu}}^{\mathrm{Ast}}$	Threshold parameter of Glu-induced astrocytic network feedback sigmoid	9 µmol
$r_{\mathrm{Glu}}^{\mathrm{Ast}}$	Rate parameter of Glu-induced astrocytic network feedback sigmoid	$0.5\ \mu\mathrm{mol}^{-1}$
Ω_{Pyr}	Network connectivity weights between Pyr	$[0; 1]$
Ω_{Ast}	Network connectivity weights between Ast	$[0; 1]$

Chapter 3 Dialogue mechanisms between astrocytic and neuronal networks — a whole brain modelling approach

3.1 Thesis storyline

This chapter builds on the rigorously parameterized network model established in the preceding chapter, exploring the impact of astrocytic networks on whole-brain activity and the emerging of functional connectivity patterns.

3.2 Abstract

Astrocytes, a major type of glia, possess assorted structural and functional properties making them inseparable from their neighbouring neurons. However, most published computational models of whole-brain activity, if not all, remain focused on neurons while ignoring astrocytes. We herewith introduce a biophysical model built upon neural mass network and compartmental modelling techniques, where large-scale astrocytic and neuronal networks couple their activity through glutamatergic and GABAergic transmission systems. We formulate a network scheme where neural dynamics are constrained by a two-layered structural network interconnecting either astrocytic or neuronal populations, and we ask how astrocytic networks contribute to whole-brain activity and emerging functional connectivity patterns. By developing a simulation approach based on bifurcation and multilayer network theories, we demonstrate that astrocytic and neuronal networks engage in a dialogue over fast and slow fluctuations or over phase-based and amplitude-based network connectivity. Our study is a step forward for more thoroughly investigating the role of glia alongside neurons in health or disease conditions.

3.3 Introduction

Astrocytes are intimately associated with neurons (De Pittà, 2020; De Pittà & Berry, 2019). To begin, astrocytes of the tripartite synapse model (Figure 3.1.a) sense synaptically released neurotransmitters (e.g., glutamate and gamma-aminobutyric acid (GABA)) by various mechanisms (e.g., membrane receptors and transporters) and signal back to presynaptic and postsynaptic terminals by gliotransmission (e.g., of glutamate and GABA) (De Pittà, 2020; De Pittà & Berry, 2019). Moreover, astrocytes delimit nonoverlapping domains (Figure 3.1.a), each domain covering 0.3–2 million synapses potentially associated with multiple neurons (De Pittà, 2020; Vasile et al., 2017). Finally, astrocytes form gap-junction-coupled syncytia (Figure 3.1.a) supporting intercellular communication through propagating calcium waves (Goldberg et al., 2010; Kastanenka et al., 2020). Together, these three examples highlight that astrocytes are equipped with diverse structural and functional properties allowing them to modulate neuronal circuits actively, strategically, and profoundly (De Pittà, 2020; De Pittà & Berry, 2019; Fields et al., 2015; Kastanenka et al., 2020), and they suggest that astrocytes and their neighbouring neurons form one functional unit rather than separate functional entities (De Pittà, 2020; De Pittà & Berry, 2019). Yet, despite them being potential signalling hubs in the neuropil, astrocytes have received limited attention in neurobiology compared to neurons (De Pittà, 2020; De Pittà & Berry, 2019; Fields et al., 2015; Kastanenka et al., 2020). Indeed, the bulk of empirical and theoretical neuroscientific studies have for long claimed they can explain many computational cerebral processes by examining neurons exclusively (De Pittà & Berry, 2019). To mitigate this (mostly) historical bias, a neuron-glial perspective has lately been proposed, prompting neuroscientists to revise current knowledge from a deeper mindset inclusive of glial cells (De Pittà & Berry, 2019) (see also (Marder, 2012) for a complementary perspective). The neuron-glial perspective aims at

describing the mutual dependence between neuronal and glial processes, which consists of the interplay between multiple signals elicited by neurons and glia at different spatiotemporal brain scales ranging from molecular to large-scale systems and from milliseconds to years (De Pittà, 2020; Fields et al., 2015). Understandably, the perspective posits the brain to be best characterized within a framework where not only neurons and glia can have a mutual dialogue, but also the structure and function of neuronal circuits can be flexibly intertwined with that of glia. In practice, because neuron-glial interactions are inherently nonlinear and multiscale, computational modelling approaches are essential to comprehend them (De Pittà & Berry, 2019; Kastanenka et al., 2020). Be that as it may, the latest reviews highlight a definite lack of computational frameworks elaborating on the neuron-glial perspective remaining to date (De Pittà & Berry, 2019; Kastanenka et al., 2020), especially at the whole-brain scale, and this is where this paper contributes.

We introduce a biophysical model of neuron-astrocyte large-scale network activity achieving a compromise between biological realism and mathematical tractability by building upon neural mass network and compartmental modelling techniques (Breakspear, 2017). In our network model, each node (i.e., brain region) has a temporal activity explained by a neuron-astrocyte mass model (Garnier et al., 2016) emulating regional activity elicited from neuronal and astrocytic populations mutually coupled through glutamatergic and GABAergic transmission systems, plus influences from stochastic fluctuations and distal regions. The distal influences are dictated by two types of network links, i.e., a two-layered structural network (Figure 3.1.b): one layer interconnecting neuronal populations from different regions and depicting white-matter tracts, and the other layer interconnecting astrocytic populations from different regions and depicting gap junctional densities. We formulate a simple large-scale network scheme whereby regional glutamate dynamics encourage adjacent astrocytic populations to couple their activity through a topology (based on gap junctional density) independent from that of neuronal populations (based on axonal density) which in turn leads to modulating whole-brain patterns of neuronal population firing rates via gliotransmission. We employ our model to theoretically investigate astrocytic network contributions to whole-brain activity and emerging functional connectivity patterns, through simulations, and bifurcation and multilayer network analyses (Figure 3.1.c–e).

3.4 Model

This section concisely lays out the fundamental principles of the mutual coupling between astrocytic and neuronal networks underlying our whole-brain model (see also the preceding chapter, Chapter 2 on page 92; the Chapter 2 mathematically details step-by-step how our network model can be analyzed and parameterized using techniques of simulation, bifurcation theory, and compartmental modelling; it graphically illustrates and discusses interesting dynamics that our network model supports).

3.4.1 Neuron-astrocyte mass model

The neuron-astrocyte mass model extended the work of (Garnier et al., 2016). It described the coarse-grained temporal activity of four coupled homogeneous populations of neural cells, namely glutamatergic pyramidal neurons (Pyr), excitatory interneurons (ExIn), GABAergic inhibitory interneurons (InIn), and astrocytes (Ast). Two high-level interactions between the different populations were expressed. On the one hand, neuron-neuron interactions which were abstracted to the dendro-somatic transformation of population firing rates (F_{Pyr}, F_{ExIn}, and F_{InIn}) into average membrane potentials (E_{Pyr}, $E_{\mathrm{ExIn}\cup\mathrm{Pyr}}$, and E_{InIn}) and vice-versa (*Equations* (2.1) and (2.2)). On

the other hand, neuron-astrocyte interactions which were abstracted to the concurrent synaptic releases and uptakes of neurotransmitters from and to an extracellular space (e). The two major excitatory and inhibitory neurotransmitters, namely glutamate (Glu) and GABA, respectively, were considered (*Equations* (2.3) and (2.4)). Glutamate release (J_{Glu}) was driven by pyramidal neurons firing-rate activity (F_{Pyr}) while GABA release (J_{GABA}) was driven by inhibitory interneurons activity (F_{InIn}). Extracellular glutamate ($\mathrm{Glu_e}$) uptakes were predominantly astrocytic while neurons had small but non-negligible contributions, while extracellular GABA ($\mathrm{GABA_e}$) uptakes were predominantly neuronal while astrocytes played a secondary role. Besides, following uptakes, neurotransmitters were degraded within astrocytes (expressed in $\mathrm{Glu_{Ast}}$ and $\mathrm{GABA_{Ast}}$ in *Equations* (2.3) and (2.4)). Of importance, and at the heart of this model, a dependency between extracellular neurotransmitter concentrations and neuronal firing rates was formulated based on the excitability level of the targeted neuronal populations (*Equation* (2.5)). This dependency was expressed in two ways in the model: on the one hand, an increase in $\mathrm{Glu_e}$ mainly resulting in the bounded (possibly transient) decrease of the excitability thresholds for both pyramidal cells and inhibitory interneurons, and conversely; on the other hand, an increase in $\mathrm{GABA_e}$ mainly resulting in the bounded (possibly transient) increase of the excitability threshold for pyramidal neurons, and conversely. Altogether, since all processes could happen concurrently, complex competitions took place between neuronal excitatory and inhibitory firings, and neuron-astrocyte uptakes and releases of neurotransmitters. These competitions in turn yielded a rich dynamic repertoire with different timescales at play.

3.4.2 Network extension for the neuronal compartment

Following common practices (Breakspear, 2017), we assumed excitatory neuronal interconnections between pyramidal cell populations exclusively (*Equation* (2.6)), and we used empirical diffusion magnetic resonance imaging (MRI) data to reconstruct white-matter tracts (see also "Defining structural layers" in Methods) and define the neuronal structural constraints (i.e., parameter matrix Ω_{Pyr}). The network interaction terms were specified as a linear combination of incoming firing rates (Q_{Pyr}) where weights were coded in Ω_{Pyr}, and a global coupling parameter ω_{Pyr} controlled the relative contributions of Ω_{Pyr} to nodal dynamics.

3.4.3 Network extension for the astrocytic compartment

Because experimental data for whole-brain modelling are lacking to date, we formulated a preliminary astrocytic network coupling model (see also the last paragraphs of Section 2.2 in Chapter 2). Concerning the astrocytic structural constraints (i.e., parameter matrix Ω_{Ast}), we extrapolated the notion of a gap-junction-coupled syncytial organization for astrocytes (Fields et al., 2015; Goldberg et al., 2010; Vasile et al., 2017). We did so by modelling Ω_{Ast} as a lattice-like network encoding physical proximity, where an astrocytic population within a region only connected to other astrocytic populations within the regions of its first neighbourhood along the cortical mantle, with weights given by geodesic distance reciprocals between region mass centers. Concerning astrocytic network feedback, we extrapolated the notions of glutamate neurotransmission mediating intercommunication flows between astrocytes, and excitatory gliotransmission acting on pre-terminal neuronal receptors. We did so by specifying linear interaction terms expressing astrocytic network modulations of nodal neuronal glutamate ($Q_{\mathrm{Glu}}^{\mathrm{Ast}}$) and GABA ($Q_{\mathrm{GABA}}^{\mathrm{Ast}}$) release rates where weights were distributed according to Ω_{Ast} (*Equations* (2.3), (2.4), and (2.7)), and where two global coupling parameters ω_{Glu} and ω_{GABA} controlled the relative contributions of Ω_{Ast} to nodal dynamics.

3.5 Results

3.5.1 Analyses overview

We were interested in quantifying astrocytic network contributions to neuron-astrocyte network activity and emerging functional connectivity patterns. Accordingly, we systematically varied two global parameters controlling the strength of relative contributions of astrocytic network activity to modulate glutamatergic (ω_{Glu}) and GABAergic (ω_{GABA}) neurotransmissions (Figure 3.1.c). When defining an exploration grid for $(\omega_{\mathrm{Glu}}; \omega_{\mathrm{GABA}})$, we adopted a criterion set so that empirically concrete model outputs such as $\mathrm{LFP} = E_{\mathrm{ExInUPyr}} - E_{\mathrm{InIn}}$, $\mathrm{Glu_e}$, and $\mathrm{GABA_e}$, would exhibit some key features (mostly qualitative) of real-world "normative" resting-state human data (see also "Constraining dynamical regimes" in Methods). Namely, we specified constraints so that LFP dynamics would depict waxing-and-waning oscillations with peak frequencies between eight and 13 hertz (i.e., a so-called electrophysiological α-band) while underlying amplitude and phase network synchronizations, and so that $\mathrm{Glu_e}$ and $\mathrm{GABA_e}$ would depict mean-quasi-stationary slow fluctuations. Ultimately, we defined 1225 unique pairs $(\omega_{\mathrm{Glu}}; \omega_{\mathrm{GABA}})$ and repeated ten times for each pair a network simulation of 120 seconds duration based on 216 nodes (see also "Simulation scheme" in Methods). We analyzed both neuron-astrocyte network activity and connectivity and developed a bifurcation-based computational approach to interpret results (Figure 3.1.d–e). To analyze activity (see also "Neuron-astrocyte network activity analysis" in Methods), we derived whole-brain quantities and spatial patterns of regional temporal standard deviations. To analyze connectivity (see also "Neuron-astrocyte functional network connectivity analysis" in Methods), we reconstructed a four-layered interconnected multiplex functional network from each simulated whole-brain activity (using the identity matrix as inter-layers and) such that each intra-layer encoded: α-band-limited phase-locking values (i.e., a similarity measure between instantaneous phases) or amplitude envelope Pearson-correlations of LFP dynamics (LFP-PLV or LFP-AEC), or Person-correlations of $\mathrm{Glu_e}$ or $\mathrm{GABA_e}$ dynamics ($\mathrm{Glu_e}$-C or $\mathrm{GABA_e}$-C).

3.5.2 Neuron-astrocyte network activity analysis

Figure 3.2.a maps whole-brain $\mathrm{Glu_e}$ or $\mathrm{GABA_e}$ levels against $(\omega_{\mathrm{Glu}}; \omega_{\mathrm{GABA}})$, showing that ω_{Glu} increases (independently of ω_{GABA}) were associated with $\mathrm{Glu_e}$ and $\mathrm{GABA_e}$ increases while ω_{GABA} increases (independently of ω_{Glu}) were associated with $\mathrm{Glu_e}$ decreases and $\mathrm{GABA_e}$ increases (see also Section 3.13.1 which further explains the links between the simulation parameters (ω_{Glu} and ω_{GABA}) and the empirically concrete state-variables ($\mathrm{Glu_e}$ and $\mathrm{GABA_e}$)). Of importance, these mappings revealed that each simulation defined by $(\omega_{\mathrm{Glu}}; \omega_{\mathrm{GABA}})$ could unambiguously be identified by $(\mathrm{Glu_e}; \mathrm{GABA_e})$, facilitating direct mappings of LFP features against $(\mathrm{Glu_e}; \mathrm{GABA_e})$ and thereby providing a pragmatical discourse of the relationships between membrane potential and neurotransmitter dynamics. Figure 3.2.b shows that LFP peak–peak amplitude and peak frequency variation patterns were mostly monotonic along either the $\mathrm{Glu_e}$-axis or $\mathrm{GABA_e}$-axis, with maximum (or minimum) peak–peak amplitude and minimum (or maximum) peak frequency when $\mathrm{Glu_e}$ and $\mathrm{GABA_e}$ were both maximum (or minimum), while exhibiting local extrema at intermediate $\mathrm{Glu_e}$ and $\mathrm{GABA_e}$ levels. A bifurcation analysis, as illustrated in Figure 3.2.c, revealed that the network model was approaching *spiking* regimes at high $\mathrm{Glu_e}$ and $\mathrm{GABA_e}$ values (thereby explaining the increasing peak–peak amplitude and decreasing peak frequency trends), while the local extrema distributions were explained by contours of limit cycle peak–peak amplitudes as well as a drastic change in network *homogeneity* due to stochastic motions (see also Sections 3.13.2 and 3.13.3; Section 3.13.2 further clarifies the links between features of membrane potential dynamics and bifurcation diagram; Section 3.13.3 further describes the links between

neurotransmission and amplitude modulations of bioelectrical neuronal activity). Ultimately, Figure 3.2 highlights dependencies between features of network activity and bifurcation diagram, and such dependencies were additionally captured by a clustering analysis of the simulation parameter plane based on a Gaussian mixture model with predictors given by regional temporal standard deviations (std) of LFP, $\mathrm{Glu_e}$, and $\mathrm{GABA_e}$. Figure 3.3.a shows four clusters (essentially spatially contiguous) primarily delineated by contours of limit cycle E_{InIn} peak–peak amplitudes, and Figure 3.4 illustrates the corresponding cluster means. For example, Figure 3.4 shows that (i) within all clusters, LFP-std patterns were different from $\mathrm{Glu_e}$-std or $\mathrm{GABA_e}$-std patterns, while $\mathrm{Glu_e}$-std and $\mathrm{GABA_e}$-std patterns were nearly identical, and whole-brain LFP-std values were higher than $\mathrm{Glu_e}$-std or $\mathrm{GABA_e}$-std values; (ii) within cluster #1, LFP-std values were minimum within precuneus regions and distributed roughly uniformly elsewhere, while $\mathrm{Glu_e}$-std and $\mathrm{GABA_e}$-std values were maximum within occipital lobe regions and distributed roughly uniformly elsewhere; (iii) across clusters #2–4, precuneus and superior parietal cortices were consistently distinguished from the rest of the brain, and notably from lateral occipital, middle frontal, or temporal cortices. In sum, Figure 3.3.a and Figure 3.4 demonstrate that the simulated whole-brain dynamics were spatiotemporally shaped diversely across the activity types (i.e., LFP, $\mathrm{Glu_e}$, or $\mathrm{GABA_e}$) and simulation parameter plane (see also Sections 3.13.4 and 3.13.5; Section 3.13.4 provides complementary results of the clustering analysis; Section 3.13.5 exposes the biophysics of spatial patterns of temporal standard deviations).

3.5.3 Neuron-astrocyte network connectivity analysis

Figure 3.5 maps four global topological properties of multilayer functional networks (i.e., clustering coefficient, path length, edge overlap, and code length) against $(\mathrm{Glu_e}; \mathrm{GABA_e})$, showing local extrema and otherwise monotonic trends consistent with contours of limit cycle E_{Pyr} peak–peak amplitudes (see also Section 3.14.1 for complementary global topological multilayer network properties). The dependencies between features of network connectivity and bifurcation diagram were further captured by a clustering analysis of the simulation parameter plane based on a Gaussian mixture model with predictors given by the global topological measures of clustering coefficient, path length, edge overlap, and code length. Figure 3.3.b shows four clusters (quasi-identical to the clusters of Figure 3.3.a, although delineated by contours of limit cycle E_{Pyr} peak–peak amplitudes) where cluster #2 mostly captured local extrema (see also Section 3.14.2 for complementary results of the clustering analysis), and Figure 3.6 illustrates one multilayer network in each cluster. For example, Figure 3.6 shows that (i) within all clusters, PLV-based layers featured connectivity patterns less pronounced than in correlation-based layers and vice-versa, such as short-range or frontal-cingulate-parietal-insula connections instead of long-range or parietal-occipital-temporal connections; (ii) within all clusters, $\mathrm{Glu_e}$-C and $\mathrm{GABA_e}$-C layers generally portrayed highly similar connection densities, slightly differing from LFP-AEC layers and greatly differing from LFP-PLV layers; (iii) across all clusters, connection densities, centralities, and communities differed. In sum, Figure 3.3.b and Figure 3.6 demonstrate that the simulated whole-brain dynamics supported diverse network topologies across the connectivity types (i.e., LFP-PLV, LFP-AEC, $\mathrm{Glu_e}$-C, or $\mathrm{GABA_e}$-C) and simulation parameter plane (see also Section 3.14.3 which further elucidates the links between phase-based and amplitude-based network connectivity patterns). To additionally highlight (connectivity) layer distinctiveness, a structural reducibility analysis was performed across all simulations, providing for each simulation an optimal multilayer network where the layers providing redundant topological information were merged. Such analysis resulted in no merging for about half of the simulations (48.1%) while for the remaining

simulations: all correlation-based layers were merged (31.7%), some (but not all) correlation-based layers were merged (17.5%), or PLV-based plus some (but not all) correlation-based layers were merged (2.7%). Importantly, investigating the set of *reduced* networks provided similar conclusions to the set of *full* networks (see also Sections 3.14.2 and 3.14.4 for complementary results of the structural reducibility analysis).

3.6 Discussion

Neuron-glial research over the past three decades has been revolutionary (De Pittà & Berry, 2019), to say the least. Collectively, it suggests that glia (e.g., microglia, oligodendrocytes, astrocytes) possess assorted structural and functional properties making them inseparable from their neighbouring neurons (De Pittà & Berry, 2019), and to go a step further, glia are pivotal modulators of brain physiology and pathology (Kugler et al., 2021), even superseding neurons as a health or disease focus in multiple scenarios (Liddelow & Sofroniew, 2019; Volman & Bazhenov, 2019). Nevertheless, despite extensive investigations, neuron-glial research has yet to flourish as the question of what the role of glia in health or disease conditions is, alongside neurons, still lingers today (Barres, 2008; De Pittà & Berry, 2019). Hereunto, many authors have communicated the dire need for computational frameworks to be able to address such a fundamental decades-old question (De Pittà & Berry, 2019; Kastanenka et al., 2020).

In this paper, we introduced a dynamical model of whole-brain activity where neuronal and astrocytic networks engage in a bidirectional dialogue, and we simulated a network scheme of gliotransmission. We determined that astrocytic networks, via gliotransmission, could not only induce diverse spatially structured neuronal dynamical states (characterized on LFP) coinciding with distinct spatially structured profiles of excitatory and inhibitory activities (probed by $\mathrm{Glu_e}$ and $\mathrm{GABA_e}$), but also induce various multilayer functional network topologies (reconstructed using PLV and Pearson-correlations) shaped by complex interactions between fast and slow dynamics. All in all, we determined that astrocytic networks biologically enrich the simulation and interpretation of whole-brain activity and connectivity patterns.

Regarding our investigation of whole-brain activity (see also Section 3.13 for an in-depth discussion), analyzing the links between $\mathrm{Glu_e}$, $\mathrm{GABA_e}$, and LFP patterns suggested that balanced excitatory and inhibitory neurotransmitter dynamics (being ruled by a competition between neuron-astrocyte uptake and release processes) were likely modulatory components of membrane potential dynamics (e.g., being reflected in their amplitude envelope fluctuations). Such findings deserve to be highlighted because it has long been appraised that multiple transmitters and modulators act in concert, synaptically and extra-synaptically, to shape the properties of neural circuits, with the ability to massively alter their output (Del Guerra et al., 2018; Diao et al., 2017; Kringelbach et al., 2020; Marder, 2012; Pacholko et al., 2020; Pierce et al., 2021; Shine, 2019; Shine et al., 2019). Thus, besides extending excitation-inhibition balance frameworks (Sohal & Rubenstein, 2019), our network modelling approach of neuron-glial interactions provides a novel computational way to investigate the biochemical basis of whole-brain dynamics at the neuroimaging data scale (Del Guerra et al., 2018; Diao et al., 2017; Kringelbach et al., 2020; Marder, 2012; Pacholko et al., 2020; Pierce et al., 2021; Shine, 2019; Shine et al., 2019). For example, our methodology could allow exploring the neuron-glial regulatory mechanisms of glutamatergic and GABAergic transmission systems underpinning the neuroimaged coupling between electrophysiological and hemodynamic rhythms (Betina Ip et al., 2017; Brookes et al., 2011; Logothetis et al., 2001).

As to our investigation of whole-brain connectivity (see also Section 3.14 for an in-depth discussion), analyzing the links between phase-based and amplitude-based network connectivity patterns suggested that they were sensitive to distinct and complementary spatiotemporal phenomena. Such findings call attention to frameworks able to comprehensively account for multiple connectivity channels, such as multilayer network modelling (De Domenico, 2017; Hallett et al., 2020; Tewarie et al., 2016, 2019), to appropriately characterize dynamical network systems. On this topic, it is noteworthy that although we employed multilayer network modelling mainly as an illustrative framework in this paper, our paper could easily be extended for a more rigorous characterization of complex brain networks as well as for a deeper understanding of emerging functional connectivity patterns (see also the last two paragraphs of Section 3.14.3 for a complementary discussion on multilayer functional network analyses). For example, our modelling approach permits us to motivate, formalize, and investigate the notion of *coupled multilayer functional networks under multilayer structural network constraints* (since our network model assumed that a two-layered structural network dictated whole-brain dynamics).

Along these lines, it is worth highlighting how the relative simplicity of our whole-brain model allowed us to employ bifurcation analyses to characterize dynamic features of network activity and connectivity that are driven by stochastic motions (see also (Forrester et al., 2020)). As we have shown, using bifurcation analysis better shapes our biophysical understanding of the interplay between compartments, dynamics, structural constraints, and emerging functional connectivity patterns. On that note, it was interesting to see the potential of clustering procedures to be particularly sensitive to bifurcation phenomena (see also Section 3.13.4 and 3.14.2), thereby providing a novel way to understand dynamical behaviours without necessarily employing stochastic bifurcation theory *per se*.

More generally, our emphasis is that glial cells must be an integral piece of biophysical models of whole-brain activity because of their intimate and active partnerships with neurons (De Pittà & Berry, 2019; Kastanenka et al., 2020). In such a neuron-glial perspective, our paper could be seen as a step forward to potentially elucidating decades-old unresolved (neuron-glial) questions through computational means whereby real-world experiments and computational modelling complement and guide each other (De Pittà & Berry, 2019; Kastanenka et al., 2020). For example, reliable experimental evidence that *neuron-glial assemblies* may be regarded as dynamic discrete brain systems governed by function-specific regimes, or a definitive experimental connection between glial signalling and higher brain functions, are both still missing and must be established (De Pittà & Berry, 2019; Kastanenka et al., 2020). In this case, it is useful to adopt a type of a (whole-brain) modelling approach (complementing empirical experiments) where the detailed neurophysiology of individual cells is not captured, but instead, collective neural activity is described in precise mathematical laws across different layers of abstractions from fully phenomenological to fully exact according to physics first principles (Breakspear, 2017). The underlying hypothesis of such modelling is that movement, cognition, and perception arise from the collective activity of neural cells within cortical circuits and across large-scale brain systems (Breakspear, 2017).

In practice, because we adopted a compartmental modelling approach, many existing neuronal models (e.g., see (Breakspear, 2017)), especially those based on population firing rates (e.g., see (Chehelcheraghi et al., 2016; Coombes & Byrne, 2016; Liley, 2015), could be upgraded with an astrocytic compartment without losing previously acquired knowledge. As a proof of concept, we designed our methodology by first showing that there were broad biophysical principles which,

when adopted, would allow qualitatively reproducing many features of real-world data (see also Chapter 2). Overall, this is an interesting modelling approach because it allows us to capture different facets of whole-brain activity conveniently and cohesively (since different neuronal (Breakspear, 2017; Chehelcheraghi et al., 2016; Coombes & Byrne, 2016; Griffiths et al., 2022; Liley, 2015) or glial (De Pittà, 2020; De Pittà & Berry, 2019; Manninen et al., 2019) compartments often intrinsically feature distinct and complementary biophysical processes). However, in such a compartmental modelling scheme, although different compartments could be swapped at will to capture precise phenomena or achieve a desired realism level, the bidirectional coupling between neuronal and astrocytic populations would always require a careful formulation. Besides, it is noteworthy that in studies mainly targeting neuroimaging data, it remains unclear how versatile or realistic models must be and what data are needed or sufficient to constrain these models (Breakspear, 2017; Hallett et al., 2020).

Indeed, the extent to which models of large-scale network dynamics are amenable to validation based on neuroimaging data primarily and critically depends on the state of empirical data analyses which is yet to flourish (Breakspear, 2017; Hallett et al., 2020). For example, because empirical methods allowing the simultaneous recordings of whole-brain or population neuronal and glial activity are lacking (Kastanenka et al., 2020), we must lean towards datasets (possibly unimodal) indirectly reflecting neuron-glial activity such as blood-oxygen-level-dependent functional MRI or non-invasive electrophysiological data (Breakspear, 2017). However, there are generic methodological challenges in making such empirical data comparable with model outputs because they require the specification of forward or inverse models (Breakspear, 2017; Palva et al., 2018; Sadaghiani et al., 2022; Sotero & Trujillo-Barreto, 2008; Valdes-Sosa et al., 2009). Besides, in our neuron-glial context, such mapping schemes to empirically constrain model outputs remain ambiguous until further research is carried out to reinterpret the acquired datasets using a perspective inclusive of glial cells (Figley & Stroman, 2011; Lu et al., 2019; Magistretti & Allaman, 2015). Within a glial context, it is also important to note the technical and analytical shortage in astrocytic population imaging (Kastanenka et al., 2020). Nevertheless, calcium dynamics being considered the primary candidate substrate for astrocytic-based computations in the brain (Kastanenka et al., 2020), it could potentially be used to partially constrain model outputs. In this regard, many proposed theoretical models (Manninen et al., 2019) could help either derive a phenomenological link or extend our model at the population level to include an explicit biophysical description of astrocytic calcium dynamics. Leaving aside the discussion of model outputs, the way astrocytic populations may structurally interconnect and the spatial heterogeneity of neuron-astrocyte populations across the whole brain remain to be (empirically) established as well (see also Section 3.12.4 for a complementary discussion on the structural layers of dynamical models of whole-brain activity). In this respect, moleculo-cellular atlases such as the BigBrain (Amunts et al., 2013) or Allen Human Brain Atlas (Arnatkevičiūtė et al., 2019) could be systematically exploited together with PET or MRI data (Figley & Stroman, 2011; Lu et al., 2019; Magistretti & Allaman, 2015), or invasive electrophysiological data (Frauscher, Von Ellenrieder, et al., 2018).

3.7 Conclusion

We extended a previously published neuron-astrocyte mass model (Garnier et al., 2016) by proposing biophysical ways in which astrocytic network dynamics could modulate neuronal network dynamics and vice-versa, and we illustrated that integrating astrocytes within a computational model of whole-brain dynamics biologically enriches whole-brain activity and

connectivity patterns. Our proposed framework expands widely. For example, our modelling perspective has the potential of generating novel hypotheses of glial contributions to observed neuroimaging signals in the aging or diseased brain, when decoupling between neuron-glial compartments occurs. We assume that during aging, large-scale brain networks exhibit signs of disrupted neuron-glial processes that render the aging brain vulnerable to many neurodegenerative disorders (Ahmed et al., 2016; Hallett et al., 2020; Mattson & Arumugam, 2018). Hence, we could envision different biologically inspired scenarios of impaired neuron-glial network interactions and assess the degree to which glial signalling may render ambiguous the detections and interpretations of neuronal activity and processes. For another example, our modelling perspective could be key in better re-examining structure-function-metabolism couplings (Giaume et al., 2010; Magistretti & Allaman, 2015; Scimemi, 2019; Suárez et al., 2020) where we put forth a neuron-glia-vascular network perspective which entails adding vascular compartments (Blanchard et al., 2016) and a third structural layer to represent vascular pathways (M. Bernier et al., 2018). We assume that observed functional activity and connectivity patterns are the results of neural signalling that not only dynamically evolves on a relatively fixed multilayer (i.e., multi-cellular) structural network topology, but is also spatiotemporally shaped by a metabolic landscape. We envision that our perspective would help to explain the seemingly unresolvable imperfect matching between structural and functional connectivity (Suárez et al., 2020), as well as to reconcile many undertaken studies over the past decades which have mostly focused on neuronal (white-matter) pathways or vascular pathways in isolation (Schmahmann et al., 2008; Sweeney et al., 2018).

3.8 Methods

3.8.1 Constraining dynamical regimes

When defining an exploration grid for $(\omega_{\mathrm{Glu}}; \omega_{\mathrm{GABA}})$, we adopted a set of criteria so that empirically concrete model outputs such as local field potential ($\mathrm{LFP} = E_{\mathrm{ExIn}\cup\mathrm{Pyr}} - E_{\mathrm{InIn}}$), $\mathrm{Glu_e}$, and $\mathrm{GABA_e}$ would exhibit some key features (mostly qualitative) of real-world "normative" resting-state human data. Briefly, the criteria ensured that (i) LFP dynamics would resemble α-band electrophysiological recordings (i.e., [8; 13] Hz) (Sadaghiani et al., 2022) underlying amplitude and phase network synchronizations, while (ii), neurotransmitter uptake and release rates would balance each other in a way that $\mathrm{Glu_e}$ and $\mathrm{GABA_e}$ dynamics could be portrayed as mean-quasi-stationary slow fluctuations. In more detail, our parametrization strategy critically exploited two ingredients: on the one hand, consensual physiologically plausible parameter sets from the literature (see also Table 2.3 in Chapter 2), and on the other hand, a former bifurcation analyses of the neuron-astrocyte mass model (Garnier et al., 2016) (see also Sections 2.3.1 and 2.3.2 in Chapter 2). These ingredients allowed us to (i) identify concentration intervals for $\mathrm{Glu_e}$ (i.e., [5; 15] µmol) and $\mathrm{GABA_e}$ (i.e., [5; 35] µmol) where the neuronal compartment would be particularly sensitive to their modulatory impacts (see also Sections 2.3.3 and 2.3.4 in Chapter 2); (ii) restrict the neuronal compartment to solely explore self-sustaining stable oscillatory regimes with fundamental frequencies within [8; 13] Hz and with moderate peak–peak amplitudes (see also Sections 2.3.3 and 2.3.5 in Chapter 2); (iii) specify an initial stable dynamical state (i.e., a stable initial state in the vicinity of a branch of supercritical Hopf bifurcation points) where the network model would exhibit *baseline* noise-modulated oscillatory activity (see also Section 2.3.5 in Chapter 2); (iv) determine a value for ω_{Pyr} (i.e., $\omega_{\mathrm{Pyr}} = 7.5$) that would guarantee the occurrence of amplitude and phase network synchronizations (see also Section 2.3.5 in Chapter 2); and (v) define pairs of values for $(\omega_{\mathrm{Glu}}; \omega_{\mathrm{GABA}})$ (i.e., $\omega_{\mathrm{Glu}} \in [2.90; 6.47]\ \mu\mathrm{mol}^{-1}$ and $\omega_{\mathrm{GABA}} \in [0.14; 1.94]\ \mu\mathrm{mol}^{-1}$) so that variations in $\mathrm{Glu_e}$ and $\mathrm{GABA_e}$ would remain in their pre-specified

bounds (see also Section 2.3.6 in Chapter 2 as well as Section 3.10). Altogether, these constraints are what allowed the network model to visit, with respect to $(\omega_{\mathrm{Glu}}; \omega_{\mathrm{GABA}})$, a variety of neuronal dynamical states characterized by stable limit cycles with different peak–peak amplitudes and frequencies, as well as distinct profiles of excitatory and inhibitory activities, and a variety of functional network architectures. It is noteworthy that these choices regarding the LFP frequency band, the concentration bounds for $\mathrm{Glu_e}$ and $\mathrm{GABA_e}$, and the initial state, were all easily generalizable but at the expense of the physiological plausibility of the neuronal compartment parameters (see also Section 2.3.7 in Chapter 2).

3.8.2 Defining structural layers

Empirical magnetic resonance imaging (MRI) data were used to define the two structural connectivity matrices of our model, i.e., Ω_{Pyr} interconnecting neuronal populations and Ω_{Ast} interconnecting astrocytic populations. For both matrices, the (anatomical) Lausanne-2018 surface-based atlas (Tourbier et al., 2022) scale three with 216 cortical parcels was used to constrain the connectivity estimates (see also Section 3.11).

To define Ω_{Pyr} (see also Section 3.12.1), we run a state-of-the-art tractography-based connectome reconstruction pipeline on the minimally preprocessed diffusion and structural MRI data of ten subjects of the Human Connectome Project Young Adult dataset (Glasser et al., 2013; Van Essen et al., 2013). The pipeline was designed to address specifically the streamline-termination and streamline-quantification biases of tractography (C. H. Yeh et al., 2021) by building upon (i) Tractoflow (Theaud et al., 2020), which is an efficient diffusion MRI processing pipeline, (ii) Surface-Enhanced Tractography (St-Onge et al., 2018), which is a surface-based tractography strategy recently proposed to address streamline termination biases, and (iii), a variant of convex optimization modelling for microstructure informed tractography, i.e., COMMIT-2 (Schiavi et al., 2020), which is a quantitative tractogram-filtering and streamline-weighting procedure based on microstructural and anatomical constraints. The pipeline was run on each subject separately, providing quantitative connectomes whereby a weight depicted an anatomo-microstructural-reflecting measure of connectivity strength. Ω_{Pyr} was computed as the mean of the connectomes taken across subjects (see also Section 3.12.3).

To define Ω_{Ast} (see also Section 3.12.2), we used a high-resolution tessellation of the mid-surface (i.e., the mid-point between the white and pial surfaces) of the ICBM-2009c-asymmetric template (Fonov et al., 2011), reconstructed thanks to FreeSurfer (Fischl, 2012). A weight between any two adjacent parcels was calculated as the inverse of the geodesic distance between parcel mass centers. Thus, Ω_{Ast} described a lattice-like network depicting the geometrical embedding of the brain, where a node connected only to its first neighbourhood along the cortical mantle, and where an edge coded physical proximity (see also Section 3.12.3). We acknowledge that using geodesic distances amounts to a coarse approximation of the paths of astrocytic interactions (through gap junctional densities). However, it provides us with a global neuron-astrocyte structure (informed by the geometry of the brain) underlying dynamics that can be heuristically understood with the analyses of the nodal model.

Before the simulations, Ω_{Pyr} and Ω_{Ast} had their diagonal set to zero and they were normalized such that coefficients sum to one on each row (i.e., they each were made right stochastic). Doing so ensured that any network node would receive network inputs with commensurate magnitudes.

3.8.3 Simulation scheme

The simulation parameter plane defined by $(\omega_{\mathrm{Glu}}; \omega_{\mathrm{GABA}})$ was sampled non-uniformly to account for the non-linear dependence between glutamate and GABA dynamics so that whole-brain $\mathrm{Glu_e}$ and $\mathrm{GABA_e}$ levels would remain within [5; 15] µmol and [5; 35] µmol, respectively. In total, 1225 unique pairs $(\omega_{\mathrm{Glu}}; \omega_{\mathrm{GABA}})$ were specified, and they conveniently allowed the uniform sampling of a grid defined by whole-brain $(\mathrm{Glu_e}; \mathrm{GABA_e})$ or $(v_{\mathrm{Glu}}; v_{\mathrm{GABA}})$ levels (see also Section 3.10).

The equations governing the time evolution of our network model formed a system of coupled stochastic differential equations. This system was numerically integrated using an in-house *MATLAB* (version R2022a (MATLAB, 2022)) implementation of a stochastic Heun's integration scheme.

Simulations of 120 seconds were performed ten times for each pair $(\omega_{\mathrm{Glu}}; \omega_{\mathrm{GABA}})$, thereby providing ten simulation batches, and each time, the initial states together with the neuronal stochastic inputs (i.e., $q_{[.]}$) were different. To minimize biases due to transients, the following procedure was adopted. First, before any of the ten simulation batches, a single (i.e., calibrated) simulation of 370 seconds was run for each pair $(\omega_{\mathrm{Glu}}; \omega_{\mathrm{GABA}})$. Then, each calibrated simulation was visually checked to ensure that steady states were reached in the last ten seconds. Finally, for each pair $(\omega_{\mathrm{Glu}}; \omega_{\mathrm{GABA}})$, the last ten seconds of the corresponding calibrated simulation were used to define (random) initial states for all subsequent ten simulation batches. In the end, 10×1225 simulations in total, of two minutes each, were retained for analyses (see also Section 3.10).

3.8.4 Neuron-astrocyte network activity analysis

For each pair $(\omega_{\mathrm{Glu}}; \omega_{\mathrm{GABA}})$ in any of the ten simulation batches, whole-brain values were derived as follows. (i) A whole-brain value of LFP peak–peak amplitude was defined as the mean of regional values, while (ii) a whole-brain value of LFP peak frequency was determined from the mean of regional Welch's power spectral density estimates, and (iii) a whole-brain value of $\mathrm{Glu_e}$ or $\mathrm{GABA_e}$ (as well as v_{Glu} or v_{GABA}) was computed as the mean of regional temporal means. These whole-brain quantities were analyzed specifically because they naturally portrayed our hypothesis that our network model could visit, with respect to $(\omega_{\mathrm{Glu}}; \omega_{\mathrm{GABA}})$, a variety of neuronal dynamical states characterized by stable limit cycles with different peak–peak amplitudes and frequencies, as well as distinct profiles of excitatory and inhibitory activities (see also Section 2.4 in Chapter 2).

Graphing any of the whole-brain values against $(\omega_{\mathrm{Glu}}; \omega_{\mathrm{GABA}})$ or $(\mathrm{Glu_e}; \mathrm{GABA_e})$ was done by first performing a scattered two-dimensional natural neighbour interpolation based on Delaunay triangulations (*MATLAB*'s *scatteredInterpolant* function) for each simulation batch, and then taking the mean of the interpolated graphs across simulation batches. Since whole-brain values of $(\mathrm{Glu_e}; \mathrm{GABA_e})$ were largely unchanged across simulation batches, the mean of interpolated graphs was found to be quasi-identical to the individual graphs.

Hard clustering analyses were performed with a Gaussian mixture model (*MATLAB*'s *fitgmdist* function). Data variables consisted of the regional temporal standard deviations of LFP, $\mathrm{Glu_e}$ and $\mathrm{GABA_e}$ dynamics (i.e., 216×3 predictors) while data observations consisted of the different simulations (i.e., 10×1225 observations). Spatial profiles of temporal standard deviations were scaled between zero and one independently for LFP, $\mathrm{Glu_e}$ and $\mathrm{GABA_e}$, and independently for each simulation (see also Section 3.13.4). The Gaussian mixture model was used to explicitly account for the natural spatial covariance in the data across simulations and the ensuing heterogeneity in cluster shapes and sizes. Accordingly, when fitting the model, we specified a full covariance

structure shared amongst all Gaussian components and performed independent fits for four, five, or six components (see also Section 3.13.4). To fit the different models (i.e., one model for each *a priori* number of components) and ensure cluster stability, we employed a heuristic based on *k*-means clustering to initialize ten independent instances of an expectation-maximization algorithm and we took the model with the largest loglikelihood across the ten replicates. In the end, we chose the (stable) fitted model between four, five, or six components that best balances low values of Akaike information criteria with simplicity.

Graphing the estimated clusters against $(\mathrm{Glu_e}; \mathrm{GABA_e})$ was done as follows. We first graphed the posterior probabilities of each Gaussian mixture component for each simulation batch, and then took the mean of interpolated (probability) graphs across simulation batches, before assigning the observations to (hard) clusters based on the highest posterior probabilities. We verified that the mean interpolated graph was similar to each individual graph.

3.8.5 Neuron-astrocyte functional network connectivity analysis

To analyze connectivity, the multilayer network modelling approach was adopted as it specifically deals with systems whose functional units couple through distinct interaction channel types. For each pair $(\omega_{\mathrm{Glu}}; \omega_{\mathrm{GABA}})$ in any of the ten simulation batches, a four-layered interconnected multiplex functional network was reconstructed. With the interconnected multiplex network topology, the same brain region is replicated along the different layers where it exhibits (different) layer-dependent connectivity patterns. The identity was chosen to define inter-layer connectivity for the sake of simplicity, and each intra-layer encoded: α-band-limited phase-locking values (Palva et al., 2018) (PLV) of LFP dynamics (LFP-PLV), α-band-limited amplitude envelope Pearson-correlations (Palva et al., 2018) (AEC) of LFP dynamics (LFP-AEC), Person-correlations of $\mathrm{Glu_e}$ dynamics ($\mathrm{Glu_e}$-C), or Pearson-correlations of $\mathrm{GABA_e}$ dynamics ($\mathrm{GABA_e}$-C). PLV is formally defined as the temporal mean of the differences in instantaneous phases and ranges 0–1: it equals one when phase differences are constant over time, and zero when phase differences are uniformly distributed. Instantaneous phases and amplitude envelopes of LFP dynamics were obtained using a Hilbert transform. Amplitude envelopes of LFP dynamics together with $\mathrm{Glu_e}$ and $\mathrm{GABA_e}$ dynamics were low-pass-filtered with a 0.5 Hz cut-off frequency. All Pearson-correlations were analyzed in absolute values for convenience, and we determined that replacing Pearson-correlations with Spearman-correlations provided similar results and conclusions. Our choices of connectivity indices (i.e., the bivariate statistical association measures encoding each intra-layer connectivity) echoed typical real-world data analyses (Palva et al., 2018; Sadaghiani et al., 2022), and they were motivated by the fact that our network model was parameterized such that LFP dynamics would underlie amplitude and phase network synchronizations (see also Section 2.3.5 in Chapter 2), while $\mathrm{Glu_e}$ and $\mathrm{GABA_e}$ would evolve on time scales different from LFP, and the fluctuations of LFP amplitude envelope would be mostly explained by the slow fluctuations of $\mathrm{Glu_e}$ and $\mathrm{GABA_e}$ (see also Sections 3.13.2–3.13.5).

For the sake of concise visualizations, given a pair $(\omega_{\mathrm{Glu}}; \omega_{\mathrm{GABA}})$, a representative *mean* multilayer network across the ten simulation batches was derived, where the mean was used for the PLV layer, and the back-transformed correlation of the mean of Fisher's z-transformed coefficients was used for the correlation layers (Corey et al., 1998). However, analyses were systematically done on both the raw (i.e., 10×1225 networks) and mean (i.e., 1225 networks) multilayer networks (e.g., see Section 3.14.2). Before any multilayer network analysis, each

functional layer was individually thresholded based on its density by retaining 25 percent of the strongest weights.

To gain insight into the emerging functional connectivity patterns, different (nodal, global, and mesoscale) topological properties of the (weighted) reconstructed multilayer functional networks were quantified. The nodal centrality of each multilayer network was characterized by estimating its eigenvector versatility (De Domenico et al., 2015) (i.e., a generalization of eigenvector centrality), while the global segregation, integration, and edge redundancy levels of each multilayer network was characterized by estimating its global clustering coefficient, path length, and edge overlap, respectively (De Domenico et al., 2014; De Domenico, Nicosia, et al., 2015). The mesoscale architecture of each multilayer network was characterized by detecting its multilayer communities using map-equation (De Domenico et al., 2015). In short, the map-equation takes advantage of the duality in information theory between finding regularities in data (i.e., finding groups of nodes) and compressing the data (i.e., minimizing the description length of a random walker's movements within and between layers) (De Domenico et al., 2015); proposing that, with respect to the walker dynamics on the multilayer network, multilayer communities are groups of nodes where flows within and between layers remain optimally trapped for a relatively long time (De Domenico et al., 2015).

Hard clustering analyses were performed with a Gaussian mixture model almost exactly as described earlier for network activity analysis except that the data variables consisted of clustering coefficient, path length, edge overlap, and code length (i.e., four predictors; z-scored independently) and a full covariance structure unshared amongst all Gaussian components was specified (see also Section 3.14.2).

Structural reducibility analysis (i.e., the optimal aggregation of some network layers according to their similarity relative to their complete aggregation, as described in (De Domenico, Nicosia, et al., 2015)) was performed on each multilayer network using the quantum Jensen-Shannon divergence to quantify similarities and the (arithmetic) mean to aggregate layers, and the topological properties of the resulting *reduced* networks were quantified exactly as for the *full* networks (see also Sections 3.14.2 and 3.14.4). Such analysis was done to account for the redundant, irrelevant, or uninformative network interactions that are inherent to our multilayer functional network reconstruction scheme (De Domenico, Nicosia, et al., 2015).

Graphing global topological properties or clusters against $(\mathrm{Glu_e}; \mathrm{GABA_e})$ was done exactly as described earlier for network activity analysis.

3.8.6 Illustrations

Throughout this paper, we used the *Scientific colour maps* package (Crameri et al., 2020) to prevent visual distortion of the data and exclusion of readers with colour-vision deficiencies. Brain maps and outlines were all based on the ICBM-2009c-asymmetric template (Fonov et al., 2011).

3.9 Figures

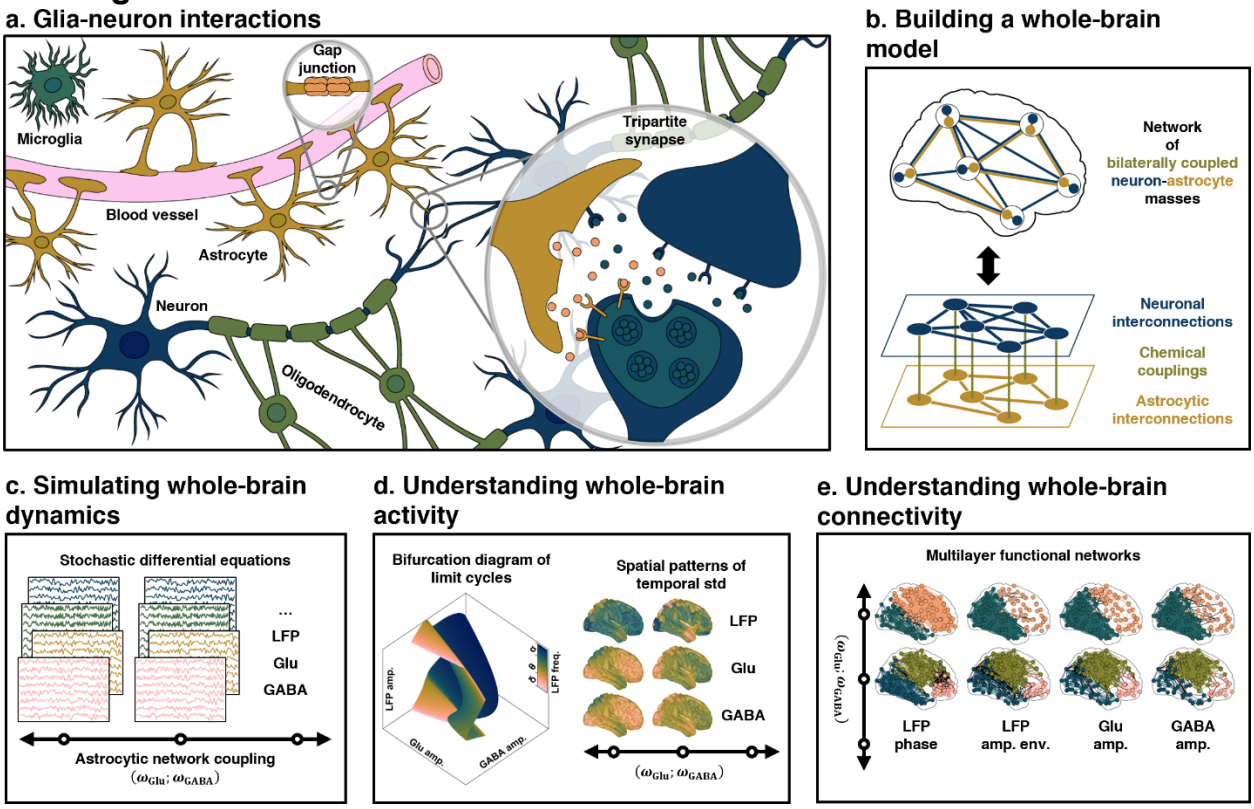

Figure 3.1. Analysis overview. (a) Astrocytes contact and ensheath synapses and blood vessels, they also provide a tiled arrangement of brain space where each tile is a mini-circuit, and they form a gap-junction-coupled syncytium supporting cell-cell (i.e., network) communication. Different types of other glia (i.e., not just astrocytes) interact with neurons and the surrounding blood vessels (altogether forming a neuron-glia-vascular unit). For example, oligodendrocytes wrap myelin around axons to speed up neuronal transmission, and microglia keep the brain under surveillance for damage or infection. (b) We introduce a biophysical model of whole-brain activity where large-scale astrocytic and neuronal networks couple their activity through glutamatergic and GABAergic transmission systems, and where neural dynamics are constrained by a two-layered structural network interconnecting either astrocytic or neuronal populations. (c) As a simulation strategy, we systematically varied two global parameters controlling the strength of relative contributions of astrocytic network activity to modulate glutamatergic (ω_{Glu}) and GABAergic (ω_{GABA}) neurotransmissions; 1225 unique pairs ($\omega_{\mathrm{Glu}}; \omega_{\mathrm{GABA}}$) were defined based on physiologically plausible criteria, and the stochastic simulations, each of 120 seconds duration and based on 216 nodes, were repeated ten times for each pair ($\omega_{\mathrm{Glu}}; \omega_{\mathrm{GABA}}$). (d) To analyze activity, we derived whole-brain quantities and spatial patterns of regional temporal standard deviations (std). Bifurcation analyses provided key biophysical insights into our findings. (e) To analyze connectivity, we reconstructed four-layered interconnected multiplex functional networks such that each layer encoded: α-band-limited phase-locking values or amplitude envelope Pearson-correlations of LFP dynamics, or Person-correlations of $\mathrm{Glu}_{\mathrm{e}}$ or $\mathrm{GABA}_{\mathrm{e}}$ dynamics. Our multilayer network analyses included quantifying clustering coefficient, path length, edge overlap, eigenvector versatility, community organization, and structural reducibility.

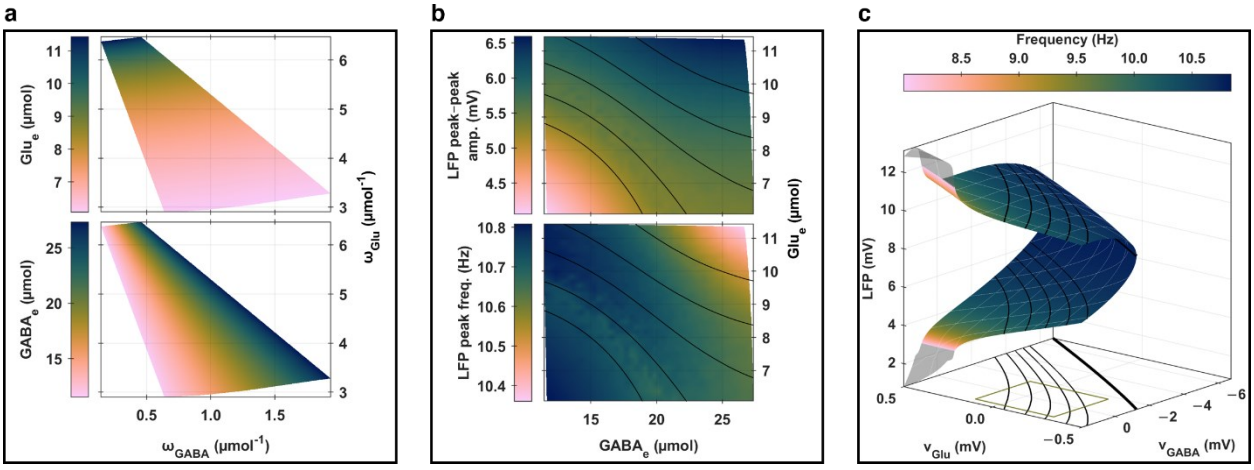

Figure 3.2. Global analysis of whole-brain neuron-astrocyte activity. (a) Links between simulation parameters and empirically concrete state-variables. The heatmaps show changes in whole-brain levels of $\mathrm{Glu_e}$ (top tile) or $\mathrm{GABA_e}$ (bottom tile) as functions of ω_{Glu} (y-axis) and ω_{GABA} (x-axis). (b) Links between membrane potential and neurotransmitter dynamics. The heatmaps show whole-brain levels of LFP peak–peak amplitudes (top tile) or peak frequencies (bottom tile) as functions of whole-brain levels of $\mathrm{Glu_e}$ (y-axis) and $\mathrm{GABA_e}$ (x-axis). The black solid curves represent contours of limit cycle LFP peak–peak amplitudes obtained through bifurcation analyses (see the panel (c)), and each contour passes through one of the following $(\mathrm{Glu_e}; \mathrm{GABA_e})$ coordinates in (µmol) × (µmol): (8; 15), (9; 15), (10; 15), (11; 15), or (11; 20). (c) Two-parameter bifurcation landscape of limit cycles drawn with LFP as state-variable, and v_{Glu} and v_{GABA} as bifurcation parameters (see also Section 3.13.2). The surface delimits the extrema of limit cycle amplitudes, and the colour bars indicate limit cycle frequencies. A portion of the surface is not coloured (i.e., is left semi-transparent), indicating frequencies lower than eight hertz, and the black solid curves represent contours of limit cycle peak–peak amplitudes. The same contours are graphed on a plane $(v_{\mathrm{Glu}}; v_{\mathrm{GABA}})$ under the surface, and each thickest black solid curve represents a locus of supercritical Hopf bifurcation points (i.e., a contour associated with the height equal to zero). As detailed in Methods, v_{Glu} and v_{GABA} are increasing monotonic (sigmoidal) functions of $\mathrm{Glu_e}$ and $\mathrm{GABA_e}$, respectively. The green rectangular outline under the surface shows the domain correspondence between $(v_{\mathrm{Glu}}; v_{\mathrm{GABA}})$ and $(\mathrm{Glu_e}; \mathrm{GABA_e})$ as drawn in (b), which further delineates the exploration grid that was defined for simulations (see also Section 3.10).

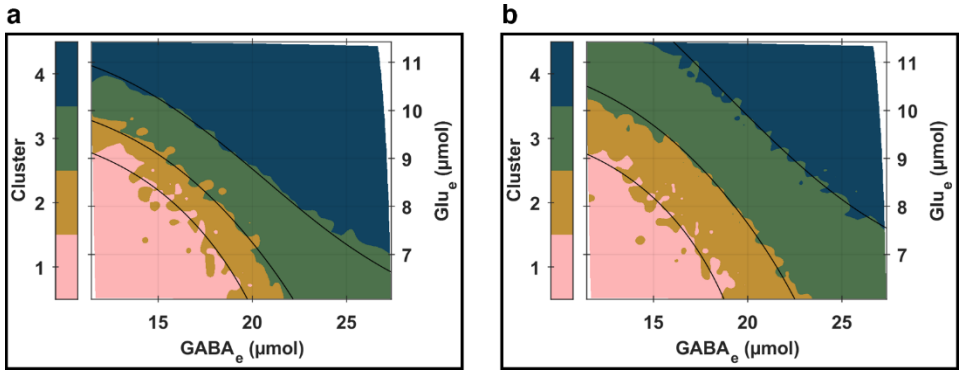

Figure 3.3. Clustering analysis of whole-brain neuron-astrocyte activity and connectivity. Clustering analysis results of (a) spatial patterns of temporal standard deviations of neuron-astrocyte network activity, and (b) global topological properties of reconstructed multilayer functional networks. In (a) and (b), each colour (i.e., cluster) represents a partition of the plane $(\mathrm{Glu_e}; \mathrm{GABA_e})$ which can be related (back) to the parameter plane $(\omega_{\mathrm{Glu}}; \omega_{\mathrm{GABA}})$ using a one-to-one mapping. The black solid curves in (a) represent contours of limit cycle E_{InIn} peak–peak amplitudes (see also Section 3.13.4), and each contour passes through one of the following $(\mathrm{Glu_e}; \mathrm{GABA_e})$ coordinates in (µmol) × (µmol): (8; 16), (8.8; 16.0), (10; 16), or (9.75; 25.00). The black solid curves in (b) represent contours of limit cycle E_{Pyr} peak–peak amplitudes (see also Section 3.14.2), and each contour passes through one of the following $(\mathrm{Glu_e}; \mathrm{GABA_e})$ coordinates in (µmol) × (µmol): (8.5; 14.0), (8.50; 18.25), or (9.5; 21.0).

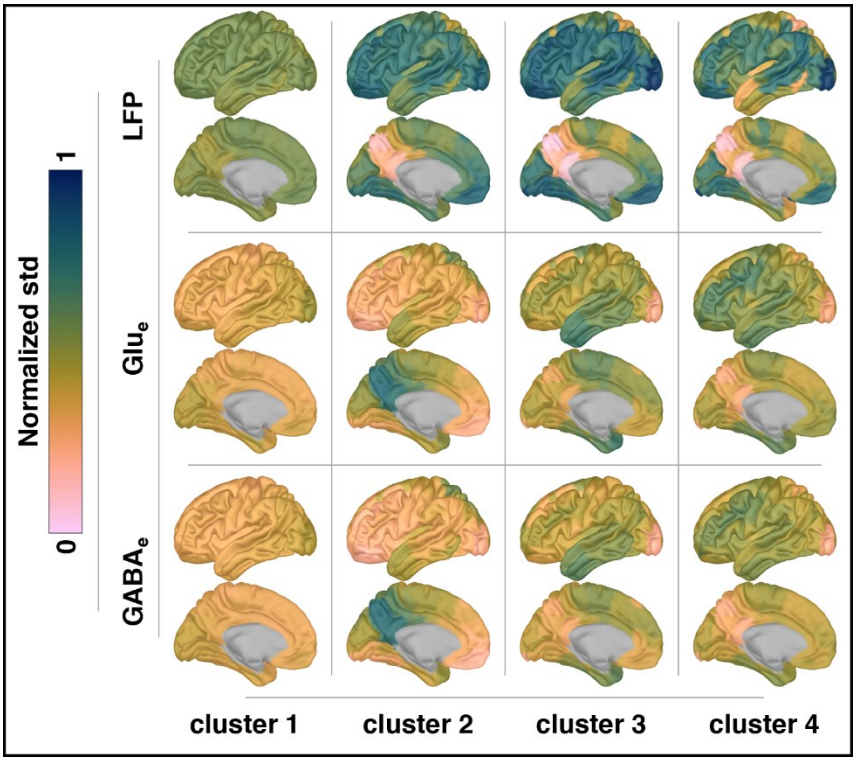

Figure 3.4. Means of Gaussian mixture model. Cluster means (as fitted by a Gaussian mixture model with four components) of LFP, Glu_e, and $GABA_e$ normalized spatial patterns of temporal standard deviations (std). This figure complements Figure 3.3.a. For clarity and simplicity, only left hemispheric patterns are displayed, noting that they are quasi-identical to right hemispheric ones (see Section 3.13.4 for full views).

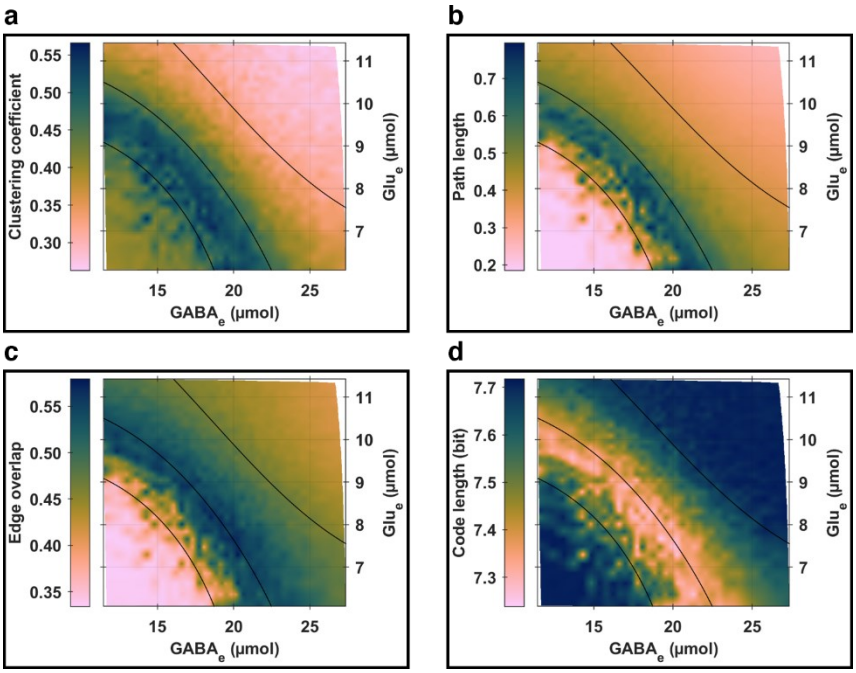

Figure 3.5. Global topological properties of reconstructed multilayer functional networks. Panel (a): clustering coefficient (an index of network segregation where higher values connote more segregated networks); panel (b): path length (an index of network integration where higher values connote more integrated networks); panel (c): edge overlap (an index of edge redundancy where higher values connote more similar weight patterns across layers); and

panel (d): code length (a quality index of community detection where lower values connote networks with more optimal data compression of a random walker's movements on them). The black solid curves in each graph represent the same contours of limit cycle E_{Pyr} peak–peak amplitudes shown in Figure 3.3.b. Complementary global topological properties are provided in Section 3.14.1.

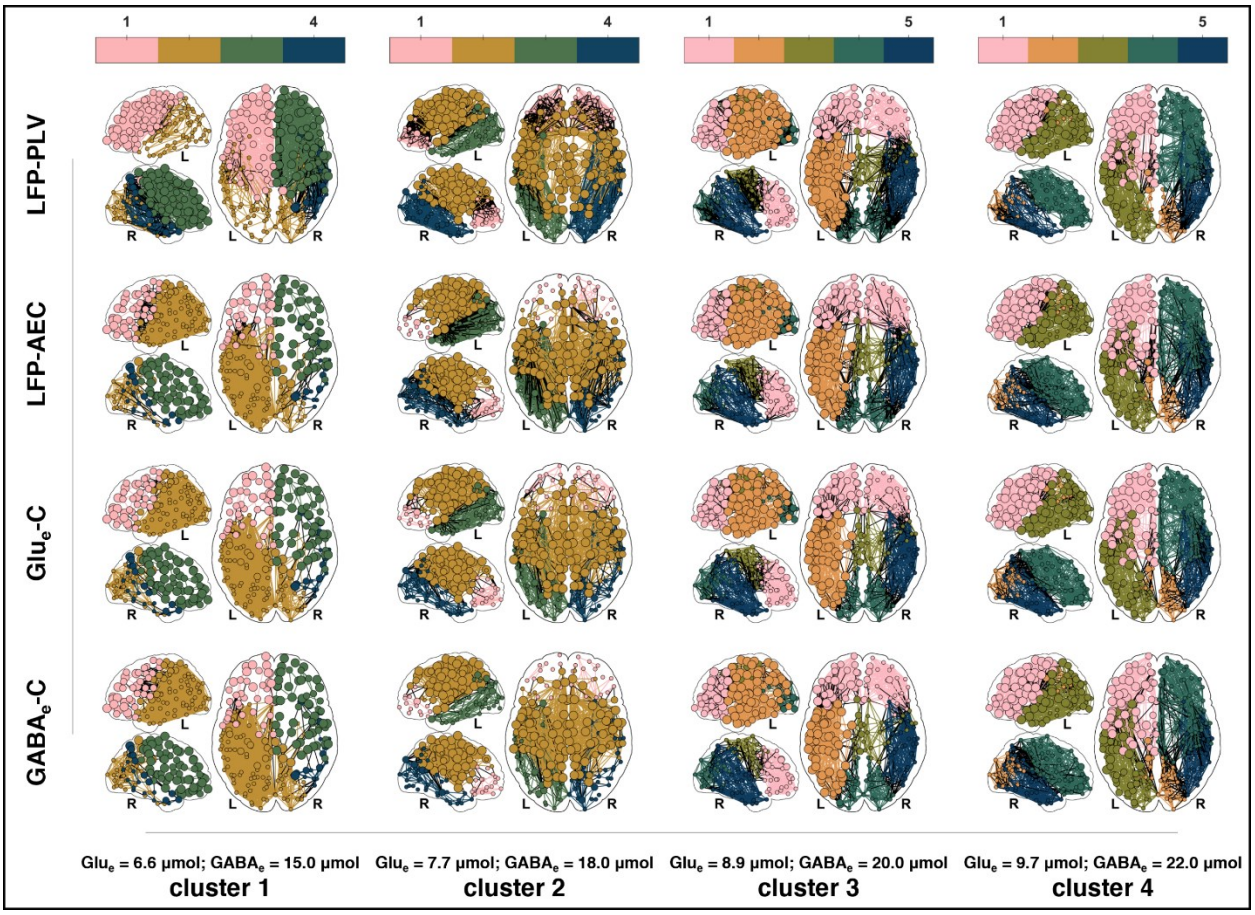

Figure 3.6. Mean multilayer functional networks for four simulations. Layers are indicated on the rows, and each simulation (and its cluster) can be identified on the columns by its whole-brain $(\mathrm{Glu}_e, \mathrm{GABA}_e)$ levels. A colour bar, on the top of each column (i.e., for each simulation), codes for detected multilayer communities. Nodes are coloured according to their community assignment. Within-community edges are colored according to their community colour while between-community edges are black. Communities across layers are most of the time but not always identical. Nodes are sized according to their eigenvector versatility for three ranges: $]0;1/3]$ (small), $]1/3\,;2/3]$ (medium), and $]2/3\,;1]$ (large). For the sake of clarity, only ten percent of the edges with the strongest weights in each layer are displayed, and edge weights are not coded (see Section 3.14.3 for full views of adjacency matrices). Additionally, only three brain views are displayed: lateral left, lateral right, and dorsal. The letters L and R below each brain indicate where the posterior left and right are located, respectively.

3.10 SI — Constraining dynamical regimes

Figure 3.7.a shows the simulation parameter plane as defined by 1225 unique pairs $(\omega_{\mathrm{Glu}}; \omega_{\mathrm{GABA}})$. Figure 3.7.b shows the uniform grid of the parameter plane defined by $(v_{\mathrm{Glu}}; v_{\mathrm{GABA}})$ with 35×35 values used for to derive the pairs $(\omega_{\mathrm{Glu}}; \omega_{\mathrm{GABA}})$. Figure 3.8.a shows, in the plane $(v_{\mathrm{Glu}}; v_{\mathrm{GABA}})$, whole-brain and regional mean states corresponding to the last ten seconds of calibrated simulations, while Figure 3.8.b shows, in the plane $(v_{\mathrm{Glu}}; v_{\mathrm{GABA}})$, whole-brain and regional mean states as calculated from ten simulation batches. As a reminder, a single (i.e., calibrated) simulation of 370 seconds was run for each pair $(\omega_{\mathrm{Glu}}; \omega_{\mathrm{GABA}})$ before performing any of the ten simulation batches on which were based the analyses exposed in the *Main Text*. Then, each calibrated simulation was visually checked to ensure that steady states were reached in the last ten seconds. Finally, for each pair $(\omega_{\mathrm{Glu}}; \omega_{\mathrm{GABA}})$, the last ten seconds of the corresponding calibrated simulation were used to define (random) initial states for all subsequent ten simulation batches.

The fact that the simulated network states in Figure 3.8.a or Figure 3.8.b are close to the calculated target states shown in Figure 3.7.b, except for high v_{Glu} and v_{GABA} values, highlights that the network model was appropriately well-constrained. Because the simulations of the ten batches were 120 seconds long, less variance between regional states were expected when comparing Figure 3.8.b to Figure 3.8.a.

Together, Figure 3.7 and Figure 3.8 also illustrate the global non-linear dependence between glutamate and GABA dynamics. In fact, the funnel-shaped parameter space defined by $(\omega_{\mathrm{Glu}}; \omega_{\mathrm{GABA}})$ in Figure 3.7.a is evidence of the highly non-linear impacts of ω_{Glu} on neuron-astrocyte activity compared to ω_{GABA}. This is understandable, given that not only do excitability thresholds of both pyramidal cells and inhibitory interneurons depend on glutamate levels, but astrocytic network feedbacks are also driven by glutamate levels.

It is also worth mentioning that although the area of low ω_{GABA} values was sampled more sparsely compared to the area of high ω_{GABA} values, there was no benefit in this study in attempting to perform more simulations including low ω_{GABA} values. An illustration of this fact is provided in Figure 3.8.b–c, showing for each simulation how the regional states spread around the whole-brain state (i.e., the orange circular dots spread around the green triangular dot). Such regional variabilities confirm the *heterogeneity* of the corresponding simulated networks which is induced by the structural layers and the stochastic components $q_{[\cdot]}$ (Figure 3.8.d better illustrates network *heterogeneity* for one simulation). In particular, the simulations corresponding to the lowest ω_{GABA} values (i.e., mapping to the area of low v_{Glu} values and low v_{GABA} values) depict the lowest regional variabilities (the dynamics of which being mostly dominated by stochastic noise). Furthermore, from Figure 3.8.a–c (together with Figure 2.5), we can observe that a line equidistant from the Hopf bifurcation locus is a good approximation of where interesting dynamical network states seem to start arising, i.e., where regional and whole-brain values start differing characteristically (akin to a network-level bifurcation phenomenon). As we further elaborate later in the next chapter, such drastic change in regional variability across the simulation parameter plane is explained by the interactions between the structural layers, the *heterogeneously* specified stochastic components $q_{[\cdot]}$, and the bifurcation diagram of limit cycles of the neuronal compartments, and its properties is such that the dynamical behaviour of an isolated node or a *homogeneously* parametrized network cannot trivially or fully explain them.

It is worth keeping in mind that although the mean states represented in Figure 3.8.a–c based on whole-brain values can map to the pairs $(\omega_{\mathrm{Glu}}; \omega_{\mathrm{GABA}})$ in a bijective way, there are in fact overlaps between states induced by the variance of the stochastic components $q_{[\cdot]}$ (as a reminder, $\mathrm{std}(q) = 10$ Hz). Besides, we understand from Figure 3.8.b and Figure 3.8.c that some interpolation artifacts can arise, especially nearby the area where simulations can have drastically different states. We also understand that it is unnecessary to simulate for v_{Glu} values higher than 0.15 (i.e., at a topologically large distance from the Hopf bifurcation locus) in our case because the resulting network dynamics and states become highly redundant with respect to the rest of the parameter plane.

Finally, given one simulation as illustrated in Figure 3.8.d, it is interesting to note the positive correlations across regions between v_{Glu}, v_{GABA}, and Q_{Pyr} and the negative correlation across regions between v_{Glu} and $p + Q_{\mathrm{Pyr}}$. These results, which conform to our simulation design exposed in Section 2.3.5 in Chapter 2, indicate that regions with higher mean $\mathrm{Glu_e}$ levels also have higher mean $\mathrm{GABA_e}$ and Q_{Pyr} levels and vice-versa, while $\mathrm{GABA_e}$ fluctuations almost exclusively dictate mean levels of total neuronal inputs (i.e., $p + Q_{\mathrm{Pyr}} = q - v_{\mathrm{GABA}}\, a/A + Q_{\mathrm{Pyr}}$) through a monotonic decreasing mapping.

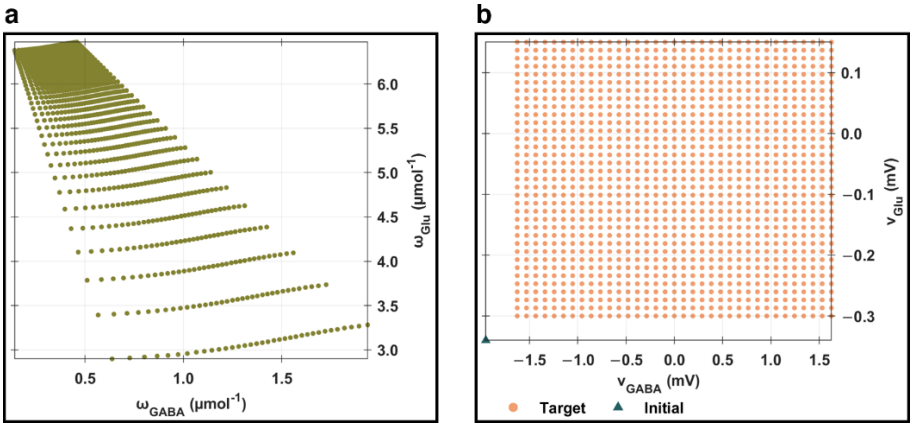

Figure 3.7. Simulation parameter planes. (a) Simulation parameter plane as defined by $(\omega_{\mathrm{Glu}}; \omega_{\mathrm{GABA}})$. (b) Parameter plane used to derive (a). The green triangular dot (on the bottom right corner) represents the initial state, which, as a reminder, was associated with ${\omega_{\mathrm{Glu}}}^{\mathrm{initial}} = {\omega_{\mathrm{GABA}}}^{\mathrm{initial}} = 10^{-2}$ µmol^{-1} (not drawn in (a)).

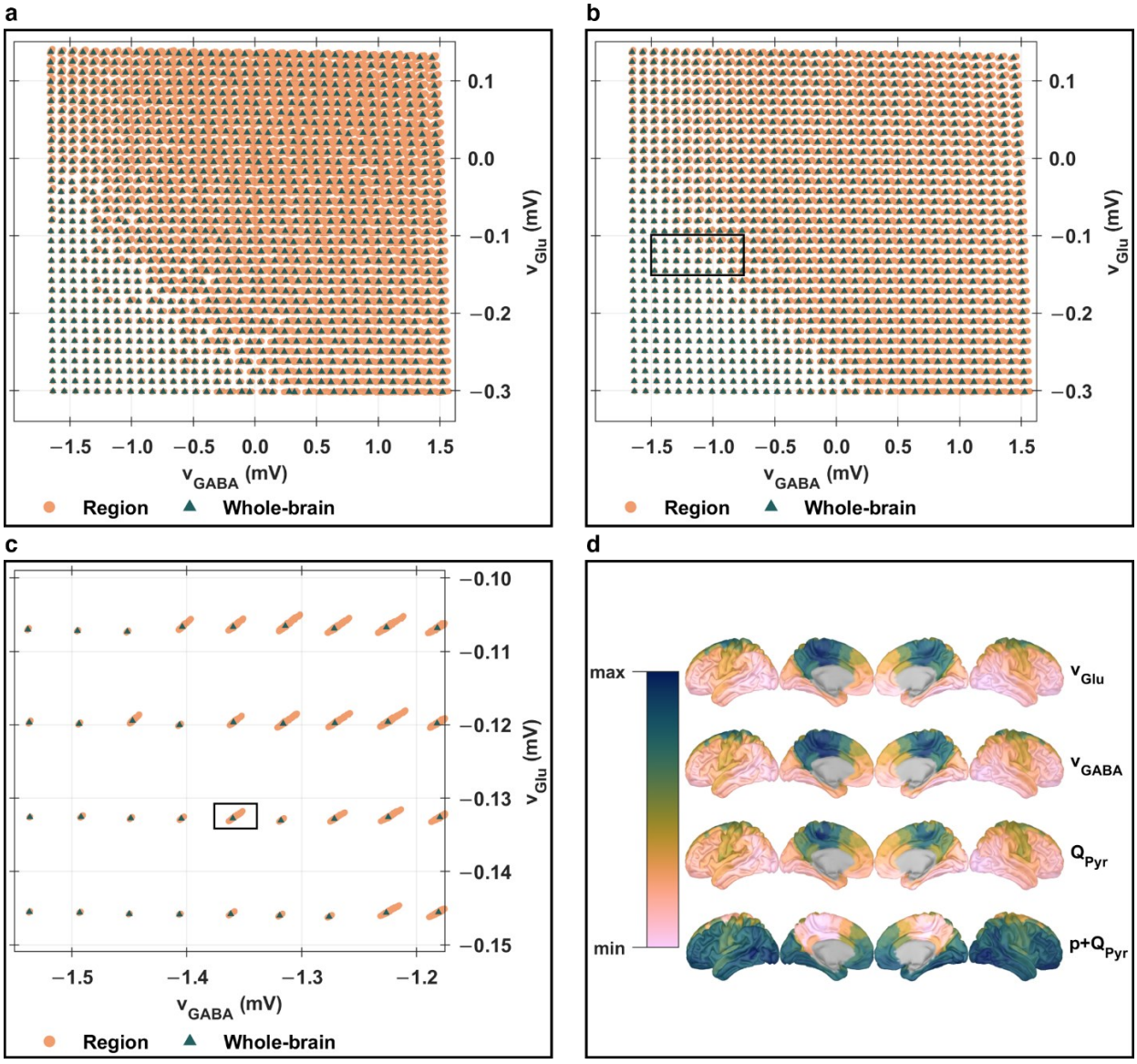

Figure 3.8. Simulated mean states. (a) Simulated mean states at the whole-brain and regional levels in the plane $(v_{\mathrm{Glu}}; v_{\mathrm{GABA}})$ as estimated from the calibrated simulations. The green dots represent whole-brain values (hence, there are 1225 green dots) while the orange dots represent regional values (hence, there are 216 orange dots for each green dot). (b) Same as (a) but simulated mean states at the whole-brain and regional levels were calculated from the ten simulation batches rather than the calibrated simulations. The rectangular black outline is represented in (c). (d) Simulated mean states at the regional level corresponding to the simulation outlined in (c). Details about the parcellation are provided in the next chapter.

3.11 SI — Parcellation

Figure 3.9 shows the parcellation we used, i.e., the (anatomical) Lausanne-2018 surface-based atlas (Tourbier et al., 2022) scale three (version 3.0.3; https://github.com/connectomicslab/connectomemapper3) with 216 cortical parcels. For convenience, parcels were uniquely assigned (irrespective of their hemispheric membership) to a lobe amongst frontal, cingulate, parietal, occipital, temporal, and insula. Table 3.1 is the tabular equivalent of Figure 3.9 and it shows how we ordered the parcels.

In the subsequent figures, parcels will be identified using the colour bar shown in Figure 3.9 with the following convention: when displayed horizontally (i.e., as in Figure 3.9), left hemispheric parcels will be on the left side while right hemispheric parcels will be on the right side; when displayed vertically, left hemispheric parcels will be on the top side while right hemispheric parcels will be on the bottom side.

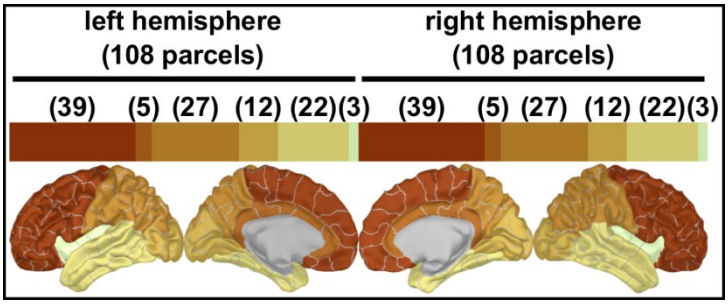

Figure 3.9. Lausanne-2018 atlas scale three. Each lobe can uniquely be identified using the colour bar (from dark red to yellow) and the numbers in parentheses indicate how many parcels are in each lobe for each hemisphere.

Table 3.1. Lausanne-2018 atlas scale three. Left hemispheric parcels are prefixed by "lh" and right hemispheric parcels are prefixed by "rh". Number ranges in brackets indicate that the corresponding parcels were ascendingly ordered.

Parcel	**Lobe**
lh.lateralorbitofrontal.[1–4]	frontal
lh.parsorbitalis.1	frontal
lh.frontalpole.1	frontal
lh.medialorbitofrontal.[1–3]	frontal
lh.parstriangularis.[1–2]	frontal
lh.parsopercularis.[1–2]	frontal
lh.rostralmiddlefrontal.[1–6]	frontal
lh.superiorfrontal.[1–8]	frontal
lh.caudalmiddlefrontal.[1–3]	frontal
lh.precentral.[1–6]	frontal
lh.paracentral.[1–3]	frontal
lh.rostralanteriorcingulate.1	cingulate
lh.caudalanteriorcingulate.1	cingulate
lh.posteriorcingulate.[1–2]	cingulate

Parcel	Lobe
lh.isthmuscingulate.1	cingulate
lh.postcentral.[1–5]	parietal
lh.supramarginal.[1–4]	parietal
lh.superiorparietal.[1–7]	parietal
lh.inferiorparietal.[1–6]	parietal
lh.precuneus.[1–5]	parietal
lh.cuneus.[1–2]	occipital
lh.pericalcarine.[1–2]	occipital
lh.lateraloccipital.[1–5]	occipital
lh.lingual.[1–3]	occipital
lh.fusiform.[1–4]	temporal
lh.parahippocampal.1	temporal
lh.entorhinal.1	temporal
lh.temporalpole.1	temporal
lh.inferiortemporal.[1–4]	temporal
lh.middletemporal.[1–4]	temporal
lh.bankssts.1	temporal
lh.superiortemporal.[1–5]	temporal
lh.transversetemporal.1	temporal
lh.insula.[1–3]	insula
rh.lateralorbitofrontal.[1–4]	frontal
rh.parsorbitalis.1	frontal
rh.frontalpole.1	frontal
rh.medialorbitofrontal.[1–3]	frontal
rh.parstriangularis.[1–2]	frontal
rh.parsopercularis.[1–2]	frontal
rh.rostralmiddlefrontal.[1–6]	frontal
rh.superiorfrontal.[1–8]	frontal
rh.caudalmiddlefrontal.[1–3]	frontal
rh.precentral.[1–6]	frontal
rh.paracentral.[1–3]	frontal
rh.rostralanteriorcingulate.1	cingulate
rh.caudalanteriorcingulate.1	cingulate
rh.posteriorcingulate.[1–2]	cingulate
rh.isthmuscingulate.1	cingulate
rh.postcentral.[1–5]	parietal

Parcel	Lobe
rh.supramarginal.[1–4]	parietal
rh.superiorparietal.[1–7]	parietal
rh.inferiorparietal.[1–6]	parietal
rh.precuneus.[1–5]	parietal
rh.cuneus.[1–2]	occipital
rh.pericalcarine.[1–2]	occipital
rh.lateraloccipital.[1–5]	occipital
rh.lingual.[1–3]	occipital
rh.fusiform.[1–4]	temporal
rh.parahippocampal.1	temporal
rh.entorhinal.1	temporal
rh.temporalpole.1	temporal
rh.inferiortemporal.[1–4]	temporal
rh.middletemporal.[1–4]	temporal
rh.bankssts.1	temporal
rh.superiortemporal.[1–5]	temporal
rh.transversetemporal.1	temporal
rh.insula.[1–3]	insula

3.12 SI — Structural layers

3.12.1 Neuronal connectome reconstruction pipeline

Diffusion and structural 3 T MRI data were obtained from the Human Connectome Project (Van Essen et al., 2013) for the following ten subjects: 101107, 105923, 108323, 111514, 116726, 140117, 146129, 156334, 158136, and 257845. Full acquisition protocol details are provided in (Van Essen et al., 2013). Briefly, diffusion data were acquired at a high spatial resolution of 1.25 mm isotropic thanks to a 2D spin-echo echo-planar imaging sequence. Diffusion-sensitization was applied with three *b*-values (1000, 2000 and 3000 s/mm^2) along 90 directions per *b*-shell, and 18 images with $b = 0$ s/mm^2 were acquired. T1-weighted images were obtained at 0.7 mm isotropic thanks to a 3D magnetization-prepared rapid gradient-echo sequence. We used the minimally processed (Glasser et al., 2013) diffusion-weighted images (DWI) where susceptibility-induced distortions, eddy currents, and subject motion were all corrected simultaneously using a non-parametric framework based on Gaussian processes. The structural data used were also the ones available in the minimally processed dataset (Glasser et al., 2013) including (but not limited to) FreeSurfer derivatives and T1-weighted images sampled at the same resolution as the diffusion data.

To obtain volumetric-based Lausanne-2018 parcellations (Tourbier et al., 2022) for each subject (see also Section 3.11), the FreeSurfer (Fischl, 2012) (version 6.0.0; https://github.com/freesurfer/freesurfer) *fsaverage* template was used as an intermediate to perform surface-to-surface (*mri_surf2surf*) then surface-to-volume (*mri_aparc2aseg*) mappings.

Our tractography-based connectome reconstruction pipeline was designed to specifically address the streamline termination and quantification biases of tractography (e.g., see (C. H. Yeh et al., 2021)). Its main steps included the following.

(i) First, we run Tractoflow (Theaud et al., 2020) (version 2.2.1; https://github.com/scilus/tractoflow) — a robust and efficient fully automatic diffusion MRI tractography pipeline — to estimate, for each subject, a set of brain maps including but not limited to fractional anisotropy, fibre orientation distribution function, and segmented T1 tissues. These maps were obtained by configuring Tractoflow with a minimum required number of steps listed hereafter and using default pipeline parameters (unless otherwise specified). The selected steps included: DWI brain extraction, DWI denoising, DWI N4 bias correction, DTI metrics based on the *b*-shells 0 and 1000 s/mm^2, fODF metrics based on the *b*-shells 1000, 2000, and 3000 s/mm^2 and with a fibre response function fixed manually in mm^2/s at $(15; 4; 4) \times 10^{-4}$, T1 brain extraction, T1 N4 bias correction, and T1 tissue segmentation for particle-filtered tractography.

(ii) Then, we fed the obtained Tractoflow maps to SET (St-Onge et al., 2018) (version 1.0; https://set-documentation.readthedocs.io/en/latest/) — a strategy recently proposed to address streamline termination biases based on particle filtering tractography — to yield a surface-based tractogram for each subject. SET operates by imposing geometrical flow constraints on reconstructed streamlines based on a model of surface flow trajectory for the white-grey matter boundary surface of the brain. By doing so, it can reconstruct tractograms benefiting from an improved cortical coverage where all streamlines intersect the white surface of the brain. The pipeline profile *freesurfer_basic* (i.e., FreeSurfer surfaces with brainstem and subcortical structures together) was chosen to constrain surface-based operations, warping from T1 to diffusion space was deactivated, and all other default optional pipeline parameters were retained. For the most essential parameters, one million streamlines were randomly seeded at a surface flow

of 100 iterations. Streamlines were probabilistically tracked, and they were excluded from the tractogram if their length was not within the 10–300 mm range.

(iii) Next, using the *scilpy* Python library (version 1.3.0; https://github.com/scilus/scilpy/), we decomposed the obtained tractograms on a parcel-to-parcel basis using the scale three of the Lausanne-2018 parcellation atlas (Tourbier et al., 2022) (*scil_decompose_connectivity.py*). The decomposition included a set of cleaning and filtering criteria based on streamline length, curvature, and winding angle (*scil_remove_invalid_streamlines.py*; *scil_detect_streamlines_loops.py*).

(iv) Thereafter, we run COMMIT-2 (Schiavi et al., 2020) (*scil_run_commit.py*) — a tractogram filtering procedure — to further filter the decomposed tractograms based on microstructural and anatomical constraints while assigning a quantitative weight to each streamline. COMMIT-2 attempts to recover the tractogram that best explains the observed diffusion MRI signal by formulating a linear forward model of tissue microstructure that embeds, through an optimization penalty, the anatomical prior that axons are organized in bundles. By tuning a global penalty coefficient (regularization constant), a solution is promoted where a minimum number of bundles explains the observed signal. This global penalization procedure is of interest as it provides a principled way to obtain biologically plausible tractograms with different levels of sparsity. In this paper, a single penalty coefficient (i.e., 0.005) was specified for all subjects to target a connectome with a density of about 25 percent on average across subjects. As a forward microstructural model, we specified a *stick* to account for the anisotropic contributions of the streamlines, and a *ball* to consider potential CSF contaminations with default diffusivities (*scil_run_commit.py --ball_stick*).

(v) Regarding the derivation of connectomes (*scil_compute_connectivity.py*), they were obtained for each subject by defining a connectome weight between any given two parcels as the sum of the COMMIT-2 weights assigned to each streamline connecting the two parcels. It is worth noting that the obtained connectomes are quantitative whereby a weight depicts an anatomo-microstructural-reflecting measure of connectivity strength.

(vi) Finally, we computed Ω_{Pyr} as the mean of the connectomes taken across subjects, and weights lower than or equal to 10^{-6} were considered null while no other threshold was applied to not further discard weak links which were assumed to be of biological significance. Before simulations, a normalization was applied such that coefficients sum to one on each row. See also Figure 3.10 and Figure 3.12.a.

3.12.2 Astrocytic connectome reconstruction pipeline

We used FreeSurfer (Fischl, 2012) (version 6.0.0; https://github.com/freesurfer/freesurfer) to reconstruct cortical surfaces (*recon-all -all*) for the ICBM-2009c-asymmetric template (Fonov et al., 2011) based on both T1-weighted and T2-weighted images. Afterwards, we derived a mid-surface, by outwardly expanding native white surfaces (i.e., consisting of about 160,000 vertices in each hemisphere) at a depth of 50 percent of cortical thickness (*mris_expand -thickness*). Meanwhile, we also mapped the scale three of the Lausanne-2018 atlas (Tourbier et al., 2022) on the ICBM-2009c-asymmetric template brain (see also Section 3.11), by performing surface-to-surface (*mri_surf2surf*) mappings using the FreeSurfer *fsaverage* template as an intermediate. We then used the mid-surface to compute coefficients of Ω_{Ast}. Coefficients in Ω_{Ast} between any two adjacent parcels were calculated as the shortest path distances weighted by Euclidean lengths.

Before simulations, a normalization was applied such that coefficients sum to one on each row. See also Figure 3.11 and Figure 3.12.b.

3.12.3 Analyses

Figure 3.10 shows the quantitative structural connectome we used to define the matrix Ω_{Pyr} (interconnecting neuronal populations). As elaborated earlier in Section 3.12.1, the connectome was derived as the mean of the connectomes taken across subjects Besides, whereas each subject's connectome was *biologically* filtered to target a density of about 25 percent, the mean connectome did not undergo filtering thereby explaining its higher density, of about 70 percent. As such, it remains unclear what the effects of averaging quantitative connectomes may be, as we did in this paper. Future studies could aim at developing an appropriate statistical model to derive group-level connectomes, which is currently lacking to the best of our knowledge. It is worth observing here that frontal-cingulate-insula regions or parietal-occipital-temporal regions strongly interconnect within and between hemispheres (i.e., qualitatively speaking, they belong to two different communities).

Figure 3.11, shows the connectivity matrix we used to define the matrix Ω_{Ast} (interconnecting astrocytic populations). It is a lattice-like network depicting the geometrical embedding of the brain, where a node connects only to its first neighbourhood along the cortical mantle, and where an edge codes physical proximity.

In our network model, because we left it to the structural layers (i.e., Ω_{Pyr} and Ω_{Ast}) to dictate all spatial patterns, it can be useful to analyze some of their basic topological properties. Figure 3.12 illustrates the community organization, participation coefficient, and degree of the two structural layers Ω_{Pyr} and Ω_{Ast}. The structural layers were analyzed before being normalized, using the default routines of BCT (2019-03-03 release; https://www.nitrc.org/projects/bct/). A spectral optimization algorithm (*modularity_und.m*) was used to perform community detections and the participation coefficients (*participation_coef.m*) were determined from the resulting communities. Figure 3.12.a, for Ω_{Pyr}, confirms that frontal-cingulate-insula and parietal-occipital-temporal regions form two elemental communities. Although expected, it is interesting to note that precuneus regions are highly connected to the rest of the brain (i.e., high participation coefficient and high degree), as opposed to occipital regions (i.e., low participation coefficient and distribution of low degrees). Additionally, Figure 3.12.b, for Ω_{Ast}, confirms that the lobar domains of the brain can explain well (but not fully) the geometry of its cortical surface. Indeed, the detected communities in Ω_{Ast} mostly delineated the lobes displayed in Figure 3.9. It is interesting to note that the communities detected in Ω_{Pyr} are, for the most part, present in Ω_{Ast}, albeit split into smaller ones. A thorough graph-theoretical analysis of these structural layers was falling out of the scope of this paper and so we decided to not report here further details. Nevertheless, it is important to consider that what we are showing in Figure 3.12, especially for Ω_{Ast}, critically depends on many factors (e.g., parcellation, communities) and as such we may not be able to meticulously conclude without further analyses.

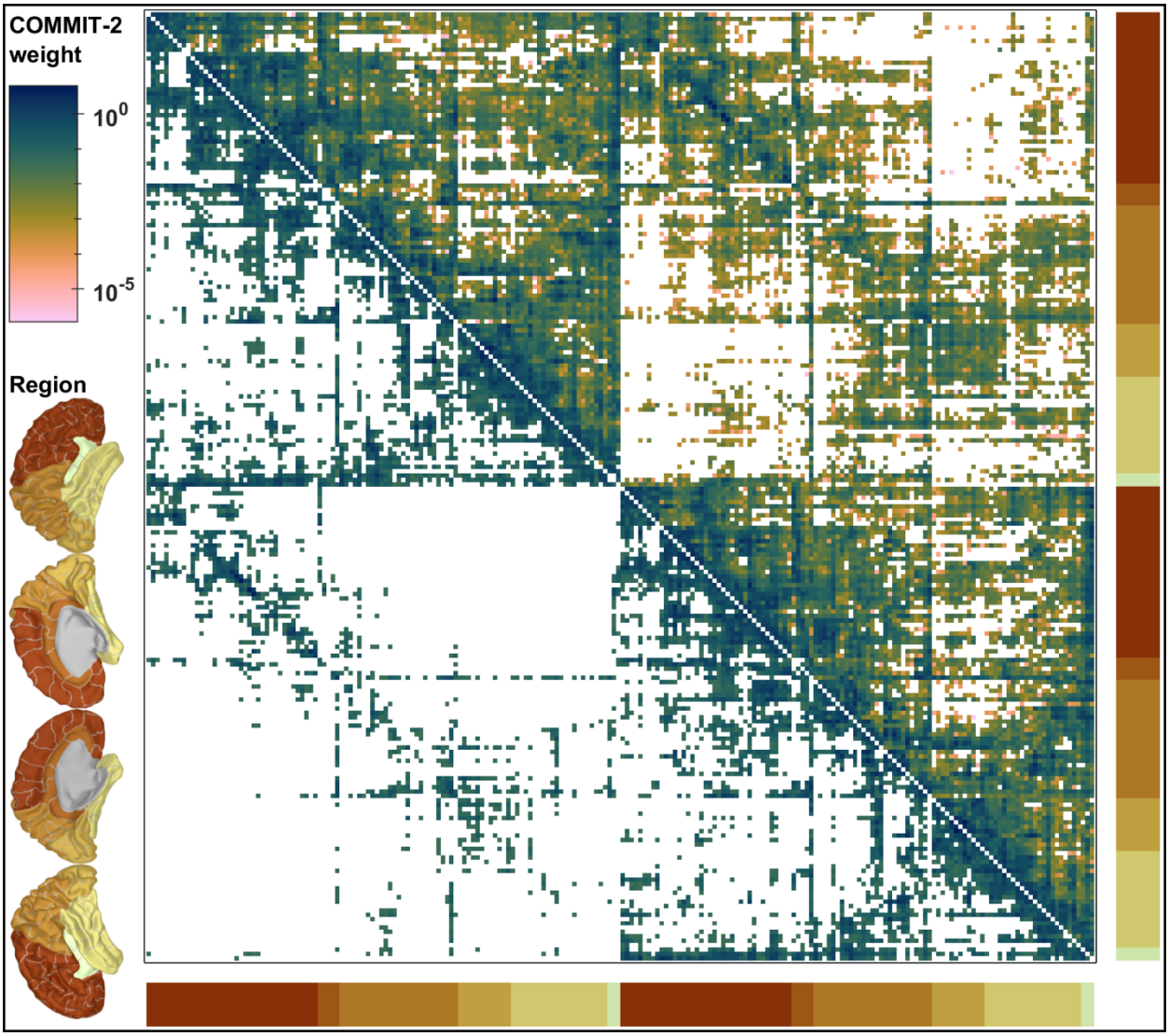

Figure 3.10. Neuronal structural layer. Quantitative structural connectome we used in this paper to define the matrix Ω_{Pyr}. As a reminder, Ω_{Pyr} is the right-stochastic variant of this connectome. A thresholded version of the connectome (retaining 25 percent of its highest weights) is displayed on the lower diagonal portion to better visualize where the strongest connections are and to interpret functional connectomes later more easily. However, note that the connectome is symmetric by construction. The parcellation and regions are shown following the conventions specified in Section 3.11.

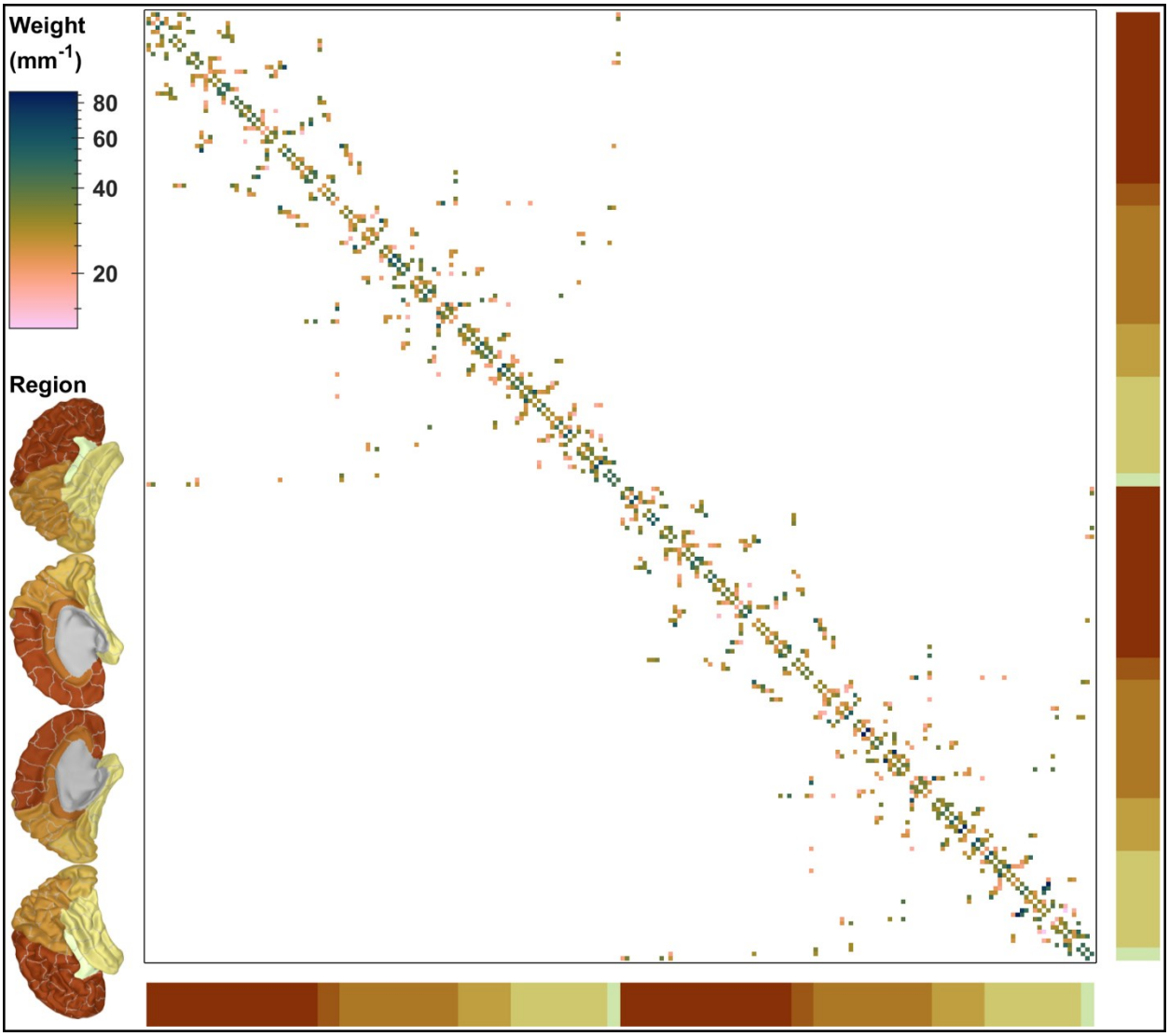

Figure 3.11. Astrocytic structural layer. Connectome we used in this paper to derive the matrix Ω_{Ast}. As a reminder, Ω_{Ast} is the right-stochastic variant of this connectome. The parcellation and regions are shown following the conventions specified in Section 3.11.

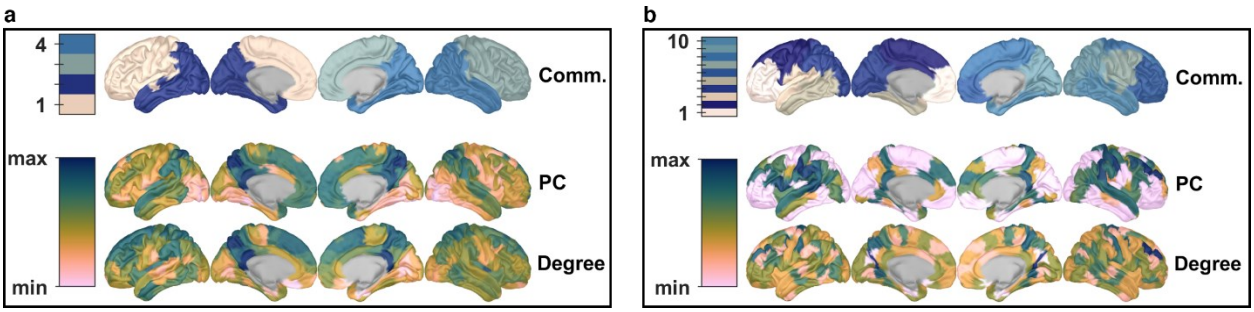

Figure 3.12. Basic topological properties for the structural layers. Panel (a): Ω_{Pyr}; and panel (b): Ω_{Ast}. Comm.: community structures; PC: participation coefficient.

3.12.4 Remarks

One crucial but oftentimes overlooked bias of dynamical models of whole-brain activity (of neuroimaging data) resides in the definition of a biophysically plausible structural layer for interconnecting neuronal populations (through white-matter tracts). The (neuronal) structural layer is a fundamentally important parameter of such models as it constrains their main spatial and temporal interactions, it is most of the time (if not always) informed by empirical data, and it seldom places the model outputs at a convenient (connectomic) scale of empirical data (Bezgin et al., 2017; Breakspear, 2017; Deco et al., 2009; Griffiths et al., 2022; Melozzi et al., 2017; Sanz-Leon et al., 2015; Shen et al., 2019). Diffusion MRI is preferentially used to define (neuronal) structural layers in the context of neuroimaging data (Breakspear, 2017). Yet all diffusion-MRI-based tractograms suffer from at least streamline termination and quantification biases which thereby decrease their biological plausibility (those are two biases that we partially addressed in this paper using state-of-art reconstruction pipelines) (C. H. Yeh et al., 2021). In addition, such tractograms are notoriously undirected whereas long-range projections between neuronal populations are established to be directed (Bezgin et al., 2017; Shen et al., 2019). To address this latter bias, some promising approaches (Bezgin et al., 2017; Shen et al., 2019) have been proposed where axonal tract-tracing datasets are used to infer directionality and we plan to integrate those in future studies. Regarding the use of tracing datasets (which mostly target primates such as macaques), it is worth noting that it further allows to potentially correct for the fact that connections between homologous brain regions are most of the time incorrectly reconstructed (due to the problem of crossing-fibres that diffusion MRI cannot fully resolve). This is of interest because homotopic connections have been shown to be critical determinants of the biological plausibility of structural connectomes (Messé et al., 2014) since they significantly increase the contribution of anatomy to the coupling between structural and functional connectivity.

Differently from the prevailing dynamical models of whole-brain activity where only interaction pathways between neuronal populations are specified (Breakspear, 2017), our network model additionally assumes a structural layer for interconnecting astrocytic populations. To the best of our knowledge, astrocytic connectivity at the population level remains hardly addressed in the literature (De Pittà, 2020; De Pittà & Berry, 2019; Fields et al., 2015; Kastanenka et al., 2020), which prompted us, in this paper, to construct a phenomenological model of gap junctional densities dictating couplings between astrocytic populations. Nevertheless, it is also worth considering how vascular networks could serve as additional (and viable) pathways for defining astrocytic interaction paths (and their couplings with neurons) at the resolution of neuroimaging data (De Pittà, 2020; De Pittà & Berry, 2019; Fields et al., 2015; Hösli et al., 2022; Kugler et al., 2021; Macvicar & Newman, 2015; Magistretti & Allaman, 2015; Nedergaard et al., 2003). It is also worth mentioning that there exist other pathways of glial interactions (De Pittà, 2020; De Pittà & Berry, 2019; Fields et al., 2015). For example, oligodendrocytes can communicate over axons while microglia (and all glia) can establish diffusion-based communications (e.g., over the extracellular matrix) (De Pittà, 2020; De Pittà & Berry, 2019; Fields et al., 2015).

Another crucial but also more generic bias in neuroimaging studies resides in the choice of a parcellation scheme (e.g., see (Arslan et al., 2018; Messé, 2020)). For example, here we used a surface-based anatomical atlas with 216 regions to define network nodes, but it is unclear how other atlases (e.g., functional, multimodal, volumetric, of different spatial resolutions) may influence our analyses.

3.13 SI — Neuron-astrocyte network activity analysis

3.13.1 Links between simulation parameters and empirically concrete state-variables

In Figure 3.2.*a* of the *Main Text*, whole-brain levels of $\mathrm{Glu_e}$ and $\mathrm{GABA_e}$ were mapped into the plane defined by ω_{Glu} and ω_{GABA}. Values of $\mathrm{Glu_e}$ were found to span the interval [6.1; 11.4] µmol while $\mathrm{GABA_e}$ varied in [11.5; 27.4] µmol. We observed that increases in ω_{Glu} were associated with increases in both $\mathrm{Glu_e}$ and $\mathrm{GABA_e}$ (independently of ω_{GABA}) while increases in ω_{GABA} were associated with decreases in $\mathrm{Glu_e}$ and increases in $\mathrm{GABA_e}$ (independently of ω_{Glu}). The increases in $\mathrm{Glu_e}$ as a function of either ω_{Glu} or ω_{GABA} remained particularly small everywhere except within a relatively tiny area characterized by high ω_{Glu} values and low ω_{GABA} values. In addition, the decreases in $\mathrm{Glu_e}$ as a function ω_{GABA} (with ω_{Glu} fixed) were particularly small with a maximum absolute difference equal to 0.7 µmol.

In our simulations, both the release and uptake dynamics of neurotransmitters were constrained to be slow. In addition, ensuing changes in $\mathrm{Glu_e}$ and $\mathrm{GABA_e}$ were constrained to be small and to happen at the same timescale. As a result, increases in ω_{Glu} were all associated with increases in both $\mathrm{Glu_e}$ and $\mathrm{GABA_e}$ independently of ω_{GABA} whereas increases in ω_{GABA} were all associated with decreases in $\mathrm{Glu_e}$ and increases in $\mathrm{GABA_e}$ independently of ω_{Glu}. Those are natural (elementary) and expected mappings as described throughout Sections 2.3.5 and 2.3.6 in Chapter 2 as well as Section 3.10.

Indeed, starting from an initial (stable) network state, any increment in ω_{Glu} amounts to (transiently and directly) increasing whole-brain levels of glutamate release rates (i.e., J_{Glu}) which in turn amounts to progressively increasing whole-brain levels of $\mathrm{Glu_e}$. Subsequently, astrocytic network feedbacks over both glutamate and GABA release rates (i.e., $Q_{\mathrm{Glu}}^{\mathrm{Ast}}$ and $Q_{\mathrm{GABA}}^{\mathrm{Ast}}$) increase while excitability thresholds for both populations of pyramidal cells and inhibitory interneurons (i.e., v_{Pyr} and v_{InIn}) decrease. In the end, concurrent increases are induced in J_{Glu} (and thereby $\mathrm{Glu_e}$) as well as J_{GABA} (and thereby $\mathrm{GABA_e}$). This temporal chain of actions, which can symbolically be summarized as $\left[\{\omega_{\mathrm{Glu}}\uparrow\} \Longrightarrow \{J_{\mathrm{Glu}}\uparrow\uparrow\} \Longrightarrow \{\mathrm{Glu_e}\uparrow\uparrow\} \Longrightarrow \left\{Q_{\mathrm{Glu}}^{\mathrm{Ast}}\uparrow; Q_{\mathrm{GABA}}^{\mathrm{Ast}}\uparrow; v_{\mathrm{Pyr}}\downarrow; v_{\mathrm{InIn}}\downarrow\right\} \Longrightarrow \{J_{\mathrm{Glu}}\uparrow; J_{\mathrm{GABA}}\uparrow\} \Longrightarrow \{\mathrm{Glu_e}\uparrow; \mathrm{GABA_e}\uparrow\} \Longrightarrow \{\ldots\}\right]$, continues until uptake rates adjust (upward) to release rates so that ultimately, increases in ω_{Glu} induce increases in both $\mathrm{Glu_e}$ and $\mathrm{GABA_e}$. It is worth noting the possibility of induced decreases in $\mathrm{Glu_e}$ following increases in $\mathrm{GABA_e}$ (and possibly due to the presence of stochastic fluctuations as well) along this temporal action chain. What guarantees that such a scenario does not occur (or at least would not be noticeable) in our simulations is the fact that all GABA-induced changes (i.e., decreases) in the firing rates of pyramidal cells are too small to provoke a significant decrease in glutamate release rates with respect to glutamate uptake rates. Said otherwise, changes in $\mathrm{GABA_e}$ are too small and slow so much so that most of the transient increases in $\mathrm{Glu_e}$ following an increment in ω_{Glu} would remain present later at equilibrium (i.e., would remain in excess). Concerning the case of an increment in ω_{GABA}, a similar logic applies where $\left[\{\omega_{\mathrm{GABA}}\uparrow\} \Longrightarrow \{J_{\mathrm{GABA}}\uparrow\uparrow\} \Longrightarrow \{\mathrm{GABA_e}\uparrow\uparrow\} \Longrightarrow \left\{v_{\mathrm{Pyr}}\uparrow\right\} \Longrightarrow \{J_{\mathrm{Glu}}\downarrow\} \Longrightarrow \{\mathrm{Glu_e}\downarrow\} \Longrightarrow \left\{Q_{\mathrm{Glu}}^{\mathrm{Ast}}\downarrow; Q_{\mathrm{GABA}}^{\mathrm{Ast}}\downarrow; v_{\mathrm{Pyr}}\uparrow; v_{\mathrm{InIn}}\uparrow\right\} \Longrightarrow \{\mathrm{Glu_e}\downarrow; J_{\mathrm{GABA}}\downarrow\} \Longrightarrow \{\ldots\}\right]$ so that ultimately, increases in ω_{GABA} induces increases in $\mathrm{GABA_e}$ and decreases in $\mathrm{Glu_e}$. We note, similarly to the earlier case of $\mathrm{Glu_e}$, that most transient increases in $\mathrm{GABA_e}$ following an increment in ω_{GABA} do not dissipate as the network model converges to an equilibrium (even

though $\mathrm{GABA_e}$ undergoes decrease periods along the temporal action chain) because all changes in neuronal firing rates are small.

3.13.2 Links between features of membrane potential dynamics and bifurcation diagram

Figure 3.13.a is the same as Figure 3.2.*b* of the *Main Text* where we highlighted that LFP peak–peak amplitudes and peak frequencies local extrema were nearly all distributed along contours of limit cycle peak–peak amplitudes. Figure 3.13.b better illustrates the distribution of some extrema by focusing on a restricted portion of the heatmaps. The results for LFP peak frequencies are clear, while the results for LFP peak–peak amplitudes show an abrupt transition between low and high values indicating that the corresponding surface gradient flows have drastically different magnitudes above, at, and below the second and third contour curves. We verified that the local extrema were in fact due to stochastic motions. Figure 3.13.c further better illustrates the distribution of some (but not all) extrema by graphing the sign of the scalar products between surface gradients and the vectors drawn in black. The vectors drawn in black capture a hypothetical overall direction flow and in this way, some local extrema are captured where the signs of the scalar products change from positive to negative and vice-versa. It is important to note that LFP peak frequency patterns are not fully explained by contours of limit cycle LFP peak–peak amplitudes because limit cycle amplitudes and frequencies are not correlated and LFP dynamics are non-linearly related to the other dynamics of the network model.

Figure 3.14.a is the same as Figure 3.2.*c* of the *Main Text* where we drew a bifurcation landscape of limit cycles with LFP as state variable, and v_{Glu} and v_{GABA} as bifurcation parameters. Figure 3.14.b–d show bifurcation landscapes with E_{Pyr}, $E_{\mathrm{ExIn}\cup\mathrm{Pyr}}$, and E_{InIn} as state variables.

Our in-depth analyses revealed that the patterns observed in Figure 3.13 were (mainly but not exclusively) explained by the ways the stochastic motions specified in our network model were acting on the nodal neuronal compartments through the neuronal structural constraints Ω_{Pyr}, and more specifically they were explained by an index of global *heterogeneity* level amongst network nodes. Figure 3.15.a–b summarizes our analysis of global network *heterogeneity* levels as a function of whole-brain levels of $\mathrm{Glu_e}$ and $\mathrm{GABA_e}$. Our analysis was based on the role of the parameter G which, as we described in Section 2.3.5 in Chapter 2, is a substitute for the parameter ω_{Pyr} when we consider a network composed of a single node or fully identical nodes. As a reminder, in our model, the parameter G can conveniently be used to understand the behaviour of a *heterogeneous* network by considering that the two scenarios of disconnected nodes (i.e., $G = 0$) and coupled fully identical nodes (i.e., $G = \omega_{\mathrm{Pyr}}$) represent two extremes of a continuum within which lie (statistically speaking) most (but not all) other *heterogeneous* network states. Our hypothesis is based on the following. Unless fully identical (i.e., unless specified with the same parameters and initial states), and as long as ω_{Pyr} values are not *too high*, nodes would never exhibit the same state (or, within a probabilistic scheme where the baseline neuronal firing rates $q_{[\cdot]}$ are independent stochastic processes, nodes would *almost surely* never exhibit the same state). Said otherwise, given any node n within a *heterogeneous* network, a proportion of the information in its input neuronal network feedback $Q_{\mathrm{Pyr}_{[n]}}$ can explain and be explained by its pyramidal firing rate $F_{\mathrm{Pyr}_{[n]}}$, while the residual proportion could *conveniently* (i.e., in some specific statistical scenarios) be considered as an *independent* input (or an *independent* source of stochastic fluctuations) alongside $q_{[n]}$. For example, within a statistical linear modelling scheme, a value for

$G_{[n]}$ could be estimated, *a posteriori*, to reflect the proportion (i.e., between 0 and 1, but then scaled by ω_{Pyr}) of information shared between $Q_{\mathrm{Pyr}_{[n]}}$ and $F_{\mathrm{Pyr}_{[n]}}$. In this case, the behaviour of the node n could be entirely understood (or reconstructed) by drawing a codimension-2 diagram as we did throughout Chapter 2 but with such an *a posteriori* value for $G_{[n]}$ to account for stochastic network interactions. Besides, such a value of $G_{[n]}$ would always (or almost surely always in the stochastic case) satisfy $G_{[n]} \leq \omega_{\mathrm{Pyr}}$. Hence, as stated earlier, the two scenarios of disconnected nodes (i.e., $G = 0$) and coupled fully identical nodes (i.e., $G = \omega_{\mathrm{Pyr}}$) represent two extremes of a continuum within which lie most (but not all) other network states, and a global statistical estimate of G (e.g., obtained using a multilevel regression model, or obtained by calculating a descriptive statistic on $G_{[\cdot]}$ values) could provide an index of global network *heterogeneity* levels.

Figure 3.15.a–b shows the results of a robust linear regression scheme (*MATLAB*'s default routine *robustfit*) specified with $q + Q_{\mathrm{Pyr}}$ as responses and F_{Pyr} as predictors, i.e., specified for any node n by $q_{[n]} + Q_{\mathrm{Pyr}_{[n]}} = \mathrm{slope}_{[n]} F_{\mathrm{Pyr}_{[n]}} + \mathrm{intercept}_{[n]} + \mathrm{residual}$. Figure 3.15.a shows whole-brain levels (i.e., mean taken across regions) of the estimated slopes (i.e., *a posteriori* G values) as a function of whole-brain levels of $\mathrm{Glu_e}$ and $\mathrm{GABA_e}$, and Figure 3.15.b shows whole-brain values (i.e., mean taken across regions) of the estimated intercepts (i.e., *a posteriori* q values). We observed that the slopes were lower than $\omega_{\mathrm{Pyr}} = 7.5$, as well as an abrupt transition from a uniform area where the slopes were relatively close to ω_{Pyr} at low $\mathrm{Glu_e}$ and $\mathrm{GABA_e}$ values to an area where the slopes started to rapidly decrease until reaching a minimum at high $\mathrm{Glu_e}$ and $\mathrm{GABA_e}$ values. We also observed that the intercepts were higher than 240 Hz (i.e., higher than $\mathrm{mean}(q)$ as specified in Table 2.3) while exhibiting variation patterns consistent with the slopes. In addition, such transition and variation patterns for the slopes and intercepts were explained by contours of limit cycle peak–peak amplitudes. We verified that such phenomena did not occur when stochastic fluctuations were *homogeneously* specified (e.g., the same q for all nodes), and when ω_{Glu} and ω_{GABA} were from different value ranges. Instead, we found that such phenomena were occurring specifically due to the specified standard deviation for q (as a reminder, we specified $\mathrm{std}(q) = 10$ Hz in Table 2.3), and due to the characteristics of the two-parameter bifurcation landscape of limit cycles. We also verified that performing a simulation with a single node (see Section 2.3.2 in Chapter 2 for equations) where G, q, $\mathrm{Glu_e}$ and $\mathrm{GABA_e}$ are specified exactly as in Figure 3.15.a–b, provided heatmaps quasi-identical to those in Figure 3.13.a (i.e., they allowed to reproduce whole-brain network states). Together, these results confirm that there are dynamical behaviours that occur (akin to bifurcations) in a *heterogeneous* network scenario which do not occur either in a non-stochastic or in a stochastic but *homogeneous* network scenario. These results also highlight a novel way to understand dynamical behaviours without necessarily employing stochastic bifurcation theory *per se*. Lastly, these results provide a solid basis for analyzing more complex network scenarios where whole-brain states no longer adequately summarize network states.

As a final note, because we were particularly interested in LFP amplitude-modulation patterns in this paper, it can be useful to link LFP envelope fluctuation patterns and the stochastic motions along the bifurcation landscape that we described so far. Figure 3.15.c–d shows that the variation patterns of LFP envelope mean amplitude levels and LFP envelope peak–peak amplitude levels are consistent with the variation patterns described earlier in Figure 3.15.a–b when analyzing global network *heterogeneity* levels, notably sharing the same critical frontier where network

properties change drastically. We further discuss the links between neurotransmission and amplitude modulations of bioelectrical neuronal activity in Section 3.13.3.

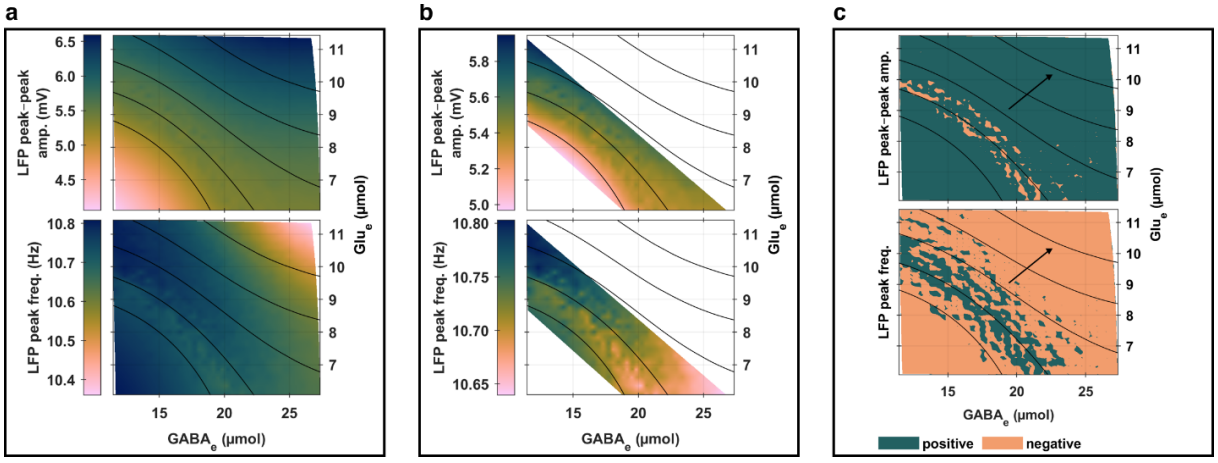

Figure 3.13. Linking electrophysiology and neurotransmission. (a)–(b) Whole-brain levels of LFP peak–peak amplitudes (top tile) or peak frequencies (bottom tile) as functions of whole-brain levels of Glu_e (y-axis) and $GABA_e$ (x-axis). (c) Sign of scalar products between surface gradients (obtained from (a)) and the vectors drawn in black. (a)–(c) The five black solid curves in each graph represent contours of limit cycle LFP peak–peak amplitudes. Each contour passes through one of the following (Glu_e; $GABA_e$) coordinates in (μmol) × (μmol): (8; 15), (9; 15), (10; 15), (11; 15), or (11; 20).

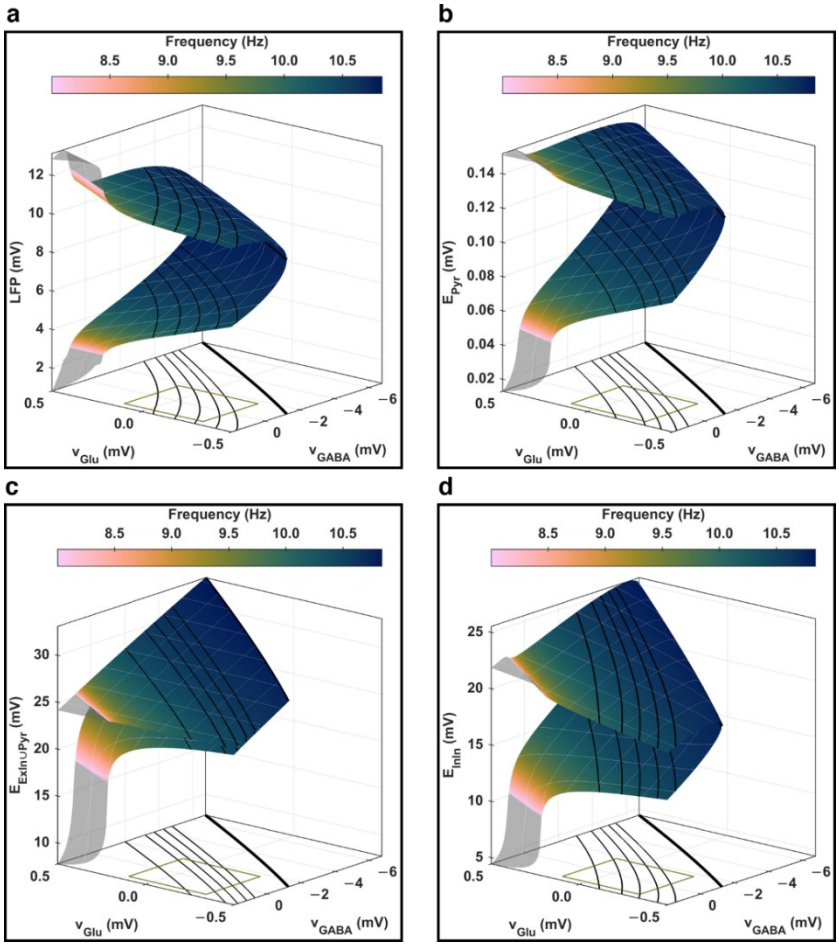

Figure 3.14. Two-parameter bifurcation landscapes of limit cycles. Drawn with (a) LFP, (b) E_{Pyr}, (c) $E_{\mathrm{ExIn\cup Pyr}}$, and (d) E_{InIn} as state variables, and v_{Glu} and v_{GABA} as bifurcation parameters. The surfaces delimit the extrema of limit cycle amplitudes, and the colour bars indicate limit cycle frequencies. A portion of each surface is not coloured (i.e., is left semi-transparent), indicating frequencies lower than eight hertz, and the black solid curves represent contours of limit cycle peak–peak amplitudes. The same contours are graphed on a plane $(v_{\mathrm{Glu}}; v_{\mathrm{GABA}})$ under the surface, and each thickest black solid curve represents a locus of supercritical Hopf bifurcation points (i.e., a contour associated with the height equal to zero). As detailed in Section 2.3.4 in Chapter 2, v_{Glu} and v_{GABA} are increasing monotonic (sigmoidal) functions of $\mathrm{Glu_e}$ and $\mathrm{GABA_e}$ respectively. The green rectangular outline under the surface shows the domain correspondence between $(v_{\mathrm{Glu}}; v_{\mathrm{GABA}})$ and $(\mathrm{Glu_e}; \mathrm{GABA_e})$ as drawn, e.g., in Figure 3.13 or Figure 3.2.*b* of the *Main Text*, and each contour (except for the Hopf locus) passes through one of the following $(\mathrm{Glu_e}; \mathrm{GABA_e})$ coordinates in (μmol) × (μmol): (8; 15), (9; 15), (10; 15), (11; 15), or (11; 20).

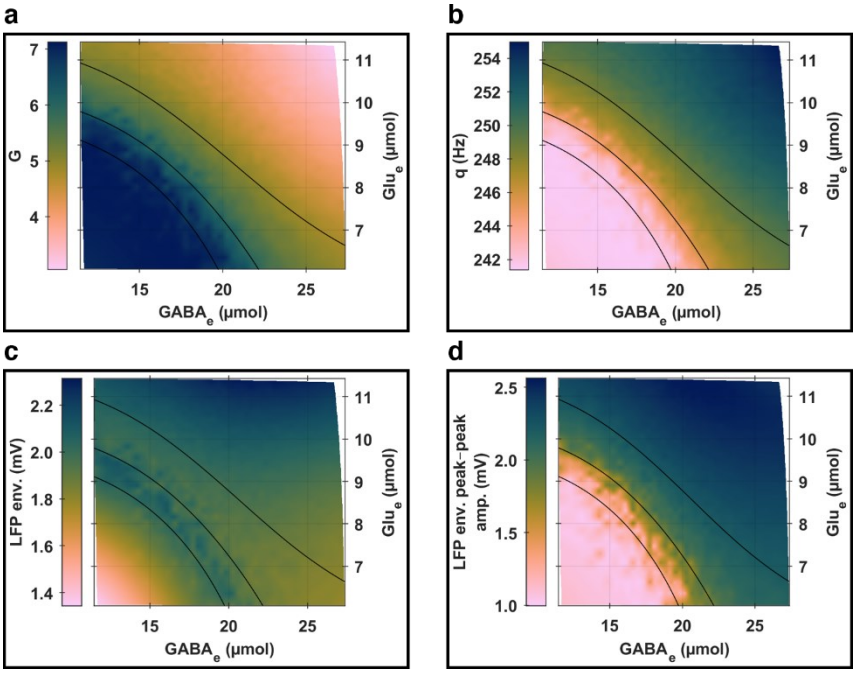

Figure 3.15. Linking amplitude modulations of bioelectrical activity and neurotransmission. (a) Whole-brain levels of *a posteriori* G estimates as functions of whole-brain levels of Glu_e (y-axis) and $GABA_e$ (x-axis). All *t*-statistics testing the null hypothesis that G is zero against the alternative that it is different from zero were ranging 14.5–98.8, and all G values were considered statistically significant. (b) Same as (a) but for *a posteriori* q estimates. All *t*-statistics testing the null hypothesis that q is zero against the alternative that it is different from zero were ranging 451–1234, and all q values were considered statistically significant. (c)–(d) Whole-brain levels of LFP envelope mean amplitudes (c) or peak–peak amplitudes (d) as functions of whole-brain levels of Glu_e (y-axis) and $GABA_e$ (x-axis). In (a)–(d) the black solid curves represent contours of limit cycle E_{InIn} peak–peak amplitudes. The contours are the same as in Figure 3.3.*a* of the *Main Text* to facilitate juxtapositions with clustering analysis results of network activity patterns. Each contour passes through one of the following (Glu_e; $GABA_e$) coordinates in (μmol) × (μmol): (8; 16), (8.8; 16.0), or (10; 16).

3.13.3 Links between neurotransmission and amplitude modulations of bioelectrical neuronal activity

As elaborated earlier in Section 3.13.2 (or throughout Sections 2.3.5 and 2.3.6 in Chapter 2 as well Section 3.10), in our network model, a natural link between LFP envelope fluctuations and Glu_e and $GABA_e$ fluctuations was provided by the facts that Glu_e and $GABA_e$ fluctuations remained almost perfectly correlated across all simulations while $GABA_e$ fluctuations almost exclusively dictated the motions along the limit cycles of the neuronal compartment across all simulations. Figure 3.16 summarizes whole-brain spatial Pearson-correlation patterns between LFP envelope and Glu_e and $GABA_e$ fluctuations where whole-brain values were calculated as the median of regional values for each simulation independently. Consistent with the results described in Section 3.13.2, we determined overall that the correlations between LFP envelope and either Glu_e (i.e., Figure 3.16.a) or $GABA_e$ (i.e., Figure 3.16.b) fluctuations were particularly strong along the critical frontier where network *heterogeneity* levels drastically change and increasingly weaker for increasing astrocytic network coupling strengths, and likewise for the correlations between Glu_e and $GABA_e$ fluctuations (i.e., Figure 3.16.c). It is worth noting the fact that we obtained the same results using Spearman-correlations, and all linear correlation values between LFP envelope fluctuations and either Glu_e or $GABA_e$ fluctuations were low to medium. Such results were expected because, as elaborated throughout Sections 3.13.1 and 3.13.2, dynamic links between

neurotransmission and amplitude modulations of bioelectrical neuronal activity are inherently non-linear.

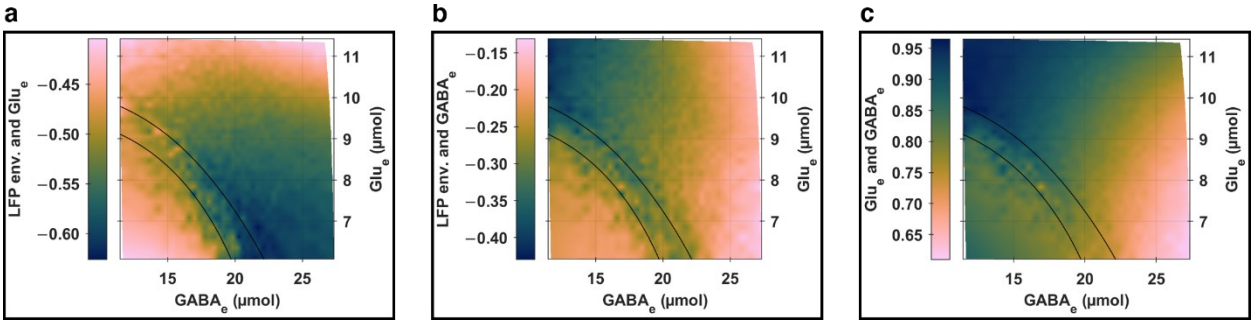

Figure 3.16. Correlational associations between amplitude modulations of bioelectrical activity and neurotransmission. Whole-brain Pearson-correlations between LFP envelope and Glu_e fluctuations (a), between LFP envelope and $GABA_e$ fluctuations (b), and between Glu_e and $GABA_e$ fluctuations (c) as functions of whole-brain levels of Glu_e (y-axis) and $GABA_e$ (x-axis). Darker colours always map to stronger absolute correlation values. The black solid curves in each graph represent contours of limit cycle E_{InIn} peak–peak amplitudes. The contours are the same as in Figure 3.3.*a* of the *Main Text* to facilitate juxtapositions with clustering analysis results of network activity patterns. Each contour passes through one of the following $(Glu_e; GABA_e)$ coordinates in (μmol) × (μmol): (8; 16), or (8.8; 16.0).

3.13.4 Clustering analysis of spatial patterns of temporal standard deviations

Figure 3.17 shows the input data used for clustering analysis, i.e., spatial patterns of LFP, Glu_e, and $GABA_e$ normalized temporal standard deviations (std).

Figure 3.18 is the same as Figure 3.4 of the *Main Text* where we illustrated cluster means as fitted by a Gaussian mixture model with four components. We can observe that the cluster means are consistent with the input data shown in Figure 3.17. For example, when focusing on LFP-std, Figure 3.17 shows that some regions of the parietal lobe had very low standard deviation values for the simulations of clusters #2–4, and we easily recognize in Figure 3.18 that those were regions of the precuneus cortices (see also Section 3.11).

Figure 3.19 shows the correlation matrix as fitted by a Gaussian mixture model with four components. We can observe high similarities between the four correlation sub-matrices involving Glu_e-std and $GABA_e$-std, confirming the overall high similarity between Glu_e and $GABA_e$ network activity patterns across all simulations. We can also observe the skeleton of the neuronal structural connectome (see Figure 3.9) in all correlation sub-matrices, confirming that, overall, simulated temporal network dynamics were consistently spatially shaped across all simulations. It is worth noting the anti-correlation patterns, especially between LFP-std and either Glu_e-std or $GABA_e$-std, distinguishing frontal-cingulate lobes from parietal-occipital-temporal-insula lobes (as we elaborate later in Section 3.13.5, anti-correlation patterns were due to the (anti-correlated) relationship between $GABA_e$ and total neuronal input fluctuations).

Figure 3.20.a is the same as Figure 3.3.*a* of the *Main Text* where we showed clusters using a Gaussian mixture model with four components. Figure 3.20.b–c shows clusters using a Gaussian mixture model with five (b) and six (c) components. It is noteworthy that clusters #2–3 in (a) remained consistent across the other two models, whereas cluster #1 in (a) became *heterogeneous* across the other two models, and cluster #4 in (a) eventually split into two clusters in (c). Besides, all clusters, for all models, were mostly spatially contiguous, and though we do not illustrate the results, we found that contours of limit cycle LFP, E_{Pyr}, and E_{ExInUPyr} peak–peak amplitudes were

delineating less well the cluster frontiers than contours of limit cycle E_{InIn} peak–peak amplitudes (suggesting that GABAergic inhibitory interneurons strongly shape activity patterns (Coronel-Oliveros et al., 2021)).

Together, these results are consistent with the network *heterogeneity* profile that we analyzed in Section 3.13.2 where we determined that within cluster #1 nodes behaved *homogeneously* (hence the rather noisy and lack of clear spatial structures) while at the frontiers between clusters #1–2 and then beyond, nodes behaved *heterogeneously*.

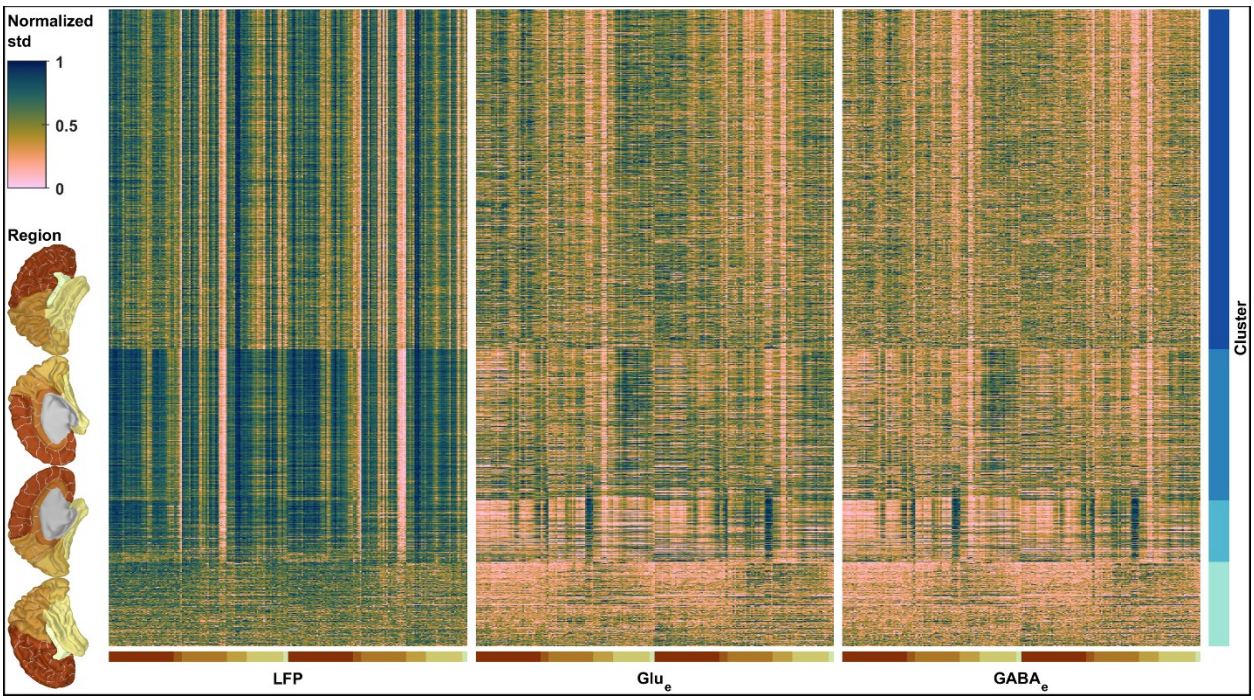

Figure 3.17. Input data for clustering analysis based on Gaussian mixture models. Spatial patterns of LFP, $\mathrm{Glu_e}$, and $\mathrm{GABA_e}$ normalized temporal standard deviations (std). Each column represents one brain region (there are 216 unique brain regions, hence 216×3 columns in total) while each row represents one simulation (there are 10×1225 rows in total). The parcellation and regions are shown following the conventions specified in Section 3.11. Here we ordered the rows (i.e., the simulations) according to their cluster assignments by a Gaussian mixture model with four components (i.e., the results shown in Figure 3.3.*a* of *Main Text*). Hence, each row (i.e., each simulation) belongs to one unique cluster that can be identified using the colour map (from light blue on the bottom, representing cluster #1, to dark blue on the top, representing cluster #4) on the right side of the figure.

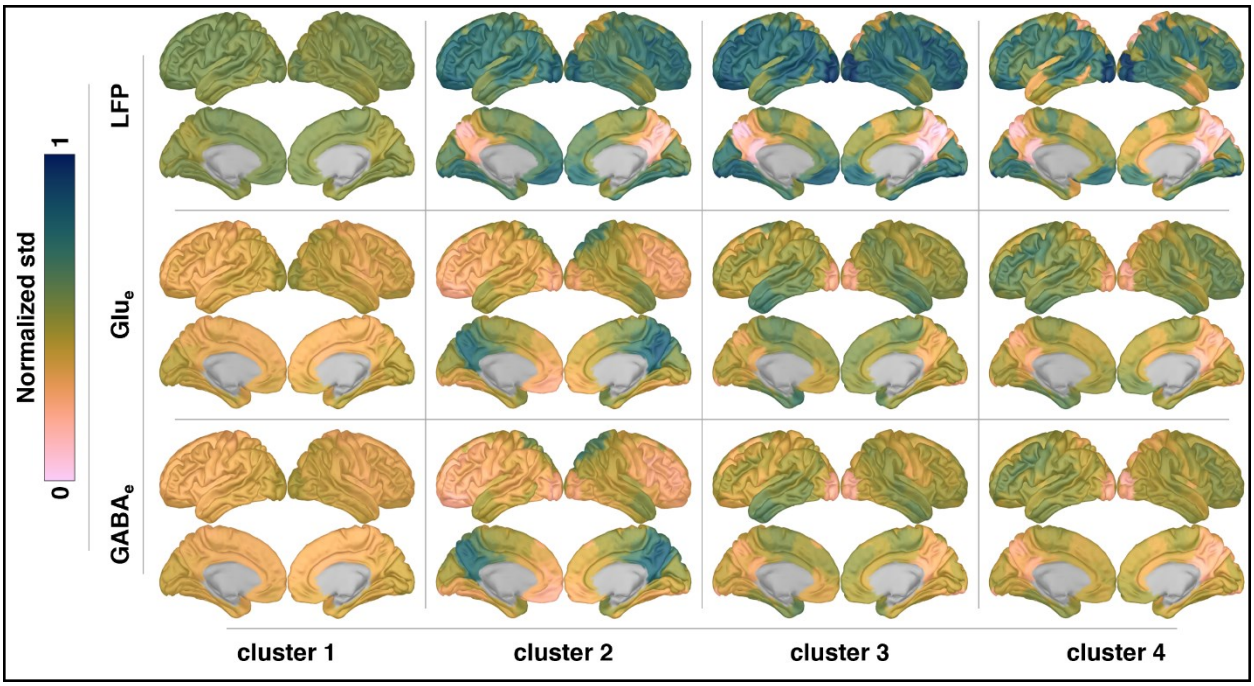

Figure 3.18. Means of Gaussian mixture model. Cluster means (as fitted by a Gaussian mixture model with four components) of LFP, Glu_e, and $GABA_e$ normalized temporal standard deviations (std).

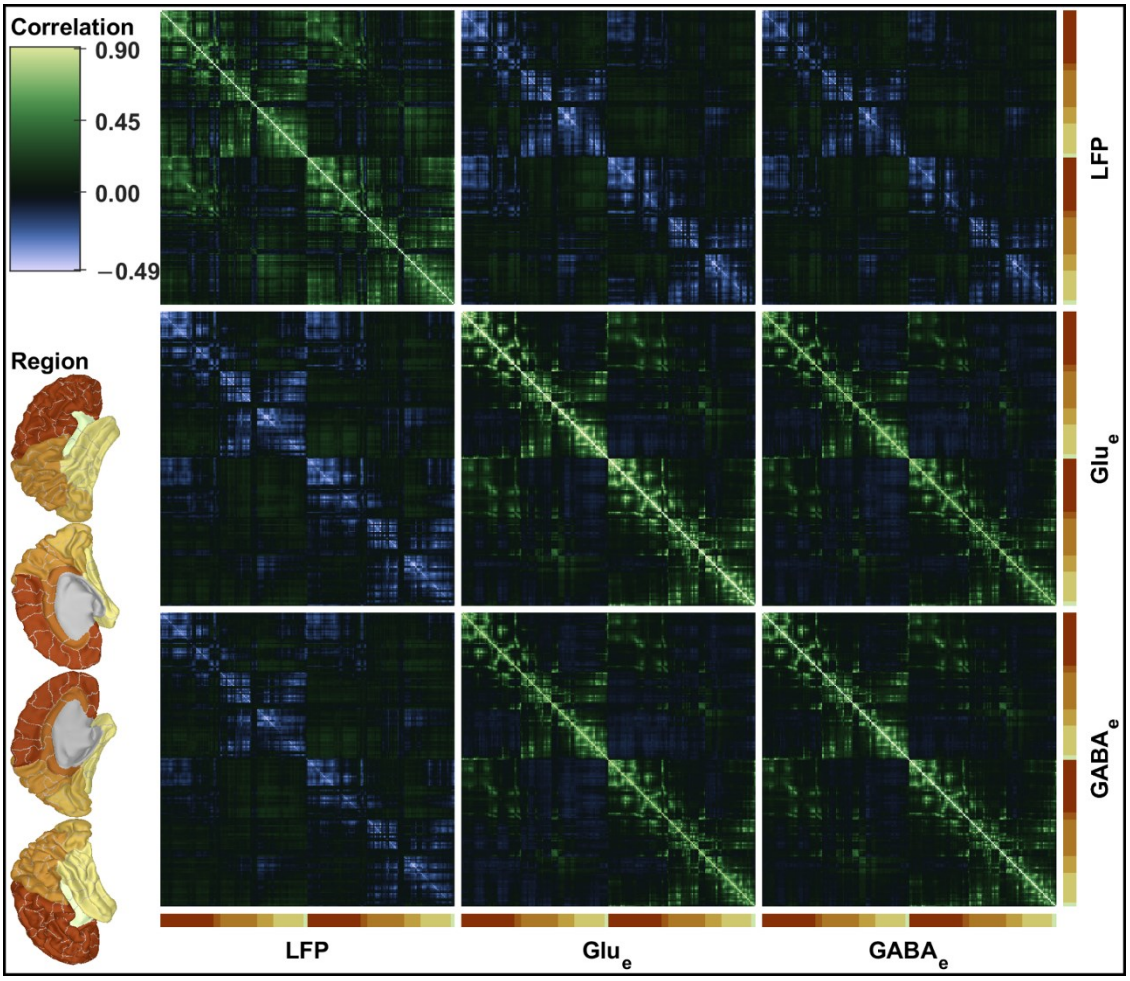

Figure 3.19. Correlation matrices of Gaussian mixture model. Correlation matrix (as fitted by a Gaussian mixture model with four components) of LFP, Glu_e, and $GABA_e$ temporal standard deviations. Diagonal values are not shown and appear in white (i.e., the background colour). As a reminder, a full covariance structure (with dimension 216×3) shared amongst all four Gaussian components was specified when fitting the model. The parcellation and regions are shown following the conventions specified in Section 3.11.

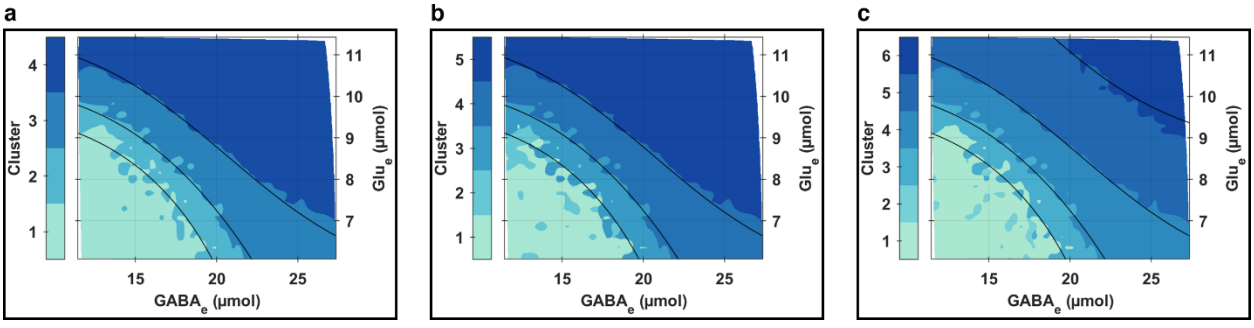

Figure 3.20. Clustering analysis results of spatial patterns of temporal standard deviations of neuron-astrocyte network activity. This analysis extends the *Main Text* using a Gaussian mixture model with four (a), five (b), and six (c) components. The black solid curves in each graph represent contours of limit cycle E_{InIn} peak–peak amplitudes. Each contour passes through one of the following (Glu_e; $GABA_e$) coordinates in (μmol) × (μmol): (8; 16), (8.8; 16.0), (10; 16), or (9.75; 25.00).

3.13.5 Biophysical description of spatial patterns of temporal standard deviations

Our network model was parameterized such that neuronal dynamics would mostly consist of stable limit cycles. Accordingly, given any simulation, the neuronal inputs at each node (which consisted of temporally structured driving network feedback with additive white noise) allowed them to visit different stable states by (smoothly) jumping over limit cycles with different peak–peak amplitudes, and very similar mean amplitudes and frequencies. In this way, patterns of LFP-std became mostly explained by LFP amplitude modulations. For example, we showed earlier in Figure 3.15.c–d, that LFP amplitude modulations were an emergent property of the stochastic and nonlinear dynamics of our network model, and their variation patterns across the simulation plane were largely explained by contours of limit cycle peak–peak amplitudes. Importantly, while the limit cycles yielded the fastest oscillations of our network model, the oscillation frequencies of the amplitude modulations were expressed on timescales that were orders of magnitude slower (e.g., see also Figure 2.10 and Figure 2.11 in Section 2.4.2 of Chapter 2). Consequently, the regions experiencing stronger amplitude modulations had the least sum of deviations from their means and hence the lowest LFP-std, and conversely. This phenomenon is clear by observing, e.g., the patterns of precuneus and lateral occipital cortices within clusters #1–4, from Figure 3.17 and Figure 3.18. Because regions of the precuneus cortices were the most strongly structurally connected (e.g., see Figure 3.12.a), they were the regions with the highest $\mathrm{Glu_e}$ and $\mathrm{GABA_e}$ levels (e.g., see Figure 3.8 in Section 3.10), thereby encountering limit cycles with the highest peak–peak amplitudes, and in the end experiencing the strongest amplitude modulations while exhibiting the lowest LFP-std. The converse was true for regions of the lateral occipital cortices, encountering limit cycles with the lowest peak–peak amplitudes, thereby experiencing the weakest amplitude modulations while exhibiting the highest LFP-std (e.g., see also Figure 2.10 and Figure 2.11 in Section 2.4.2 of Chapter 2). Hence, we understand that the ability of a brain region to experience LFP amplitude modulations depends on both its bifurcation landscape properties and its topological network attributes with respect to the structural layers of our model. This is an interplay between temporal dynamics and structural network constraints. Resultingly, we understand how patterns of LFP-std reflected spatially shaped temporal neuronal dynamics.

Additionally, by simulation design, motions on the bifurcation landscape of any region were mostly (but not entirely) explained by their $\mathrm{Glu_e}$ and $\mathrm{GABA_e}$ activity, thereby providing a natural link between $\mathrm{Glu_e}$-std and $\mathrm{GABA_e}$-std and LFP-std patterns. As illustrated in Figure 3.17, Figure 3.18, and Figure 3.19, there were global anti-correlations between profiles of $\mathrm{Glu_e}$-std or $\mathrm{GABA_e}$-std and LFP-std across all simulations. This was so because, overall, $\mathrm{Glu_e}$ and $\mathrm{GABA_e}$ fluctuations remained almost perfectly correlated across all simulations while increases in the standard deviations of $\mathrm{GABA_e}$ fluctuations were associated with increases in the standard deviations of total neuronal input fluctuations (e.g., as described in Section 2.3.2 in Chapter 2 and Section 3.10) which in turn were associated with increases in LFP amplitude modulations and therefore decreases in the standard deviations of LFP fluctuations (e.g., see also Section 3.13.2 together with Section 3.13.3). However, whereas these anti-correlation patterns were largely reflected within clusters #1–2, they were less so within clusters #3–4 (see Figure 3.17 and Figure 3.18). We determined that such dichotomy was due to how temporal standard deviations were spatially shaped across the simulation parameter plane (see Figure 3.17). Indeed, within clusters #1–2 compared to clusters #3–4, the neuronal dynamics were governed by limit cycles exhibiting the most differences in their patterns of peak–peak amplitudes (e.g., see Figure 3.14), while the astrocytic structural constraints contributed the least to shaping temporal dynamics because ω_{Glu} or ω_{GABA} values were the lowest

(e.g., see Figure 3.7 in Section 3.10). Additionally, as elaborated in Section 3.13.2, within cluster #1, network nodes mostly behaved *homogeneously*, while within clusters #3–4 nodes mostly behaved *heterogeneously*, and within cluster #2 nodes behaviours were mixed (akin to a bifurcation). Accordingly, we determined that the interplays between neuronal dynamics and structural constraints dictated different patterns of Glu_e-std and $GABA_e$-std between clusters #1–2 and clusters #3–4. More specifically, within clusters #3–4, they were overall fewer contrasts between regional values and stronger *homogeneity* between neighbouring regions thereby diluting the anti-correlation patterns that we mentioned earlier. This was due to the stronger astrocytic structural constraints within clusters #3–4, enforcing coherent glutamatergic and GABAergic release rates between neighbouring regions. For example, regions of the precuneus cortices were found to exhibit the highest standard deviations within clusters #1–2 but one of the lowest standard deviations within clusters #3–4 (i.e., a trend opposite to LFP-std), while regions of the occipital cortices were found to exhibit the lowest standard deviations within all clusters except #1 where it was rather the regions of the frontal lobe (i.e., again, a trend opposite to LFP-std).

Altogether, we understand how the astrocytic network regulation of glutamatergic and GABAergic neurotransmission induced diverse whole-brain spatial patterns of temporal standard deviations.

3.14 SI — Neuron-astrocyte functional network connectivity analysis

As a reminder, our network model was parameterized such that LFP dynamics would underlie amplitude and phase network synchronizations (see also (Liuzzi et al., 2019; Tewarie et al., 2021)) while $\mathrm{Glu_e}$ and $\mathrm{GABA_e}$ would underlie linear network co-variations. In addition, $\mathrm{Glu_e}$ and $\mathrm{GABA_e}$ would evolve on time scales different from LFP, while the fluctuations of LFP amplitude envelope would be mostly explained by the slow fluctuations of $\mathrm{Glu_e}$ and $\mathrm{GABA_e}$.

To account for the ensuing multivariate (neuron-astrocyte) network connectivity patterns and to cope with the subsequent high amount of underlying complexity, we adopted the mathematical framework of multilayer network analysis and we explored how local, mesoscale, and global network features would vary with respect to the parameter plane defined by $(\omega_{\mathrm{Glu}}; \omega_{\mathrm{GABA}})$ and equivalently $(\mathrm{Glu_e}; \mathrm{GABA_e})$ whole-brain levels.

Overall, we found evidence that our network model could exhibit, with respect to $(\omega_{\mathrm{Glu}}; \omega_{\mathrm{GABA}})$, a variety of functional network architectures (as characterized by clustering coefficient, path length, edge overlap, structural reducibility indices, entropies, community measures, and eigen-centralities) that further relates to bifurcation features. The following sections provide supplementary information for the *Main Text*.

3.14.1 Global topological multilayer network properties

Figure 3.21 is like Figure 3.5 of the *Main Text* where we highlighted that the variation patterns of four global topological properties of reconstructed multilayer functional networks (i.e., clustering coefficient, path length, edge overlap, and code length) were explained by contours of limit cycle E_{Pyr} peak–peak amplitudes. Figure 3.21 shows three complementary properties, namely, Von Neuman entropy (De Domenico, Nicosia, et al., 2015) (an extension of the Shannon information entropy to a graph), code length savings (Neuman et al., 2022) (an index of how much data compression is obtained from a network when it is optimally organized in modules compared to when it is organized in a single module), and modularity (Clauset et al., 2004) (defined as the fraction of within-community edges minus the fraction expected by chance). As in the *Main Text*, we observed that all three measures depicted local extrema and otherwise monotonic trends consistent with contours of limit cycle E_{Pyr} peak–peak amplitudes.

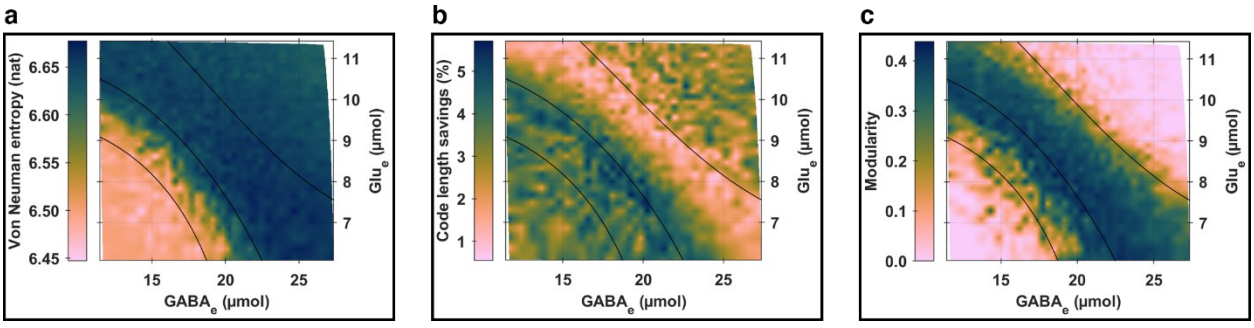

Figure 3.21. Global topological properties of reconstructed multilayer functional networks. Panel (a): Von Neuman entropy; panel (b): code length savings; and panel (c): modularity. The properties are graphed as functions of whole-brain levels of $\mathrm{Glu_e}$ (y-axis) and $\mathrm{GABA_e}$ (x-axis). The black solid curves in each graph represent contours of limit cycle E_{Pyr} peak–peak amplitudes. The contours are the same as in Figure 3.3.*b* of the *Main Text* to facilitate juxtapositions with clustering analysis results of network connectivity measures. Each contour passes through one of the following $(\mathrm{Glu_e}; \mathrm{GABA_e})$ coordinates in (μmol) × (μmol): (8.5; 14.0), (8.50; 18.25), or (9.5; 21.0).

3.14.2 Clustering analysis of global topological multilayer network properties

Figure 3.22.a is the same as Figure 3.3.*b* of the *Main Text* where we showed clusters using a Gaussian mixture model with four components. Figure 3.22 shows the effects of increasing the number of Gaussian components (four, five, or six), as well as the effects of analyzing all multilayer networks across all ten simulation batches (i.e., 10×1225 networks) versus analyzing either structurally reduced multilayer networks (i.e., also 10×1225 networks) or multilayer networks averaged across simulation batches (i.e., 1225 networks). Overall, we observed that the Gaussian mixture models were consistent with each other although the cluster frontiers for reduced networks were best explained by contours of limit cycle E_{InIn} peak–peak amplitudes rather than contours of limit cycle E_{Pyr} peak–peak amplitudes. Though we do not illustrate the results, we found, upon closer inspection, that a combination between contours of limit cycle E_{Pyr} and E_{InIn} peak–peak amplitudes were better at outlining cluster frontiers for all Gaussian mixture models. This is consistent with the fact that we expect neither excitatory nor inhibitory dynamics to solely explain all connectivity patterns across the simulation parameter plane, rather a combination of the different neuronal dynamics (due to excitation-inhibition balance) shapes such patterns. By including the investigations of reduced multilayer networks, we confirmed that our results and interpretations were not biased by redundant topological information (e.g., between $\mathrm{Glu_e}$-C and $\mathrm{GABA_e}$-C layers), incidentally highlighting the fact that reducibility operations did not throw away the informative topological information of the different multilayer networks across simulations. It was also interesting to observe that analyzing multilayer networks averaged across simulation batches instead of all the networks provided qualitatively comparable results and conclusions, suggesting that the stochastic components of our network model were appropriately specified. Finally, consistent with the analyses of network activity described throughout Section 3.13, it is noteworthy that all Gaussian mixture models identified the critical frontier where network *heterogeneity* levels drastically change.

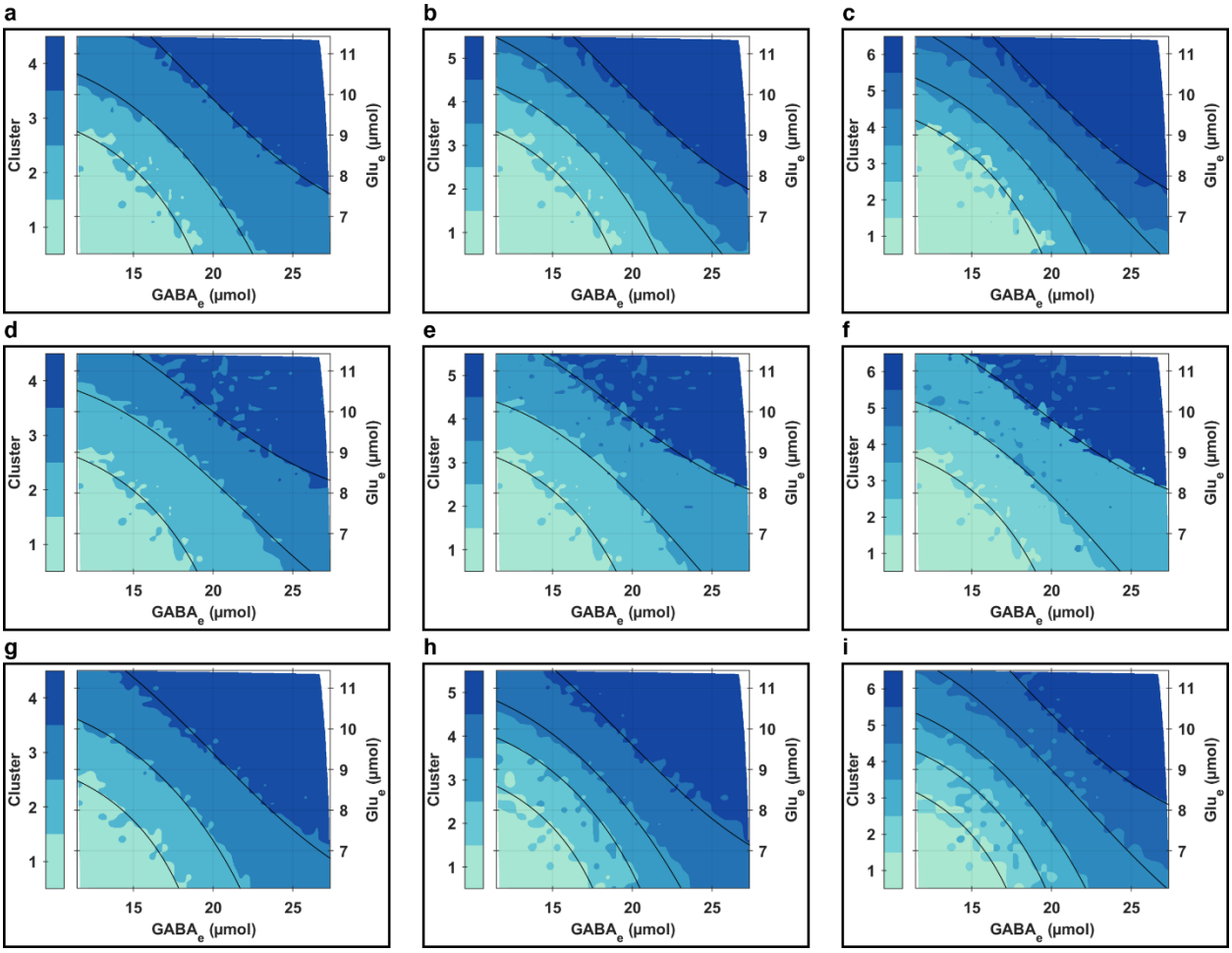

Figure 3.22. Clustering analysis results of global topological properties of multilayer functional networks. This analysis focuses on clustering coefficient, path length, edge overlap, and code length, using a Gaussian mixture model with four (first column), five (second column), or six components (third column). The tiles of the first column, i.e., (a), (d), and (g), are for four components. The tiles of the second column, i.e., (b), (e), and (h), are for five components. The tiles of the third column, i.e., (c), (f), and (i), are for six components. The tiles of the first row, i.e., (a)–(c) were obtained by analyzing all multilayer networks across all ten simulation batches (i.e., 10×1225 networks). The tiles of the second row, i.e., (d)–(f) were obtained after performing structural reducibility analysis of multilayer functional networks (i.e., also 10×1225 networks). The tiles of the third row, i.e., (g)–(i) were obtained by analyzing multilayer networks averaged across simulation batches (i.e., 1225 networks). The black solid curves in (a)–(c) and (g)–(i) represent contours of limit cycle E_{Pyr} peak–peak amplitudes. The black solid curves in (d)–(f) represent contours of limit cycle E_{InIn} peak–peak amplitudes. Each contour was visually selected to coincide with cluster frontiers.

3.14.3 Links between phase-based and amplitude-based network connectivity patterns

Figure 3.23 is like Figure 3.6 of the *Main Text* where we represented mean multilayer networks for four simulations by combining three different pieces of information: adjacency matrices, eigenvector versatilities, and communities.

From the adjacency matrices, consistent with our discourse in the *Main Text*, we observed varying topologies across layers and simulations. Overall, $\mathrm{Glu_e}$-C and $\mathrm{GABA_e}$-C layers were found to always display high spatial similarity although their respective edge weight distributions slightly differed (e.g., weights of $\mathrm{Glu_e}$-C layers were on average slightly higher than for $\mathrm{GABA_e}$-C layers, owing to higher ω_{Glu} values). In addition, $\mathrm{Glu_e}$-C and $\mathrm{GABA_e}$-C layers also displayed high spatial

similarity with LFP-AEC layers, although in general, weights distributions for LFP-AEC layers were the most skewed with the lowest first moment of all three layers. Interestingly, LFP-PLV layers depicted topologies bearing the least similarity to all three correlation layers across simulations. This suggests complementary functional links between amplitude and phase network synchrony. Besides, it is worth noting that LFP-PLV layers had generally the most consistent connectivity patterns across simulations where we could always identify the skeleton of the structural layers (i.e., consisting of highly densely connected regions within the frontal-cingulate lobes across hemispheres together with highly densely connected regions within the other lobes within hemispheres) whereas all other three correlation layers would display highly similar connectivity patterns to LFP-PLV layers only within a restricted region of the parameter plane (e.g., where edge overlap are high, i.e., mostly at the frontier between cluster #2 and cluster #3, as identified in Figure 3.22.a). This is due to phase synchrony being intrinsic to network models of spatial coupling.

From the detected multilayer communities, we determined that functional modules consisted of mostly frontal-cingulate-parietal-insula regions versus parietal-occipital-temporal regions, and they were highly intra-hemispheric. This is understandable because, as we illustrated in Section 3.12.3, the two groups of regions formed manifest structural mesoscale domains, and the astrocytic structural constraints strongly enforced intra-hemispheric functional couplings by design. Interestingly, communities within the LFP-PLV layers slightly differed from all other correlation layers, while the communities within the correlation layers highly coincided. This, again, further illustrated the fact that functional connectivity metrics based on amplitude or phase capture different topologies. We also illustrated the community profile of the aggregate functional network to highlight how an enriched representation of functional connectivity across multiple layers can be more valuable than an aggregated representation. Though we are not illustrating the results, by carefully analyzing adjacency matrices and community profiles, we determined that inter-hemispheric modules emerged whenever inter-hemispheric frontal connections were fewer in density (further coinciding with portions of parameter plane where integration and segregation levels peaked, i.e., mostly within cluster #2 as identified in Figure 3.22.a). This means that reduced inter-hemispheric connections within frontal mesoscale domains seemed to coincide with the ability of the functional networks to diversify their ties across hemispheres and to further coincide with portions of the parameter plane where nodal dynamics would drastically (qualitatively) change.

Finally, from the mapping of eigenvector versatilities, we determined consistent patterns with respect to the community profiles. We observed how the centralities could most of the time distinguish between the two hemispheres as well as between frontal-cingulate-parietal-insula regions versus parietal-occipital-temporal regions. Upon closer inspections (not illustrated), we determined that across simulations, the least central nodes changed their locations from parietal to occipital to temporal lobes while the highly central nodes were consistently located within the frontal lobe. We noted how the consistency of highly central frontal regions mirrored our previous observations (when analyzing communities) of high connection densities within the frontal lobe.

Altogether, the results of Figure 3.23 provided evidence that our network model could exhibit, with respect to $(\omega_{\mathrm{Glu}}; \omega_{\mathrm{GABA}})$, a variety of functional network architectures.

It is worth emphasizing that topologies captured by PLV complemented topologies captured by correlations. These complementarities are further related to how the structural layers (mostly the

neuronal one) induced different basins of attractions on a bifurcation plane that consisted of limit cycles with different peak–peak amplitudes and frequencies. The phenomena are similar to what we extensively discussed already in Section 3.13.5. The main idea is that because regions in frontal-cingulate-parietal-insula and parietal-occipital-temporal lobes belong to two basic communities that manifestly differ, two basic attractors are formed in a bifurcation plane. The basic attractors differ such that one of them is more sensitive to changes in limit cycle peak–peak amplitudes due to stochastic motions. In this way, the phase and amplitude relationships within the two communities of regions become two measures to distinguish between the communities. For example, for the simulation of cluster #1 illustrated in Figure 3.23, regions of the parietal-occipital-temporal left-lobes and occipital right-lobe were found to be associated with the highest Glu_e and $GABA_e$ levels (i.e., where limit cycle peak–peak amplitudes get increasingly larger) thereby exhibiting consistent amplitude relationships between each other but inconsistent phase relationships, whereas regions of the remaining lobes were found to be associated with the lowest Glu_e and $GABA_e$ levels thereby exhibiting consistent phase relationships between each other but inconsistent amplitude relationships. It is worth noting that although in our simulations the neuronal structural layer dictated most of the main functional connectivity patterns, the astrocytic structural layer provided varying levels of uniformity for intra-hemispheric and short-range connectivity (not illustrated).

In this paper, for the sake of simplicity, we provided illustrations in Figure 3.6 of the *Main Text* (or in Figure 3.23 of this Section) for one mean multilayer network within each cluster, instead of illustrating all the multilayer networks across the ten simulation batches for each cluster. However, one mean multilayer network cannot by itself always capture the features of the different networks from which it was built. Hence, in such analyses, it is essential to examine the variability across networks, which in our simulations are particularly influential due to bifurcation phenomena (e.g., see Figure 3.24 and Figure 3.25).

Figure 3.24 shows the effects of consensus analysis on eigenvector versatilities. Consensus analyses consisted of averaging eigenvector versatilities across simulation batches. Although there is generally no direct correspondence between analyzing one mean multilayer network versus performing consensus analysis on multiple multilayer networks, we can still appreciate that our main conclusions based on how frontal-cingulate-parietal-insula regions are consistently distinguished from parietal-occipital-temporal regions hold.

Figure 3.25 shows the effects of consensus analysis on communities. Consensus analyses (i.e., consensus clustering) were done using the default routines of BCT (2019-03-03 release; https://www.nitrc.org/projects/bct/). The idea of consensus analysis (*consensus_und.m*) is to seek a consensus partition of a probabilistic agreement matrix. Here, the agreement matrix was thresholded at a level of 0.5 to remove weak elements and the resulting matrix was then partitioned 100 times using the Louvain algorithm. The final Louvain-based clustering produced a set of partitions from which a new agreement is built which we are showing here as consensus communities. Consistent with the previous analysis of eigenvector versatilities, although there is generally no direct correspondence between analyzing one mean multilayer network versus performing consensus analysis on multiple multilayer networks, we can still appreciate that our main conclusions based on how frontal-cingulate-parietal-insula regions are consistently distinguished from parietal-occipital-temporal regions hold.

We did not proceed further into investigating the effects of averaging networks because a rigorous network analysis was falling out of the scope of this paper.

It is important to keep in mind that other connectivity indices could be used (e.g., coherence or mutual information) and potentially capture different topologies from the ones captured by linear correlations and phase locking values (depending of course on the activity of specific functional agents, e.g., neurons, astrocytes, or their interface through glutamatergic and GABAergic transmissions). Additionally, a full multilayer network reconstruction could be used and potentially reveal the cohesions that exist between functional relationships of different natures. In this paper, we adopted the intuitive case of multiplex networks due to the lack of established procedures to generally define inter-layer connectivity or relate to each other the different connectivity indices used for network reconstructions (e.g., see (Brookes et al., 2016; De Domenico, 2017; Palva et al., 2018; Sadaghiani et al., 2022; Tewarie et al., 2016), there are diverse connectivity measures relating instantaneous phase-phase, or amplitude-amplitude, or phase-amplitude, but their joint analysis requires a dedicated paper). In addition, it is also important to remember that there are still considerable theoretical challenges to tackle for the study of multilayer functional networks, especially when analyzing real-world data, such as the definition of appropriate null models to avoid mapping spurious connectivity patterns or the quantification of topological descriptors under uncertainty and stochastic conditions (De Domenico, 2017; Raimondo & De Domenico, 2021). In this paper, because a rigorous network analysis was falling out of our scope, we did not attempt to quantify the statistical significance of either our topological descriptors or our functional connectivity scores.

As a final note and related to the illustrations provided in Section 2.4.1 of Chapter 2, the frameworks of time-resolved and dynamic functional connectivity analysis (e.g., see (Heitmann & Breakspear, 2018; Preti et al., 2017)) are best suited to characterize our network model given the non-stationary nature of $\mathrm{Glu_e}$ and $\mathrm{GABA_e}$ over short time windows. Besides, with slight variations in parameter constraints, our network model no longer satisfies the trivial mappings between $(\omega_{\mathrm{Glu}}; \omega_{\mathrm{GABA}})$ and $(\mathrm{Glu_e}; \mathrm{GABA_e})$ as elaborated in Section 3.13.1. In this case, transitions between states may occur across different temporal scales and a static analysis would be misleading. In a real-world setting, transitions between states, as provided in our model through neurotransmission and gliotransmission, could be linked to various phenomena such as tasks, physical activity, circadian rhythmicity, sleep, etc. Those are considerations that we will include in our future studies.

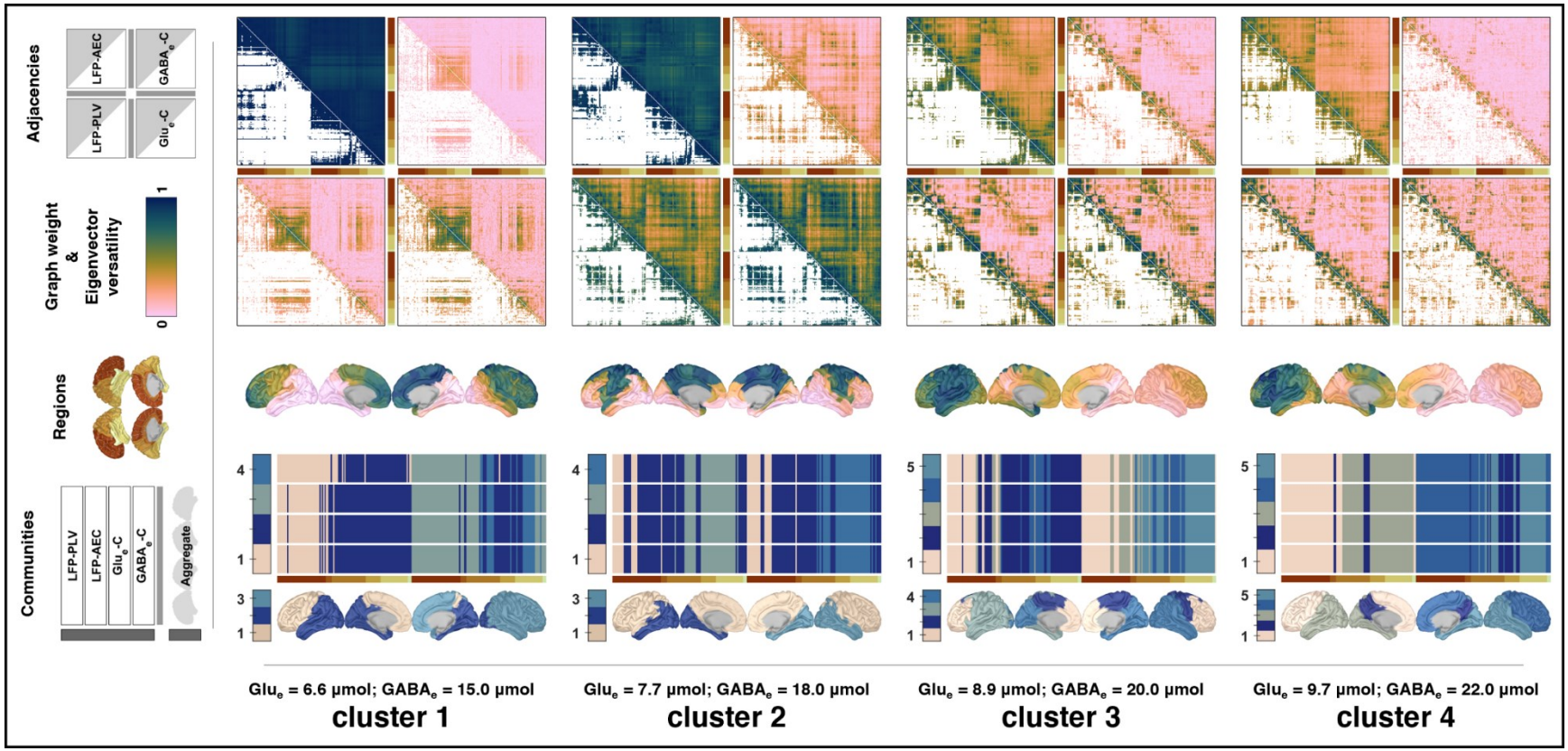

Figure 3.23. Mean multilayer functional networks for four simulations. Each simulation can be identified by its whole-brain (Glu_e; $GABA_e$) levels. Three distinct pieces of information are represented: adjacency matrices (the matrices on the top), eigenvector versatilities (the brain maps in the middle), and communities (the heatmaps and brain maps on the bottom). For each simulation, there are four adjacency matrices, each corresponding to one functional layer (i.e., LFP-PLV, LFP-AEC, Glu_e-C, or $GABA_e$-C) as indicated on the legend schematic on the top left. A thresholded version of each functional layer (retaining 25 percent of their highest weights) is displayed on the lower diagonal portions (i.e., exactly as analyzed in this paper). Note that for the sake of conciseness, we are not showing here the full multilayer networks, which would be of dimension 4×216. Instead, we are showing only the intra-layers (i.e., the diagonal blocks of the rank-2 tensor representation of the multilayer networks), each being of dimension 216. However, we reiterate that all inter-layers were in fact identity matrices (i.e., the state nodes of a single physical node build a clique). For each simulation, there are two community profiles: one for the multilayer functional network and one for the aggregate network, as indicated on the legend schematic on the bottom left. For each community profile, the number and colour of communities are indicated by colour bars. For both the adjacency matrices and community profiles, the parcellation and regions are shown following the conventions specified in Section 3.11.

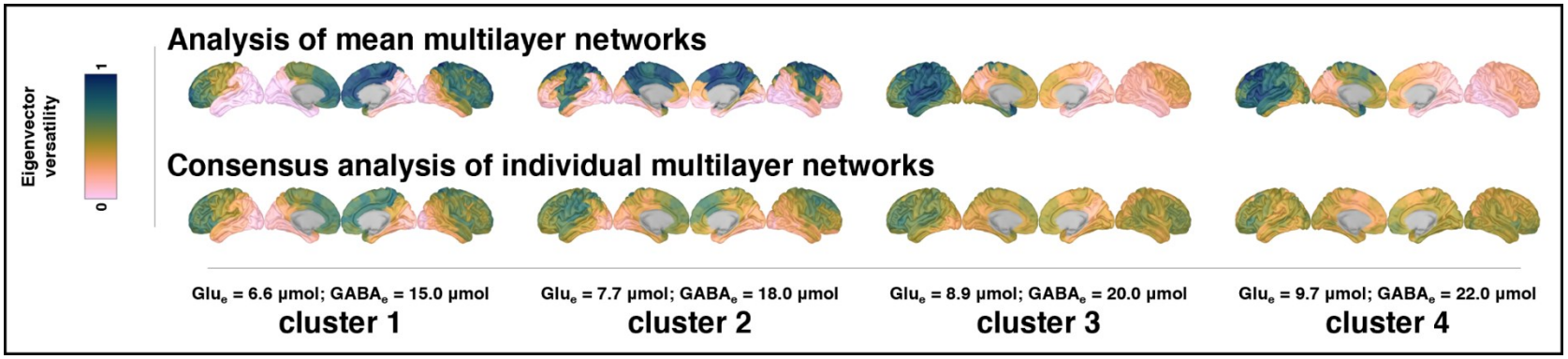

Figure 3.24. Effects of connectome-averaging on eigenvector versatilities for four simulations. Each simulation can be identified by its whole-brain (Glu_e; $GABA_e$) levels. The first row is the same as in Figure 3.23 which was obtained by estimating eigenvector versatilities on mean multilayer networks. The second row was obtained by performing consensus analysis on the multilayer eigenvector versatilities obtained across simulation batches.

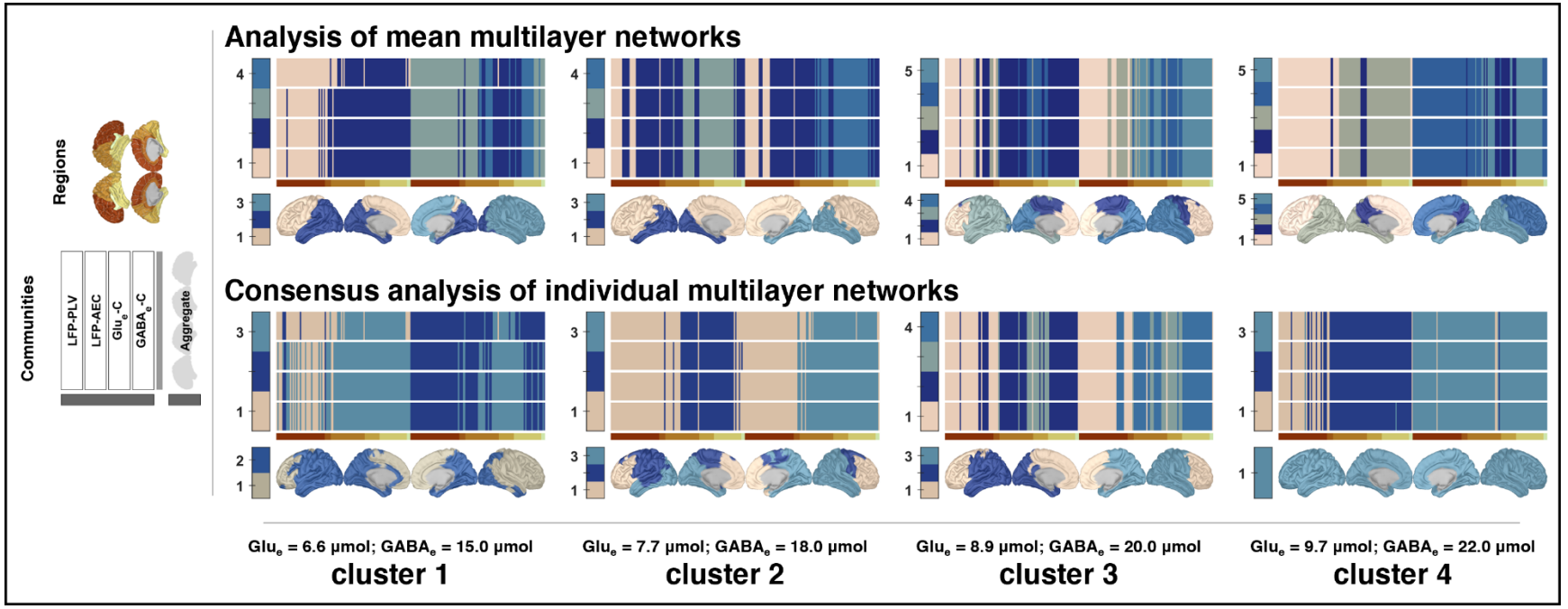

Figure 3.25. Effects of connectome-averaging on community detections for four simulations. Each simulation can be identified by its whole-brain (Glu_e; $GABA_e$) levels. For each simulation, there are two community profiles: one for the multilayer functional network and one for the aggregate network, as indicated on the

legend schematic on the left. For each community profile, the number and colour of communities are indicated by colour bars. The parcellation and regions are shown following the conventions specified in Section 3.11. The first row is the same as in Figure 3.23 which was obtained by performing multilayer community detections on mean multilayer networks. The second row was obtained by performing consensus clustering on the multilayer communities obtained across simulation batches.

3.14.4 Structural reducibility analysis of multilayer functional networks

One important observation was the fact that $\mathrm{Glu_e}$ and $\mathrm{GABA_e}$ connectivity (or activity) patterns were highly similar across simulations (e.g., see Figure 3.16.c). The analysis of the structural reducibility of a multilayer network (De Domenico, Nicosia, et al., 2015) allows us to find layers that provide redundant topological information, suggesting how to merge some layers with other ones, to obtain an optimal multilayer network.

Figure 3.26.a shows reducibility scores (i.e., indexing the distinguishability level of a network from its aggregate counterpart) graphed against whole-brain levels of $\mathrm{Glu_e}$ and $\mathrm{GABA_e}$. We observed that local maxima coincided with cluster #2 determined in Figure 3.22.a. Figure 3.26.b shows (average) optimal number of layers after reducibility operations graphed against whole-brain levels of $\mathrm{Glu_e}$ and $\mathrm{GABA_e}$, and it illustrates our discourse in the *Main Text*, where we summarized the results of structural reducibility by reporting the number of layers merged across simulations. For example, we understand from Figure 3.26.b that no layers were merged (i.e., they did not have redundant topological information) for a relatively large number of simulations (i.e., the optimal number of layers is about four), while three layers out of four (in fact all correlation layers) were merged (i.e., they had redundant topological information) for the simulations where the network model behaved *homogeneously* (i.e., below the first contour, as elaborated in Section 3.13.2). We also understand from Figure 3.26.a–b that the simulations of cluster #2 compared to the other clusters underlay networks that were both maximally distinguishable from their aggregate counterparts and without redundant topological information (i.e., there was virtually no merging between layers). This is consistent with the fact that we expected critical dynamical network behaviours within cluster #2 (as elaborated throughout Sections 3.13.2, 3.14.2, and 3.14.3).

Figure 3.27 shows that all our conclusions obtained from performing the analysis of the full networks remained mostly unchanged after reducibility operations (i.e., reducibility operations preserved essential topological features). We can observe that the global topological properties of reduced networks are highly similar to those of the full networks (as shown in Figure 3.5 of the *Main Text*), and therefore consistent with the clustering results that we interpreted in the *Main Text* and in Section 3.14.2. For example, within cluster #1, the networks were found to depict medium segregation levels, lowest integration levels, medium edge redundancy levels, and medium community detection quality levels. Within cluster #2, the networks were found to depict maximum segregation and integration levels, medium-to-high edge redundancy levels, and highest community detection quality levels. Far from cluster #2, the networks were found to depict decreasing segregation, integration, and edge redundancy levels, as well as decreasing community detection quality levels. The decreases were larger the further away from cluster #2.

Altogether, Figure 3.26 and Figure 3.27 suggest that functional networks exhibit optimal properties when the network model operates at a critical dynamical border (here determined by limit cycle peak–peak amplitudes as elaborated throughout Section 3.13.2).

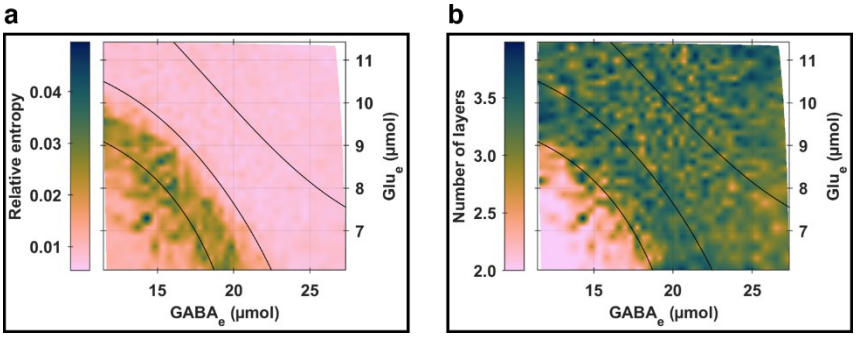

Figure 3.26. Structural reducibility analysis of multilayer functional networks. The relative entropy in (a) indexes the distinguishability level of an optimally reduced multilayer network from its aggregate counterpart where higher values connote networks whose layers provide less redundant topological information. The optimal number of layers after reducibility operations in (b) were obtained by averaging across simulation batches. The black solid curves in each graph represent contours of limit cycle E_{Pyr} peak–peak amplitudes. The contours are the same as in Figure 3.3.*b* of the *Main Text* to facilitate juxtapositions with clustering analysis results of network connectivity measures. Each contour passes through one of the following $(\mathrm{Glu_e}; \mathrm{GABA_e})$ coordinates in (μmol) × (μmol): (8.5; 14.0), (8.50; 18.25), or (9.5; 21.0).

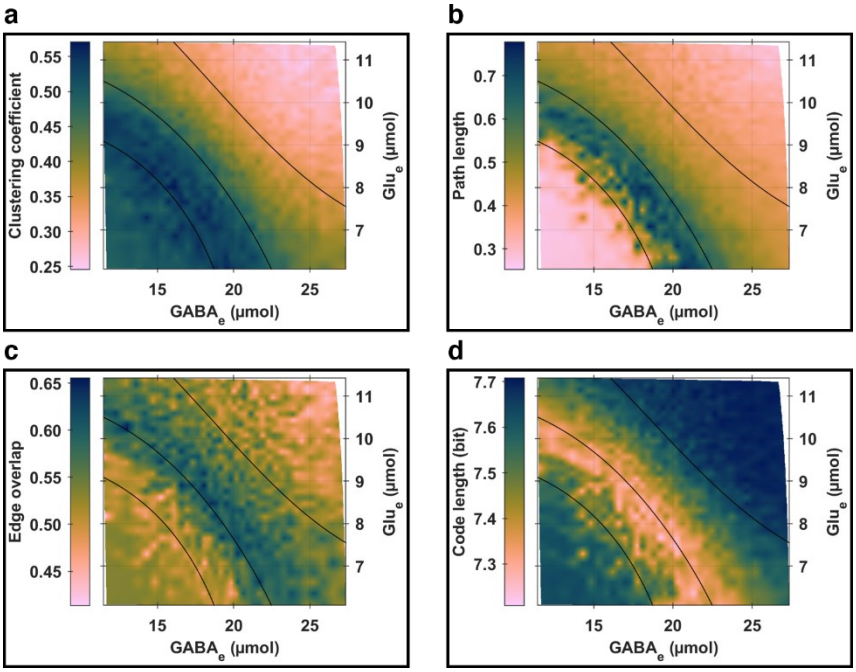

Figure 3.27. Global topological properties of reduced multilayer functional networks. The properties are graphed as functions of whole-brain levels of $\mathrm{Glu_e}$ (y-axis) and $\mathrm{GABA_e}$ (x-axis): (a) clustering coefficient (an index of network segregation where higher values connote more segregated networks), (b) path length (an index of network integration where higher values connote more integrated networks), (c) edge overlap (an index of edge redundancy where higher values connote more similar weight patterns across layers), and (d) code length (a quality index of community detection where lower values connote networks with more optimal data compression of a random walker's movements on them). The black solid curves in each graph represent contours of limit cycle E_{Pyr} peak–peak amplitudes. The contours are the same as in Figure 3.3.*b* of the *Main Text* to facilitate juxtapositions with clustering analysis results of network connectivity measures. Each contour passes through one of the following $(\mathrm{Glu_e}; \mathrm{GABA_e})$ coordinates in (μmol) × (μmol): (8.5; 14.0), (8.50; 18.25), or (9.5; 21.0).

Chapter 4 A neuron-glial perspective of MEG connectomics — establishing a biologically plausible computational framework to guide and evaluate empirical methodologies

4.1 Thesis storyline

This chapter marks the first of two segments dedicated to neuroimaging applications, building upon the previously introduced biophysical model that elucidates whole-brain neuron-astrocyte network dynamics. Here, the coupling of neuronal and astrocytic networks through glutamatergic and GABAergic transmission systems is pivotal. Our objective is to shed light on the role of astrocytic networks in the non-invasive electrophysiological reconstruction of resting-state functional networks, thereby proposing a biologically plausible computational framework aimed at enhancing and evaluating empirical approaches within whole-brain electrophysiological connectomics.

To appreciate the emphasis on electrophysiological connectomics, it is pertinent to revisit a key discovery from the previous chapter. A crucial insight from our earlier work highlighted the interplay between glutamatergic and GABAergic neurotransmissions, and the dynamics of neuronal membrane potentials within the alpha frequency band (8–13 Hz). We posited that the nuanced balance of excitatory and inhibitory neurotransmitter dynamics, governed by the intricate interplay of neuron-astrocyte uptake and release mechanisms, plays a modulatory role in neuronal membrane potential dynamics. Notably, our in-depth analysis of whole-brain network activity and functional connectivity revealed that neurotransmitter dynamics could statistically explain fluctuations in the amplitude envelope of neuronal membrane potential dynamics.

Building on this pivotal discovery and leveraging insights from empirical multimodal neuroimaging research, we felt compelled to confront our model's predictions to empirical electrophysiological findings. Moreover, we sought to explore the intricate relationships between these findings and other functional neuroimaging approaches, most notably BOLD fMRI. This inclination towards electrophysiology is driven by its more immediate applicability in our network model, unlike neurotransmitter dynamics which remain elusive at the whole-brain scale in humans. A well-recognized example of the interconnection between different neuroimaging modalities is the established correlational links between electrophysiological activities and hemodynamic changes, a topic frequently cited in the field.

Over the last decade, a significant observation has been the concordance of network patterns found in the band-limited amplitude envelopes of MEG rhythms, particularly within the alpha and beta (13–30 Hz) bands, with those identified in BOLD fMRI rhythms (Brookes et al., 2011; Hipp et al., 2012; Sadaghiani et al., 2022). This discovery was groundbreaking, establishing a multimodal bridge between non-invasive electrophysiological connectomics and the established domain of fMRI connectomics, and underscoring the relevance of whole-brain MEG analyses in understanding functional connectivity patterns (Sadaghiani et al., 2022).

In parallel, within a distinct yet lesser-known research community, numerous studies have argued that fMRI signals, which include but are not limited to the BOLD signal, cannot solely be interpreted through neuronal activity (Figley & Stroman, 2011; Lu et al., 2019; Magistretti & Allaman, 2015; Schaeffer & Iadecola, 2021). These findings suggest the necessity for a more

encompassing theory that integrates glial signaling to accurately describe the mechanisms behind fMRI signal generation.

Collectively, these insights motivated our previous work to propose that our neuron-astrocyte whole-brain modeling approach could pioneer the exploration of neuron-glial regulatory mechanisms governing glutamatergic and GABAergic transmissions. We argue these mechanisms are crucial for the empirically observed associations between MEG and BOLD signals. We emphasized the existence of a biochemical foundation, carefully orchestrated by neuron-astrocyte networks, for these empirical correlational relationships. We posited that a neuron-glial perspective is essential for unraveling the intricate mechanisms at play.

Thus, it is anticipated that our whole-brain model will generate outputs that, to some extent, mirror empirical electrophysiological data like MEG or EEG, provided that current electrophysiological forward and inverse models are suitable. These models typically involve defining an electromagnetic lead field model to transform the aggregated membrane potentials of neuronal populations, represented as intracellular current dipoles (i.e., sources), into observable data at the electrode level; or its dual, i.e., formulating a source reconstruction model to estimate neuronal sources from the observed electrode-level data; or both (Sadaghiani et al., 2022).

For the purpose of this chapter, we will primarily address the topic of fitting MEG data, leaving the integration of BOLD fMRI data for later discussion, to simplify our focus on electrophysiology. To this end, we assume that neuronal and astrocytic activities are sufficiently coupled to make current electrophysiological forward models viable. This assumption, which implicitly frames astrocytes as *passive* components within prevailing head tissue conductivity models, is contentious due to astrocytes' dynamic impact on neuronal field potentials at the brain mesoscales and macroscales (De Pittà & Berry, 2019; Kastanenka et al., 2020; Verkhratsky & Nedergaard, 2018). Nevertheless, this simplification is a necessary compromise for the model's practical use and partial validation, considering the absence of techniques to simultaneously record neuronal and glial activity across the whole brain (De Pittà & Berry, 2019; Kastanenka et al., 2020). Moreover, this stance acknowledges the complexity of brain tissue modeling and the active research dedicated to developing more sophisticated models that incorporate a richer array of tissue characteristics (Antonakakis et al., 2019; Coquelet et al., 2020; McCann et al., 2019; Morales et al., 2018; Stenroos & Nummenmaa, 2016; Unal et al., 2021; Vorwerk et al., 2014).

Our methodology in the previous chapter already adopted this assumption, expressing it mathematically as a dynamic balance where neurotransmitter uptake and release rates equilibrate, portraying glutamatergic and GABAergic dynamics as mean quasi-stationary slow fluctuations.

Under this framework, one might anticipate a straightforward mapping between our model's outputs and empirical electrophysiological data, given the previous successes of Jansen–Rit-based whole-brain models in approximating empirical observations (Griffiths et al., 2022). Our model's neuronal compartment is mathematically equivalent to these models once the criterion of stationary neurotransmitter dynamics is applied.

However, the reality of source-level analysis in non-invasive electrophysiological data, particularly in the domain of resting-state studies, is fraught with inherent challenges (B. He et al., 2018; Palva et al., 2018; Sadaghiani et al., 2022). These complexities render the mapping between model outputs and empirical data less clear-cut, even when employing neuronal-only or phenomenological whole-brain models. The task is especially daunting when attempting to match

model outputs with empirical data based on the fit of functional network connectivity patterns (B. He et al., 2018; Palva et al., 2018; Sadaghiani et al., 2022).

For instance, the accuracy of source-level functional network reconstruction techniques in capturing true functional network patterns remains uncertain, even within the basic spectral range of 1–100 Hz, despite the potential for frequencies up to 1000 Hz (B. He et al., 2018; Palva et al., 2018; Sadaghiani et al., 2022). The primary hurdles in assessing these reconstruction techniques include the spatial resolution limitations and signal leakage common to non-invasive electrophysiological measurements, along with the inevitable methodological decisions required in the activity and connectivity reconstruction processes (B. He et al., 2018; Palva et al., 2018; Sadaghiani et al., 2022). These issues highlight the lack of standardized analytical approaches in electrophysiological connectomics research (Meunier et al., 2020; van Diessen et al., 2015).

However, we propose that a significant part of the challenge also lies in developing a robust simulation framework that allows for a comprehensive evaluation of these source-level functional network reconstruction methods. Despite some efforts, existing frameworks have been limited in their conceptual depth. Addressing this gap is a key aim of our work.

As we will outline, the task of evaluating source-level functional network reconstruction methods is both a recent area of scientific investigation and an exciting opportunity to highlight the neuron-glial modelling perspective. It is important to note that these evaluations, while related, are distinct from the assessments of whole-brain computational models' capacity to replicate empirical functional connectivity patterns; a field that constitutes its own area of research, which we will also briefly discuss.

4.2 Abstract

This physiologically constrained simulation study evaluates the performance of traditional MEG source-level functional network reconstructions across multiple spatial resolutions, using both a linear (weighted minimum norm, MN) inverse operator, and a non-linear (wavelet-based maximum entropy on the mean, MEM) one able to accommodate biological priors. Focusing on the intricate neuron-astrocyte interactions within whole-brain resting-state dynamics, our computational neural mass network model integrates astrocytic structural and functional constraints to provide a more biophysically plausible framework for network analysis. Utilizing the MEG setup from the Human Connectome Project for nine subjects, we explore the consistency and precision of MEG network reconstructions in simultaneously capturing phase and amplitude coupling patterns, summarized in a multilayer network model, across four spatial resolutions informed by the Schaefer-Yeo atlases. Our comprehensive analysis, encompassing macro-scale and micro-scale multilayer network properties, reveals that MN reconstructions slightly outperform MEM, especially at finer dipolar resolutions. However, the effectiveness of these reconstructions is heavily dependent on the use of appropriate priors for inverse operator parameters, challenging standard practices in the field. We observe that the accuracy of network reconstructions is influenced by various factors, including resolution, connectivity measures corrected or not for zero-lag synchronization, and the underlying network dynamics. A notable finding is the critical role of biological priors, such as the brain's geometrical structure, in enhancing the fidelity of reconstructions at micro-scales. This underscores the importance of selecting inverse operators based on their ability to integrate such priors rather than solely on their comparative performance. Additionally, our study suggests that optimal connectome densities can significantly improve reconstruction accuracy, pointing towards methodological advancements for

high-resolution electrophysiological data analysis. This research advocates for a nuanced approach to electrophysiological network reconstruction, emphasizing the integration of neuron-glial perspectives and the consideration of brain geometry. By addressing current methodological limitations and opportunities, our findings contribute to advancing network reconstruction techniques and deepening our understanding of brain dynamics.

4.3 Introduction

Astrocytes, a major type of glial cells, are organized into networks primarily connected by gap junctions that facilitate intercellular communication. Their anatomical positioning in relation to neurons is strategically optimized to enhance functional interactions, such as those mediated by glutamatergic and GABAergic transmission systems (De Pittà, 2020; De Pittà & Berry, 2019; Fields et al., 2015; Kastanenka et al., 2020; Poskanzer & Yuste, 2011, 2016; Vasile et al., 2017; Verkhratsky & Nedergaard, 2018). Despite evidence indicating that astrocytic networks can decode and modulate neuronal network activities, as well as respond independently of neuronal activity changes, astrocytes often remain underrepresented in discussions surrounding electrophysiological studies, particularly in non-invasive human studies using techniques like EEG or MEG (De Pittà, 2020; De Pittà & Berry, 2019; Fields et al., 2015; Kastanenka et al., 2020; Poskanzer & Yuste, 2011, 2016; Robertson, 2018; Vasile et al., 2017; Verkhratsky & Nedergaard, 2018).

Foundational texts like “Niedermeyer’s Electroencephalography” acknowledge the diverse cellular contributions to brain electrophysiology, glial cells included (Amzica & Lopes da Silva, 2017). Yet, the bulk of EEG and MEG research remains focused on neuronal activities, often relegating the role of non-neuronal cells to brief mentions (Baillet, 2017; Biasiucci et al., 2019; Gross, 2019; F. Lopes da Silva, 2013, 2022; Okada, 2020; Wadman & Lopes da Silva, 2017; Wendling & Lopes da Silva, 2017). This neuron-centric view persists despite acknowledgments that EEG and MEG signals encapsulate contributions from neurons, glia, and even blood vessels (Buzsáki, 2009; Buzsáki et al., 2012; F. Lopes da Silva, 2022; Okada, 2020; Robertson, 2018; Wadman & Lopes da Silva, 2017; Wendling & Lopes da Silva, 2017). The emphasis on neuronal dynamics is partly due to these techniques’ sensitivity to electrical activities of neurons and is exacerbated by current technological limitations, which hinder simultaneous monitoring of both neuronal and glial activities across the entire brain (De Pittà, 2020; De Pittà & Berry, 2019; Fields et al., 2015; Kastanenka et al., 2020; Poskanzer & Yuste, 2011, 2016; Vasile et al., 2017).

However, glial cells gain prominence in research concerning neurological disorders and in investigations at the cellular and assembly levels, where their contributions to neural circuit functionalities and dysfunctions are more thoroughly examined (Amhaoul et al., 2014; Brazhe et al., 2023; Devinsky et al., 2013; Obenaus, 2013; Purnell et al., 2023; Vezzani et al., 2022; Volman & Bazhenov, 2019). This discrepancy underscores the need for advancing research methodologies to capture the comprehensive roles of both neuronal and glial populations in brain electrophysiology, promoting a more holistic understanding of neural network operations.

This chapter explores the mapping of whole-brain functional connectivity through non-invasive electrophysiological imaging, a field also known as *connectomics* (Sadaghiani et al., 2022). It aims to broaden the traditional neuronal-centric view by incorporating neuron-astrocyte network dynamics into the analysis of electrophysiological data (De Pittà & Berry, 2019; Kastanenka et al., 2020; Robertson, 2018). Unlike the direct graphical mapping achievable with BOLD fMRI, whole-brain imaging in non-invasive human electrophysiology relies on inverse modeling, or

reconstruction, of data from EEG or MEG (Baillet, 2017; B. He et al., 2018). This thesis chapter specifically harnesses MEG to propose and examine novel hypotheses regarding the potential interplay between astrocytic networks and neuronal circuits, and how this interaction influences the resting-state functional networks reconstructed from MEG data.

Our objective is to critically evaluate the fidelity of existing MEG source-level functional network reconstruction techniques in capturing the intricate and biologically plausible dynamics of our computational model of whole-brain resting-state networks, with a particular focus on neuron-astrocyte interactions manifested through amplitude and phase synchronizations. The typical reconstruction process adopts a sequential method, starting with solving the inherently ill-posed inverse problem to obtain time-series data, followed by constructing functional networks from these time-series.

Our aim is to *establish a biologically plausible computational framework that can rigorously test and refine empirical electrophysiological connectomics approaches*. This initiative is part of a broader research agenda aimed at integrating our biophysical whole-brain model with real-world data, employing optimized electrophysiological connectomics techniques, even if this integration remains partial at this stage. We also explore how adopting a neuron-astrocyte perspective augments the modeling process by factoring in the brain's geometrical structure. This consideration allows us to account for fundamental structural constraints that extend beyond neuronal fiber connectivity (Pang et al., 2023). Furthermore, we utilize multilayer network modeling to coherently integrate different types of functional interactions (De Domenico, 2017), particularly those characterized by amplitude and phase coupling measures, and apply dynamic systems theory to elucidate the various modes of dynamic interactions between astrocytic and neuronal networks within our model. The ensuing sections will detail how these methodological advancements significantly improve our understanding of source-level functional network reconstruction within a simulated environment, underpinned by our computational model of neuron-astrocyte network interactions.

Our methodology unfolds in two primary stages: the simulation of α-band MEG activity and the subsequent evaluation of network reconstructions.
Simulation of α-band MEG activity — We initiate our study by simulating α-band MEG activity across 248 electrodes, employing a distributed source model that spans the entire cortical surface. This is done at five different resolutions, involving 100, 200, 300, 400, and 8,000 dipoles, respectively. The simulation aims to reflect complex amplitude and phase interactions within neural networks. These interactions are influenced by three core principles governing network community organization: (i) we use the Yeo-7 BOLD fMRI resting-state network atlas (Schaefer et al., 2018; Yeo et al., 2011), to encourage functional integration within distinct neural communities; (ii) we incorporate neuronal constraints derived from diffusion-MRI data to enhance functional integration between different neural communities; and (iii) we apply astrocytic constraints that are informed by the brain's cortical folding patterns, which introduces deformations in functional integration within communities to ensure alignment with the brain's geometric structure.
Evaluation of network reconstructions — The second stage involves a systematic evaluation of the reconstructed networks. We aim to meticulously compare these reconstructed networks with the original (ground-truth) source-level functional networks. This comparison takes into account the effects of different inverse operators and connectivity measures used in the reconstruction process: (i) for inverse modelling, we employ two distinct MEG inverse operators, including a linear

operator, the weighted minimum norm (wMN) (M. S. Hämäläinen & Ilmoniemi, 1994; B. He et al., 2018), and a non-linear operator, the wavelet-based maximum entropy on the mean (wMEM) (Afnan et al., 2023; Lina et al., 2014); and (ii) for quantifying connectivity, we apply four connectivity measures (Palva et al., 2018), comprising, for phase coupling, the phase locking value (PLV) and the weighted phase lag index (wPLI), and for amplitude coupling, the amplitude envelope correlation (AEC) and orthogonalized amplitude envelope correlation (oAEC).
By structuring our methodology in this manner, we aim to provide a flexible framework for simulating and evaluating the dynamics of neural networks, with a particular emphasis on the integration of neuron-astrocyte interactions and the geometric constraints of the brain's structure.

Evaluating source-level functional network reconstruction schemes is a dynamic area of research. A compelling illustration of this is provided by two studies published in 2023 by (Vallarino et al., 2023) and (Allouch et al., 2023), which collectively advance our understanding of the complexities involved in reconstructing functional brain networks in non-invasive electrophysiology, pointing to the critical role of methodological choices and the potential for optimization beyond standard software capabilities.
Study by Vallarino and colleagues — (Vallarino et al., 2023) expanded upon the work of (A. S. Hincapié et al., 2016), employing a more nuanced simulation framework. This study meticulously examined the wMN Tikhonov regularization parameter to enhance the reconstruction of functional connectivity patterns. The analysis focused on the cross-power spectrum, imaginary part of coherence, corrected imaginary part of PLV, and wPLI. The research utilized a single-subject MEG setup with 102 sensors and a multivariate autoregressive model to simulate neuronal activity. Their strategy featured a distributed source model with 6940 dipoles to simulate spectral coherence patterns between two regions of interest, under various conditions including changes in regional spatial extents, locations, and coherence levels, as well as different signal-to-noise ratios at both source and sensor levels. The study relied on seed-based connectivity mappings to reconstruct functional patterns. A key finding was that the optimal parameters for reconstructing activity and connectivity differ significantly, with the optimal values for each being orders of magnitude apart. Upon reviewing their work, we also noted a discrepancy between their optimal reconstruction parameters and the default settings recommended by widely used electrophysiological software like *Brainstorm* (Tadel et al., 2011), *FieldTrip* (Oostenveld et al., 2011), and *MNE-Python* (Gramfort et al., 2013). This gap underscores the need for external optimization schemes, beyond the built-in functionalities of these tools, for improved connectivity reconstruction.
Study by Allouch and colleagues — The study conducted by (Allouch et al., 2023) builds upon previous research by (Hassan et al., 2014), examining the influence of EEG channel density, inverse solutions, and functional connectivity measures on the accuracy of network reconstructions. The authors explored the effects of varying EEG channel densities (19, 32, 64, 128, 256), employing three inverse solutions (wMN, exact low-resolution brain electromagnetic tomography, and linearly constrained minimum variance beamforming), and assessing four functional connectivity measures (PLV, PLI, AEC, and oAEC). Utilizing a neural mass network model constrained by empirical diffusion MRI-derived connectomes, the researchers simulated whole-brain neuronal dynamics. Their distributed source model comprised 66 dipoles, focusing on amplitude and phase couplings within the default mode network (with six dipoles) or the dorsal attention network (with six dipoles), separately. The findings suggest that higher EEG channel densities generally improve connectivity reconstruction fidelity, particularly beyond 64 channels. However, variations in analytical choices, such as the selection of inverse solutions or connectivity measures, introduced significant variability in connectivity reconstructions. The study did not

recommend specific analytical approaches outside particular contexts, and it relied on the default settings of popular electrophysiological software for connectivity reconstructions.

Considering these recent studies, it becomes evident that the field of source-level functional network reconstruction is fraught with unresolved challenges, as highlighted by the authors themselves. These challenges persist both in simulation techniques and in the reconstruction methodologies. While these studies offer valuable insights for methodologists (most notably, the potential of reconstruction schemes to capture meaningful connectivity patterns despite inherent biases), they represent divergent approaches within non-invasive electrophysiological connectomics. This divergence often leads to confusion among experimental researchers. Moreover, the continuous introduction of new inverse operators and connectivity metrics, each purporting significant advancements over predecessors, exacerbates the lack of standardization in the field. This situation frequently results in inconsistent findings across studies, underscoring the pressing need for consensus and uniformity in methodological approaches.

However, certain trends are becoming increasingly prominent.
Simulation trends. — Employing biophysical whole-brain models emerges as a particularly effective approach for evaluating empirical reconstruction techniques (Breakspear, 2017; Griffiths et al., 2022; Næss et al., 2021). These models encapsulate our biological understanding of the brain comprehensively, being both informed by empirical data and capable of scaling in complexity (Breakspear, 2017; Griffiths et al., 2022). Their utility has grown to the extent that they are now a cornerstone in neuroimaging research, often employed alongside real-world experiments (Breakspear, 2017; Griffiths et al., 2022). Furthermore, the last two decades have seen the development of numerous software packages and tutorials aimed at both methodologists and experimental researchers (Sanzleon et al., 2013). These resources have democratized access to whole-brain biophysical models, which, despite their mathematical complexity (e.g., non-linearities, large number of variables and parameters and their interdependencies, …), remain practical for research applications. This includes models that are more mathematically sophisticated than the one utilized in our study, yet still tractable.
Reconstruction trends. — (i) The wMN inverse operator continues to serve as a standard benchmark for evaluating other operators, a trend that persists despite its longstanding presence in the field, as evidenced by recent studies like (Vallarino et al., 2023) focusing on wMN. (ii) In resting-state studies, distributed source models are the preferred choice for dissecting the spatiotemporal dynamics of electrophysiological data. These models typically define a large number of sources, ranging from 4,000 to 164,000 per hemisphere (for a reference, see https://www.fieldtriptoolbox.org/tutorial/sourcemodel/), to ensure comprehensive coverage of the brain volume or cortical surface. This approach, while contributing to the inverse problem's complexity, remains a tractable and widely accepted practice (B. He et al., 2018). (iii) Graph theoretical methods are increasingly recognized as effective for exploring resting-state network dynamics. This approach circumvents potential neuroanatomical misinterpretations and leverages a robust theoretical foundation capable of accommodating various spatiotemporal scales with minimal assumptions (Bassett & Sporns, 2017; Palva et al., 2018). Functional interactions are commonly analyzed between regions defined by anatomical or functional parcellations, with resolutions typically ranging from one hundred to several hundred regions (Palva et al., 2018; Sadaghiani et al., 2022). This balance reflects the spatial resolution constraints of standard EEG or MEG setups and the requirements for resolving the brain's large-scale resting-state networks. (iv) Phase and amplitude coupling measures are widely adopted for quantifying functional

interactions within the brain (Palva et al., 2018; Sadaghiani et al., 2022). It is crucial to understand that these interactions are often interdependent, necessitating a combined analysis to fully capture their dynamics, despite the fact that examining them individually can still yield meaningful biological insights (Palva et al., 2018). To address the complexity of these interactions, multilayer network modeling has been introduced as an effective framework (Brookes et al., 2016; De Domenico, 2017; Vaiana & Muldoon, 2020). This approach transcends the mere aggregation of different connectivity graphs, such as one layer for PLV and another for AEC, by explicitly modeling the interactions between these layers. This enables the exploration of cross-frequency, cross-measure, and cross-modality functional interactions, offering significant insights into the intricate nature of electrophysiological connectomics. (v) The presence of instantaneous field spread and volume conduction introduces spurious correlations, complicating the accurate estimation of phase and amplitude couplings. These artifacts present themselves in two forms: zero-lag correlations, which can be mitigated by measures like the wPLI or oAEC, and *ghost* interactions, which are false positive connections in the vicinity of true interactions but for which no definitive solution exists yet. Consequently, a comprehensive approach that incorporates multiple connectivity measures, both sensitive and insensitive to zero-phase-lag interactions, is advocated (Palva et al., 2018). This strategy allows for a more reliable interpretation of connectivity patterns, acknowledging the limitations and strengths of each measure. This approach represents a significant advancement from previous practices in non-invasive electrophysiology, which overly relied on specific measures to avoid false positives, without recognizing the inherent complexity of phase and amplitude interactions in brain connectivity.

In this chapter, we embrace the current trends in the field and extend the research summarized earlier (along with additional studies discussed later) by simulating biologically plausible functional patterns of neuron-astrocyte interactions across the whole brain. We place a special emphasis on the influence of the brain's geometric structure and fiber connectivity, recognizing their critical roles in shaping the electrophysiological dynamics that govern complex phase and amplitude network interactions. A detailed introduction to the significance of the brain's geometrical embedding in our model is provided in the *Methods* section as we describe our simulation approach.

4.4 Methods

4.4.1 Neuron-astrocyte mass network model

Our biophysical whole-brain model has been delineated in previous chapters. In summary, the model conceptualizes each node within the network as a mesoscopic cortical region, encapsulated by a mass model comprising four densely interconnected neural subpopulations: glutamatergic pyramidal neurons, GABAergic inhibitory interneurons, excitatory interneurons, and astrocytes. In this model, glutamatergic pyramidal neurons are positioned at the forefront, integrating feedback from both excitatory and GABAergic inhibitory interneurons via synaptic firing. It is posited that the aggregate of excitatory and inhibitory postsynaptic potentials at these pyramidal cells constitutes the principal source of electrophysiological signal that can be recorded at the macroscale by MEG. Moreover, the model posits a dynamic interplay where pyramidal and inhibitory neurons are subject to modulation by astrocytic feedback via glutamatergic gliotransmission. This interaction stimulates neurotransmitter release into the extracellular milieu, influencing the excitability of both pyramidal and inhibitory neurons. Notably, while extracellular glutamate modulates the excitability of both neuron types, GABA specifically affects pyramidal neurons. The neurotransmitter dynamics, including uptake mechanisms by pyramidal neurons,

inhibitory neurons, and astrocytes, are meticulously accounted for, ensuring neurochemical equilibrium. On a broader scale, the model encapsulates macroscopic network connectivity, with pyramidal neuron interconnections across regions depicted via white-matter tracts, and astrocytic connectivity modeled through gap junction densities, indicative of a syncytial organizational pattern. The governing equations of the model can be found in Section 2.2 in Chapter 2.

4.4.2 Structural layers

In this study, empirical MRI data were employed to derive the interconnection matrices for neuronal and astrocytic networks, building upon the approach outlined in the preceding chapter. This time, connectivity estimates for both matrices were constrained by Schaefer-7 functional atlases (Schaefer et al., 2018), incorporating 100, 200, 300, and 400 cortical regions. These regions are intrinsically organized into 7 functional networks as identified by (Yeo et al., 2011), enabling a detailed exploration of the impact of spatial resolution on network connectivity.

The neuronal interconnection matrix, representing synaptic connectivity among pyramidal neurons, was derived from a state-of-the-art tractography-based connectome reconstruction pipeline (Schiavi et al., 2020; St-Onge et al., 2018; Theaud et al., 2020) applied to diffusion and structural MRI data from nine subjects in the Human Connectome Project Young Adult dataset (Glasser et al., 2013; Van Essen et al., 2013). This matrix reflects an anatomical and microstructural measure of neuronal connectivity strength.

The astrocytic interconnection matrix was constructed to reflect the brain's cortical surface geometry, based on a high-resolution tessellation of the cortical mid-surface derived from the same dataset.

To manage computational demands and reduce sources of variabilities in our statistical analyses, we computed single representative matrices for both pyramidal neurons and astrocytes by averaging across the subject cohort, as done in the preceding chapter. These matrices underwent normalization to ensure their right-stochastic properties. The network model parameters were carefully selected to produce simulations that remain consistent across different parcellation sizes, with further elaboration on these adjustments provided in subsequent sections.

4.4.3 Constraining dynamical regimes

In this study, the model's outputs were constrained using a biologically plausible parameterization, as detailed in preceding chapters (e.g., Section 3.8.1 in Chapter 3). This parameterization was derived from a combination of bifurcation analysis of limit cycles and a consensus of physiologically realistic parameter sets sourced from existing literature. Such an approach enables our network model to generate α-band local field potential (LFP) dynamics that underpin both amplitude and phase network synchronizations, alongside depicting quasi-stationary slow fluctuations in extracellular glutamate and GABA neurotransmitter dynamics.

Crucially, this parameterization allows the model to produce consistent outputs across different parcellation sizes, primarily because it is anchored in the bifurcation analysis of a homogeneous network model. To accommodate the variability inherent in biological systems, we allowed three parameters to remain adjustable: two parameters governing astrocytic network coupling and one parameter defining the variance of the normally distributed neuronal firing rates.

We explored 27 unique sets of astrocytic network coupling parameters. These sets were categorized into two separate oscillatory regimes, corresponding to two distinct families of

periodic orbits. Specifically, one family was represented by 16 unique parameter combinations, while the other comprised 11. These dynamic regimes were selected to position the network model at critical dynamical junctures, fostering the emergence of functional networks characterized by optimal properties such as clustering coefficient, path length, and community organization. Detailed visual representations of these dynamical regimes and their implications for network functionality are provided in Section 4.8.1, which is in the *Supplementary Information* accompanying this chapter.

In this study, we introduce a novel approach by treating the variance of neuronal firing rates as a variable parameter, diverging from the methodology presented in the previous chapter. We established two distinct global variance levels to modulate the multivariate normally distributed baseline neuronal firing rates. These variance levels act as multiplicative constants applied to a spatially constraining covariance matrix, which is structured as a block diagonal matrix with unity blocks corresponding to each Yeo-7 community. This configuration serves as a functional spatial prior, offering an innovative alternative to direct manipulations of structural layers or the specification of heterogeneous nodal priors.

The utility of this functional prior is best understood by imagining a hypothetical scenario where the network model lacks structural constraints: the prescribed covariance matrix would then compel the model to generate functional networks with perfect intra-community correlations and complete inter-community orthogonality. However, given the model's incorporation of structural constraints though a two-layered network, this covariance matrix merely promotes intra-community functional integration to a certain extent, allowing the model the flexibility to either distort these patterns or foster inter-community integration.

To explore two distinct modes of network dynamics, we set the global variance levels such that in one scenario (with the standard deviation level set to 10 Hz), the baseline neuronal firing rates are marginally lower than the levels induced by neuronal network feedback (guided by the diffusion-MRI-based connectome). This setup inherently biases the model towards stronger inter-community functional integration. Conversely, in the second scenario (with the standard deviation level set to 20 Hz), the baseline firing rates exceed the feedback-induced levels, promoting enhanced intra-community integration. Consequently, the ratio between the variance of neuronal network feedback and the baseline firing rates acts as a global index to gauge the balance between functional integration and segregation. Further elaboration on this aspect and its implications is provided in Section 4.8.2 in the *Supplementary Information*.

To summarize, in this study, we constructed a total of 54 unique network configurations, divided into two distinct sets based on their functional integration patterns. The first set, comprising 27 network simulations, predominantly exhibits complex patterns of inter-community functional integration. Conversely, the second set, also consisting of 27 simulations, is characterized by intricate patterns of intra-community functional integration.

For both sets of simulations, the astrocytic structural layer, derived from empirical data on cortical folding, plays a pivotal role in modulating the intra-community functional integration patterns. This modulation occurs in a geometrically consistent manner across all 27 pairs of astrocytic network coupling parameters. Notably, the set of networks emphasizing inter-community functional integration is more significantly influenced by these geometrical constraints due to its inherent reliance on long-range neuronal projections.

Detailed visual representations and further elaboration on the network configurations and their resultant functional integration patterns are provided in Sections 4.8.1 and 4.8.2 in the *Supplementary Information* section of this chapter.

4.4.4 Simulation scheme

In the preceding section, we delineated a total of 54 distinct network configurations. For each spatial resolution across the Schaefer atlases encompassing 100, 200, 300, and 400 cortical regions, we conducted simulations of 54 reference network dynamics, also termed ground-truth networks, resulting in a cumulative total of 216 reference simulations across all resolutions.

Each simulation spanned a duration of 5 minutes, a timeframe selected to align with conventional durations in empirical studies and to provide an adequate number of data points for the reliable estimation and statistical evaluation of connectivity metrics such as AEC and oAEC. The data from these simulations were sampled at an effective frequency of 256 Hz, a rate deemed appropriate for analyses based on MEG data.

4.4.5 MEG source space and forward projection

In this study, we utilized MEG data from nine subjects selected from the Human Connectome Project dataset, as detailed in Section 4.4.2. The MEG recordings were conducted using a whole-head MAGNES 3600 system (4D Neuroimaging, San Diego, California), situated in a magnetically shielded room at the Saint Louis University medical campus. The system comprised 248 magnetometers. Spatial digitization, encompassing anatomical landmarks, head localization coils, and a head shape scan with approximately 2400 points, was performed using a Polhemus FASTRAK-III system. Further information on sensor placement and the co-registration process between MEG and MRI structural scans, are referred in (Larson-Prior et al., 2013; Van Essen et al., 2013). Briefly, during the MEG scans, participants were positioned supine in the scanner, with the crown of their head gently touching the back of the MEG dewar. The co-registration process involved a 3-point reference system (nasion and left and right peri-auricular points) and five MEG position-sensor coils. Co-registrations were executed using an unmasked T1-weighted anatomical image with 1 mm resolution, which was not released to comply with anonymity requirements.

For each participant, a native cortical sheet-based source model was generated, comprising approximately 4,000 vertices per hemisphere to facilitate distributed source reconstructions. These source models were derived by downsampling from a more detailed cortical sheet containing 32,000 vertices per hemisphere, an output from the structural processing pipeline of the Human Connectome Project (Glasser et al., 2013; Van Essen et al., 2013). The source spaces were established by morphing surfaces from a standard template space to each subject's T1-weighted anatomical space. This approach ensures that dipole positions are aligned across subjects in surface-space, permitting direct averaging across subjects when necessary. The cortical sheets represent tessellations of the mid-surfaces, defined as the midpoint between the white and pial surfaces.

Lead field matrices for each subject were created with 8,000 dipoles using a single-shell boundary element model (BEM) that incorporates the inner skull layer (representing the brain) with 2,432 vertices and the aforementioned cortical surface with 8,000 vertices (Gramfort et al., 2010; Kybic et al., 2005; Tadel et al., 2011). Dipole orientations were constrained to be perpendicular to the cortical surface at each vertex location.

Additional lead field matrices with 400, 300, 200, or 100 dipoles were generated by restricting source estimations to lead field vectors from the 8,000-dipole model that correspond to the centroids of predefined regions of interest. Specifically, from the 8,000-vertex source model, reduced models with 400, 300, 200, or 100 vertices were constructed by identifying centroid vertices within each region defined by the Schaefer atlases. Utilizing these reduced source models within the BEM framework, lead field matrices with 400, 300, 200, or 100 dipoles were then established for each subject, facilitating analyses at various spatial resolutions.

MEG data for each subject was directly simulated using the lead field matrices corresponding to 400, 300, 200, or 100 dipoles, reflecting the linear projection of reference networks at these resolutions. Consequently, for each resolution and subject, 54 simulated networks were generated.

For simulations constrained by the Schaefer-100 and Schaefer-200 atlases, MEG data within the 8,000-dipole source space were also derived by assigning identical time-series to all dipoles within each region defined by the Schaefer-100 or Schaefer-200 atlas, respectively. Given the potential for signal cancellation due to opposing dipole orientations within the same region, a two-step process was employed to mitigate this effect. First, the predominant dipole orientation within each region was identified. Subsequently, time-series for dipoles oriented in opposition to this dominant direction were sign-flipped to minimize cancellation. The choice of 100 and 200 regions of interest aligns with common practices in current literature (Palva et al., 2018; Sadaghiani et al., 2022).

No sensor-level noise was introduced to the simulated MEG data. Ultimately, MEG datasets were generated through forward modeling for nine subjects across six resolutions (RES-100, RES-200, RES-300, RES-400, RES-8K-100, and RES-8K-200), resulting in a total of 9×6×54 five-minute MEG simulations for subsequent reconstruction analysis.

4.4.6 MEG functional network reconstructions

Overview. In this study, we extensively utilized the wMN operator for all simulations (i.e., 27×2 simulations per resolution for each of the 9 subjects, across 6 resolutions) due to its computational efficiency. This efficiency is attributed to the wMN's linear kernel, which is constructed from a limited number of matrix multiplications, unlike the wMEM operator. The wMEM operator, as detailed subsequently, necessitates a nonlinear programming solver and a data-driven cortical parcellation, which significantly increases computational demands.
The notation 27×2, rather than 54, is used deliberately to underscore the separate statistical analyses conducted for the two distinct sets of simulations. To reiterate, each set comprises 27 simulations; one set is predominantly influenced by brain geometry, showcasing primarily inter-community functional integration patterns (referred to as the *between-integration batch*), while the other set exhibits mainly intra-community functional integration patterns, with minimal geometric constraints (referred to as the *within-integration batch*).

Weighted minimum norm. The minimum norm approach (Lin et al., 2006) aims to solve a least-squares optimization problem using MEG data M and an orientation-free lead field matrix G. The MEG data M consists of N_{C} channels over N_{T} time samples, while the lead field matrix G encompasses N_{D} dipolar sources with unconstrained orientations. The objective is to determine a unique source configuration $\hat{J}_{\mathrm{MN}} \in \mathbb{R}^{(3N_{\mathrm{D}})\times N_{\mathrm{T}}}$ that minimizes the energy among all possible configurations fitting the MEG data equally. Formally, the solution is given by:

$$\hat{J}_{\mathrm{MN}} = G^{\top}(GG^{\top} + \lambda^2 I)^{+}M \tag{4.1}$$

where I is the identity matrix, $^\top$ denotes matrix transpose, $^+$ indicates the Moore–Penrose inverse, and λ^2 is the Tikhonov regularization parameter. The choice of λ balances spatial smoothness and sensitivity to noise, with larger values resulting in smoother but weaker current amplitudes, and smaller values leading to data fidelity but increased sensitivity to noise. This minimum norm solution assumes spatial whitening of the data and the gain matrix, which is reflected in the identity matrix scaled by λ^2 in Equation (4.1). Additionally, anatomical priors are often incorporated, constraining current dipole orientations to be perpendicular to the cortical surface at each vertex location. This leads to using the gain matrix $G_{\text{fixed}} = G\Theta \in \mathbb{R}^{N_\text{C} \times N_\text{D}}$ in Equation (4.1), where Θ contains unit vectors representing the direction of current for each dipole. Consequently, $\hat{J}_{\text{MN}}$ has N_D rows.

In the minimum norm solution, superficial sources tend to produce stronger fields with less energy due to their proximity to the sensors. To counteract this bias, the introduction of a depth-weighting prior, represented by the matrix, A, adjusts the contribution of each lead field vector based on the depth of the corresponding source. This ensures that deeper sources, which may be less prominent in the sensor data, are appropriately accounted for in the reconstruction process. The depth-weighted minimum norm solution is formulated as follows:

$$\hat{J}_{\text{wMN}} = AG^\top(GAG^\top + \lambda^2 I)^+ M \tag{4.2}$$

In this equation, the diagonal matrix A scales each lead field vector i with a factor proportional to $\left(g_{x,i}{}^\top g_{x,i} + g_{y,i}{}^\top g_{y,i} + g_{z,i}{}^\top g_{z,i}\right)^{-\gamma}$, where $g_{x,i}$, $g_{y,i}$, and $g_{z,i}$ are the three columns of the non-oriented lead field matrix G at the source location i, and γ is a depth weighting exponent (chosen as 0.8 in this study). An upper bound on depth weighting is typically specified, set to 10 in this case. For more details, refer to (Lin et al., 2006).

In the work of (Vallarino et al., 2023), a theoretical procedure is proposed to choose λ for optimal connectivity reconstructions when ground-truth is known. They demonstrated that the best λ values for connectivity reconstructions differed significantly from the traditional approach of $\lambda^2 = \text{tr}(GG^\top)/(N_C \times \text{SNR}^2)$, where SNR is the amplitude signal-to-noise ratio of the whitened data (typically set to 3), and tr denotes the matrix trace operator (Lin et al., 2006). For simplicity, we present results only for λ values that best reconstruct activity, determined by minimizing the Frobenius norm of the difference between the ground-truth and wMN solutions. While this choice may not be optimal, it significantly outperforms the default setting with $\text{SNR} = 3$, as demonstrated in the *Supplementary Information*, and it serves the purposes of our discussion and analysis.

Wavelet-based maximum entropy on the mean. Consider a continuous random variable X, for which the only available data are $\{m_0 = 1, m_1, \dots, m_N\}$. Furthermore, suppose that the data represent the expectations of some known functions $\{\phi_0(X) = 1, \phi_1(X), \dots, \phi_N(X)\}$. Given a prior probability density ρ_0, if we aim to determine, *a posteriori*, a probability density ρ that best represents the data and the prior knowledge, then the *maximum (relative) entropy approach* (M. Djafari, 1994; Gamboa, 1989) suggests choosing ρ maximizing the relative entropy:

$$-\int \rho(x) \ln\left(\frac{\rho(x)}{\rho_0(x)}\right) \mathrm{d}x \tag{4.3}$$

subject to:

$$\int \phi_k(x)\rho(x)\,\mathrm{d}x = m_k, \quad k \in [\![0; N]\!] \tag{4.4}$$

The solution to this problem has an exponential form:

$$\rho(x) = \frac{1}{Z(\lambda_1, \dots, \lambda_N)} \rho_0(x) \exp\left(-\sum_{k=1}^{N} \lambda_k \phi_k(x)\right)$$
$$Z(\lambda_1, \dots, \lambda_N) = \exp(\lambda_0) = \int \exp\left(-\sum_{k=1}^{N} \lambda_k \phi_k(x)\right) \rho_0(x)\, \mathrm{d}x \tag{4.5}$$

where Z is the partition function, and the Lagrange multipliers $\{\lambda_1, \dots, \lambda_N\}$ are obtained by solving the non-linear system of equations:

$$-\frac{\partial \ln\big(Z(\lambda_1, \dots, \lambda_N)\big)}{\partial \lambda_k} = m_k, \quad k \in [\![1; N]\!] \tag{4.6}$$

Denoting by λ the vector $(\lambda_1, \dots, \lambda_N) \in \mathbb{R}^{N\times 1}$, in practice, the following unconstrained dual optimization problem is solved:

$$\hat{\lambda} = \underset{\lambda}{\operatorname{argmin}} \big\{\ln\big(Z(\lambda)\big) + \lambda^\top m\big\}, \quad m = (m_1, \dots, m_N) \in \mathbb{R}^{N\times 1} \tag{4.7}$$

The constant $\lambda_0 = \ln Z$ ensures that ρ integrates to 1 over its support, while $\hat{\lambda}$ control the compromise between the data fit and the relative entropy. Depending on the presumed form for ρ_0 (e.g., multivariate normal distribution) and the constrains (e.g., constrains expressed on first-order or second-order moments), ρ can yield simple forms (M. Djafari, 1994; Gamboa, 1989). Additionally, this overall approach becomes the *maximum entropy on the mean* when the constraints pertain to the mean (first-order moment) of the distribution (M. Djafari, 1994; Gamboa, 1989).

In this study, the maximum entropy on the mean approach is employed to solve the inverse problem as proposed in (Amblard et al., 2004). We aim to approximate the probability density ρ that is closest to a given prior density ρ_0, for current sources j at specific time instants or intervals. This approximation, where $\tilde{\rho} \neq \rho_0$, is based on the relative entropy criteria, as outlined in Equation (4.3), while ensuring consistency with the corresponding MEG data m, given the lead field matrix, G:

$$G j_{\mathrm{MEM}} = m$$
$$j_{\mathrm{MEM}} = \int j \tilde{\rho}(j)\, \mathrm{d}j \tag{4.8}$$

To facilitate this, we introduce the log-partition function F_{ρ_0} defined by:

$$F_{\rho_0}(G^\top \lambda) = \ln\big(Z(\lambda)\big) = \ln\left(\int \exp(\lambda^\top G j)\, \rho_0(j)\, \mathrm{d}j\right) \tag{4.9}$$

Assuming that the noise in the measurement follows a centered normal distribution with covariance C, the optimal density $\tilde{\rho}$ is derived as:

$$\tilde{\rho}(j) = \frac{1}{Z(\tilde{\lambda})} \rho_0(j) \exp\big(\tilde{\lambda}^\top G j\big)$$
$$\tilde{\lambda} = \underset{\lambda}{\operatorname{argmin}} \left\{F_{\rho_0}(G^\top \lambda) - \left(\lambda^\top m - \frac{1}{2}\lambda^\top C \lambda\right)\right\} \tag{4.10}$$

Consequently, the MEM current source estimation j_{MEM} is determined by:

$$j_{\mathrm{MEM}} = \frac{\mathrm{d}}{\mathrm{d}x} F_{\rho_0}(x)\Big|_{x = G^\top \tilde{\lambda}} \tag{4.11}$$

In the wavelet-based MEM approach (Afnan et al., 2023; Lina et al., 2014), discrete wavelet transforms on the MEG data are first performed, the MEM framework is then applied within the

wavelet domain. This process effectively introduces temporal sparsity and facilitates the reconstruction of oscillatory patterns inherent in the data.

The prior density, ρ_0, is defined based on a fixed cortical parcellation, grouping dipoles according to spatially independent parcels informed by MEG data and the lead field matrix, as detailed in (Afnan et al., 2023; Lina et al., 2014). For P parcels, each k-th parcel is associated with a time-dependent (or in the wavelet domain, a time-scale dependent) latent state S_k, from a state vector $S = (S_1, \dots, S_P)$ with density $\pi(S)$, indicating either active $S_k = 1$ or inactive $S_k = 0$ states. Assuming the current sources j_k within the k-th parcel depend solely on its state S_k (Lina et al., 2014), the joint prior density is expressed as:

$$\rho_0(j, S) = \pi(S) \prod_{k=1}^{P} \rho_0(j_k | S_k) \tag{4.12}$$

It is crucial to acknowledge that this model's assumption of activity independence across parcels is inconsistent with the interconnected nature of resting-state network dynamics, which typically involve dependencies across network nodes. However, the prior formulation in Equation (4.12) does not preclude the possibility of functional couplings between activities across different brain regions. Although such coupling configurations are not emphasized in the bulk of the distribution, they can still be accommodated within the model's framework given appropriate parameterization (explained below), allowing this MEM model to produce insightful results. For advanced discussions on enhancing the MEM framework to more explicitly model connectivity, refer to the work by (Deslauriers-Gauthier et al., 2019, 2020), which explores significant extensions of the MEM approach in the context of network activity and connectivity.

To describe the current sources or their wavelet coefficients within each parcel, normal distributions, $\mathcal{N}(\text{mean}, \text{covariance})$, are adopted with different mean and covariance parameters for active and inactive states (Afnan et al., 2023; Lina et al., 2014):

$$\begin{matrix} \mathcal{N}\left(0, \sigma_0 I_{N_k}\right) & \text{when } S_k = 0 \\ \mathcal{N}(\mu_k, \Sigma_k) & \text{when } S_k = 1 \end{matrix} \tag{4.13}$$

where I_{N_k} is the identity matrix with size N_k, the number of dipoles in the k-th parcel. This yields the following log-partition function for the k-th parcel:

$$F_{\rho_k}(x) = \ln\left((1 - \alpha_k) \exp\left(\frac{\sigma_0}{2} x^\top x\right) + \alpha_k \exp\left(x^\top \mu_k + \frac{1}{2} x^\top \Sigma_k x\right)\right) \tag{4.14}$$

where α_k denotes the probability of the k-th parcel being active.

Given the optimal solution $\tilde{\lambda}$ from Equation (4.10), the current sources, j_k, for the k-th parcel is derived as:

$$\begin{aligned} j_k &= (1 - \widetilde{\alpha_k})\sigma_0 {G_k}^\top \tilde{\lambda} + \widetilde{\alpha_k} \mu_k + \widetilde{\alpha_k} \Sigma_k {G_k}^\top \tilde{\lambda} \\ \widetilde{\alpha_k} &= \frac{\alpha_k}{(1 - \alpha_k) \exp(-\Delta F_k) + \alpha_k} \\ \Delta F_k &= \tilde{\lambda}^\top G_k \mu_k + \frac{1}{2} \tilde{\lambda}^\top G_k \left(\Sigma_k - \sigma_0 I_{N_k}\right) {G_k}^\top \tilde{\lambda} \end{aligned} \tag{4.15}$$

with the updated probability $\widetilde{\alpha_k}$ adjusted for the energy difference ΔF_k. Here, G_k represents the lead field submatrix corresponding to the dipoles of the k-th parcel. In our simulations, all network nodes maintain a meaningful temporal activity, and there are no periods of *background* activity. This design premise enables us to set all activation probabilities, $\{\alpha_k\}_k$, to 1, reflecting an active state for every parcel throughout the simulation.

It is important to note that the spatial covariance matrices $\{\Sigma_k\}_k$ are designed to model functional couplings within parcels but do not extend to inter-parcel or global brain region interactions (Lina et al., 2014). These matrices are constructed based on cortical geometry, utilizing the graph Laplacian (A) derived from the cortical surface mesh adjacency matrix, as defined by:

$$\Sigma_k = \sigma_1 {\mu_k}^2 {\Gamma_k}^\top \Gamma_k$$
$$\Gamma = \sum_{n=0}^{L} \frac{(-\gamma)^n}{n!} A^n \tag{4.16}$$

Here $\sigma_1 = 0.05$ locally adjusts the variance within each parcel, $\gamma = 0.5$ controls the extent of spatial smoothing, and Γ_k is the truncated version of Γ, retaining only the columns corresponding to the dipoles in the k-th parcel. As detailed in *Supplementary Information*, the critical parameter for achieving meaningful connectivity reconstructions in this MEM model is the set of parcel means $\{\mu_k\}_k$. Incorrect settings for $\{\mu_k\}_k$ can lead to the model's inability to reconstruct functional networks, regardless of other parameter configurations. This limitation highlights the role of $\{\mu_k\}_k$ in guiding the solution towards configurations that reflect functional couplings between temporal activities across different brain regions.

Following (Lina et al., 2014), we initially consider $\{\mu_k\}_k$ as minimum norm estimates. However, we diverge from their approach by optimally adjusting the underlying Tikhonov parameters to match those determined for the wMN solution, as discussed earlier. Without this optimization, the MEM model fails to produce insightful outcomes, as demonstrated in the *Supplementary Information*, for the same reasons highlighted by (Vallarino et al., 2023) for the wMN model. This adjustment also ensures depth-weighting is considered in the MEM solution, enhancing its interpretability.

It is also important to recognize that the data-driven cortical parcellation scheme employed by (Afnan et al., 2023; Lina et al., 2014) does not inherently account for functional connectivity patterns, leading to potential discrepancies with the simulated brain activity parcellation. This discrepancy becomes critical when data-driven parcels are overly large, imposing local spatial smoothing and functional couplings that misalign with the simulated patterns. To counter this bias while preserving the current MEM implementations, we adjust the parcellation procedure to yield the smallest possible parcel sizes, opting for a neighborhood order of one during the region-growing steps, as opposed to the default value of four. An alternative strategy involves directly using a predefined parcellation atlas (e.g., the one employed during simulations) as a more meaningful and accessible prior. However, even in this case, caution is advised to prevent the MEM model from favoring solutions that imply independent activities across parcels, which can be mitigated by appropriately setting $\{\mu_k\}_k$. An important observation in our study is that the MEM solution can perfectly align with wMN solution when each dipole is its own parcel. This convergence underscores the critical role that parcel size and configuration play in determining the efficacy of our modeling approach.

For the wavelet analysis, we employed a discrete wavelet transform using Daubechies wavelets with four vanishing moments. Our approach did not incorporate wavelet denoising, resulting in a null shrinkage coefficient. We focused exclusively on the time-frequency boxes corresponding to the α-band frequencies (8–13 Hz), in line with our simulation constraints. It is worth noting that exploring other time-frequency boxes from different scales did not alter the functional connectivity estimations, due to the specific design of our simulations.

The noise covariance matrix was set to an identity matrix, effectively treated as a scalar matrix through a scaling factor that maintains the original data units. This scaling was achieved by

inputting a white noise data segment with comparable overall mean and variance to the data of interest into the MEM implementation interface. This approach yields results equivalent compared to the shuffling procedure described in (Afnan et al., 2023), but offers a significant advantage in computational efficiency. However, it is important to note that this step is not critical for our analysis, given that all brain regions are considered to be in an active state throughout the simulations.

Multilayer functional network modelling. In our study, we constructed two types of multiplex functional connectomes from both reference and reconstructed (via wMN or wMEM) network time-series. These connectomes were distinguished based on the bi-variate connectivity measures used to define the intra-layer connections: one connectome utilized phase locking value (PLV) and amplitude envelope correlation (AEC), which are *standard* connectivity measures sensitive to zero-lag couplings. The other employed the weighted phase lag index (wPLI) and orthogonalized amplitude envelope correlation (oAEC) as *corrected* connectivity measures insensitive to zero-lag couplings. An identity matrix defined the inter-layer connections in both types of connectomes.
The approach to analyzing reconstructed dipolar time-series in our study varies depending on the resolution. For resolutions RES-100, RES-200, RES-300, and RES-400, each region of interest (ROI) corresponds to a single dipole, allowing the reconstructed time-series to be directly analyzed without the need for further dimension reduction. However, for higher resolutions such as RES-8K-100 and RES-8K-200, the scenario becomes more complex due to the presence of 8000 dipoles. To align these dipoles with the Schaefer-100 or Schaefer-200 atlas, a process of aggregation is necessary to reduce the dimensionality of the reconstructed time-series to match the intended atlas resolution. Two primary aggregation operators were employed in this study to consolidate the dipolar time-series into ROI-conforming time-series: average operator and principal component analysis (PCA) operator. The average operator computes the mean of the dipolar time-series within each ROI. To counteract potential signal cancellation effects that might occur due to dipole orientation within an ROI, a sign-flip correction was applied before averaging. The time-series aggregated through this method were exclusively utilized for estimating oAEC. The first principal component from a PCA performed on the dipolar time-series within each ROI served as the aggregated time-series. The time-series derived through PCA were utilized for PLV, wPLI, and AEC analyses. The choice of using the average operator for oAEC and the PCA operator for PLV, wPLI, and AEC was informed by extensive preliminary analyses. These analyses evaluated the efficacy and suitability of each aggregation method for the respective connectivity measures, ensuring the most accurate and representative outcomes. Although the detailed findings from these preliminary studies are beyond the scope of this chapter, they were instrumental in guiding the methodological decisions made in our network modeling process. For readers interested in the theoretical underpinnings and empirical validation of these aggregation methods, we recommend consulting the work of (Brkić et al., 2023), which provides comprehensive insights into the subject.
For any two nodes within a network, denoted as ▲ and ■, we consider their respective time-series, $y_{\blacktriangle}$ and $y_{\blacksquare}$. To analyze the α-band (8–13 Hz) dynamics, we first apply a band-pass filter to obtain the α-band limited versions of these time-series, denoted as $y_{\blacktriangle,\alpha}$ and $y_{\blacksquare,\alpha}$. This filtering is performed using MATLAB's *bandpass* function. Subsequently, we apply a Hilbert transform (using MATLAB's *hilbert* function) to the filtered signals to extract their instantaneous amplitudes m and phases ϕ at any given time t. The transformed signal for node ▲ in the α-band at time t is represented as $Y_{\blacktriangle,\alpha}(t) = m_{\blacktriangle,\alpha}(t)\exp\left(j\phi_{\blacktriangle,\alpha}(t)\right)$, and similarly for node ■. Here, j denotes the

imaginary unit. The cross-spectrum between nodes ▲ and ■ at any time t is estimated by $P_{▲,■}(t) = Y_{▲,\alpha}(t)\bar{Y}_{■,\alpha}(t)$, where the overbar indicates the complex conjugate. We define E as the expectation operator.

The PLV (Palva et al., 2018), a measure of the consistency of phase differences between the two nodes over time, is calculated as $\mathrm{PLV}_{▲,■} = \left|\mathrm{E}\left\{P_{▲,■}/\left|P_{▲,■}\right|\right\}\right|$. The PLV value ranges from 0 to 1, indicating perfect phase synchronization when equal to 1 and complete desynchronization when equal to 0.

The wPLI quantifies the asymmetry in the distribution of phase differences between the signals from nodes ▲ and ■. It is defined as $\mathrm{wPLI}_{▲,■} = \left|\mathrm{E}\left\{\mathrm{Im}\left(P_{▲,■}\right)\right\}\right|/\mathrm{E}\left\{\left|\mathrm{Im}\left(P_{▲,■}\right)\right|\right\}$, where Im denotes the imaginary part operator (Palva et al., 2018). The wPLI is insensitive to zero-lag coupling, requiring a non-zero phase-delay between signals to be non-zero. Its values range from 0, indicating an equal balance of leading and lagging relationships, to 1, denoting consistent lead or lag behavior (Vinck et al., 2011).

The AEC between nodes ▲ and ■ is calculated as the absolute value of the Pearson-correlation between their respective signal envelopes, $m_{▲,\alpha}$ and $m_{■,\alpha}$ (Palva et al., 2018). Prior to correlation, the envelopes are processed by applying a 2-second non-overlapping moving average filter, followed by a logarithmic transformation (Colclough et al., 2015). We found that substituting the moving average filter with a 0.5-Hz-cutoff low-pass filter yields similar results, as does using Spearman-correlations in place of Pearson-correlations. Absolute values were used for convenience.

For the oAEC calculation, we first orthogonalize the full set of band-passed time-series $\left(y_{\cdot,\alpha}\right)_{\cdot}$ across all nodes using singular value decomposition, resulting in a set of orthogonalized time-series $\left(\tilde{y}_{\cdot,\alpha}\right)_{\cdot}$ (Colclough et al., 2015). The oAEC between nodes ▲ and ■ is then determined by applying the AEC pipeline to the orthogonalized time-series $\tilde{y}_{▲}$ and $\tilde{y}_{■}$, including the Hilbert transform, moving average filtering, and log transformation. It is crucial to note that the oAEC may not always be meaningful, especially when the ensemble of time-series $\left(y_{\cdot,\alpha}\right)_{\cdot}$ is not full rank, such as when the number of dipoles exceeds the number of sensors for wMN timeseries.

4.4.7 STATIStical investigations

Overview. Our approach to multivariate statistical analysis aimed to methodically assess the congruence and divergence among various reconstructed networks in relation to their reference counterparts. This evaluation was facilitated by employing STATIS (a French acronym: structuration des tableaux à trois indices de la statistique), which extends PCA to accommodate multi-table datasets. This methodology enabled us to conduct a comprehensive joint analysis across multiple datasets, including one reference network dataset and additional datasets for each of the nine subjects' networks reconstructed using both the wMN and, where applicable, the wMEM inverse operators.

Specifically, our analysis encompassed either 10 (1 reference + 9 wMN reconstructions) or 19 (1 reference + 9 wMN reconstructions + 9 wMEM reconstructions) data tables, allowing for a thorough examination of the variations attributable to individual subjects and, when pertinent, the differences engendered by the choice of inverse operator. These statistical investigations were meticulously conducted for each spatial resolution (RES-100, RES-200, RES-300, RES-400, RES-8K-100, and RES-8K-200) and were further delineated based on the type of multilayer functional networks examined: those constructed using standard connectivity measures sensitive to zero-lag

coupling (PLV and AEC) and those utilizing corrected measures insensitive to zero-lag coupling (wPLI and oAEC).
Additionally, our analysis spanned two distinct network scales frequently referenced in neuroscientific research, macro and micro scales, allowing for a nuanced exploration of network dynamics at different levels of granularity. By separating the investigations based on resolution, connectivity measure type, and network scale, we aimed to provide a detailed and stratified understanding of the underlying network structures and their properties.

STATIS. The STATIS (structuration des tableaux à trois indices de la statistique) method extends PCA to effectively handle multi-table datasets, facilitating the analysis of complex multivariate data. In STATIS, each data table is composed of rows representing observations and columns representing variables. It is essential that all tables share the same set of observations, although the nature of the variables and their numbers may differ from one table to another. The STATIS approach unfolds in two primary steps. Initially, STATIS examines the interrelationships among the data tables, focusing on their similarity structure. This step is crucial for understanding how each table relates to the others within the dataset. Subsequently, STATIS leverages the identified similarity structure to determine an optimal set of weights. These weights are then applied to combine the individual tables into a unified representation, known as the compromise or consensus. The objective is to ensure that this combined representation is as reflective of the entire dataset as possible. Following the establishment of the compromise, PCA is applied to this *synthesized dataset* to derive factor scores, which represent the positions of observations within the compromise space. These positions can be visualized in a map-like format, where the proximity between points corresponds to the similarity between observations. Moreover, the observations from individual data tables can be integrated into this compromise space as supplementary elements, allowing for a comprehensive visualization that includes both the consensus and the unique contributions of each table. The contribution of each variable to the principal components is quantified through loadings, indicating the variable's importance for a given component. These loadings can be utilized to construct maps reflecting the relationships among variables or to produce biplots that simultaneously display both factor scores and loadings. Additionally, the process of computing weights for the compromise also allows for the representation of the data-tables themselves as points within a multidimensional space, offering another perspective on their interrelations. For detailed insights into the application and interpretation of STATIS, re(Abdi et al., 2012; Abdi & Valentin, 2007)l., 2012; Abdi & Valentin, 2007).
For the purposes of this analysis, the notation $^\top$ denotes matrix transpose, tr signifies the matrix trace operator, I represents the identity matrix, and $\mathbf{1}$ is a vector of ones.
Consider a collection of K tables, where each table Y_k consists of I rows (observations) and J_k columns (variables), and $k \in [\![1, K]\!]$. Initially, each raw data matrix Y_k undergoes preprocessing (e.g., centering and normalization) to yield the matrices X_k upon which the analysis is based. Each preprocessed matrix X_k is then transformed into a cross-product matrix $S_k = X_k {X_k}^\top \in \mathbb{R}^{I \times I}$.
To explore the similarity structure across the K tables, a between-table cosine matrix $C = \left(c_{i,j}\right)_{1 \le i \le K, 1 \le j \le K}$, representing inner products, is constructed as follows:

$$c_{i,j} = \frac{\mathrm{tr}\left({S_i}^\top S_j\right)}{\sqrt{\mathrm{tr}\left({S_i}^\top S_i\right) \times \mathrm{tr}\left({S_j}^\top S_j\right)}} \tag{4.17}$$

The eigen-decomposition of the cosine matrix C unveils the inter-table similarity structure:

$$C = U\Theta U^{\top} \quad \text{with } UU^{\top} = I \tag{4.18}$$

Here, U is the eigenvector matrix and Θ is the diagonal matrix of eigenvalues, sorted in descending order. This decomposition, akin to a non-centered PCA, elucidates the similarity among the tables. The weights for constructing the compromise matrix are derived from the eigen-decomposition of C. Given that C is positive semidefinite with all-positive elements, the first eigenvector u_1's elements will share the same sign (positive by convention). The first eigenvector essentially encapsulates the *communality* among the tables, suggesting its use in weighting the tables to emphasize those that best represent the group and de-emphasize outlier tables.

The weights $\boldsymbol{\alpha} = (\alpha_k)_k$ are normalized elements of u_1, ensuring their sum equals one: $\boldsymbol{\alpha} = u_1/({u_1}^{\top}\mathbf{1}) \in \mathbb{R}^{K\times 1}$. Utilizing these weights, the compromise matrix S_+ is formulated as:

$$S_+ = \sum_{k=1}^{K} \alpha_k S_k \tag{4.19}$$

This compromise matrix S_+ serves as a unified representation that encapsulates the commonalities across the diverse data tables, providing a foundation for subsequent multivariate analyses. This compromise matrix, being a probabilistic sum of the cross-product matrices, retains the property of being positive semi-definite. Consequently, its eigen-decomposition is analogous to performing a PCA:

$$S_+ = V\Lambda V^{\top} \quad \text{with } VV^{\top} = I \tag{4.20}$$

From this decomposition, we calculate the loadings (Q) using the formula $Q = X^{\top}V\Lambda^{-1/2}$, where X is the concatenation of all preprocessed data tables $\{X_k\}_k$ along their columns. The factor scores (F) are derived as $F = V\Lambda^{1/2}$, which can also be expressed as $F = S_+V\Lambda^{-1/2}$, illustrating that $P = V\Lambda^{-1/2}$acts as a projection operator.

The loadings for the variables from the k-th table are obtained by:

$$Q_k = {X_k}^{\top}P \tag{4.21}$$

Correspondingly, the partial factor scores for table k are calculated using:

$$F_k = X_kQ_k = S_kP \tag{4.22}$$

In our analysis (see below, macro-scale and micro-scale analyses), we will present various graphical representations including plots of the inner product matrices and their PCA, maps depicting variable loadings, as well as visualizations of both the compromise and the partial factor scores. These visual tools will facilitate the interpretation of the multivariate relationships within and across the datasets, highlighting the underlying structure captured by the STATIS approach.

It is noteworthy to acknowledge the versatility of the STATIS framework and its various extensions, which cater to a broad spectrum of statistical modeling scenarios beyond the analysis of data tables based on the same set of observations. These extensions enrich the applicability of STATIS across different research contexts, enabling tailored analyses that align with specific research needs. Notable extensions include: dual-STATIS (tailored for analyzing data tables that share the same set of variables), X-STATIS or triadic partial analysis (designed for the simultaneous analysis of data tables that share both variables and observations), DISTATIS or COVSTATIS (aimed at analyzing covariance or distance matrices that are based on the same observations), STATICO or COSTATIS (focused on the analysis of paired data tables), (K+1)-STATIS or STATIS-4 or CANOSTATIS (geared towards integrating external data tables into the analysis), INTER-STATIS or CLUSTATIS (specialized in grouping data tables). These extensions, as referenced in (Abdi et al., 2012; González-Narváez et al., 2021), demonstrate the adaptability of STATIS to various analytical challenges, making it a powerful tool in the arsenal of multivariate

analysis. Each extension serves a unique purpose, from enhancing the depth of analysis within a single dataset to enabling the integration and comparison of multiple datasets, thereby broadening the horizons of statistical investigation.

Macro-scale analysis. In this analysis, we aim to assess the efficacy of various network reconstruction methods in preserving essential global properties of multilayer networks. This assessment helps to gauge the fidelity of reconstructed networks in reflecting the overall structure and dynamics of the reference networks. The analysis encompasses several key macro-scale properties of multilayer networks, including (De Domenico et al., 2014; De Domenico, Lancichinetti, et al., 2015; De Domenico, Nicosia, et al., 2015): global clustering coefficient (a measure of the degree to which nodes in the network tend to cluster together), global path length (the average shortest path length between all pairs of nodes in the network, providing insight into the network's overall connectivity), global edge overlap (the extent of edge conservation across different layers of the multilayer network), functional clustering ratio (the proportion of interactions within each functional communities, relative to between them; this is a multilayer network extension of the measure developed by (Marrelec et al., 2008) and applied in (Boly et al., 2012), by assuming that the graph Laplacian of the multilayer networks are covariance matrices of a degenerate multivariate normal distribution), modularity (the degree to which the network can be divided into distinct communities or modules with dense intra-module connections and sparse inter-module connections; (Clauset et al., 2004)). For each resolution considered, the statistical analysis is structured around data tables comprising 27 rows and 5 columns. The 27 rows correspond to the simulated networks within a specific batch, representing the observational units in our analysis. The 5 columns are dedicated to the macro-scale network properties listed above, serving as the variables under investigation. Depending on the scope of the reconstruction methods evaluated, the analysis involves either 10 (1 reference network + 9 reconstructed networks for wMN) or 19 (1 reference network + 9 wMN + 9 wMEM reconstructed networks) data tables for each resolution. This arrangement allows for a comprehensive comparison across different reconstruction approaches and their impact on the global properties of multilayer networks.

Micro-scale analysis. In contrast to the macro-scale analysis, our micro-scale analysis delves into the extent to which network reconstruction methods successfully retain properties at the nodal level within multilayer networks. This finer-scale examination is pivotal for understanding the local effects of reconstruction accuracy on individual nodes and their immediate connections. The micro-scale analysis encompasses several critical nodal properties of multilayer networks, notably (De Domenico et al., 2014; De Domenico, Lancichinetti, et al., 2015; De Domenico, Nicosia, et al., 2015): multi-strength (a multilayer network extension of strength), eigenvector versatility (a multilayer network extension of eigenvector centrality), and closeness versatility (a multilayer network extension of closeness centrality). For each network resolution under study, the statistical analysis employs data tables structured with 27×(size of resolution) rows and 3 columns. The rows represent the network nodes across all simulated networks within a batch, thereby capturing observations at the nodal level. The columns are dedicated to the micro-scale properties outlined above. We found that performing a separate analysis for each simulation yields analogous conclusions.

4.5 Results

In the interest of brevity and clarity, this *Results* section presents the findings of our statistical analyses for select key network configurations. Detailed results for additional configurations are

available in the *Supplementary Information*. For simplicity, weighted minimum norm will henceforth be referred to as MN, and wavelet-based maximum entropy on the mean as MEM.

4.5.1 Macro-scale analysis of MN reconstructions across all simulations and resolutions

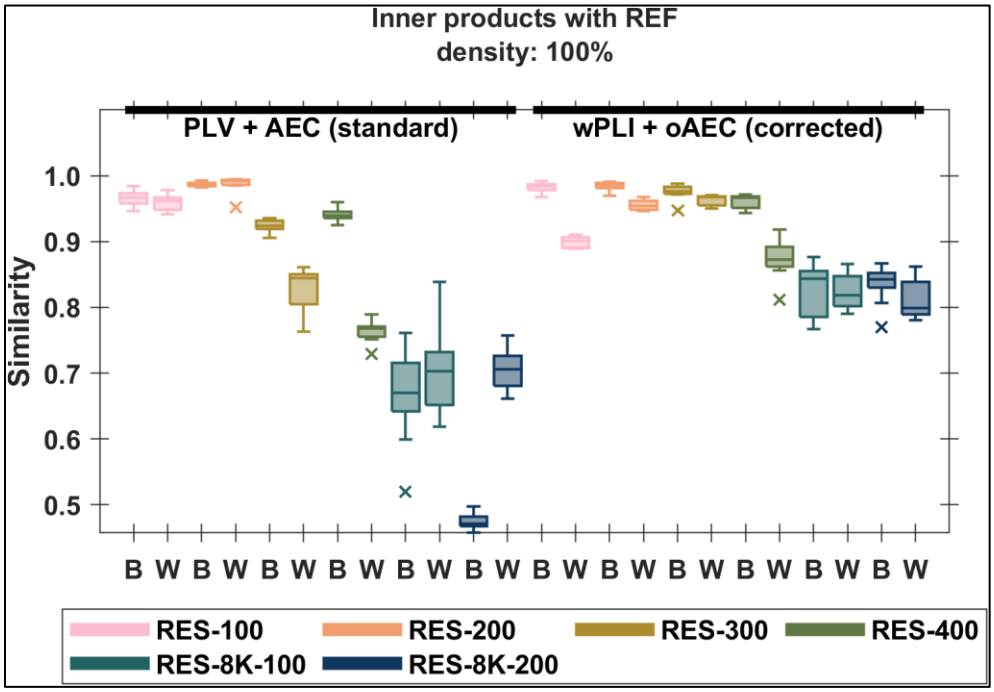

Figure 4.1. Cosine similarity analysis of MN networks at macro-scale. This figure presents box plots depicting the cosine similarities between reference networks and MN-reconstructed networks across 9 subjects, with each network retaining 100% of its graph weights. The colors represent different resolutions (RES). The x-axis categorizes the data into two simulation batches: *B* for the between-community integration batch and *W* for the within-community integration batch. Black horizontal lines above the x-axis delineate two analytic groups: the left side pertains to multilayer functional networks derived using standard connectivity measures, while the right side pertains to those derived using corrected connectivity measures. Each box plot in the figure represents a statistical summary of the cosine similarity scores for a specific simulation batch and resolution. The central line within each box denotes the median of the data, providing a measure of central tendency. The bottom and top edges of the box correspond to the first (0.25) and third (0.75) quantiles, respectively, with the distance between them defining the interquartile range (IQR), which measures data spread. Outliers, represented as individual points, are defined as observations that fall more than 1.5 times the IQR above the third quartile or below the first quartile. The whiskers extending from the box indicate the range of nonoutlier data, with the top whisker marking the maximum and the bottom whisker the minimum nonoutlier values.

Figure 4.1 focuses on macro-scale network properties and presents the cosine similarity scores for MN-reconstructed networks, illustrating the impact of various factors: parcellation sizes (RES-100, RES-200, RES-300, RES-400, RES-8K-100, and RES-8K-200, indicated by different colors), the treatment of zero-phase lag interactions (grouped on the x-axis as standard or corrected connectivity measures), the balance of functional integration and segregation (denoted by *B* for between-community integration and *W* for within-community integration batches on the x-axis), and inter-subject variability (represented by individual box plots).

Key observations include:

- High similarity scores, close to 1, for RES-100 and RES-200, suggesting nearly perfect MN reconstructions of macro-scale features. This high performance is attributed to these

configurations where the number of sensors (data) surpasses the number of dipoles (unknown), simplifying the inverse problem.

- As parcellation granularity increases, similarity scores tend to decline, reflecting the inherent complexity and ill-posed nature of the inverse problem at finer resolutions, with the lowest scores observed for RES-8K-100 and RES-8K-200.
- Reconstructions utilizing corrected connectivity measures generally outperform those using standard measures, likely due to better handling of signal mixing and volume conduction effects, which are especially pronounced in high-resolution settings such as RES-8K-100 and RES-8K-200.
- A noticeable trend is the reduction in similarity scores from the between-integration batch (*B*) to the within-integration batch (*W*), suggesting a bias in reconstructions towards the brain's geometrical structure, and indicating that long-range functional interactions misaligned with cortical geometry are more prone to distortion.

In the *Supplementary Information*, Figure 4.15 illustrates the impact of varying connectome densities (100%, 75%, 50%, and 25%) on network reconstructions. Our analysis reveals a notable trend: as the percentage of the weakest graph weights excluded from the analysis increases (e.g., at connectome densities of 50% or 25%), reconstructions based on corrected connectivity measures exhibit decreased accuracy compared to those based on standard measures. This suggests that the strongest graph weights are less susceptible to zero-lag biases, which predominantly distort the weakest graph weights. In contrast, the strongest graph weights appear more vulnerable to non-zero-lag biases, whereas the weakest weights are less affected.

Figure 4.16, also in the *Supplementary Information*, extends this analysis to the impact of the choice of inverse operator on network reconstructions. The trends observed with MEM reconstructions mirror those seen with MN reconstructions, with the notable difference that cosine similarities for MN reconstructions consistently outperform those for MEM reconstructions.

These findings underscore a critical aspect of network reconstruction: the challenge of accurately reconstructing networks increases with the number of dipoles relative to the number of channels. Given that MN reconstructions approach near-perfection when the number of channels exceeds the number of dipoles, further analysis at such resolutions may not yield additional insights. Therefore, our subsequent analysis will concentrate on the RES-8K-100 resolution, commonly employed in the literature and representative of the most challenging reconstruction scenarios.

4.5.2 Macro-scale analysis of MN and MEM reconstructions at RES-8K-100

In this section, we present a detailed analysis of our statistical findings for the RES-8K-100 resolution, concentrating specifically on standard connectivity measures within the between-integration simulation batch, and maintaining a connectome density of 100% (whereby all graph weights are included in the analyses). Comprehensive results for other conditions, connectivity measures, simulation batches, and connectome densities are systematically detailed in the *Supplementary Information*.

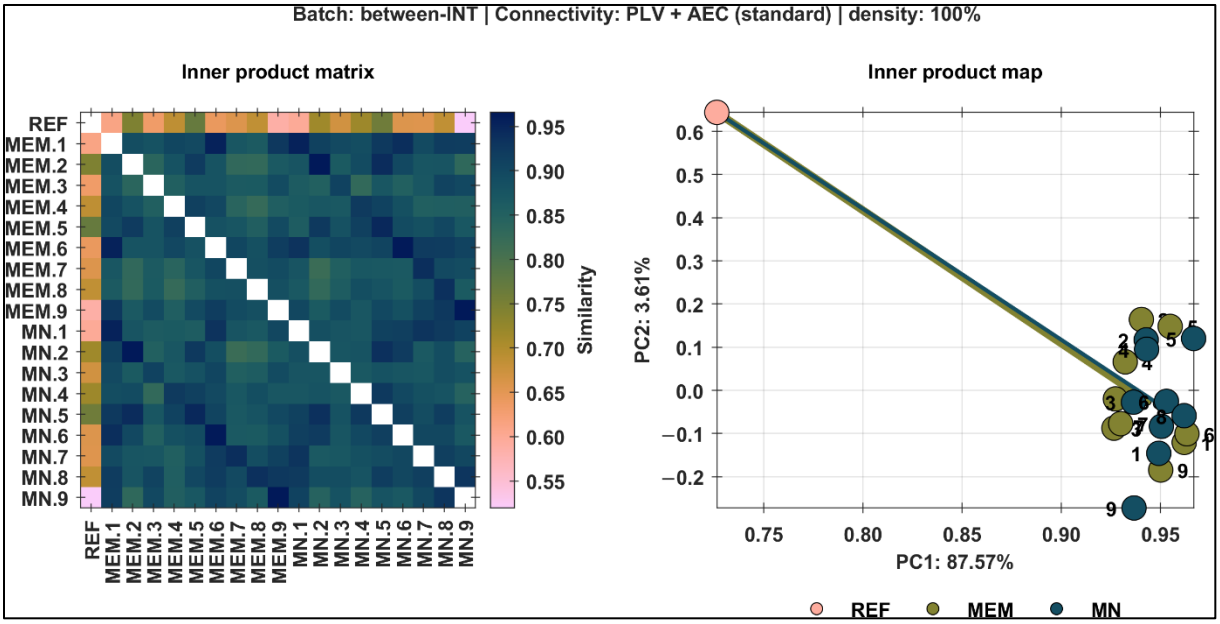

Figure 4.2. Comparative analysis of MN and MEM networks using the between-integration simulation batch with standard connectivity measures and full connectome density. On the left, the heat map displays the similarity matrix (excluding the diagonal) calculated via the STATIS method, highlighting inter-network comparisons. The right panel features a plot derived from the first two principal components of the similarity matrix, illustrating the spatial distribution of the reference network (represented by the pink dot), MN networks (blue dots), and MEM networks (green dots). The percentages of variance explained by each principal component are denoted along the respective axes. Line segments extend from the reference network to the centroid (fictive dot) of the MN and MEM network sets, with the shortest segment emphasized by increased thickness, indicating closer proximity to the reference network in the (full) principal component space.

In Figure 4.2, the left panel presents the pairwise similarities among the reference, MN, and MEM networks, quantified by their inner product matrix. The first row (and column) highlights the similarities relative to the reference network, revealing that MEM reconstructions marginally surpass MN reconstructions on average, largely due to an *outlier* (subject-9). This panel also underscores that the relative similarity rankings among subjects are maintained across both inverse operators, with subject-5 exhibiting the highest resemblance and subject-9 the lowest to the reference network for both MN and MEM.

The subsequent rows (and columns) delineate the intra-operator and inter-operator similarities, illustrating a high degree of consistency in reconstructions within individual subjects across both MN and MEM operators. The right panel, featuring a PCA of the inner product matrix, encapsulates these insights. Here, the second principal component distinctly separates the reference network from the reconstructions, indicating the challenges inherent in reconstruction accuracy. The clustering of reconstructed networks for both operators into a cohesive group reflects uniform reconstruction quality across subjects, with the dispersion within this cluster representing inter-subject variability.

In the *Supplementary Information*, Figure 4.17 presents a comprehensive complementary analysis of network reconstructions across connectivity measures, connectome densities, and simulation batches. Our observations highlight several key points:

- MN reconstructions consistently exhibit a slight advantage over MEM reconstructions, maintaining this trend across different connectivity measures, connectome densities, and

simulation batches. This advantage is coupled with reduced variability among subjects in the MN reconstructions.

- The relative differences observed between subjects, both within and across inverse operator, vary significantly with connectivity measure, connectome density, and simulation batch. This suggests that subject-specific variability in reconstructed networks is not a trivial function of the lead field and vertex connectivity matrices, but it is also influenced by the specific functional interaction patterns present within each simulation.

Our statistical framework enables an in-depth exploration beyond mere comparison. It allows for the precise identification of variables and observations that underpin the similarities and discrepancies between the reconstructed networks and the ground-truths. We delve into this detailed analysis in the following sections, aiming to uncover the underlying factors that drive these observed patterns in network reconstruction.

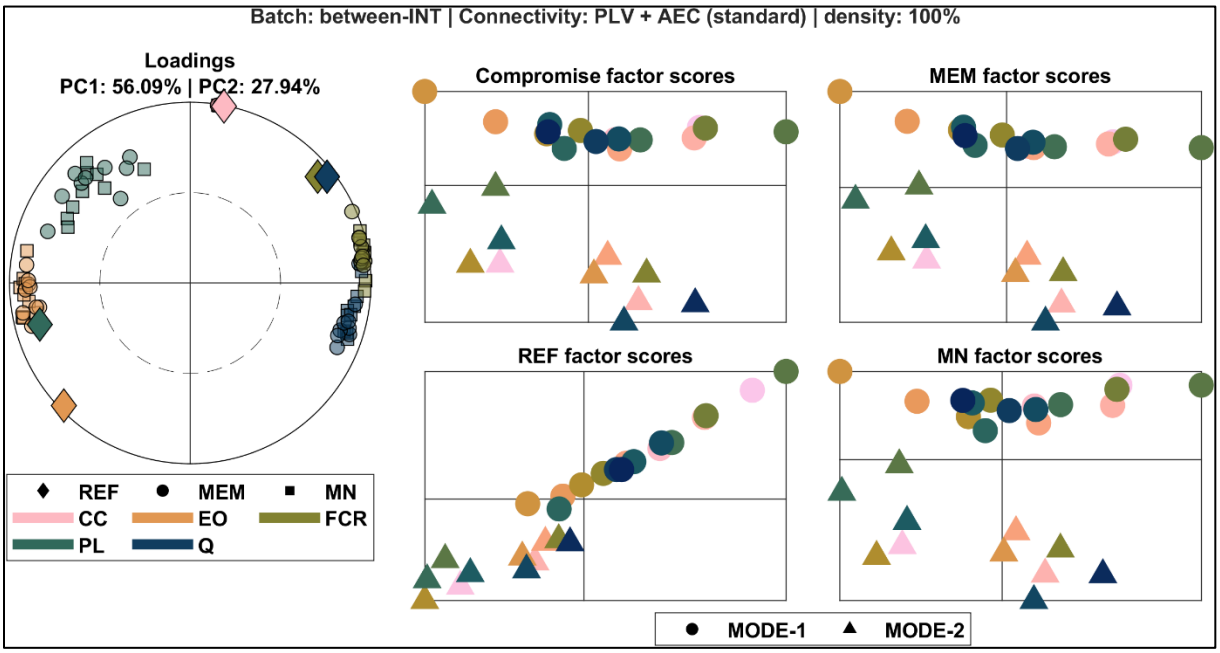

Figure 4.3. Analyses of loadings and factor scores for MN and MEM networks using the between-integration simulation batch with standard connectivity measures and full connectome density, at the macro-scale. The circular graph (left) illustrates the variable loadings on the first two principal dimensions within the compromise space, displaying five network metrics: global clustering coefficient (CC), global edge overlap (EO), functional clustering ratio (FCR), global path length (PL), and modularity (Q), each distinguished by unique colors. The 19 dots per color represent the reference network (largest dot), and the 9 MN and 9 MEM reconstructed networks (smallest dots). The outer circle denotes a perfect correlation (radius = 1), while the inner dashed circle marks correlations of 0.5. Adjacent to this, the right side comprises four plots showcasing factor scores: the top-left graph presents the compromise of all data tables; the bottom-left focuses solely on the reference network; the top-right and bottom-right are dedicated to MEM and MN reconstructions, respectively. Each plot contains 27 data points, symbolized by circles and triangles to differentiate between the two distinct dynamical regimes they represent, based on their mapping onto two families of periodic orbits (16 circles and 11 triangles).

The left panel of Figure 4.3 presents correlation loadings, which elucidate the variables significantly contributing to the observed similarities and differences between the reference and reconstructed networks. Notably, both MN and MEM reconstructions closely preserve CC, suggesting a faithful representation of local connectivity patterns. However, distortions are observed in other metrics, particularly those reflecting long-range interactions, such as PL and EO.

This aligns with the known tendency of inverse methods to be influenced by the brain's geometrical constraints, favoring short-range connections. The first principal component effectively differentiates between community structure indices (FCR and Q) and long-range interaction indices (PL and EO), with the latter two often conflated in both MN and MEM reconstructions.

The right-side plots of Figure 4.3 detail factor scores, shedding light on specific observations underpinning the previously discussed network characteristics. Both inverse methods (MN and MEM) consistently differentiate between the two simulated dynamical regimes across subjects, as evident in the separation along the second principal component. This differentiation underscores the reconstruction algorithms' capability to capture distinct dynamical behaviors. Further analysis (by superimposing correlation loadings and factor scores) reveals that the first dynamical regime is predominantly characterized by community structure and short-range connectivity metrics (FCR and Q, and CC), while the second regime is defined by metrics indicative of long-range connectivity (PL and EO). This observation is in harmony with our simulation design intentions, emphasizing the distinct network properties fostered by each dynamical mode.

In the extended analysis presented in Figure 4.18 (refer to *Supplementary Information*), we delve deeper into the nuances of network reconstructions, considering the impact of connectivity measures, connectome densities, and simulation batches on the preservation of graph metrics. A striking observation is the superior preservation of all graph metrics when corrected connectivity measures are employed, as opposed to standard connectivity measures. Specifically, CC is consistently well-preserved across all scenarios when standard connectivity measures are used, highlighting its robustness in the face of varying reconstruction approaches. However, the preservation of other graph metrics introduces subject-specific variability, indicating that factors such as long-range connectivity and network integration may be differentially affected by the reconstruction process. Furthermore, an inverse relationship is observed between connectome density and reconstruction quality; as connectome density decreases, the fidelity of the reconstructed networks to the reference models improves, suggesting that sparser connectomes may facilitate more accurate reconstructions under standard connectivity measures.

While the detailed results are not presented here, it is important to note that the trends and patterns observed in the analyses for RES-8K-100 also hold true for the RES-8K-200 resolution. This consistency across resolutions reinforces the reliability of our findings. However, such consistencies do not necessarily imply the generalizability of the observed trends due to, e.g.: non-trivial signal cancellation and dipole depth effects across different levels of network granularity, as well as the ratio between number of sensors (~250) and number of regions of interest (100–400).

Exemplar reconstructions for MN and MEM are provided in Figure 4.11, Figure 4.12, Figure 4.13, and Figure 4.14.

4.5.3 Micro-scale analysis of MN reconstructions across all simulations and resolutions

In this section and the next, we focus on the micro-scale and follow a structure similar to the previous macro-scale sections.

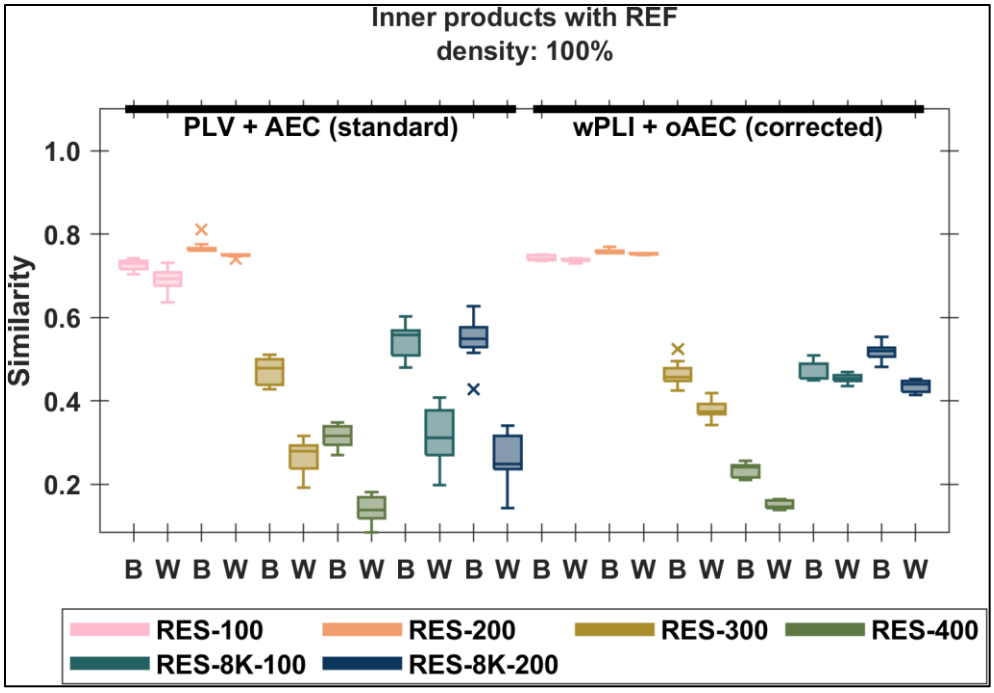

Figure 4.4. Cosine similarity analysis of MN networks at micro-scale. This figure presents box plots depicting the cosine similarities between reference networks and MN-reconstructed networks across 9 subjects, with each network retaining 100% of its graph weights. The colors represent different resolutions (RES). The x-axis categorizes the data into two simulation batches: *B* for the between-community integration batch and *W* for the within-community integration batch. Black horizontal lines above the x-axis delineate two analytic groups: the left side pertains to multilayer functional networks derived using standard connectivity measures, while the right side pertains to those derived using corrected connectivity measures. For each simulation batch, a joint STATIS analysis was conducted, pulling data from all simulations within the batch.

Transitioning to a micro-scale perspective, we examine the finer details of network reconstructions, akin to our macro-scale analysis approach. Figure 4.4 delves into the micro-scale network properties, displaying cosine similarity scores for MN-reconstructed networks. This figure mirrors the macro-scale analysis structure presented in Figure 4.1 but shifts focus to the nuances of micro-scale network attributes. The figure elucidates the effect of various factors, including parcellation sizes, zero-phase lag interaction treatments, functional integration and segregation balances, and inter-subject variability.

A consistent observation is the decline in similarity scores with increasing parcellation granularity, highlighting the escalating complexity and the ill-posed nature of the inverse problem at finer resolutions. The similarity decreases from between-integration to within-integration batches further support the hypothesis that reconstructions exhibit a bias towards the brain's geometrical structure.

Interestingly, the fidelity of wMN reconstructions in capturing micro-scale features for RES-100 and RES-200, at a connectome density of 100%, falls short of perfection, contrasting with the relative success observed in macro-scale feature preservation. A pivotal finding from further investigations is the marked improvement in reconstruction quality when a minor percentage of graph weights is excluded from the analysis (e.g., maintaining a density of 75% by discarding the weakest 25% of graph weights). This indicates a reconstruction bias towards the weakest network

links and underscores the heightened challenge in preserving micro-scale network properties compared to macro-scale ones.

The analysis also reveals that, aside from reduced variance, the choice between standard and corrected connectivity measures does not significantly influence the overall accuracy of the reconstructions. This insight underscores the complexity of micro-scale network reconstruction and the importance of considering both macro-scale and micro-scale analyses to comprehensively evaluate reconstruction fidelity.

Figure 4.19 in the *Supplementary Information* explores the influence of varying connectome densities (100%, 75%, 50%, and 25%) on the quality of network reconstructions. Contrary to macro-scale analysis outcomes, we observe a notable peak in similarity scores at a 75% density. This finding was initially unexpected but aligns with graph theoretical research advocating for a percentile-based proportional thresholding approach (a method, which excludes both the strongest and weakest links rather than solely the weakest).

Further analysis provided in Figure 4.20 investigates the performance of the MEM versus MN operator across different resolutions and connectivity measures. Interestingly, the MEM operator outperforms the MN operator at RES-300 and RES-400 resolutions when standard connectivity measures are employed. A deeper examination reveals that the spatial priors inherent in the MEM operator are instrumental in amplifying micro-scale features at these specific resolutions. The MEM's data-driven parcels, defined with a neighborhood order of one, are congruent with the astrocytic structural constraints of our whole-brain model, enhancing the operator's efficacy. In practical terms, this means that for any selected seed dipole within the brain model, the corresponding parcel generated by the MEM operator will include not only the seed dipole but also the dipoles in its immediate vicinity, effectively its first neighborhood. This parcellation strategy mirrors the astrocytic structural layer within our whole-brain model, where astrocytic networks are characterized by their nearest-neighbor connectivity patterns. By capturing this connectivity in the parcellation process, the MEM operator inherently incorporates a critical aspect of the brain's structural organization into the reconstruction process.

However, this alignment is not observed at higher resolutions, RES-8K-100 and RES-8K-200, where MEM's data-driven parcels, being agnostic to functional connectivity, do not coincide with the underlying parcellations comprising 100 and 200 cortical regions, respectively. Consequently, the spatial kernel of the MEM operator cannot consistently leverage the structural constraints of the whole-brain model at these finer resolutions due also to the high density of dipoles within each parcel or region of interest. To understand this, consider that the local covariance matrices used by the MEM operator, which are pivotal for reconstructing the network's micro-scale features, cannot be confined to merely include a seed dipole and its immediate neighbors (its first neighborhood). Instead, due to the sheer number of dipoles present within each parcel or region of interest at these resolutions, the local covariance matrices inevitably encompass a broader array of dipoles, extending beyond the immediate neighborhood. This expansion beyond the first neighborhood dilutes the MEM operator's ability to leverage the specific structural constraints that mimic astrocytic networks, which are fundamentally characterized by their nearest-neighbor connectivity patterns.

This observation underscores the potential for refining the MEM operator and the simulation framework, especially for scenarios involving high dipolar resolutions. The challenges encountered at these finer resolutions offer a valuable perspective on the limitations of current

reconstruction techniques and the complexities inherent in modeling the brain's intricate network structures.

4.5.4 Micro-scale analysis of MN and MEM reconstructions at RES-8K-100

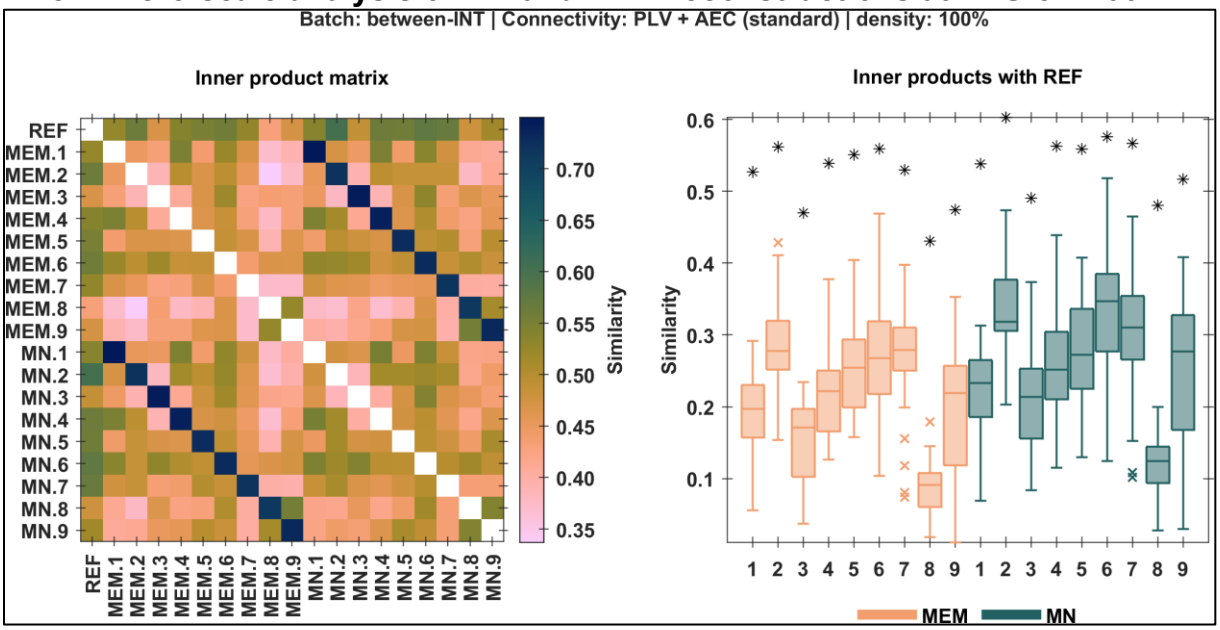

Figure 4.5. Comparative analysis of MN and MEM networks at micro-scale with full connectome density. On the left, a heat map visualizes the similarity matrix (diagonal excluded) derived from a joint STATIS analysis of all simulations within the between-integration batch, using standard connectivity measures. On the right, box plots provide a statistical summary of similarity scores for each inverse operator (MN and MEM) across subjects, based on individual STATIS analyses for each simulation within the batch. Black star dots overlaying the box plots correspond to similarity scores from the joint STATIS analysis, aligning with the values in the first row and column of the heat map, thereby offering a dual perspective on network similarity assessments.

With the insights gained from Figure 4.5, it is evident that, at the RES-8K-100 resolution, MN reconstructions of micro-scale network properties exhibit a slight advantage over MEM reconstructions. Echoing findings from the macro-scale analysis, we observe that the relative similarity rankings among subjects remain consistent irrespective of the chosen inverse operator, underscoring a high degree of fidelity in reconstructions within individual subjects for both MN and MEM operators. Further substantiation of these findings is provided in Figure 4.21 in the *Supplementary Information*, which extends the analysis to encompass varying connectome densities, connectivity measures, and simulation batches. This comprehensive overview reinforces the observed trends, highlighting the robust performance of MN reconstructions across a spectrum of conditions. Figure 4.22, also available in the *Supplementary Information*, delves into the correlation loadings associated with micro-scale network properties, such as closeness versatility (CV), eigenvector versatility (EV), and multi-strength (S). This analysis reveals that corrected connectivity measures generally ensure better preservation of all examined micro-scale properties, albeit with notable variabilities observed under standard connectivity measures. Notably, the analysis distinguishes between CV, which primarily reflects short-range connectivity, and EV and S, which encapsulate the effects of long-range connectivity. This distinction is consistently maintained across the reconstructions, highlighting the nuanced differences in how various connectivity measures capture the intricate web of neural interactions at the micro-scale.

Exemplar reconstructions for MN and MEM are provided in Figure 4.11, Figure 4.12, Figure 4.13, and Figure 4.14.

4.6 Discussion

This study offers novel insights into the reconstruction of complex and biologically plausible whole-brain MEG functional networks, particularly concerning amplitude-based and phase-based functional connectivity. The findings have significant implications for empirical studies and methodological approaches in the field of resting-state EEG and MEG research.

Rethinking zero-lag couplings. A prevalent recommendation in the methodology of functional connectivity research has been to avoid measures susceptible to volume conduction effects, equating this to the avoidance of zero-lag couplings analysis (Palva et al., 2018). This caution stems from the understanding that volume conduction, spatial leakage, or linear mixing can significantly confound connectivity measures, leading to artificially inflated consistency metrics within and across subjects or groups (Colclough et al., 2016). Contrary to these general recommendations, our simulation-based study demonstrates that true zero-lag couplings can indeed be *reliably* recovered despite the presence of volume conduction. More interestingly, our results suggest that under certain conditions, measures sensitive to zero-lag couplings may offer more reliability than those designed to negate such effects. For instance, the comparison between PLV and wPLI or AEC and oAEC revealed a nuanced dependency on network densities.

Impact on network weight distribution — Our findings specifically highlight a differential impact of zero-lag biases on the network's weight distribution: stronger graph weights (top 50%) are less likely to be influenced by zero-lag biases, which instead tend to affect the weaker graph weights. Conversely, stronger graph weights appear more susceptible to non-zero-lag biases, while the weaker weights remain largely unaffected. This nuanced understanding challenges the prevailing notion of uniformly avoiding zero-lag sensitive measures and calls for a more sophisticated approach to selecting connectivity measures based on the specific network properties and research objectives.

Reevaluation of methodologies and theoretical work — The revelation that true zero-lag couplings can be discerned amidst volume conduction challenges opens new avenues for re-evaluating methodologies that have been sidelined in neuroscientific research (Palva et al., 2018). This discovery not only invites a reexamination of previously disregarded methods but also beckons a reevaluation of experimental and theoretical work on zero-lag synchronization of neural oscillations (Palva et al., 2018). Such a reassessment can be undertaken with a refined understanding of the limitations and potential biases inherent in reconstruction techniques, enriching our grasp of neural coherence mechanisms (Palva et al., 2018).

Addressing spurious connections — Our findings also resonate with research (Palva et al., 2018) that uncovers a prevalence of spurious connections due to field spread near actual interaction sites (the *ghost* interactions), despite the immunity of certain connectivity measures to linear mixing. This observation underscores the intricate challenge of distinguishing genuine neural interactions from artefactual correlations induced by methodological constraints (S. H. Wang et al., 2018). Notably, our explorations of the ground-truth networks, unmarred by linear mixing biases, illuminates the distinct yet complementary nature of PLV and wPLI. Contrary to a common misconception in the neuroscience community, these measures do not merely serve as alternatives to each other but rather unveil unique connectivity patterns. This insight emphasizes the need for a broader analytical perspective that transcends the conventional dichotomy of measure selection based on perceived strengths or vulnerabilities.

Advocating for a comprehensive approach — The synthesis of our findings advocates for a comprehensive approach to analyzing functional connectivity, integrating multiple measures to encapsulate the multifaceted nature of neural interactions (De Domenico, 2017; Vaiana & Muldoon, 2020). This holistic strategy, encompassing both amplitude and phase coupling metrics, promises to provide a richer and more nuanced understanding of brain dynamics than the reliance on a select few measures predicated on their theoretical robustness (Palva et al., 2018).

Revisiting phase-based connectivity measures. Phase-based connectivity measures, despite their potential for revealing precise temporal relationships between neural oscillations, have often been criticized for their noisier nature and the statistical challenges they present (Colclough et al., 2016). Contrary to these criticisms, our analysis illuminated that, with properly optimized inverse operators, phase network couplings exhibit remarkable consistency in their reconstructions. This aligns with findings from other scholars who have sought the most effective combinations of inverse operators and connectivity measures for electrophysiological network analysis (Hassan et al., 2014). It is important to acknowledge that our simulations were conducted in an idealized, noise-free environment and were underpinned by a parameterized whole-brain model inherently conducive to strong phase network couplings (as opposed, e.g., to a weakly coupled oscillator network model (Forrester et al., 2020)). This context may have inadvertently favored the reconstruction of phase-based interactions. Recognizing this limitation, we advocate for future investigations to adopt more nuanced simulation environments that rigorously test the robustness of phase coupling reconstructions, incorporating factors such as additive noise at the source or sensor levels, and dynamic models that permit greater variability in phase relationships (in our model this would involve a different parameterization). Such considerations would provide a more rigorous assessment of the fidelity with which phase couplings are reconstructed, especially under varying brain states and cognitive conditions.

Interplay between amplitude and phase couplings. A growing body of literature suggests that the inherent signal mixing in EEG and MEG data can constrain the distinctiveness of neuronal phase and amplitude couplings, challenging the physiological interpretation of connectivity analyses (Brookes et al., 2014). Contrary to viewing this as a limitation, our study advocates for a paradigm shift from comparing to integrating connectivity measures. By embracing the principle of complementarity, we posit that amplitude and phase couplings offer unique yet interrelated insights into brain connectivity (De Domenico, 2017; Vaiana & Muldoon, 2020). Our simulations were intentionally designed to explore this hypothesis, illustrating how astrocytic activity influences the relationship between amplitude and phase couplings in neuronal networks. The findings suggest that electrophysiological reconstruction methods are adept at capturing the nuanced interplay between these connectivity measures, potentially unveiling the complex dynamics of neural communication. This approach aligns with the notion that the brain employs multiple concurrent communication channels among neural assemblies. Hence, different connectivity measures might be tapping into diverse facets of information transfer, each revealing distinct aspects of the underlying neural interactions. From a mathematical perspective, it is conceivable that these connectivity measures are not entirely independent but rather provide complementary estimations of the brain's coupling mechanisms (Colclough et al., 2016; Palva et al., 2018; Sadaghiani et al., 2022).

Reevaluating inverse modeling in electrophysiology. The traditional approach to inverse modeling in non-invasive electrophysiology has often grappled with the challenge of signal leakage, which has historically led to a preference, in connectomics, for connectivity measures that

are robust against zero-lag couplings. This preference has given rise to a conventional methodology that depends heavily on the selection of an appropriate inverse operator. Numerous studies have been conducted to identify the most effective combinations of inverse operators and connectivity measures for accurately characterizing neural networks, particularly in resting-state contexts or in pathological conditions such as epilepsy (Allouch et al., 2022, 2023; Fraschini et al., 2020; Hassan et al., 2014, 2017; A.-S. Hincapié et al., 2017; Mahjoory et al., 2017; Pellegrini et al., 2023; Tabbal et al., 2022; Yu, 2020). This chapter proposes a paradigm shift from the conventional comparative approach to one that prioritizes the selection of methods based on their capacity to incorporate biological priors (Deslauriers-Gauthier et al., 2019, 2020; Gonzalez-Moreira, Paz-Linares, Areces-Gonzalez, Wang, & Valdes-Sosa, 2018; Gonzalez-Moreira, Paz-Linares, Areces-Gonzalez, Wang, Bosch-Bayard, et al., 2018; Gonzalez-Moreira, Paz-Linares, Martinez-Montes, et al., 2018). This perspective is informed by our comparative analysis of the wMN estimate and the wMEM, where MEM's inherent consideration of geometrical attributes led to more accurate recovery of nodal functional patterns in some conditions. This underscores the limited utility (from a modeling perspective) of comparing wMN, which does not account for geometrical information, with wMEM, which explicitly does.

The role of model priors. Notably, the discussion extends to the evolution of inverse modeling techniques over the last decade, highlighting the introduction of models capable of integrating structural and functional network priors (Deslauriers-Gauthier et al., 2019, 2020; Gonzalez-Moreira, Paz-Linares, Areces-Gonzalez, Wang, & Valdes-Sosa, 2018; Gonzalez-Moreira, Paz-Linares, Areces-Gonzalez, Wang, Bosch-Bayard, et al., 2018; Gonzalez-Moreira, Paz-Linares, Martinez-Montes, et al., 2018; Sanchez-Bornot et al., 2024). This advancement enables a more simultaneous estimation of source activity and connectivity in EEG and MEG data, aligning closely with whole-brain simulation frameworks. These next-generation models can redefine signal leakage beyond mere zero-lag couplings, incorporating biological insights such as cortical geodesic distances, thereby offering a more refined and biologically consistent framework for understanding electrophysiological connectivity (Gonzalez-Moreira, Paz-Linares, Areces-Gonzalez, Wang, Bosch-Bayard, et al., 2018).

Implications for clinicians and experimental researchers. While the aforementioned perspectives largely cater to research teams with methodological expertise, the findings presented herein hold significant implications for clinicians and experimental researchers. Despite its longstanding presence in the field and its simplicity, the wMN operator has demonstrated its continued viability and convenience (B. He et al., 2018; Lin et al., 2006; Vallarino et al., 2023). Our analyses indicate that the wMN can yield results comparable to those derived from more sophisticated operators, yet with substantially lower computational demands. This revelation underscores the potential of the wMN to serve as a robust tool in clinical and experimental settings, where computational resources or methodological expertise might be limited. The efficacy of the wMN operator in handling complex network simulations, as evidenced in this study, positions it as a particularly valuable asset for non-methodologists engaged in electrophysiological research. Given the utility of the wMN demonstrated in this study, future research should endeavor to elucidate the operator's strengths and limitations more comprehensively. Such studies could provide invaluable insights for experimental researchers and clinicians, facilitating more informed choices of analytical tools in electrophysiological studies. It is noteworthy that, to our knowledge, this study represents the first application of the wMN within a sophisticated network simulation framework, marking a significant contribution to the field and paving the way for further explorations of its potential.

Innovations in functional network analysis and future directions. This study introduces a pioneering approach to analyzing complex brain networks by integrating multilayer network modeling with STATIS (Abdi et al., 2012; De Domenico, 2017; González-Narváez et al., 2021; Vaiana & Muldoon, 2020). This combination addresses the critique of complexity in graph-based functional connectivity analysis, offering a nuanced method to explore the intricate web of neural interactions. Multilayer network theory enables a sophisticated examination of the brain's complexity across different scales, modalities, and dimensions, enriching our understanding of structural and functional connectivity. Simultaneously, STATIS serves as a versatile analytical tool, adaptable to various statistical modeling scenarios, enhancing our ability to synthesize and interpret multi-faceted neuroimaging data. This methodological advancement is significant for its ability to make complex network analyses more accessible and comprehensible, potentially broadening the appeal and applicability of such analyses across neuroscience disciplines. By presenting these complex models in an intuitive and scientifically engaging manner, we aim to facilitate broader discussions and collaborations within the scientific community. Addressing another common critique of graph-based analyses, the challenge of quantifying statistical significance, our study prioritizes descriptive statistics for simplicity (Bassett & Sporns, 2017; Brookes et al., 2014; De Domenico, 2017; Mandke et al., 2018). However, recognizing the critical need for rigor in statistical evaluations, we advocate for future research to develop and standardize methods for assessing the statistical significance of network properties and comparisons. This is particularly pertinent given the active developments in network neuroscience and the current diversity in statistical approaches (Bassett & Sporns, 2017; Brookes et al., 2014; De Domenico, 2017; Mandke et al., 2018; Sadaghiani et al., 2022).

Revising the discussion on simulation approaches and literature. In our exploration of whole-brain modeling for electrophysiological studies, we delved beyond traditional simulations that primarily focus on neuronal structural connectivity patterns. By incorporating a dynamic astrocytic compartment, we explicitly accounted for the influence of cortical geometry, a factor often underrepresented in simulation studies yet critical for understanding brain function (Pang et al., 2023).

Geometrical embedding and its implications — The geometrical structure of the brain, particularly its lobar organization, plays a significant role in shaping similarities across multimodal structural and functional networks. Empirical studies have consistently shown that areas such as the visual and somatomotor cortices exhibit dense functional connections, aligning with structural diffusion MRI and functional BOLD MRI networks (Cioli et al., 2014; Mesmoudi et al., 2013; Shafiei et al., 2022, 2023; Suárez et al., 2020). This convergence within unimodal cortices underscores the intertwined nature of structural, functional, and metabolic networks, pointing to a fundamental influence of brain geometry on neural dynamics. However, relying solely on structural diffusion MRI constraints in dynamical models can lead to an oversimplified understanding of brain function, as such models often overlook the intricate role of brain geometry (Griffiths et al., 2022; Pang et al., 2023; Roberts et al., 2016). Recent advancements in neural-field whole-brain computational models have begun to address this by integrating both geometrical and axonal fiber connectivity, suggesting that brain geometry may be a more critical determinant of dynamics than previously understood (Pang et al., 2023).

Astrocytes as functional entities — We propose that astrocytes, with their gap-junctional network organization, provide a biologically plausible framework for mapping the brain's geometrical embedding. This perspective marks a significant shift from conventional models that depict brain sources as purely neuronal (Griffiths et al., 2022; Marder, 2012; Pacholko et al., 2020; Schroeder

et al., 2022; Shine et al., 2019). By considering both neurons and astrocytes, and acknowledging the dual constraints of axonal fiber and gap-junctional connectivity, our model offers a more comprehensive and biologically plausible approach to whole-brain modeling for electrophysiological studies (De Pittà & Berry, 2019).
Methodological implications — Our approach challenges previous notions of *realism* in whole-brain models or electrophysiological simulation studies, which often hinge on empirical head models, sensor noise, and isolated or structurally constrained neural mass models. Thus, this present discussion underscores the need for a more holistic view of brain function that encompasses the complex interplay between neuronal and astrocytic networks, and the fundamental constraints imposed by brain geometry. Our findings not only contribute to the theoretical understanding of brain dynamics but also have practical implications for the design and interpretation of electrophysiological studies.

Key limitations. Our study presents several avenues for enhancement to more closely align with physiological realities and improve the robustness of our findings.
Incorporation of noise and background activity — A more nuanced approach to modeling noise at both source and sensor levels could enhance the realism of our simulations for challenging MEG reconstructions. This includes specifying types of noise beyond white noise and accurately defining noise covariance matrices for inverse operators, tailored to the physiological characteristics of neural activity.
Enrichment of temporal patterns — By integrating electrophysiological insights, such as peak frequency distributions from brain atlases (Frauscher, von Ellenrieder, et al., 2018)), our simulations could better reflect the diverse spectral characteristics of electrophysiological rhythms (Griffiths et al., 2022). Additionally, incorporating regional heterogeneities, such as variations in synaptic densities or neurotransmitter receptor distributions based on multimodal brain maps (Shafiei et al., 2023), would add another layer of physiological detail to our model.
Model parameter adjustments and extensions — To accommodate a wider range of neural oscillations, updating the model's neuronal compartments, possibly by extending the Jansen–Rit model to include broad-band and multi-band spectra (Griffiths et al., 2022), could provide a more comprehensive representation of brain dynamics.
Quantification of bias factors in pattern reconstructions — A deeper analysis of the reconstructed patterns, specifically quantifying the impact of signal leakage and source mixing on the results, would offer insights into the inherent biases of our methodology and potential corrective measures relevant for empirical settings (Hauk et al., 2022).
By addressing these aspects, our study could significantly advance the fidelity and physiological relevance of MEG source-level functional network reconstructions, paving the way for more accurate interpretations of the brain electrophysiological activity and connectivity.

4.7 Conclusion

In this study, we delved into traditional MEG source-level functional network reconstruction, aiming to capture the complex interplay between neuron-astrocyte interactions in whole-brain resting-state dynamics. Guided by a computational model that reflects the biological realism of these interactions, we sought to provide a fresh perspective for assessing empirical electrophysiological connectomics methodologies.

Our analysis foregrounded the neuron-astrocyte dynamic as a critical element in shaping the brain's structural and functional architecture, moving beyond mere neuronal connectivity to

include the impact of brain geometry and the layered nature of functional interactions, particularly through amplitude and phase couplings.

Utilizing sophisticated analytical tools such as multilayer network modeling and STATIS, we explored the nuanced interactions within the brain, evaluating the fidelity of traditional MEG reconstruction methods under diverse simulation scenarios. Our investigation spanned various network scales, dissecting functional integration patterns within and between communities and their potential representation in empirical electrophysiological connectomics.

Through a critical review of existing literature and a reflective analysis of our study's constraints, we aim to foster discussion within the neuroscience community. We call for a shift towards integrating neuron-glial perspectives in electrophysiological data analysis, challenging current interpretations of brain dynamics.

As we conclude, our aspiration is to ignite renewed interest and expand the investigative lens in the study of electrophysiological data's spatiotemporal organization. By advocating for a neuron-astrocyte network approach, we encourage the scientific community to embark on this journey with us, leading to deeper understanding and more comprehensive views of the brain's functional networks.

4.8 Supplementary Information

4.8.1 Selected dynamic regimes

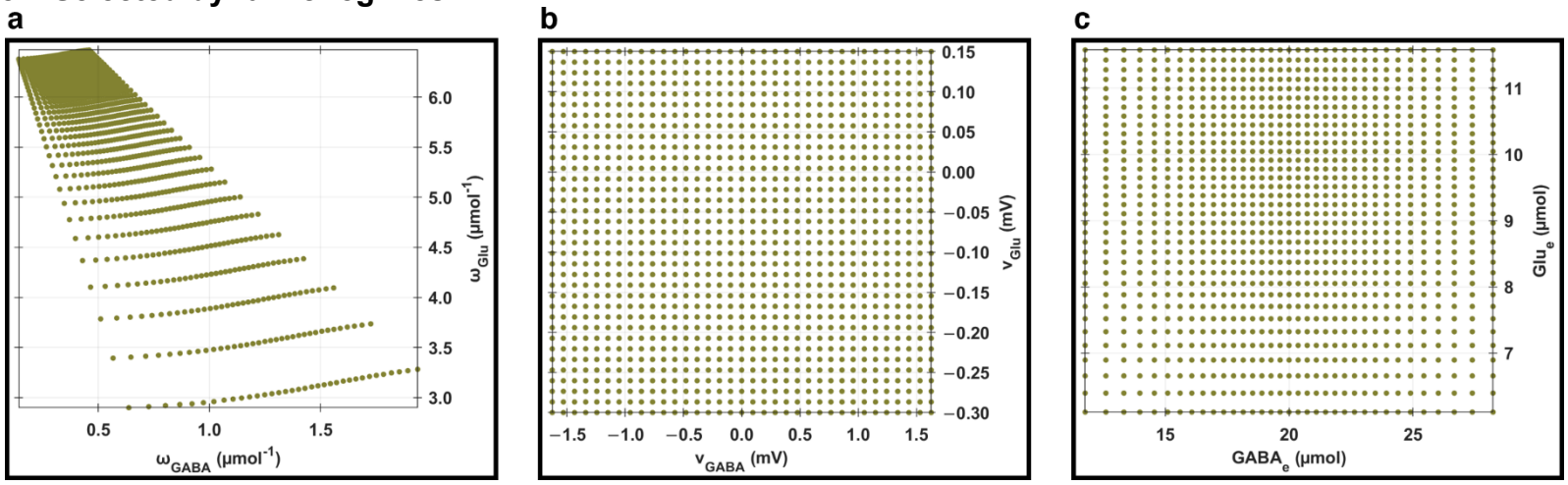

Figure 4.6. Original parameter plane with 1225 configurations. This figure shows the initial parameter plane obtained from Chapter 3 (for instance, refer to Section 3.10 on page 134), using three equivalent coordinate systems of steady-state calculations. Panel (a) uses $(\omega_{\mathrm{Glu}}; \omega_{\mathrm{GABA}})$, panel (b) uses $(v_{\mathrm{Glu}}; v_{\mathrm{GABA}})$, and panel (c) uses $(\mathrm{Glu_e}; \mathrm{GABA_e})$.

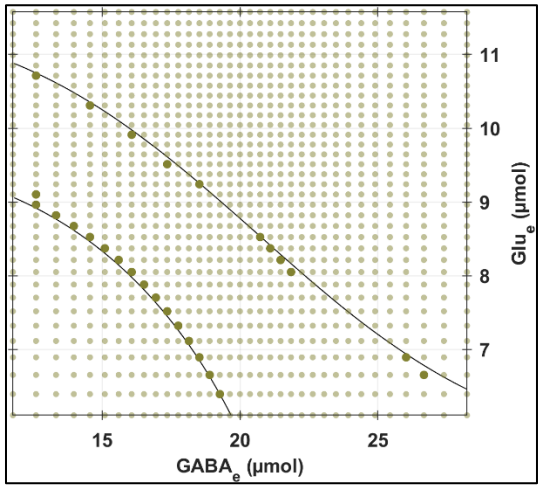

Figure 4.7. New parameter plane with 27 configurations. In this chapter only, 27 out of the 1225 configurations shown in Figure 4.6 were used. These (16+11) configurations map to two distinct contours of limit cycles drawn as black solid curves.

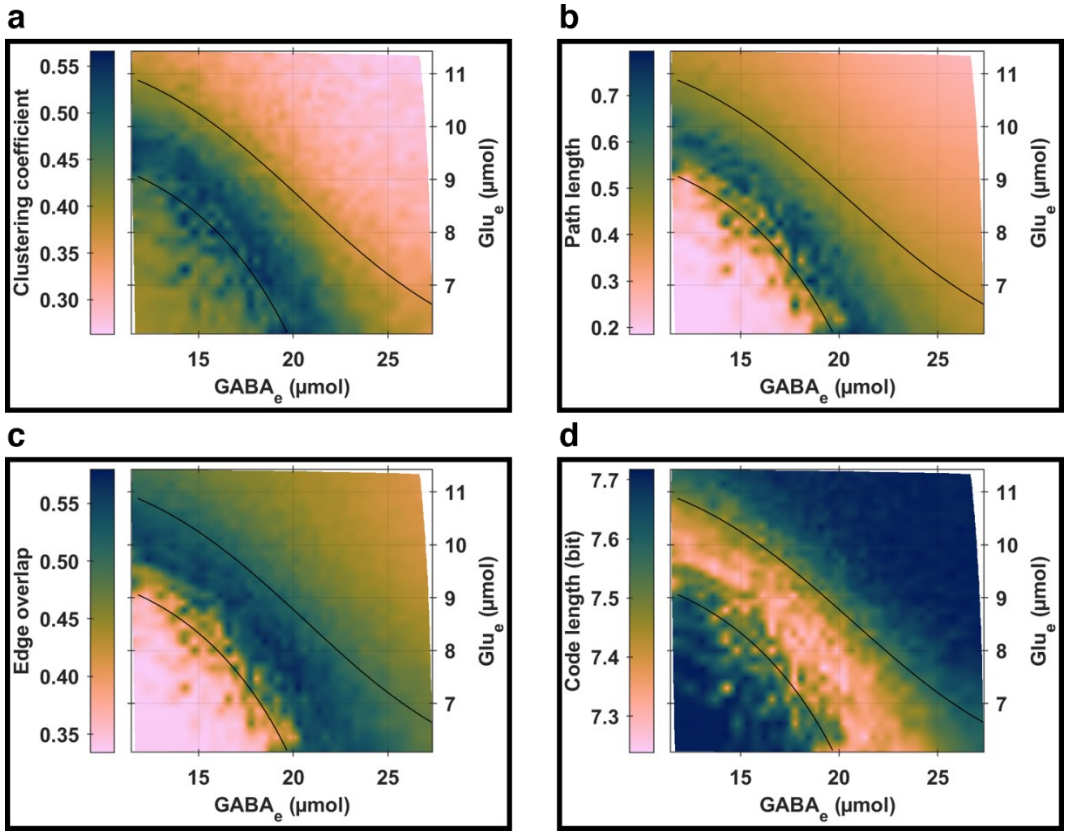

Figure 4.8. Global topological properties of multilayer functional networks. The two contours discussed in Figure 4.7 reflect two dynamical modes, where simulated networks exhibit a broad range of attributes that are particularly relevant to this work. This four-panel figure is the same one as in Chapter 3, except for the two contours of limit cycles. Panel (a): clustering coefficient (an index of network segregation where higher values connote more segregated networks); panel (b): path length (an index of network integration where higher values connote more integrated networks); panel (c): edge overlap (an index of edge redundancy where higher values connote more similar weight patterns across layers); and panel (d): code length (a quality index of community detection where lower values connote networks with more optimal data compression of a random walker's movements on them).

4.8.2 Simulated functional connectomes

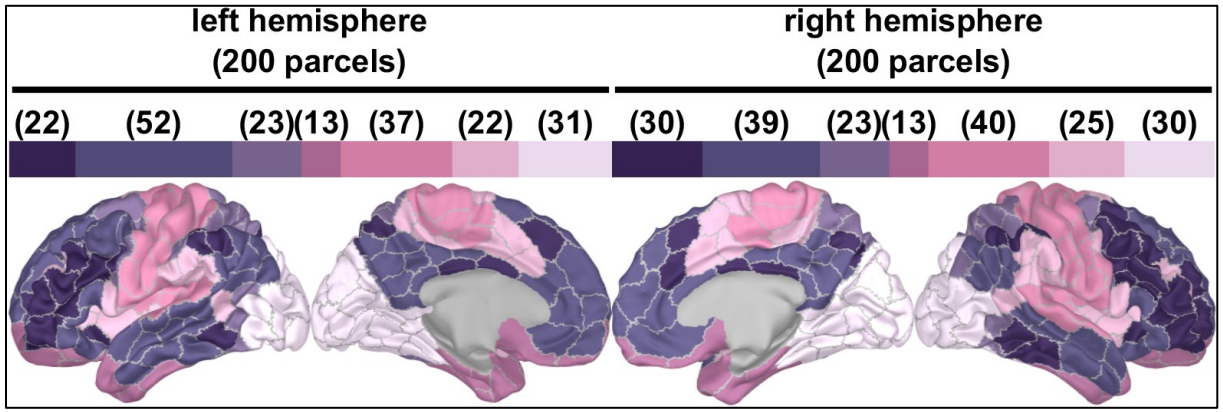

Figure 4.9. Schaefer-400 atlas. Each color indicates a Yeo-7 network. Numbers in brackets indicate how many parcels are in each network across the two hemispheres.

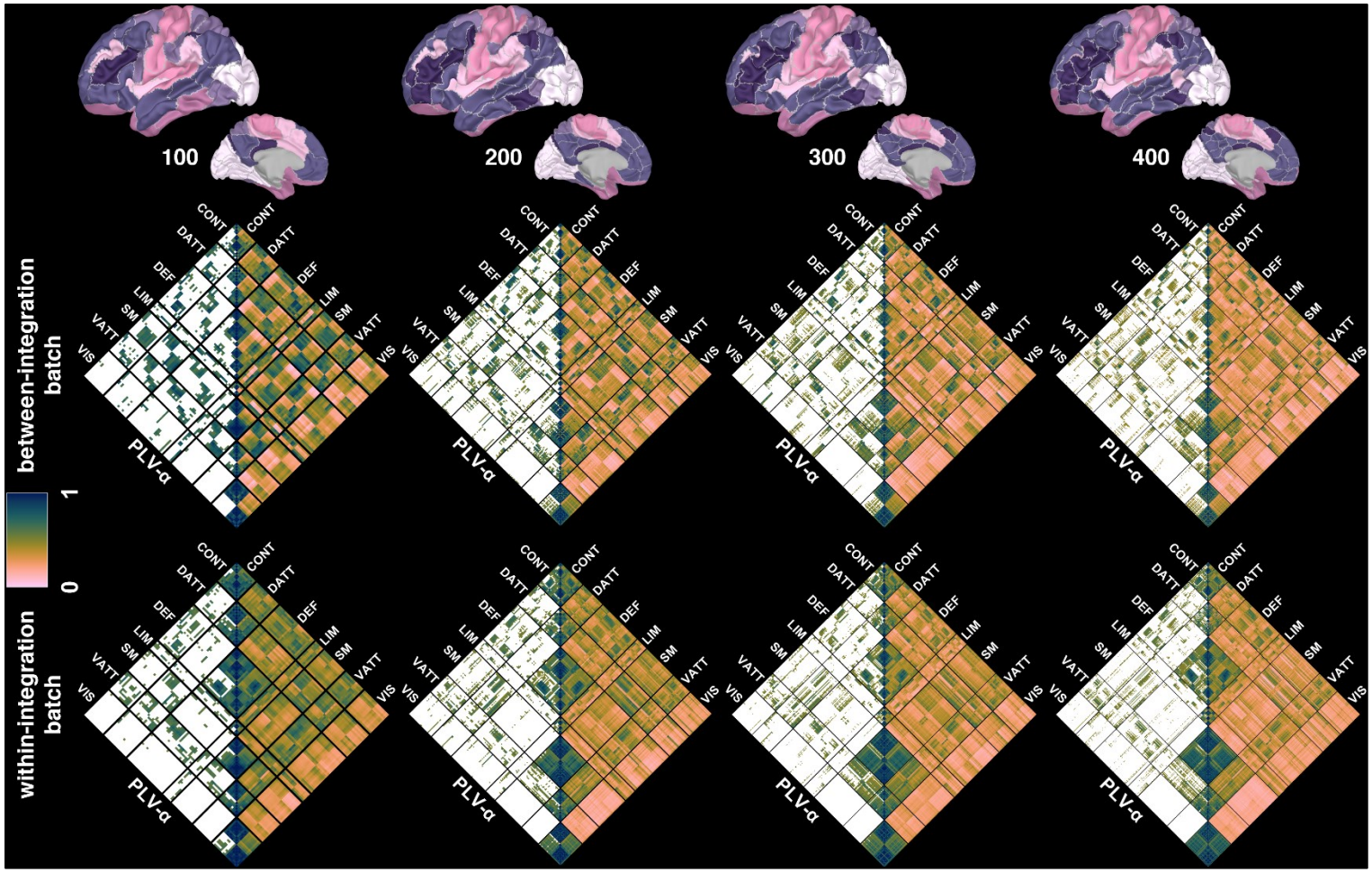

Figure 4.10. Scaling of simulations across spatial resolutions and simulation batches. The figure provides a comparative view of simulations across four spatial resolutions: RES-100, RES-200, RES-300, and RES-400, delineated by columns. The first row displays the parcellation atlases, with each color representing a distinct Yeo-7 subnetwork, consistent with the color scheme in Figure 4.9. The second row showcases a simulation from the between-integration batch for each resolution, all sharing identical parameters except for their structural layers. Here, the matrices exhibit α-band phase locking values, with the upper diagonal representing full density and the lower diagonal showing 25% density, revealing consistent connectivity patterns across all resolutions. The regions within these matrices are organized by subnetworks, with left-hemispheric regions preceding right-hemispheric ones in alphabetical order within each subnetwork, when reading from top to bottom. The third row presents simulations from the within-integration batch at each resolution, differing only in structural layers. The parameters for all eight simulations are the same, only differing in structural layers (the spatial resolutions), or in the variances of the stochastic components of the model (the batches). A comparative analysis between the batches highlights distinct connectivity trends: within the within-integration batch, stronger connections are

predominantly intra-subnetwork and hemispheric. Conversely, the between-integration batch exhibits more pronounced functional interconnections across different subnetworks, showcasing the role of the variance in network dynamics attributed to the stochastic component of the model, as well as the ability of the neuronal structural layer to induce between subnetwork functional integration patterns. In the between-integration batch, the intra-subnetwork connectivity patterns are even more hemispheric than in the within-integration batch, reflecting the influence of the astrocytic structural layer's geometrical constraints.

4.8.3 Reconstructed functional connectomes

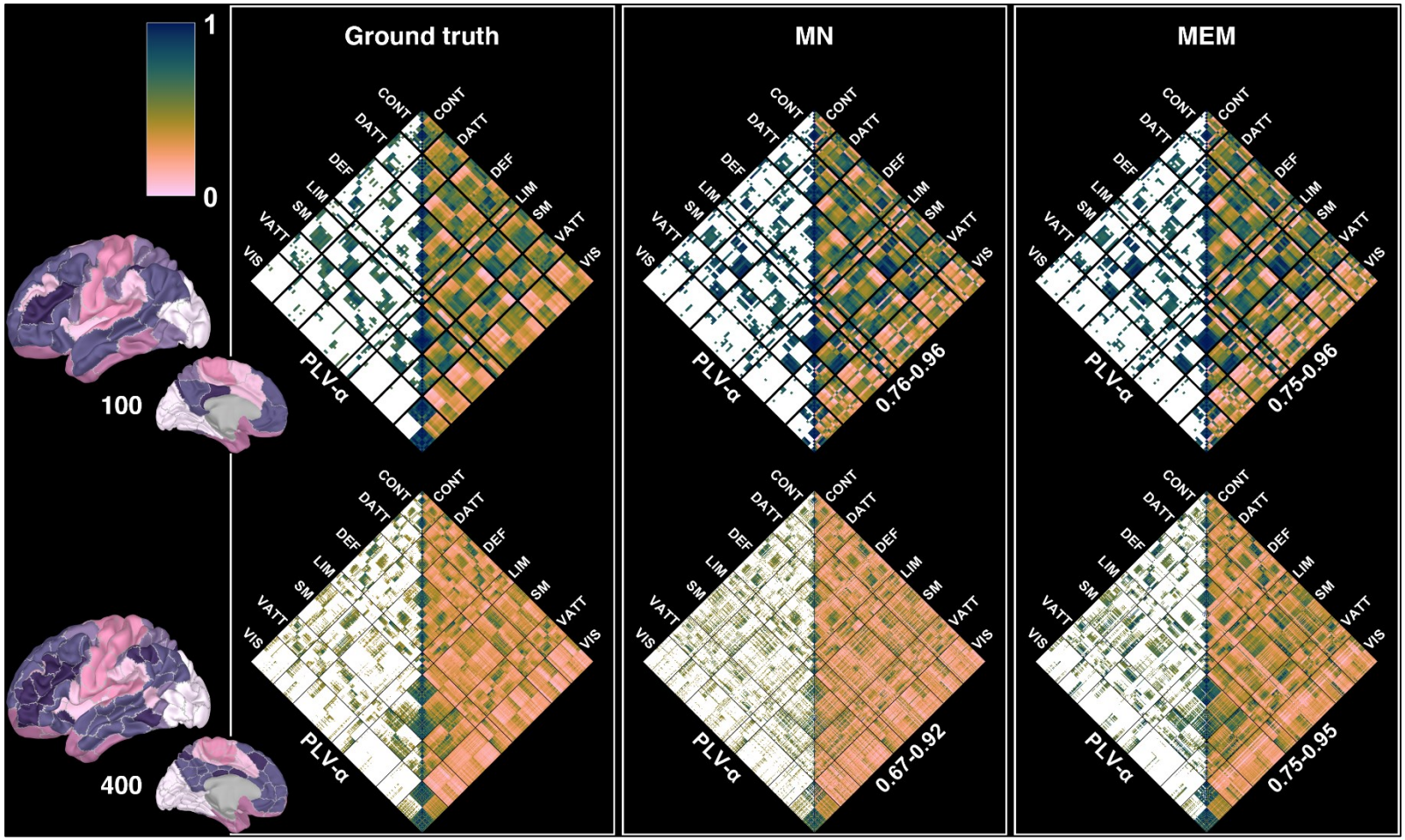

Figure 4.11. Network reconstructions of PLV. This figure juxtaposes MN and MEM reconstructions against the ground truth for two distinct resolutions: RES-8K-100 (displayed in the first row) and RES-400 (shown in the second row), using MEG data reconstructed from the same subject. The matrices illustrate connectivity patterns by depicting the α-band phase locking values. Below each reconstructed connectome, two similarity scores are provided: the first score quantifies the

similarity between thresholded graphs at 25% density, and the second score evaluates the similarity between unthresholded graphs, both in comparison to the ground truth. These simulations, belonging to the between-integration batch, differ only in their structural layers, underscoring the impact of resolution on the fidelity of network reconstructions.

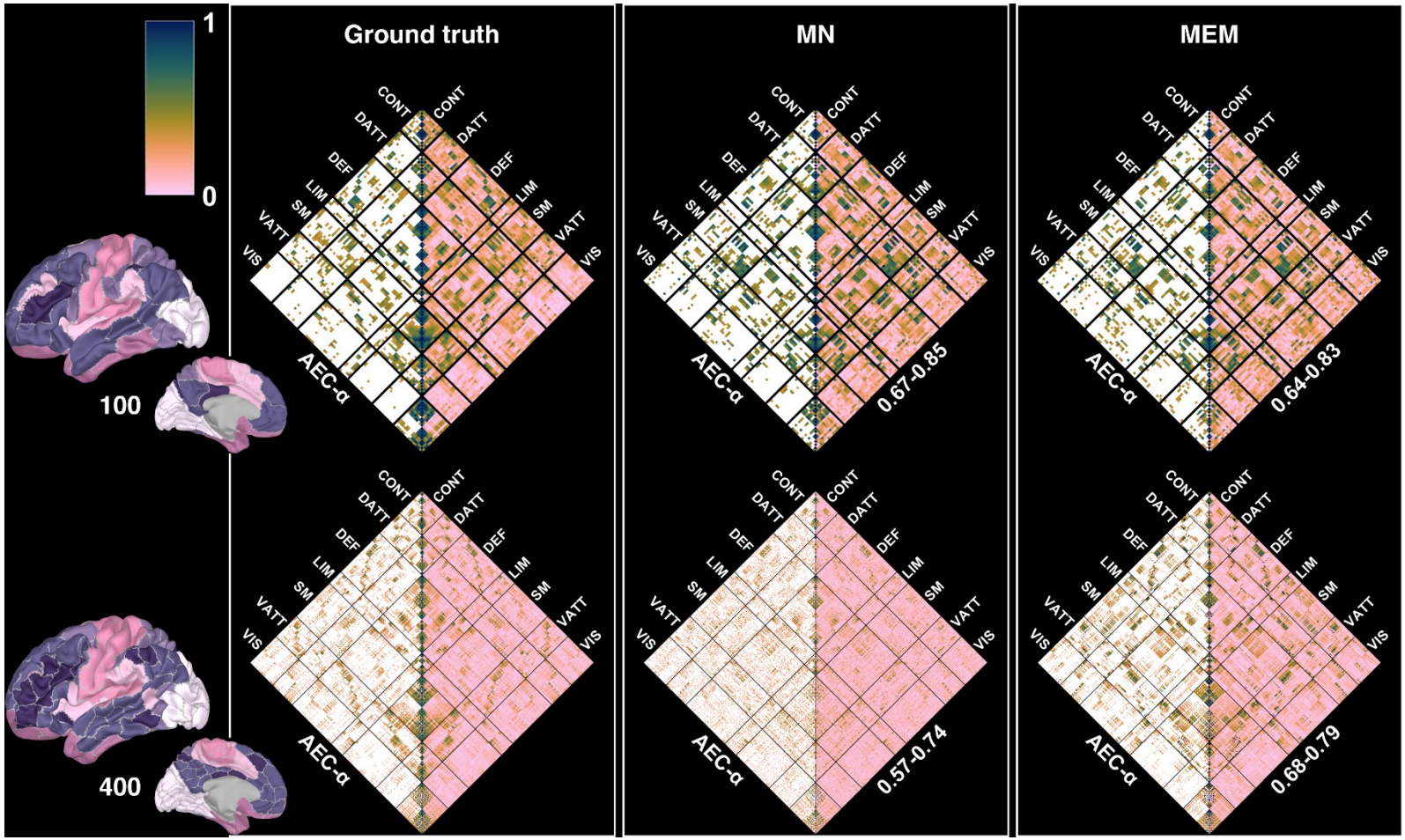

Figure 4.12. Network reconstructions of AEC. This is the same as Figure 4.11, but featuring α-band amplitude envelope correlations (instead of phase-locking values).

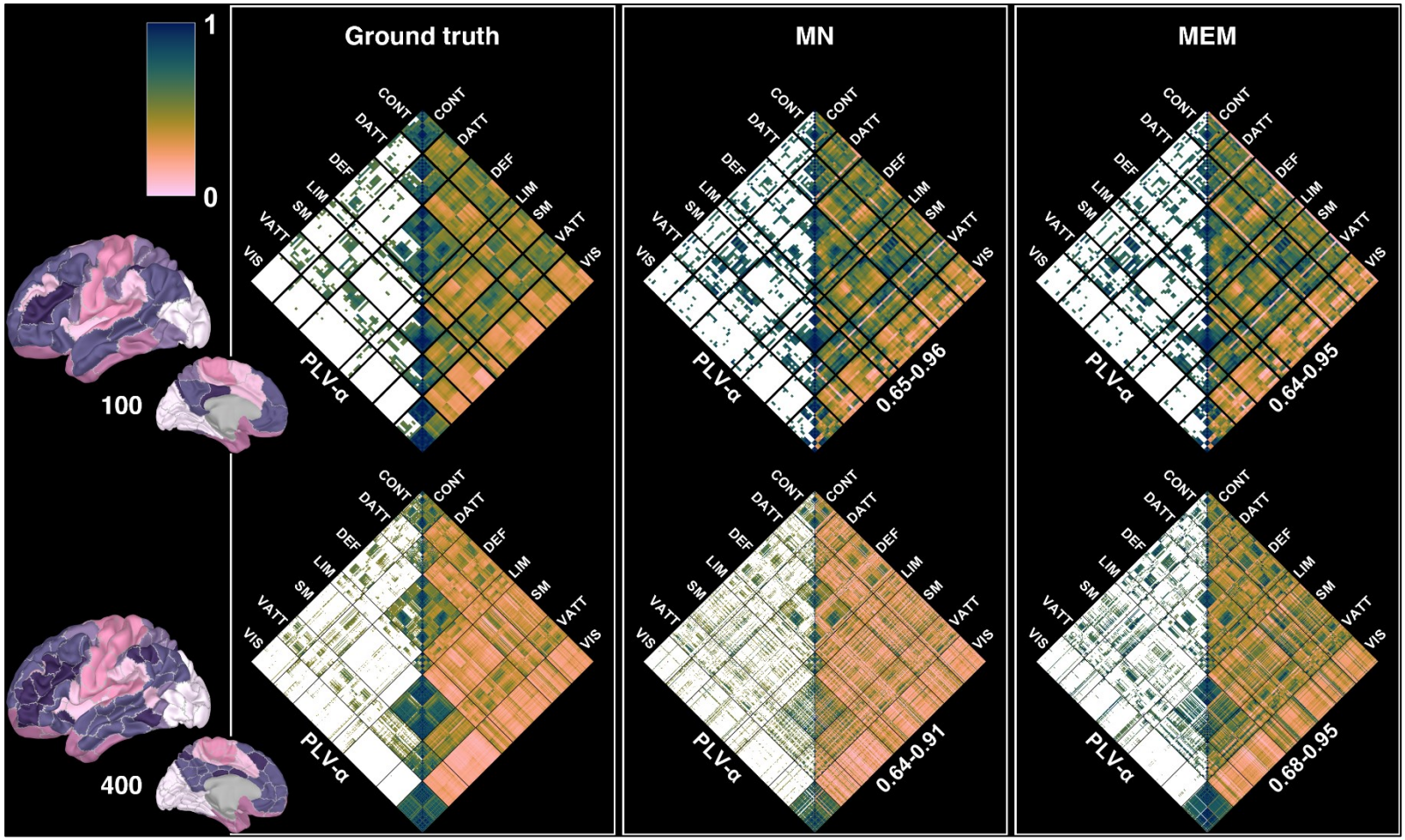

Figure 4.13. Network reconstructions of PLV. Compared to Figure 4.11, this figure features simulations belonging to the within-integration batch.

Figure 4.14. Network reconstructions of AEC. This is the same as Figure 4.13, but featuring α-band amplitude envelope correlations (instead of phase-locking values).

4.8.4 Macro-scale analyses

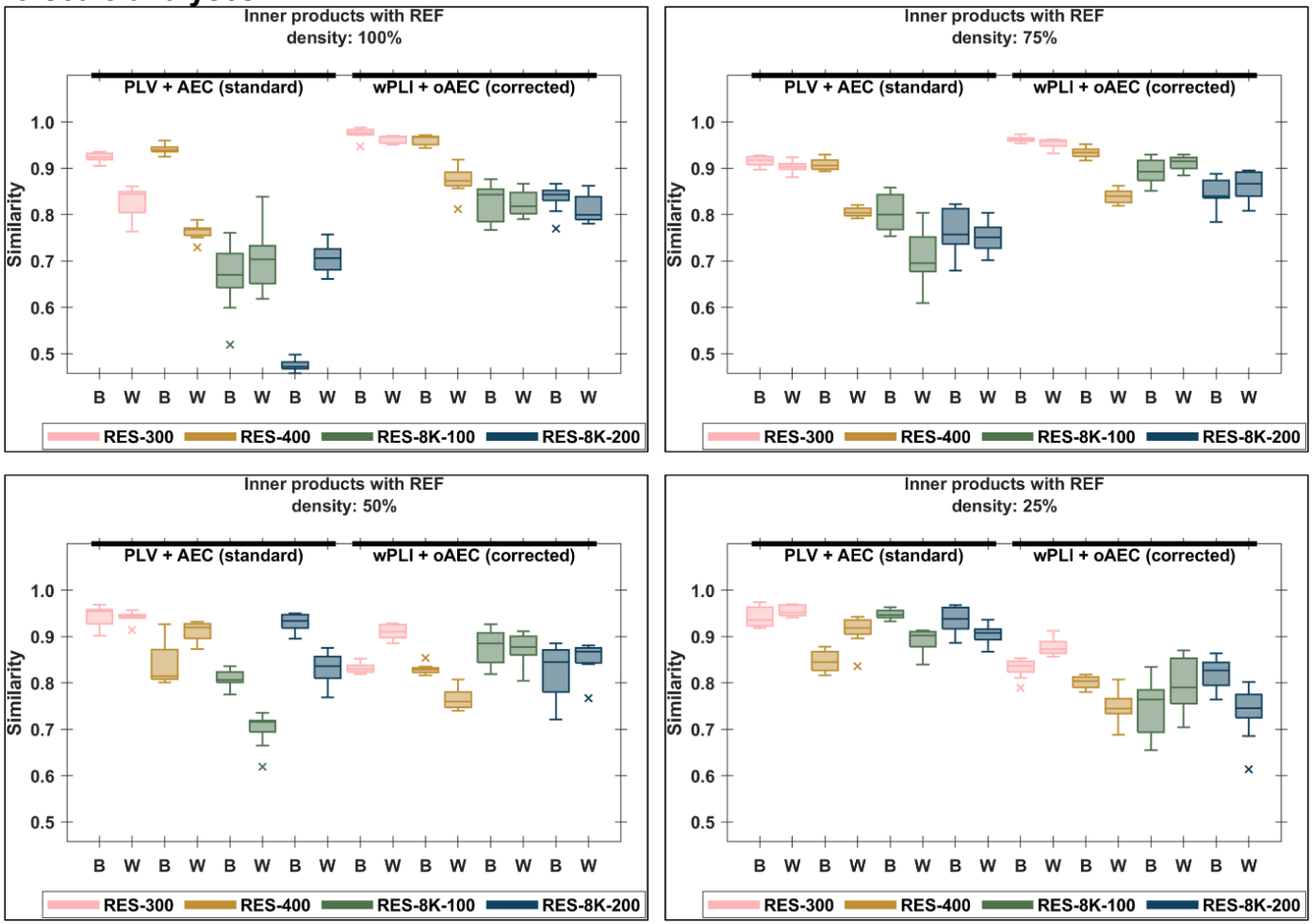

Figure 4.15. Cosine similarity analysis of MN networks at macro-scale. This figure extends the analysis presented in Figure 4.1 by examining the impact of varying connectome densities (100%, 75%, 50%, and 25%) on the cosine similarity scores of MN-reconstructed networks. For clarity, results for RES-100 and RES-200 are omitted, as reconstructions at these resolutions, where the number of sensors surpasses the number of dipoles, tend to approach near-perfect accuracy with decreasing connectome density.

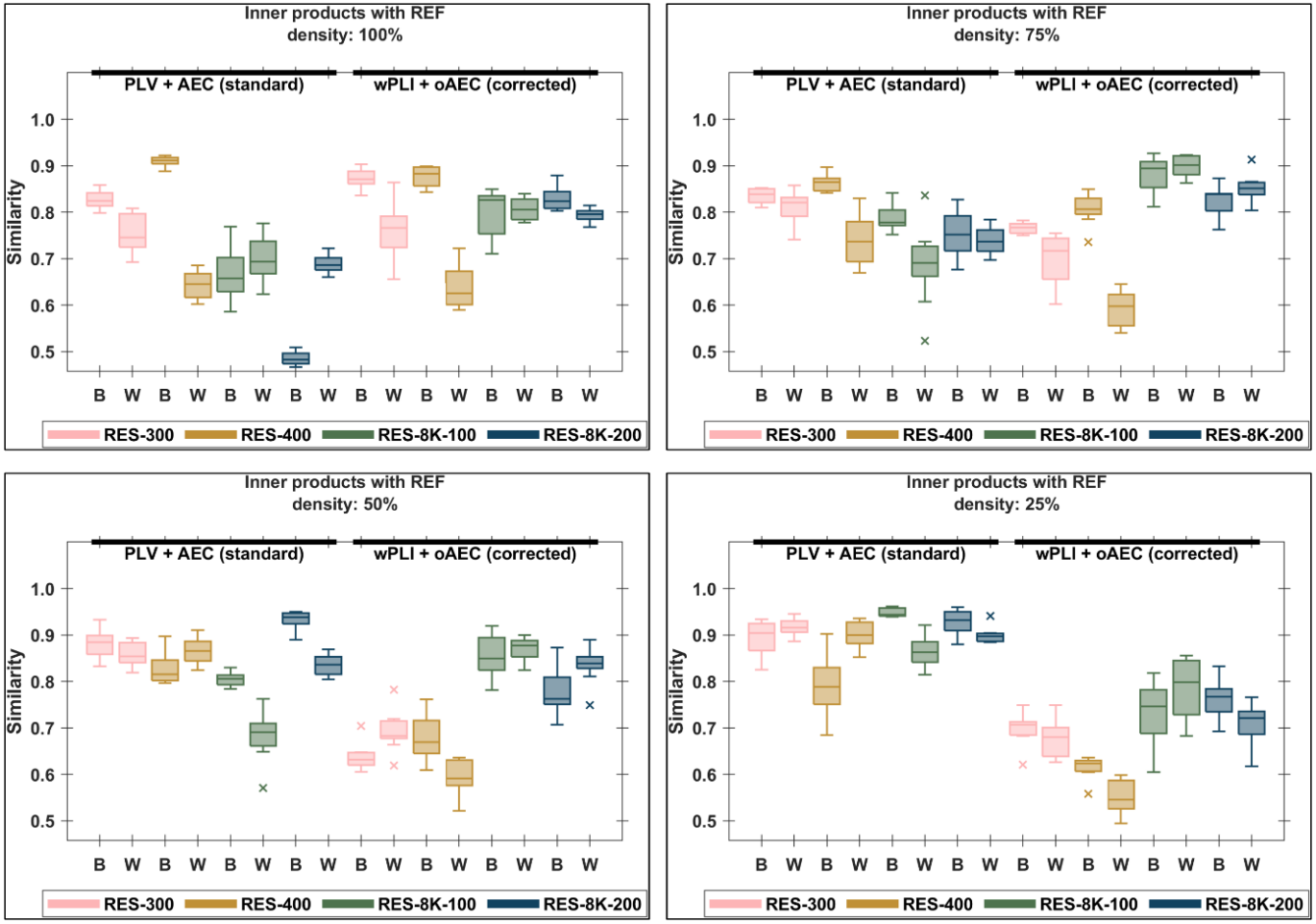

Figure 4.16. Cosine similarity analysis of MEM networks at macro-scale. This figure builds upon the analysis in Figure 4.15 by exploring the effects of employing the MEM inverse operator on network reconstruction accuracy. The analysis compares cosine similarity scores across varying connectome densities, illustrating the performance of MEM in capturing the underlying network structures in comparison to the MN approach detailed previously.

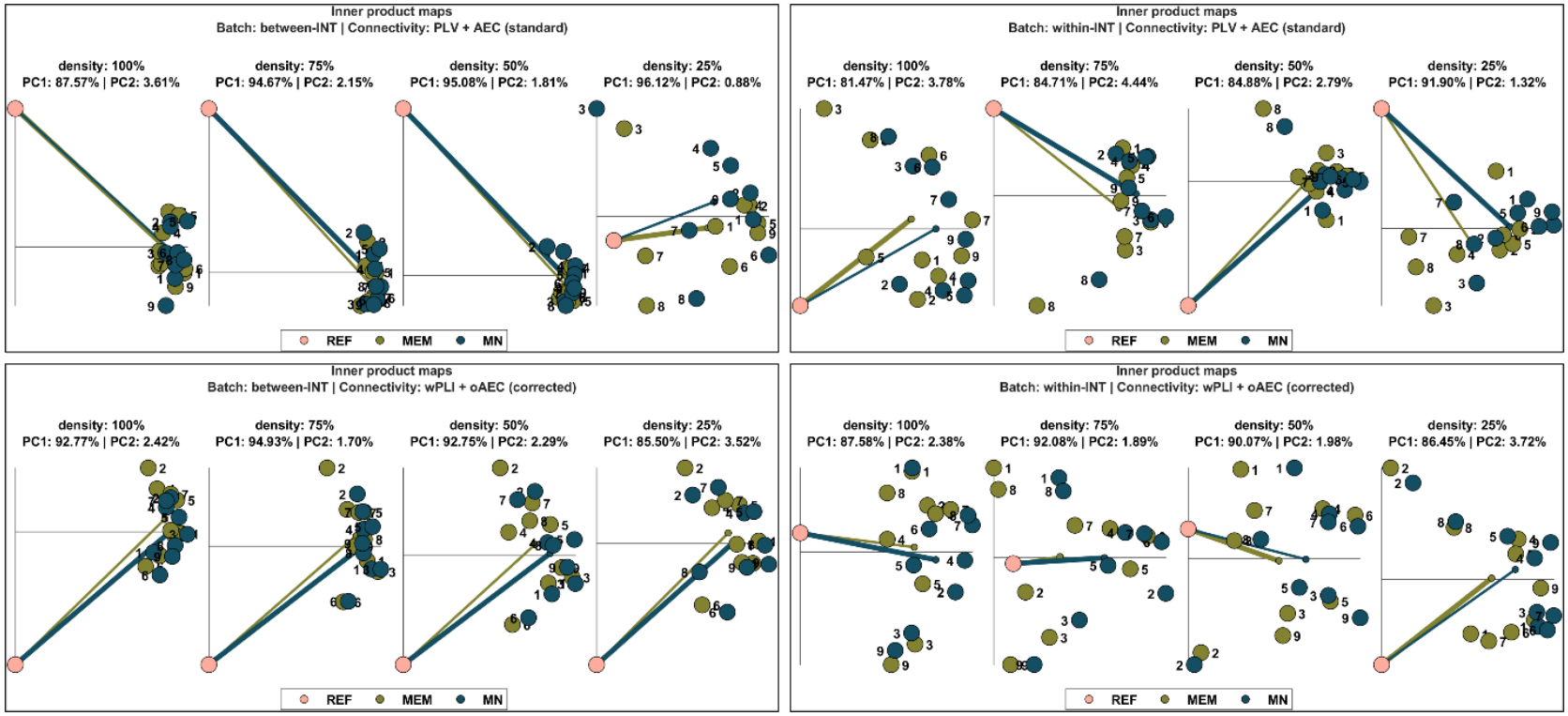

Figure 4.17. Principal component analysis of MN and MEM network reconstructions. This figure builds upon the analysis in Figure 4.2, providing a more nuanced comparison between MN and MEM networks across various dimensions: connectivity measures (standard vs. corrected), simulation batches (between-community vs. within-community integration), and connectome densities (100%, 75%, 50%, and 25%).

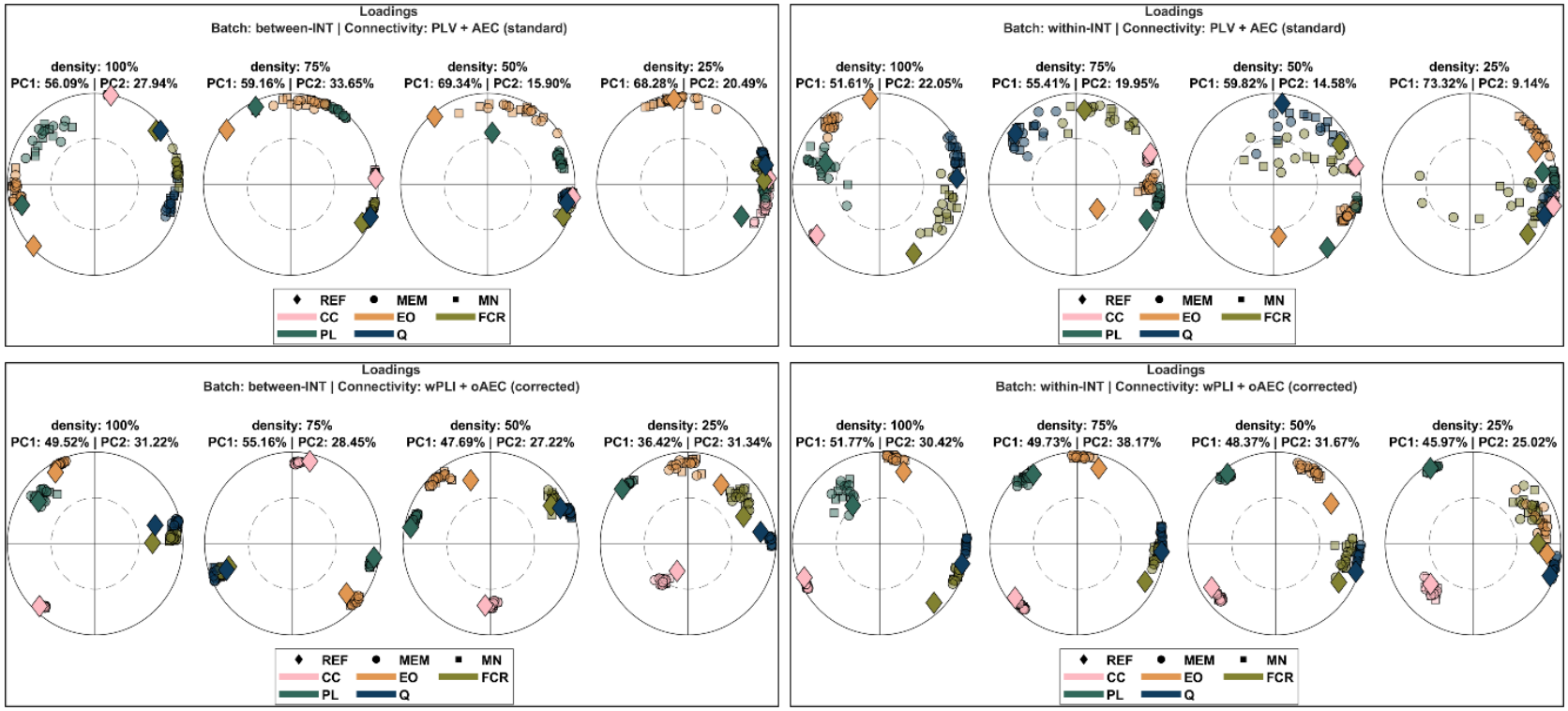

Figure 4.18. Comparative analyses of loadings across MN and MEM network reconstructions. This figure extends the insights from Figure 4.3, by factoring in the effects of connectivity measures (standard vs. corrected), simulation batches (between-community vs. within-community integration), and connectome densities (100%, 75%, 50%, and 25%).

4.8.5 Micro-scale analyses

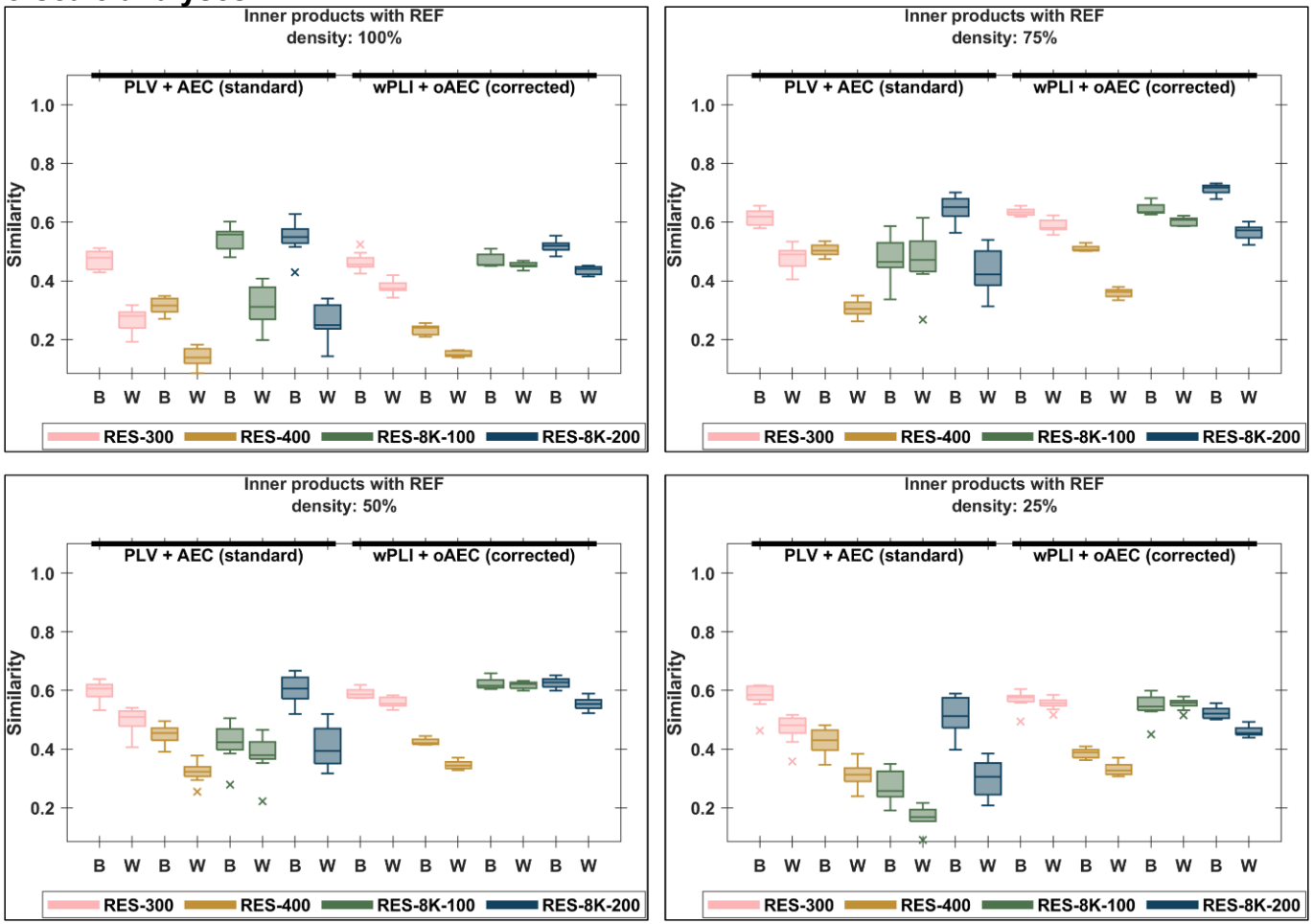

Figure 4.19. Cosine similarity analysis of MN networks at micro-scale. This figure extends the analysis presented in Figure 4.4 by examining the impact of varying connectome densities (100%, 75%, 50%, and 25%) on the cosine similarity scores of MN-reconstructed networks. For each simulation batch, a joint STATIS analysis was conducted, pulling data from all simulations within the batch.

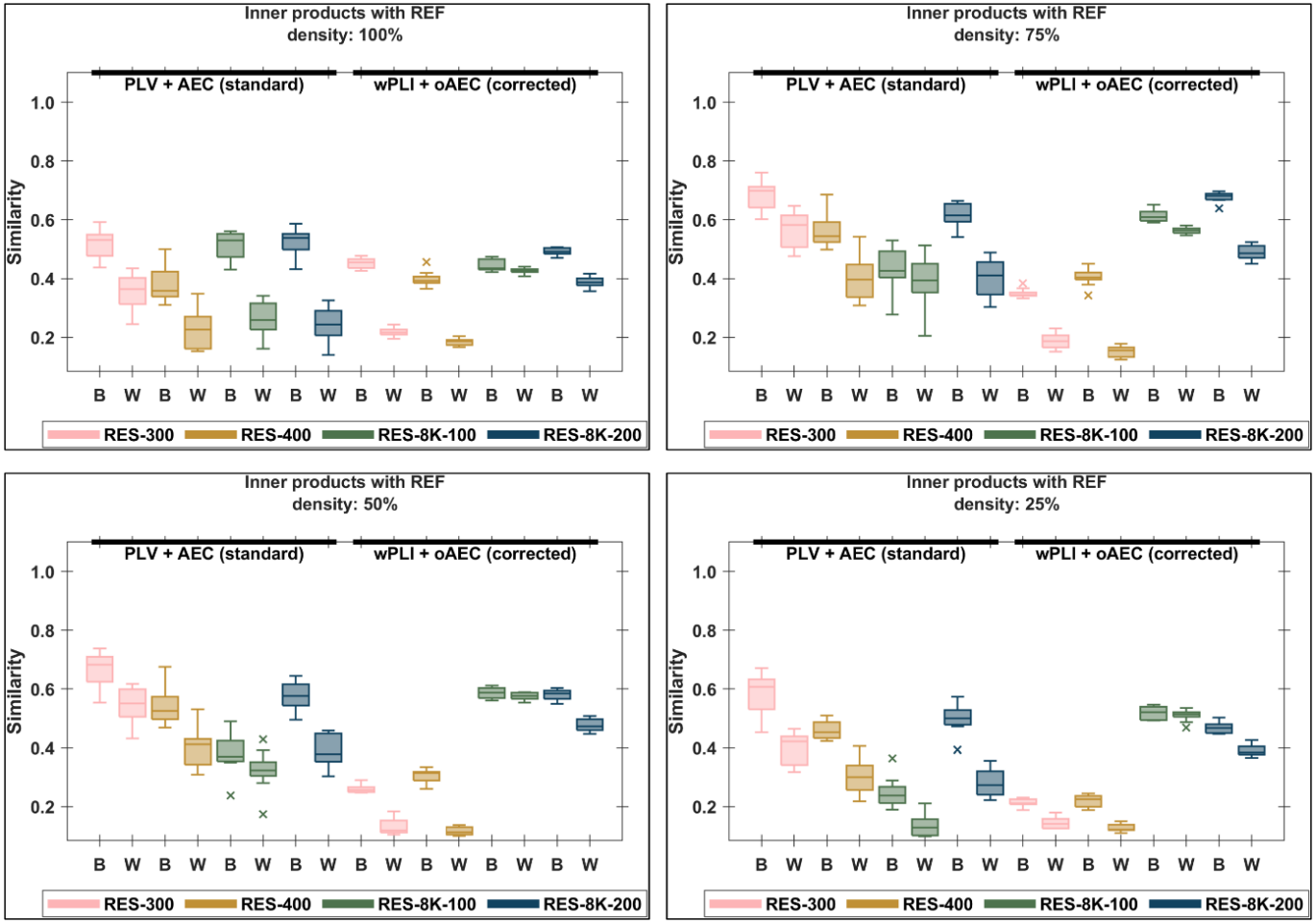

Figure 4.20. Cosine similarity analysis of MEM networks at micro-scale. This figure builds upon the analysis in Figure 4.19 by exploring the effects of employing the MEM inverse operator on network reconstruction accuracy. The analysis compares cosine similarity scores across varying connectome densities, illustrating the performance of MEM in capturing the underlying network structures in comparison to the MN approach detailed previously. For each simulation batch, a joint STATIS analysis was conducted, pulling data from all simulations within the batch.

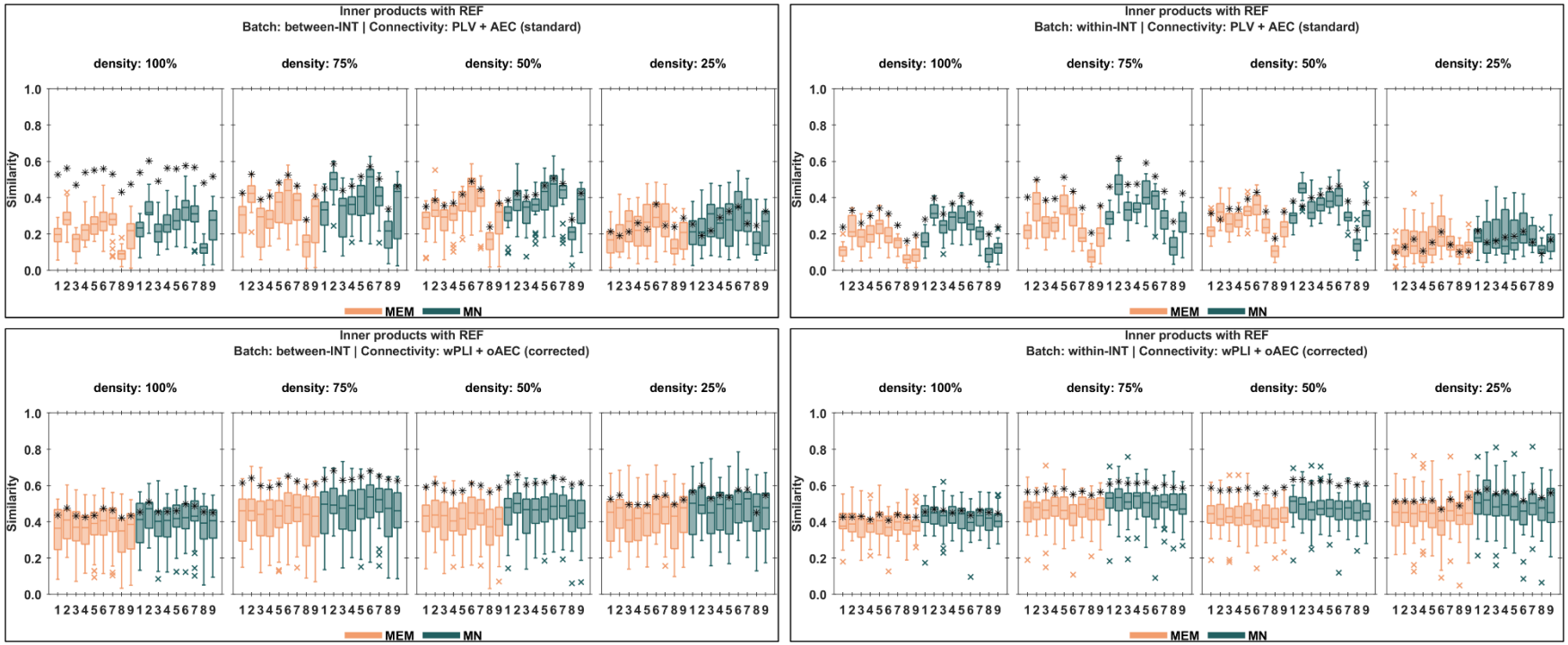

Figure 4.21. Comparative analyses of loadings across MN and MEM network reconstructions. This figure extends the insights from Figure 4.5, by factoring in the effects of connectivity measures (standard vs. corrected), simulation batches (between-community vs. within-community integration), and connectome densities (100%, 75%, 50%, and 25%).

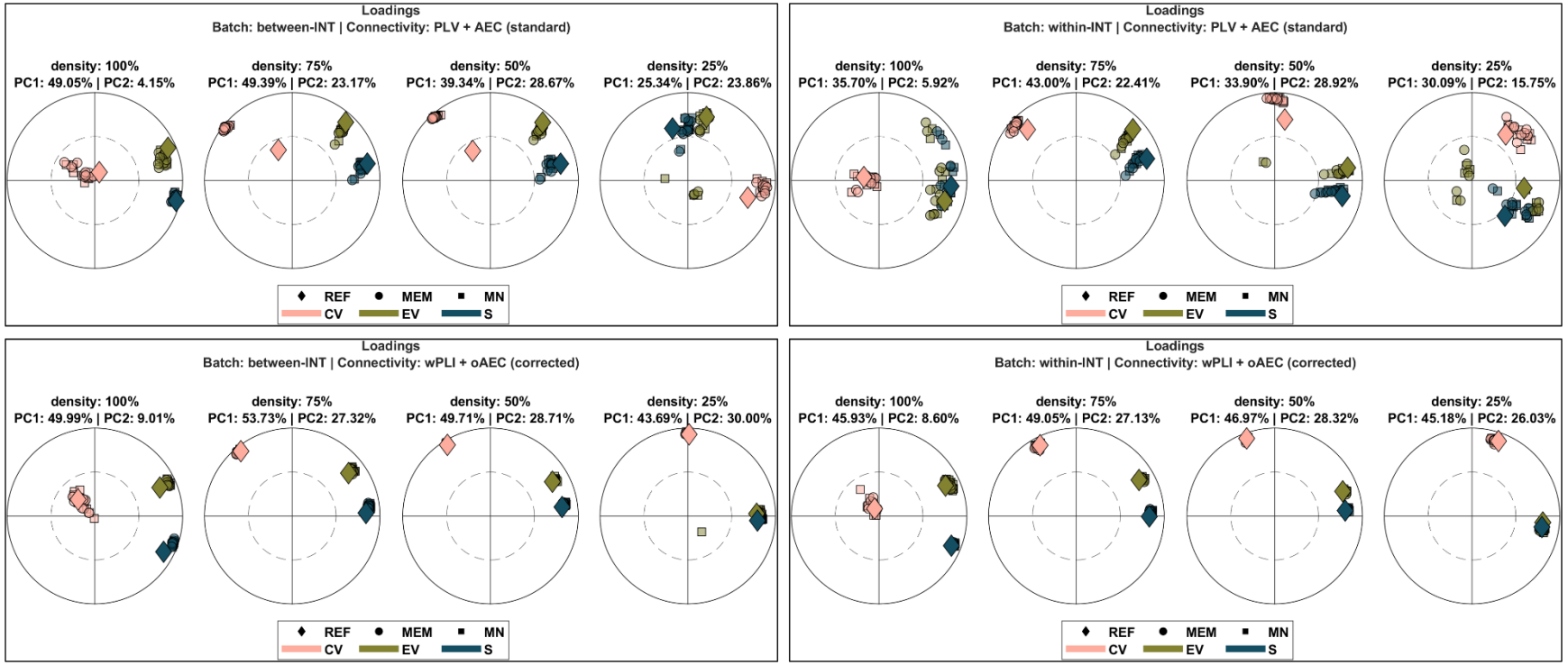

Figure 4.22. Comparative analyses of loadings across MN and MEM network reconstructions. This figure illustrates the effects of connectivity measures (standard vs. corrected), simulation batches (between-community vs. within-community integration), and connectome densities (100%, 75%, 50%, and 25%). For each simulation batch, a joint STATIS analysis was conducted, pulling data from all simulations within the batch. Three network metrics were considered: closeness versatility (CV), eigenvector versatility (EV), and multi-strength (S).

Chapter 5 Exploring mechanisms of network dysfunction, resistance, and adaptation in Alzheimer disease — a research proposal for empirical insight

5.1 Thesis storyline

This chapter represents a departure from the preceding three, serving as a prospective segment of the thesis. It lays the groundwork for an extensive modeling framework designed to tackle critical aspects of Alzheimer disease pathology.

Specifically, in this segment of my thesis, I aspire to unveil a sophisticated modeling framework that encapsulates two pivotal aspects of Alzheimer disease pathology: the synaptic dysfunction and the ensuing neuronal death precipitated by the buildup of extracellular glutamate, alongside the alterations in the brain's white-matter structural integrity.

This endeavor draws inspiration from a series of whole-brain modeling studies (Arbabyazd et al., 2021; de Haan et al., 2017; Demirtaş et al., 2017; Frässle et al., 2018; Hallett et al., 2020; Stefanovski et al., 2019, 2021; van Nifterick et al., 2021; Yalcinkaya et al., 2023; Zimmermann et al., 2018) that have laid the groundwork by exploring these hallmarks, often leveraging the wealth of data from neuronal white-matter fiber connectomes. These studies have adeptly adjusted the excitation-to-inhibition balance within neuronal models, aiming to mirror the hyperactivity induced by glutamate through modifications in neuronal dynamical behavior. Despite their invaluable contributions, these models stop short of delving into the underlying causes of the shifts in excitation-to-inhibition balance, primarily due to their design limitations, such as the absence of variables representing neurotransmitter dynamics or a neural compartment capable of modulating neurotransmission.

In a bid to build upon and innovate beyond these studies, and others such as (Iturria-Medina et al., 2017), my proposal encompasses a comprehensive research agenda that stretches beyond the confines of this doctoral thesis.

5.2 Preliminary investigations

This preliminary section is dedicated to visually demonstrating the complexities of the proposed research agenda through an initial simulation approach that extends the work presented in the preceding chapters. The objective here is to simulate Alzheimer disease (AD) pathology, focusing on glutamate excitotoxicity, to explore the potential role of astrocytic networks in the progression of the disease. This preliminary examination sets the stage for a detailed exposition of my research proposal, which commences on page 230.

While the detailed scientific underpinnings and rationales behind the forthcoming simulations will be thoroughly addressed starting on page 230, this preliminary section emphasizes the intuitive understanding of my research through visual means. Readers are encouraged to engage with these visuals as an entry point into the complex phenomena that I aim at investigating, with the assurance that a comprehensive scientific discussion awaits in the subsequent sections, providing a seamless bridge between visual intuition and scientific rationale.

At this juncture of the thesis, it is crucial to underscore that real data have been utilized only for constructing the structural layers of the whole-brain model, and not for constraining its other

parameters. As delineated in Chapter 2, and reiterated in Chapter 3 and Chapter 4, our model's parameters were derived from a combination of physiologically plausible scalar values sourced from the existing literature (as outlined in Table 2.3) and extensive bifurcation analyses. Consequently, the biologically relevant interpretations presented in the upcoming sections should be regarded as a foundation for hypothesis generation. In this context, the computational model is employed as a tool for conceptual exploration, rather than as a faithful replica of biological reality. The model is specifically tuned to simulate phenomena that may not directly mirror biological reality but provide valuable insights into potential mechanisms and behaviors. The research proposal, detailed starting from page 230, will advance this discourse by illustrating how the insights garnered from the computational model can be further enriched and validated through empirical biological research, thereby bridging the gap between theoretical modeling and real-world biological phenomena.

5.2.1 Regional simulations

In a preliminary simulation scheme (in Figure 5.1, Figure 5.2, Figure 5.3, Figure 5.4, and Figure 5.5), we explore the effects of diminished astrocytic glutamate uptake rates and a concurrent decrease in neuronal synaptic density within an isolated brain region. Here, we first focus on intrinsic regional changes before considering the complexities of network interactions. Additionally, for these preliminary analyses, we employ the following criterion for virtual neuronal death: defined by a prolonged period of minimal activity. This criterion, while unconventional, offers a unique perspective on neuronal viability and glutamate dynamics in the absence of a hard threshold for neuronal death.

Over a span of 120 seconds, we simulate a progressive decrease in astrocytic glutamate uptake from an initial rate of 4.5 μM/s, reducing it gradually until cessation, alongside a simultaneous reduction in global synaptic density from 135 to 125 (the other parameters are mostly like in Table 2.3). The simulation's key variables, the astrocytic self-coupling constants (ω_{Glu} and ω_{GABA}), is adjusted to examine its influence on excitatory gliotransmission at glutamatergic (ω_{Glu}) and GABAergic (ω_{GABA}) synapses. This manipulation provides insights into potential network effects once the region is reintegrated.

Our preliminary simulations (Figure 5.1, Figure 5.2, Figure 5.3, Figure 5.4, and Figure 5.5) reveal distinct dynamical behaviors in neuronal populations under varying astrocytic coupling conditions.

Initially, in Figure 5.1, we observe an abrupt transition from normal oscillatory activity to a quiescent state around 75 seconds, prompted by increasing extracellular glutamate levels. This transition, characterized by a cusp bifurcation, leaves neurons in a minimally active state, isolated from their previously accessible dynamic regimes.

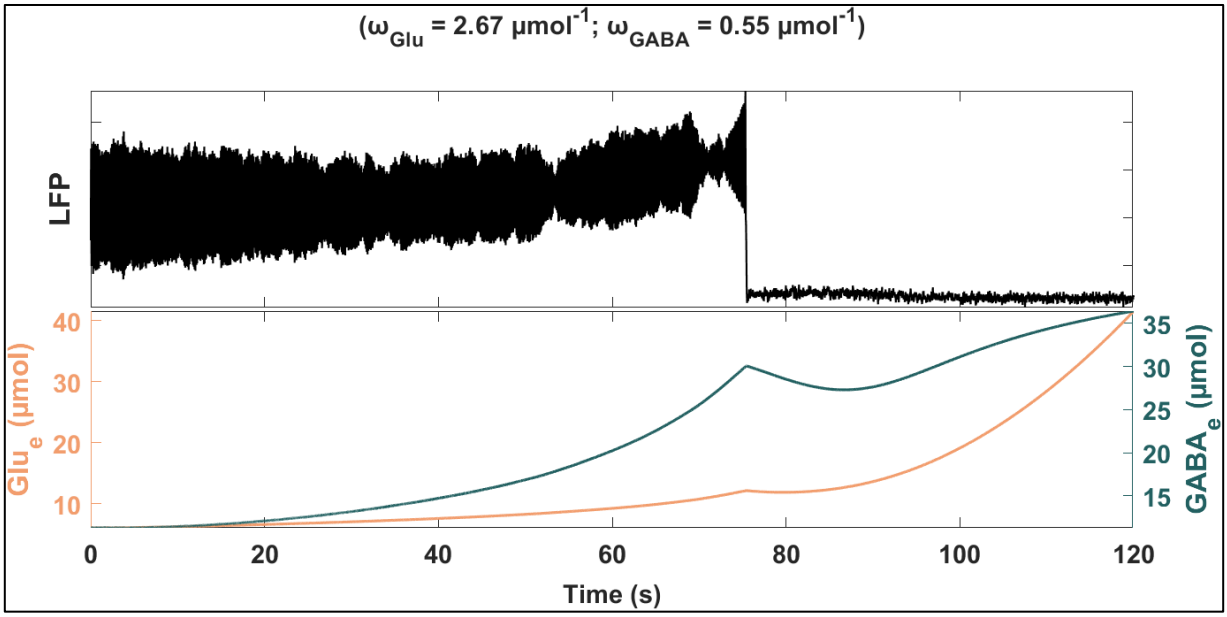

Figure 5.1. Regional simulation experiment #1. This figure shows the membrane potential of pyramidal neurons LFP, extracellular glutamate concentration Glu_e, and extracellular GABA concentration $GABA_e$. The astrocytic self-coupling constants ω_{Glu} and ω_{GABA} are indicated in the figure title.

With enhanced astrocytic coupling's impact on GABAergic neurons, in Figure 5.2, we noted a shift that temporarily restored some neuronal dynamics through a saddle-node bifurcation, albeit followed by inevitable neuronal death due to unmitigated glutamate accumulation.

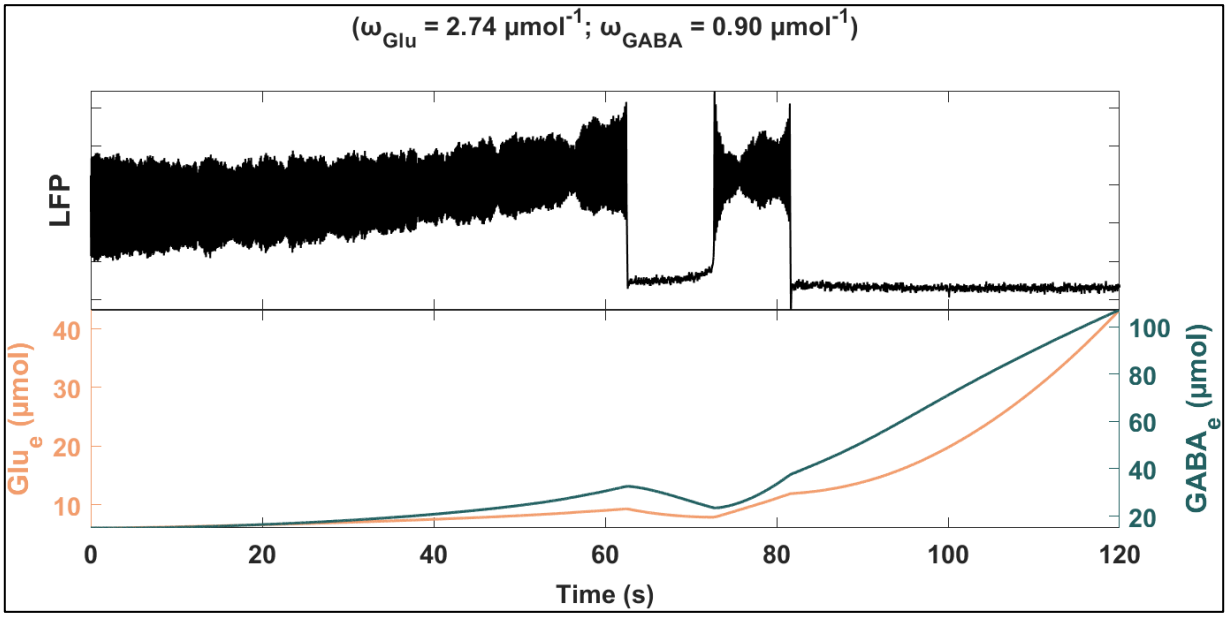

Figure 5.2. Regional simulation experiment #2. Same as Figure 5.1 for different values of ω_{Glu} and ω_{GABA}, increasing astrocytic feedback on GABAergic neurons.

Intriguingly, in Figure 5.3, certain astrocytic coupling settings could hypothetically sustain the neuronal population in a continuous spiking mode, suggesting a potential mechanism for excitotoxicity, if not for a predefined glutamate threshold that would indicate neuronal death.

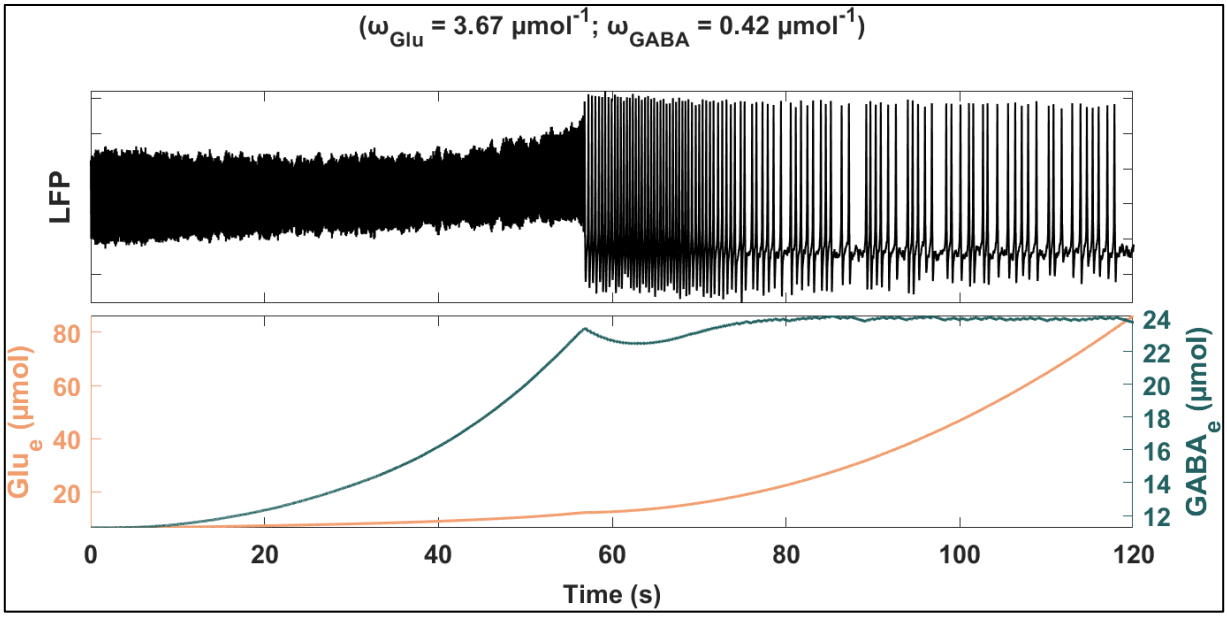

Figure 5.3. Regional simulation experiment #3. Same as Figure 5.1 for different values of ω_{Glu} and ω_{GABA}, highlighting how astrocytic feedback sustain neurons in a spiking regime.

These varied dynamics, from transient recoveries to sustained excitatory states, underscore the pivotal role of astrocytic coupling in neuronal network behavior under stress. Figure 5.4 further demonstrates how astrocytic coupling levels modulate these transitions, offering potential insights into neuroprotective strategies.

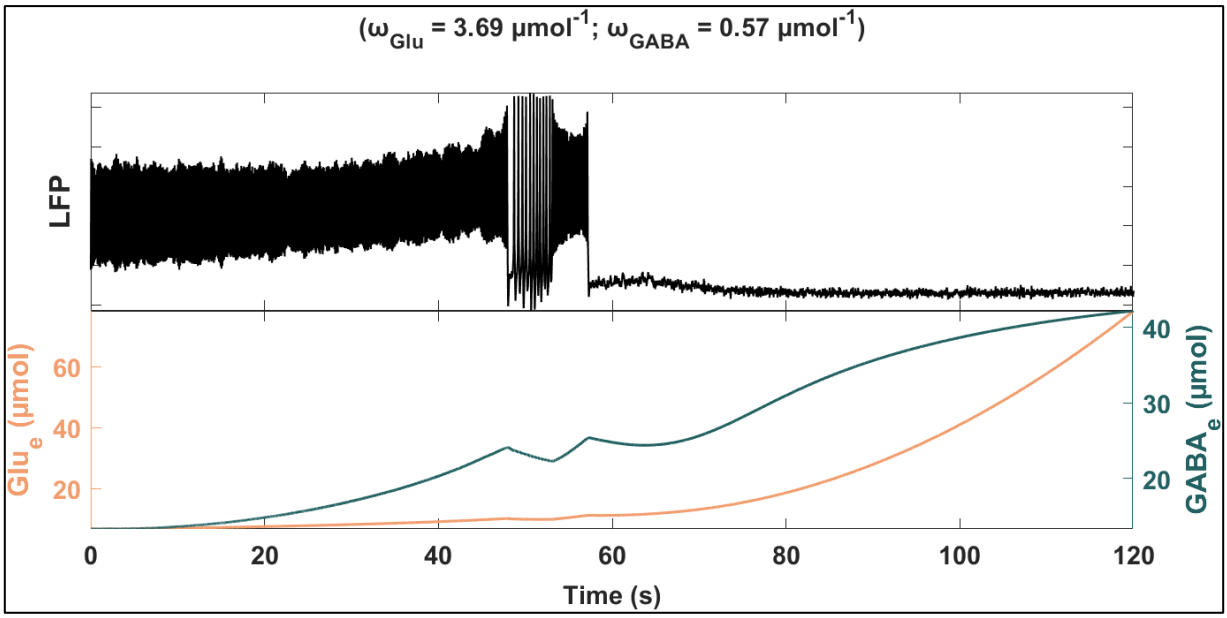

Figure 5.4. Regional simulation experiment #4. Same as Figure 5.1 for different values of ω_{Glu} and ω_{GABA}, highlighting how astrocytic feedback accelerates neuronal losses.

Moreover, we explored a scenario where neurons stabilize in a periodic attractor post-crisis, highlighting the complex interplay between astrocytic influences and neuronal resistance, as depicted in Figure 5.5.

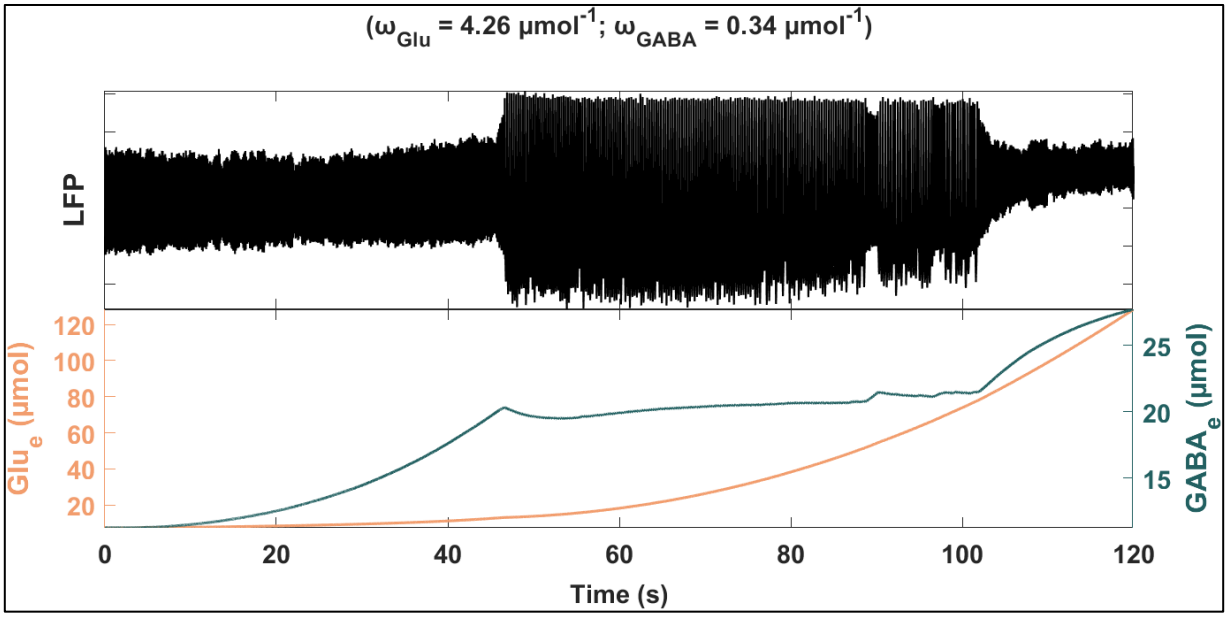

Figure 5.5. Regional simulation experiment #5. Same as Figure 5.1 for different values of ω_{Glu} and ω_{GABA}, highlighting how astrocytic feedback halts neuronal losses.

These simulation scenarios, underpinned by bifurcation analysis as detailed in an earlier chapter (Chapter 2, from page 92), provide a foundational understanding of the nonlinear dynamics at play in neurodegenerative conditions like AD, pointing towards astrocytic coupling as a key modulator of neuronal fate under pathological conditions.

It is important to reiterate that for these preliminary simulations, we made a deliberate choice not to impose a limit on glutamate levels. This approach allows us to explore the full range of neuronal dynamics under conditions of unchecked excitatory neurotransmitter accumulation, providing a baseline understanding of how escalating glutamate levels impact neuronal activity and network stability. However, recognizing the critical role of glutamate-induced excitotoxicity in neurodegenerative conditions such as AD, our next simulations will adopt a more biologically meaningful framework. We will introduce a threshold for neuronal death (which will be modelled as null membrane potentials), triggered by prolonged glutamate exposure, irrespective of the current state of neuronal activity. This threshold will be carefully defined based on a combination of literature review and theoretical modeling, ensuring its relevance to pathological conditions (we partially addressed this topic already in the Chapter 2, on page 92). Incorporating this threshold will significantly enhance the realism and applicability of our simulations, allowing us to more accurately model the processes leading to neuronal death and network degradation in neurodegenerative diseases. By comparing the outcomes of simulations with and without the constraints of a predefined glutamate threshold, we aim to gain deeper insights into the mechanisms of neurodegeneration and the potential for intervention strategies that target glutamate dynamics.

5.2.2 Whole-brain simulations

In exploring a network comprising 216 nodes (in Figure 5.6, Figure 5.7, Figure 5.8, Figure 5.9, Figure 5.10, and Figure 5.11), we next focused on abnormal nodes within the entorhinal and parahippocampal cortices of both hemispheres, regions critical to memory and navigation and often implicated in the early stages of AD. These four network nodes were subjected to

perturbations mirroring those described previously in (Figure 5.1, Figure 5.2, Figure 5.3, Figure 5.4, and Figure 5.5), involving gradual changes in glutamate dynamics.

Our simulations in Figure 5.6 reveal that despite the perturbations, the affected nodes managed to sustain oscillatory behavior compared to the preceding simulations where the nodes were not in a network. This is a testament to the intricate feedback mechanisms within the network, particularly the astrocytic modulation of extracellular GABA. This finding suggests a potential neuroprotective role of astrocytic networks in maintaining neural function under stress. However, this stability was contingent upon the neighboring nodes' capacity to buffer the excess glutamate, as evidenced by transient spiking patterns observed in these nodes.

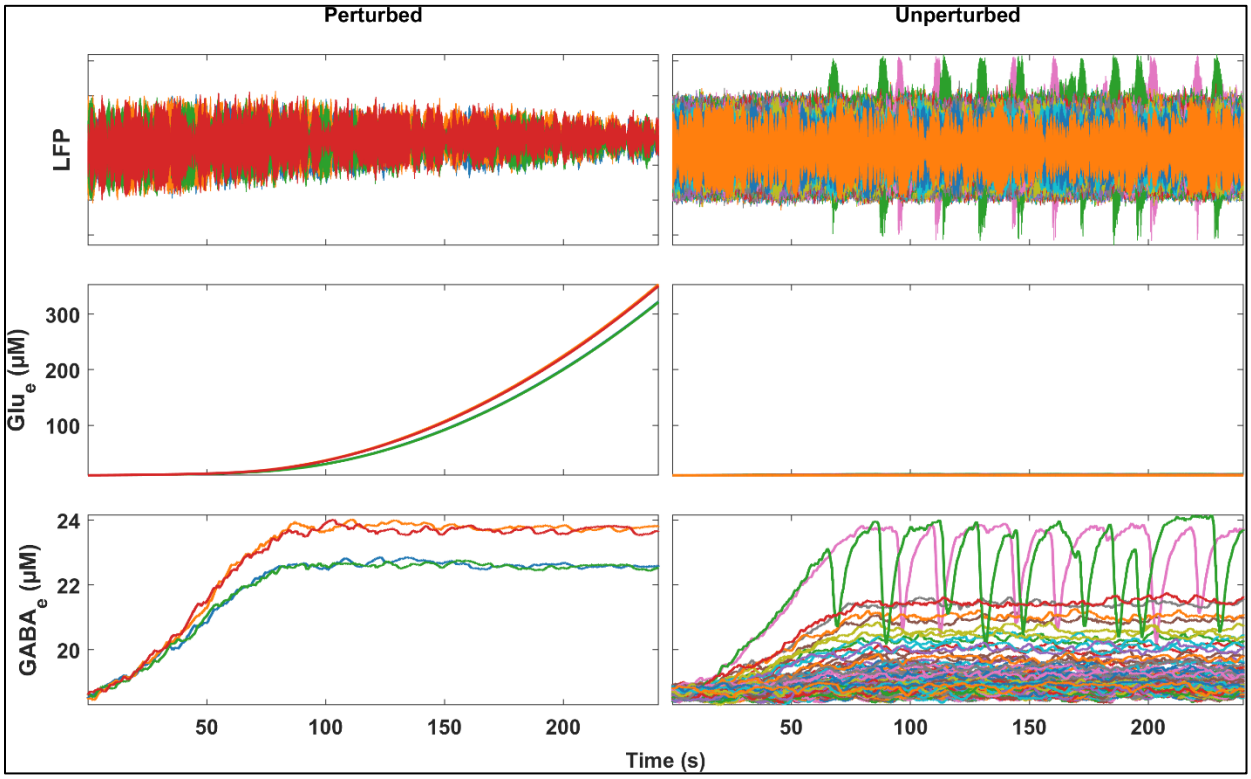

Figure 5.6. Network simulation experiment #1. Same as Figure 5.1 for now within a network of 216 nodes. The perturbed nodes are on the left panels (there are four perturbed nodes). The non-perturbed nodes are on the right panels.

Subsequent simulations in Figure 5.7 showed an expansion of this buffering behavior to more neighboring nodes, highlighting the network's distributed response to localized perturbations. Despite normal local glutamate levels, these nodes exhibited spiking activity, underscoring the complexity of network interactions and the non-local effects of neural perturbations.

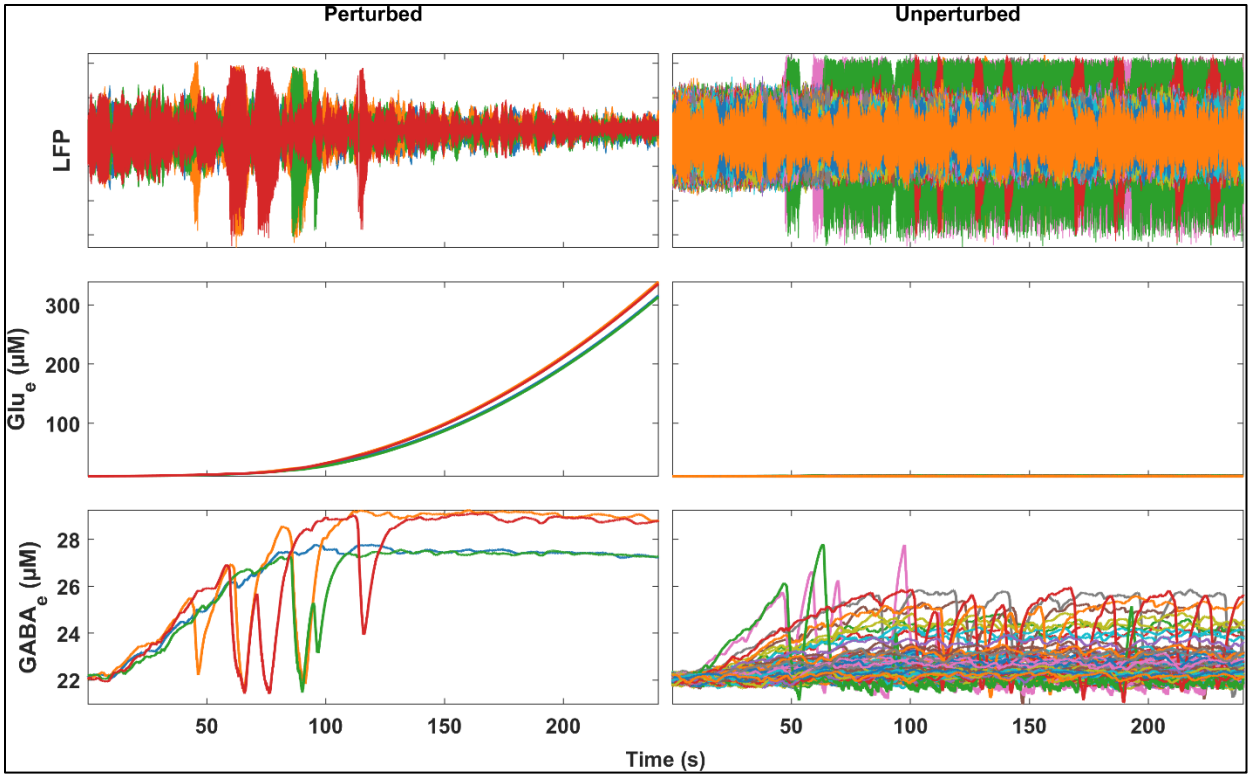

Figure 5.7. Network simulation experiment #1. Same as Figure 5.6 for different values of ω_{Glu} and ω_{GABA}.

In Figure 5.8 and Figure 5.9, we extend our analysis (of Figure 5.6 and Figure 5.7, respectively) to include the critical factor of neuronal death, implemented when glutamate exposure surpasses a defined threshold (e.g., 50 μM, which is about three times larger than the physiologically motivated value of 15μM proposed in Table 2.3). This addition reveals that post-neuronal death, the spiking behavior in neighboring nodes persists due to the continued presence of extracellular glutamate, underscoring the network's challenge (lack of ability) in clearing neurotransmitter surpluses even after cell loss.

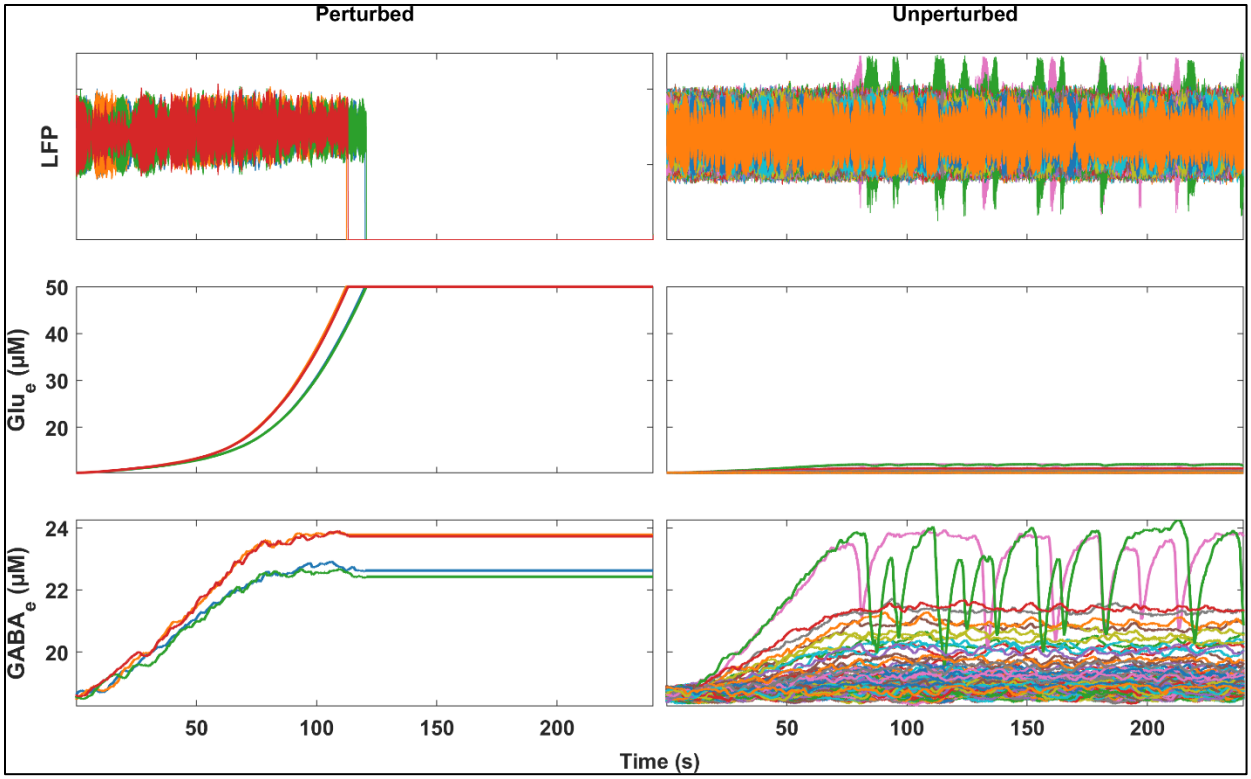

Figure 5.8. Network simulation experiment #2. Complements Figure 5.6 by implementing neuronal death.

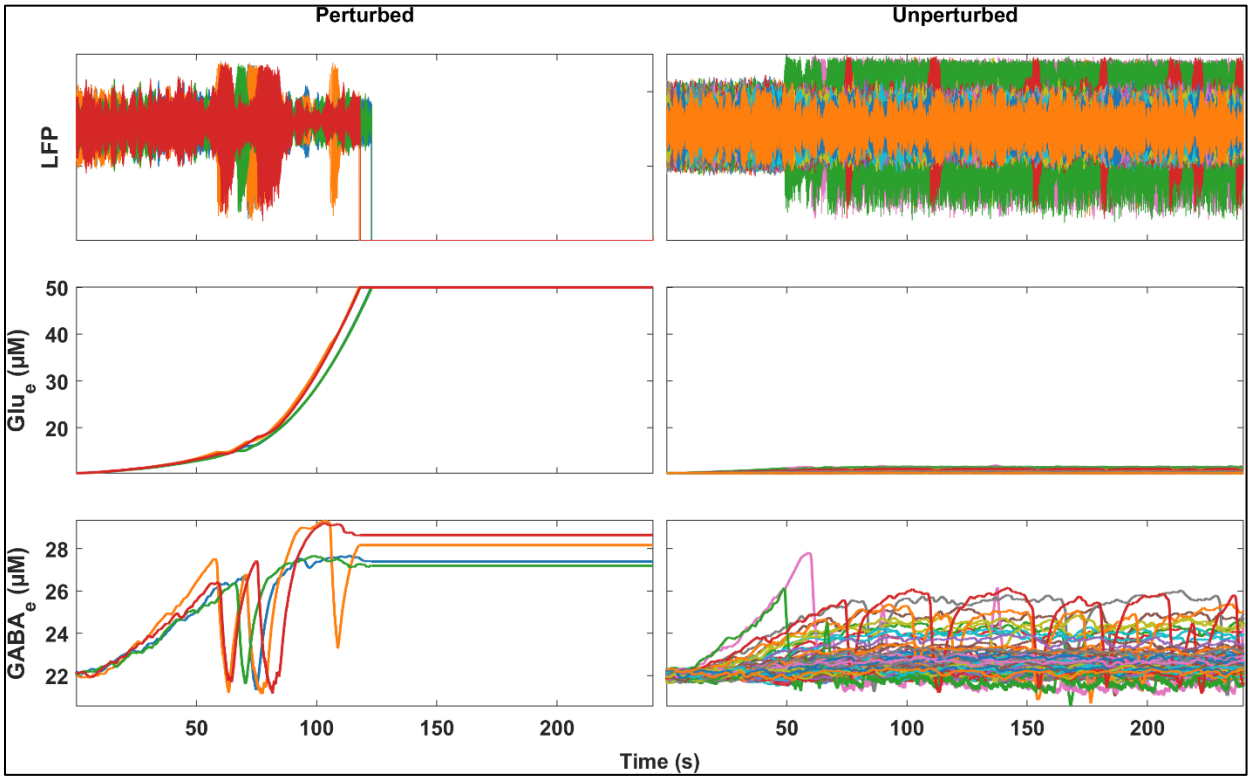

Figure 5.9. Network simulation experiment #2. Complements Figure 5.7 by implementing neuronal death.

Assuming a neurotransmitter clearance mechanism post-mortem in Figure 5.10 and Figure 5.11, such as volume transmission, we observe a nuanced change in the network's dynamics. Neighboring nodes exhibit a slight reduction in extracellular glutamate and GABA levels, albeit not returning to baseline. This modest decrease reflects the diminished astrocytic feedback following the loss of adjacent neurons, highlighting the intricate interplay between neuronal and astrocytic networks in maintaining neural homeostasis.

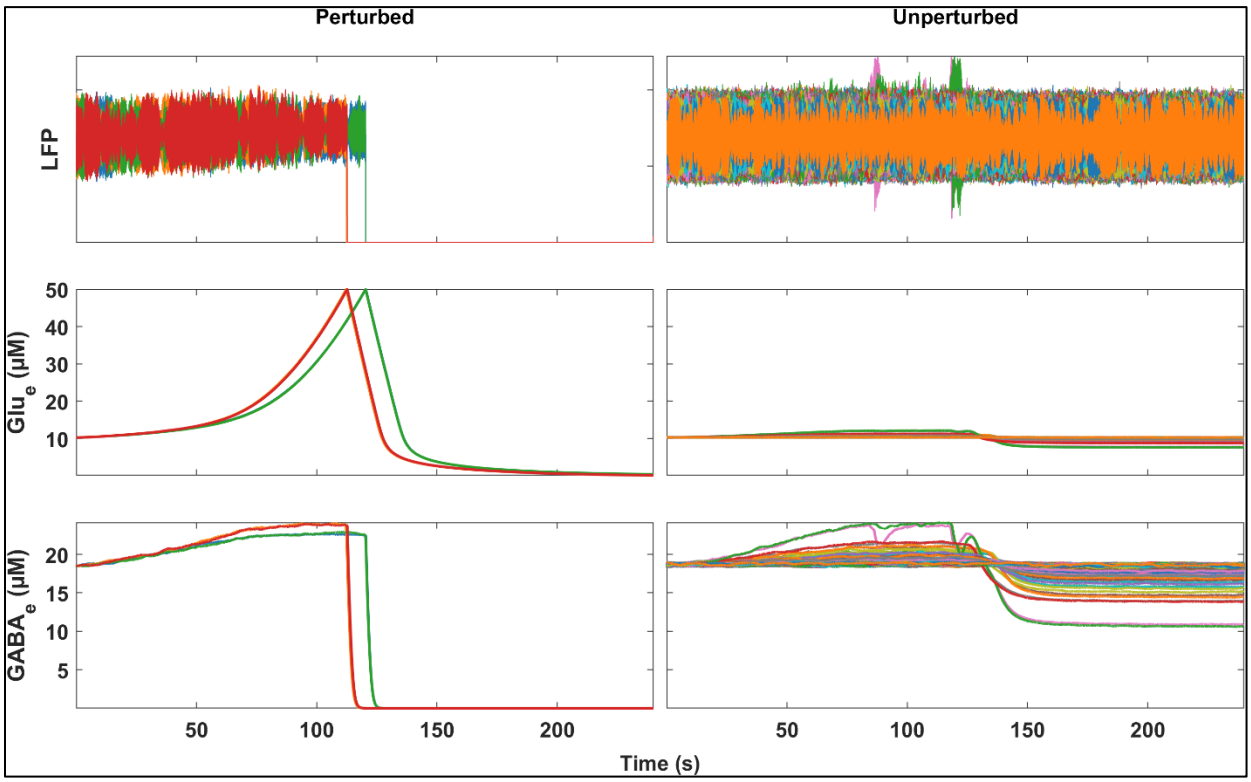

Figure 5.10. Network simulation experiment #3. Complements Figure 5.6 by implementing neuronal death and neurotransmitter clearance.

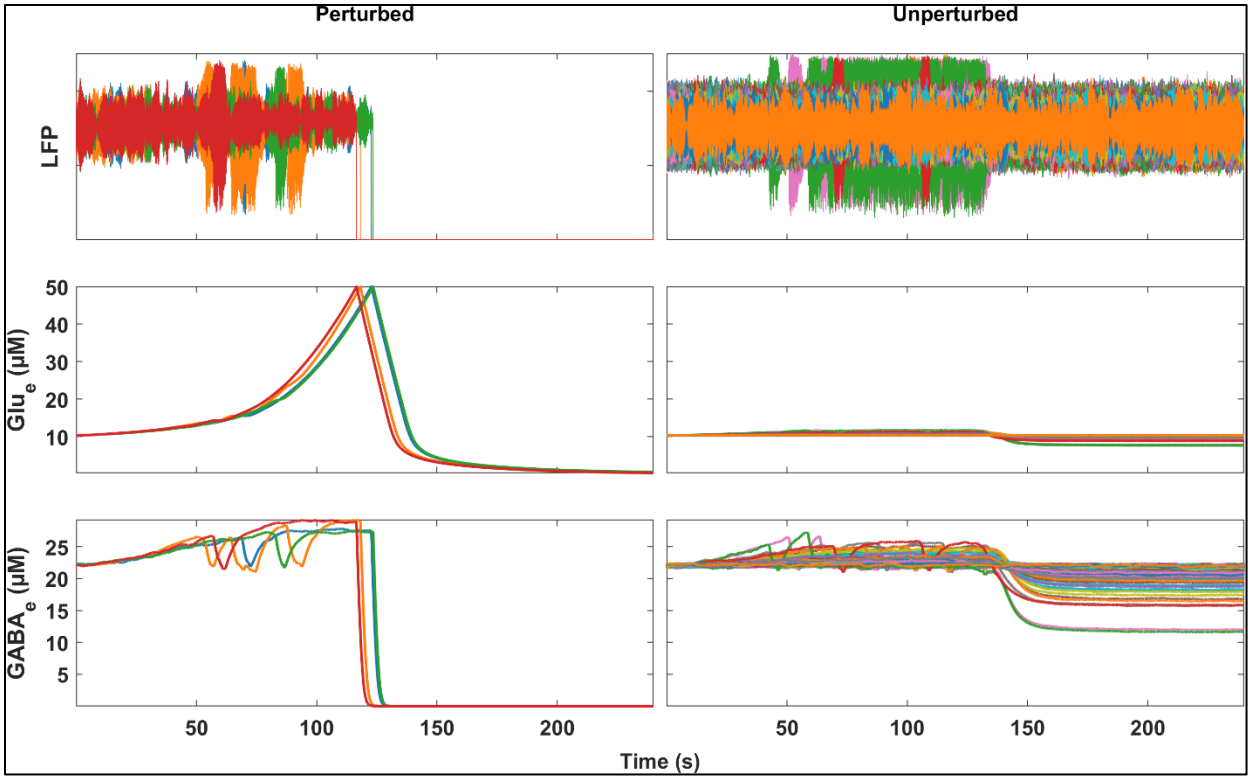

Figure 5.11. Network simulation experiment #3. Complements Figure 5.7 by implementing neuronal death and neurotransmitter clearance.

This scenario opens avenues for exploring the resistance and vulnerability of the network's remaining nodes and the emergent properties of the new network architecture post-neuronal death. By closely examining these dynamics, we gain insights into the network's adaptive capacities and the potential for recovery or further degradation under continued pathological conditions.

Overall, these network-level observations, from Figure 5.6 to Figure 5.11, underscore the network's remarkable ability to adapt and buffer against abnormal perturbations, up to a certain threshold. This resistance, however, is dependent on the network's overall connectivity and the functionality of its astrocytic components. Understanding these dynamics offers insights into the potential mechanisms underlying the progression of neurodegenerative conditions and highlights the importance of considering network interactions in the study of brain pathologies.

In forthcoming simulations, we plan to systematically introduce perturbations to subsequent nodes within the network alongside their structural white-matter fiber connections, aiming to simulate the progressive nature of AD as it extends (from entorhinal and parahippocampal cortices) to more regions of the neocortex in its later stages. This approach will involve carefully selecting nodes for perturbation based on their anatomical and functional relevance to AD's known progression pathway, potentially guided by established models such as the Braak staging. These simulations will not only reflect the spatial and temporal degeneration patterns observed in AD but will also consider the brain network's inherent compensatory mechanisms. By doing so, we aim to capture the complex interplay between disease progression, network degradation, and the brain's adaptive responses. As the disease model encompasses broader neocortical involvement, we anticipate observing significant changes in network dynamics, potentially shedding light on the mechanisms underlying the clinical manifestations of AD's advanced stages. This meticulous modeling effort

will integrate current neuropathological insights as well as empirically derived constraints, offering a detailed and realistic computational exploration of AD's progression and its impact on neural networks.

The upcoming sections provide a comprehensive narrative of my research program.

5.3 Alzheimer disease

Alzheimer disease (AD) is a grave neurodegenerative condition that, despite extensive research efforts, lacks effective treatments to halt or reverse its progression ("2023 Alzheimer's Disease Facts and Figures," 2023). Between 2002 and 2012, the global scientific community initiated more than four hundred clinical trials in search of a cure, yet a staggering 99.6% failed to meet their primary endpoints (Cummings et al., 2014). This high failure rate underscores the urgent need for novel therapeutic strategies and a deeper understanding of the disease's multifaceted nature (Bredesen, 2014; Canter et al., 2016; Fonseca-Santos et al., 2015; Selkoe, 2011). As global life expectancy rises, the incidence of AD is projected to increase dramatically, further amplifying its social and economic burden. For instance, current estimates by (*Dementia Statistics | Alzheimer's Disease International (ADI)*, n.d.) suggest that every 3 seconds, someone develops dementia, with more than 55 million individuals affected worldwide in 2020, a number expected to nearly double every 20 years. The financial impact is equally staggering, with the global cost of dementia surpassing US$ 1.3 trillion, a figure set to double by 2030.

The prevailing research paradigm, heavily focused on neuronal dysfunction, may need to broaden its scope to encompass other aspects of brain health, including the role of glial cells and vascular factors (Acosta et al., 2017; Allaman et al., 2010; Allen & Lyons, 2018; Iadecola, 2017; Kugler et al., 2021; Lago-Baldaia et al., 2020; Liddelow & Barres, 2017; Liddelow & Sofroniew, 2019; C.-C. Liu et al., 2013; Nelson et al., 2016; Sarkar et al., 2022; Schaeffer & Iadecola, 2021; St-Pierre et al., 2022; Sweeney et al., 2018; Verkhratsky & Nedergaard, 2018; Volman & Bazhenov, 2019; Zlokovic, 2011). This shift could pave the way for more comprehensive and potentially successful therapeutic interventions.

AD is defined by its complex neurodegenerative pathology, notably the accumulation of amyloid-β (Aβ) plaques and neurofibrillary tangles composed of tau protein (Ahmed et al., 2016). Interestingly, a significant proportion of patients diagnosed with probable AD do not exhibit the classical levels of Aβ plaques and tau tangles typically associated with the disease (Mattson & Arumugam, 2018). Instead, these individuals may show substantial neuronal loss in regions like the hippocampus, with only a moderate presence of tau-positive neurons (Mattson & Arumugam, 2018). Conversely, some elderly individuals display considerable Aβ plaque accumulation post-mortem yet retain cognitive function, hinting at potential neuroprotective mechanisms against Aβ toxicity (Mattson & Arumugam, 2018). Emerging evidence suggests that factors such as neurotrophic factor signaling, particularly involving brain-derived neurotrophic factor, and adaptive cellular stress response pathways might underlie the resilience observed in certain aging brains (Mattson & Arumugam, 2018). These insights underscore the intricate interplay between aging, Aβ and tau pathologies, and the body's adaptive responses, challenging the notion of a linear pathway to synaptic dysfunction and neuronal death in AD (Mattson & Arumugam, 2018).

In AD, it is posited that Aβ propagates in a manner reminiscent of prions, marking distinct pathological stages (Ahmed et al., 2016). Initially, Aβ deposition is seen in the basal temporal and orbitofrontal neocortex, subsequently extending across the neocortex, and eventually impacting

the hippocampus, amygdala, diencephalon, and basal ganglia. In advanced stages, it even reaches the mesencephalon, lower brainstem, and cerebellar cortex (Ahmed et al., 2016). Neuroimaging studies, including resting-state fMRI, EEG, and MEG, reveal that these regional pathologies disrupt key brain networks (namely the salience, default mode, and executive control networks) leading to the characteristic cognitive impairments and behavioral anomalies of AD (Ahmed et al., 2016). The disruption of neural synchrony, particularly within the default network and its medial temporal lobe regions, is closely associated with the episodic memory deficits that are emblematic of AD (Ahmed et al., 2016). Notably, there is often a mismatch between the extent of Aβ pathology and the degree of cognitive (network) dysfunction, suggesting that the spatial distribution of Aβ might not fully explain the clinical diversity observed in AD presentations (Ahmed et al., 2016).

As for tau pathology, its progression in AD is similarly systematic, beginning with neuronal tau inclusions in the locus coeruleus and entorhinal regions, advancing through the hippocampal formation and select neocortical areas, and ultimately enveloping a vast expanse of the neocortex (Ahmed et al., 2016). This progression of tau pathology parallels the deepening cognitive decline, further elucidating the multifaceted nature of neurodegeneration in AD.

In the landscape of AD research, the spotlight is increasingly on the role of glial cells (microglia, oligodendrocytes, and astrocytes) not just as bystanders but as active participants in the disease's unfolding narrative (Acosta et al., 2017; Allaman et al., 2010; Kugler et al., 2021; Lago-Baldaia et al., 2020; Liddelow & Barres, 2017; Liddelow & Sofroniew, 2019; C.-C. Liu et al., 2013; Patro et al., 2022; Sarkar et al., 2022; St-Pierre et al., 2022). These cells, which are cornerstones of the brain's immune defense, exhibit a dynamic range of actions that straddle the line between protecting the neural environment and contributing to its distress. They engage in the clearance and degradation of Aβ, with microglia and astrocytes at the forefront of this regulatory battle. Initially, astrocytes appear as guardians, sequestering and dismantling the Aβ. However, this protective mechanism has its costs: the relentless uptake of Aβ can divert astrocytes from their critical support functions, leading to a metabolic crisis for neurons and subsequent degeneration (Allaman et al., 2010).

This duality in glial function, where they can oscillate between being neuroprotective allies and drivers of neurodegeneration, adds a layer of complexity to our understanding of AD. Moreover, the plot thickens with the involvement of astrocytes in the production of apolipoprotein E (ApoE), a molecule with deep ties to AD's genetic risk landscape (C.-C. Liu et al., 2013). The presence of the ApoE4 variant, in particular, markedly elevates the risk of AD, underscoring a genetic vulnerability orchestrated by astrocytes.

This intricate interplay between glial function, Aβ dynamics, and genetic factors like ApoE4 paints a multifaceted picture of AD pathogenesis, where glial cells play pivotal, albeit ambivalent, roles (Acosta et al., 2017; Allaman et al., 2010; Kugler et al., 2021; Lago-Baldaia et al., 2020; Liddelow & Barres, 2017; Liddelow & Sofroniew, 2019; C.-C. Liu et al., 2013; Patro et al., 2022; Sarkar et al., 2022; St-Pierre et al., 2022).

Recent insights have illuminated the diverse and complex roles of glial cells in the progression of AD, with particular emphasis on the nuanced interactions between these cells and the broader neural environment (Acosta et al., 2017; Liddelow & Barres, 2017; Liddelow & Sofroniew, 2019; Sarkar et al., 2022; St-Pierre et al., 2022). In AD, the pathological accumulation of Aβ not only induces a reactive phenotype in astrocytes but also precipitates a cascade of functional disruptions. These include alterations in astrocytic morphology, calcium dynamics, potassium regulation, and

glutamate handling, as well as in the mechanisms governing Aβ clearance and neuronal energy support (Acosta et al., 2017; Sarkar et al., 2022). The resultant environment is marked by excitotoxicity due to impaired glutamate clearance, compromised synaptic functionality, energy shortages for neuronal activity, and misaligned neurovascular communication.

In this intricate milieu, reactive astrocytes serve dual roles, initially as buffers against Aβ accumulation but potentially as contributors to the Aβ burden in later stages (Acosta et al., 2017; Sarkar et al., 2022). The interaction between Aβ and astrocytic receptors like metabotropic-glutamate-receptor-5 and α7-nicotinic-acetylcholine-receptor amplifies calcium signaling disturbances within astrocytes, further entangling them in the disease's pathology. This astrocytic dysfunction leads to an excess of synaptic glutamate, either by hindering its reuptake or by promoting its astrocyte-driven release, thus exacerbating neuronal and synaptic distress.

Moreover, the astrocytic contribution to neuronal energy metabolism becomes compromised in AD (Acosta et al., 2017; Sarkar et al., 2022). Disruptions in glucose and lactate transport, alongside glutamine synthesis, undercut the energy supply essential for neuronal function and glutamate recycling. Additionally, the dysregulated calcium signaling in astrocytes extends its impact to the cerebrovasculature, where abnormal responses can arise. The downregulation of astrocytic potassium channels by Aβ further disrupts the delicate balance of extracellular potassium, contributing to the cerebrovascular anomalies observed in AD.

Though less studied than astrocytes, oligodendrocytes also play a crucial role in the pathology of AD, impacting disease progression and offering potential therapeutic targets (Abd-Elrahman et al., 2023; Butt et al., 2019; Ferrer, 2018; J. Rodríguez et al., 2016; Kahlson & Colodner, 2015; LoPresti, 2018; Maitre et al., 2023; Matute et al., 2006). These cells, vital for myelination and energy support to neurons, are affected in AD, leading to white matter atrophy, demyelination, and axonal loss. Damage to oligodendrocytes often results from abnormal tau protein deposits and Aβ peptides, contributing to cognitive dysfunction and dementia severity in AD patients. The protein aggregates not only damage oligodendrocytes directly but also increase their vulnerability to glutamate toxicity, exacerbating white matter damage (Abd-Elrahman et al., 2023; Butt et al., 2019; Ferrer, 2018; J. Rodríguez et al., 2016; Kahlson & Colodner, 2015; LoPresti, 2018; Maitre et al., 2023; Matute et al., 2006). Abnormal calcium regulation (calcium dyshomeostasis) within oligodendrocytes further contributes to their dysfunction and death. This calcium dysregulation, along with glutamate and ATP excitotoxicity, can lead to oligodendrocyte apoptosis and myelin breakdown, highlighting the complex interplay between oligodendrocytes, neuronal signaling, and AD pathology.

To summarize, the diverse responses of glial cells to the pathological features of AD underscore their complex involvement in the disease's progression. The dynamic interplay between glial cells and AD's hallmark pathologies, Aβ accumulation and tau protein aggregation, reveals a spectrum of glial functions that range from protective to detrimental. This nuanced understanding of glial cell behavior in the AD context highlights their potential as pivotal players in the disease's mechanisms and opens up innovative avenues for therapeutic exploration. By targeting the regulatory functions of glial cells, there is a promising opportunity to influence the course of AD. Future research focused on elucidating the precise mechanisms of glial involvement in AD can pave the way for the development of glia-centric therapies, potentially offering new hope for modulating this complex neurodegenerative condition (Acosta et al., 2017; Allaman et al., 2010;

Kugler et al., 2021; Lago-Baldaia et al., 2020; Liddelow & Barres, 2017; Liddelow & Sofroniew, 2019; C.-C. Liu et al., 2013; Patro et al., 2022; Sarkar et al., 2022; St-Pierre et al., 2022).

5.4 Proposed main focus

My research proposal is underpinned by the following foundational ideas: initiating with the baseline of a healthy older adult brain predisposed to neurodegenerative conditions, we aim to chart the trajectory towards AD. This will be achieved by concurrently modeling critical phenomena across the entire brain: synaptic loss, neural network disruptions, and neuronal death. Given our objective to align with the spatiotemporal resolutions of neuroimaging data, we translate these biological phenomena into observable neuroimaging correlates: diminished synaptic densities among neuron subpopulations, compromised functional connectivity within and across neural communities (e.g., resting-state networks), deteriorated white matter integrity, and the demise of axonal pathways. Through these translations, our discourse centers on the concept of neural communities, offering a tangible framework for our simulations.

As an initial step, we postulate that these three phenomena (synaptic loss, neural network disruptions, and neuronal death), which sequentially manifest within a single brain region but might overlap across multiple regions, correlate (not strictly in a linear manner) with extended glutamate exposure. This hypothesis introduces a degree of contention, as it is widely recognized that these manifestations are also the culmination of a multifaceted cascade involving intracellular accumulations of Aβ and tau, oxidative stress, mitochondrial anomalies, and sustained neuroinflammation (Abd-Elrahman et al., 2023; Acosta et al., 2017; Allaman et al., 2010; Kugler et al., 2021; Lago-Baldaia et al., 2020; Liddelow & Barres, 2017; Liddelow & Sofroniew, 2019; C.-C. Liu et al., 2013; Matute et al., 2006; Patro et al., 2022; Sarkar et al., 2022; St-Pierre et al., 2022). These processes can either independently or in conjunction instigate the degeneration and demise of neuronal networks. Despite the multifactorial nature of these processes, our modeling approach centers on glutamate due to its critical role as the primary excitatory neurotransmitter in the brain and its established association with AD (Abd-Elrahman et al., 2023; Acosta et al., 2017; Allaman et al., 2010; Kugler et al., 2021; Lago-Baldaia et al., 2020; Liddelow & Barres, 2017; Liddelow & Sofroniew, 2019; C.-C. Liu et al., 2013; Matute et al., 2006; Patro et al., 2022; Sarkar et al., 2022; St-Pierre et al., 2022). Focusing on glutamate aids in reducing the complexity of the phenomena that we aim to model without significantly compromising their relevance, given glutamate's significance in the context of AD pathology. This simplified approach facilitates a more manageable exploration of the disease's mechanisms, which will be further highlighted in the section "Beyond glutamate and GABA neurotransmission" of the Discussion starting on page 241.

Thus, in this research program, the discourse pivots to the concept of neural communities, a pivotal element that bridges the gap between the whole-brain neuron-astrocyte network modeling approach developed throughout this thesis and the neuroimaging data ubiquitously collected in both clinical and research settings. These neural communities not only resonate with the data derived from neuroimaging techniques but also align with cognitive and behavioral evaluations, providing a rich tapestry of insights into brain function and organization (Breakspear, 2017; Hallett et al., 2020).

The primary objective delineated here is to construct a model that elucidates the adaptive mechanisms of multilayer network communities in the face of gradual changes, akin to those observed in the biological aging process. Complex dynamical systems, including the brain, often

exhibit emergent properties where groups of nodes, or neural communities, form interconnected layers, facilitating robust information exchange (Bassett & Bullmore, 2017; Bassett & Sporns, 2017; Boccaletti et al., 2014; De Domenico, 2017; Fan et al., 2021; Ghavasieh & Domenico, 2021; Han et al., 2017). This multilayered modular organization, evident across various spatiotemporal scales, plays a crucial role in system resistance and adaptability. Yet, the dynamics of how these modular architectures evolve in response to slow and continuous perturbations (assuming that *biological aging* can be modelled as slow-continuous *perturbations*), and the underlying topological features that underpin the emergence and temporal reconfiguration of these functional modules, remain areas ripe for exploration.

My research proposal endeavors to shed light on the emergent multilayer network communities within the brain, probing their relationship with the brain's resistance to *slow-scale perturbations* (explained in Section 5.6), such as those that are characteristic of *biological aging*. Employing a physiologically constrained computational modeling approach, we aim to simulate the dynamic evolution of these network communities in response to defined perturbation paradigms. The simulations will build on the foundations laid in preceding chapters, which demonstrated our whole-brain neuron-astrocyte network model's capacity to mimic a diverse array of network dynamics across multiple scales. While previous chapters have successfully replicated key aspects of empirical networks through principled parameterization, a critical next step involves directly comparing these model simulations to actual neuroimaging data, a process integral to this research program. Thus, this research program seeks to extend these simulations to more closely mirror real-world neuroimaging data. Moreover, this research program will explore the application of network control theory to systematically manipulate and understand the principles governing network dynamics within our model.

By leveraging a modeling framework deeply intertwined with non-invasive neuroimaging modalities such as diffusion MRI, functional MRI, PET, EEG, and MEG, we enhance the potential for empirical validation of our theoretical constructs (Breakspear, 2017; Griffiths et al., 2022; Hallett et al., 2020), paving the way for groundbreaking insights into the adaptive capacities of neural networks in the face of aging and other perturbations.

At the heart of this ambitious program is also the integration of a vascular component into the whole-brain neuron-astrocyte network model conceived in this thesis. However, to maintain continuity with the concepts and methodologies introduced in the previous chapters, I choose to postpone the discussion of incorporating a vascular dimension. We will delve into the complexities of integrating this vascular component in the Discussion chapter starting on page 239. This vascular addition is crucial, given the significant role that vascular dysfunction plays in the AD landscape, marking a critical area for exploration in our quest to understand and ultimately combat this multifaceted disease (Acosta et al., 2017; Allaman et al., 2010; Allen & Lyons, 2018; Iadecola, 2017; Kugler et al., 2021; Lago-Baldaia et al., 2020; Liddelow & Barres, 2017; Liddelow & Sofroniew, 2019; C.-C. Liu et al., 2013; Nelson et al., 2016; Sarkar et al., 2022; Schaeffer & Iadecola, 2021; St-Pierre et al., 2022; Sweeney et al., 2018; Verkhratsky & Nedergaard, 2018; Volman & Bazhenov, 2019; Zlokovic, 2011).

5.5 Proposed primary objectives

In this research program, the exploration begins with the investigation of healthy aging brains, utilizing real-world behavioral and resting-state neuroimaging data from MEG and fMRI sources. The primary aim is to discern if age-dependent patterns in resting-state functional multilayer neural

communities manifest over the adult lifespan and to understand the relationship between these dynamic network reorganizations and cognitive performance shifts. The underlying hypothesis posits that the natural progression of healthy aging is marked by notable changes in the brain's network architecture, characterized by enhanced community integration, diminished segregation, and an ensuing decline in cognitive faculties (Bagarinao et al., 2019; Stumme et al., 2020).

Moving forward, the focus shifts to aligning our computational model with the empirical neuroimaging data patterns previously dissected. This second step involves examining if the optimized parameters of our whole-brain model accurately reflect the observed modular network patterns. We hypothesize (consistent with the literature review of the preceding sections) that these network changes are partially attributable to alterations in neuron-astrocyte interactions, a phenomenon our model aims to elucidate through its latent variables and parameters, once calibrated against empirical data.

The third objective aims to delve into the dynamic responses of multilayer neural communities to biologically inspired, age-related perturbations through computational simulations. We propose specific hypotheses to guide this exploration (Bagarinao et al., 2019; Fan et al., 2021; Ghavasieh & Domenico, 2021; Gilarranz et al., 2017; Stumme et al., 2020). (i) The balance between integration and segregation in neural communities may influence their vulnerability and adaptability to perturbations. (ii) Multilayer communities' ability to rewire in response to "injuries" decreases with increased global integration. (iii) Structural-functional multilayer hubs are pivotal in the network's resistance to targeted perturbations, more so than hubs with only structural or functional prominence. (iv) Perturbation propagation is likely less extensive in networks with lattice topology, characterized by local interactions, compared to those with small-world topology, which facilitates efficient long-range information exchange.

In the fourth objective, we extend our investigation to empirically validate the simulated multilayer community dynamics using real-world behavioral and neuroimaging data across various age groups. This validation process will involve the following. (i) Methodical comparison of simulated network trajectories with empirical data to identify patterns and discrepancies. (ii) Examination of statistical associations between model parameters and cognitive performance shifts, assessing the plausibility of perturbation schemes used in the simulations.

Finally, we propose to expand our research to include clinic-based cohorts, ranging from cognitively unimpaired older adults to individuals with mild cognitive impairment and AD. This approach will allow us to do the following. (i) Simulate network trajectories that reflect the progression from healthy aging to mild cognitive impairment and AD, using perturbation schemes that mimic AD pathology. (ii) Identify network pathways that facilitate or prevent the transition to AD, offering potential insights into lifestyle interventions that could bolster cognitive resilience against neurodegenerative diseases.

The rationale behind simulating a transition from healthy aging to AD, rather than modeling AD in isolation, is twofold and will be elaborated throughout my research proposal. Primarily, it aligns with the proactive stance of preventative health research (Mattson & Arumugam, 2018), positing that lifestyle interventions can beneficially influence brain network dynamics over time, thereby preserving cognitive functions and bolstering the brain's resilience against vulnerabilities to AD (Arenaza-Urquijo & Vemuri, 2018). Should this modeling endeavor prove successful, it would pave the way for investigating how lifestyle factors, such as regular physical exercise, impact the

organization and properties of multilayer brain network communities, thereby contributing to the maintenance of functional and cognitive capacities throughout the adult lifespan.

This overall approach aims not only to enhance our understanding of neural network dynamics in aging and AD but also to contribute to preventative health strategies by identifying modifiable factors that influence brain network resistance.

5.6 Proposed overall methodology

To achieve the defined objectives, we will harness data from two sources: the Cambridge Centre for Ageing and Neuroscience project (Shafto et al., 2014; Taylor et al., 2017) and the Lifespan Human Connectome Project Aging Study (Bookheimer et al., 2019). These datasets collectively offer a rich array of neural imaging data across a broad adult age spectrum, complemented by detailed lifestyle and cognitive performance metrics.

The Cambridge Centre for Ageing and Neuroscience project (Shafto et al., 2014; Taylor et al., 2017) serves as a foundational dataset for this research, encompassing a diverse cohort of 700 participants aged 18 to 88. This dataset is notable for its extensive assessment of neural structure and function through various imaging techniques, including T1, T2, and diffusion MRI, alongside functional MRI and MEG. It also includes detailed evaluations of lifestyle factors and cognitive performance, offering a multidimensional view of aging's impact on the brain. Complementing this, the Lifespan Human Connectome Project Aging Study (Bookheimer et al., 2019) provides additional depth with its inclusion of 725 subjects aged 36 to 100+, focusing on detailed structural and functional MRI data. This dataset's unique offerings, such as high-resolution hippocampal imaging and arterial spin labeling, afford critical insights into the neurobiological substrates of aging. Coupled with extensive demographic and behavioral data, this dataset enriches our understanding of the aging process from a multifaceted perspective.

Our analytical framework to resolve the first objective will primarily focus on resting-state MEG and fMRI data to discern age-related shifts in brain network communities. Advanced resting-state neuroimaging analysis techniques will be employed to extract functional connectivity patterns. Concurrently, diffusion MRI data will inform on the structural underpinnings of these functional networks, providing a more complete view of the brain's multilayer community architecture. Behavioral data, encompassing a wide range of cognitive assessments, will be statistically associated with neural community attributes to uncover potential links between brain network dynamics and cognitive abilities. This analysis will leverage robust statistical methods, ensuring a thorough examination of the relationships between network properties, including integration-segregation balance, and cognitive performance metrics (Abdi et al., 2012; González-Narváez et al., 2021). Clustering-like analyses will be pivotal in identifying group-level patterns of network communities across different age cohorts. We will explore various clustering-like methodologies to best capture the complex architecture of multilayer networks (De Domenico, 2017; Huang et al., 2021; Interdonato et al., 2017; Mucha et al., 2010; Tagarelli et al., 2017; Ting et al., 2021; H. Zhang et al., 2017). Moreover, the impact of demographic factors on these network patterns will be meticulously analyzed, considering variables such as gender and education, to elucidate the diversity of aging trajectories.

Following the analysis of real-world neuroimaging data, we will proceed to personalize model fits for each subject using both structural and functional data (Arbabyazd et al., 2021; de Haan et al., 2017; Demirtaş et al., 2017; Frässle et al., 2018; Hallett et al., 2020; Stefanovski et al., 2019, 2021;

van Nifterick et al., 2021; Yalcinkaya et al., 2023; Zimmermann et al., 2018). Initially, we'll identify global network coupling coefficients as the model's free parameters for each individual, a choice grounded in its demonstrated efficacy in existing literature. This process aims to construct a *virtual brain* for each participant, upon which we'll explore statistical associations between model parameters and cognitive performance metrics. Building on these personalized models, we will generate hypotheses regarding the impact of aging on network modular organization. This will involve applying biologically inspired perturbations, informed by literature precedents, to simulate age-related changes within the brain networks of specific age cohorts. These perturbations might include gradually adjusting structural link weights or altering nodal parameters (e.g., pertaining to impaired glutamate neurotransmission) to induce dysregulated dynamics, reflective of aging processes. Simulated multilayer communities will then undergo a temporal analysis akin to our real-data approach, examining their evolution under the influence of strategic perturbations. A key part of this phase will involve comparing the simulated community dynamics with those observed in real-world data, adjusting perturbation schemes as necessary to enhance congruence. Upon achieving a satisfactory alignment between simulated and empirical data, we will delve into the potential associations between the parameters of our whole-brain model and cognitive performance changes. This step will not only validate the model's accuracy but also shed light on the plausibility of the employed perturbation schemes in reflecting real-world aging processes.

In exploring the effects of temporal perturbations on multilayer community organization, our focus will be on delineating how specific perturbations alter the activity patterns of key network nodes (particularly those with strong structural or functional connections to perturbation sites) and the integrity of associated network links. We will quantify the impact of these perturbations on network integration and segregation to gauge the balance between these two critical aspects of network organization. Additionally, the reassignment of nodes to different modules post-perturbation will be monitored using advanced community detection and dynamic network analysis techniques, providing insights into the network's adaptive mechanisms. To comprehensively assess the ramifications of perturbations, we will map and quantify their spread within and across network modules. This will involve the development of a quantitative index to evaluate the robustness of the modular architecture and its sensitivity to various perturbation types. This index will be instrumental in comparing the effects of different perturbations, allowing us to rank them based on their impact on network functionality and structure.

To address our final objective, we will leverage datasets from patients with AD, notably from the Alzheimer's Disease Neuroimaging Initiative (ADNI; https://adni.loni.usc.edu/). While electrophysiological data are scarce in AD datasets, the ADNI provides a rich array of neuroimaging data, including functional MRI and PET scans for amyloid and tau, which are pivotal in AD research. Additionally, the BrainLat dataset (Prado et al., 2023), a unique compilation of data from a multicentric effort across five Latin American countries including both fMRI and EEG, will offer invaluable insights into the neuroimaging aspects of AD in diverse populations. Integrating this neuroimaging data with our whole-brain model, we aim to elucidate the network modular organization in AD-affected brains. Through simulations informed by this integrated model, we will generate causal hypotheses on the progression from healthy to AD-specific network organizations. These simulations will specifically focus on glutamate-mediated perturbations, mirroring the gradual onset of synaptic loss, network disruptions, and neuronal death characteristic of AD. By meticulously modeling these perturbations, we aim to uncover the mechanistic pathways through which healthy brain networks transition to states resembling those observed in

AD. This methodological approach will not only enhance our understanding of AD pathology but also provide a computational framework for exploring potential interventions that could mitigate the progression of this debilitating disease.

Discussion

This general discussion augments the analyses presented within the individual manuscript chapters, and synthesizes the strengths and limitations of my work, evaluating its academic impact and relevance. It assesses how my findings align with, differ from, or add to existing research, suggesting ways to integrate them into the broader field. This section also proposes directions for future research, building on the insights provided.

Overall summary

The foundational premise of this thesis was anchored in a mesoscopic neuron-astrocyte mass model (Garnier et al., 2016), designed to simulate the reciprocal dynamics between neuronal and astrocytic populations mediated by glutamatergic and GABAergic neurotransmission pathways. This initial model served as a mesoscopic representation of the complex interplay between neuronal and glial elements, setting the stage for a more expansive exploration of whole-brain functioning.

In the course of this thesis, the mesoscopic model was transformed and extended into a whole-brain mass network model. This evolution was achieved by implementing a sophisticated coupling scheme that facilitated interactions across distinct brain regions. Specifically, neuronal populations were interconnected via white matter tracts, emblematic of the brain's structural connectivity, while astrocytic populations were linked through densities of gap junctions. This approach to astrocytic coupling drew inspiration from microscale investigations of the brain, particularly the structural notion of astrocytes forming a gap-junction-coupled syncytium. It also considered the pivotal role of glutamate neurotransmission in mediating astrocytic intercommunication and the consequential effects of excitatory gliotransmission on neuronal pre-terminal receptors.

This expansion of the mesoscopic model into a whole-brain framework heralded a groundbreaking conceptualization of cerebral organization: envisioning the brain as a dynamic *network-of-networks* orchestrated by a two-layered structural architecture. This innovative perspective emphasizes that neural dynamics are intricately shaped by the interplay between neuronal and astrocytic networks, each constituting a layer in the overarching structural network of the brain.

The inaugural manuscript-chapter of this thesis meticulously dissected the mathematical underpinnings of the resulting whole-brain model. It elucidated the core biophysical principles that regulate the reciprocal interactions between astrocytes and neurons within this large-scale network. A detailed mathematical procedure for the model's parameterization was outlined, leveraging an array of methodologies including simulation techniques, bifurcation theory, and compartmental modeling. This parameterization process was specifically tailored to meet specific criteria designed to enhance utility for subsequent chapters, ensuring the model's outputs, notably the local field potential, and extracellular glutamate and GABA, accurately emulate characteristics typically observed in empirical resting-state human data.

The criteria established for the model's parameterization were designed to fulfill dual objectives. Firstly, they aimed to ensure that the dynamics of the local field potentials closely mirrored the characteristics of the α-band (8–13 Hz) as observed in electrophysiological studies. This included capturing the nuances of amplitude and phase network synchronizations that are indicative of coherent neural activity within this frequency band, a hallmark of resting-state brain network dynamics. Secondly, the criteria sought to achieve a harmonious balance in neurotransmitter

dynamics, characterized by quasi-stationary slow fluctuations of extracellular glutamate and GABA. This balance is crucial for maintaining the homeostasis of excitatory and inhibitory influences within the brain, ensuring that neural networks operate within optimal physiological parameters. Furthermore, this chapter illuminated potential avenues for broadening these criteria to extend the model's applicability to a wider array of scientific inquiries.

Advancing into the second manuscript-chapter, the thesis embraced the intricate nature of the whole-brain model, proposing a simulation approach that integrates multilayer network modeling with bifurcation theory. This strategy aimed to dissect the nuanced contributions of astrocytic networks to the modulation of whole-brain activity and the emergent patterns of functional connectivity. Through this approach, the thesis ventured into uncharted territories, exploring the profound impact of astrocytic network dynamics on the cerebral landscape, thereby shedding light on the pivotal role these glial networks play in orchestrating the symphony of brain activity and connectivity. The findings from this chapter were profound, illustrating the dynamic interplay between astrocytic and neuronal networks through both fast and slow fluctuations, as well as through phase-based and amplitude-based network connectivity.

A significant revelation from the analysis of whole-brain activity was the posited hypothesis that glutamatergic and GABAergic neurotransmissions act as critical modulators of the amplitude envelope of neuronal membrane potential dynamics. This insight underscores the pivotal role of neurotransmission in influencing neuronal oscillations and their associated amplitude envelope fluctuations. In the realm of whole-brain connectivity, the examination of amplitude and phase couplings unveiled with remarkable biophysical detail that these modes of connectivity underscore distinct yet complementary spatiotemporal phenomena within the brain's architecture.

These pivotal findings not only captivate the neuroimaging community's interest, particularly in the nexus between amplitude and phase neural synchrony, but they also set a foundational tone for subsequent investigations within the thesis. The chapter compellingly argues that the inclusion of glial cells in biophysical models substantially enriches the interpretation of whole-brain activity and connectivity patterns, whereas their exclusion could lead to ambiguous interpretations of cerebral processes.

With the theoretical groundwork laid in the first and second chapters, the thesis then transitioned towards evaluating the practical applicability and realism of the whole-brain model from a neuron-glial perspective. This evaluation necessitated consideration of the types of data required to both constrain and validate the model, particularly in the context of predicting the interplay between neurotransmission and neuronal amplitude modulation.

Addressing these considerations, the third manuscript-chapter ventured into the domain of empirical electrophysiological connectomics. The intrinsic alignment between electrophysiological data and the state variables of our whole-brain model underscores the unique utility of such data for model validation and refinement. In light of this, the third chapter embarked on an exploration of empirical electrophysiological connectomics, seizing the opportunity to infuse neuron-glial perspectives into a domain traditionally dominated by neuronal-centric analyses.

Acknowledging the methodological constraints inherent in the field of non-invasive electrophysiology, this chapter endeavored to establish a biologically informed simulation environment. This setting was designed to scrutinize and enhance existing electrophysiological connectomics methodologies, with the overarching aim of surmounting some of the field's

prevalent limitations. The chapter was dedicated to pinpointing an optimal analytical framework that could later be applied to real-world data, facilitating a rigorous comparison between model predictions and empirical observations.

One of the pivotal revelations of this chapter was the elucidation of conditions under which complex yet biologically plausible patterns of amplitude and phase couplings could be accurately detected using conventional empirical electrophysiological connectomics techniques. The analysis highlighted several critical factors influencing the reliability of these techniques, including the dimension of the functional networks (measured in terms of the number of nodes), the density of functional network connections, the underlying nature of network dynamics (such as the balance between functional integration and segregation), and the specific types of network properties under investigation (ranging from macro-scale to micro-scale phenomena).

The following discussion sections enrich this overall summary.

Beyond glutamate and GABA neurotransmission

Our modeling approach relied on the explicit integration of excitatory and inhibitory neurotransmitter dynamics (through glutamate and GABA, respectively) to capture the intricate coupling between neurons and astrocytes. By focusing on these two neurotransmitters, we effectively employed a dimension reduction approach to navigate the complex landscape of neurochemicals in the brain (Brezina, 2010; Katz, 1999; Kondziella, 2017). Glutamate stands as the primary excitatory neurotransmitter within the human cortex, playing a pivotal role in processes such as memory formation, neuronal development, and synaptic plasticity. Its ubiquity and involvement in critical brain functions suggest that glutamate could serve as a biomarker for various cerebral processes (Crupi et al., 2019; Meldrum, 2000; Morris, 2013; Pankevich et al., 2011; Petroff, 2002; Riedel, 2003; Robbins & Murphy, 2006). Conversely, GABA, as the principal inhibitory neurotransmitter, introduces a counterbalance to the excitatory actions of glutamate, contributing to the overall homeostasis of neural activity (Angulo et al., 2008; Olsen & Sieghart, 2008; Petroff, 2002; Yoon & Lee, 2014). The metabolic pathway from glutamate to GABA underlines their intertwined roles, where glutamate is not only a neurotransmitter but also a precursor for GABA synthesis, highlighting the biochemical interdependence within the brain's neurochemical framework. Despite the critical role of GABA in maintaining neural circuit stability and its involvement in processes such as anxiety regulation, sleep, and muscle tone, it has historically been overshadowed by the extensive research focus on glutamate (Angulo et al., 2008; Petroff, 2002; Yoon & Lee, 2014). However, recent studies are increasingly acknowledging the significance of GABA, especially as a gliotransmitter, striving to balance the research attention between these two pivotal transmitters (Angulo et al., 2008; Petroff, 2002; Yoon & Lee, 2014).

Overall, neuroscientific research has dedicated substantial efforts to understanding the roles of glutamate and GABA, reflecting the broader endeavor to decipher the neurochemical underpinnings of human physiology in both health and disease (Angulo et al., 2008; Duman et al., 2019; Guerriero et al., 2015; Katz, 1999; Kondziella, 2017; Mattson & Arumugam, 2018; Meldrum, 2000; Morris, 2013; Pankevich et al., 2011; Petroff, 2002; Riedel, 2003; Robbins & Murphy, 2006; Rowley et al., 2012; Yoon & Lee, 2014). The exploration of neurotransmitter dynamics extends beyond glutamate and GABA, encompassing a broad spectrum of molecules with diverse roles in the nervous system. Key neurotransmitters such as acetylcholine, serotonin, and dopamine exhibit dual functions, acting as both excitatory and inhibitory agents depending on the receptor types and neural contexts they engage with (Brezina, 2010; Katz, 1999; Kondziella,

2017; Marder, 2012). This duality underscores the complexity of neurochemical interactions and their implications for brain function and behavior. This pursuit is also not limited to neurotransmitters but also encompasses neuromodulators like neuropeptides and endocannabinoids, which fine-tune neural activity without directly inducing excitatory or inhibitory postsynaptic potentials (Bargmann, 2012; Brezina, 2010; Katz, 1999; Marder, 2012). These compounds modulate the strength and efficacy of synaptic transmission, influencing a wide range of brain functions and contributing to the dynamic regulation of neural networks.

This discussion not only highlights the critical importance of glutamate and GABA in neurochemical research but also opens avenues for investigating how neuromodulators, such as neuropeptides and endocannabinoids, contribute to the nuanced orchestration of brain activity. As we delve deeper into the neurochemical landscape, it becomes evident that understanding the interplay between neurotransmitters, neuromodulators, and neural dynamics is pivotal for unraveling the complexities of neural function and dysfunction.

Glial pertinence

The neurochemical perspective has catalyzed the development of advanced dynamic whole-brain models and neuroscientific investigations that transcend traditional neuronal-centric views, aligning more closely with the scales used in neuroimaging studies. Notable contributions in this domain include the work of (J. Y. Hansen et al., 2022; Kringelbach et al., 2020; Lawn et al., 2023; Shine et al., 2019), see also the *Background* chapter for an extensive review, which collectively underscore the interconnection between neural network dynamics, neurochemical systems, and their implications on behavior and cognition.

However, the contributions of glial cells in modulating the brain's neurochemical milieu often remain underappreciated in these studies (J. Y. Hansen et al., 2022; Kringelbach et al., 2020; Lawn et al., 2023; Shine et al., 2019). Glial cells, with their extensive and dynamic roles in the central nervous system, are uniquely equipped and positioned to monitor, regulate, and profoundly influence the brain's neurochemical milieu (De Pittà & Berry, 2019; Fields et al., 2015; Pacholko et al., 2020; Verkhratsky & Nedergaard, 2018). These cells, which include astrocytes, microglia, and oligodendrocytes, surpass neurons in their multifaceted functions. They are pivotal in maintaining neural homeostasis, orchestrating the delicate balance of neurotransmitters, and ensuring the structural and functional integrity of the blood-brain barrier (Kugler et al., 2021; Sweeney et al., 2018). Their involvement also extends to facilitating neuroplasticity and regulating synaptic function. Astrocytes, for instance, directly regulate synaptic transmission and neurotransmitter recycling, while microglia monitor and respond to changes in the neural environment, playing a key role in neuroinflammation and neuroprotection. Oligodendrocytes contribute to neuron function by insulating axons, thus facilitating rapid signal transmission. Collectively, glial cells contribute to the fine-tuning of neural circuits and large-scale networks, and they are integral to the brain's adaptability and health, challenging the neuron-centric dogma that has long dominated neuroscience while opening new avenues for understanding and treating neurological disorders (Amhaoul et al., 2014; Barres, 2008; Brazhe et al., 2023; Devinsky et al., 2013; Fields et al., 2015; Kugler et al., 2021; Liddelow & Barres, 2017; Liddelow & Sofroniew, 2019; Mattson & Arumugam, 2018; Obenaus, 2013; Purnell et al., 2023; Vezzani et al., 2022; Volman & Bazhenov, 2019).

The emerging recognition of glial cells as fundamental to brain function necessitates a more inclusive neuron-glial network modeling approach (De Pittà & Berry, 2019), as we proposed in

this thesis. This approach aims at offering a comprehensive framework for understanding the dynamic neurochemical landscape of the brain through intricate neuron-glial interactions. Further enriching this perspective, the consideration of neuro-glial–vascular interactions unveils the foundational elements of brain functionality (Brazhe et al., 2023; Fields et al., 2015; Giaume et al., 2010; Iadecola, 2017; Kugler et al., 2021; Schaeffer & Iadecola, 2021). The brain's intricate architecture comprises billions of neurons and glial cells, all supported by an extensive vascular network. These trilateral interactions are essential for synaptic modulation, meeting the brain's metabolic needs, and maintaining overall homeostasis. This holistic view of the neuro-glial–vascular nexus highlights the complex, interdependent mechanisms underpinning brain activity and offers a broader canvas for neuroscientific exploration.

Towards the neuro-glial–vascular network unit

Understanding the intricate workings of the brain requires a comprehensive view that extends beyond neurons to include the essential contributions of glial cells and the vascular system (Brazhe et al., 2023; De Pittà & Berry, 2019; Fields et al., 2015; Giaume et al., 2010; Iadecola, 2017; Kugler et al., 2021; Schaeffer & Iadecola, 2021; Verkhratsky & Nedergaard, 2018). The concept of the neuro-glial-vascular network unit emphasizes the trilateral interactions among these components, providing a cohesive framework that has the potential to reconcile various independently conducted studies within the neuroscience field, as well as unify their respective research communities. In this unit, the vascular component, consisting of a complex network of blood vessels, ensures the delivery of glucose, oxygen, and other nutrients while removing waste products, a process that is critical for sustaining the energetic demands of both neuronal and glial activity.

The interactions within the neuro-glial–vascular unit are pivotal for understanding brain function in health and disease. This unit underlies mechanisms such as neurovascular coupling, where changes in neural activity lead to corresponding changes in blood flow, a principle that forms the basis of functional neuroimaging techniques like fMRI (Figley & Stroman, 2011; Lu et al., 2019). Disruptions in the neuro-glial–vascular interactions are implicated in various neurological disorders, including stroke, Alzheimer disease, and multiple sclerosis, highlighting the importance of this unit in pathology (Amhaoul et al., 2014; Barres, 2008; Brazhe et al., 2023; Devinsky et al., 2013; Iadecola, 2017; Kugler et al., 2021; Liddelow & Barres, 2017; Liddelow & Sofroniew, 2019; Mattson & Arumugam, 2018; Obenaus, 2013; Purnell et al., 2023; Schaeffer & Iadecola, 2021; Vezzani et al., 2022; Volman & Bazhenov, 2019).

Recent advances in modeling efforts have aimed to capture the complexity of the neuro-glial–vascular unit, especially at scales relevant to human neuroimaging. These models integrate data from molecular, cellular, and systems neuroscience to simulate the interactions within this unit, providing insights into the underlying mechanisms of brain function and the pathophysiology of brain disorders (Blanchard et al., 2016; Jolivet et al., 2015; Volman & Bazhenov, 2019). Such models hold promise for the development of new therapeutic strategies targeting the neuro-glial–vascular unit (Allen & Lyons, 2018; Lago-Baldaia et al., 2020).

It is worth highlighting, Iadecola's review on the neurovascular unit (Iadecola, 2017), which has been instrumental in expanding our understanding of the interactions between neural activity and cerebral blood flow, emphasizing the multidimensional nature of these processes. This conceptual framework has paved the way for further research into the roles of astrocytes in neurovascular coupling and the maintenance of the blood-brain barrier. Likewise, De Pitta and Berry's review

(De Pittà & Berry, 2019) uniquely enriches our comprehension of the intricate signaling mechanisms within the brain, particularly focusing on the astrocytic modulation of synaptic activity and plasticity. Their research delves into the biophysical and biochemical pathways through which astrocytes contribute to the fine-tuning of synaptic transmission, revealing the astrocytes' pivotal role in modulating neuronal networks and their implications for cognitive functions. These two works are complemented by studies demonstrating the critical role of the vascular system in responding to neural metabolic demands, as highlighted in reviews by (Kugler et al., 2021; Sweeney et al., 2018; Zlokovic, 2011) on the blood-brain barrier and neurodegeneration.

Thus, we may posit that the neuro-glial-vascular network unit offers a comprehensive framework for understanding the complex interactions that underpin brain function and disease. By integrating insights from diverse studies and leveraging advanced modeling techniques, this framework holds the potential to unify the field of neuroscience and pave the way for innovative treatments targeting the intricate web of neuronal, glial, and vascular interactions.

Concretely speaking, in our whole-brain neuron-astrocyte model, which currently integrates two distinct structural layers representing neuronal and astrocytic networks, we are poised to incorporate a third, innovative layer dedicated to vascular pathways. This addition aims to enhance the model's realism and functionality, drawing inspiration from existing vascular atlases like the one proposed by (M. Bernier et al., 2018). However, to align with our model's scale and objectives, we anticipate adapting the atlas's detailed micro-scale vascular information into more generalized meso-scale and macro-scale representations suitable for our modeling framework. To mathematically depict the cerebral vasculature as an independent entity within our model, we are considering the adoption of a multigraph approach. This type of graph architecture allows for multiple connections, or edges, between network nodes, thus more accurately reflecting the complex interconnectivity of the brain's vascular system. For this aspect of the model, we can leverage the vascular graph modeling frameworks established by (Reichold et al., 2009), which detail the micro-scale dynamics of blood pressure, flow, and scalar transport processes, including oxygen transport, within the cerebral vasculature. To dynamically link the vascular layer with the neuron-astrocyte interactions in our model, we plan to draw upon the framework established by (Jolivet et al., 2015), who modelled activity-dependent metabolic coupling within the neuro-glial–vascular mesoscopic unit, while carefully considering the multiple timescales at which this unit operates. We also plan to incorporate principles from (Blanchard et al., 2016), who introduced a neural mass model that couples neuron-astrocyte activity with cerebral blood flow. Similarly, the work of (Tesler et al., 2023) provides a valuable reference for integrating mean-field models that connect neuronal activity with the BOLD signal, incorporating the influence of astrocyte calcium dynamics. By intertwining these elements, our model will offer a holistic view of brain function, positing that the observed functional activity and connectivity patterns at macro-scales are emergent properties of neural signaling processes unfolding within a structurally intricate multi-layer (multi-cellular) network topology. The inclusion of a vascular layer, represented as a multigraph, not only enriches the model's complexity but also opens avenues for simulating whole-brain neuro-glial–vascular dynamics. This approach, grounded in neural mass or field models and informed by empirical vascular network data, holds significant promise for advancing our understanding of the brain's integrated function and its perturbations in various pathologies. Additionally, this modelling perspective has other implications as outlined in the next section.

Vascular networks as surrogates of astrocytic networks

Our network model introduces a novel dimension to the conventional dynamic models of whole-brain activity, which typically focus solely on the neuronal interactions (Breakspear, 2017; Griffiths et al., 2022). Unlike these traditional approaches, our model incorporates an additional structural layer specifically designed to represent the interconnected networks of astrocytic populations. This inclusion is predicated on the understanding that astrocytes, much like neurons, form extensive networks, albeit through a mechanism of gap junctions.

Gap junctions are intricate cellular structures that facilitate direct cell-to-cell communication by allowing the passage of ions and small molecules (Lallouette et al., 2019; Stephan et al., 2021; Vasile et al., 2017). These junctions are composed of connexin proteins that assemble into channels with the capability to modulate their opening, thus regulating intercellular communication. The diversity in connexin types, such as connexin 30 and 43 (Cx30 and Cx43) found in astrocytes, dictates the functional characteristics of these gap junctions, including the specificity and efficiency of signal transmission between astrocytes. Although the understanding of connexin expression, particularly Cx43, has been primarily gleaned from studies on pathological brain tissues, such as those affected by epilepsy and tumors, this knowledge base underscores the pivotal role of gap junctional communication within glial networks (Lallouette et al., 2019; Stephan et al., 2021; Vasile et al., 2017).

The significance of astrocytic gap junctions has garnered attention from numerous research teams dedicated to unraveling the complexities of glial interconnectivity (Stephan et al., 2021). (Stephan et al., 2021) provided a comprehensive review of both classical and cutting-edge methodologies enabling the investigation of gap junctional coupling in acute tissue slices through electrophysiological and imaging techniques. Despite these advancements, the precise mapping of astrocytic network topology within the brain remains an elusive goal, as highlighted by the reviews of (Lallouette et al., 2019; Vasile et al., 2017). This challenge has motivated our research in this thesis to develop a phenomenological model that hypothesizes the densities of gap junctions as the underlying mechanism governing the interactions among astrocytic populations throughout the brain.

In the endeavor to elucidate the complexities inherent within the brain's neuro-glial–vascular matrix, the intricate vascular networks present a novel paradigm through which one might delineate astrocytic interaction pathways and their subsequent couplings with neuronal assemblies, particularly within the confines of neuroimaging data resolution (De Pittà, 2020; De Pittà & Berry, 2019; Fields et al., 2015; Hösli et al., 2022; Kugler et al., 2021; Macvicar & Newman, 2015; Magistretti & Allaman, 2015; Nedergaard et al., 2003). This perspective is substantiated by the investigation conducted by (Hösli et al., 2022), wherein the utilization of *in vivo* two-photon imaging in conjunction with immunohistological analyses elucidated the extent of astrocytic association with cerebral vasculature within mice models. Their research elucidated that a preponderance of cortical astrocytes, 99.8%, to be precise, forge connections with at least one vascular entity. It was observed that protoplasmic astrocytes predominantly establish direct contacts with trios of blood vessels, with the density of these vessels, rather than the astrocytes' dimensional attributes, dictating the quantity of vascular contacts. Regions devoid of direct astrocytic-vascular contacts were exclusively noted within the hippocampus, attributed to its relatively diminished vascular density.

This pivotal study intimates that knowledge of vascular architecture permits inference regarding the spatial positioning of cortical astrocytes. Considering astrocytes' proclivity for organizing into gap-junction-coupled syncytia, it is proposed to utilize the vasculature's network as a template to empirically define astrocytic structural interconnectivity within the cerebral gray matter for our whole-brain model. For this purpose, a vascular atlas akin to that proposed by (M. Bernier et al., 2018) could be instrumental. As an initial foray, the weights within the resultant structural network might be constituted as binary or predicated upon geodesic distances between nodal points along the vascular arboretum, serving as proxies for signal propagation and its attendant attenuation.

In a subsequent phase, when this astrocytic network is amalgamated with the vascular compartment previously discussed, the inter-astrocytic population couplings might be conceptualized as a phenomenological function contingent upon vascular densities or other salient features of the vascular anatomy. To further refine the structural network, recourse to high-definition molecular-cellular brain atlases, such as BigBrain (Amunts et al., 2013) and the Allen Human Brain Atlas (Arnatkevičiūtė et al., 2019), could be invaluable. These atlases could offer profound insights into the heterogeneous distribution of astrocytic densities across the cerebral expanse, thereby augmenting the fidelity of our neuro-glial–vascular interaction model.

Revisiting electrophysiology for model validation

A pivotal insight derived from the Chapter 3 of this thesis elucidated the dynamic interplay between glutamatergic and GABAergic neurotransmissions and their influence on the oscillatory behavior of neuronal membrane potentials within the alpha frequency band (8–13 Hz). We proposed that the equilibrium between excitatory and inhibitory neurotransmitter activities, orchestrated by the complex interactions involving neuron-astrocyte uptake and release processes, exerts a modulatory effect on the dynamics of neuronal membrane potentials. A salient outcome of our comprehensive examination of whole-brain network activity and functional connectivity was the identification that neurotransmitter dynamics could statistically account for variations in the amplitude envelope of neuronal membrane potential oscillations.

This discovery holds transformative potential within two interrelated research themes. The first theme explores the correlation between non-invasive electrophysiological measurements and BOLD fMRI data. Over the last decade, a significant observation has been the concordance of network configurations within the band-limited amplitude envelopes of MEG rhythms, particularly within the alpha and beta (8–30 Hz) bands, with those discerned in BOLD fMRI signals (Brookes et al., 2011; Hipp et al., 2012; Sadaghiani et al., 2022). This breakthrough established a multimodal bridge linking electrophysiological connectomics with the established domain of fMRI connectomics, underscoring the critical role of whole-brain MEG source-space analyses in elucidating patterns of functional connectivity (Sadaghiani et al., 2022). The second theme delves into the association between BOLD fMRI signals and glial activities, positing that glial cells, particularly astrocytes, rather than neurons, constitute the primary sources of fMRI signals (Figley & Stroman, 2011; Lu et al., 2019; Tesler et al., 2023; M. Wang et al., 2018). Integrating these themes, we hypothesize that the biochemical underpinnings of the observed congruence between MEG and BOLD fMRI signals are predominantly influenced by glutamate and GABA. Moreover, this biochemical foundation mirrors the sophisticated intercommunication between astrocytic networks and neuronal circuits, suggesting a deeper, more integrated level of brain function analysis. Thus, we embarked upon a rigorous endeavor to juxtapose the predictions of our model against empirical data derived from MEG and BOLD fMRI. This emphasis on the

nexus between MEG and BOLD fMRI was further motivated by the current absence of empirical methodologies capable of capturing temporally resolved neurotransmitter activity across the entire human brain (J. Y. Hansen et al., 2022; Lawn et al., 2023; Lea-Carnall et al., 2023).

In the realm of whole-brain modeling, traditional methodologies for constraining model outputs have predominantly utilized BOLD fMRI and non-invasive electrophysiological data (Breakspear, 2017; Griffiths et al., 2022). A predilection for BOLD fMRI over electrophysiological data has been evident, attributed to various factors elucidated below. Specifically, in the context of BOLD fMRI, a hemodynamic forward model, such as the balloon model proposed by (Buxton et al., 1998), is implemented to transform model-derived neuronal activity into predicted BOLD fMRI signals. It is crucial to recognize, within the context of glial involvement, that such hemodynamic models often presuppose that dynamic changes in vasodilation, blood flow, and subsequent alterations in volume and deoxyhemoglobin content are exclusively driven by neuronal activity (see also integrative biophysical or analytical approaches (Sotero & Trujillo-Barreto, 2008; Valdes-Sosa et al., 2009)). This assumption overlooks potential contributions from glial cells, notwithstanding emerging research that reevaluates fMRI data from a neuro-glial–vascular perspective (Blanchard et al., 2016; De Pittà & Berry, 2019; Figley & Stroman, 2011; Jolivet et al., 2015; Kastanenka et al., 2020; Lu et al., 2019; Tesler et al., 2023; M. Wang et al., 2018). Therefore, within the framework of our whole-brain neuron-astrocyte model, the utilization of traditional BOLD fMRI as a means to constrain model outputs is considered less than ideal. This is primarily because the conventional forward models employed do not explicitly incorporate the astrocytic component, thereby potentially omitting critical aspects of neuro-glial interactions.

Consequently, given the more straightforward correspondence of the model's state variables to electrophysiological data, we initially aimed to align our whole-brain model with such data.

However, this endeavor was anticipated to be arduous, as the analysis of electrophysiological data is beset with numerous challenges (Baillet, 2017; B. He et al., 2018). For the purpose of this thesis, we focused on the task of fitting our model to functional connectivity patterns derived from electrophysiological data, acknowledging the lack of established methodologies for fitting the temporal dynamics of whole-brain network activity during resting-state conditions.

Contrary to the more intuitive graphical representation afforded by BOLD fMRI, the analysis of non-invasive human electrophysiological data, such as EEG or MEG, necessitates the employment of inverse modeling techniques (Baillet, 2017; B. He et al., 2018). The traditional approach to connectomics analysis involves a sequential methodology that commences with the resolution of the inherently ill-posed inverse problem to generate time-series data, subsequently utilized to construct functional networks (Baillet, 2017; B. He et al., 2018). The efficacy and limitations of this two-step process remain partially obscured due to the myriad of approaches available for solving the inverse problem and for reconstructing functional networks. This obscurity is compounded by the fact that the simulation environments utilized for validation often lack the requisite biological realism (Allouch et al., 2022, 2023; Fraschini et al., 2020; Hassan et al., 2014, 2017; A.-S. Hincapié et al., 2017; Mahjoory et al., 2017; Pellegrini et al., 2023; Tabbal et al., 2022; Yu, 2020).

To address these challenges, we endeavored to critically assess and refine these methodologies through the integration of a biologically coherent computational framework, informed by our biophysical whole-brain neuron-astrocyte model. Our ultimate ambition was to identify and later employ the most efficacious reconstruction strategies for real data analysis, potentially facilitating

the integration of our biophysical model with empirical data, albeit in a preliminary fashion at this juncture.

Our investigation revealed that traditional reconstruction methodologies are intrinsically constrained by their reliance on inverse models that do not always inherently incorporate critical biological priors pertinent to the data under investigation, such as fiber connectivity, cortical geometry, and cortical parcellation. Despite these limitations, we discovered that reconstruction methods could yield reliable outcomes, provided that the inverse models are suitably parameterized or adapted to include proxies or substitutes for the essential biological priors underpinning the data.

In addressing the pivotal questions of whether we are now poised to undertake the task of partially fitting empirical MEG data, and the strategic approach and modeling assumptions that would underlie such an endeavor, we conclude that while further research is imperative, the simplifications adopted, in the Chapter 4, during our simulation and evaluation phases have positioned us more favorably to engage with the challenges of electrophysiological connectomics. Our proposed strategy hinges on the utilization of reconstruction models that incorporate structural connectivity priors derived from diffusion MRI and cortical geometry (Deslauriers-Gauthier et al., 2019, 2020; Gonzalez-Moreira, Paz-Linares, Areces-Gonzalez, Wang, & Valdes-Sosa, 2018; Gonzalez-Moreira, Paz-Linares, Areces-Gonzalez, Wang, Bosch-Bayard, et al., 2018; Gonzalez-Moreira, Paz-Linares, Martinez-Montes, et al., 2018), predicated on the hypothesis that these structural elements significantly influence neural network dynamics (Griffiths et al., 2022; Pang et al., 2023; Roberts et al., 2016).

Conclusion

In drawing this doctoral thesis to a close, I endeavor to extend beyond a mere recapitulation of the original contributions underscored within the preceding overall summary and discussions. My aim is to underscore the paramount importance of integration, collaboration, and the ethos of perpetual learning as cornerstone principles in the pursuit of unraveling the complexities of one of the most sophisticated constructs known to humankind: the human brain. It is my fervent hope that this multidisciplinary work will serve as a catalyst, encouraging future researchers to intricately interlace their focused inquiries with the broader scientific mosaic of their respective laboratories, collaborative networks, disciplines, departments, and the global scientific community.

The human brain, a masterpiece of biological complexity, represents an elaborate nexus comprised of billions of neurons, each intricately woven into a vast network and bolstered by the support of glial cells, all ensconced within an elaborate vascular system. Within this intricate network, glial cells emerge as pivotal actors, not merely fulfilling supportive roles but actively contributing to the brain's functionality and its myriad capabilities. This paradigm shift, recognizing the integral contributions of glial cells alongside neurons, marks a significant advancement in our understanding of cerebral architecture and dynamics.

Recent breakthroughs in neuroimaging technologies, the evolution of computational modeling, the maturation of network science, and enriched insights into the neuro-glial–vascular interplay have collectively illuminated the multifaceted mechanisms through which this remarkable organ orchestrates the spectrum of cognition, emotion, and behavior. Yet, the task of effectively leveraging this extensive body of knowledge presents a formidable challenge. It necessitates a multidisciplinary approach, drawing upon the collective expertise of neuroscientists, computational biologists, physicists, and engineers, among others, to forge a cohesive understanding of the brain's operational principles.

This thesis has placed a particular emphasis on computational modeling as a tool for simulating and understanding the brain's intricate dynamics. These models, which integrate data from various sources, offer predictive insights and help guide experimental endeavors. Nonetheless, computational modeling faces challenges such as the need for precise data, the inherent complexity of brain dynamics, and the ethical considerations associated with simulating brain activity.

Moreover, as a field in rapid evolution, neuroscience is characterized by ongoing controversies and debates, ranging from the roles of different brain components to the interpretation of cerebral data and the ethical implications of neuromodulation and brain-computer interfaces. This dynamic landscape necessitates a flexible and adaptive scientific approach, where neuroscientists are receptive to new data, willing to revise theories, and vigilant in maintaining ethical standards.

Considering these aspects collectively allows for a more comprehensive evaluation of neuroscience's broader impact. Insights from neuroscience have influenced and been influenced by a wide array of disciplines, leading to innovations in artificial intelligence, network theory, psychology, and medicine, among others. As neuroscientists delve deeper into the brain's complexities, they are likely to uncover new functional principles, develop novel treatments for neurological disorders, and continue to engage in a fruitful exchange with diverse scientific fields. The anticipated contributions of the *glial revolution* to this interdisciplinary dialogue are particularly noteworthy.

In this era of exponential scientific growth, the essence of our endeavor lies not solely in the accumulation of data but in our ability to synthesize, integrate, and apply this knowledge towards unraveling the myriad mysteries of the brain. As we stand on the cusp of new scientific frontiers, the journey ahead calls for a collaborative spirit, an interdisciplinary mindset, and a commitment to innovation and discovery. It is through this collective endeavor that we can hope to demystify the complexities of the brain, paving the way for transformative breakthroughs that will enhance our understanding of this enigmatic organ and its profound impact on the human experience.

Bibliography

2023 Alzheimer's disease facts and figures. (2023). *Alzheimer's & Dementia*, *19*(4), 1598–1695. https://doi.org/10.1002/alz.13016

Abd-Elrahman, K. S., Sarasija, S., & Ferguson, S. S. G. (2023). The Role of Neuroglial Metabotropic Glutamate Receptors in Alzheimer's Disease. *Current Neuropharmacology*, *21*(2), 273–283. https://doi.org/10.2174/1570159X19666210916102638

Abdi, H., & Valentin, D. (2007). The STATIS Method. *Encyclopedia of Measurement and Statistics*, *January*, 17. https://www.researchgate.net/publication/239547120_The_STATIS_Method

Abdi, H., Williams, L. J., Valentin, D., & Bennani-Dosse, M. (2012). STATIS and DISTATIS: optimum multitable principal component analysis and three way metric multidimensional scaling. *WIREs Computational Statistics*, *4*(2), 124–167. https://doi.org/10.1002/wics.198

Ableidinger, M., Buckwar, E., & Hinterleitner, H. (2017). A Stochastic Version of the Jansen and Rit Neural Mass Model: Analysis and Numerics. *The Journal of Mathematical Neuroscience*, *7*(1), 8. https://doi.org/10.1186/s13408-017-0046-4

Acosta, C., Anderson, H. D., & Anderson, C. M. (2017). Astrocyte dysfunction in Alzheimer disease. *Journal of Neuroscience Research*, *95*(12), 2430–2447. https://doi.org/10.1002/jnr.24075

Afnan, J., von Ellenrieder, N., Lina, J., Pellegrino, G., Arcara, G., Cai, Z., Hedrich, T., Abdallah, C., Khajehpour, H., Frauscher, B., Gotman, J., & Grova, C. (2023). Validating MEG source imaging of resting state oscillatory patterns with an intracranial EEG atlas. *NeuroImage*, *274*(March), 120158. https://doi.org/10.1016/j.neuroimage.2023.120158

Agid, Y., & Magistretti, P. (2020). *Glial Man: A Revolution in Neuroscience* (Cory, R.N.). Oxford University Press. https://books.google.ca/books?id=HfoFEAAAQBAJ

Ahmed, R. M., Devenney, E. M., Irish, M., Ittner, A., Naismith, S., Ittner, L. M., Rohrer, J. D., Halliday, G. M., Eisen, A., Hodges, J. R., & Kiernan, M. C. (2016). Neuronal network disintegration: Common pathways linking neurodegenerative diseases. *Journal of Neurology, Neurosurgery and Psychiatry*, *87*(11), 1234–1241. https://doi.org/10.1136/jnnp-2014-308350

Allaman, I., Gavillet, M., Bélanger, M., Laroche, T., Viertl, D., Lashuel, H. A., & Magistretti, P. J. (2010). Amyloid-β Aggregates Cause Alterations of Astrocytic Metabolic Phenotype: Impact on Neuronal Viability. *The Journal of Neuroscience*, *30*(9), 3326–3338. https://doi.org/10.1523/JNEUROSCI.5098-09.2010

Allen, N. J., & Barres, B. A. (2009). Glia — more than just brain glue. *Nature*, *457*(7230), 675–677. https://doi.org/10.1038/457675a

Allen, N. J., & Lyons, D. A. (2018). Glia as architects of central nervous system formation and function. *Science*, *362*(6411), 181–185. https://doi.org/10.1126/science.aat0473

Allouch, S., Duprez, J., Khalil, M., Hassan, M., Modolo, J., & Kabbara, A. (2022). Methods Used to Estimate EEG Source-Space Networks: A Comparative Simulation-Based Study.

Proceedings of the Annual International Conference of the IEEE Engineering in Medicine and Biology Society, EMBS, *2022-July*, 3590–3593. https://doi.org/10.1109/EMBC48229.2022.9871047

Allouch, S., Kabbara, A., Duprez, J., Khalil, M., Modolo, J., & Hassan, M. (2023). Effect of channel density, inverse solutions and connectivity measures on EEG resting-state networks reconstruction: A simulation study. *NeuroImage*, *271*(October 2022), 120006. https://doi.org/10.1016/j.neuroimage.2023.120006

Amblard, C., Grangeat, P., Benali, H., & Bendriem, B. (1999). Hyperfixation point-source reconstruction by the maximum entropy on the mean method. *1998 IEEE Nuclear Science Symposium Conference Record. 1998 IEEE Nuclear Science Symposium and Medical Imaging Conference (Cat. No.98CH36255)*, *2*, 1372–1376. https://doi.org/10.1109/NSSMIC.1998.774408

Amblard, C., Lapalme, E., & Lina, J. M. (2004). Biomagnetic Source Detection by Maximum Entropy and Graphical Models. *IEEE Transactions on Biomedical Engineering*, *51*(3), 427–442. https://doi.org/10.1109/TBME.2003.820999

Amhaoul, H., Staelens, S., & Dedeurwaerdere, S. (2014). Imaging brain inflammation in epilepsy. *Neuroscience*, *279*, 238–252. https://doi.org/10.1016/j.neuroscience.2014.08.044

Amunts, K., Lepage, C., Borgeat, L., Mohlberg, H., Dickscheid, T., Rousseau, M.-É., Bludau, S., Bazin, P.-L., Lewis, L. B., Oros-Peusquens, A.-M., Shah, N. J., Lippert, T., Zilles, K., & Evans, A. C. (2013). BigBrain: An Ultrahigh-Resolution 3D Human Brain Model. *Science*, *340*(6139), 1472–1475. https://doi.org/10.1126/science.1235381

Amzica, F., & Lopes da Silva, F. H. (2017). Cellular Substrates of Brain Rhythms. In D. L. Schomer & F. H. Lopes da Silva (Eds.), *Niedermeyer's Electroencephalography: Basic Principles, Clinical Applications, and Related Fields* (Vol. 1). Oxford University Press. https://doi.org/10.1093/med/9780190228484.003.0002

Angulo, M. C., Le Meur, K., Kozlov, A. S., Charpak, S., & Audinat, E. (2008). GABA, a forgotten gliotransmitter. *Progress in Neurobiology*, *86*(3), 297–303. https://doi.org/10.1016/j.pneurobio.2008.08.002

Antonakakis, M., Schrader, S., Wollbrink, A., Oostenveld, R., Rampp, S., Haueisen, J., & Wolters, C. H. (2019). The effect of stimulation type, head modeling, and combined EEG and MEG on the source reconstruction of the somatosensory P20/N20 component. *Human Brain Mapping*, *40*(17), 5011–5028. https://doi.org/10.1002/hbm.24754

Aquino, K. M., Schira, M. M., Robinson, P. A., Drysdale, P. M., & Breakspear, M. (2012). Hemodynamic Traveling Waves in Human Visual Cortex. *PLoS Computational Biology*, *8*(3), e1002435. https://doi.org/10.1371/journal.pcbi.1002435

Arbabyazd, L., Shen, K., Wang, Z., Hofmann-Apitius, M., Ritter, P., McIntosh, A. R., Battaglia, D., & Jirsa, V. (2021). Virtual Connectomic Datasets in Alzheimer's Disease and Aging Using Whole-Brain Network Dynamics Modelling. *Eneuro*, *8*(4), ENEURO.0475-20.2021. https://doi.org/10.1523/ENEURO.0475-20.2021

Arenaza-Urquijo, E. M., & Vemuri, P. (2018). Resistance vs resilience to Alzheimer disease. *Neurology*, *90*(15), 695–703. https://doi.org/10.1212/WNL.0000000000005303

Arnatkevičiūtė, A., Fulcher, B. D., & Fornito, A. (2019). A practical guide to linking brain-wide gene expression and neuroimaging data. *NeuroImage*, *189*(July 2018), 353–367. https://doi.org/10.1016/j.neuroimage.2019.01.011

Arslan, S., Ktena, S. I., Makropoulos, A., Robinson, E. C., Rueckert, D., & Parisot, S. (2018). Human brain mapping: A systematic comparison of parcellation methods for the human cerebral cortex. *NeuroImage*, *170*, 5–30. https://doi.org/10.1016/j.neuroimage.2017.04.014

Aydin, Ü., Pellegrino, G., Ali, O. B. K., Abdallah, C., Dubeau, F., Lina, J.-M., Kobayashi, E., & Grova, C. (2020). Magnetoencephalography resting state connectivity patterns as indicatives of surgical outcome in epilepsy patients. *Journal of Neural Engineering*, *17*(3), 035007. https://doi.org/10.1088/1741-2552/ab8113

Aydin, Ü., Vorwerk, J., Dümpelmann, M., Küpper, P., Kugel, H., Heers, M., Wellmer, J., Kellinghaus, C., Haueisen, J., Rampp, S., Stefan, H., & Wolters, C. H. (2015). Combined EEG/MEG Can Outperform Single Modality EEG or MEG Source Reconstruction in Presurgical Epilepsy Diagnosis. *PLOS ONE*, *10*(3), e0118753. https://doi.org/10.1371/journal.pone.0118753

Aydin, Ü., Vorwerk, J., Küpper, P., Heers, M., Kugel, H., Galka, A., Hamid, L., Wellmer, J., Kellinghaus, C., Rampp, S., & Wolters, C. H. (2014). Combining EEG and MEG for the Reconstruction of Epileptic Activity Using a Calibrated Realistic Volume Conductor Model. *PLoS ONE*, *9*(3), e93154. https://doi.org/10.1371/journal.pone.0093154

Bagarinao, E., Watanabe, H., Maesawa, S., Mori, D., Hara, K., Kawabata, K., Yoneyama, N., Ohdake, R., Imai, K., Masuda, M., Yokoi, T., Ogura, A., Taoka, T., Koyama, S., Tanabe, H. C., Katsuno, M., Wakabayashi, T., Kuzuya, M., Ozaki, N., … Sobue, G. (2019). Reorganization of brain networks and its association with general cognitive performance over the adult lifespan. *Scientific Reports*, *9*(1), 1–15. https://doi.org/10.1038/s41598-019-47922-x

Baillet, S. (2017). Magnetoencephalography for brain electrophysiology and imaging. *Nature Neuroscience*, *20*(3), 327–339. https://doi.org/10.1038/nn.4504

Baillet, S., Mosher, J. C., & Leahy, R. M. (2001). Electromagnetic brain mapping. *IEEE Signal Processing Magazine*, *18*(6), 14–30. https://doi.org/10.1109/79.962275

Banavar, J., & Maritan, A. (2007). *The maximum relative entropy principle*. *5*, 5–8. http://arxiv.org/abs/cond-mat/0703622

Bandyopadhyay, A., Rabuffo, G., Calabrese, C., Gudibanda, K., Depannemaecker, D., Ivanov, A., Bernard, C., Jirsa, V. K., & Petkoski, S. (2022). Mean-field approximation of network of biophysical neurons driven by conductance-based ion exchange. *BioRxiv*, 2021.10.29.466427. https://doi.org/10.1101/2021.10.29.466427

Bargmann, C. I. (2012). Beyond the connectome: How neuromodulators shape neural circuits. *BioEssays*, *34*(6), 458–465. https://doi.org/10.1002/bies.201100185

Barres, B. A. (2008). The Mystery and Magic of Glia: A Perspective on Their Roles in Health and Disease. *Neuron*, *60*(3), 430–440. https://doi.org/10.1016/j.neuron.2008.10.013

Barreto, G., E. White, R., Ouyang, Y., Xu, L., & G. Giffard, R. (2012). Astrocytes: Targets for Neuroprotection in Stroke. *Central Nervous System Agents in Medicinal Chemistry*, *11*(2), 164–173. https://doi.org/10.2174/187152411796011303

Bassett, D. S., & Bullmore, E. T. (2017). Small-World Brain Networks Revisited. *The Neuroscientist*, *23*(5), 499–516. https://doi.org/10.1177/1073858416667720

Bassett, D. S., & Sporns, O. (2017). Network neuroscience. *Nature Neuroscience*, *20*(3), 353–364. https://doi.org/10.1038/nn.4502

Bastos, A. M., & Schoffelen, J.-M. (2016). A Tutorial Review of Functional Connectivity Analysis Methods and Their Interpretational Pitfalls. *Frontiers in Systems Neuroscience*, *9*(January), 1–23. https://doi.org/10.3389/fnsys.2015.00175

Bernier, L.-P., Brunner, C., Cottarelli, A., & Balbi, M. (2021). Location Matters: Navigating Regional Heterogeneity of the Neurovascular Unit. *Frontiers in Cellular Neuroscience*, *15*, 696540. https://doi.org/10.3389/fncel.2021.696540

Bernier, M., Cunnane, S. C., & Whittingstall, K. (2018). The morphology of the human cerebrovascular system. *Human Brain Mapping*, *39*(12), 4962–4975. https://doi.org/10.1002/hbm.24337

Betina Ip, I., Berrington, A., Hess, A. T., Parker, A. J., Emir, U. E., & Bridge, H. (2017). Combined fMRI-MRS acquires simultaneous glutamate and BOLD-fMRI signals in the human brain. *NeuroImage*, *155*(April), 113–119. https://doi.org/10.1016/j.neuroimage.2017.04.030

Betzel, R. F., & Bassett, D. S. (2017). Multi-scale brain networks. *NeuroImage*, *160*(November 2016), 73–83. https://doi.org/10.1016/j.neuroimage.2016.11.006

Beurle, R. L. (1956). Properties of a mass of cells capable of regenerating pulses. *Philosophical Transactions of the Royal Society of London. Series B, Biological Sciences*, *240*(669), 55–94. https://doi.org/10.1098/rstb.1956.0012

Bezgin, G., Solodkin, A., Bakker, R., Ritter, P., & McIntosh, A. R. (2017). Mapping complementary features of cross-species structural connectivity to construct realistic "Virtual Brains." *Human Brain Mapping*, *38*(4), 2080–2093. https://doi.org/10.1002/hbm.23506

Biasiucci, A., Franceschiello, B., & Murray, M. M. (2019). Electroencephalography. *Current Biology*, *29*(3), R80–R85. https://doi.org/10.1016/j.cub.2018.11.052

Blanchard, S., Saillet, S., Ivanov, A., Benquet, P., Bénar, C.-G., Pélégrini-Issac, M., Benali, H., & Wendling, F. (2016). A New Computational Model for Neuro-Glio-Vascular Coupling: Astrocyte Activation Can Explain Cerebral Blood Flow Nonlinear Response to Interictal Events. *PLOS ONE*, *11*(2), e0147292. https://doi.org/10.1371/journal.pone.0147292

Blanco-Suárez, E., Caldwell, A. L. M., & Allen, N. J. (2017). Role of astrocyte–synapse interactions in CNS disorders. *Journal of Physiology*, *595*(6), 1903–1916. https://doi.org/10.1113/JP270988

Boccaletti, S., Bianconi, G., Criado, R., del Genio, C. I., Gómez-Gardeñes, J., Romance, M., Sendiña-Nadal, I., Wang, Z., & Zanin, M. (2014). The structure and dynamics of multilayer networks. *Physics Reports*, *544*(1), 1–122. https://doi.org/10.1016/j.physrep.2014.07.001

Bojak, I. (2014). Neural Population Models and Cortical Field Theory: Overview. In *Encyclopedia of Computational Neuroscience* (pp. 1–3). Springer New York. https://doi.org/10.1007/978-1-4614-7320-6_759-1

Bojak, I., & Breakspear, M. (2015). Neuroimaging, Neural Population Models for. In *Encyclopedia of Computational Neuroscience* (pp. 1919–1944). Springer New York. https://doi.org/10.1007/978-1-4614-6675-8_70

Boly, M., Perlbarg, V., Marrelec, G., Schabus, M., Laureys, S., Doyon, J., Pélégrini-Issac, M., Maquet, P., & Benali, H. (2012). Hierarchical clustering of brain activity during human nonrapid eye movement sleep. *Proceedings of the National Academy of Sciences of the United States of America*, *109*(15), 5856–5861. https://doi.org/10.1073/pnas.1111133109

Bookheimer, S. Y., Salat, D. H., Terpstra, M., Ances, B. M., Barch, D. M., Buckner, R. L., Burgess, G. C., Curtiss, S. W., Diaz-Santos, M., Elam, J. S., Fischl, B., Greve, D. N., Hagy, H. A., Harms, M. P., Hatch, O. M., Hedden, T., Hodge, C., Japardi, K. C., Kuhn, T. P., … Yacoub, E. (2019). The Lifespan Human Connectome Project in Aging: An overview. *NeuroImage*, *185*(July 2018), 335–348. https://doi.org/10.1016/j.neuroimage.2018.10.009

Brazhe, A., Verisokin, A., Verveyko, D., & Postnov, D. (2023). Astrocytes: new evidence, new models, new roles. *Biophysical Reviews*, *15*(5), 1303–1333. https://doi.org/10.1007/s12551-023-01145-7

Breakspear, M. (2017). Dynamic models of large-scale brain activity. *Nature Neuroscience*, *20*(3), 340–352. https://doi.org/10.1038/nn.4497

Bredesen, D. E. (2014). Reversal of cognitive decline: A novel therapeutic program. *Aging*, *6*(9), 707–717. https://doi.org/10.18632/aging.100690

Brezina, V. (2010). Beyond the wiring signalling through complex neuromodulator networks. *Philosophical Transactions of the Royal Society B: Biological Sciences*, *365*(1551), 2363–2374. https://doi.org/10.1098/rstb.2010.0105

Brkić, D., Sommariva, S., Schuler, A.-L., Pascarella, A., Belardinelli, P., Isabella, S. L., Pino, G. Di, Zago, S., Ferrazzi, G., Rasero, J., Arcara, G., Marinazzo, D., & Pellegrino, G. (2023). The impact of ROI extraction method for MEG connectivity estimation: Practical recommendations for the study of resting state data. *NeuroImage*, *284*(September), 120424. https://doi.org/10.1016/j.neuroimage.2023.120424

Brookes, M. J., Tewarie, P. K., Hunt, B. A. E., Robson, S. E., Gascoyne, L. E., Liddle, E. B., Liddle, P. F., & Morris, P. G. (2016). A multi-layer network approach to MEG connectivity analysis. *NeuroImage*, *132*, 425–438. https://doi.org/10.1016/j.neuroimage.2016.02.045

Brookes, M. J., Woolrich, M., Luckhoo, H., Price, D., Hale, J. R., Stephenson, M. C., Barnes, G. R., Smith, S. M., & Morris, P. G. (2011). Investigating the electrophysiological basis of resting state networks using magnetoencephalography. *Proceedings of the National Academy*

of Sciences of the United States of America, *108*(40), 16783–16788. https://doi.org/10.1073/PNAS.1112685108

Brookes, M. J., Woolrich, M. W., & Price, D. (2014). An Introduction to MEG Connectivity Measurements. In *Magnetoencephalography* (Vol. 9783642330, pp. 321–358). Springer Berlin Heidelberg. https://doi.org/10.1007/978-3-642-33045-2_16

Butt, A. M., De La Rocha, I. C., & Rivera, A. (2019). Oligodendroglial Cells in Alzheimer's Disease. In *Advances in Experimental Medicine and Biology* (Vol. 1175, pp. 325–333). Springer Singapore. https://doi.org/10.1007/978-981-13-9913-8_12

Buxton, R. B., Frank, L. R., Wong, E. C., Siewert, B., Warach, S., & Edelman, R. R. (1998). A general kinetic model for quantitative perfusion imaging with arterial spin labeling. *Magnetic Resonance in Medicine*, *40*(3), 383–396. https://doi.org/10.1002/mrm.1910400308

Buzsáki, G. (2009). Rhythms of the Brain. In *Rhythms of the Brain*. https://doi.org/10.1093/acprof:oso/9780195301069.001.0001

Buzsáki, G., Anastassiou, C. A., & Koch, C. (2012). The origin of extracellular fields and currents-EEG, ECoG, LFP and spikes. *Nature Reviews Neuroscience*, *13*(6), 407–420. https://doi.org/10.1038/nrn3241

Byrne, Á., O'Dea, R. D., Forrester, M., Ross, J., & Coombes, S. (2020). Next-generation neural mass and field modeling. *Journal of Neurophysiology*, *123*(2), 726–742. https://doi.org/10.1152/jn.00406.2019

Byrne, Á., Ross, J., Nicks, R., & Coombes, S. (2022). Mean-Field Models for EEG/MEG: From Oscillations to Waves. *Brain Topography*, *35*(1), 36–53. https://doi.org/10.1007/s10548-021-00842-4

Cabral, J., Kringelbach, M. L., & Deco, G. (2014). Exploring the network dynamics underlying brain activity during rest. *Progress in Neurobiology*, *114*, 102–131. https://doi.org/10.1016/j.pneurobio.2013.12.005

Cai, Z., Machado, A., Chowdhury, R. A., Spilkin, A., Vincent, T., Aydin, Ü., Pellegrino, G., Lina, J.-M., & Grova, C. (2022). Diffuse optical reconstructions of functional near infrared spectroscopy data using maximum entropy on the mean. *Scientific Reports*, *12*(1), 2316. https://doi.org/10.1038/s41598-022-06082-1

Canter, R. G., Penney, J., & Tsai, L.-H. (2016). The road to restoring neural circuits for the treatment of Alzheimer's disease. *Nature*, *539*(7628), 187–196. https://doi.org/10.1038/nature20412

Caticha, A. (2008). *Lectures on Probability, Entropy, and Statistical Physics*. http://arxiv.org/abs/0808.0012

Caticha, A., & Giffin, A. (2006). Updating Probabilities. *AIP Conference Proceedings*, *872*, 31–42. https://doi.org/10.1063/1.2423258

Chavoshnejad, P., Li, X., Zhang, S., Dai, W., Vasung, L., Liu, T., Zhang, T., Wang, X., & Razavi, M. J. (2021). Role of axonal fibers in the cortical folding patterns: A tale of variability and regularity. *Brain Multiphysics*, *2*, 100029. https://doi.org/10.1016/j.brain.2021.100029

Cheeseman, P. (2004). On The Relationship between Bayesian and Maximum Entropy Inference. *AIP Conference Proceedings*, *735*, 445–461. https://doi.org/10.1063/1.1835243

Chehelcheraghi, M., Nakatani, C., Steur, E., & van Leeuwen, C. (2016). A neural mass model of phase–amplitude coupling. *Biological Cybernetics*, *110*(2–3), 171–192. https://doi.org/10.1007/s00422-016-0687-5

Chowdhury, R. A., Lina, J. M., Kobayashi, E., & Grova, C. (2013). MEG Source Localization of Spatially Extended Generators of Epileptic Activity: Comparing Entropic and Hierarchical Bayesian Approaches. *PLoS ONE*, *8*(2), e55969. https://doi.org/10.1371/journal.pone.0055969

Chowdhury, R. A., Merlet, I., Birot, G., Kobayashi, E., Nica, A., Biraben, A., Wendling, F., Lina, J. M., Albera, L., & Grova, C. (2016). Complex patterns of spatially extended generators of epileptic activity: Comparison of source localization methods cMEM and 4-ExSo-MUSIC on high resolution EEG and MEG data. *NeuroImage*, *143*, 175–195. https://doi.org/10.1016/j.neuroimage.2016.08.044

Chowdhury, R. A., Zerouali, Y., Hedrich, T., Heers, M., Kobayashi, E., Lina, J.-M., & Grova, C. (2015). MEG–EEG Information Fusion and Electromagnetic Source Imaging: From Theory to Clinical Application in Epilepsy. *Brain Topography*, *28*(6), 785–812. https://doi.org/10.1007/s10548-015-0437-3

Chung, W. S., Welsh, C. A., Barres, B. A., & Stevens, B. (2015). Do glia drive synaptic and cognitive impairment in disease? *Nature Neuroscience*, *18*(11), 1539–1545. https://doi.org/10.1038/nn.4142

Chung, Y. S., Hyatt, C. J., & Stevens, M. C. (2017). Adolescent maturation of the relationship between cortical gyrification and cognitive ability. *NeuroImage*, *158*(July), 319–331. https://doi.org/10.1016/j.neuroimage.2017.06.082

Cioli, C., Abdi, H., Beaton, D., Burnod, Y., & Mesmoudi, S. (2014). Differences in Human Cortical Gene Expression Match the Temporal Properties of Large-Scale Functional Networks. *PLoS ONE*, *9*(12), e115913. https://doi.org/10.1371/journal.pone.0115913

Clarke, C. J. S. (1989). Probabilistic methods in a biomagnetic inverse problem. *Inverse Problems*, *5*(6), 999–1012. https://doi.org/10.1088/0266-5611/5/6/008

Clarke, C. J. S., & Janday, B. S. (1989). The solution of the biomagnetic inverse problem by maximum statistical entropy. *Inverse Problems*, *5*(4), 483–500. https://doi.org/10.1088/0266-5611/5/4/005

Clauset, A., Newman, M. E. J., & Moore, C. (2004). Finding community structure in very large networks. *Physical Review E - Statistical Physics, Plasmas, Fluids, and Related Interdisciplinary Topics*, *70*(6), 6. https://doi.org/10.1103/PhysRevE.70.066111

Clewley, R. (2012). Hybrid Models and Biological Model Reduction with PyDSTool. *PLoS Computational Biology*, *8*(8), e1002628. https://doi.org/10.1371/journal.pcbi.1002628

Colclough, G. L., Brookes, M. J., Smith, S. M., & Woolrich, M. W. (2015). A symmetric multivariate leakage correction for MEG connectomes. *NeuroImage*, *117*, 439–448. https://doi.org/10.1016/j.neuroimage.2015.03.071

Colclough, G. L., Woolrich, M. W., Tewarie, P. K., Brookes, M. J., Quinn, A. J., & Smith, S. M. (2016). How reliable are MEG resting-state connectivity metrics? *NeuroImage*, *138*, 284–293. https://doi.org/10.1016/j.neuroimage.2016.05.070

Contreras, D., & Steriade, M. (1995). Cellular basis of EEG slow rhythms: a study of dynamic corticothalamic relationships. *The Journal of Neuroscience*, *15*(1), 604–622. https://doi.org/10.1523/JNEUROSCI.15-01-00604.1995

Cook, B. J., Peterson, A. D. H., Woldman, W., & Terry, J. R. (2022). Neural Field Models: A mathematical overview and unifying framework. *Mathematical Neuroscience and Applications*, *Volume 2*(2), 1–67. https://doi.org/10.46298/mna.7284

Coombes, S. (2023). Next generation neural population models. *Frontiers in Applied Mathematics and Statistics*, *9*. https://doi.org/10.3389/fams.2023.1128224

Coombes, S., & Byrne, Á. (2016). Next generation neural mass models. *PoliTO Springer Series*, *September*, 1–16. https://doi.org/10.1007/978-3-319-71048-8_1

Coombes, S., & Wedgwood, K. C. A. (2023). *Neurodynamics* (Vol. 75). Springer International Publishing. https://doi.org/10.1007/978-3-031-21916-0

Coquelet, N., De Tiège, X., Destoky, F., Roshchupkina, L., Bourguignon, M., Goldman, S., Peigneux, P., & Wens, V. (2020). Comparing MEG and high-density EEG for intrinsic functional connectivity mapping. *NeuroImage*, *210*(January), 116556. https://doi.org/10.1016/j.neuroimage.2020.116556

Corey, D. M., Dunlap, W. P., & Burke, M. J. (1998). Averaging correlations: Expected values and bias in combined pearson rs and fisher's z transformations. *Journal of General Psychology*, *125*(3), 245–261. https://doi.org/10.1080/00221309809595548

Coronel-Oliveros, C., Cofré, R., & Orio, P. (2021). Cholinergic neuromodulation of inhibitory interneurons facilitates functional integration in whole-brain models. *PLOS Computational Biology*, *17*(2), e1008737. https://doi.org/10.1371/journal.pcbi.1008737

Cowan, J. D., Neuman, J., & van Drongelen, W. (2016). Wilson–Cowan Equations for Neocortical Dynamics. *The Journal of Mathematical Neuroscience*, *6*(1), 1. https://doi.org/10.1186/s13408-015-0034-5

Crameri, F., Shephard, G. E., & Heron, P. J. (2020). The misuse of colour in science communication. *Nature Communications*, *11*(1), 1–10. https://doi.org/10.1038/s41467-020-19160-7

Crupi, R., Impellizzeri, D., & Cuzzocrea, S. (2019). Role of metabotropic glutamate receptors in neurological disorders. *Frontiers in Molecular Neuroscience*, *12*(February), 1–11. https://doi.org/10.3389/fnmol.2019.00020

Cummings, J. L., Morstorf, T., & Zhong, K. (2014). Alzheimer's disease drug-development pipeline: few candidates, frequent failures. *Alzheimer's Research & Therapy*, *6*(4), 37. https://doi.org/10.1186/alzrt269

Daducci, A., Dal Palù, A., Lemkaddem, A., & Thiran, J.-P. (2015). COMMIT: Convex optimization modeling for microstructure informed tractography. *IEEE Transactions on Medical Imaging*, *34*(1), 246–257. https://doi.org/10.1109/TMI.2014.2352414

David, O., & Friston, K. J. (2003). A neural mass model for MEG/EEG: coupling and neuronal dynamics. *NeuroImage*, *20*(3), 1743–1755. https://doi.org/10.1016/j.neuroimage.2003.07.015

De Domenico, M. (2017). Multilayer modeling and analysis of human brain networks. *GigaScience*, *6*(5), 1–8. https://doi.org/10.1093/gigascience/gix004

De Domenico, M. (2020). *Multilayer Networks Illustrated*. https://doi.org/10.17605/OSF.IO/GY53K

De Domenico, M., Lancichinetti, A., Arenas, A., & Rosvall, M. (2015). Identifying modular flows on multilayer networks reveals highly overlapping organization in interconnected systems. *Physical Review X*, *5*(1), 1–11. https://doi.org/10.1103/PhysRevX.5.011027

De Domenico, M., Nicosia, V., Arenas, A., & Latora, V. (2015). Structural reducibility of multilayer networks. *Nature Communications*, *6*, 1–9. https://doi.org/10.1038/ncomms7864

De Domenico, M., Solé-Ribalta, A., Cozzo, E., Kivelä, M., Moreno, Y., Porter, M. A., Gómez, S., & Arenas, A. (2014). Mathematical formulation of multilayer networks. *Physical Review X*, *3*(4), 1–15. https://doi.org/10.1103/PhysRevX.3.041022

De Domenico, M., Solé-Ribalta, A., Omodei, E., Gómez, S., & Arenas, A. (2015). Ranking in interconnected multilayer networks reveals versatile nodes. *Nature Communications*, *6*, 1–6. https://doi.org/10.1038/ncomms7868

de Haan, W., van Straaten, E. C. W., Gouw, A. A., & Stam, C. J. (2017). Altering neuronal excitability to preserve network connectivity in a computational model of Alzheimer's disease. *PLOS Computational Biology*, *13*(9), e1005707. https://doi.org/10.1371/journal.pcbi.1005707

De Pittà, M. (2020). Neuron-Glial Interactions. In *Encyclopedia of Computational Neuroscience* (Vol. 2020, pp. 1–30). Springer New York. https://doi.org/10.1007/978-1-4614-7320-6_100691-1

De Pittà, M., & Berry, H. (2019). A Neuron–Glial Perspective for Computational Neuroscience. In M. De Pittà & H. Berry (Eds.), *Computational Glioscience* (pp. 3–35). Springer, Cham. https://doi.org/10.1007/978-3-030-00817-8_1

De Pittà, M., Volman, V., Berry, H., & Ben-Jacob, E. (2011). A Tale of Two Stories: Astrocyte Regulation of Synaptic Depression and Facilitation. *PLoS Computational Biology*, *7*(12), e1002293. https://doi.org/10.1371/journal.pcbi.1002293

Deco, G., Cabral, J., Woolrich, M. W., Stevner, A. B. A., van Hartevelt, T. J., & Kringelbach, M. L. (2017). Single or multiple frequency generators in on-going brain activity: A mechanistic whole-brain model of empirical MEG data. *NeuroImage*, *152*(February), 538–550. https://doi.org/10.1016/j.neuroimage.2017.03.023

Deco, G., & Jirsa, V. K. (2012). Ongoing Cortical Activity at Rest: Criticality, Multistability, and Ghost Attractors. *The Journal of Neuroscience*, *32*(10), 3366–3375. https://doi.org/10.1523/JNEUROSCI.2523-11.2012

Deco, G., Jirsa, V. K., Robinson, P. A., Breakspear, M., & Friston, K. (2008). The dynamic brain: From spiking neurons to neural masses and cortical fields. *PLoS Computational Biology*, *4*(8). https://doi.org/10.1371/journal.pcbi.1000092

Deco, G., Jirsa, V., McIntosh, A. R., Sporns, O., & Kötter, R. (2009). Key role of coupling, delay, and noise in resting brain fluctuations. *Proceedings of the National Academy of Sciences*, *106*(25), 10302–10307. https://doi.org/10.1073/pnas.0901831106

Del Guerra, A., Ahmad, S., Avram, M., Belcari, N., Berneking, A., Biagi, L., Bisogni, M. G., Brandl, F., Cabello, J., Camarlinghi, N., Cerello, P., Choi, C.-H., Coli, S., Colpo, S., Fleury, J., Gagliardi, V., Giraudo, G., Heekeren, K., Kawohl, W., … Ziegler, S. (2018). TRIMAGE: A dedicated trimodality (PET/MR/EEG) imaging tool for schizophrenia. *European Psychiatry*, *50*, 7–20. https://doi.org/10.1016/j.eurpsy.2017.11.007

Delettre, C., Messé, A., Dell, L.-A., Foubet, O., Heuer, K., Larrat, B., Meriaux, S., Mangin, J.-F., Reillo, I., de Juan Romero, C., Borrell, V., Toro, R., & Hilgetag, C. C. (2019). Comparison between diffusion MRI tractography and histological tract-tracing of cortico-cortical structural connectivity in the ferret brain. *Network Neuroscience*, *3*(4), 1038–1050. https://doi.org/10.1162/netn_a_00098

Dementia statistics | Alzheimer's Disease International (ADI). (n.d.). Retrieved February 18, 2024, from https://www.alzint.org/about/dementia-facts-figures/dementia-statistics/

Demirtaş, M., Falcon, C., Tucholka, A., Gispert, J. D., Molinuevo, J. L., & Deco, G. (2017). A whole-brain computational modeling approach to explain the alterations in resting-state functional connectivity during progression of Alzheimer's disease. *NeuroImage: Clinical*, *16*(March), 343–354. https://doi.org/10.1016/j.nicl.2017.08.006

Deng, P.-Y., & Lei, S. (2008). Serotonin increases GABA release in rat entorhinal cortex by inhibiting interneuron TASK-3 K+ channels. *Molecular and Cellular Neuroscience*, *39*(2), 273–284. https://doi.org/10.1016/j.mcn.2008.07.005

Deslauriers-Gauthier, S., Costantini, I., & Deriche, R. (2020). Non–invasive inference of information flow using diffusion MRI, functional MRI, and MEG. *Journal of Neural Engineering*, *17*(4), 045003. https://doi.org/10.1088/1741-2552/ab95ec

Deslauriers-Gauthier, S., Lina, J.-M., Butler, R., Whittingstall, K., Gilbert, G., Bernier, P.-M., Deriche, R., & Descoteaux, M. (2019). White matter information flow mapping from diffusion MRI and EEG. *NeuroImage*, *201*(February), 116017. https://doi.org/10.1016/j.neuroimage.2019.116017

Destexhe, A., & Sejnowski, T. J. (2009). The Wilson–Cowan model, 36 years later. *Biological Cybernetics*, *101*(1), 1–2. https://doi.org/10.1007/s00422-009-0328-3

Devinsky, O., Vezzani, A., Najjar, S., De Lanerolle, N. C., & Rogawski, M. A. (2013). Glia and epilepsy: excitability and inflammation. *Trends in Neurosciences*, *36*(3), 174–184. https://doi.org/10.1016/j.tins.2012.11.008

Dhooge, A., Govaerts, W., Kuznetsov, Y. A., Meijer, H. G. E., & Sautois, B. (2008). New features of the software MatCont for bifurcation analysis of dynamical systems. *Mathematical and Computer Modelling of Dynamical Systems*, *14*(2), 147–175. https://doi.org/10.1080/13873950701742754

Diao, F., Elliott, A. D., Diao, F., Shah, S., & White, B. H. (2017). Neuromodulatory connectivity defines the structure of a behavioral neural network. *ELife*, *6*(1984), 1–30. https://doi.org/10.7554/eLife.29797

Djafari, A. M. (1994). Maximum Entropy and Inverse Problems in Image Reconstruction. *Traitement Du Signal*, *11*(2), 87. https://api.semanticscholar.org/CorpusID:124775983

Dudkowski, D., Jafari, S., Kapitaniak, T., Kuznetsov, N. V., Leonov, G. A., & Prasad, A. (2016). Hidden attractors in dynamical systems. *Physics Reports*, *637*, 1–50. https://doi.org/10.1016/j.physrep.2016.05.002

Duman, R. S., Sanacora, G., & Krystal, J. H. (2019). Altered Connectivity in Depression: GABA and Glutamate Neurotransmitter Deficits and Reversal by Novel Treatments. *Neuron*, *102*(1), 75–90. https://doi.org/10.1016/j.neuron.2019.03.013

Ermentrout, G. B., & Terman, D. H. (2010). Firing Rate Models. In *Interdisciplinary Applied Mathematics* (Vol. 35, pp. 331–367). https://doi.org/10.1007/978-0-387-87708-2_11

Fan, Y., Fan, Q., Zhou, L., Wang, R., Lin, P., & Wu, Y. (2021). Cohesive communities in dynamic brain functional networks. *Physical Review E*, *104*(1), 014302. https://doi.org/10.1103/PhysRevE.104.014302

Faugeras, O., Touboul, J., & Cessac, B. (2009). A constructive mean-field analysis of multi-population neural networks with random synaptic weights and stochastic inputs. *Frontiers in Computational Neuroscience*, *3*(FEB), 1–28. https://doi.org/10.3389/neuro.10.001.2009

Ferrat, L. A., Goodfellow, M., & Terry, J. R. (2018). Classifying dynamic transitions in high dimensional neural mass models: A random forest approach. *PLOS Computational Biology*, *14*(3), e1006009. https://doi.org/10.1371/journal.pcbi.1006009

Ferrer, I. (2018). Oligodendrogliopathy in neurodegenerative diseases with abnormal protein aggregates: The forgotten partner. *Progress in Neurobiology*, *169*(March), 24–54. https://doi.org/10.1016/j.pneurobio.2018.07.004

Fields, R. D. (2011). *The Other Brain: The Scientific and Medical Breakthroughs That Will Heal Our Brains and Revolutionize Our Health*. Simon & Schuster. https://books.google.ca/books?id=alTuRAAACAAJ

Fields, R. D., Woo, D. H., & Basser, P. J. (2015). Glial regulation of the neuronal connectome through local and long-distant communication. *Neuron*, *86*(2), 374–386. https://doi.org/10.1016/j.neuron.2015.01.014

Figley, C. R., & Stroman, P. W. (2011). The role(s) of astrocytes and astrocyte activity in neurometabolism, neurovascular coupling, and the production of functional neuroimaging signals. *European Journal of Neuroscience*, *33*(4), 577–588. https://doi.org/10.1111/j.1460-9568.2010.07584.x

Fischl, B. (2012). FreeSurfer. *NeuroImage*, *62*(2), 774–781. https://doi.org/10.1016/j.neuroimage.2012.01.021

Fonov, V., Evans, A. C., Botteron, K., Almli, C. R., McKinstry, R. C., & Collins, D. L. (2011). Unbiased average age-appropriate atlases for pediatric studies. *NeuroImage*, *54*(1), 313–327. https://doi.org/10.1016/j.neuroimage.2010.07.033

Fonseca-Santos, B., Gremião, M. P. D., & Chorilli, M. (2015). Nanotechnology-based drug delivery systems for the treatment of Alzheimer's disease. *International Journal of Nanomedicine*, *10*, 4981–5003. https://doi.org/10.2147/IJN.S87148

Fornito, A., Arnatkevičiūtė, A., & Fulcher, B. D. (2019). Bridging the Gap between Connectome and Transcriptome. *Trends in Cognitive Sciences*, *23*(1), 34–50. https://doi.org/10.1016/j.tics.2018.10.005

Forrester, M., Crofts, J. J., Sotiropoulos, S. N., Coombes, S., & O'Dea, R. D. (2020). The role of node dynamics in shaping emergent functional connectivity patterns in the brain. *Network Neuroscience*, *4*(2), 467–483. https://doi.org/10.1162/netn_a_00130

Fraschini, M., La Cava, S. M., Didaci, L., & Barberini, L. (2020). On the Variability of Functional Connectivity and Network Measures in Source-Reconstructed EEG Time-Series. *Entropy*, *23*(1), 5. https://doi.org/10.3390/e23010005

Frässle, S., Yao, Y., Schöbi, D., Aponte, E. A., Heinzle, J., & Stephan, K. E. (2018). Generative models for clinical applications in computational psychiatry. *WIREs Cognitive Science*, *9*(3), 1–21. https://doi.org/10.1002/wcs.1460

Frauscher, B., Von Ellenrieder, N., Zelmann, R., Doležalová, I., Minotti, L., Olivier, A., Hall, J., Hoffmann, D., Nguyen, D. K., Kahane, P., Dubeau, F., & Gotman, J. (2018). Atlas of the normal intracranial electroencephalogram: Neurophysiological awake activity in different cortical areas. *Brain*, *141*(4), 1130–1144. https://doi.org/10.1093/brain/awy035

Frauscher, B., von Ellenrieder, N., Zelmann, R., Doležalová, I., Minotti, L., Olivier, A., Hall, J., Hoffmann, D., Nguyen, D. K., Kahane, P., Dubeau, F., & Gotman, J. (2018). Atlas of the normal intracranial electroencephalogram: neurophysiological awake activity in different cortical areas. *Brain*, *141*(4), 1130–1144. https://doi.org/10.1093/brain/awy035

Freeman, W. J. (1972). Linear Analysis of the Dynamics of Neural Masses. *Annual Review of Biophysics and Bioengineering*, *1*(1), 225–256. https://doi.org/10.1146/annurev.bb.01.060172.001301

Freeman, W. J. (1975). Mass Action in the Nervous System. In *Mass Action in the Nervous System*. Elsevier. https://doi.org/10.1016/C2009-0-03145-6

Gamboa, F. (1989). *Méthode du maximum d'entropie sur la moyenne et applications* [Theses, Université Paris-Sud]. https://theses.hal.science/tel-04163504

Gamboa, F., & Gassiat, E. (1997). Bayesian methods and maximum entropy for ill-posed inverse problems. *The Annals of Statistics*, *25*(1), 328–350. https://doi.org/10.1214/aos/1034276632

Garcia, K. E., Wang, X., & Kroenke, C. D. (2021). A model of tension-induced fiber growth predicts white matter organization during brain folding. *Nature Communications*, *12*(1), 6681. https://doi.org/10.1038/s41467-021-26971-9

Garcia-Hernandez, R., Cerdán Cerdá, A., Trouve Carpena, A., Drakesmith, M., Koller, K., Jones, D. K., Canals, S., & De Santis, S. (2022). Mapping microglia and astrocyte activation in vivo using diffusion MRI. *Science Advances*, *8*(21). https://doi.org/10.1126/sciadv.abq2923

Garnier, A., Vidal, A., & Benali, H. (2016). A Theoretical Study on the Role of Astrocytic Activity in Neuronal Hyperexcitability by a Novel Neuron-Glia Mass Model. *The Journal of Mathematical Neuroscience*, *6*(1), 10. https://doi.org/10.1186/s13408-016-0042-0

Garnier, A., Vidal, A., Huneau, C., & Benali, H. (2015). A Neural Mass Model with Direct and Indirect Excitatory Feedback Loops: Identification of Bifurcations and Temporal Dynamics. *Neural Computation*, *27*(2), 329–364. https://doi.org/10.1162/NECO_a_00696

Gautam, P., Anstey, K. J., Wen, W., Sachdev, P. S., & Cherbuin, N. (2015). Cortical gyrification and its relationships with cortical volume, cortical thickness, and cognitive performance in healthy mid-life adults. *Behavioural Brain Research*, *287*, 331–339. https://doi.org/10.1016/j.bbr.2015.03.018

Ghavasieh, A., & Domenico, M. De. (2021). *Multiscale Information Propagation in Emergent Functional Networks*. *June*, 1–11. https://doi.org/10.20944/preprints202106.0668.v1

Giaume, C., Koulakoff, A., Roux, L., Holcman, D., & Rouach, N. (2010). Astroglial networks: A step further in neuroglial and gliovascular interactions. *Nature Reviews Neuroscience*, *11*(2), 87–99. https://doi.org/10.1038/nrn2757

Giffin, A., & Caticha, A. (2007). Updating Probabilities with Data and Moments. *AIP Conference Proceedings*, *954*, 74–84. https://doi.org/10.1063/1.2821302

Gilarranz, L. J., Rayfield, B., Liñán-Cembrano, G., Bascompte, J., & Gonzalez, A. (2017). Effects of network modularity on the spread of perturbation impact in experimental metapopulations. *Science*, *357*(6347), 199–201. https://doi.org/10.1126/science.aal4122

Glasser, M. F., Sotiropoulos, S. N., Wilson, J. A., Coalson, T. S., Fischl, B., Andersson, J. L., Xu, J., Jbabdi, S., Webster, M., Polimeni, J. R., Van Essen, D. C., & Jenkinson, M. (2013). The minimal preprocessing pipelines for the Human Connectome Project. *NeuroImage*, *80*, 105–124. https://doi.org/10.1016/j.neuroimage.2013.04.127

Goldberg, M., De Pittà, M., Volman, V., Berry, H., & Ben-Jacob, E. (2010). Nonlinear Gap Junctions Enable Long-Distance Propagation of Pulsating Calcium Waves in Astrocyte Networks. *PLoS Computational Biology*, *6*(8), e1000909. https://doi.org/10.1371/journal.pcbi.1000909

Gonzalez-Moreira, E., Paz-Linares, D., Areces-Gonzalez, A., Wang, R., Bosch-Bayard, J., Bringas-Vega, M. L., & Valdes-Sosa, P. A. (2018). *Caulking the Leakage Effect in MEEG Source Connectivity Analysis*. *September*. https://doi.org/10.48550/arXiv.1810.00786

Gonzalez-Moreira, E., Paz-Linares, D., Areces-Gonzalez, A., Wang, R., & Valdes-Sosa, P. A. (2018). Third Generation MEEG Source Connectivity Analysis Toolbox (BC-VARETA 1.0) and Validation Benchmark. *ArXiv*. http://arxiv.org/abs/1810.11212

Gonzalez-Moreira, E., Paz-Linares, D., Martinez-Montes, E., Valdes-Hernandez, P., Bosch-Bayard, J., Bringas-Vega, M. L., & Valdés-Sosa, P. (2018). Populational Super-Resolution Sparse M/EEG Sources and Connectivity Estimation. *BioRxiv*, 1–2. https://doi.org/10.1101/346569

González-Narváez, M., Fernández-Gómez, M. J., Mendes, S., Molina, J.-L., Ruiz-Barzola, O., & Galindo-Villardón, P. (2021). Study of Temporal Variations in Species–Environment Association through an Innovative Multivariate Method: MixSTATICO. *Sustainability*, *13*(11), 5924. https://doi.org/10.3390/su13115924

Gramfort, A., Luessi, M., Larson, E., Engemann, D. A., Strohmeier, D., Brodbeck, C., Goj, R., Jas, M., Brooks, T., Parkkonen, L., & Hämäläinen, M. (2013). MEG and EEG data analysis with MNE-Python. *Frontiers in Neuroscience*, *7*(7 DEC), 1–13. https://doi.org/10.3389/fnins.2013.00267

Gramfort, A., Papadopoulo, T., Olivi, E., & Clerc, M. (2010). OpenMEEG: opensource software for quasistatic bioelectromagnetics. *BioMedical Engineering OnLine*, *9*(1), 45. https://doi.org/10.1186/1475-925X-9-45

Gregory, M. D., Kippenhan, J. S., Dickinson, D., Carrasco, J., Mattay, V. S., Weinberger, D. R., & Berman, K. F. (2016). Regional Variations in Brain Gyrification Are Associated with General Cognitive Ability in Humans. *Current Biology*, *26*(10), 1301–1305. https://doi.org/10.1016/j.cub.2016.03.021

Griffiths, J. D., Bastiaens, S. P., & Kaboodvand, N. (2022). Whole-Brain Modelling: Past, Present, and Future. In *Advances in Experimental Medicine and Biology* (Vol. 1359, pp. 313–355). https://doi.org/10.1007/978-3-030-89439-9_13

Grisot, G., Haber, S. N., & Yendiki, A. (2021). Diffusion MRI and anatomic tracing in the same brain reveal common failure modes of tractography. *NeuroImage*, *239*(April), 118300. https://doi.org/10.1016/j.neuroimage.2021.118300

Gross, J. (2019). Magnetoencephalography in Cognitive Neuroscience: A Primer. *Neuron*, *104*(2), 189–204. https://doi.org/10.1016/j.neuron.2019.07.001

Guerriero, R. M., Giza, C. C., & Rotenberg, A. (2015). Glutamate and GABA imbalance following traumatic brain injury. *Current Neurology and Neuroscience Reports*, *15*(5), 27. https://doi.org/10.1007/s11910-015-0545-1

Hagmann, P., Jonasson, L., Maeder, P., Thiran, J.-P., Wedeen, V. J., & Meuli, R. (2006). Understanding Diffusion MR Imaging Techniques: From Scalar Diffusion-weighted Imaging to Diffusion Tensor Imaging and Beyond. *RadioGraphics*, *26*(suppl_1), S205–S223. https://doi.org/10.1148/rg.26si065510

Haim, L. Ben, Carrillo-de Sauvage, M. A., Ceyzériat, K., & Escartin, C. (2015). Elusive roles for reactive astrocytes in neurodegenerative diseases. *Frontiers in Cellular Neuroscience*, *9*(AUGUST), 1–27. https://doi.org/10.3389/fncel.2015.00278

Hallett, M., de Haan, W., Deco, G., Dengler, R., Di Iorio, R., Gallea, C., Gerloff, C., Grefkes, C., Helmich, R. C., Kringelbach, M. L., Miraglia, F., Rektor, I., Strýček, O., Vecchio, F., Volz, L. J., Wu, T., & Rossini, P. M. (2020). Human brain connectivity: Clinical applications for

clinical neurophysiology. *Clinical Neurophysiology*, *131*(7), 1621–1651. https://doi.org/10.1016/j.clinph.2020.03.031

Hämäläinen, M., Hari, R., Ilmoniemi, R. J., Knuutila, J., & Lounasmaa, O. V. (1993). Magnetoencephalography—theory, instrumentation, and applications to noninvasive studies of the working human brain. *Reviews of Modern Physics*, *65*(2), 413–497. https://doi.org/10.1103/RevModPhys.65.413

Hämäläinen, M. S., & Ilmoniemi, R. J. (1994). Interpreting magnetic fields of the brain: minimum norm estimates. *Medical & Biological Engineering & Computing*, *32*(1), 35–42. https://doi.org/10.1007/BF02512476

Han, X., Cao, S., Shen, Z., Zhang, B., Wang, W. X., Cressman, R., & Stanley, H. E. (2017). Emergence of communities and diversity in social networks. *Proceedings of the National Academy of Sciences of the United States of America*, *114*(11), 2887–2891. https://doi.org/10.1073/pnas.1608164114

Hansen, J. Y., Shafiei, G., Markello, R. D., Smart, K., Cox, S. M. L., Nørgaard, M., Beliveau, V., Wu, Y., Gallezot, J. D., Aumont, É., Servaes, S., Scala, S. G., DuBois, J. M., Wainstein, G., Bezgin, G., Funck, T., Schmitz, T. W., Spreng, R. N., Galovic, M., … Misic, B. (2022). Mapping neurotransmitter systems to the structural and functional organization of the human neocortex. *Nature Neuroscience*, *25*(11), 1569–1581. https://doi.org/10.1038/s41593-022-01186-3

Hansen, P. C. (1992). Analysis of Discrete Ill-Posed Problems by Means of the L-Curve. *SIAM Review*, *34*(4), 561–580. https://doi.org/10.1137/1034115

Hartmann, D. A., Berthiaume, A.-A., Grant, R. I., Harrill, S. A., Koski, T., Tieu, T., McDowell, K. P., Faino, A. V., Kelly, A. L., & Shih, A. Y. (2021). Brain capillary pericytes exert a substantial but slow influence on blood flow. *Nature Neuroscience*, *24*(5), 633–645. https://doi.org/10.1038/s41593-020-00793-2

Hassan, M., Dufor, O., Merlet, I., Berrou, C., & Wendling, F. (2014). EEG Source Connectivity Analysis: From Dense Array Recordings to Brain Networks. *PLoS ONE*, *9*(8), e105041. https://doi.org/10.1371/journal.pone.0105041

Hassan, M., Merlet, I., Mheich, A., Kabbara, A., Biraben, A., Nica, A., & Wendling, F. (2017). Identification of Interictal Epileptic Networks from Dense-EEG. *Brain Topography*, *30*(1), 60–76. https://doi.org/10.1007/s10548-016-0517-z

Hauk, O., Stenroos, M., & Treder, M. S. (2022). Towards an objective evaluation of EEG/MEG source estimation methods – The linear approach. *NeuroImage*, *255*(April), 119177. https://doi.org/10.1016/j.neuroimage.2022.119177

He, B., Sohrabpour, A., Brown, E., & Liu, Z. (2018). Electrophysiological Source Imaging: A Noninvasive Window to Brain Dynamics. *Annual Review of Biomedical Engineering*, *20*, 171–196. https://doi.org/10.1146/annurev-bioeng-062117-120853

He, J., & Kolovos, A. (2018). Bayesian maximum entropy approach and its applications: a review. *Stochastic Environmental Research and Risk Assessment*, *32*(4), 859–877. https://doi.org/10.1007/s00477-017-1419-7

Heitmann, S., & Breakspear, M. (2018). Putting the “dynamic” back into dynamic functional connectivity. *Network Neuroscience*, *2*(2), 150–174. https://doi.org/10.1162/netn_a_00041

Hincapié, A. S., Kujala, J., Mattout, J., Daligault, S., Delpuech, C., Mery, D., Cosmelli, D., & Jerbi, K. (2016). MEG connectivity and power detections with minimum norm estimates require different regularization parameters. *Computational Intelligence and Neuroscience*, *2016*, 12–18. https://doi.org/10.1155/2016/3979547

Hincapié, A.-S., Kujala, J., Mattout, J., Pascarella, A., Daligault, S., Delpuech, C., Mery, D., Cosmelli, D., & Jerbi, K. (2017). The impact of MEG source reconstruction method on source-space connectivity estimation: A comparison between minimum-norm solution and beamforming. *NeuroImage*, *156*(May), 29–42. https://doi.org/10.1016/j.neuroimage.2017.04.038

Hipp, J. F., Hawellek, D. J., Corbetta, M., Siegel, M., & Engel, A. K. (2012). Large-scale cortical correlation structure of spontaneous oscillatory activity. *Nature Neuroscience*, *15*(6), 884–890. https://doi.org/10.1038/nn.3101

Hori, T., & Takahashi, T. (2012). Kinetics of Synaptic Vesicle Refilling with Neurotransmitter Glutamate. *Neuron*, *76*(3), 511–517. https://doi.org/10.1016/j.neuron.2012.08.013

Hösli, L., Zuend, M., Bredell, G., Zanker, H. S., Porto de Oliveira, C. E., Saab, A. S., & Weber, B. (2022). Direct vascular contact is a hallmark of cerebral astrocytes. *Cell Reports*, *39*(1), 110599. https://doi.org/10.1016/j.celrep.2022.110599

Huang, X., Chen, D., Ren, T., & Wang, D. (2021). A survey of community detection methods in multilayer networks. In *Data Mining and Knowledge Discovery* (Vol. 35, Issue 1). Springer US. https://doi.org/10.1007/s10618-020-00716-6

Hutt, A. (2015). Neural Field Model, Continuum. In *Encyclopedia of Computational Neuroscience* (pp. 1888–1895). Springer New York. https://doi.org/10.1007/978-1-4614-6675-8_67

Iadecola, C. (2017). The Neurovascular Unit Coming of Age: A Journey through Neurovascular Coupling in Health and Disease. *Neuron*, *96*(1), 17–42. https://doi.org/10.1016/j.neuron.2017.07.030

Interdonato, R., Tagarelli, A., Ienco, D., Sallaberry, A., & Poncelet, P. (2017). Local community detection in multilayer networks. In *Data Mining and Knowledge Discovery* (Vol. 31, Issue 5). Springer US. https://doi.org/10.1007/s10618-017-0525-y

Iturria-Medina, Y., Carbonell, F. M., Sotero, R. C., Chouinard-Decorte, F., & Evans, A. C. (2017). Multifactorial causal model of brain (dis)organization and therapeutic intervention: Application to Alzheimer’s disease. *NeuroImage*, *152*(February), 60–77. https://doi.org/10.1016/j.neuroimage.2017.02.058

Izhikevich, E. (2007). Equilibrium. *Scholarpedia*, *2*(10), 2014. https://doi.org/10.4249/scholarpedia.2014

J. Rodríguez, J., M. Butt, A., Gardenal, E., Parpura, V., & Verkhratsky, A. (2016). Complex and Differential Glial Responses in Alzheimers Disease and Ageing. *Current Alzheimer Research*, *13*(4), 343–358. https://doi.org/10.2174/1567205013666160229112911

Jansen, B. H., & Rit, V. G. (1995). Electroencephalogram and visual evoked potential generation in a mathematical model of coupled cortical columns. *Biological Cybernetics*, *73*(4), 357–366. https://doi.org/10.1007/BF00199471

Jaynes, E. (1968). Prior Probabilities. *IEEE Transactions on Systems Science and Cybernetics*, *4*(3), 227–241. https://doi.org/10.1109/TSSC.1968.300117

Jaynes, E. T. (1988). The Relation of Bayesian and Maximum Entropy Methods. In *Maximum-Entropy and Bayesian Methods in Science and Engineering* (Vol. 1, pp. 25–29). Springer Netherlands. https://doi.org/10.1007/978-94-009-3049-0_2

Jizba, P., & Korbel, J. (2019). Maximum Entropy Principle in Statistical Inference: Case for Non-Shannonian Entropies. *Physical Review Letters*, *122*(12), 120601. https://doi.org/10.1103/PhysRevLett.122.120601

Jolivet, R., Coggan, J. S., Allaman, I., & Magistretti, P. J. (2015). Multi-timescale Modeling of Activity-Dependent Metabolic Coupling in the Neuron-Glia-Vasculature Ensemble. *PLoS Computational Biology*, *11*(2), 1–23. https://doi.org/10.1371/journal.pcbi.1004036

Kahlson, M. A., & Colodner, K. J. (2015). Glial Tau Pathology in Tauopathies: Functional Consequences. *Journal of Experimental Neuroscience*, *9s2*, JEN.S25515. https://doi.org/10.4137/JEN.S25515

Kalucka, J., de Rooij, L. P. M. H., Goveia, J., Rohlenova, K., Dumas, S. J., Meta, E., Conchinha, N. V., Taverna, F., Teuwen, L.-A., Veys, K., García-Caballero, M., Khan, S., Geldhof, V., Sokol, L., Chen, R., Treps, L., Borri, M., de Zeeuw, P., Dubois, C., … Carmeliet, P. (2020). Single-Cell Transcriptome Atlas of Murine Endothelial Cells. *Cell*, *180*(4), 764-779.e20. https://doi.org/10.1016/j.cell.2020.01.015

Kastanenka, K. V., Moreno-Bote, R., De Pittà, M., Perea, G., Eraso-Pichot, A., Masgrau, R., Poskanzer, K. E., & Galea, E. (2020). A roadmap to integrate astrocytes into Systems Neuroscience. *Glia*, *68*(1), 5–26. https://doi.org/10.1002/glia.23632

Katz, P. (Ed.). (1999). *Beyond Neurotransmission: Neuromodulation and its Importance for Information Processing*. Oxford University Press. https://doi.org/10.1093/acprof:oso/9780198524243.001.0001

Kilpatrick, Z. P. (2015). Wilson-Cowan Model. In *Encyclopedia of Computational Neuroscience* (pp. 3159–3163). Springer New York. https://doi.org/10.1007/978-1-4614-6675-8_80

Kivela, M., Arenas, A., Barthelemy, M., Gleeson, J. P., Moreno, Y., & Porter, M. A. (2014). Multilayer networks. *Journal of Complex Networks*, *2*(3), 203–271. https://doi.org/10.1093/comnet/cnu016

Kiyoshi, C., & Zhou, M. (2019). Astrocyte syncytium: a functional reticular system in the brain. *Neural Regeneration Research*, *14*(4), 595. https://doi.org/10.4103/1673-5374.247462

Kondziella, D. (2017). The Top 5 Neurotransmitters from a Clinical Neurologist's Perspective. *Neurochemical Research*, *42*(6), 1767–1771. https://doi.org/10.1007/s11064-016-2101-z

Kotyrba, M. (2015). Influence of changes in initial conditions for the simulation of dynamic systems. *AIP Conference Proceedings*, *1648*, 550003. https://doi.org/10.1063/1.4912758

Koutsoyiannis, D., & Sargentis, G. F. (2021). Entropy and wealth. *Entropy*, *23*(10). https://doi.org/10.3390/e23101356

Kringelbach, M. L., Cruzat, J., Cabral, J., Knudsen, G. M., Carhart-Harris, R., Whybrow, P. C., Logothetis, N. K., & Deco, G. (2020). Dynamic coupling of whole-brain neuronal and neurotransmitter systems. *Proceedings of the National Academy of Sciences of the United States of America*, *117*(17), 9566–9576. https://doi.org/10.1073/pnas.1921475117

Kugler, E. C., Greenwood, J., & MacDonald, R. B. (2021). The "Neuro-Glial-Vascular" Unit: The Role of Glia in Neurovascular Unit Formation and Dysfunction. *Frontiers in Cell and Developmental Biology*, *9*. https://doi.org/10.3389/fcell.2021.732820

Kybic, J., Clerc, M., Abboud, T., Faugeras, O., Keriven, R., & Papadopoulo, T. (2005). A common formalism for the Integral formulations of the forward EEG problem. *IEEE Transactions on Medical Imaging*, *24*(1), 12–28. https://doi.org/10.1109/TMI.2004.837363

Lago-Baldaia, I., Fernandes, V. M., & Ackerman, S. D. (2020). More Than Mortar: Glia as Architects of Nervous System Development and Disease. *Frontiers in Cell and Developmental Biology*, *8*(December), 1–26. https://doi.org/10.3389/fcell.2020.611269

Lallouette, J., De Pittà, M., & Berry, H. (2019). *Astrocyte Networks and Intercellular Calcium Propagation* (pp. 177–210). Springer International Publishing. https://doi.org/10.1007/978-3-030-00817-8_7

Larson-Prior, L. J., Oostenveld, R., Della Penna, S., Michalareas, G., Prior, F., Babajani-Feremi, A., Schoffelen, J.-M., Marzetti, L., de Pasquale, F., Di Pompeo, F., Stout, J., Woolrich, M., Luo, Q., Bucholz, R., Fries, P., Pizzella, V., Romani, G. L., Corbetta, M., & Snyder, A. Z. (2013). Adding dynamics to the Human Connectome Project with MEG. *NeuroImage*, *80*, 190–201. https://doi.org/10.1016/j.neuroimage.2013.05.056

Lawn, T., Howard, M. A., Turkheimer, F., Misic, B., Deco, G., Martins, D., & Dipasquale, O. (2023). From neurotransmitters to networks: Transcending organisational hierarchies with molecular-informed functional imaging. *Neuroscience and Biobehavioral Reviews*, *150*(April), 105193. https://doi.org/10.1016/j.neubiorev.2023.105193

Le Bihan, D. (2014). Diffusion MRI: What water tells us about the brain. *EMBO Molecular Medicine*, *6*(5), 569–573. https://doi.org/10.1002/emmm.201404055

Le Bihan, D., Breton, E., Lallemand, D., Grenier, P., Cabanis, E., & Laval-Jeantet, M. (1986). MR imaging of intravoxel incoherent motions: application to diffusion and perfusion in neurologic disorders. *Radiology*, *161*(2), 401–407. https://doi.org/10.1148/radiology.161.2.3763909

Le Bihan, D., & Iima, M. (2015). Diffusion Magnetic Resonance Imaging: What Water Tells Us about Biological Tissues. *PLOS Biology*, *13*(7), e1002203. https://doi.org/10.1371/journal.pbio.1002203

Le Bihan, D., & Johansen-Berg, H. (2012). Diffusion MRI at 25: Exploring brain tissue structure and function. *NeuroImage*, *61*(2), 324–341. https://doi.org/10.1016/j.neuroimage.2011.11.006

Le Bihan, D., Poupon, C., Amadon, A., & Lethimonnier, F. (2006). Artifacts and pitfalls in diffusion MRI. *Journal of Magnetic Resonance Imaging*, *24*(3), 478–488. https://doi.org/10.1002/jmri.20683

Lea-Carnall, C. A., El-Deredy, W., Stagg, C. J., Williams, S. R., & Trujillo-Barreto, N. J. (2023). A mean-field model of glutamate and GABA synaptic dynamics for functional MRS. *NeuroImage*, *266*(December 2022), 119813. https://doi.org/10.1016/j.neuroimage.2022.119813

Liddelow, S. A., & Barres, B. A. (2017). Reactive Astrocytes: Production, Function, and Therapeutic Potential. *Immunity*, *46*(6), 957–967. https://doi.org/10.1016/j.immuni.2017.06.006

Liddelow, S. A., & Sofroniew, M. V. (2019). Astrocytes usurp neurons as a disease focus. *Nature Neuroscience*, *22*(4), 512–513. https://doi.org/10.1038/s41593-019-0367-6

Liley, D. T. J. (2015). Neural Population Model. In D. Jaeger & R. Jung (Eds.), *Encyclopedia of Computational Neuroscience* (pp. 1898–1912). Springer New York. https://doi.org/10.1007/978-1-4614-6675-8_69

Liley, D. T. J., Bojak, I., Dafilis, M. P., van Veen, L., Frascoli, F., & Foster, B. L. (2010). Bifurcations and state changes in the human alpha rhythm: Theory and experiment. In *Modeling Phase Transitions in the Brain* (pp. 117–145). Springer New York. https://doi.org/10.1007/978-1-4419-0796-7_6

Liley, D. T. J., Cadusch, P. J., & Dafilis, M. P. (2002). A spatially continuous mean field theory of electrocortical activity. *Network: Computation in Neural Systems*, *13*(1), 67–113. https://doi.org/10.1088/0954-898X/13/1/303

Liley, D. T. J., Foster, B. L., & Bojak, I. (2012). Co-operative Populations of Neurons: Mean Field Models of Mesoscopic Brain Activity. In *Computational Systems Neurobiology* (pp. 317–364). Springer Netherlands. https://doi.org/10.1007/978-94-007-3858-4_11

Lin, F.-H., Witzel, T., Ahlfors, S. P., Stufflebeam, S. M., Belliveau, J. W., & Hämäläinen, M. S. (2006). Assessing and improving the spatial accuracy in MEG source localization by depth-weighted minimum-norm estimates. *NeuroImage*, *31*(1), 160–171. https://doi.org/10.1016/j.neuroimage.2005.11.054

Lina, J. M., Chowdhury, R., Lemay, E., Kobayashi, E., & Grova, C. (2014). Wavelet-based localization of oscillatory sources from magnetoencephalography data. *IEEE Transactions on Biomedical Engineering*, *61*(8), 2350–2364. https://doi.org/10.1109/TBME.2012.2189883

Liu, B., Teschemacher, A. G., & Kasparov, S. (2017). Astroglia as a cellular target for neuroprotection and treatment of neuro-psychiatric disorders. *Glia*, *65*(8), 1205–1226. https://doi.org/10.1002/glia.23136

Liu, C.-C., Kanekiyo, T., Xu, H., & Bu, G. (2013). Apolipoprotein E and Alzheimer disease: risk, mechanisms and therapy. *Nature Reviews Neurology*, *9*(2), 106–118. https://doi.org/10.1038/nrneurol.2012.263

Liu, Z.-Q., Shafiei, G., Baillet, S., & Misic, B. (2023). Spatially heterogeneous structure-function coupling in haemodynamic and electromagnetic brain networks. *NeuroImage*, *278*(July), 120276. https://doi.org/10.1016/j.neuroimage.2023.120276

Liuzzi, L., Quinn, A. J., O'Neill, G. C., Woolrich, M. W., Brookes, M. J., Hillebrand, A., & Tewarie, P. (2019). How sensitive are conventional MEG functional connectivity metrics with sliding windows to detect genuine fluctuations in dynamic functional connectivity? *Frontiers in Neuroscience*, *13*(JUL), 1–16. https://doi.org/10.3389/fnins.2019.00797

Llinares-Benadero, C., & Borrell, V. (2019). Deconstructing cortical folding: genetic, cellular and mechanical determinants. *Nature Reviews Neuroscience*, *20*(3), 161–176. https://doi.org/10.1038/s41583-018-0112-2

Logothetis, N. K., Pauls, J., Augath, M., Trinath, T., & Oeltermann, A. (2001). Neurophysiological investigation of the basis of the fMRI signal. *Nature*, *412*(6843), 150–157. https://doi.org/10.1038/35084005

Lopes da Silva, F. (2013). EEG and MEG: Relevance to Neuroscience. *Neuron*, *80*(5), 1112–1128. https://doi.org/10.1016/j.neuron.2013.10.017

Lopes da Silva, F. (2022). EEG: Origin and Measurement. In *EEG - fMRI* (pp. 23–48). Springer International Publishing. https://doi.org/10.1007/978-3-031-07121-8_2

Lopes da Silva, F. H., Hoeks, A., Smits, H., & Zetterberg, L. H. (1974). Model of brain rhythmic activity: the alpha-rhythm of the thalamus. *Kybernetik*, *15*(1), 27–37. https://doi.org/10.1007/BF00270757

Lopes da Silva, F. H., van Rotterdam, A., Barts, P., van Heusden, E., & Burr, W. (1976). Models of Neuronal Populations: The Basic Mechanisms of Rhythmicity. In *Progress in Brain Research* (Vol. 45, Issue C, pp. 281–308). https://doi.org/10.1016/S0079-6123(08)60995-4

LoPresti, P. (2018). Tau in Oligodendrocytes Takes Neurons in Sickness and in Health. *International Journal of Molecular Sciences*, *19*(8), 2408. https://doi.org/10.3390/ijms19082408

Lu, H., Jaime, S., & Yang, Y. (2019). Origins of the Resting-State Functional MRI Signal: Potential Limitations of the "Neurocentric" Model. *Frontiers in Neuroscience*, *13*(October), 1–8. https://doi.org/10.3389/fnins.2019.01136

Macvicar, B. A., & Newman, E. A. (2015). Astrocyte regulation of blood flow in the brain. *Cold Spring Harbor Perspectives in Biology*, *7*(5), 1–15. https://doi.org/10.1101/cshperspect.a020388

Magistretti, P. J., & Allaman, I. (2015). A Cellular Perspective on Brain Energy Metabolism and Functional Imaging. *Neuron*, *86*(4), 883–901. https://doi.org/10.1016/j.neuron.2015.03.035

Mahjoory, K., Nikulin, V. V., Botrel, L., Linkenkaer-Hansen, K., Fato, M. M., & Haufe, S. (2017). Consistency of EEG source localization and connectivity estimates. *NeuroImage*, *152*(February), 590–601. https://doi.org/10.1016/j.neuroimage.2017.02.076

Maier-Hein, K. H., Neher, P. F., Houde, J.-C., Côté, M.-A., Garyfallidis, E., Zhong, J., Chamberland, M., Yeh, F.-C., Lin, Y.-C., Ji, Q., Reddick, W. E., Glass, J. O., Chen, D. Q.,

Feng, Y., Gao, C., Wu, Y., Ma, J., He, R., Li, Q., … Descoteaux, M. (2017). The challenge of mapping the human connectome based on diffusion tractography. *Nature Communications*, *8*(1), 1349. https://doi.org/10.1038/s41467-017-01285-x

Maitre, M., Jeltsch-David, H., Okechukwu, N. G., Klein, C., Patte-Mensah, C., & Mensah-Nyagan, A.-G. (2023). Myelin in Alzheimer's disease: culprit or bystander? *Acta Neuropathologica Communications*, *11*(1), 56. https://doi.org/10.1186/s40478-023-01554-5

Mandke, K., Meier, J., Brookes, M. J., O'Dea, R. D., Van Mieghem, P., Stam, C. J., Hillebrand, A., & Tewarie, P. (2018). Comparing multilayer brain networks between groups: Introducing graph metrics and recommendations. *NeuroImage*, *166*(November 2017), 371–384. https://doi.org/10.1016/j.neuroimage.2017.11.016

Manninen, T., Havela, R., & Linne, M.-L. (2019). *Computational Models of Astrocytes and Astrocyte–Neuron Interactions: Characterization, Reproducibility, and Future Perspectives*. Springer International Publishing. https://doi.org/10.1007/978-3-030-00817-8_16

Mansouri, S., Alharbi, Y., Haddad, F., Chabcoub, S., Alshrouf, A., & Abd-Elghany, A. A. (2021). Electrical Impedance tomography – recent applications and developments. *Journal of Electrical Bioimpedance*, *12*(1), 50–62. https://doi.org/10.2478/joeb-2021-0007

Marder, E. (2012). Neuromodulation of Neuronal Circuits: Back to the Future. *Neuron*, *76*(1), 1–11. https://doi.org/10.1016/j.neuron.2012.09.010

Marrelec, G., Bellec, P., Krainik, A., Duffau, H., Pélégrini-Issac, M., Lehéricy, S., Benali, H., & Doyon, J. (2008). Regions, systems, and the brain: Hierarchical measures of functional integration in fMRI. *Medical Image Analysis*, *12*(4), 484–496. https://doi.org/10.1016/j.media.2008.02.002

Martínez-Cancino, R., & Sotero Diaz, R. C. (2011). Dynamical Mean Field approximation of a canonical cortical model for studying inter-population synchrony. *Nature Precedings*, 1–15. https://doi.org/10.1038/npre.2011.5583.1

MATLAB. (2022). *Version 9.12.0 (R2022a)*. Natick, Massachusetts: The MathWorks Inc.

Mattson, M. P., & Arumugam, T. V. (2018). Hallmarks of Brain Aging: Adaptive and Pathological Modification by Metabolic States. *Cell Metabolism*, *27*(6), 1176–1199. https://doi.org/10.1016/j.cmet.2018.05.011

Matute, C., Domercq, M., & Sánchez-Gómez, M. (2006). Glutamate-mediated glial injury: Mechanisms and clinical importance. *Glia*, *53*(2), 212–224. https://doi.org/10.1002/glia.20275

McCann, H., Pisano, G., & Beltrachini, L. (2019). Variation in Reported Human Head Tissue Electrical Conductivity Values. *Brain Topography*, *32*(5), 825–858. https://doi.org/10.1007/s10548-019-00710-2

McCulloch, W. S., & Pitts, W. (1943). A logical calculus of the ideas immanent in nervous activity. *The Bulletin of Mathematical Biophysics*, *5*(4), 115–133. https://doi.org/10.1007/BF02478259

Meldrum, B. S. (2000). Glutamate as a Neurotransmitter in the Brain: Review of Physiology and Pathology. *The Journal of Nutrition*, *130*(4), 1007S-1015S. https://doi.org/10.1093/jn/130.4.1007S

Melozzi, F., Woodman, M. M., Jirsa, V. K., & Bernard, C. (2017). The virtual mouse brain: A computational neuroinformatics platform to study whole mouse brain dynamics. *ENeuro*, *4*(3), 1–14. https://doi.org/10.1523/ENEURO.0111-17.2017

Mendler, M., Falk, J., & Drossel, B. (2018). Analysis of stochastic bifurcations with phase portraits. *PLoS ONE*, *13*(4), 1–20. https://doi.org/10.1371/journal.pone.0196126

Mesmoudi, S., Perlbarg, V., Rudrauf, D., Messe, A., Pinsard, B., Hasboun, D., Cioli, C., Marrelec, G., Toro, R., Benali, H., & Burnod, Y. (2013). Resting State Networks' Corticotopy: The Dual Intertwined Rings Architecture. *PLoS ONE*, *8*(7), e67444. https://doi.org/10.1371/journal.pone.0067444

Messé, A. (2020). Parcellation influence on the connectivity-based structure–function relationship in the human brain. *Human Brain Mapping*, *41*(5), 1167–1180. https://doi.org/10.1002/hbm.24866

Messé, A., Rudrauf, D., Benali, H., & Marrelec, G. (2014). Relating Structure and Function in the Human Brain: Relative Contributions of Anatomy, Stationary Dynamics, and Non-stationarities. *PLoS Computational Biology*, *10*(3), e1003530. https://doi.org/10.1371/journal.pcbi.1003530

Meunier, D., Pascarella, A., Altukhov, D., Jas, M., Combrisson, E., Lajnef, T., Bertrand-Dubois, D., Hadid, V., Alamian, G., Alves, J., Barlaam, F., Saive, A. L., Dehgan, A., & Jerbi, K. (2020). NeuroPycon: An open-source python toolbox for fast multi-modal and reproducible brain connectivity pipelines. *NeuroImage*, *219*(June). https://doi.org/10.1016/j.neuroimage.2020.117020

Mohammad-Djafari, A. (2006). Maximum Entropy and Bayesian inference: Where do we stand and where do we go? *AIP Conference Proceedings*, *872*, 3–14. https://doi.org/10.1063/1.2423255

Mohammad-Djafari, A. (2015). Entropy, Information Theory, Information Geometry and Bayesian Inference in Data, Signal and Image Processing and Inverse Problems. *Entropy*, *17*(6), 3989–4027. https://doi.org/10.3390/e17063989

Morales, E. C., Villar, Y. R. C., Cardona, H. F. T., Acosta, C. D., & Dominguez, G. C. (2018). Influence of Realistic Head Modeling on EEG Forward Problem. In *Lecture Notes in Computer Science (including subseries Lecture Notes in Artificial Intelligence and Lecture Notes in Bioinformatics): Vol. 11309 LNAI* (pp. 32–40). https://doi.org/10.1007/978-3-030-05587-5_4

Moran, R. J., Kiebel, S. J., Stephan, K. E., Reilly, R. B., Daunizeau, J., & Friston, K. J. (2007). A neural mass model of spectral responses in electrophysiology. *NeuroImage*, *37*(3), 706–720. https://doi.org/10.1016/j.neuroimage.2007.05.032

Mori, S., Crain, B. J., Chacko, V. P., & Van Zijl, P. C. M. (1999). Three-dimensional tracking of axonal projections in the brain by magnetic resonance imaging. *Annals of Neurology*, *45*(2), 265–269. https://doi.org/10.1002/1531-8249(199902)45:2<265::AID-ANA21>3.0.CO;2-3

Morrens, J., Van Den Broeck, W., & Kempermann, G. (2012). Glial cells in adult neurogenesis. *Glia*, *60*(2), 159–174. https://doi.org/10.1002/glia.21247

Morris, R. G. M. (2013). NMDA receptors and memory encoding. *Neuropharmacology*, *74*, 32–40. https://doi.org/10.1016/j.neuropharm.2013.04.014

Mota, B., Dos Santos, S. E., Ventura-Antunes, L., Jardim-Messeder, D., Neves, K., Kazu, R. S., Noctor, S., Lambert, K., Bertelsen, M. F., Manger, P. R., Sherwood, C. C., Kaas, J. H., & Herculano-Houzel, S. (2019). White matter volume and white/gray matter ratio in mammalian species as a consequence of the universal scaling of cortical folding. *Proceedings of the National Academy of Sciences*, *116*(30), 15253–15261. https://doi.org/10.1073/pnas.1716956116

Mucha, P. J., Richardson, T., Macon, K., Porter, M. A., & Onnela, J. P. (2010). Community structure in time-dependent, multiscale, and multiplex networks. *Science*, *328*(5980), 876–878. https://doi.org/10.1126/science.1184819

Muñoz-Cobo, J.-L., Mendizábal, R., Miquel, A., Berna, C., & Escrivá, A. (2017). Use of the Principles of Maximum Entropy and Maximum Relative Entropy for the Determination of Uncertain Parameter Distributions in Engineering Applications. *Entropy*, *19*(9), 486. https://doi.org/10.3390/e19090486

Næss, S., Halnes, G., Hagen, E., Hagler, D. J., Dale, A. M., Einevoll, G. T., & Ness, T. V. (2021). Biophysically detailed forward modeling of the neural origin of EEG and MEG signals. *NeuroImage*, *225*(September 2020), 117467. https://doi.org/10.1016/j.neuroimage.2020.117467

Nagy, J. I., Pereda, A. E., & Rash, J. E. (2018). Electrical synapses in mammalian CNS: Past eras, present focus and future directions. *Biochimica et Biophysica Acta (BBA) - Biomembranes*, *1860*(1), 102–123. https://doi.org/10.1016/j.bbamem.2017.05.019

Nedergaard, M., Ransom, B., & Goldman, S. A. (2003). New roles for astrocytes: Redefining the functional architecture of the brain. *Trends in Neurosciences*, *26*(10), 523–530. https://doi.org/10.1016/j.tins.2003.08.008

Nelson, A. R., Sweeney, M. D., Sagare, A. P., & Zlokovic, B. V. (2016). Neurovascular dysfunction and neurodegeneration in dementia and Alzheimer's disease. *Biochimica et Biophysica Acta (BBA) - Molecular Basis of Disease*, *1862*(5), 887–900. https://doi.org/10.1016/J.BBADIS.2015.12.016

Neuman, M., Jonsson, V., Calatayud, J., & Rosvall, M. (2022). Cross-validation of correlation networks using modular structure. *Applied Network Science*, *7*(1). https://doi.org/10.1007/s41109-022-00516-5

Nir, Y., Staba, R. J., Andrillon, T., Vyazovskiy, V. V., Cirelli, C., Fried, I., & Tononi, G. (2011). Regional Slow Waves and Spindles in Human Sleep. *Neuron*, *70*(1), 153–169. https://doi.org/10.1016/j.neuron.2011.02.043

Nunez, P. L. (1974). The brain wave equation: a model for the EEG. *Mathematical Biosciences*, *21*(3–4), 279–297. https://doi.org/10.1016/0025-5564(74)90020-0

Obenaus, A. (2013). Neuroimaging biomarkers for epilepsy: Advances and relevance to glial cells. *Neurochemistry International*, *63*(7), 712–718. https://doi.org/10.1016/j.neuint.2013.05.001

Ocampo-Pineda, M., Schiavi, S., Rheault, F., Girard, G., Petit, L., Descoteaux, M., & Daducci, A. (2021). Hierarchical Microstructure Informed Tractography. *Brain Connectivity*, *11*(2), 75–88. https://doi.org/10.1089/brain.2020.0907

Okada, Y. (2020). Physiological Bases of Magnetoencephalography and Electroencephalography. In *Fifty Years of Magnetoencephalography* (pp. 35–65). Oxford University Press. https://doi.org/10.1093/oso/9780190935689.003.0004

Olsen, R. W., & Sieghart, W. (2008). International Union of Pharmacology. LXX. Subtypes of γ-Aminobutyric Acid A Receptors: Classification on the Basis of Subunit Composition, Pharmacology, and Function. Update. *Pharmacological Reviews*, *60*(3), 243–260. https://doi.org/10.1124/pr.108.00505

Oostenveld, R., Fries, P., Maris, E., & Schoffelen, J.-M. (2011). FieldTrip: Open Source Software for Advanced Analysis of MEG, EEG, and Invasive Electrophysiological Data. *Computational Intelligence and Neuroscience*, *2011*, 1–9. https://doi.org/10.1155/2011/156869

Pacholko, A. G., Wotton, C. A., & Bekar, L. K. (2020). Astrocytes—The Ultimate Effectors of Long-Range Neuromodulatory Networks? *Frontiers in Cellular Neuroscience*, *14*(September), 1–12. https://doi.org/10.3389/fncel.2020.581075

Palva, J. M., Wang, S. H., Palva, S., Zhigalov, A., Monto, S., Brookes, M. J., Schoffelen, J.-M., & Jerbi, K. (2018). Ghost interactions in MEG/EEG source space: A note of caution on inter-areal coupling measures. *NeuroImage*, *173*(February), 632–643. https://doi.org/10.1016/j.neuroimage.2018.02.032

Pang, J. C., Aquino, K. M., Oldehinkel, M., Robinson, P. A., Fulcher, B. D., Breakspear, M., & Fornito, A. (2023). Geometric constraints on human brain function. *Nature*, *618*(7965), 566–574. https://doi.org/10.1038/s41586-023-06098-1

Pankevich, D. E., Davis, M., Altevogt, B. M., Diana E. Pankevich, Miriam Davis, and B. M. A., & Rapporteurs. (2011). Glutamate-Related Biomarkers in Drug Development for Disorders of the Nervous System. In *Neuroscience and Nervous System Disorders*. National Academies Press. https://doi.org/10.17226/13146

Park, H.-J., & Friston, K. (2013). Structural and Functional Brain Networks: From Connections to Cognition. *Science*, *342*(6158). https://doi.org/10.1126/science.1238411

Patro, I., Seth, P., Patro, N., & Tandon, P. N. (2022). The Biology of Glial Cells: Recent Advances. In I. Patro, P. Seth, N. Patro, & P. N. Tandon (Eds.), *The Biology of Glial Cells: Recent Advances*. Springer Singapore. https://doi.org/10.1007/978-981-16-8313-8

Pellegrini, F., Delorme, A., Nikulin, V., & Haufe, S. (2023). Identifying good practices for detecting inter-regional linear functional connectivity from EEG. *NeuroImage*, *277*(June), 120218. https://doi.org/10.1016/j.neuroimage.2023.120218

Petroff, O. A. C. (2002). Book Review: GABA and Glutamate in the Human Brain. *The Neuroscientist*, *8*(6), 562–573. https://doi.org/10.1177/1073858402238515

Phillips, A. J. K. (2015). Sleep, Neural Population Models of. In *Encyclopedia of Computational Neuroscience* (pp. 2710–2715). Springer New York. https://doi.org/10.1007/978-1-4614-6675-8_76

Pierce, S., Kadlaskar, G., Edmondson, D. A., McNally Keehn, R., Dydak, U., & Keehn, B. (2021). Associations between sensory processing and electrophysiological and neurochemical measures in children with ASD: an EEG-MRS study. *Journal of Neurodevelopmental Disorders*, *13*(1), 1–11. https://doi.org/10.1186/s11689-020-09351-0

Pinotsis, D., Robinson, P., Graben, P. B., & Friston, K. (2014). Neural masses and fields: Modeling the dynamics of brain activity. *Frontiers in Computational Neuroscience*, *8*(NOV), 2013–2015. https://doi.org/10.3389/fncom.2014.00149

Poskanzer, K. E., & Yuste, R. (2011). Astrocytic regulation of cortical UP states. *Proceedings of the National Academy of Sciences*, *108*(45), 18453–18458. https://doi.org/10.1073/pnas.1112378108

Poskanzer, K. E., & Yuste, R. (2016). Astrocytes regulate cortical state switching in vivo. *Proceedings of the National Academy of Sciences of the United States of America*, *113*(19), E2675–E2684. https://doi.org/10.1073/pnas.1520759113

Prado, P., Medel, V., Gonzalez-Gomez, R., Sainz-Ballesteros, A., Vidal, V., Santamaría-García, H., Moguilner, S., Mejia, J., Slachevsky, A., Beherens, M. I., Aguillon, D., Lopera, F., Parra, M. A., Matallana, D., Maito, M. A., Garcia, A. M., Custodio, N., Funes, A. Á., Piña-Escudero, S., … Ibañez, A. (2023). The BrainLat project, a multimodal neuroimaging dataset of neurodegeneration from underrepresented backgrounds. *Scientific Data*, *10*(1), 1–13. https://doi.org/10.1038/s41597-023-02806-8

Preti, M. G., Bolton, T. A., & Van De Ville, D. (2017). The dynamic functional connectome: State-of-the-art and perspectives. *NeuroImage*, *160*(December 2016), 41–54. https://doi.org/10.1016/j.neuroimage.2016.12.061

Puce, A., & Hämäläinen, M. (2017). A Review of Issues Related to Data Acquisition and Analysis in EEG/MEG Studies. *Brain Sciences*, *7*(12), 58. https://doi.org/10.3390/brainsci7060058

Purnell, B. S., Alves, M., & Boison, D. (2023). Astrocyte-neuron circuits in epilepsy. *Neurobiology of Disease*, *179*(March), 106058. https://doi.org/10.1016/j.nbd.2023.106058

Quon, E. F., Wotton, C. A., & Bekar, L. K. (2018). Evidence for astrocyte purinergic signaling in cortical sensory adaptation and serotonin-mediated neuromodulation. *Molecular and Cellular Neuroscience*, *88*(March 2017), 53–61. https://doi.org/10.1016/j.mcn.2017.12.008

Raimondo, S., & De Domenico, M. (2021). Measuring topological descriptors of complex networks under uncertainty. *Physical Review E*, *103*(2), 1–15. https://doi.org/10.1103/PhysRevE.103.022311

Reichold, J., Stampanoni, M., Lena Keller, A., Buck, A., Jenny, P., & Weber, B. (2009). Vascular graph model to simulate the cerebral blood flow in realistic vascular networks. *Journal of*

Cerebral Blood Flow and Metabolism, *29*(8), 1429–1443. https://doi.org/10.1038/jcbfm.2009.58

Riedel, G. (2003). Glutamate receptor function in learning and memory. *Behavioural Brain Research*, *140*(1–2), 1–47. https://doi.org/10.1016/S0166-4328(02)00272-3

Rioux, G., Choksi, R., Hoheisel, T., Marechal, P., & Scarvelis, C. (2020). The Maximum Entropy on the Mean Method for Image Deblurring. *Inverse Problems*, *37*(1), 1–34. https://doi.org/10.1088/1361-6420/abc32e

Robbins, T. W., & Murphy, E. R. (2006). Behavioural pharmacology: 40+ years of progress, with a focus on glutamate receptors and cognition. *Trends in Pharmacological Sciences*, *27*(3), 141–148. https://doi.org/10.1016/j.tips.2006.01.009

Roberts, J. A., Perry, A., Lord, A. R., Roberts, G., Mitchell, P. B., Smith, R. E., Calamante, F., & Breakspear, M. (2016). The contribution of geometry to the human connectome. *NeuroImage*, *124*, 379–393. https://doi.org/10.1016/j.neuroimage.2015.09.009

Robertson, J. M. (2018). The gliocentric brain. *International Journal of Molecular Sciences*, *19*(10). https://doi.org/10.3390/ijms19103033

Rowley, N. M., Madsen, K. K., Schousboe, A., & Steve White, H. (2012). Glutamate and GABA synthesis, release, transport and metabolism as targets for seizure control. *Neurochemistry International*, *61*(4), 546–558. https://doi.org/10.1016/j.neuint.2012.02.013

Rubinov, M., & Sporns, O. (2010). Complex network measures of brain connectivity: Uses and interpretations. *NeuroImage*, *52*(3), 1059–1069. https://doi.org/10.1016/j.neuroimage.2009.10.003

Sadaghiani, S., Brookes, M. J., & Baillet, S. (2022). Connectomics of human electrophysiology. *NeuroImage*, *247*(December 2021), 118788. https://doi.org/10.1016/j.neuroimage.2021.118788

Sanchez-Bornot, J., Sotero, R. C., Kelso, J. A. S., Şimşek, Ö., & Coyle, D. (2024). Solving large-scale MEG/EEG source localisation and functional connectivity problems simultaneously using state-space models. *NeuroImage*, *285*(1), 120458. https://doi.org/10.1016/j.neuroimage.2023.120458

Sanz-Leon, P., Knock, S. A., Spiegler, A., & Jirsa, V. K. (2015). Mathematical framework for large-scale brain network modeling in The Virtual Brain. *NeuroImage*, *111*, 385–430. https://doi.org/10.1016/j.neuroimage.2015.01.002

Sanzleon, P., Knock, S. A., Woodman, M. M., Domide, L., Mersmann, J., Mcintosh, A. R., & Jirsa, V. (2013). The virtual brain: A simulator of primate brain network dynamics. *Frontiers in Neuroinformatics*, *7*(MAY). https://doi.org/10.3389/fninf.2013.00010

Sarkar, S., Guha, S., & Biswas, S. C. (2022). Role of Reactive Astrocytes in Alzheimer's Disease. In *The Biology of Glial Cells: Recent Advances* (pp. 199–242). Springer Singapore. https://doi.org/10.1007/978-981-16-8313-8_9

Sarvas, J. (1987). Basic mathematical and electromagnetic concepts of the biomagnetic inverse problem. *Physics in Medicine and Biology*, *32*(1), 11–22. https://doi.org/10.1088/0031-9155/32/1/004

Schaefer, A., Kong, R., Gordon, E. M., Laumann, T. O., Zuo, X.-N., Holmes, A. J., Eickhoff, S. B., & Yeo, B. T. T. (2018). Local-Global Parcellation of the Human Cerebral Cortex from Intrinsic Functional Connectivity MRI. *Cerebral Cortex*, *28*(9), 3095–3114. https://doi.org/10.1093/cercor/bhx179

Schaeffer, S., & Iadecola, C. (2021). Revisiting the neurovascular unit. *Nature Neuroscience*, *24*(9), 1198–1209. https://doi.org/10.1038/s41593-021-00904-7

Schiavi, S., Ocampo-Pineda, M., Barakovic, M., Petit, L., Descoteaux, M., Thiran, J.-P., & Daducci, A. (2020). A new method for accurate in vivo mapping of human brain connections using microstructural and anatomical information. *Science Advances*, *6*(31), eaba8245. https://doi.org/10.1126/sciadv.aba8245

Schilling, K. G., Daducci, A., Maier-Hein, K., Poupon, C., Houde, J.-C., Nath, V., Anderson, A. W., Landman, B. A., & Descoteaux, M. (2019). Challenges in diffusion MRI tractography – Lessons learned from international benchmark competitions. *Magnetic Resonance Imaging*, *57*(November 2018), 194–209. https://doi.org/10.1016/j.mri.2018.11.014

Schilling, K. G., Nath, V., Hansen, C., Parvathaneni, P., Blaber, J., Gao, Y., Neher, P., Aydogan, D. B., Shi, Y., Ocampo-Pineda, M., Schiavi, S., Daducci, A., Girard, G., Barakovic, M., Rafael-Patino, J., Romascano, D., Rensonnet, G., Pizzolato, M., Bates, A., … Landman, B. A. (2019). Limits to anatomical accuracy of diffusion tractography using modern approaches. *NeuroImage*, *185*(August 2018), 1–11. https://doi.org/10.1016/j.neuroimage.2018.10.029

Schilling, K. G., Petit, L., Rheault, F., Remedios, S., Pierpaoli, C., Anderson, A. W., Landman, B. A., & Descoteaux, M. (2020). Brain connections derived from diffusion MRI tractography can be highly anatomically accurate—if we know where white matter pathways start, where they end, and where they do not go. *Brain Structure and Function*, *225*(8), 2387–2402. https://doi.org/10.1007/s00429-020-02129-z

Schmahmann, J. D., Smith, E. E., Eichler, F. S., & Filley, C. M. (2008). Cerebral White Matter. *Annals of the New York Academy of Sciences*, *1142*(1), 266–309. https://doi.org/10.1196/annals.1444.017

Schroeder, M. E., Bassett, D. S., & Meaney, D. F. (2022). A multilayer network model of neuron-astrocyte populations in vitro reveals mGluR5 inhibition is protective following traumatic injury. *Network Neuroscience*, *6*(2), 499–527. https://doi.org/10.1162/netn_a_00227

Schurr, R., & Mezer, A. A. (2021). The glial framework reveals white matter fiber architecture in human and primate brains. *Science*, *374*(6568), 762–767. https://doi.org/10.1126/science.abj7960

Scimemi, A. (2019). *The Role of Astrocytes in Neurotransmitter Uptake and Brain Metabolism*. Springer International Publishing. https://doi.org/10.1007/978-3-030-00817-8_12

Selkoe, D. J. (2011). Resolving controversies on the path to Alzheimer's therapeutics. *Nature Medicine*, *17*(9), 1060–1065. https://doi.org/10.1038/nm.2460

Shafiei, G., Baillet, S., & Misic, B. (2022). Human electromagnetic and haemodynamic networks systematically converge in unimodal cortex and diverge in transmodal cortex. *PLOS Biology*, *20*(8), e3001735. https://doi.org/10.1371/journal.pbio.3001735

Shafiei, G., Fulcher, B. D., Voytek, B., Satterthwaite, T. D., Baillet, S., & Misic, B. (2023). Neurophysiological signatures of cortical micro-architecture. *Nature Communications*, *14*(1). https://doi.org/10.1038/s41467-023-41689-6

Shafto, M. A., Tyler, L. K., Dixon, M., Taylor, J. R., Rowe, J. B., Cusack, R., Calder, A. J., Marslen-Wilson, W. D., Duncan, J., Dalgleish, T., Henson, R. N., Brayne, C., & Matthews, F. E. (2014). The Cambridge Centre for Ageing and Neuroscience (Cam-CAN) study protocol: a cross-sectional, lifespan, multidisciplinary examination of healthy cognitive ageing. *BMC Neurology*, *14*(1), 204. https://doi.org/10.1186/s12883-014-0204-1

Shen, K., Bezgin, G., Schirner, M., Ritter, P., Everling, S., & McIntosh, A. R. (2019). A macaque connectome for large-scale network simulations in TheVirtualBrain. *Scientific Data*, *6*(1), 123. https://doi.org/10.1038/s41597-019-0129-z

Shimbel, A., & Rapoport, A. (1948). A statistical approach to the theory of the central nervous system. *The Bulletin of Mathematical Biophysics*, *10*(1), 41–55. https://doi.org/10.1007/BF02478329

Shine, J. M. (2019). Neuromodulatory Influences on Integration and Segregation in the Brain. *Trends in Cognitive Sciences*, *23*(7), 572–583. https://doi.org/10.1016/j.tics.2019.04.002

Shine, J. M., Breakspear, M., Bell, P. T., Ehgoetz Martens, K., Shine, R., Koyejo, O., Sporns, O., & Poldrack, R. A. (2019). Human cognition involves the dynamic integration of neural activity and neuromodulatory systems. *Nature Neuroscience*, *22*(2), 289–296. https://doi.org/10.1038/s41593-018-0312-0

Shinmyo, Y., Saito, K., Hamabe-Horiike, T., Kameya, N., Ando, A., Kawasaki, K., Duong, T. A. D., Sakashita, M., Roboon, J., Hattori, T., Kannon, T., Hosomichi, K., Slezak, M., Holt, M. G., Tajima, A., Hori, O., & Kawasaki, H. (2022). Localized astrogenesis regulates gyrification of the cerebral cortex. *Science Advances*, *8*(10), 1–14. https://doi.org/10.1126/sciadv.abi5209

Sohal, V. S., & Rubenstein, J. L. R. (2019). Excitation-inhibition balance as a framework for investigating mechanisms in neuropsychiatric disorders. *Molecular Psychiatry*, *24*(9), 1248–1257. https://doi.org/10.1038/s41380-019-0426-0

Sotero, R. C., & Trujillo-Barreto, N. J. (2008). Biophysical model for integrating neuronal activity, EEG, fMRI and metabolism. *NeuroImage*, *39*(1), 290–309. https://doi.org/10.1016/j.neuroimage.2007.08.001

Sotero, R. C., Trujillo-Barreto, N. J., Iturria-Medina, Y., Carbonell, F., & Jimenez, J. C. (2007). Realistically Coupled Neural Mass Models Can Generate EEG Rhythms. *Neural Computation*, *19*(2), 478–512. https://doi.org/10.1162/neco.2007.19.2.478

Spiegler, A., & Jirsa, V. (2013). Systematic approximations of neural fields through networks of neural masses in the virtual brain. *NeuroImage*, *83*, 704–725. https://doi.org/10.1016/j.neuroimage.2013.06.018

Stefanovski, L., Meier, J. M., Pai, R. K., Triebkorn, P., Lett, T., Martin, L., Bülau, K., Hofmann-Apitius, M., Solodkin, A., McIntosh, A. R., & Ritter, P. (2021). Bridging Scales in Alzheimer's Disease: Biological Framework for Brain Simulation With The Virtual Brain. *Frontiers in Neuroinformatics*, *15*(April), 1–30. https://doi.org/10.3389/fninf.2021.630172

Stefanovski, L., Triebkorn, P., Spiegler, A., Diaz-Cortes, M.-A., Solodkin, A., Jirsa, V., McIntosh, A. R., & Ritter, P. (2019). Linking Molecular Pathways and Large-Scale Computational Modeling to Assess Candidate Disease Mechanisms and Pharmacodynamics in Alzheimer's Disease. *Frontiers in Computational Neuroscience*, *13*(August), 1–27. https://doi.org/10.3389/fncom.2019.00054

Stenroos, M., & Nummenmaa, A. (2016). Incorporating and Compensating Cerebrospinal Fluid in Surface-Based Forward Models of Magneto- and Electroencephalography. *PLOS ONE*, *11*(7), e0159595. https://doi.org/10.1371/journal.pone.0159595

Stephan, J., Eitelmann, S., & Zhou, M. (2021). Approaches to Study Gap Junctional Coupling. *Frontiers in Cellular Neuroscience*, *15*(March). https://doi.org/10.3389/fncel.2021.640406

Steyn-Ross, D. A., Steyn-Ross, M., & Sleigh, J. (2015). Gap Junctions, Neural Population Models and. In *Encyclopedia of Computational Neuroscience* (pp. 1266–1270). Springer New York. https://doi.org/10.1007/978-1-4614-6675-8_62

Stimberg, M., Goodman, D. F. M., Brette, R., & Pittà, M. De. (2019). *Modeling Neuron–Glia Interactions with the Brian 2 Simulator*. 471–505. https://doi.org/10.1007/978-3-030-00817-8_18

St-Onge, E., Al-Sharif, N., Girard, G., Theaud, G., & Descoteaux, M. (2021). Cortical Surfaces Integration with Tractography for Structural Connectivity Analysis. *Brain Connectivity*, *11*(7), 505–517. https://doi.org/10.1089/brain.2020.0930

St-Onge, E., Daducci, A., Girard, G., & Descoteaux, M. (2018). Surface-enhanced tractography (SET). *NeuroImage*, *169*(December 2017), 524–539. https://doi.org/10.1016/j.neuroimage.2017.12.036

St-Pierre, M.-K., VanderZwaag, J., Loewen, S., & Tremblay, M.-È. (2022). All roads lead to heterogeneity: The complex involvement of astrocytes and microglia in the pathogenesis of Alzheimer's disease. *Frontiers in Cellular Neuroscience*, *16*(August). https://doi.org/10.3389/fncel.2022.932572

Strogatz, S. H. (2018). Nonlinear Dynamics and Chaos. In *Nonlinear Dynamics and Chaos: With Applications to Physics, Biology, Chemistry, and Engineering*. CRC Press. https://doi.org/10.1201/9780429492563

Stumme, J., Jockwitz, C., Hoffstaedter, F., Amunts, K., & Caspers, S. (2020). Functional network reorganization in older adults: Graph-theoretical analyses of age, cognition and sex. *NeuroImage*, *214*(September 2019), 116756. https://doi.org/10.1016/j.neuroimage.2020.116756

Suárez, L. E., Markello, R. D., Betzel, R. F., & Misic, B. (2020). Linking Structure and Function in Macroscale Brain Networks. *Trends in Cognitive Sciences*, *24*(4), 302–315. https://doi.org/10.1016/j.tics.2020.01.008

Swanson, L. W., & Lichtman, J. W. (2016). From Cajal to Connectome and beyond. *Annual Review of Neuroscience*, *39*, 197–216. https://doi.org/10.1146/annurev-neuro-071714-033954

Sweeney, M. D., Kisler, K., Montagne, A., Toga, A. W., & Zlokovic, B. V. (2018). The role of brain vasculature in neurodegenerative disorders. *Nature Neuroscience*, *21*(10), 1318–1331. https://doi.org/10.1038/s41593-018-0234-x

Tabbal, J., Kabbara, A., Yochum, M., Khalil, M., Hassan, M., & Benquet, P. (2022). Assessing HD-EEG functional connectivity states using a human brain computational model. *Journal of Neural Engineering*, *19*(5). https://doi.org/10.1088/1741-2552/ac954f

Tadel, F., Baillet, S., Mosher, J. C., Pantazis, D., & Leahy, R. M. (2011). Brainstorm: A User-Friendly Application for MEG/EEG Analysis. *Computational Intelligence and Neuroscience*, *2011*, 1–13. https://doi.org/10.1155/2011/879716

Tagarelli, A., Amelio, A., & Gullo, F. (2017). Ensemble-based community detection in multilayer networks. In *Data Mining and Knowledge Discovery* (Vol. 31, Issue 5). Springer US. https://doi.org/10.1007/s10618-017-0528-8

Taylor, J. R., Williams, N., Cusack, R., Auer, T., Shafto, M. A., Dixon, M., Tyler, L. K., Cam-CAN, & Henson, R. N. (2017). The Cambridge Centre for Ageing and Neuroscience (Cam-CAN) data repository: Structural and functional MRI, MEG, and cognitive data from a cross-sectional adult lifespan sample. *NeuroImage*, *144*, 262–269. https://doi.org/10.1016/j.neuroimage.2015.09.018

Tesler, F., Linne, M. L., & Destexhe, A. (2023). Modeling the relationship between neuronal activity and the BOLD signal: contributions from astrocyte calcium dynamics. *Scientific Reports*, *13*(1), 1–17. https://doi.org/10.1038/s41598-023-32618-0

Tewarie, P., Hillebrand, A., van Dijk, B. W., Stam, C. J., O'Neill, G. C., Van Mieghem, P., Meier, J. M., Woolrich, M. W., Morris, P. G., & Brookes, M. J. (2016). Integrating cross-frequency and within band functional networks in resting-state MEG: A multi-layer network approach. *NeuroImage*, *142*, 324–336. https://doi.org/10.1016/j.neuroimage.2016.07.057

Tewarie, P., Liuzzi, L., O'Neill, G. C., Quinn, A. J., Griffa, A., Woolrich, M. W., Stam, C. J., Hillebrand, A., & Brookes, M. J. (2019). Tracking dynamic brain networks using high temporal resolution MEG measures of functional connectivity. *NeuroImage*, *200*(June), 38–50. https://doi.org/10.1016/j.neuroimage.2019.06.006

Tewarie, P., Prasse, B., Meier, J., Byrne, ine, De Domenico, M., Stam, C. J., Brookes, M. J., Hillebrand, A., Daffertshofer, A., Coombes, S., & Van Mieghem, P. (2021). Interlayer connectivity reconstruction for multilayer brain networks using phase oscillator models. *New Journal of Physics*, *23*(6). https://doi.org/10.1088/1367-2630/ac066d

Theaud, G., Houde, J.-C., Boré, A., Rheault, F., Morency, F., & Descoteaux, M. (2020). TractoFlow: A robust, efficient and reproducible diffusion MRI pipeline leveraging Nextflow & Singularity. *NeuroImage*, *218*(April), 116889. https://doi.org/10.1016/j.neuroimage.2020.116889

Thurner, S., Corominas-Murtra, B., & Hanel, R. (2017). Three faces of entropy for complex systems: Information, thermodynamics, and the maximum entropy principle. *Physical Review E*, *96*(3), 1–12. https://doi.org/10.1103/PhysRevE.96.032124

Thurner, S., Hanel, R., & Klimekl, P. (2018). Statistical Mechanics and Information Theory for Complex Systems. In *Introduction to the Theory of Complex Systems* (Vol. 1). Oxford University Press. https://doi.org/10.1093/oso/9780198821939.003.0006

Ting, C. M., Samdin, S. B., Tang, M., & Ombao, H. (2021). Detecting dynamic community structure in functional brain networks across individuals: A multilayer approach. *IEEE Transactions on Medical Imaging*, *40*(2), 468–480. https://doi.org/10.1109/TMI.2020.3030047

Toda, A. A. (2011). *Unification of Maximum Entropy and Bayesian Inference via Plausible Reasoning*. 1–10. http://arxiv.org/abs/1103.2411

Touboul, J., Wendling, F., Chauvel, P., & Faugeras, O. (2011). Neural Mass Activity, Bifurcations, and Epilepsy. *Neural Computation*, *23*(12), 3232–3286. https://doi.org/10.1162/NECO_a_00206

Tourbier, S., Rue-Queralt, J., Glomb, K., Aleman-Gomez, Y., Mullier, E., Griffa, A., Schöttner, M., Wirsich, J., Tuncel, M. A., Jancovic, J., Cuadra, M. B., & Hagmann, P. (2022). Connectome Mapper 3: A Flexible and Open-Source Pipeline Software for Multiscale Multimodal Human Connectome Mapping. *Journal of Open Source Software*, *7*(74), 4248. https://doi.org/10.21105/joss.04248

Uludağ, K., & Blinder, P. (2018). Linking brain vascular physiology to hemodynamic response in ultra-high field MRI. *NeuroImage*, *168*(February 2017), 279–295. https://doi.org/10.1016/j.neuroimage.2017.02.063

Unal, G., Swami, J. K., Canela, C., Cohen, S. L., Khadka, N., FallahRad, M., Short, B., Argyelan, M., Sackeim, H. A., & Bikson, M. (2021). Adaptive current-flow models of ECT: Explaining individual static impedance, dynamic impedance, and brain current density. *Brain Stimulation*, *14*(5), 1154–1168. https://doi.org/10.1016/j.brs.2021.07.012

Uttley, A. M. (1955). The probability of neural connexions. *Proceedings of the Royal Society of London. Series B - Biological Sciences*, *144*(915), 229–240. https://doi.org/10.1098/rspb.1955.0054

Vaiana, M., & Muldoon, S. F. (2020). Multilayer Brain Networks. *Journal of Nonlinear Science*, *30*(5), 2147–2169. https://doi.org/10.1007/s00332-017-9436-8

Vaisbourd, Y., Choksi, R., Goodwin, A., Hoheisel, T., & Schönlieb, C.-B. (2022). *Maximum Entropy on the Mean and the Cram\'er Rate Function in Statistical Estimation and Inverse Problems: Properties, Models, and Algorithms*. 1–41. http://arxiv.org/abs/2211.05205

Valdes-Sosa, P. A., Sanchez-Bornot, J. M., Sotero, R. C., Iturria-Medina, Y., Aleman-Gomez, Y., Bosch-Bayard, J., Carbonell, F., & Ozaki, T. (2009). Model driven EEG/fMRI fusion of brain oscillations. *Human Brain Mapping*, *30*(9), 2701–2721. https://doi.org/10.1002/hbm.20704

Vallarino, E., Hincapié, A. S., Jerbi, K., Leahy, R. M., Pascarella, A., Sorrentino, A., & Sommariva, S. (2023). Tuning Minimum-Norm regularization parameters for optimal MEG connectivity

estimation. *NeuroImage*, *281*(August), 120356. https://doi.org/10.1016/j.neuroimage.2023.120356

van den Heuvel, M. P., Scholtens, L. H., & Kahn, R. S. (2019). Multiscale Neuroscience of Psychiatric Disorders. *Biological Psychiatry*, *86*(7), 512–522. https://doi.org/10.1016/j.biopsych.2019.05.015

van Diessen, E., Numan, T., van Dellen, E., van der Kooi, A. W., Boersma, M., Hofman, D., van Lutterveld, R., van Dijk, B. W., van Straaten, E. C. W., Hillebrand, A., & Stam, C. J. (2015). Opportunities and methodological challenges in EEG and MEG resting state functional brain network research. *Clinical Neurophysiology*, *126*(8), 1468–1481. https://doi.org/10.1016/j.clinph.2014.11.018

Van Essen, D. C. (2020). A 2020 view of tension-based cortical morphogenesis. *Proceedings of the National Academy of Sciences*, *117*(52), 32868–32879. https://doi.org/10.1073/pnas.2016830117

Van Essen, D. C., Smith, S. M., Barch, D. M., Behrens, T. E. J., Yacoub, E., & Ugurbil, K. (2013). The WU-Minn Human Connectome Project: An overview. *NeuroImage*, *80*, 62–79. https://doi.org/10.1016/j.neuroimage.2013.05.041

van Nifterick, A. M., Gouw, A. A., de Haan, W., Stam, C. J., & Scheltens, P. (2021). EEG slowing in predementia Alzheimer's disease is compatible with neuronal hyperactivity: A multiscale computational modeling study. *Alzheimer's & Dementia : The Journal of the Alzheimer's Association*, *17*, e053535. https://doi.org/10.1002/alz.053535

Vanlandewijck, M., He, L., Mäe, M. A., Andrae, J., Ando, K., Del Gaudio, F., Nahar, K., Lebouvier, T., Laviña, B., Gouveia, L., Sun, Y., Raschperger, E., Räsänen, M., Zarb, Y., Mochizuki, N., Keller, A., Lendahl, U., & Betsholtz, C. (2018). A molecular atlas of cell types and zonation in the brain vasculature. *Nature*, *554*(7693), 475–480. https://doi.org/10.1038/nature25739

Vannitsem, S. (2017). Predictability of large-scale atmospheric motions: Lyapunov exponents and error dynamics. *Chaos: An Interdisciplinary Journal of Nonlinear Science*, *27*(3). https://doi.org/10.1063/1.4979042

Vasile, F., Dossi, E., & Rouach, N. (2017). Human astrocytes: structure and functions in the healthy brain. *Brain Structure and Function*, *222*(5), 2017–2029. https://doi.org/10.1007/s00429-017-1383-5

Verkhratsky, A., & Nedergaard, M. (2018). Physiology of Astroglia. *Physiological Reviews*, *98*(1), 239–389. https://doi.org/10.1152/physrev.00042.2016

Vezzani, A., Ravizza, T., Bedner, P., Aronica, E., Steinhäuser, C., & Boison, D. (2022). Astrocytes in the initiation and progression of epilepsy. *Nature Reviews Neurology*, *18*(12), 707–722. https://doi.org/10.1038/s41582-022-00727-5

Vigneault, É., Poirel, O., Riad, M., Prud'homme, J., Dumas, S., Turecki, G., Fasano, C., Mechawar, N., & El Mestikawy, S. (2015). Distribution of vesicular glutamate transporters in the human brain. *Frontiers in Neuroanatomy*, *9*(MAR), 1–13. https://doi.org/10.3389/fnana.2015.00023

Vinck, M., Oostenveld, R., Van Wingerden, M., Battaglia, F., & Pennartz, C. M. A. (2011). An improved index of phase-synchronization for electrophysiological data in the presence of

volume-conduction, noise and sample-size bias. *NeuroImage*, *55*(4), 1548–1565. https://doi.org/10.1016/j.neuroimage.2011.01.055

Virkar, Y. S., Shew, W. L., Restrepo, J. G., & Ott, E. (2016). Feedback control stabilization of critical dynamics via resource transport on multilayer networks: How glia enable learning dynamics in the brain. *Physical Review E*, *94*(4), 042310. https://doi.org/10.1103/PhysRevE.94.042310

Voigt, K., Liang, E. X., Misic, B., Ward, P. G. D., Egan, G. F., & Jamadar, S. D. (2023). Metabolic and functional connectivity provide unique and complementary insights into cognition-connectome relationships. *Cerebral Cortex*, *33*(4), 1476–1488. https://doi.org/10.1093/cercor/bhac150

Volman, V., & Bazhenov, M. (2019). *Computational Models of Pathophysiological Glial Activation in CNS Disorders* (pp. 289–305). Springer International Publishing. https://doi.org/10.1007/978-3-030-00817-8_11

Volterra, A., & Meldolesi, J. (2005). Astrocytes, from brain glue to communication elements: the revolution continues. *Nature Reviews Neuroscience*, *6*(8), 626–640. https://doi.org/10.1038/nrn1722

Vorwerk, J., Cho, J.-H., Rampp, S., Hamer, H., Knösche, T. R., & Wolters, C. H. (2014). A guideline for head volume conductor modeling in EEG and MEG. *NeuroImage*, *100*, 590–607. https://doi.org/10.1016/j.neuroimage.2014.06.040

Wadman, W. J., & Lopes da Silva, F. H. (2017). Biophysical Aspects of EEG and MEG Generation. In D. L. Schomer & F. H. Lopes da Silva (Eds.), *Niedermeyer's Electroencephalography: Basic Principles, Clinical Applications, and Related Fields* (Vol. 1). Oxford University Press. https://doi.org/10.1093/med/9780190228484.003.0004

Waldrip, S., & Niven, R. (2017). Comparison Between Bayesian and Maximum Entropy Analyses of Flow Networks†. *Entropy*, *19*(2), 58. https://doi.org/10.3390/e19020058

Wang, M., He, Y., Sejnowski, T. J., & Yu, X. (2018). Brain-state dependent astrocytic Ca2+ signals are coupled to both positive and negative BOLD-fMRI signals. *Proceedings of the National Academy of Sciences of the United States of America*, *115*(7), E1647–E1656. https://doi.org/10.1073/pnas.1711692115

Wang, Q., Jie, W., Liu, J. H., Yang, J. M., & Gao, T. M. (2017). An astroglial basis of major depressive disorder? An overview. *Glia*, *65*(8), 1227–1250. https://doi.org/10.1002/glia.23143

Wang, S. H., Lobier, M., Siebenhühner, F., Puoliväli, T., Palva, S., & Palva, J. M. (2018). Hyperedge bundling: A practical solution to spurious interactions in MEG/EEG source connectivity analyses. *NeuroImage*, *173*(November 2017), 610–622. https://doi.org/10.1016/j.neuroimage.2018.01.056

Wendling, F., & Chauvel, P. (2008). Transition to Ictal Activity in Temporal Lobe Epilepsy: Insights From Macroscopic Models. In *Computational Neuroscience in Epilepsy* (pp. 356–386). https://doi.org/10.1016/B978-012373649-9.50026-0

Wendling, F., Hernandez, A., Bellanger, J.-J., Chauvel, P., & Bartolomei, F. (2005). Interictal to ictal transition in human temporal lobe epilepsy: insights from a computational model of intracerebral EEG. *Journal of Clinical Neurophysiology : Official Publication of the American Electroencephalographic Society*, *22*(5), 343–356. https://doi.org/10.1016/0022-2836(87)90238-5

Wendling, F., & Lopes da Silva, F. H. (2017). Dynamics of EEGs as Signals of Neuronal Populations. In D. L. Schomer & F. H. Lopes da Silva (Eds.), *Niedermeyer's Electroencephalography: Basic Principles, Clinical Applications, and Related Fields* (Vol. 1). Oxford University Press. https://doi.org/10.1093/med/9780190228484.003.0003

White, T., & Hilgetag, C. C. (2011). Gyrification and neural connectivity in schizophrenia. *Development and Psychopathology*, *23*(1), 339–352. https://doi.org/10.1017/S0954579410000842

Wilson, H. R., & Cowan, J. D. (1972). Excitatory and Inhibitory Interactions in Localized Populations of Model Neurons. *Biophysical Journal*, *12*(1), 1–24. https://doi.org/10.1016/S0006-3495(72)86068-5

Wilson, H. R., & Cowan, J. D. (1973). A mathematical theory of the functional dynamics of cortical and thalamic nervous tissue. *Kybernetik*, *13*(2), 55–80. https://doi.org/10.1007/BF00288786

Wong-Lin, K. F., Wang, D. H., & Joshi, A. (2021). Multiscale modeling and analytical methods in neuroscience: Molecules, neural circuits, cognition and brain disorders. *Journal of Neuroscience Methods*, *359*, 109225. https://doi.org/10.1016/j.jneumeth.2021.109225

Wotton, C. A., Quon, E. F., Palmer, A. C., & Bekar, L. K. (2018). Corticosterone and serotonin similarly influence GABAergic and purinergic pathways to affect cortical inhibitory networks. *Journal of Neuroendocrinology*, *30*(4), 1–10. https://doi.org/10.1111/jne.12592

Yalcinkaya, B. H., Ziaeemehr, A., Fousek, J., Hashemi, M., Lavanga, M., Solodkin, A., McIntosh, R. A., Jirsa, V. K., & Petkoski, S. (2023). Personalized virtual brains of Alzheimer's Disease link dynamical biomarkers of fMRI with increased local excitability. *MedRxiv*, *1*, 1–52. https://doi.org/10.1101/2023.01.11.23284438

Yeh, C. H., Jones, D. K., Liang, X., Descoteaux, M., & Connelly, A. (2021). Mapping Structural Connectivity Using Diffusion MRI: Challenges and Opportunities. *Journal of Magnetic Resonance Imaging*, *53*(6), 1–17. https://doi.org/10.1002/jmri.27188

Yeh, C., Jones, D. K., Liang, X., Descoteaux, M., & Connelly, A. (2021). Mapping Structural Connectivity Using Diffusion MRI: Challenges and Opportunities. *Journal of Magnetic Resonance Imaging*, *53*(6), 1666–1682. https://doi.org/10.1002/jmri.27188

Yeo, B. T. T., Krienen, F. M., Sepulcre, J., Sabuncu, M. R., Lashkari, D., Hollinshead, M., Roffman, J. L., Smoller, J. W., Zöllei, L., Polimeni, J. R., Fischl, B., Liu, H., & Buckner, R. L. (2011). The organization of the human cerebral cortex estimated by intrinsic functional connectivity. *Journal of Neurophysiology*, *106*(3), 1125–1165. https://doi.org/10.1152/jn.00338.2011

Yoon, B. E., & Lee, C. J. (2014). GABA as a rising gliotransmitter. *Frontiers in Neural Circuits*, *8*(DEC), 1–8. https://doi.org/10.3389/fncir.2014.00141

Youssofzadeh, V., Prasad, G., & Wong-Lin, K. F. (2015). On self-feedback connectivity in neural mass models applied to event-related potentials. *NeuroImage*, *108*, 364–376. https://doi.org/10.1016/j.neuroimage.2014.12.067

Yu, M. (2020). Benchmarking metrics for inferring functional connectivity from multi-channel EEG and MEG: A simulation study. *Chaos: An Interdisciplinary Journal of Nonlinear Science*, *30*(12). https://doi.org/10.1063/5.0018826

Zaman, A., Zhang, L., Yan, J., & Zhu, D. (2020). Multi-modal Image Prediction via Spatial Hybrid U-Net. In *Lecture Notes in Computer Science (including subseries Lecture Notes in Artificial Intelligence and Lecture Notes in Bioinformatics): Vol. 11977 LNCS* (pp. 1–9). Springer International Publishing. https://doi.org/10.1007/978-3-030-37969-8_1

Zerouali, Y., Herry, C. L., Jemel, B., & Lina, J. M. (2013). Localization of Synchronous Cortical Neural Sources. *IEEE Transactions on Biomedical Engineering*, *60*(3), 770–780. https://doi.org/10.1109/TBME.2011.2176938

Zetterberg, L. H., Kristiansson, L., & Mossberg, K. (1978). Performance of a model for a local neuron population. *Biological Cybernetics*, *31*(1), 15–26. https://doi.org/10.1007/BF00337367

Zhang, H., Wang, C.-D., Lai, J.-H., & Yu, P. S. (2017). Modularity in complex multilayer networks with multiple aspects: a static perspective. *Applied Informatics*, *4*(1). https://doi.org/10.1186/s40535-017-0035-4

Zhang, Y., Chen, K., Sloan, S. A., Bennett, M. L., Scholze, A. R., O'Keeffe, S., Phatnani, H. P., Guarnieri, P., Caneda, C., Ruderisch, N., Deng, S., Liddelow, S. A., Zhang, C., Daneman, R., Maniatis, T., Barres, B. A., & Wu, J. Q. (2014). An RNA-sequencing transcriptome and splicing database of glia, neurons, and vascular cells of the cerebral cortex. *Journal of Neuroscience*, *34*(36), 11929–11947. https://doi.org/10.1523/JNEUROSCI.1860-14.2014

Zimmermann, J., Perry, A., Breakspear, M., Schirner, M., Sachdev, P., Wen, W., Kochan, N. A., Mapstone, M., Ritter, P., McIntosh, A. R., & Solodkin, A. (2018). Differentiation of Alzheimer's disease based on local and global parameters in personalized Virtual Brain models. *NeuroImage: Clinical*, *19*(November 2017), 240–251. https://doi.org/10.1016/j.nicl.2018.04.017

Zlokovic, B. V. (2011). Neurovascular pathways to neurodegeneration in Alzheimer's disease and other disorders. *Nature Reviews Neuroscience*, *12*(12), 723–738. https://doi.org/10.1038/nrn3114